Vortex Development for a 65° swept back Delta Wing with Varying Thickness and Maximum Thickness Location

JANA STUCKE

A thesis submitted in partial fulfilment of the requirements of the University of the West of England, Bristol for the degree of Doctor of Philosophy

Faculty of Environment and Technology

University of the West of England, Bristol

June 2020

Abstract

Low signature, unmanned combat aerial vehicles (UCAV) are foreseen to play an important role in future military missions. Most UCAV concepts feature some sort of delta or lambda type of wing with high or moderately swept leading edge, where the fuselage is part of the lifting surface, thus, forming a blended wing body. These configurations have advantageous characteristics at high speeds and a low radar signature, making them desirable shapes for military purposes. However, blended wing bodies are known for having a serious problem with their longitudinal static stability and their performance at low speeds. Initial wing design or the ability to change the wing shape in flight, by means of wing morphing, could be utilised to overcome these issues. Therefore, with the technology readiness level of morphing configurations increasing, an understanding of the effect of slight changes to the aerofoil design need to be more thoroughly established. Therefore, to understand the change in aerodynamics when altering the thickness/chord ratio (3.4%, 6% and 12%), spanwise thickness distribution and maximum thickness location/chord (30% and 50%) a computational investigation of a 65° delta wing with different profiles of different thicknesses was undertaken. Here, the maximum thickness location was investigated on two biconvex wings with maximum thickness locations at 30% and 50% root chord, whilst a tip taper study was conducted using the NATO's AVT-113 VFE-2 configuration and a derivation of it. The effect of thickness was investigated on all configurations. Particular emphasis was placed on the longitudinal stability and lift to drag (L/D) ratio as they both impact aircraft design. The former due to its impact on the positioning and size of control surfaces and the latter due to its impact on thrust, maximum range and maximum take-off weight considerations. The investigation was carried out at Mach number 0.1 and Reynolds number of 750,000 with the former being representative for take-off and landing conditions for some military aircraft incorporating slender wing flows. The numerical results were validated for selected configurations in the University of the West of England's wind tunnel. For the numerical simulations ANSYS FLUENT was used with an unstructured hybrid mesh approach. The steady state runs were conducted using the k-ω Shear Stress turbulence (SST) model with curvature and low Reynolds number corrections.

The study showed that tip taper, thickness and maximum thickness location affect the L/D ratio and longitudinal stability. For the biconvex wings an increase in thickness was found to increase the L/D at higher angles of attack whilst the maximum attainable L/D ratio was found to be a function of both, thickness and maximum thickness location. For wings with mainly flat upper and lower surface L/D decreased with increase in thickness and so did the maximum L/D ratio. This was irrespective of tip taper. The angle of attack at which the maximum L/D was reached moved to a slightly higher angle (α=1°) when thickness was increased on the biconvex configurations, whereby the tapered VFE-2 configuration experienced a shift of up to α= 3°. Having a constant thickness distribution further

enhanced this effect moving the angle of maximum L/D from α= 5° to α= 15°. Moving the maximum thickness location forward resulted in an overall increase in L/D for the 6% and 12% configuration whilst not having a significant effect for thin wings, with the same being true for the maximum attainable L/D ratio. The angle of attack at which maximum L/D was reached moved to a lower angle by 1° for the 3.4% and 12% wing whilst being unaffected for the 6% wing. Tip taper showed to improve L/D and maximum L/D irrespective of thickness whilst the angle of attack at which maximum L/D could be achieved moved to lower angles when tip taper was introduced. This effect showed to enhance with increase in thickness.

The stability was evaluated at a lift coefficient C_L=0.5 typical for take-off and landing. It was found that stability improved with increase in thickness indicated by a rearward movement of the aerodynamic centre. These improvements were more significant when maximum thickness location was moved forward and resulted in up to 1.82% increase in static margin. Similar observations were made for the VFE-2 configuration and its adapted model with span taper. Here, the static margin increased by 3.21% when introducing tip taper. This was due to increased rear loading. In particular moving the maximum thickness location forward resulted in a delay in vortex onset, thus, further improving stability. Increase in thickness also resulted in enhanced stability (by up to 6.68%) but was strongly dependent on maximum thickness location and spanwise thickness distribution.

The flow pattern was also affected by increasing thickness, resulting in primary vortex stretching and domination of separation bubbles especially close to the apex. On the biconvex profiles shifting the maximum thickness location rearward helped in maintaining non-linear lift generation even when thickness was increased. It further resulted in delayed onset of vortex breakdown. Increase in thickness on wings with a flat profile was found to cause the formation of an inner co-rotating vortex similar to that observed for delta wings with round leading edges.

The main finding of the study was the demonstration that by alteration of the upper surface, leading edge suction can be recovered despite having a sharp leading edge, a phenomenon normally attributed to wings with round leading edges. This, in combination with the finding that the vortex flow pattern can be altered by reducing it to separation bubbles is not only valuable for future delta wing design but also for the implementation of wing morphing. Here, depending on the flight condition, wing shape could be altered by moving the maximum thickness location or introducing tip taper to get the desired flight performance.

Acknowledgements

To my Director of Studies Dr. Chris Toomer, a simple “thank you” does not seem adequate for your continuous advice, trust and support during the last years. The experience gained under your wing, during my time at UWE, is exceptionally valuable in its variety and applicability and I will be forever grateful for this.

I would also like to thank Dr. Sean Tuling for the additional guidance and feedback throughout the project. A huge thank you to Dr. Raj Nangia, who showed me the importance of polar plots, and opened my eyes to the vast number of variables which can be plotted against each other and for being a great and passionate teacher.

I would like to thank Zac Kanaa for his assistance in setting up experiments and his advice on experimental techniques throughout the years. For putting up with my countless requests such as wind tunnel rig and mounting changes, manufacturing parts, ordering materials, having an open ear when times were hard (to name a few) I would like to thank Mark Allonby.

Finally, I would like to thank the European Space Agency (ESA) and the International Space University (ISU) for giving me not only a sizzling summer in space and NLarging my universe but also for giving me a new family. I further would like to thank Issie Lloyd, for getting me through the last year and for showing me how to live the dream.

Laura Maybury for enhancing my PhD experience and for the laughs and jokes shared on a daily basis over a Starbucks coffee. Marie-Therese Schmidt, for supporting me like a supervisor and without whom I would have gone insane.

Last but not least I would like to thank my family, particularly my mum and dad who have supported me emotionally and financially throughout my educational career, pulling me through the hard times and never letting me lose sight of the ultimate goal. I would not have made it to where I am now if it was not for them.

There are many more I would like to thank but as I am tight to a word limit, I will do this in person over a hot or cold beverage of choice.

Table of Contents

Table of Figures

Table of Tables

Table of Equations

List of Abbreviations

AVT	Applied Vehicle Technology Panel
BoI	Body of Influence
BSL	Baseline Two-Equation Model
CG	Centre of gravity
CFD	Computational Fluid Dynamics
D	Drag force (wind axes), N
DDES	Delayed Detached Eddy Simulation
DES	Detached Eddy Simulation

DNS	Direct Numerical Simulations
DSM	Differential Stress Model
EVM	Eddy Viscosity Model
FEM	Finite Element Method
FVM	Finite Volume Method
GCI	Grid Convergence Index
LES	Large Eddy Simulation
LEV	Leading-edge vortex
L/D	Lift to drag ratio
MRLE	Medium Round Leading-edge
NATO	North Atlantic Treaty Organisation
N-S	Navier-Stokes equations
PDE	Partial Differential Equation
PIV	Particle Image Velocimetry
RANS	Reynolds Averaged Navier-Stokes Equations
RLE	Round Leading-edge
RSM	Reynolds Stress Model
SLE	Sharp Leading-edge
SA	Spalart- Allmaras
SST	Shear stress transport
TE	Trailing Edge
TUM	TU Munich
t/c	Thickness to chord ratio, %

UCAV	Unmanned Combat Aerial Vehicle
UWE	University of the West of England Bristol
VBD	Vortex Breakdown
VFE-2	Vortex Flow Experiment 2
VST	Varying Spanwise Thickness
x/c	Root chord location, %

List of Symbols

a	Slope of the normal force curve, $a = \frac{\partial C_N}{\partial \alpha}$, $^1/_{deg}$
A	Axial Force, N
AR	Aspect ratio, $\frac{b^2}{S}$
b	Wingspan, m
c	Local chord, m
c_{mac}	Mean aerodynamic chord, m, $c = \frac{2}{3} c_{root}$
C_A	Axial force coefficient, $C_A = \frac{A}{\frac{1}{2}\rho V^2 S}$
C_{A_0}	Axial force coefficient at α= 0°
C_D	Drag coefficient (wind axes), $C_D = \frac{D}{\frac{1}{2}\rho V^2 S}$
C_L	Lift coefficient (wind axes), $C_L = \frac{L}{\frac{1}{2}\rho V^2 S}$
C_{l_p}	Theoretical lift coefficient for attached flow
C_{l_v}	Theoretical lift coefficient for vortex lift

C_m	Pitching moment coefficient, about leading-edge of c , $C_m = \frac{M}{\frac{1}{2}\rho V^2 S\bar{c}}$
$C_{m_{ref}}$	Reference pitching moment coefficient
$C_{m_{0.58c_r}}$	Pitching moment coefficient around 0.58c
C_N	Normal force coefficient (body axes), $C_N = \frac{N}{\frac{1}{2}\rho V^2 S}$
$C_{N_{linear}}$	Linear Component of the Normal Force, $C_N = a\alpha$
$C_{N_{non-linear}}$	Non-Linear Component of the Normal Force, $C_{N_{non-linear}} = \frac{C_N}{\alpha} - a$
C_p	Pressure coefficient, $C_p = \frac{P-P_\infty}{\frac{1}{2}\rho_\infty V_\infty^2}$
C_S	Leading-edge suction coefficient
c_r	Root chord, m
D	Drag force, N
K	Induced drag coefficient
K_p	Lift coefficient slope at zero angle of attack
K_v	Suction Factor
k	Turbulence kinetic energy, $(kgm^2)/ s^2$
L	Lift force, N
M	Mach Number/ Pitching Moment, Nm
N	Normal Force, N
P_∞	Freestream pressure, Pa
R	Ideal Gas Constant, R= $287\frac{J}{kg\,K}$ for air
Re	Reynolds Number, Re= $\frac{\rho V c}{\mu}$
Re_{mac}	Reynolds Number based on mean aerodynamic chord

S	Reference area (planform of wing), m^2
S_L	Lower limit of the solution
S_{mac}	Recovered suction factor
S_U	Upper limit of the solution
T	Static Temperature, K
t	Student t-distribution Value
U	Uncertainty
u_i	Velocity component in direction i, m/s
V, v	Velocity magnitude, m/s
x/c	Root chord location, %
x_a	Distance between apex and centre of area, m
x_{ac}	Aerodynamic centre location, m
x_{cp}	Centre-of-pressure location, m
x_{ref}	Reference length, m
Λ	Leading-edge sweep angle, degrees
ζ	Notch ratio
α_{up}	Upwash Angle, degrees
γ	Specific Heat Ratio, $\gamma = 1.4$ for air
δ_{ij}	Kronecker Delta
ε	Dissipation rate, m^2/s^3
η, η_S	Non- dimensional spanwise position
λ	Taper ratio
μ	Dynamic Viscosity, kg/(ms)

μ_t	Turbulence Eddy Viscosity, kg/(ms)
ξ	Notch Ratio
ρ	Density of air, kg/m^3
σ	Normal Stress, N/mm^2
τ_{ij}	Reynolds Stress, N/mm^2
υ_t	Turbulence Kinetic Viscosity
ω	Specific turbulence dissipation rate m^2/s^3

Chapter 1 Introduction

1.1. Background

Delta wings and blended wing body configurations are of particular interest for military applications, due to their good performance at high speeds. The latter is of particular interest due to its economy (up to 30% less fuel consumption), improved lift-to-drag ratio (L/D) and stealth qualities (Nasir et al., 2014). However, these configurations show significant problems with longitudinal static stability and flying qualities due to not having a horizontal control surface (Bolsunovsky et al., 2001; Jung and Lowenberg, 2005; Saephan and Van Dam, 2008). These issues are enhanced at low speeds normally encountered during take-off, landing and loitering, thus, making improvements in this speed regime by means of wing design and flow control techniques necessary. A significant characteristic of delta wings and thus blended wing body configurations is the formation of two counter-rotating leading-edge vortices which can significantly augment the lift generation (Muir et al., 2017).

The development of these leading-edge vortices has been the focus of numerous numerical and experimental investigations in the recent past. Flow features such as subsonic and supersonic leading-edges (Szodruch and Peake, 1980), primary and secondary vortices (Szodruch and Peake, 1980), and vortex breakdown (Jones and Cohen, 1960) have been identified. Modelling global forces and moments such as the attached flow lift curve slope (Stallings, 1986) and those accounting for the leading-edge vortex (LEV) (Polhamus, 1966; Polhamus, 1971; Lamar, 1968; Lamar, 1976) have been undertaken. This is in addition to the development of a wide range of theoretical methods (Legendre, 1952; Adams, 1953; Brown and Michael, 1955; Edwards, 1954; Pershing, 1964; Sack et al., 1967).

Slender ($\Lambda \geq 60°$) configurations with small aerofoil thicknesses and flat upper surfaces (Szodruch and Peake, 1980; Muir et al., 2017) have been studied extensively, in order to understand the driving flow physics before extending research to more complex designs. In the more recent past, the VFE-2 configuration was studied by the NATO Research and Technology Organization's Applied Vehicle Technology (AVT) Task Group (Hummel, 2007). From 2003 to 2007, the Second International Vortex Flow Experiment (VFE-2) was performed (Luckring, 2009). The investigation, both numerical and experimental, were aimed at extending the knowledge of vortical flows for the 65° delta wing configuration with sharp and various rounded leading-edges and to create a research configuration for future studies (Chu and Luckring, 1996; Luckring, 2002; Le Roy et al., 2007; Luckring and Hummel, 2008).

Simple delta wings with non-flat lee side surfaces have not been studied as extensively, despite being more practical for aircraft application. Kirby and Kirkpatrick (1969) investigated the effect of thickness (4% to 16% of chord) on the longitudinal stability of a 70° biconvex delta wing configuration with a view to applying thicker profiles to practical aircraft layouts. The effects of thickness on lift and drag were also considered; reporting a loss of lift as the thickness increased. This is the opposite to that seen in two-dimensional flows, where an increase in aerofoil thickness results in an increase in lift.

In recent years, several research projects involving more complex delta wing designs have been undertaken to expand aerodynamic understanding of, especially, Unmanned Combat Aerial Vehicles (UCAVs). One of the biggest was conducted by NATO from 2007 to 2014. The research was conducted on a Stability And Control CONfiguration (SACCON) (Luckring and Boelens, 2015) to show the state of the art in predicting highly non-linear flow and the challenges for these types of simulations.

Configurations such as SACCON are practical designs for future UCAVs and have thickness to chord ratios of order 12%, with maximum thickness locations other than 50% chord and non-flat lee side surfaces. The leading-edge of these configurations may even be non-sharp. The SACCON configuration has highlighted the difficulties of numerically predicting the onset of leading-edge vortices (LEVs) for intermediate swept and non-sharp-edged wings for a configuration of practical thickness (Frink, 2014).

For aircraft design purposes it is crucial to be able to model the flow physics correctly without using excessive computational resources. Using numerical simulations requires a high grid resolution as the upper surface pressure distribution is very sensitive to correct modelling of the viscous flow region as concluded by Hummel (2009). Multiple studies further showed that modelling of the viscous region is affected by turbulence model choice and therefore needs to be taken into account when modelling vortex dominated flows, which can make them computationally expensive (Hummel, 2008b; Hummel and Redeker, 2003; Fritz,2009; Lamar, 2002; Lamar and Abdol-Hamid, 2009).

Overcoming the challenge of accurately modelling the vortical flow over a wide range of angles of attack and speeds could make delta wing configurations a more compatible planform for current military and commercial aircraft. However, to do so requires a comparable design process with regards to costs, computationally as well as experimentally. Therefore, understanding the influence of aerofoil as well as planform shape on the generation and

location of LEVs is crucial as it enables flow control devices and/or shape changes to be used to make a more adaptable aircraft in flight.

This doctoral study extends the studies of Le Roy et al. (2007) and Kirby and Kirkpatrick, (1971) by investigating how the dominant flow phenomena and global loads change with maximum thickness location. This is particularly useful for the design of UCAVs and future blended wing body transport aircraft especially when the technology for wing morphing matures.

Furthermore, this thesis intents to focus on low speed flight for take-off, landing and loitering as this is where delta wings perform worst and where the LEV is prone to be unstable (Gudmundsson, 2014).

The baseline configuration for this study is the aforementioned VFE-2 configuration as a vast amount of numerical and experimental data is already available for comparison and is depicted in Figure 1.1. It is used to validate the numerical grid and the accuracy of the experimental data of this study.

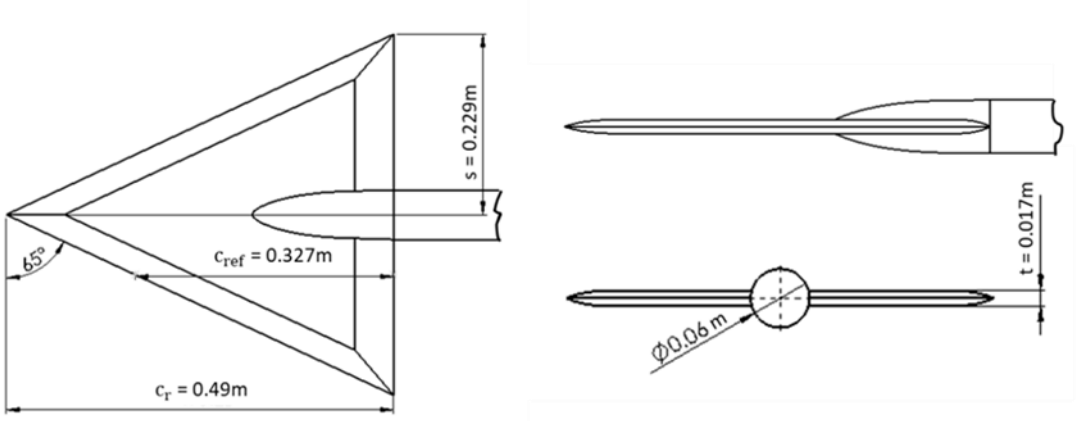

Figure 1.1 VFE-2 configuration with wind tunnel sting mount (Le Roy et al., 2007).

Derived from this is the VFE-2 model without sting mount and the so called VST configuration, which varies from the VFE-2 by having span taper and is depicted in Figure 1.3. The VST and VFE-2 configurations are sharp-edged and flat topped in profile and have a thickness of 3.4% of local chord (for the VST) or root chord (for the VFE-2). These configurations were used to investigate the impact of change in thickness and span taper. The configurations studying the effect of thickness and thickness location have biconvex profiles and are also depicted in Figure 1.3.

The VST, VFE-2 and biconvex configurations, all with a sharp leading-edge (SLE), are simulated at a Reynolds Number of 750000, speed of 34m/s and angles of attack from -10° to 18°. The biconvex configurations have thickness/chord ratios of 3.4%, 6% and 12%.

Symmetric profiles were adopted so as to focus on the chosen geometry change effect. The thicknesses of 3.4% and 6% were selected because configurations designed for supersonic flight generally have thicknesses between 3% and 6% (Nangia et al., 2002). As the VFE-2 has a thickness of 3.4% this thickness was also adopted for the biconvex wings to enable cross-comparison. The average thickness for subsonic and transonic aircraft is between 10-16% dependent on sweep angle, where reduced thickness is associated with low sweep (Sforza, 2014). The configuration of 12% thickness is therefore representative of subsonic configurations. The typical thickness ratio as function of Mach number is shown in Figure 1.2 (Raymer, 1992).

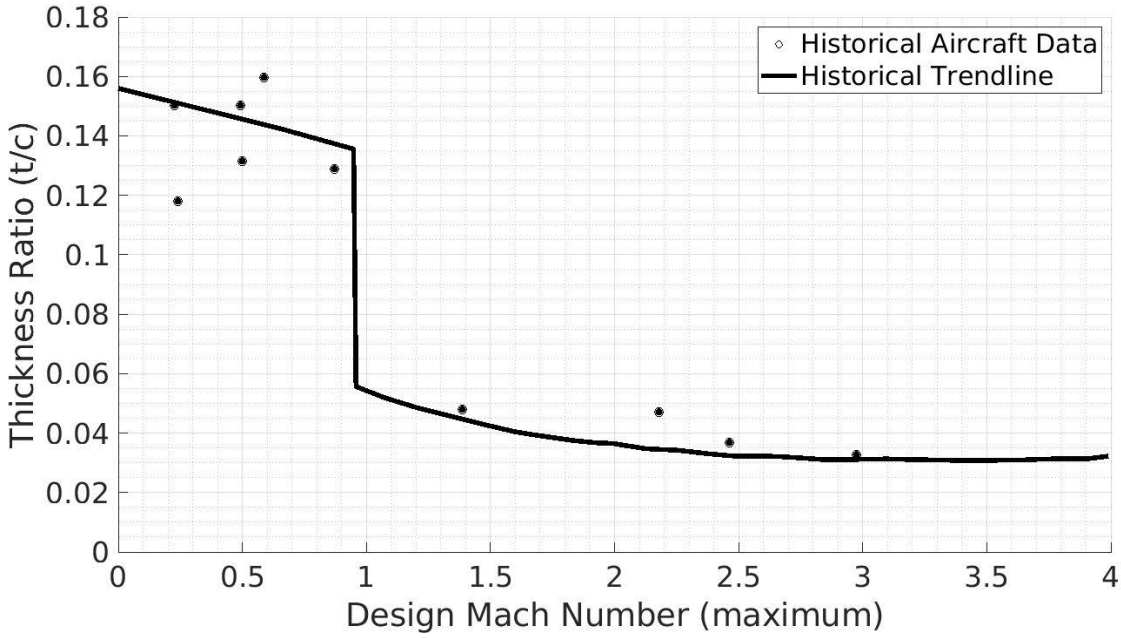

Figure 1.2 Thickness to chord ratio as a function of Mach Number for a series of historical aircraft (adapted from Raymer,1992).

Two maximum thickness/chord (t/c) locations for the 6% and 12% thick biconvex configurations are used, namely 30% (“B03”) and 50% (“B05”), whereas for the VFE-2 and VST configurations the maximum t/c location is at 15%. Also, the spanwise thickness location varies for the VST, B03 and B05 configurations compared to the VFE-2 where it is constant. This is depicted in Figure 1.3. Here, the top, side and rear views are shown on the left and bottom right, with Figure 1.3 (c) displaying the differences in spanwise thickness distribution.

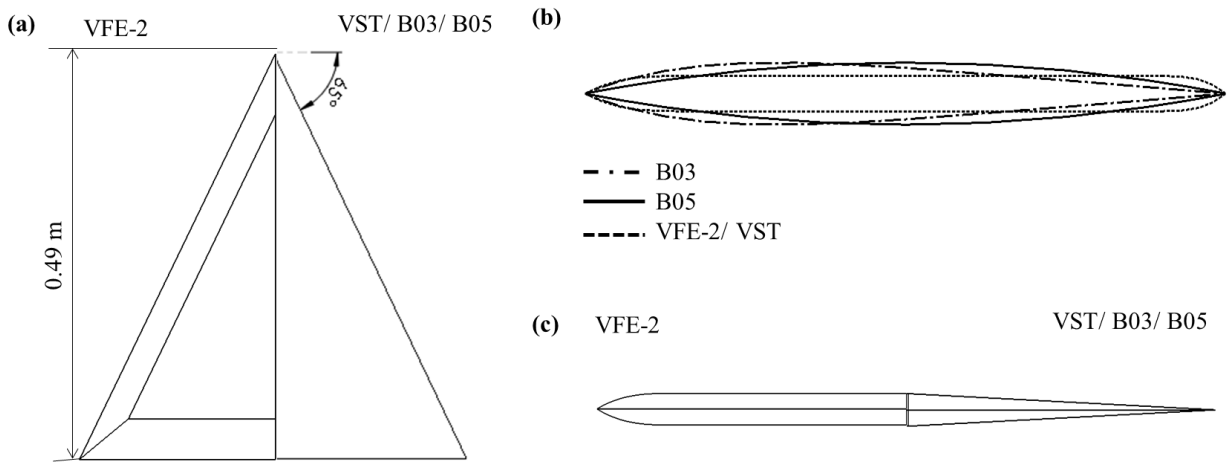

Figure 1.3 (a) Planform (b) Profile and (c) Back View of the three different geometries.

Based on the above, the focus of this thesis can be summarised to lie on slender delta wing planforms with:

- sharp-leading-edges (SLE): as this fixes separation to the leading-edge.
- 0° trailing edge (TE) sweep: as trailing edge sweep and shape further affect LEV behaviour.
- Symmetrical aerofoils: as the effects of change in thickness and maximum thickness location are not biased by an additional geometric change and because symmetric aerofoils are commonly used for stealth aircraft. The benchmark configuration VFE-2 uses a symmetric aerofoil.

Also, only subsonic speeds are considered as the interest is in high lift configurations for take-off, landing and loitering for reasons discussed earlier.

1.2. Determination of the Research Questions

Slender and non-slender delta wings have been explored extensively in the past, however there is no work investigating the effect of maximum thickness location. Despite the effect of maximum thickness being studied by Kirby and Kirkpatrick (1969), this has not been done comprehensively as a function of sweep angle. The overall aim of the research project is formulated as follows:

To demonstrate the effect of thickness and maximum thickness location on the aerodynamic performance and longitudinal stability of slender delta wings at low speeds.

To achieve the overall aim, the following objectives have been established:

i) Establish the current knowledge base on the effect of geometrical changes on slender delta wings.

ii) Investigate the current capabilities of Computational Fluid Dynamics (CFD) and in particular RANS turbulence models to predict vortical flow development accurately.

iii) Investigate the effect of spatial discretisation on the accuracy of vortical flow prediction.

iv) Design and manufacturing of wind tunnel models, mounting system and rig for the conduction of wind tunnel experiments at the University of the West of England, Bristol.

v) Validation of the CFD simulations based on the findings in objective (ii) and (iii)

With the above objectives and main aim being defined it is possible to state the two key research questions of the PhD;

1. To what extent does changing the thickness as well as the maximum thickness location of a delta wing configuration with sharp leading-edge have an effect on its performance and longitudinal stability at low speeds?
2. What is the confidence level of the prediction above, that could facilitate UCAV design by knowing the major flow parameters as well as flow features in advance?

1.3. Thesis Structure

An introduction to the thesis and its main research question is presented in Chapter 1. Background information regarding the importance of the investigation and understanding of vortex dominated flows for military aircraft design is given and aims and objectives are identified.

Chapter 2 presents a review of open literature on slender and non-slender wings, the flow physics governing delta wings, the effects of different geometrical features on these flow physics, and the current state of Computational Fluid Dynamics (CFD) and the prediction of vortical flow.

An overview of important aspects of CFD such as y^+ value, turbulence modelling and relevant turbulence models is given in Chapter 3. Further details on the geometries of the benchmark configurations VFE-2 and VST as well as the biconvex configurations are also presented.

Chapter 4 contains a description of the computational grid used and includes the details of the final grid based on the Grid Convergence Index (GCI). The accuracy of the flow that can be attained using this grid is discussed. Two different turbulence models are used with the grid and the numerical data obtained is compared with the experimental findings of TU Munich (TUM).

The experimental set up is described in Chapter 5. This includes the rig design and statistical analysis of tare and air-on runs as well as the correction undertaken to arrive at the final data. The chapter is concluded by comparing the experimental findings with the numerical ones, to display their validity.

Chapter 6 contains an evaluation of the numerical findings where the differences between the configurations with regards to maximum thickness, maximum thickness location and spanwise thickness distribution are presented.

The thesis culminates in Chapter 7 by answering the research questions and satisfying the aims and objectives of Chapter1, naming the limitations of the study and making suggestions for future work.

Chapter 2 Literature Review/ State-of-the-Art

In this chapter, the aim is to give an overview about the understanding to date of leading-edge vortices (LEVs) which form above delta wings. Firstly, the flow physics affecting the LEV are introduced. Next, the aerodynamic principles by which LEVs conform are explained by means of leading-edge geometry. Then delta wings are categorised into slender and non-slender wings before attention is drawn to the general flow physics and how the delta wings are affected by different geometric changes. These changes can either occur in the geometric plane of the wing, meaning changes in sweep angle or overall planform shape (i.e. arrow-wing, delta wing or diamond wing) or in its cross-section (i.e. the change of the aerofoil profile by change in thickness to chord ratio, nose radius, camber or overall profile change).

2.1 Flow physics affecting the vortex

Three-dimensional separation is an important phenomenon occurring on any type of three-dimensional body. On the object's surface this creates a herringbone streamline pattern near the attachment line of the separated flow (A) as illustrated in Figure 2.1 (Küchemann, 1978). Part of this reattached flow is within the viscous region, thus, altering the state of the boundary layer either from laminar to turbulent or vice versa (Colak-Antic, 1971).

Figure 2.1 Pattern of attachment flows (Küchemann, 1978).

Away from the attachment line and in the outer flow the streamlines are curved. These curved flows are subject to centrifugal forces whilst the pressure remains approximately constant throughout the boundary layer. This causes the flow molecules nearer the surface to take a more curved path due to their reduced velocity which can lead to flow separation when the

pressure rises rearwards as well as inwards (normally behind the suction peak) causing the near surface streamlines to run in the same direction and to run tangentially into a single line (Küchemann, 1978).

Depending on the sweep angle, different separation patterns can be observed on a wing normal to the leading-edge. These are depicted Figure 2.2 in where S_1 marks the initial separation. Figure 2.2 a) shows the separation surface of a wing of low sweep, where the flow behaves nearly two-dimensionally and a closed bubble may be formed. The flow re-attaches to the body surface and contains a slowly rotating flow that is separate from the surrounding air (Küchemann, 1978).

Figure 2.2 b) shows the separation surface of a wing of moderate sweep. It shows a bubble formation with at least two eddies of opposite direction inside it and a free surface of separation with a rolled up vortex core (Küchemann, 1978).

The other extreme is shown in Figure 2.2 c) showing the separation surface of highly swept wings. Here, the flow is highly three-dimensional with the separation surfaces being all open and the whole space being filled by mainstream air. This type of flow is considered quite steady. The separation surfaces can be interpreted as vortex sheets which roll up along their free edges into vortex cores. The vortex cores grow in space as further vorticity is fed into them (Küchemann, 1978). It is also characterised by high axial forces and low static pressure. The high gradients in the cross-flow velocities cause high velocity fluctuations, which are concentrated in the viscous sub-core of the vortex (Koelzsch and Breitsamter, 2014). Generally, there is another attachment surface, intersecting the body at A_1. This attachment line divides the flow which is drawn into the vortex core from that which passes it by. A secondary separation line S_2 and a secondary vortex sheet are formed on highly swept configurations. This is because the air near the surface of the body is not able to overcome the adverse pressure gradient generated by the air traveling below the vortex core, thus, generating a suction peak on the surface. This process can be repeated infinitely but is terminated when the boundary layers and vortex sheets are no longer thin and when the sheets are swallowed up by the viscous fluid surrounding them (Küchemann, 1978).

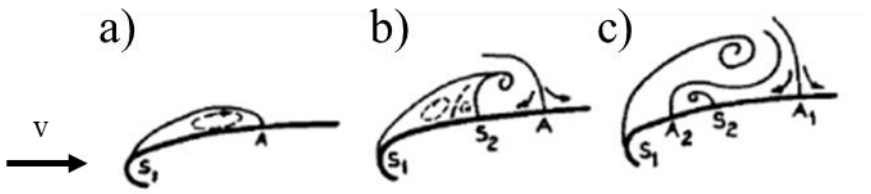

Figure 2.2 Three-dimensional separation surfaces for different sweep angles a) low sweep, b) moderate sweep and c) high sweep wing (Küchemann, 1978).

The main effects of sweep apart from the generation of a LEV are the reduction of the perturbation velocities. This is due to the velocity components parallel and perpendicular to the leading-edge having a sine and cosine components which are smaller than zero for swept wings. Another feature of swept back wings is that the perturbation velocities vary more slowly with Mach number with increase in sweep angle and the critical Mach number is reached at higher speeds compared to a non-swept wing (Küchemann, 1978).

The flow over a conventional finite delta wing is highly influenced by the shape of the tip and the sweep back angle. The pressure distribution is very different at the centre in comparison to locations further outwards. The same is true for the wing tips. The tip section behaves like the centre section of the wing with the reverse angle of sweep. Thus, whilst the centre effect shifts the minimum pressure backwards along the chord and reducing it slightly, the tip effect shifts it forward whilst increasing the suction peak (Küchemann, 1978).

Additionally, the pressure drag generated by the centre section is considerably higher than at the tips. It has also been found that the pressure drag is approximately proportional to $(t/c)^2$ (Küchemann, 1978).

When designing a swept wing it is thought to be beneficial to have straight and swept pressure isobars all along the span and right into the centre as depicted in Figure 2.3 b) and c). However, an untreated wing's isobar surface pattern would look as depicted in Figure 2.3 a). The non-uniformities in the isobar pattern are mainly due to the centre and tip effects. The loss of isobar sweep is resulting in a lower critical Mach number as well as to premature flow separation near the wing tips which in turn results in high suction peaks and steep adverse pressure gradients. This causes a tendency of the wing to pitch up (Küchemann, 1978).

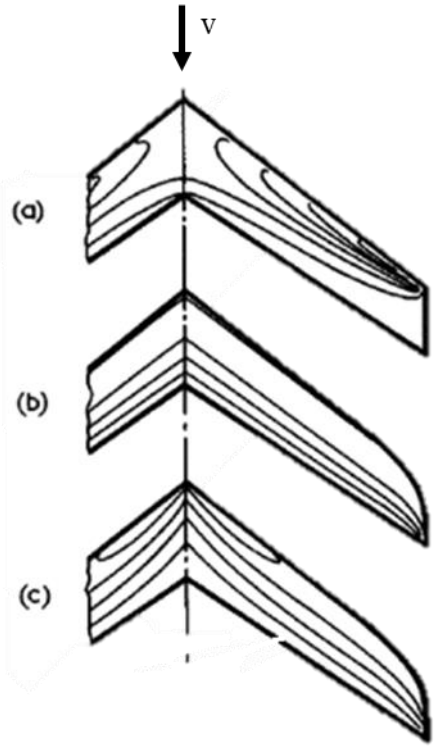

Figure 2.3 Various isobar patterns on swept wings for a) untreated tip, b) and c) different tip alterations (Küchemann, 1978).

For delta wings with SLEs the position and strength of the vortex system depends mostly on α. At a given angle the vortex structure changes and VBD occurs. This is due to a combination of high circumferential velocities, high radial pressure gradients and low total pressure at the vortex axis which results in a transition from a stable vortex to an unstable one. The trailing edge has generally a decelerating effect on the vortex system due to the increasing axial pressure gradient towards the trailing edge. This in conjunction with a strong radial expansion of the vortex core results in vortex burst. With increasing α the breakdown position moves upstream (Koelzsch and Breitsamter, 2014).

2.2 Aerofoil Shape Effects: Leading-edge shape for delta wings

2.2.1 Flow Physics for Delta Wings with Sharp Leading-edges

Slender delta wings with SLEs are of interest particularly for supersonic flight (Peckham, 1958). The flow topology of such wings with leading-edge separation operating at subsonic conditions is well established and a vast volume of data is available both experimentally and computationally, with some of it being reviewed in this chapter (Schiavetta et al.; Escudier, 1988; Hoeijmakers, 1991; Delery, 1992; Delery, 1994, Gursul, 2004).

The dominant aspects of delta wing flow are the two vortices occurring on the highly swept leading-edges (sweep angle $\geq 45°$). They are created as the flow tries to curl over the leading-edge when there is a pressure difference between upper and lower surfaces. At SLEs this will result in separated flow along the entire span as the flow cannot follow the sharp curvature of the leading-edge. The vortex produced by this is called the primary vortex and occurs inboard of each leading-edge as shown in Figure 2.4 and Figure 2.5. The flow which has separated at the leading-edge (shown as the primary separation line S_1 in Figure 2.4) curls around the wing and reattaches again along the attachment streamline A_1. The primary vortex can then be found within the free shear layer, which is created by the flow separating from the leading-edge and the departing boundary layer. It consists of a viscous core, with the vortex flow around it being nearly inviscid. This behaviour was derived by Hall (1961) analytically. He reasoned that towards the vortex core the gradients of vorticity become larger, thus giving more importance to viscous diffusion and hence viscosity. Viscosity essentially describes the process of transferring the momentum from a fast-moving region to a slow-moving region, which is happening when moving from the core of the vortex outside. This can best be understood when looking at the Navier-Stokes equation for an incompressible Newtonian fluid (Anderson, 2011):

$$\frac{\partial \mathbf{M}}{\partial t} = \frac{\mu}{\rho}\nabla^2\mathbf{M} - \mathbf{v}\cdot\nabla\mathbf{M} + (\mathbf{f} - \nabla\mathbf{P}) \qquad (2.1)$$

where **M** is the momentum of the fluid (per unit volume) at each point, μ is the dynamic viscosity, ρ is the density, **v** is the velocity vector, P is the fluid pressure, and **f** is any body force such as gravity.

The primary vortex is fed with vorticity along the entire length of the leading-edge which is transported through the free shear layer into the vortex core. This increases the strength of the vortex as well as its cross-section in the downstream direction (Anderson, 2011).

When examining Figure 2.4 and Figure 2.5 it can also be seen that the surface streamlines flow away from the attachment lines A_1 and A_2 and towards the separation lines S_1 and S_2 from where they separate. It is also shown that the surface streamlines are attached inboard of the leading-edge vortices whereas outboard of the attachment lines, the flow entrained in the primary vortex moves outward, towards the leading-edge (Anderson, 2011). Those streamlines may then separate near the surface at S_2 due to the high adverse pressure gradient in the spanwise

direction, forming an oppositely rotating secondary vortex. This in turn causes the primary vortex to move further inboard and away from the surface of the wing.

The secondary vortices can also form tertiary vortices following the same process as described above. Outboard of the secondary vortex the flow attaches again whilst approaching the leading-edge, where it separates again and joins the flow from the lower surface in the shear layer. For secondary vortices at low speed there is a dependency between Reynolds number (Re) and secondary separation location. An increase in Re resulting in the starting point of the secondary separation moving forward (Goertz, 2005).

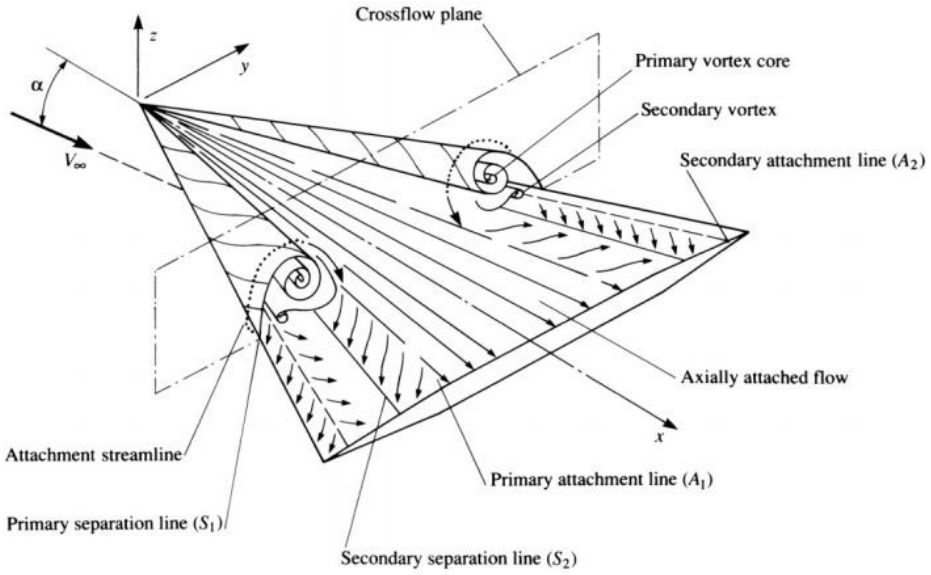

Figure 2.4 Leading-edge vortices with the primary separation S_1 occurring at the leading-edge, followed by the reattachment of the flow at A_1. A secondary vortex forms due to secondary separation S_2 with secondary reattachment at A_2 (Anderson, 2011).

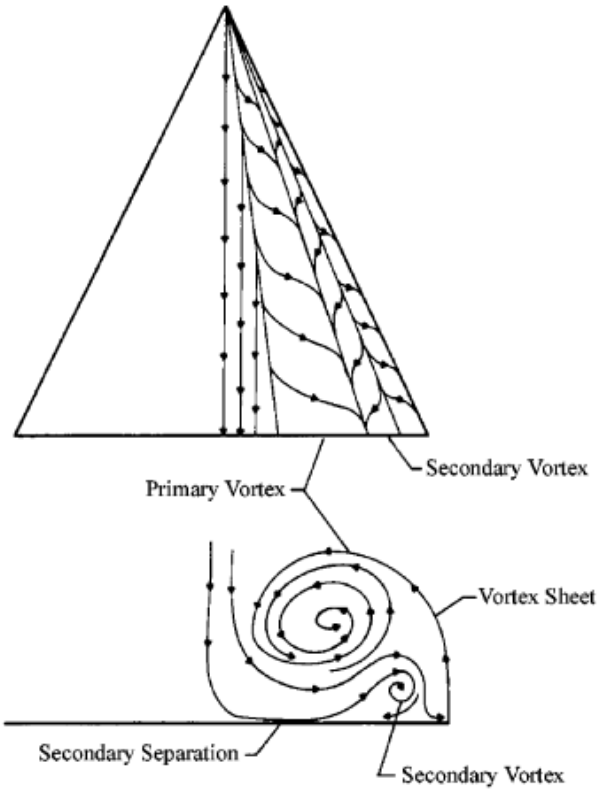

Figure 2.5 Leading-edge flow structure close to the surface of a slender delta wing (Nelson and Pelletier, 2003).

A general feature of primary vortices created on delta wings is that they are strong and stable. They are a source of high energy, high vorticity and low local pressure in the vicinity of the vortices. This results in an additional reduction of surface pressure on the upper surface near the leading-edge whereas the pressure stays constant over the middle of the wing as depicted in Figure 2.6. Note that the spanwise variation of pressure over the lower surface is constant and higher than the free stream pressure (Anderson, 2011).

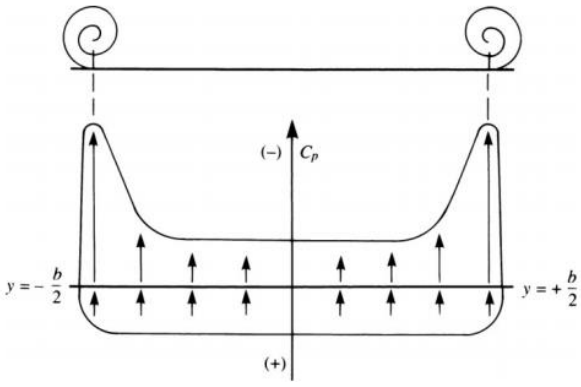

Figure 2.6 Spanwise pressure coefficient distribution of a delta wing (Anderson,2011).

The suction effect of the leading-edge vortices described above produces a local increase in lift, also known as vortex lift, in addition to that achieved with fully attached flow.

The suction analogy developed by Polhamus (1966) shows the effect of vortex lift on the lift curve and is shown in Figure 2.7.

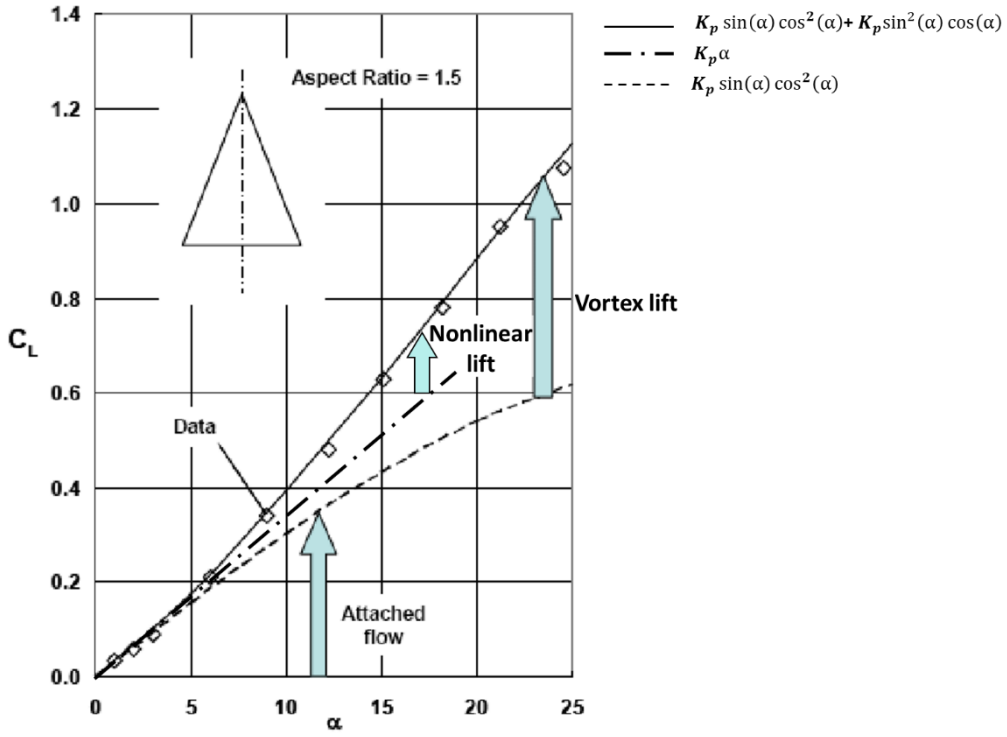

Figure 2.7 Difference between vortex lift and nonlinear lift (adapted from Luckring, 2010; Hemsch and Luckring, 1990).

The lift coefficient for attached flow is given by Polhamus, (1966) as:

$$C_{l_p} = K_p \sin(\alpha) \cos^2(\alpha) \qquad (2.2)$$

Where K_p is the lift coefficient slope at zero angle of attack, α. Hence the lift associated with the LEV (C_{l_v}) is given by (Polhamus, 1966)

$$C_{l_v} = C_l - K_p \sin(\alpha) \cos^2(\alpha) \qquad (2.3)$$

Polhamus showed that C_{l_v} can be expressed as (Polhamus, 1966)

$$C_{l_v} = K_v \cos(\alpha) \sin^2(\alpha) \quad (2.4)$$

Where K_v is directly related to the coefficient for leading-edge suction. Both values for K_p and K_v can be calculated using the potential lift formula (see Kulfan, 1979) and pre-calculated values of both coefficients can be found in Polhamus' (1966) paper for delta wings of different sweep angles (for a 65° delta wing, where A= 1.87, these values can be found to be $K_p \approx 2.2$ and $K_V \approx 3.1$).

From Equation (2.4) can be seen that the relation between lift and α is nonlinear for vortex dominated flows. The effect of the secondary separation on the surface pressure distribution depends strongly on whether the boundary layer is laminar or turbulent. For a laminar boundary layer the secondary separation effects are largest (Hummel, 1978). Also, the presence of the secondary vortex may influence the location of the primary suction peak. This means that the primary suction peak is not necessarily located exactly below the location of the primary vortex core (Hummel, 1978).

The leading-edge vortices also provide the wing with "fresh air ", counteracting the tendency of boundary layer separation which is the main factor for "stall" on conventional planforms. In addition to the suction effect of the leading-edge vortices, this enables delta wings to achieve higher lift coefficient, C_L, and angle of attack, α, values than conventional planform wings (Goertz, 2005). An example for such a C_L vs. α graph is shown for a slender delta wing of 75° sweep in Figure 2.8. The typical value for the maximum lift coefficient $C_{L_{max}}$ is of the order of 1.0 to 1.4, depending on the sweep angle and between 30% and 60% of the total lift at high α is produced by the leading-edge vortices (Wentz et al., 1971).

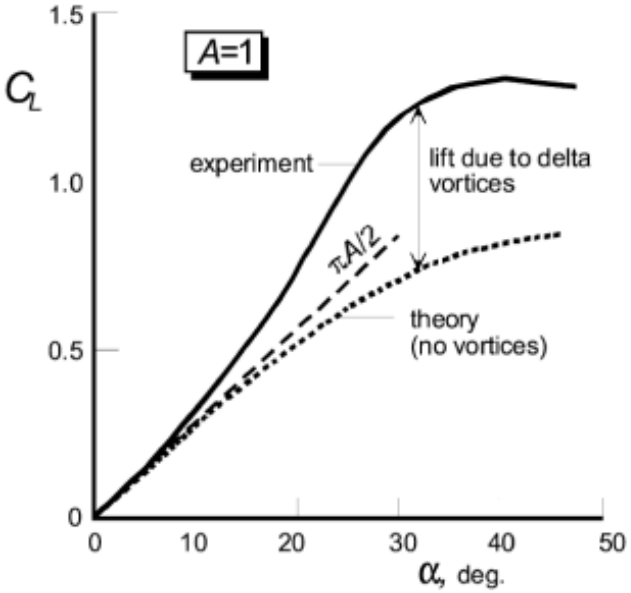

Figure 2.8 Lift coefficient for a delta Wing of aspect ratio A=1 equivalent to a sweep back angle of 75° (Polhamus, 1966).

The C_l vs. α graph for delta wings is characterised by a much more shallow slope than that seen for conventional aircraft. The shallow lift curve slope is the reason why delta wings have to land at high α in order to produce sufficient lift. This also results in high induced drag making delta wings inefficient for subsonic flight (i.e. there is a small L/D ratio). Nonetheless, they have excellent performance at high speeds due to shock minimisation and wave drag reduction (Anderson, 2011).

At very high α, however, a limit of the above described favourable effects is reached and a large-scale VBD occurs near the trailing edge causing the flow field to become unsteady (Delery, 1994, O'Neil, 1989). A detailed description of VBD and the factors affecting it can be found in Appendix A.1.1.

Furthermore, swept wings have unique characteristics in the high angle-of-attack regime, normally encountered during landing and take-off phases or during combat manoeuvring. The aerodynamic forces created during these flight regimes are highly nonlinear and related to the values of α, sideslip angle, and/or roll angle as well as their rates of change. Even the time history of those quantities plays an important role. Hence, even small changes in angle of attack result in a change in vortex position and VBD location. This requires new mathematical models in order to predict the aerodynamic forces and force distributions (Nelson and Pelletier, 2003). Numerically VBD location has been found to be predicted reasonable by RANS simulation (see Chapter 3 for details on the turbulence models mentioned here) however more advanced turbulence models such as SA-DDES showed to be more promising when a full understanding

of the flow field at VBD was required (Cummings and Schütte, 2009). Generally, it has been found that VBD is predicted to occur at lower angles of attack in numerical simulations compared to experimental data. This may be due to an underprediction of the axial velocity in the vortex core, which is predicted more accurately when using DES methods (Fritz, 2013).

Numerical studies have also been carried out on the VFE-2 configuration with RLE and SLE. Here, Crippa and Rizzi (2006) simulated the VFE-2 configuration at M=0.4 Re_{mac}= 6x10^6 and α= 18.5° and 23°, angles of attack where it is known for VBD to have reached the trailing edge. The study was conducted using RANS (EARSM) and DES based turbulence models and adaptive grid refinement. It was found that neither DES nor EARSM predicted the pressure distribution correctly, with the EARSM resolving the secondary separation better than the DES. The same was found for the Medium Round leading Edge (MRLE) configuration. Again, the DES overpredicted the primary vortex suction near the leading-edge whereas the EARSM model showed a better match. Close to the trailing edge it was found that the EARSM model underpredicted the suction peak whilst the DES resulted in a better match with experimental data. It was concluded that no substantial benefit can be obtained using DES regarding the surface pressure and its advantages were solely found regarding position and topology of VBD. It was further found that RANS models are superior when predicting the flow at lower angles of attack, but vortex core development was more accurately predicted by DES at higher α (Crippa and Rizzi, 2006).

Saha and Majumdar (2012) conducted an experimental and numerical study to evaluate the accuracy in the CFD prediction using the RANS SST k-ω model at Re= 1×10^6. Focus lay on the surface flow visualisation at α= 15° and α= 20°. Their study concluded that the SST k-ω turbulence model predicted the flow topological structure and the VBD phenomenon up to moderate angles of attack with considerable accuracy (Saha and Majumdar, 2012).

Next to this, the understanding of the relationship between the separated flow field and the aerodynamic loads needs to be established as they are the underlying causes for unwanted flight dynamic behaviour limiting the operational capability of an aircraft. Additionally, separated flow can cause flight dynamic phenomena such as wing rock, wing drop, heavy wing, nose slice, and buffet, further limiting the manoeuvring capability, due to increased structural loads and pilot safety. Methods to predict the onset and severity of these phenomena early in the design process are still under development and most flight dynamic problems are discovered during flight testing. The arising issues are then usually overcome by a “quick fix approach”

rather than by understanding the underlying physics of the problem (Nelson and Pelletier, 2003).

More information regarding the vortex structure and the impact of the boundary layer status on sharp-edged wings is presented in Appendix A.1.2.

2.2.2 Flow Physics for Delta Wings with Round Leading-edges

The flow physics around round-edged delta wings are very different compared to those around sharped-edged ones, in particular in the region near the leading-edge and apex. On configurations with round leading-edges the flow stays attached to the wing surface until a certain chordwise position which depends on Reynolds number, α, Mach number and leading-edge profile (Hummel, 2004 & 2008a; Chu and Luckring, 1996, 2002 &2004a).

Chu and Luckring (1996) conducted experiments on a delta wing with various leading-edge geometries in order to investigate the effect of bluntness. The delta wing investigated became later the benchmark geometry of the Second Vortex Flow Experiment (VFE-2), which also is the benchmark geometry of this research project. Figure 2.9 shows the effect of leading-edge shape on the surface pressure distribution. Pressure peaks are indicators for the presence of leading-edge vortices as was already shown in Figure 2.6. It can be seen from Figure 2.9 (a) that a leading-edge vortex is already present near the apex for the wing with SLE. A blunt leading-edge, however, delays vortex onset up until $x/c_r=0.6$ (see middle of Figure 2.9 and Figure 2.9 (b)). The close up of the C_p distribution in Figure 2.9 further shows the formation of a secondary vortex for the wing with RLE, indicated by a smaller pressure peak (blue curve). It can be seen that this is not the case for the SLE configuration (green curve). In fact, a multiple vortex structure is indicative for delta wings with blunt leading-edges (Luckring and Hummel, 2008). For the wing with a SLE, a pressure distribution characteristic for a leading-edge vortex is already visible close to the apex.

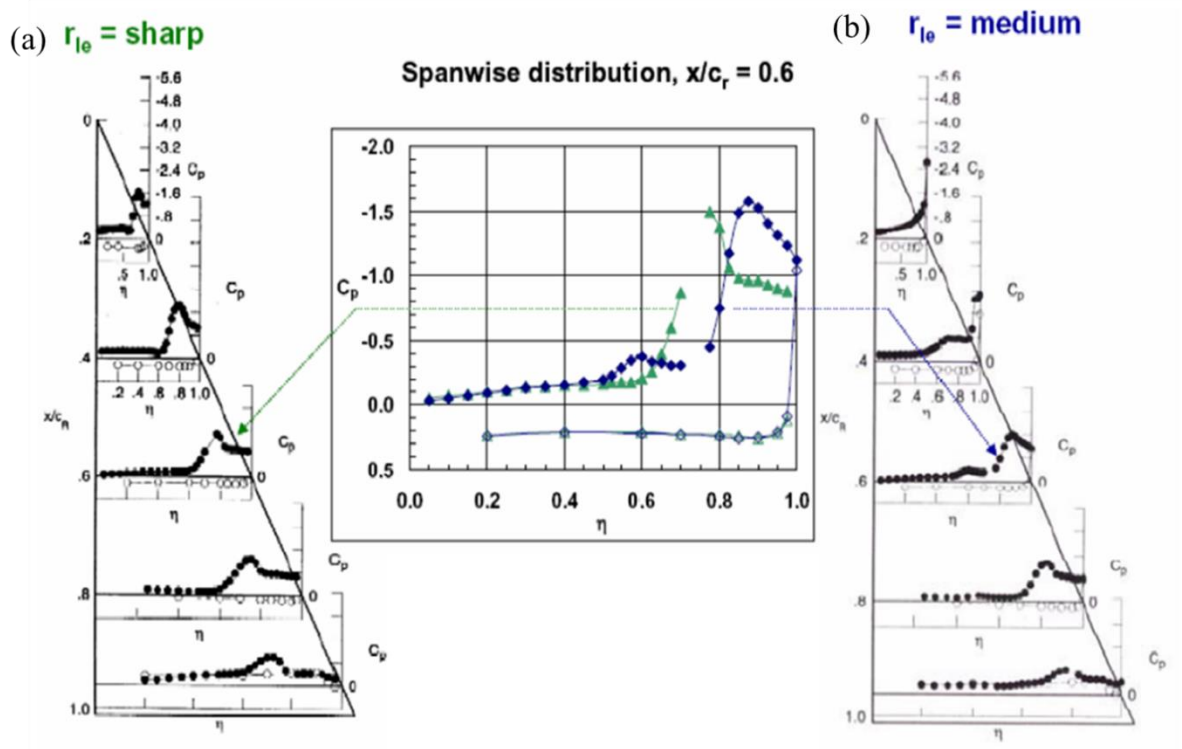

Figure 2.9 Effect of leading-edge bluntness on the pressure distribution at Mach Number 0.4, Re_{mac}= 6x10^6 and α=13°. For each test case, five Cp distributions are shown as a function of normalised span, η. A close up of the Cp distribution at mid root chord x/c=0.6 is shown in the middle of the figure including both geometries, highlighting the differences in the vortex position and strength (Chu and Luckring, 1996).

The formation of an inner vortex has been observed on the VFE-2 with medium rounded leading-edge (MRLE) for certain Reynolds numbers and angles of attack. It is observed for relatively low Reynolds numbers in the medium angle of attack range. The inboard vortex extends over the entire chord length and its strength and trajectory strongly depend on α. It is found to co-rotate with the primary vortex and as picked up by oil flow pictures (in the wind tunnel) or vorticity contours (CFD) but does not necessarily affect the surface pressure distribution (Furman and Breitsamter, 2013). An example of the flow structure is shown in Figure 2.10 for M=0.4 and $\mathrm{Re_{mac}} = 3 \times 10^6$.

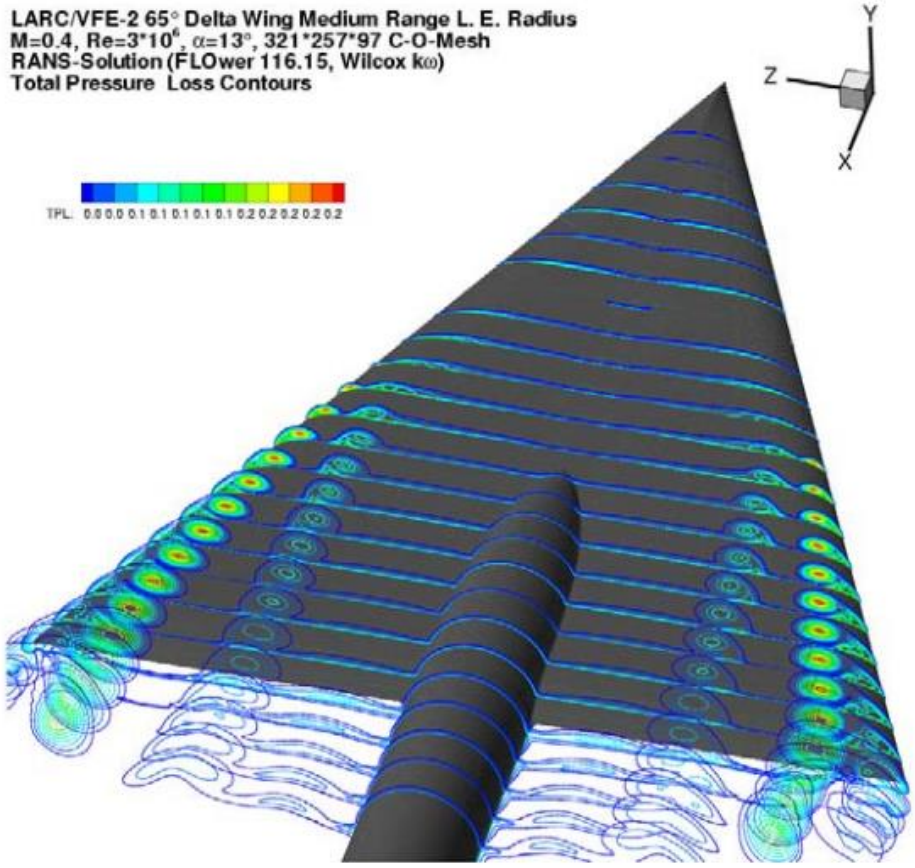

Figure 2.10 Total pressure loss contours distribution showing the formation of the primary and inner vortex of the VFE-2 with MRLE for M=0.4 $Re_{mac} = 3 \times 10^6$ α = 13° (Hummel, 2006).

Researchers have found that with increasing angle of attack, the flow at the leading-edge first separates at the rear part of the wing as the ratio of leading-edge radius over the local wing span is small. With increase in angle of attack the vortex onset moves upstream until it reaches the apex of the wing.

A more detailed review on the flow physics of delta wings with round leading-edges is given in Appendix A.1.3, which covers the effect of blunting the nose on primary and secondary vortex structure and development, including, separation onset and the effect of boundary layer status.

2.3 Effect of varying Leading-edge Radius

Multiple investigations by NASA (Luckring, 2008), ONERA and TUBITAK-SAGE (Le Roy et al. 2008) have shown that there exist only minor differences between sharp (SLE) and medium radius (MRLE) leading-edges regarding normal force coefficient, C_N, as displayed in Figure 2.11. The centre of pressure of the MRLE wing is located slightly more forward, thus,

reducing longitudinal stability compared to configurations with SLEs, and the axial force, C_A, is larger than for the SLE wing. This is due to the suction area in the leading-edge region. It is also worth noting that the theoretical values for C_A for attached flow were calculated and plotted in Figure 2.11. The values were obtained by fitting the measured data for the blunt leading-edge between 3° to 6° to the function $C_A = k_0 - k_1 \sin^2\alpha$, where k_0 and k_1 are the coefficients of the curve fit. The function is derived from three-dimensional potential flow theory and was done as the flow is attached for the blunt leading-edge in that angle of attack region and thus provides a tramline of a wing with fully attached flow to compare the results to. This helps to showcase that the blunt leading-edge uses attached flow suction until about 7° α, whereas a SLE develops separated flow already at lower α (around 5°) (Hummel and Luckring, 2008).

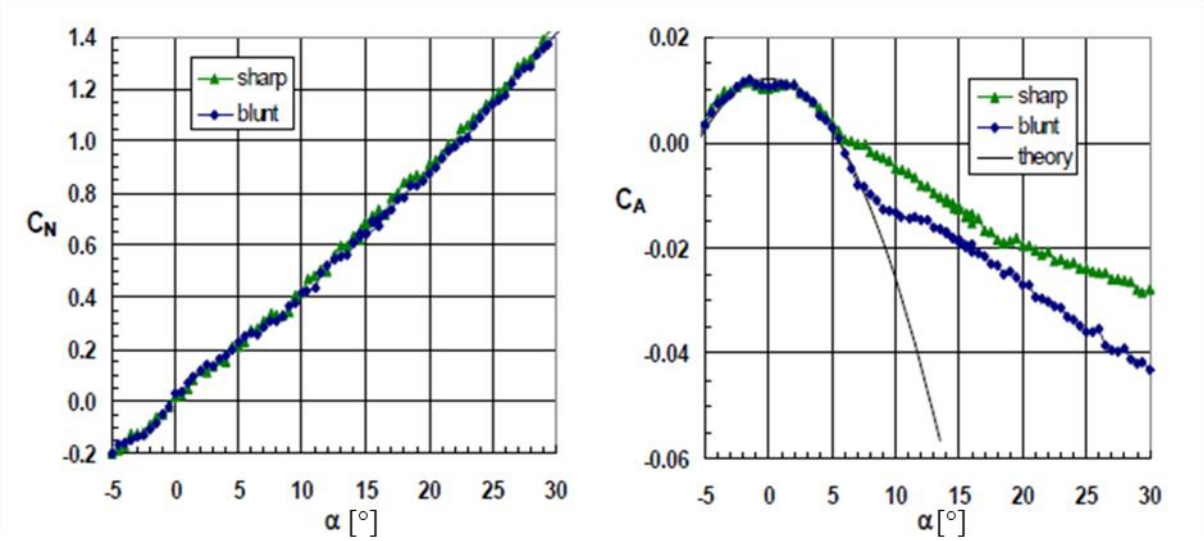

Figure 2.11 Effect of Bluntness on Experimental Normal and Axial Force Coefficients for the VFE-2 Configuration with SLE and MRLE at M=0.1 Re=1 × 10^6 from Onera L1 (Rodriguez, 2008).

Furthermore, multiple numerical studies have been conducted on delta wings with MRLEs of different nose radius, investigating the vortex development on such wings. The findings are detailed in Appendix A.1.3 but are summarised here before continuing with the findings obtained using experiments. One major difference between SLE and MRLE wings is that the separation at the leading-edge is not fixed (Hummel, 2004). This results in delay in vortex onset, and is a function of Mach number, Re number and leading-edge radius, which is not the case for wings with SLEs (Luckring, 2004 a). Furthermore, it results in a shift of the primary vortex outboard and size and strength of the primary vortex were found to decrease (Furman and Breitsamter, 2008). Predicting the vortex onset numerically proved to be challenging for most codes and turbulence models at low Re numbers (Fritz, 2013). This is opposed to findings

on wings with SLEs, where experimental and numerical findings are shown to be in good agreement (investigated were α= 10.4° and α= 15°) (Boelens, 2009). It was assumed that this may be to boundary layer transition not being modelled and the sensitivity of wings with RLEs to Re number (Fritz, 2013).

Another observation was that the rounding of the leading-edge resulted in the formation of an inner co-rotating vortex structure, which forms prior the primary vortex (Fritz, 2008; Hummel, 2006) due to boundary layer separation near the apex. However, it decays once the primary vortex starts forming further downstream and is pushed further inboard (Konrath et al., 2008 a & 2008 b). It is hypothesised that the inner vortex is caused by a separation bubble close to the apex, where the wing as higher effective leading-edge radius (leading-edge radius/ local span) (Hummel, 2007). During the literature review this phenomenon was not reported by other researchers and may be due to the flat upper and lower surface of the VFE-2 configuration on which most of the numerical findings in this report are based.

Kegelman and Roos (1989) showed that the lift coefficients are insensitive to change in leading-edge bluntness which is in contrast to the findings made by Rinoie (1996a), Wang (2005), Erickson and King (1992), Fletcher (1958) and Henderson (1976). Findings by Rodriguez (2008) and Luckring (2010) suggest also an insensitivity, though it is not explicitly stated. Rinoie (1996a), Wang (2005), Erickson and King (1992), Fletcher (1958) and Henderson (1976) findings suggest that the bluntness lowered the normal force coefficient. This can be explained by the bigger size and higher strength of the primary vortex on sharp leading-edged wings. Also, attached flow is present on the front part of the round-edged wing contributing to the reduction in normal force (Luckring and Hummel, 2008).

Little research has been published on the effect of leading-edge bluntness on the drag and pitching moment coefficient. It is assumed that the larger vortex structure on wings with SLEs yields to higher drag (Rinoei, 1996a; Wang and Lu, 2005). With regards to the pitching moment, investigations by Rinoei (1996a) and Erickson and King (1992) showed that round-edged wings experience a lower nose down pitching moment compared to sharp-edged wings. This was also confirmed during VFE-2. Figure 2.12 shows the pitching moment coefficient for the VFE-2 for both sharp and round leading-edges between α= 0°-20°. It can be seen that the round leading-edge causes a reduction in static margin with increase in angle of attack, indicated by a positive slope, compared to that of the VFE-2 with SLE, which shows a negative slope between α=0° and α=3°. After that the slope is very similar though offset, resulting in the

pitching moment coefficient being up to 50% higher for the wing with round leading-edge. This leads to a significant decrease in longitudinal stability, which is usually undesirable when designing an aircraft.

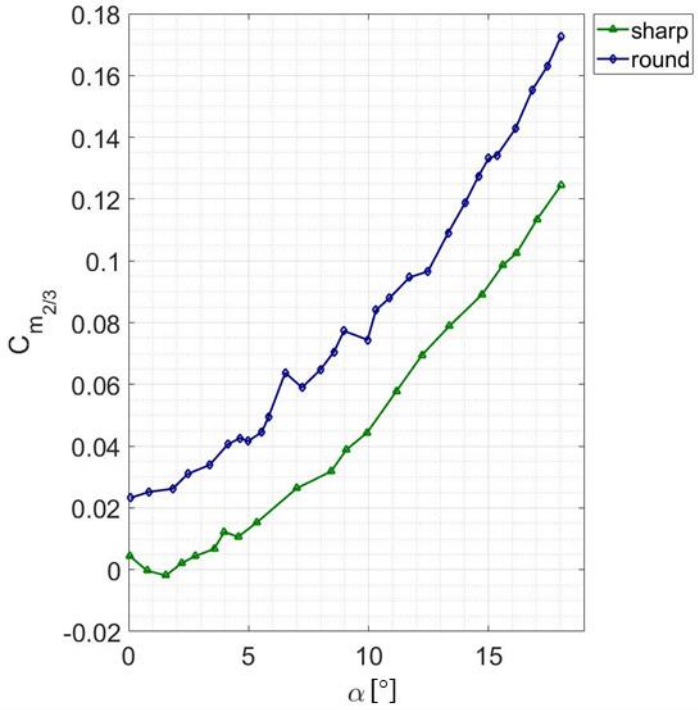

Figure 2.12 Pitching moment coefficient taken around $2/3c_r$ versus α at M=0.1 Re=1×10^6 replotted from the Onera L1 wind tunnel (Rodriguez, 2008).

It has also been shown that configurations with round leading-edges experience delayed VBD at all angles of attack compared to sharp-edged wings (Kegelman and Roos, 1989; O'Neil et al., 1989). Also, O'Neil et al. (1989) concluded that leading-edge bluntness delays the upstream progression of the primary vortex. This is favourable for aircraft design as it allows for increased controlled manoeuvrability.

Kulfan (1979) investigated the effect of a variety of geometric parameters on the vortex formation over delta wings using different profiles and sweep back angles. The studies were conducted at subsonic speeds. A summary of the configurations tested is given in Appendix A.1.4.

When investigating the aerofoil nose radius Kulfan (1979) found that an increase in nose radius has a very powerful effect on reducing the development of the LEV (Figure 2.13). Figure 2.13 visualises this by plotting the lift coefficient against the semi-span fraction η_s. It can be seen that for NASA's Arrow Wing Aerofoil (AWA) configuration (rounded nose) the vortex

development starts at the tip at a higher lift coefficient and thus higher angle of attack than the configuration with a sharper leading-edge, such as the NACA 0003.36. (see for Figure 2.14 for the aerofoil shapes).

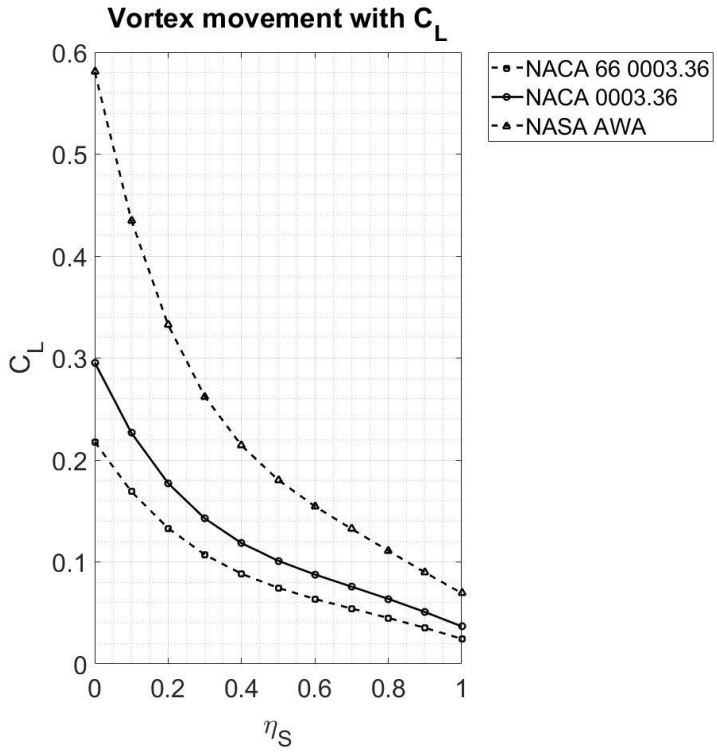

Figure 2.13 Effect of nose radius as a function of lift coefficient plotted against semispan fraction η_s adapted from Kulfan (1979).

Figure 2.14 shows that the lift is decreased when nose radius is increased. Here, t/c=0 and C_p are used as tramlines obtained from theoretical calculations using thin aerofoil theory and Polhamus' leading-edge suction analogy. Figure 2.14 indicates that the vortex induced drag decreases drastically with an increase in leading-edge radius (Kulfan, 1979), which is in accordance with the findings by Rinoei (1996a) and Wang and Lu (2005). In Figure 2.14, S_{REC} is the recovered suction factor (non-dimensional), where a value of one resembles little induced vortex drag and zero indicates high induced vortex drag.

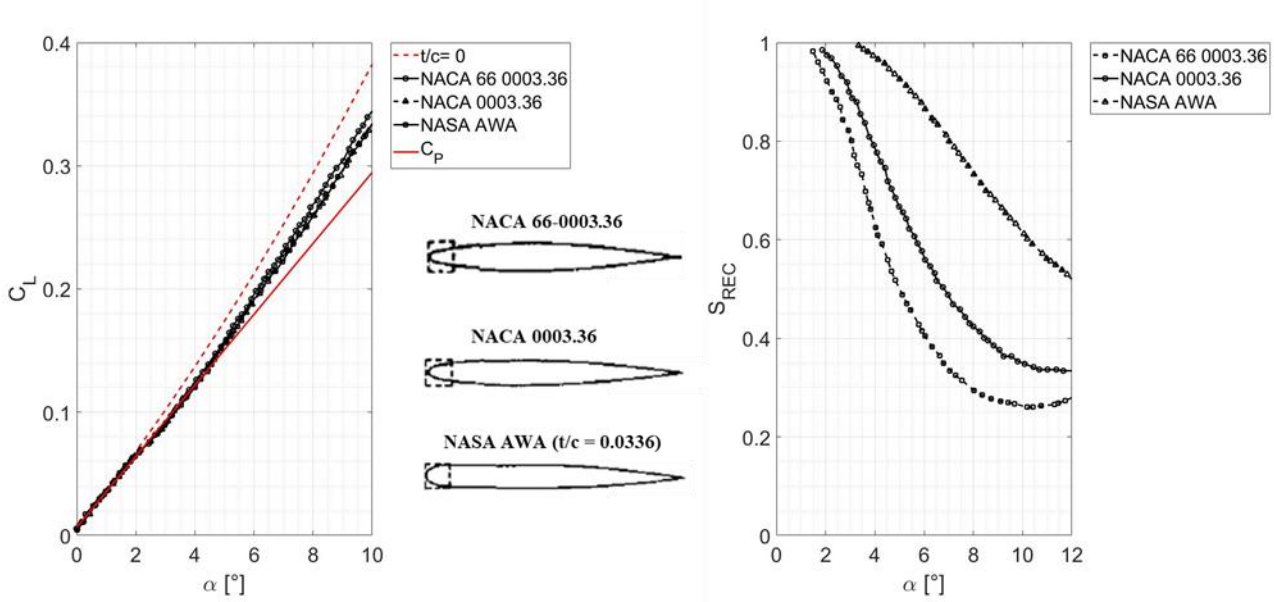

Figure 2.14 Lift curve slope for aerofoils of different leading-edge radius (Kulfan, 1979).

Kulfan (1979) also found that the amount of lift-induced drag generated depends on the LEV onset, indicating that the further downstream the onset point is, the higher the reduction in induced vortex drag.

Ridder (1971) examined the effects of different nose radius variations on the aerodynamic performance, whereby different nose radius variations were added to a thin flat delta wing. This resulted in bulbous type aerofoil sections as depicted in Figure 2.15.

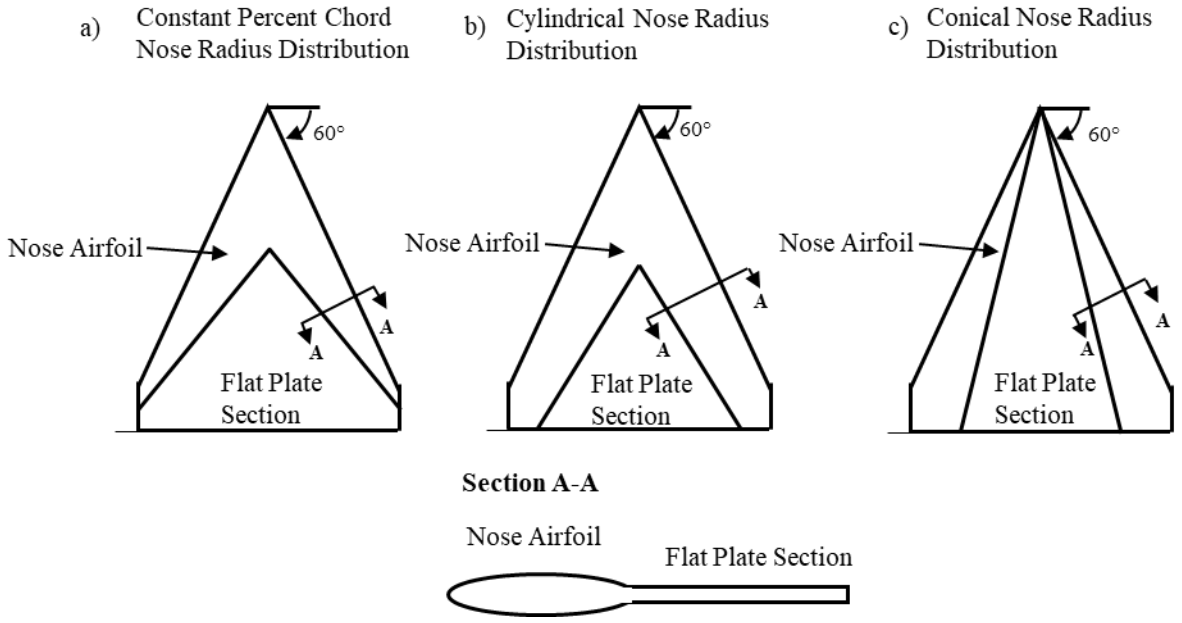

Figure 2.15 a) Conical Nose radius b) Cylindrical Nose radius c) Constant percent chord nose radius adapted from Kulfan (1979).

The nose radius variations included: constant percent chord nose radius, meaning the radius decreased linearly from root to tip, a cylindrical nose radius, which is constant across the span and a conical nose radius that increased linearly from root to tip and is depicted in Figure 2.15 above (Kulfan,1979).

Experimental investigations by Kulfan (1979) found that the vortex development rate varied significantly for each configuration. In particular the vortex onset varied in angle when it started occurring, as well as in location. For the two wings with nose radius down to the tip the vortex growth was retarded and it was concluded that an increased nose radius may be beneficial near the tip. Additional studies were conducted for wing warp effects such as twist, flap and camber effects (Kulfan, 1979).

2.3.1 Summary: Effects of leading-edge shape

Table 2.1 summarises the findings within the literature for different leading-edge radii. The structure of the tables is then the same throughout the chapter for different geometrical parameter effects investigated on delta wings. It will be explained here how to read the two tables and it is assumed that this should suffice to understand the tables in the following sections. The purpose of these tables is not only to visualise the current issue of finding relevant information easily but also to highlight the benefit of having a benchmark configuration such as AVT-113's VFE-2 configuration. It further showcases parameters which still require investigation in order to complete the tables, which by doing so, will enable researchers to detect patterns and make predictions fostering an easier design process.

The cell in the first column in row one in Table 2.1 shows the parameter which is changed, for Table 2.1 this is the nose radius, r. In The remainder, column one lists the specific parameters used to measure the changes in the flow when the nose radius, r, is increased.

The other columns show the observed relation between those parameters and the change in nose radius where:

- red indicates a decrease in parameter when increasing nose radius,
- yellow indicates that no change has been observed and
- green that the parameter increases with nose radius.

Notes in a coloured cell indicate the special conditions for which this change was observed. A cell is left blank when no information is available on that parameter.

Other columns are used to display the results from various studies which have investigated the same parameter change. For example, in Table 2.1, the results of six different papers are presented. Column five captures the results from paper 4 which details results of a delta wing with a 70° sweep. Looking down column five it can be seen that as the nose radius increases, the value of the lift coefficient Cl is unaffected (yellow cell) but the angle of attack at which VBD is seen, α_{VBD} increases in value (green cell).

It is important to state that these papers were chosen based on whether they explicitly mentioned to investigate the effect of a certain geometric parameter and only their conclusions have been marked in the table. This is particularly relevant as a lot of these papers do provide additional data but do not evaluate it regarding their change with the parameter under investigation. Also, the tables presented here are not showcasing every paper published on this topic but is limited to those which could be easily obtained, mentioned that they investigated the change in a geometric parameter, and focused on a simple delta wing geometry only.

In the legend to Table 2.1 the set-up information on the profile shape, Reynolds number etc. are detailed. So e.g. column five presents data from the Kegelman & Roos (1989) paper.

It can be seen that most studies test for different features and there is rarely consistency in leading-edge shape, thickness or Reynolds number. This makes cross-comparison impossible. Note the discrepancy in findings by Kulfan (1979) and Kegelman and Roos (1989). The former claims there is a decrease in lift coefficient with increasing nose radius whereas the latter established that the lift is independent of nose radius. However, Kulfan (1979) investigated wings with a curved profile whereas Kegelman and Roos (1989) used a flat plate configuration. Also, the speeds were significantly different. However, this may hint that overall profile shape may have an effect on lift generation and shall be further investigated. The key findings for RLEs are summarised in Table 2.2. Note, that studies on the effect of different leading-edge radii are ongoing, most of them using the VFE-2 configuration as a test case as it is designed for interchangeable leading-edges. Therefore, the year of publication is not an indicator of the latest research conducted in this field.

Table 2.1 Comparison of different nose radius studies.

increase / r	Paper 1 Λ= 70°	Paper 2 Λ= 50°	Paper 3 Λ= 65°	Paper 4 Λ= 70°	Paper 5 Λ= 60°	Paper 6 Λ=60°, 76°, 76.5°
C_l						
C_d						
C_m						
$C_{d_{vortex}}$						
C_S **Vortex Lift:** $C_{l_v} = C_s \cos(\alpha)$						
α_{VBD}						
Vortex size						
C_a						
C_n						
Vortex location			outboard			
Vortex Onset						
Longitudinal Stability						

Increase in Value
Decrease in Value
No change in Value
No Data Available

Legend						
	Paper 1	Paper 2	Paper 3	Paper 4	Paper 5	Paper 6
Re_{MAC}		2.1×10^5		$Re_{root} = 3.9 \times 10^5$	$Re_{root} = 2 \times 10^6, 3 \times 10^6$	2.3×10^6
t or t/c	3.36%	2%, 6%, 7%, 10%	3.4%	1.77%	4.8%	N/A
LE Profile	RLE	Windward bevel and leeward bevel	VFE-2	Round, square leeward bevel windward bevel, symmetric bevel	MRLE and RLE	Round and symmetric bevel
LE Radius	MRLE, RLE	SLE	SLE/ RLE	SLE, RLE	2.5mm and 7.5mm	SLE/RLE
Profile	NACA 66-00-XX NACA 00XX NASA Arrow Wing Aerofoil	Windward bevel and leeward bevel	Flat Plate	Flat Plate	Flat Plate	Flat Plate
M	0.2		0.25			
Λ	70	50	65	70	60	60, 76, 76.5
Author	Kulfan (1979)	Wang (2005)	Hummel (2008)	Kegelman and Roos (1989)	Rinoie (1996a)	Ericsson and King (1992)

Table 2.2 Special Remarks regarding RLEs.

Special Remarks for rounded leading-edges (RLEs)
Multiple vortex structure
Secondary vortex forms after primary vortex
An inner vortex forms ahead of the primary vortex, which rotates in the same direction as the primary vortex and decays once the primary vortex forms

Flow stays attached until a certain chord position which is a function of Re, M, α and leading-edge profile
Flow structure is dependent on boundary layer status (laminar or turbulent)
Flow separates at the tip first at high α

2.4 Delta Wing Aerodynamics: Slender and Non-slender Wings

Literature addressing the vortical flow around delta wings makes a distinction between slender and non-slender planforms, depending on their sweep angle.

Williams (2008) and Gursul (2007) explicitly state that a slender wing is defined as a wing with sweep angle equal to or greater than 65° and a non-slender wing with sweep angle equal or below 55°. However, no explanation or derivation of why is offered in these papers. It is also not clear as what configurations are defined which have a sweep angle of $55° \leq \Lambda \leq 65°$. In numerous investigations an angle between 65° and 70° is used for the sweep angle, however, again, no explanation is given as to why (Luckring, 2003; Saha and Majumdar, 2012; Gresham et al., 2010). Williams (2008) and Gursul (2007) offer some explanation why specific angles are defined, by referring to the work done by Earnshaw and Lawford (1966), Huang et al. (n.d.) and Taylor et al. (2003). Gursul et al. (2005) compared the normal force coefficient obtained in the studies by the aforementioned authors, who were investigating the effect of wing sweep on different profiles. The studies of Earnshaw and Lawford (1966) were conducted at Re=$(0.2 - 0.5) \times 10^6$, whereas the studies by Taylor et al. (2003) were conducted at $\mathrm{Re_c} = [4{,}300 - 34{,}700]$ and no information was found for Huang et al. (n.d.). To investigate the effect of sweep at low Re the difference between maximum normal force coefficient at stall and at zero incidence, $\mathrm{C_{N,max}} - \mathrm{C_{N\,0}}$, was plotted as a function of sweep angle (Figure 2.16), to account for the different profile shapes used in each study. It can be seen that the slope in Figure 2.16 is steepest between 55° and 60°, indicating that these results are due to a change in behaviour between slender and non-slender wings (Williams, 2008).

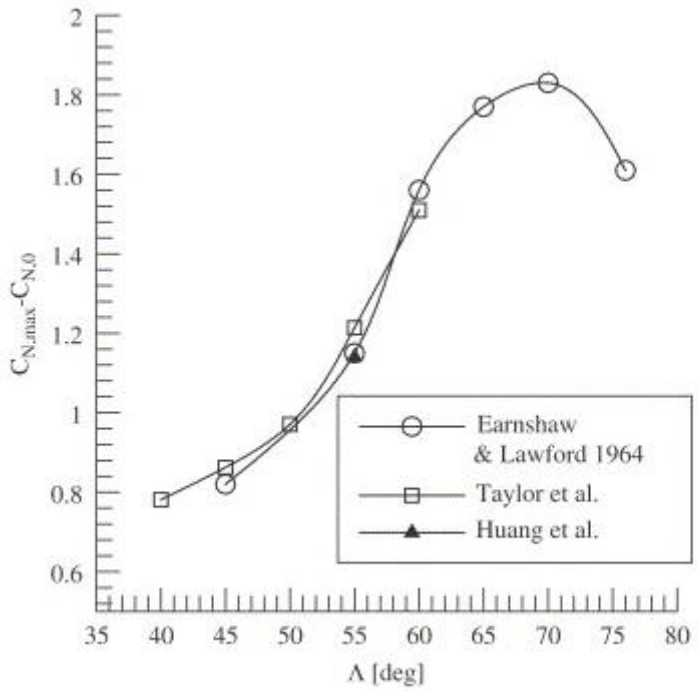

Figure 2.16 Effect of sweep angle on normal force coefficient (Gursul et al.,2005).

Earnshaw and Lawford (1966) investigated additionally the normal force fluctuations for different sweep angles, which are relevant to the problem of buffeting. They observed sharp kinks in the curves for 55° and 60° at angles of attack of about 12° and 15° as highlighted by the circled area in Figure 2.17. Also, a sharp rise in the normal force is observed between 10° and 20° (and subsequent steep drops between 30° and 40°) for leading-edge sweep angles of less than 65° (Figure 2.19). Note that the graphs are reproduced from the original paper and may not be fully accurate. Also note, that though pitching moment and drag force were provided in this study the axial force component was not.

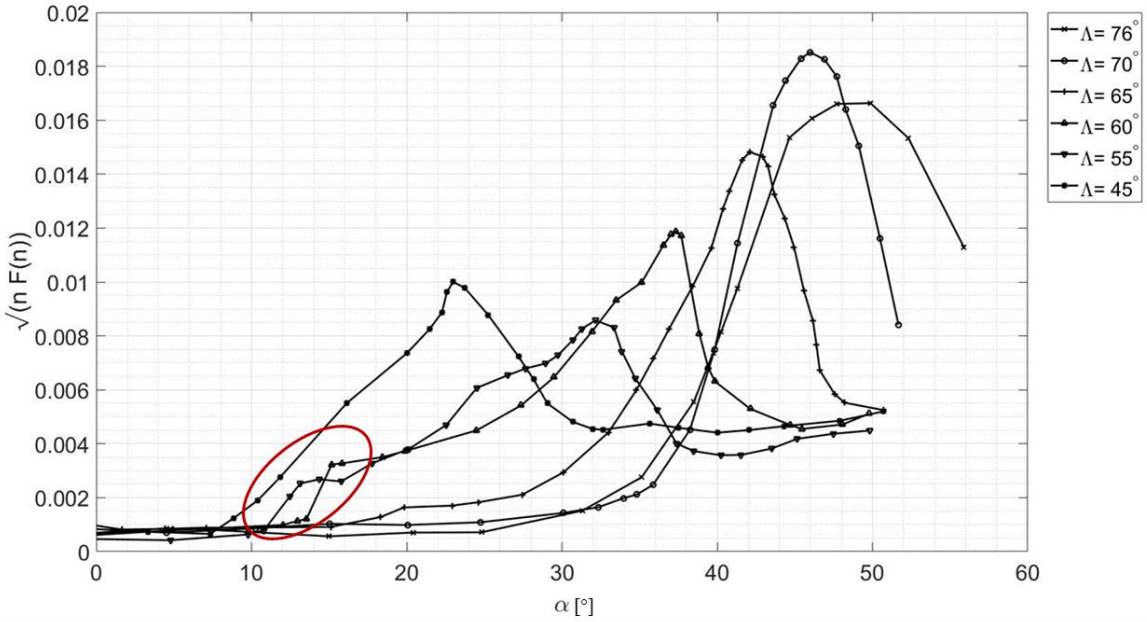

Figure 2.17 Variation of low-frequency component of normal- force fluctuation with angle of attack at frequency parameter n=0.05, where $\sqrt{\Delta C_N{}^2} = \sqrt{\left(nF(n)\right)}$ (Earnshaw and Lawford, 1966).

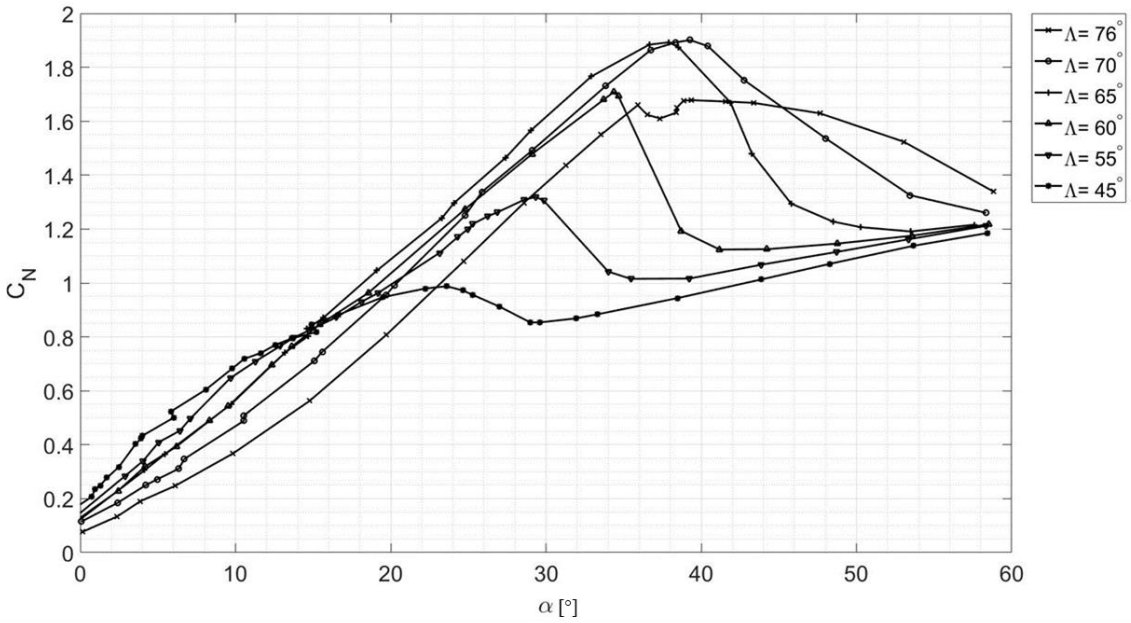

Figure 2.18 Variation of Normal Force with angle of attack adapted from Earnshaw and Lawford (1966).

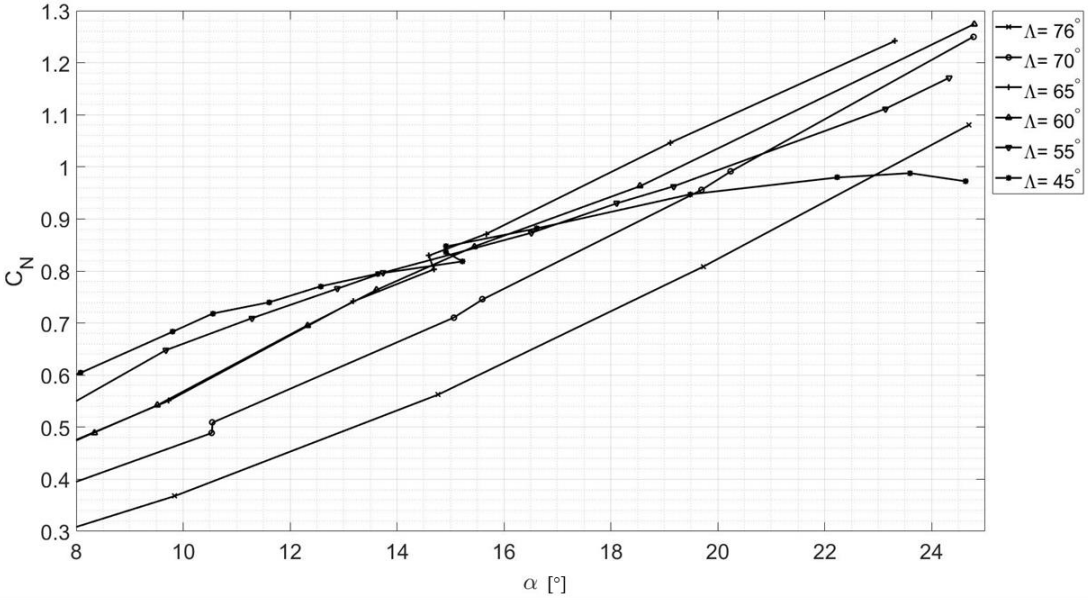

Figure 2.19 Replotted variation of Normal Force with angle of attack between 10° and 20° angle of attack using data from Earnshaw and Lawford, (1966).

Also, Taylor and Gursul (2004) and Huang and Hanff (1998) analysed the effect of wing sweep on the maximum normal force on delta wings. According to Williams (2008) the greatest rate of change in normal force coefficient with sweep angle occurs between 55 and 60 degrees. He assumes that this could be the result due to change in behaviour between non-slender and slender wings, thus defining non-slender wings as having sweep back angles $\Lambda \leq 55°$.

Another approach of distinguishing slender from non-slender wings is made by Gursul (2005) as discussed in section 2.3.1 "Flow Physics of Slender Delta Wings". He suggests that the breaking point between slender and non-slender wings is at an angle at which the VBD starts whilst the flow does not reattach again. However, Yaniktepe and Rockwell (2004) determined that VBD starting at the apex of the wing occurs more explicitly for high angles of attack for delta wings with sweep angle $\Lambda \leq 50°$, thus giving a different distinction criterion for slender and non-slender wings.

Ol (2001) conducted water tunnel tests on a 50° and 65° delta wing. He reported that the flow field features progressively diverged for the two sweep angles as incidence increased (as shown in Figure 2.20).

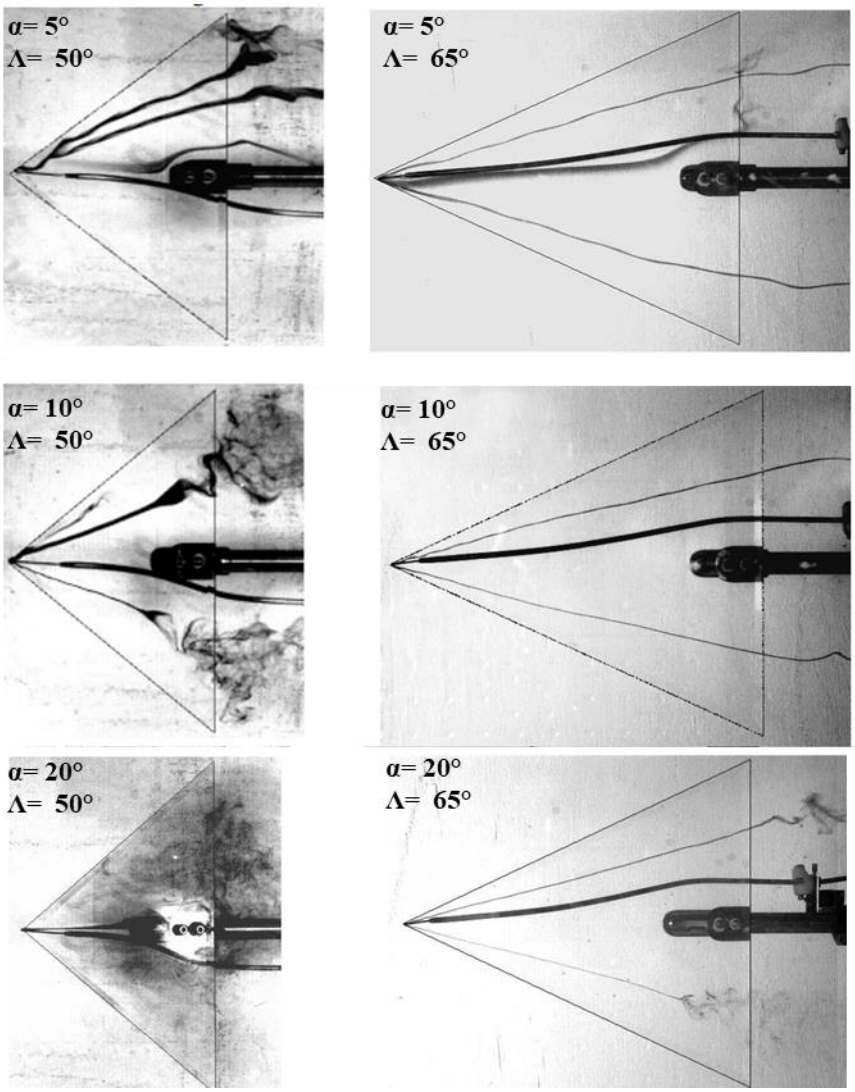

Figure 2.20 Dye streaks following primary leading-edge vortices for 50° (left column) and 65° (right column) wings at α=5°, 10° and 20° with nominal turbulence intensity of 1% in the test section (Ol, 2001).

A stable separated vortical flow can be observed for the 50° wing at $\alpha \leq 10°$. However, the axial velocity component of their vortex core never exceeds free stream velocity. By increasing α, first a decay of the secondary vortex can be observed accompanied by an upward movement of the VBD point. Ol (2001) concluded that between 12.5-15° the VBD becomes unsteady, meaning its onset location is oscillating. By 15° the breakdown-like state appears over the entire planform as shown by the left picture for 20°. Also, the leading-edge shear layer and the leading-edge vortices are close to the wing surface for low angles of attack and move further above the wing with increasing incidence. Another feature of wings having low sweep angle is that the axial velocity profile of the vortices is "wave-like" rather than "jet-like" as observed for slender wings (Ol, 2001).

Ol (2001) established three factors which are indications for the transition between a slender and a non-slender wing:

1. Stall is more abrupt for non-slender wings.
2. Non-slender wings show high unsteadiness prior to stall.
3. A coherent leading-edge shear layer is present long after VBD for non-slender wings.

As can be seen from the discussion of current literature, there is no consensus about the angle criteria distinguishing slender from non-slender wings.

However, there seems to be a general agreement that under 55 degrees is non-slender and over 65 degrees is slender, which leaves a range between these angles which is unaccounted for.

2.4.1 Flow Physics of Slender Delta Wings

For small α, the primary reattachment line is located inboard of the leading-edge vortex, as shown in Figure 2.21. With increasing α, the reattachment point A, in Figure 2.21 (a), moves further inboard until it reaches the centreline at a certain angle of attack α_R. For $\alpha > \alpha_R$ the reattachment point moves away from the wing surface as depicted in Figure 2.21 (b) (Gursul et al., 2007).

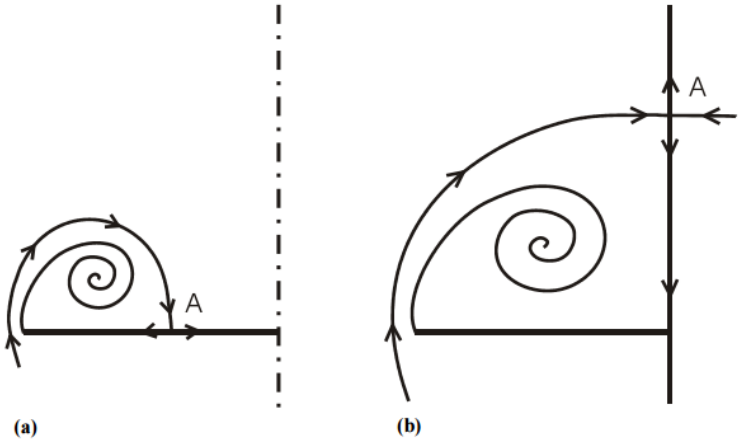

Figure 2.21 Schematic Streamline patterns for a slender delta wing (a) with reattachment at small α, (b) with no reattachment at high α (Gursul et al., 2007).

Figure 2.22 shows that α_R for slender wings (defined as $\Lambda \geq 65°$), decreases with increasing sweep (Mangler and Smith, 1959). It can be seen, that for highly swept wings no reattachment occurs beyond very small α. For wings with $\Lambda < 67°$ the reattachment of the LEV has not been measured and thus the dashed line is just theoretical. It can be seen though that for $\Lambda = 50°$ reattachment has been observed until about α=22°. Furthermore, Figure 2.22 shows that with the increase in sweep the onset of VBD is delayed. For slender delta wings, VBD is the main

cause for decreased lift and unsteadiness whereby the latter may result in wing and fin buffeting (Gursul, 2005).

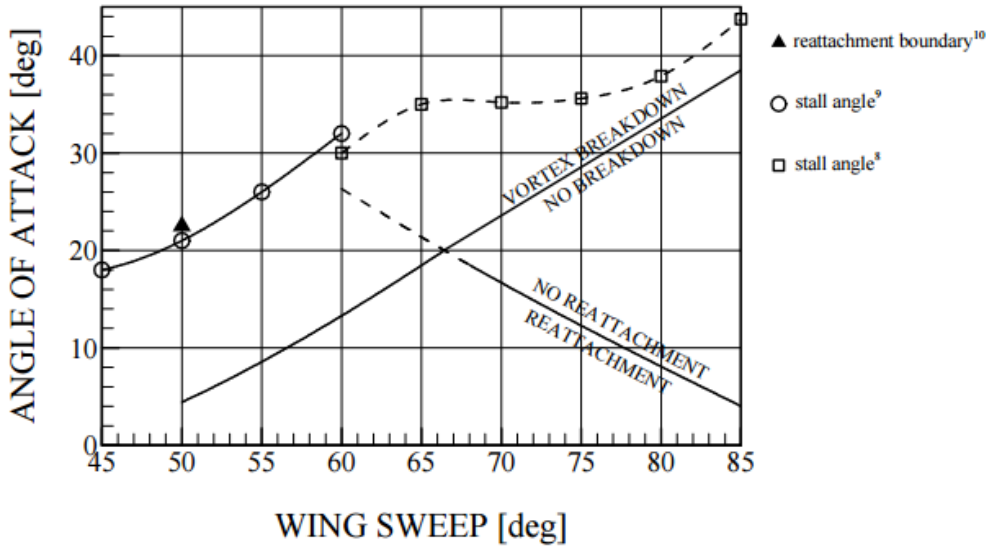

Figure 2.22 Boundaries of VBD and flow reattachment for slender wings as a function of sweep angle (Mangler and Smith, 1959).

2.4.2 Flow Physics of Non-slender Delta Wings

Non-slender delta wings are characterised by a wing sweep $\Lambda \leq 55°$ and are the subject of current research as their flow physics are less well understood than those of slender delta wings (Gursul et al., 2005). On non-slender wings vortical flows develop at very low α and form closer to the wing surface. The main difference in flow physics between non-slender and slender delta wings is on non-slender wings reattachment of the separated flow is possible even after VBD has reached the wing's apex. This is due to the fact that non-slender wings have a higher aspect ratio, resulting in a larger area thus allowing the flow to become more turbulent. The additional energy is fed into the boundary layer, resulting in reattachment.

For non-slender wings, the vortex lift contribution becomes smaller as sweep angle decreases. Also, VBD occurs at smaller α but there is no correlation between vortex burst onset and change in lift coefficient. This means the VBD is not a limiting factor with regards to lift and thus surface pressure distribution. As can be seen from Figure 2.22, for non-slender wings the flow reattaches almost until stall. This suggests that reattachment can be manipulated in contrast to slender wings where the flow does not reattach at low angles of attack (Gursul, 2005).

2.5 Geometry Effects

The following sections deal with the effects of different geometrical design aspects on the aerodynamic characteristics of delta wing configurations. Here, the focus lies on the forces and moments as well as on the change in flow physics. The geometric parameters considered are: sweep angle, maximum thickness, notch ratio and taper ratio.

2.5.1 Sweep angle effects

For slender sharp-edged wings the aerodynamic characteristics are non-linear and a significant amount of the lift is generated by the leading-edge vortices, as illustrated in Figure 2.23. Studies by Wentz and Kohlman (1968) for a series of 15° wedge-shaped flat plate delta wings with a 0.254 mm blunt edge of 25.4 mm thickness at Re=1×10^6 showed that an increase in sweep is accompanied by a decrease in lift curve slope as the circulation decreases with increasing sweep for a given α. Next to this, there is less area on a highly swept delta wing which behaves like a "normal", high aspect ratio, wing, meaning there is less attached flow. Also, the strength of the vortices is greater for lower sweep angles. However, stall is delayed for higher sweep back angles and the maximum lift obtained increases with sweep angle until a critical sweep angle is reached (75 degrees). After this a decrease in lift curve slope as well as in $C_{l_{max}}$ can be observed. It should be noted that it is unclear how and if the critical sweep angle of 75° still holds when leading-edge radius or thickness is changed nor how it varies with increasing Mach number. This may be particularly important as high swept back angles are more often used for high Mach number fighter aircraft rather than for subsonic aircraft (Kwak and Nelson, 2010). No studies have been found yet, which would investigate this and it can be seen from Figure 2.23 and Figure 2.24 that the lift and pitching moment coefficients are linear for low α, but turn non-linear when α is further increased (Polhamus, 1966; Kegelman and Roos, 1989; Wentz and Kohlman, 1968; Kohlman and Wentz, 1971). Here, the non-linear lift component seems to increase with increase in sweep. From Figure 2.24 can further be seen that the longitudinal stability increases with increase in sweep angle, indicated by the reduced pitching moment coefficient. Kulfan (1979) also conducted sweep studies for a NACA 0003.36 aerofoil and a thin delta with 14° lower surface bevel at M=0.1 (and an intermediate rounded leading-edge (RLE)) and additionally observed that the vortex induced drag increases with sweep.

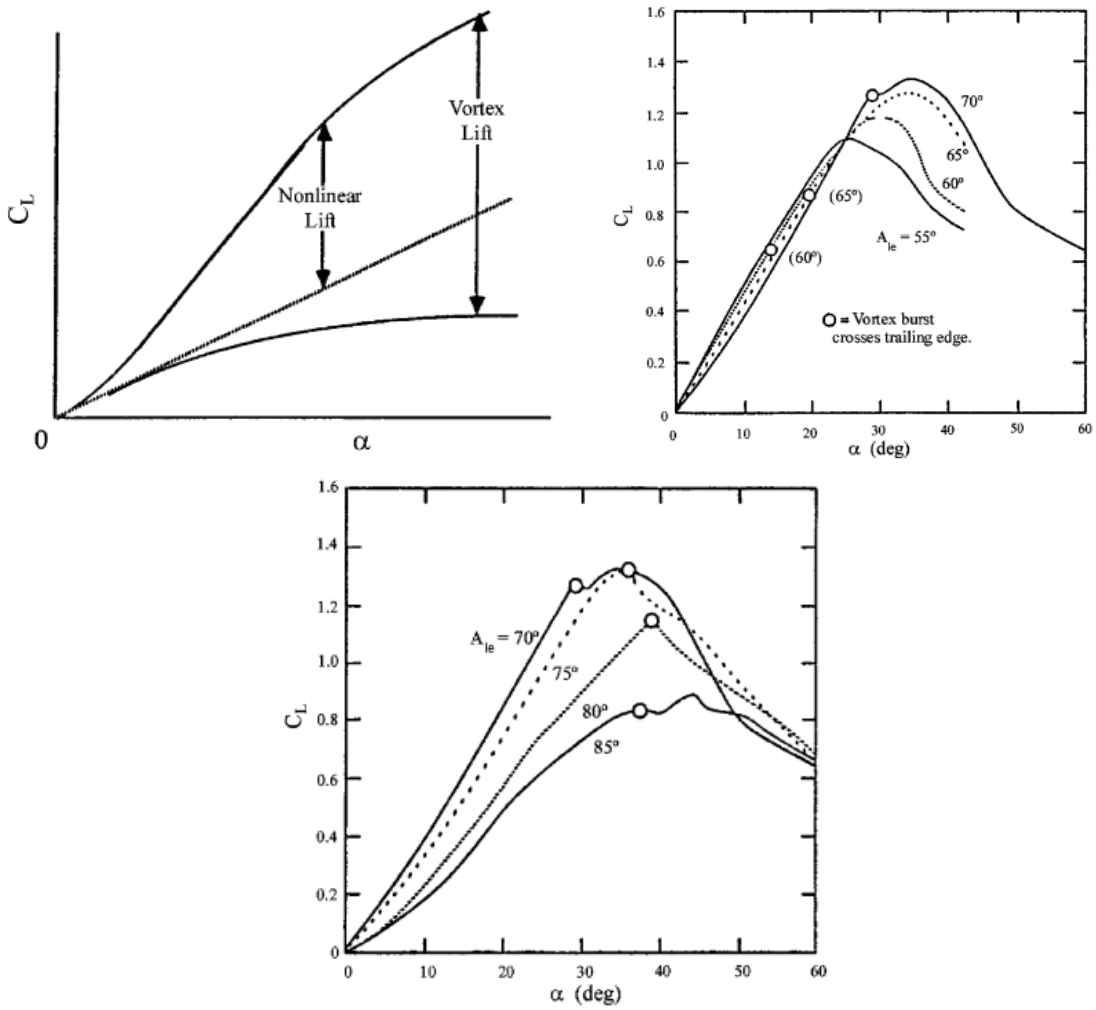

Figure 2.23 Top left: Sketch of non-linear lift, Top righ and Bottom left: Lift coefficient for a family of flat plate delta wings replotted by Kegelman and Roos (1989). Original by Kohlman and Wentz (1971).

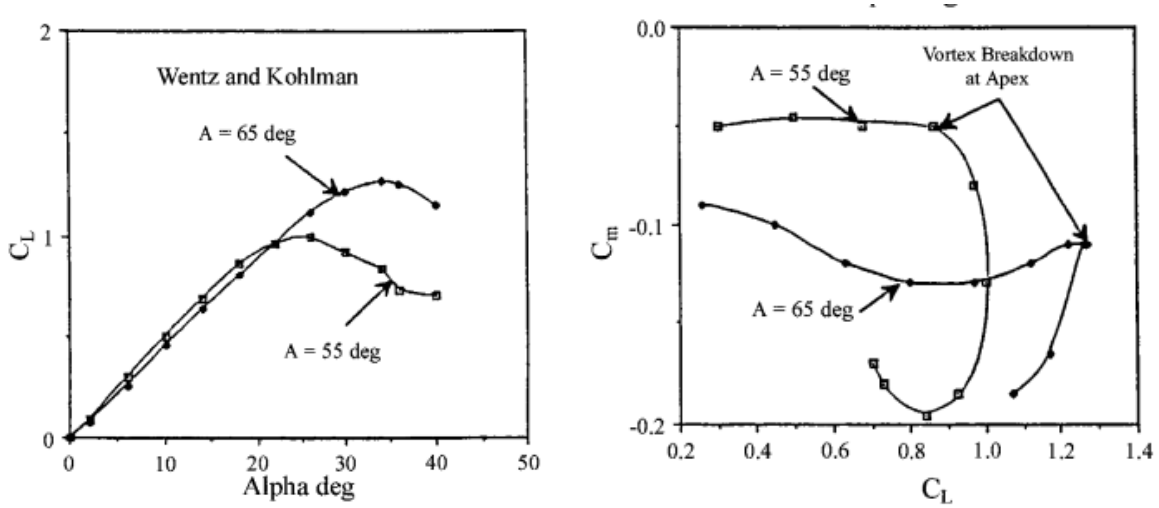

Figure 2.24 Lift and Pitching moment characteristics for two delta wings, Λ= 55° and Λ= 65° (Wentz and Kohlmann, 1969).

The lift coefficient of a cambered biconvex delta wing of 6% thickness is plotted against α for different sweep angles in Figure 2.25. It can be seen that lift increases when sweep decreases. This is due to the higher aspect ratio and larger potential for wings of reduced sweep.

In Figure 2.26 and Figure 2.27 the drag polar and the moment coefficient were replotted from Earnshaw and Lawford (1964). It can be seen that the lift-to-drag ratio L/D is more favourable for lower angles of attack and lower sweep back. However, this changes at higher α, presumably because for higher angles VBD has reached the trailing edge for lower sweep angles and is progressively moving towards the apex.

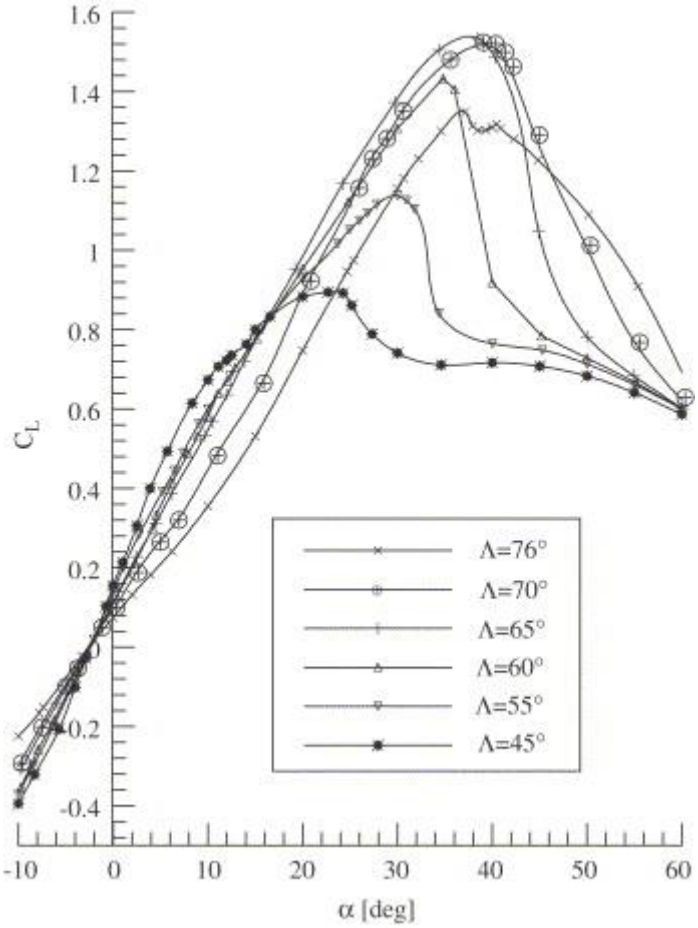

Figure 2.25 Lift coefficient vs. α at Re= 0.25- 0.5× 10^6 for different sweep back angles adapted from Earnshaw and Lawford (1964) by Gursul (2005).

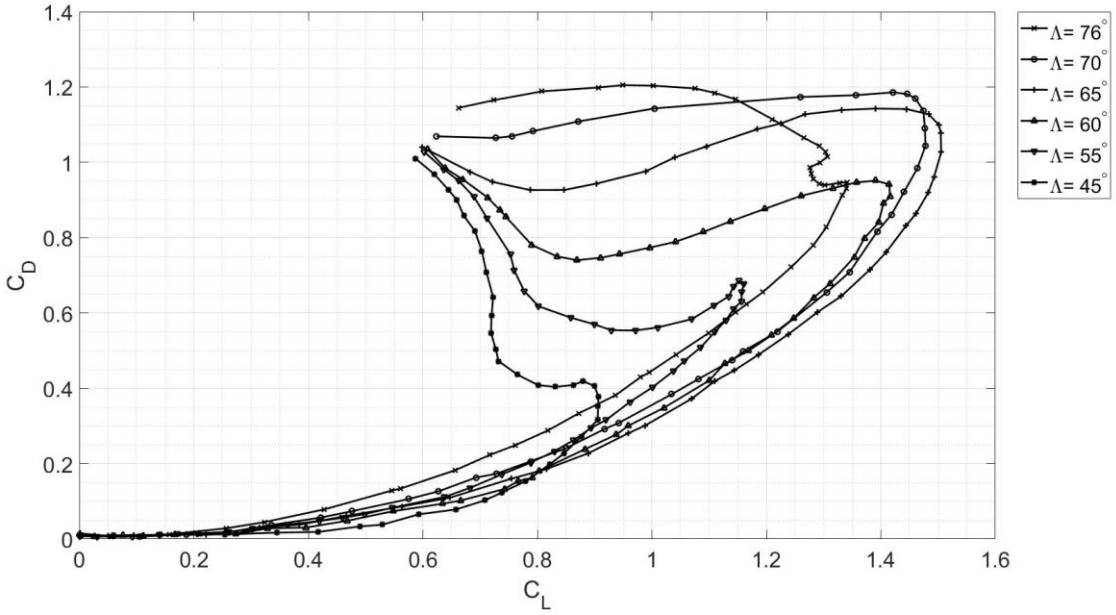

Figure 2.26 Drag polar for wings of different sweep angle adapted from Earnshaw and Lawford (1964).

Figure 2.27 shows the pitching moment coefficient for different sweep angles. Note, that it is not stated around which point the moment was measured. It is believed that the reference point may be $0.5c_{root}$ as it was stated that the model was positioned centrally between the struts (Earnshaw and Lawford, 1964). It can be seen that the slope is steeper for wings with low sweep, meaning that the suction force at the region close to the apex is higher for those configurations. This could be a result of increased circulation and thus increased lift for low sweep configurations (Goertz, 2005). Figure 2.27 shows that increase in sweep angle is beneficial with regards to longitudinal stability especially at high α with the effect becoming more impactful with increasing sweep back.

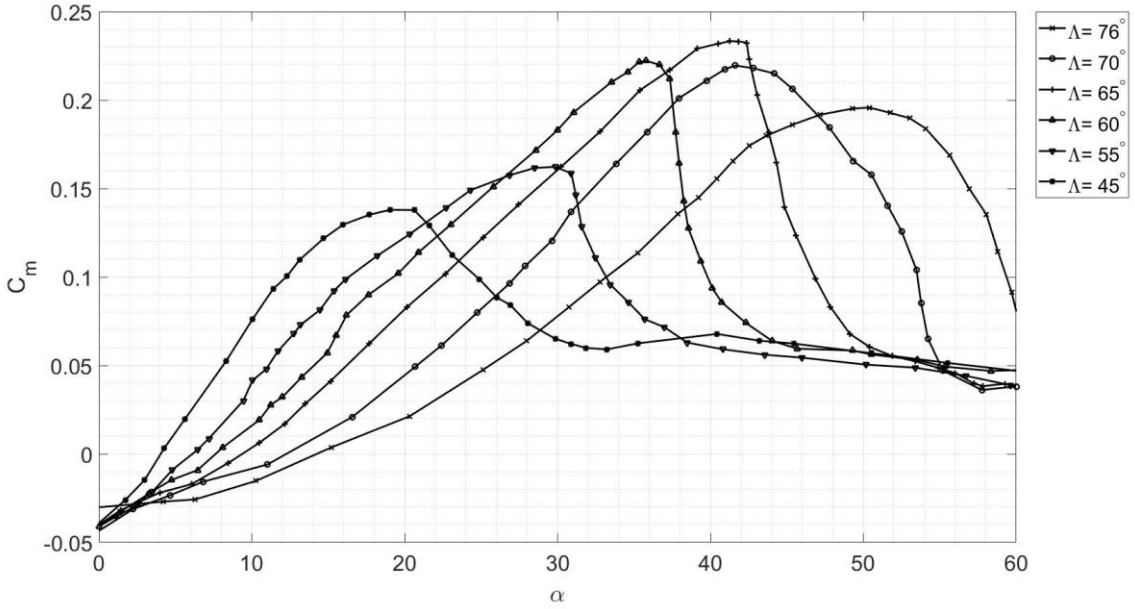

Figure 2.27 Change of pitching moment coefficient with α adapted from Earnshaw and Lawford (1964).

There is a decrease in vortex lift and vortex strength with increasing sweep angle for a given incidence (Hemsch and Luckring, 1990).

Zohar and Er-El (1988) investigated the influence of aspect ratio or sweep back on the loading of the delta wing and how the LEVs contribute to that loading and the effect of VBD on this. The wind tunnel tests were done at Technion at 32 m/s for wings with 55, 60, 70 and 74 degree sweep back and a thickness to chord ratio of 0.0192, 0.0187, 0.0172 and 0.0152 respectively. The angle of attack ranged from 0 degrees to the respective angles when VBD occurred. No information with regards to the profile shape is given in the published paper. However, Zohar refers to his Master thesis (Zohar, 1984) for more details, which is not available to the public. Figure 2.28 (from Kulfan, 1979) shows the influence of sweep (the lower the AR the higher the sweep angle) on the average L/D ratio, the angle at which VBD occurs at the trailing edge (α_{VB}) and the ability of VBD, when it crosses the trailing edge, to reduce the lift curve slope ($\Delta C_{N_{VB}}$). It indicates that the effect of VBD on the suction force generated by the LEVs decreases with increase in sweep angle. For highly swept wings the slope of $\Delta C_{N_{VB}}$ is lower than for wings with high AR. This may indicate that wings with high sweep back angle are preferable for aircraft designed for post-stall flight. The L/D ratio increases with a decrease in sweep angle. In highly swept wings the vortex-induced suction continues to increase with α (Zohar and Er-El, 1988). These findings are in accordance with those of Wentz and Kohlman (1968) and Earnshaw and Lawford (1964). The latter did their investigation on a plano-convex

wing with 6% thickness at $\mathrm{Re_{mac}} = [0.25 - 0.5] \times 10^6$. This suggests that although leading-edge radius, thickness and Reynolds number varied the same trends were observed.

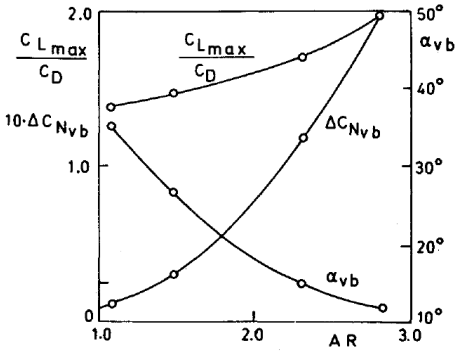

Table 1 Geometrical data for the experimental models

Model wing sweep angles, deg	A	CR, mm	t/Cr
55	2.80	239	0.0192
60	2.31	246	0.0187
70	1.46	268	0.0172
74	1.07	302	0.0152

Figure 2.28 Influence of sweep angle on the average L/D ratio (Kulfan, 1979).

Kulfan (1979) investigated the effect of the geometry on the vortex formation over delta wings. Delta wings with different profiles and sweep back angles were investigated and compared. The main focus was on a NACA 0003.36 aerofoil, which has an intermediate rounded leading-edge, and the studies were conducted at subsonic speeds. Again, the reader is referred to Appendix A.1.4 for a summary of the configurations tested. It was found that the net vortex drag equals the net vortex lift for a wide range of α and for various sweep angles, thus, making vortex lift production relatively inefficient. The study also concluded that for sweep angles smaller than 80° the induced drag ($\frac{\Delta C_D}{C_L^2}$ due to the LEV shown in Figure 2.29 (a)) is a minimum when the leading-edge suction force C_s is in the plane of the wing (see Figure 2.29 (b)). For sweep angles above 80 degrees, minimum induced drag is generated when the suction force is at 90 degrees, normal to the plane of the wing. A general observation for a variety of sweep angles is that when reducing the orientation angle of the suction force, the vortex force changes from a lifting component to a drag reducing component. Thus, the vortex lift vector will sacrifice lift but reduce drag. The results also indicate that tilting the vortex lift vector forward has the highest benefits in terms of induced drag reduction for lower lift coefficients. They also imply that for sweep angles which are of interest to aircraft design (less than 76 degrees) minimum induced drag is achieved when vortex formation is suppressed completely, which is the case for a suction force acting in the plane of the wing. However, it is difficult to retain fully attached flow out to the wing tip for delta wing configurations. Therefore, the best solution would be to reduce the vortex development (Kulfan, 1979).

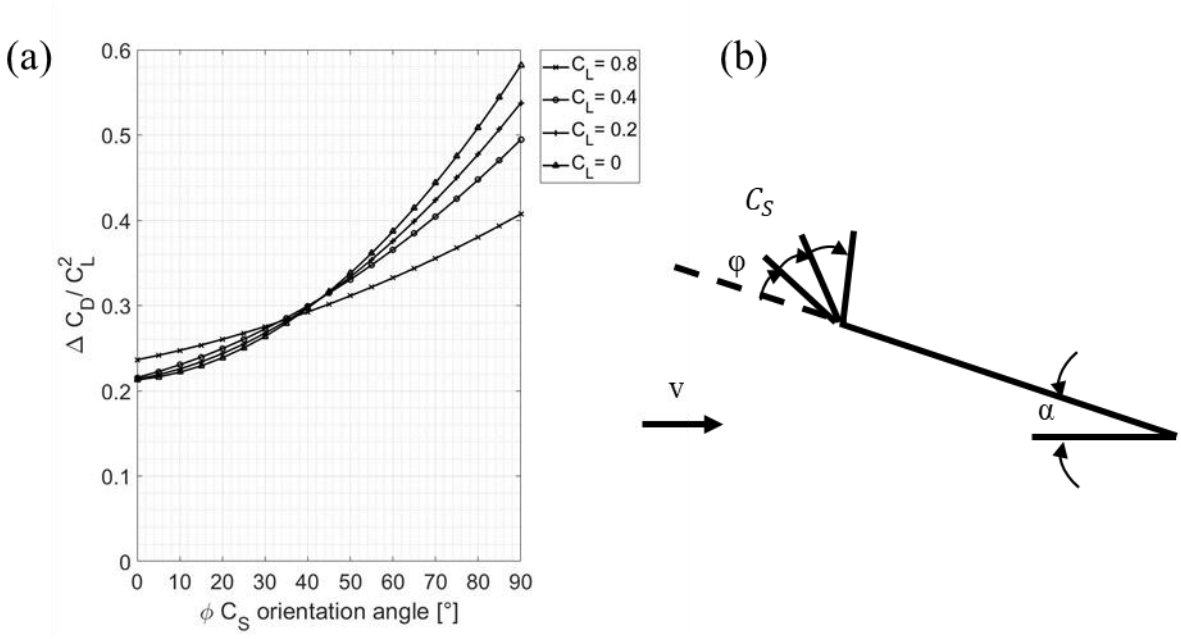

Figure 2.29 (a) Orientation angle of the leading-edge suction force (b) Effect of vortex lift angle for a 70° Delta Wing with $\Delta C_D = C_D - C_{D_0}$ adapted from Kulfan (1979).

Generally, it was observed that the suction factor K_v (see Polhamus suction analogy equation in equation (2.4)) of the vortex seems to be insensitive to sweep angle. As the vortex lift of thin sharp-edged delta wings is directly related to K_v for sharp-edged wings it can be said that they are not sensitive to change in sweep.

With regards to the flow physics Kulfan (1979) observed that for equal α it is shown that the LEV moves inboard when sweep angle is reduced but that the vortex onset is insensitive to change in sweep angle. However, no inboard movement is observed when plotting the vortex origin against the lift coefficient. The reason for the inboard movement of the vortex for reduced sweep angle is not given by Kulfan nor is it clear how the vortex position is measured. Findings by Brett and Ooi (2014) suggest that the increased velocity component normal to the leading-edge delays the reattachment of the separated flow.

Investigations on the VFE-2 configuration for sweep angles 43°, 45°, 50°, 55°, 60° and 65° were conducted at $Re_{mac} = 2.85 \times 10^6$ and M= 0.25 computationally as well as experimentally (Brett and Ooi, 2014). Only an angle of attack of 10° was investigated. The study mainly focused on the change in flow physics with sweep angle. It is found that with decrease in sweep back the leading-edge vortex generated a stronger suction near the apex and a reduced strength near the trailing edge as depicted by the surface Cp plot in Figure 2.30, where reduced surface pressure is associated with the presence of a LEV. However, drawing conclusions from Cp contours and surface streamlines alone is difficult. For a more thorough

evaluation of vortex onset the use of other visualisation techniques, such as the spanwise Cp distribution and vorticity/Q- criterion contours at different chord positions, would be required. The Q-criterion is a method of identifying vortex structures. The method is used to identify vortices as areas where the vorticity magnitude is greater than the magnitude of the rate-of-strain. Therefore, the Q-criterion represents the local balance between shear strain rate and vorticity magnitude. Mathematically, this is described by a positive second invariant of the velocity gradient tensor (Hunt et al., 1988; Kolar, 2007).

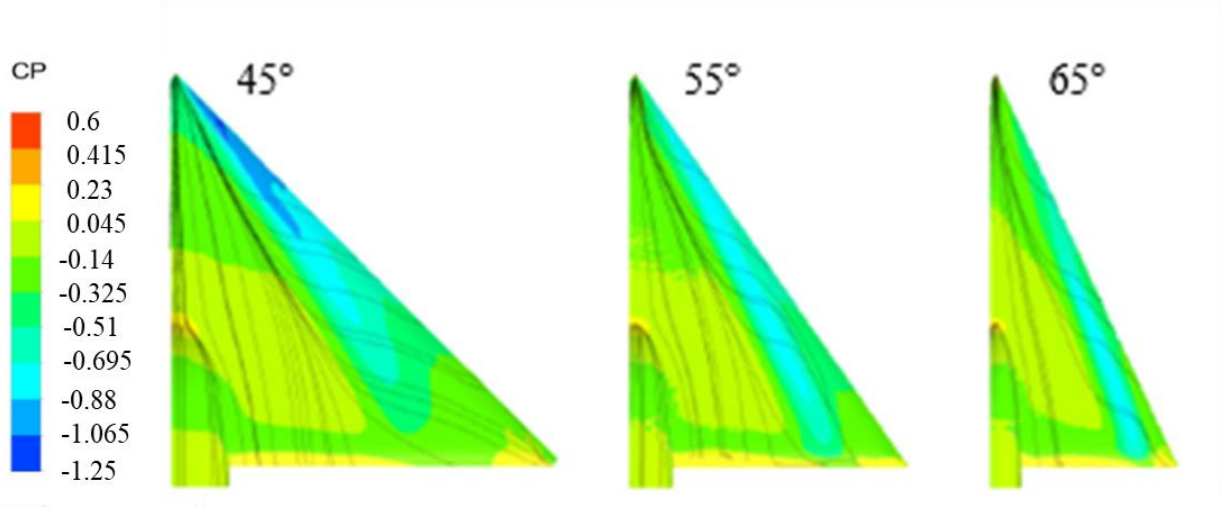

Figure 2.30 Coefficient of pressure and wall shear surface streamlines at α=10°, Re=2.85× 10^6 and M=0.25 for three different sweep angles (Brett and Ooi, 2014) (blue lowest pressure, orange highest).

Figure 2.31 visualises the vortex for two different sweep angles. The most apparent difference is that for the 45° delta wing three vortices can be observed. The primary vortex is labelled A and the more concentrated vortical structure formed by the separation of the shear layer at the leading-edge is labelled B. They can be observed for both delta wings. The vortex structure labelled C forms between the leading-edge and primary vortex for the 45° configuration and is referred to as a shadow vortex. It is weaker than the primary vortex and follows approximately the path the primary vortex would take if it did not detach. A decrease in sweep increases the free stream velocity component perpendicular to the leading-edge which results in a primary vortex which is further stretched towards the centre line. At a critical sweep angle combined with a certain α, the vortex becomes over-stretched and an additional roll up occurs forming the shadow vortex, resulting in vortex bursting of the primary vortex (Brett and Ooi, 2014).

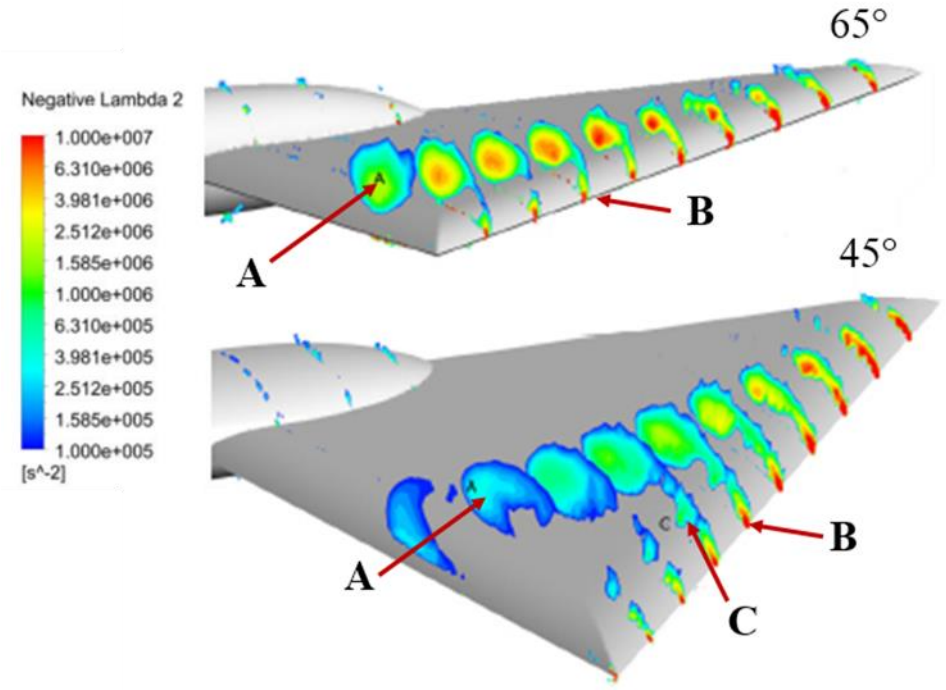

Figure 2.31 Vortex visualisation using the negative λ_2 criterion at different chordwise locations for a 45° and 65° delta wing with SLE. (Brett and Ooi, 2014).

The shadow vortex is weaker in strength, thus, generating less vortex induced lift. This is visualised in the surface Cp by the higher pressure at the outer regions of the wing. The shift in Cp distribution yields a shift in pitching moment towards the apex. It can also be seen that the shadow vortex forms at a chordwise location where vortex bursting occurs (see Figure 2.31). Vortex bursting is characterised by a reduced vorticity in the vortex core combined with a growth in diameter. It can also be seen from Figure 2.31 that the vortex rapidly increases in diameter around the 50-60% chord mark, which is further upstream than the point where the vortex moves away/detaches from the surface. Hence, when aiming to prevent vortex detachment a control mechanism has to suppress vortex stretching and forming of the shadow vortex (Brett and Ooi, 2014). It is worth noting that a similar effect, the generation of an additional vortex, appears for changing the leading-edge radius from sharp to round. However, the secondary vortex formed lies outboard of the primary vortex and not inboard. The formation of a shadow vortex has not been mentioned in any other papers which have been investigated for this literature review. This may be due to the fact that the main focus was on higher sweep back angles. However, it would be beneficial to know if other authors made the same observation or whether the shadow vortex is due to the geometrical features and ambient conditions of this particular study.

2.5.2 Summary: Sweep angle effects

From the literature review it can be seen that there is a variety of experimental data available for delta wings of different sweep angles. It could also be seen that many studies covered the effect of sweep. However, different wing profiles, sweep angles, thicknesses, and Reynolds numbers were used. Additionally, different papers focused on different flow aspects. A summary of the findings for different studies is presented in Table 2.3. Here the effects on different flow features can be seen with increase in sweep angle (Λ). It is also stated whether the geometries had a round or a SLE. It can be concluded that there is not a great consistency in the features measured although it seems that apart from the vortex onset location all papers agree on the trend of certain features when increasing sweep angle. The legend, also shown in Table 2.3, states the author of the papers as well as the test conditions. It can be seen that the experiments were done on thin wings only and at low Reynolds numbers. It is known that the vortex behaviour depends on the type of boundary layer (Hummel, 2004). However, the studies presented here did not test for boundary layer type (i.e. laminar or turbulent) which is another limitation when wanting to draw general conclusions from the studies. As for the leading-edge shape the key findings are summarised in Table 2.4.

Table 2.3 Comparison of different sweep angle studies.

increase Λ	Paper 1 RLE		Paper 2 SLE	Paper3 SLE	Paper 4 SLE	
C_l						
$C_{l_{max}}$	Λ $< 75°$	Λ $> 75°$				
C_d						
C_m						
$C_{d_{vortex}}$						
C_S Vortex Lift: $C_{l_v} = C_s \cos(\alpha)$			in plane for min $C_{d_{vortex}}$ for Λ< 80 normal for min $C_{d_{vortex}}$ for Λ< 80			
α_{Stall}						
L/D			At low α			
Vortex strength						
α_{Stall}						
L/D			At low α		At low α	
C_a						
C_n						
Vortex location			Inboard			
Vortex Onset						
Velocity perpendicular to LE						
Normal force fluctuation					Λ $< 65°$ sharply	Λ $> 65°$ slowly

Increase in Value
Decrease in Value
No change in Value
No Data Available

Legend				
	Paper 1	Paper 2	Paper 3	Paper 4
Re_{MAC}	1×10^6		0.285×10^6	$0.25 - 0.5 \times 10^6$
t/c	~1.6%	1%	3.4%	6%
LE Profile	15° wedge	14 ° lower surface bevel	VFE-2	
LE Radius	RLE	SLE	SLE	SLE
Profile	Flat Plate	Flat Plate	Flat Plate	Plano-convex
M		0.1	0.25	
Λ	50, 55, 60, 65, 70, 75, 80, 85	67.4, 71.6, 76	45, 55,65	45, 55, 60, 65, 70, 76
Author	Wentz and Kohlmann (1971)	Kuflan (1979)	Brett and Ooi (2014)	Earnshaw and Lawford (1964)

Table 2.4 Special remarks regarding change in sweep angle.

Special Remarks
A shadow vortex is observed for the VFE-2 facet for $\Lambda <= 45°$
The LEV detaches on the VFE-2 facet for $\Lambda <= 45°$

2.6 Maximum Thickness and its effects

Kirby and Kirkpatrick (1969) investigated the effect of thickness on the subsonic longitudinal stability characteristics of a 70° swept back delta wing. For this, five symmetrical wings were investigated of which three were biconvex. They tested four wings with the same thickness distribution with the maximum thickness to chord ratios being 4, 8, 12 and 16 percent and a fifth wing of 4% thickness, where the edge angle was changed to be similar to that of the 8% thick wing (Figure 2.32). The tests were conducted at two speeds resulting in a Reynolds number, based on the root chord, of $2.24x10^6$ and $1.14x10^6$ over an α range from α= -5° to 26°. They concluded that with increasing thickness the forward component of the suction forces generated by the leading-edge vortices increases in the direction of the plane of the wing resulting in reduced induced drag. Also, with increase in thickness the centre of pressure moves upstream when being within the linear region of the lift curve (low lift coefficients), whereas it moves downstream when being in the non-linear region (high lift coefficients). Thus, the longitudinal stability is reduced for low α with increasing thickness but increased for high α, which are encountered during rapid manoeuvring and take-off and landing (Kirby and Kirkpatrick, 1969). Wang (2005) investigated the effect of thickness on a 50° swept back delta wing with blunt trailing edge and different leading-edge bevel angles (wings were bevelled leeward and windward) at $Re_{c_r}=2.1x\ 10^5$. Wind tunnel tests were conducted (in-coming flow turbulence intensity was less than 0.3%, no wind tunnel corrections were made) on thicknesses t/c=2%, 6.7% and 10% and only lift and drag were measured. It was found that C_D increases with thickness, thus, resulting in a decrease in the L/D ratio value (Wang, 2005).

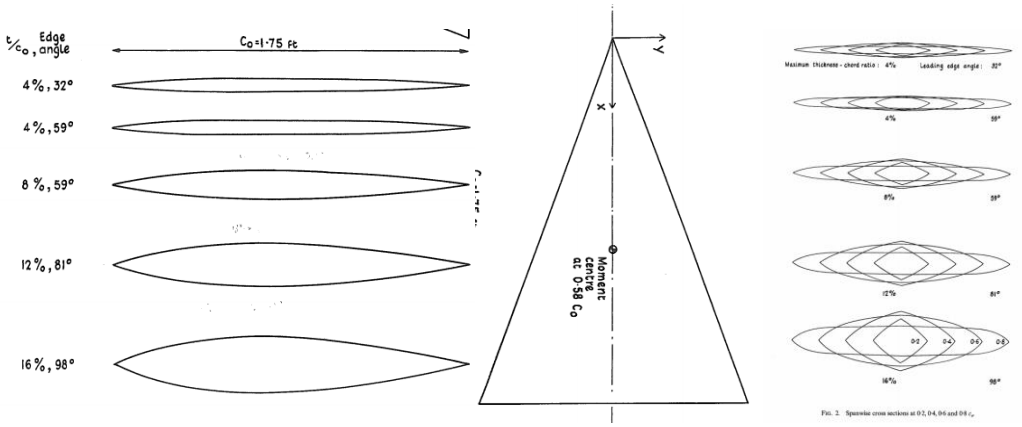

Figure 2.32 Kirby and Kirkpatrick (1969) a) chord b) planform c) spanwise cross-sections.

2.6.1 Summary: Thickness effects

An overview of the effects of thickness on different aerodynamic features is shown in Table 2.5 with the legend showing the geometric details and operating conditions. Unfortunately, there is no overlapping in the features investigated in the two studies. It would have been particularly useful as one study deals with a slender and the other one with a non-slender wing. However, there are major differences in the profile as the slender wing is biconvex (Kirby and Kirkpatrick, 1969) whereas the non-slender delta wing is a flat plate (Wang, 2005).

Table 2.5 Comparison of studies using different wing thicknesses.

increase / t/c	Paper 1 SLE Λ=70°		Paper 2 SLE Λ=50°
C_l			
$C_{l_{max}}$			
C_d			
C_m	At high α	At low α	
$C_{d_{vortex}}$			
C_S Vortex Lift: $C_{l_v} = C_s \cos(\alpha)$			
α_{Stall}			
L/D			
Vortex strength			
α_{Stall}			
L/D			
C_a			
C_n			
Vortex location			
Vortex Onset			
Longitudinal Stability	At high α	At low α	

Increase in Value
Decrease in Value
No change in Value
No Data Available

Legend		
	Paper 1	Paper 2
Re_{Root}	2.24×10^6, 1.14×10^6	2.1×10^5
t/c	4%, 8%, 12%, 16%	2%, 6%, 7%, 10%
LE Profile	biconvex	Beveled windward and beveled leeward
LE Radius	SLE	SLE
Profile	biconvex	Beveled windward and beveled leeward
Λ	70	50
Author	Kirby and Kirkpatrick (1969)	Wang (2005)

2.7 Effect of varying notch ratio

Kulfan (1979) further conducted studies on the NACA0003.36 for different notch ratios ζ. The notch ratio was calculated using

$$\zeta = \frac{\Delta c}{c_r} \tag{2.5}$$

Where Δc is the cut-out chord length and c_r is the root chord (also depicted in Figure 2.33).

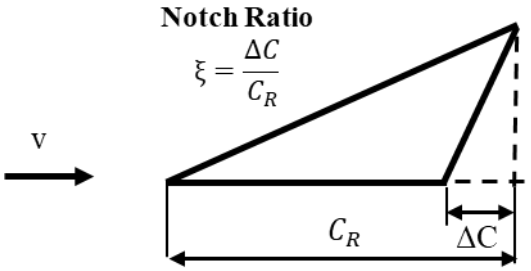

Figure 2.33 Definition of notch ratio adapted from Kulfan (1979).

It was found that the vortex delay is independent of notch ratio. Notching seems to have a slight effect on the lift generation whereby C_L increases with notch ratio. Additionally, the vortex induced drag is smaller for higher lift ratios for a given C_L .

2.7.1 Summary: Varying notch ratio effects

For consistency the findings are summarised in Table 2.6. The key findings are that lift increases and that the drag due to vortex lift decreases with increase in notch angle. The vortex retardation (delay in vortex onset) is independent of the notch angle. No further investigations on the effect of notch ratio have been undertaken as it is not relevant for the present study.

Table 2.6 Summary of findings for different notch ratios.

increase ζ	Paper 1 RLE Λ=70°
C_l	
$C_{d_{vortex}}$	

	Increase in Value
	Decrease in Value
	No change in Value

Legend	
	Paper 1
M	0.2
t/c	3.36%
LE Profile	RLE
LE Radius	RLE
Profile	NACA 0003.36
Λ	70
ζ	0, 0.2, 0.4
Author	Kulfan (1979)

2.8 Effect of varying Taper ratio

Next, wing taper ratio was investigated at M=0.2 as depicted in Figure 2.34. It was found that tapered wings experience a vortex on the streamwise tip. This vortex is not affected by aerofoil shape as it is parallel to the streamwise flow. However, it contributes to the vortex lift. Though the leading-edge suction factor decreases with increase in taper ratio the overall vortex lift remains the same due to the increase in suction force generated by the tapered tip. This, is due to the formation of a tip vortex which contributes to the vortex lift. The pressure distribution is affected by an increase in taper and decreases in magnitude with taper increase. The peak of the suction distribution moves outboard with taper ratio and so does the vortex for tapered

wings. The vortex onset point is independent of taper ratio whilst the lift decreases and the drag increases with taper.

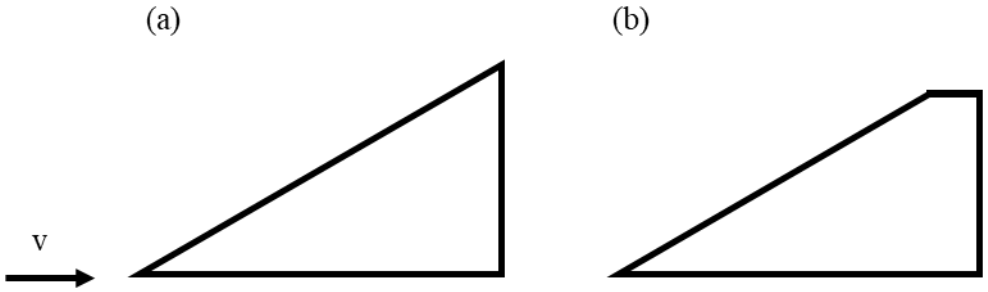

Figure 2.34 (a) Un-tapered and (b) tapered delta wing (Kulfan, 1979).

2.8.1 Summary: Taper Ratio Effects

As for the notch ratio the major correlations are summarised in Table 2.7. It can be seen that Kulfan (1979) tested for the most important aerodynamic parameters in her study. One of the key findings of the study is the generation of a tip vortex due to taper, which compensates for the LEV lift loss.

Table 2.7 Summary of findings for varying taper ratios.

increase / λ	Paper 1 RLE Λ=70°
C_l	
C_d	
$C_{d_{vortex}}$	
C_s	
Nose suction distribution	
Vortex Location	outboard
Vortex Lift	
Kv	

Increase in Value
Decrease in Value
No change in Value
No Data Available

Legend	
	Paper 1
M	0.2
t/c	0.0336
LE Profile	RLE
LE Radius	RLE
Profile	NACA 0003.36
Λ	70
λ	0, 0.1, 0.3
Author	Kulfan (1979)

2.9 Summary Geometrical Effects

It can be concluded that aerofoil shape, thickness, nose radius and wing warp have important effects on controlling the formation and strength of the LEV on delta wings (Kulfan, 1979).

Though Kulfan (1979) did a thorough analysis of different geometry effects the effect of maximum thickness location was not covered. Additionally, no other investigations on the effect of maximum thickness location on delta wings is found. It is also worth noting that the investigated aerofoil NACA0003.36 has a slightly rounded nose, which affects the leading-edge separation significantly. Therefore, the investigations in this thesis focus on the effect of maximum thickness location and maximum thickness on the flow physics of delta wings. Also, the investigation is carried out on a configuration with a SLE and symmetric profile, thus, adding more features to the investigation of vortical flow around delta wings. A SLE is chosen as slender delta wings are commonly used for supersonic flight, which require a SLE. Furthermore, having a SLE results in the primary separation being fixed, thus, making the flow steady (Peckham, 1958). This is beneficial as steady CFD runs can be used which are less computationally expensive than time dependent runs. Additionally, computational methods are challenged by the accurate prediction of the initial separation (Hitzel et al., 2015), which in turn has an effect on consecutive separations, thus, adding additional errors when evaluating the effect of thickness and maximum thickness location.

2.10 Conclusion of the Literature Review/ State of the Art

This literature review on leading-edge vortices over delta wings reveals that a significant amount of research has been conducted in this area including different sweep angles, planform shapes and aerofoil geometries. Wings have been tested computationally as well as experimentally for several speeds and α ranges. However, it appears that although there is a vast majority of data no cross-comparison has been done so far. This proves to be difficult as the focus of papers varies and certain data, though available, is not evaluated. In the age where big data and machine learning is popular it appears that a delta wing database would be feasible as it could yield a better understanding of the interdependencies of geometric parameters on different vortex features. It has also been found that up until now the most consistent research and most popular benchmark configurations are provided by the NATO research group, which is of great benefit for the scientific community as it provides consistency.

2.11 Capabilities and Limitations of the methodologies used in the Literature Review

2.11.1 Computational Fluid Dynamics

The majority of papers reviewed in this chapter were using experimental data, whilst only a few also were based on numerical simulations or a combination of both; experimental data and numerical data. These studies were mainly conducted on the VFE-2 configuration. Studies have shown, that vortical flow prediction for delta wings is highly dependent on grid quality and turbulence model choice affecting the initial prediction of separation (Hitzel et al., 2015). A thorough review of the state of the art on predicting external, vortical flows using CFD is provided in Chapter 3 and covers the effect of discretisation and turbulence model choice on the flow field around delta wings.

2.11.2 Wind Tunnel testing

In sections 2.1. to 2.8. the focus lies on data gathered during wind tunnel testing. Wind tunnel tests are commonly used to evaluate aerodynamic performance of vehicles and are of particular advantage in determining "off-design" conditions. Despite of the advancements in CFD, experiments are still required for validation purposes and are not expected to be fully replaced by CFD within the next 20 to 40 years (Kegelman and Danehz, 2010). The limitations of wind tunnel testing are the tunnel wall interference/blockage, the details of the model and the distortion of the model (Wanan, 2003). These require corrections of the results, to what extend depends on the researcher. Most papers reviewed here stated of having used wind tunnel corrections of some form, whereas others did not. The aforementioned limitations are disadvantages, hard to overcome and will always prove to be restricting factors. However, their validity has been proven over decades. As distinct from CFD, wind tunnel limitations are relatively insensitive to the problem under investigation. For delta wing investigations the most common parameters measured in the wind tunnel include; the aerodynamic forces, the surface pressure, the surface streamlines, general flow field data using PIV and hot wire techniques and 3D boundary layer investigations (Hummel, 2008a). However, most of the sources in section 2.1 to 2.8 are from a time where measurements using PIV etc. were not as popular. Thus, the data focuses on other aspects. This however, does not diminish the validity of their data. In particular when considering the aircraft developed in that time using delta wings, such as Concorde. The new capabilities of measuring the flow field mainly contribute to the ability to verify and improve numerical methods.

2.12 Summary Limitations of Numerical and Experimental findings

It has been shown in section 2.11.1 and 2.11.2 that both experimental and numerical testing are needed in order to make valid claims about a delta wing model. For a good validation as many different parameters as possible should be measured in the tunnel by the use of i.e. PIV (to obtain velocity and velocity vectors in a given plane) and hot wire anemometry (to investigate the status of the boundary layer).

2.13 Conclusion Chapter 2

This chapter gave a thorough review of research done on slender and non-slender wings, with the focus lying on the former. A variety of configurations have been studied ranging from sweep angle over nose radius to notch angle. However, most configurations varied in profile shape or test conditions. It was found that maximum thickness location without and in combination with overall thickness has not been investigated yet. To minimise computational error, it was decided to conduct a study on the effects of thickness and maximum thickness location on two biconvex configurations with SLE and a maximum thickness location at t/c=0.3 and t/c=0.5 for a thickness of 3.4%, 6% and 12%. Additionally, investigations are performed on the VFE-2 configuration using the three different thicknesses mentioned above. This serves as a benchmark case which is compared to the findings of AVT-113. A configuration based on the VFE-2 profile is used, which includes tip taper, to investigate its effects on the flow physics, as this is also found to not have been addressed by previous papers.

Aspects regarding the numerical modelling of vortical flow, as discussed in sub-section 2.2.1 and section 2.3, are considered. These were identified to be the prediction of VBD and primary vortex onset. The former is true for wings with SLE and RLEs whereas the latter is only true for configurations with RLE. However, similar issues may arise for geometries with maximum thickness location located close to the leading-edge due to the increased leading-edge slope. Care is taken during the discretisation process based on the findings by Goertz (2005) that vortical flow and VBD in particular are highly sensitive to local grid resolution and grid topology. Turbulence model choice and benefits will be discussed in Chapter 3, however, it is noted that DES was found to be promising when a full understanding of the flow field at VBD was required, though RANS models still provide reasonable results (Cummings and Schütte, 2009). It is emphasised though that researchers should use the level of modelling that is

appropriate for the level of detail required given the application as the expense and computer resources required for certain turbulence models may not be warranted for every application.

The investigations in the following chapters are carried out using Re= 750,000 and M=0.1 as these matches the Re and Mach number range found in the literature review. Studies are carried out using CFD, and the wind tunnel is used to validate the numerical findings for a selection of configurations. The findings are then compared to findings in the literature review. The thickness effects are compared with those of Kirby and Kirkpatick (1969). Thickness alteration results in the change of the frontal area, hence comparisons between the findings by Kulfan (1979) and the AVT-113 research group are made. The flow physics are investigated using surface streamline plots, spanwise pressure distribution as well as normalised Q-criterion and vorticity contours. This adds to the findings by Kirby and Kirkpatrick (1969), whose investigation did not detail the flow physics. The numerical as well as the experimental data uses the polar, moment and force plots based on the literature review for reasons of comparison and consistency.

The next chapter is reviewing the current state of CFD. This includes the discussion of the grid, including element types and near wall modelling. Relevant turbulence models such as the SST model and Reynolds Stress models are reviewed and convergence, imbalances and residuals of CFD solvers are discussed. Finally, the VFE-2 benchmark configurations and the derived geometries are introduced before overall conclusions are drawn regarding the CFD set up.

Chapter 3 Computational Fluid Dynamics (CFD)

This chapter deals with the fundamentals of Computational Fluid Dynamics (CFD) and provides the necessary background knowledge to understand the investigations undertaken from there on. CFD is defined as the numerical analysis of fluid flow and related phenomena which replaces the partial differential equations (PDEs) governing a fluid flow by a set of algebraic equations. These PDEs represent the conservation of mass, momentum and energy. CFD is often used to study flow patterns which are difficult, expensive or impossible to investigate using experimental techniques (Kuzmin, 2010). However, before any CFD code can be used with confidence, it is crucial to verify its accuracy in predicting the flow physics and to validate it against accurate and reliable experimental data (Huang and Verhaagen, 2009).

3.1 Inviscid vs. Viscid Flows

Flow in which viscous effects can be neglected is known as inviscid flow. When applying the assumption of the flow being inviscid, boundary layer effects are neglected. Normally these assumptions are valid when dealing with high Re number flows or slender bodies where the boundary layer is thin (Cousteix, 2003). Assuming inviscid flow reduces the governing equations of a fluid (discussed in section 3.3) to the so-called Euler equations. These are first order accurate methods which are less computationally expensive than when the boundary layer is accounted for but were found not to be the appropriate method for low speed vortical flows (Blazek, 2005; Verhaagen, 2002). Although it was established that the numerical viscosity in Euler codes can trigger leading-edge separation and VBD and therefore produce a similar flow structure, the actual physics and many important flow features, such as secondary separation, cannot be captured at the correct flow conditions (Lee and Brandt, 1992; LeRoy et al., 2003). The findings above resulted in the decision to run viscous simulations, which in turn resulted in the necessity of modelling the turbulence within the boundary layer.

3.2 Turbulence

Turbulence can be defined as fluctuations of the flow field in time and space. It is characterised by high Reynolds (Re) numbers and occurs when the inertial forces of the fluid become significant in comparison to the viscous forces. Turbulence is also a complex process as it is three dimensional, unsteady, consists of many scales and has a significant impact on the flow characteristics (Coleman and Sandberg, 2010).

The Navier- Stokes (N-S) equations are the basic governing equations for a fluid and are described by the continuity (equation (3.1)), momentum (equation (3.2)) and energy (equation (3.3)) equation for a compressible fluid as follows (Łukaszewicz and Kalita, 2016):

$$\frac{\partial \rho}{\partial t} + \frac{\partial}{\partial x_j}(\rho u_j) = 0 \tag{3.1}$$

$$\frac{\partial}{\partial t}(\rho u_i) + \frac{\partial}{\partial x_j}\left[\rho u_i u_j + p\delta_{ij} - \tau_{ji}\right] = 0 \qquad \text{i=1, 2, 3} \tag{3.2}$$

$$\frac{\partial}{\partial t}(\rho e_0) + \frac{\partial}{\partial x_j}\left[\rho u_j e_0 + u_j p - u_i \tau_{ij}\right] = 0 \tag{3.3}$$

With τ_{ji} being the viscous stress, ρ being the density of the fluid, t being the time, u_i being the velocity components in the respective directions, p being the pressure, e_0 being the total energy and δ_{ij} being the Kronecker delta.

Łukaszewicz and Kalita describe both laminar and turbulent flows with turbulent flows involving a large range of length and time scales. Therefore, in order to ensure that turbulence is modelled properly computational grids or length scales need to be sufficiently small (Gatsis, 2000). This is particularly true near the wall, where variables have large gradients and the momentum and other scalar transports occur more vigorously, due to the wall being the main source of vorticity and turbulence (Al-Garni et al., 2008). This is referred to as the boundary layer and a detailed description of it as well as of the related y^+ value and near wall modelling can be found in Appendix 2.2 and 2.3.

The governing flow equations mentioned above can be solved either directly or by averaging the flow characteristics by means of adding an additional time varying fluctuation component and are summarised in Figure 3.1. (Sodja, 2007). The two direct methods calculating the fluctuating quantities are called Large-Eddy Simulation (LES) and Direct Numerical Simulation (DNS).

The DNS model computes the fluctuating quantities directly by resolving all scales starting from the smallest scales. This requires a large number of grid points making it computationally

very expensive (Gatski, 1996; Sodja, 2007). Therefore, this approach is currently limited to low Reynolds number flows and simple problems (Argyropoulos and Markatos, 2015), but is a preferred choice when investigating the physics of turbulence due to its high accuracy (Gatski, 1996).

The LES is the most promising approach as it does not require to resolve for the smaller scales. Instead, it uses some sort of parameterisation or model and, as DNS, is three- dimensional and time-dependent. As it is more cost efficient than DNS, LES is a good choice when investigating flows too complicated to compute economically by DNS (Gatski, 1996).

A simpler approach to turbulence modelling is the application of perturbations to the complete set of governing flow equations and the Reynolds decomposition of the instantaneous velocities, pressure and temperature into averaged and fluctuating parts.

$$u_j = \overline{u_j} + u_j' \tag{3.4}$$

$$p = \bar{p} + p' \tag{3.5}$$

$$T = \bar{T} + T' \tag{3.6}$$

where u_j represents the velocity components, p represents the pressure and T the temperature. By time averaging the Navier-Stokes equations and replacing the flow variables by the mean and fluctuating parts obtained in Equation (3.4) to (3.6) the Reynolds Averaged Navier-Stokes equations (RANS) are obtained. The continuity equation is thus transformed into (Anderson, 1995):

$$\frac{\partial \overline{u_j}}{\partial x_j} + \frac{\partial u_j'}{\partial x_j} = 0 \tag{3.7}$$

whilst the momentum equation transforms into (Pitsch, 2014):

$$\frac{\partial \overline{u_j}}{\partial t} + \overline{u_\iota}\frac{\partial \overline{u_j}}{\partial x_i} = -\frac{1}{\rho}\frac{\partial p}{\partial x_j} + \frac{\partial}{\partial x_i}\left(\upsilon \frac{\partial u_j}{\partial x_i} - \overline{u_i' u_j'}\right) \tag{3.8}$$

As can be seen from Equation (3.8) Reynolds averaging results in an additional term the so-called turbulent Reynolds stress $\overline{u_i' u_j'}$ and also an additional term in the energy equation, the so called turbulent heat fluxes, not shown here (however a thorough derivation and explanation of arriving at the RANS equations can be found in Appendix A.2.3). Those extra variables result in the closure problem, by having more unknown than equations. To overcome this problem two different methods have been developed to achieve closure; both solving for the Reynolds stresses. The first one, the so-called Differential Stress Models (DSM), model the Reynolds stress tensor directly, whereas the second one, the so-called Eddy-Viscosity Models (EVM), use the Boussinesq assumption and thus model velocity and length scales in order to obtain the eddy viscosity (Sodja, 2007). Since the RANS are not simulating the detailed instantaneous flow, they are the most computational efficient CFD modelling approaches for viscous flows (Yang, 2015).

Experiencing difficulties when using the standard LES models, in particular in the near-wall regions, led to the development of hybrid models combining the desirable aspects of RANS and LES methodologies. One example of this is the Detached Eddy Simulation (DES) (Spalart et al., 1997). Here, RANS models are used in the near wall region whereas the regions away from the wall use LES modelling (Baker et al., 2019).

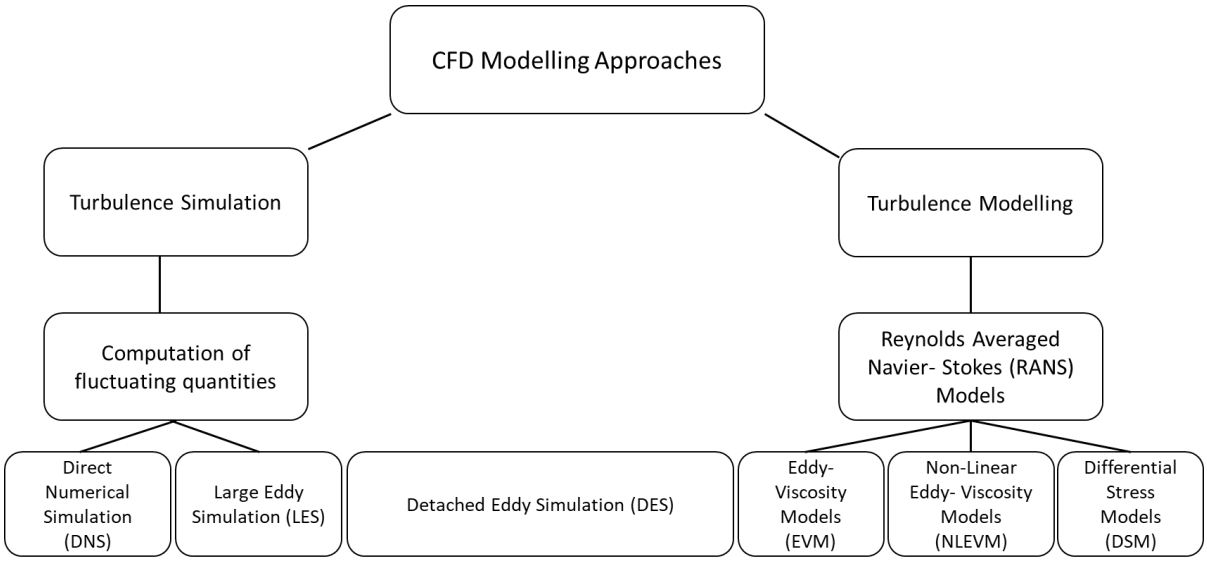

Figure 3.1 Turbulence Modelling Flow Chart.

This research project primarily uses the EVMs and DSMs because turbulence models in this category are more than adequate in solving most aerodynamic computational problems (Gatski, 2000; Brett and Ooi, 2014). The most popular EVMs and DSMs are described in the following section. Additionally, Appendix A.2.4 provides more information about other popular EVMs.

3.3 Popular RANS turbulence models

3.3.1 The Spalart- Allmaras Model

The Spalart- Allmaras (SA) turbulence model is a one-equation model solving the transport equation for the kinematic eddy (turbulent) viscosity without making use of the turbulence kinetic energy k (Bigarella and Azevedo, 2007). It was designed with aerospace applications in mind hence showing good results for wall-bounded flows with boundary layers subject to adverse pressure gradients. Originally, this turbulence model was created for low Re flows, therefore, its success relies on the accurate modelling of the boundary layer region (y^+ ~1) (FLUENT Theory Guide, 2009). For FLUENT the SA model has been extended so that it is y^+ insensitive (Enhanced Wall Treatment) which enables the application of the model irrespective of the near wall resolution. This is possible as the code automatically blends from a viscous sublayer formulation to a logarithmic formulation based on the y^+ value. However, the y^+ value has to lie in a range between 1< y^+ <30 and it is recommended to resolve the boundary layer with a minimum resolution of 10-15 cells (FLUENT Theory Guide, 2009).

Note, that the SA model produces relatively larger errors for some free shear flows, such as plane and round jet flows. Also, it cannot reliably predict the decay of homogenous, isotropic turbulence (Argyropoulos and Markatos, 2015).

3.3.2 Shear Stress Transport (SST) Model

The SST model is a blend of the k-ω model in the near wall region and the standard k-ε model with its free-stream independence in the far field. This is done by moving from the k- ω model into the k-ε formulation. Albeit, being similar to the k-ω model, the SST model has some differences in its formulation. The standard two-equation models are not capable of accurately predicting the adverse-pressure gradients or separated flows (Menter, 1993). They require a stronger pressure gradient or a longer running length to separation than has been shown in experiments. Investigations showed that this is because turbulent shear-stress transport has not been taken into account (Johnson and King, 1985). Therefore, the SST model is refined to account for the transport of the turbulent shear stress by implementing a measure of the flow strain rate within the definition of the turbulent viscosity (FLUENT Theory Guide, 2009; Menter, 1993). Additionally, another blending function is used to turn on this criterion only inside the boundary layer (Bigarella and Azevedo, 2007). This makes the SST model more accurate and reliable for adverse pressure gradient flows, aerofoils and transonic shock waves

than the standard k-ω formulation. It has been validated and provided good results for applications such as turbomachinery blades, wind turbines, free shear layers, zero pressure gradient and adverse pressure gradient boundary layers (Argyropoulos and Markatos, 2015). Another derivative of the k- ω model is the two-equation Baseline (BSL) model but it does not account for the turbulent shear stress in the eddy-viscosity coefficient (Menter, 1993). Both models are designed for $y^+ \sim 1$ (Bigarella and Azevedo, 2007), with the formulation of the k-ω SST model being described in Appendix 2.4.5.

3.3.3 Reynolds Stress Models (RSM)

Reynolds stress models are superior over EVM for flows with sudden changes in mean strain rate, curved surfaces, secondary motions, rotating and stratified flows, separated and three-dimensional flows. This is because they are not based on the assumptions of local isotropy and local equilibrium. Those assumptions imply that the normal Reynolds stresses are equal and that historic effects on the Reynolds stresses are negligible. These downfalls of the RANS models led to the development of the algebraic stress models and the second order closure models.

By abandoning the isotropic eddy-viscosity hypothesis the RSM uses the transport equation for the Reynolds stresses together with an equation for the dissipation rate in order to close the RANS equations. This requires that five additional transport equations are required in 2D flows whereas 3D flows will require seven additional transport equations (FLUENT Theory Guide, 2009).

The advantage of RSM models is there is greater potential for giving more accurate predictions of complex flows. However, the fidelity of those models is still limited as closure assumptions are used in order to model various terms in the exact transport equations for the Reynolds stresses. This is particularly true for the pressure-strain and dissipation-rate terms.

The RSM needs to be used when the flow features of interest are caused by anisotropy in the Reynolds stresses, such is the case for flows in combustors or rotating flow passages. This makes RSM models a preferred choice for internal flows (Kundu et al., 2016).

The Reynolds stress transport equation may be derived by taking the momentum equations and multiplying those by a fluctuating property; the product then being Reynolds averaged. This has been done in the section “Statistical Turbulence Modelling” and the reader is referred to Appendix A.2.3.1. As described in this section the derivation yields to several unknowns and modelling assumptions are required to close the equations (FLUENT Theory Guide, 2009).

This gives the RSM a higher degree of flexibility but also results in a higher degree of mathematical complexity. The increased number of transport equations yields to reduced numerical robustness and is computationally more expensive (Eisfeld, 2006).

The RSM available in FLUENT are:

- The Linear Pressure-Strain Model
- The Quadratic Pressure-Strain Model
- The Low Reynolds Number Stress-Omega Model
- The Stress BSL Model

The former two are ε- based whereas the latter two are ω- based.

3.4 Turbulence Model Choice for the flow investigation around Delta Wings

As could be seen from above, turbulence models are based on assumptions in order to reduce the computational costs of the simulation. Therefore, they do not represent the actual physical modes of turbulence such as eddies, velocity patterns or high-vorticity regions, but obscure them (Argyropoulos and Markatos, 2015). The assumptions and simplifications made in different turbulence models differ and thus make different turbulence models more or less suitable to predict certain flows. Therefore, the accuracy of the solution of the flow field depends upon the chosen turbulence model.

For vortex dominated flows, it has been shown in the past that inviscid and viscous flow solvers can be used to predict the primary vortices accurately for geometries with discontinuities; such as SLEs prior to VBD. This is not the case for geometries which do not possess this feature: like wings with round leading-edges. Here, the LEVs form due to boundary layer separation near the leading-edge which is controlled by momentum transport and thus extremely sensitive to the Reynolds number. Therefore, a failure of modelling this flow feature accurately results in inaccurate prediction of the strength of the vortices and details of the flow field, leading to incorrect predictions of the aerodynamic forces (Dzanic and Martinelli, 2019). Therefore, turbulence model choice and grid resolution are very important for type of flows where the separation is not fixed.

One of the aims of the NATO research initiative AVT-113 was the evaluation of CFD in modelling vortical flows, thus, a variety of turbulence models were used to investigate the vortical flow around the VFE-2. Turbulence models included: transient models such as DES,

DDES and LES as well as different steady state simulations using different forms of the Baldwin-Lomax, k-ω, k-ε and SST model as well as the Spalart-Almaras (SA) model with different correction factors and Reynolds stress models such as EARSM and CC-EARSM. All calculations have been conducted for fully turbulent boundary layers and regions with laminar boundary layers have not been taken into account. The best suitable turbulence model for calculations of vortical flow, however, still needs to be found. It has been suggested by Hummel (2008) that attempts should be made to predict laminar/turbulent transition in fully developed vortical flow without VBD. For this the test case of α=18° is suggested as the numerical data can be compared to already existing Hot-Wire-Anemometry results conducted by TU Munich (TUM). It has been further recommended by Hummel (2008) that the CFD codes need validation for partly separated vortical flow at α=13°. Here, the flow field near the onset of the outer primary vortex for delta wings with rounded leading-edges should be analysed to validate the schematic shown in Figure 3.3 (Hummel, 2008 b).

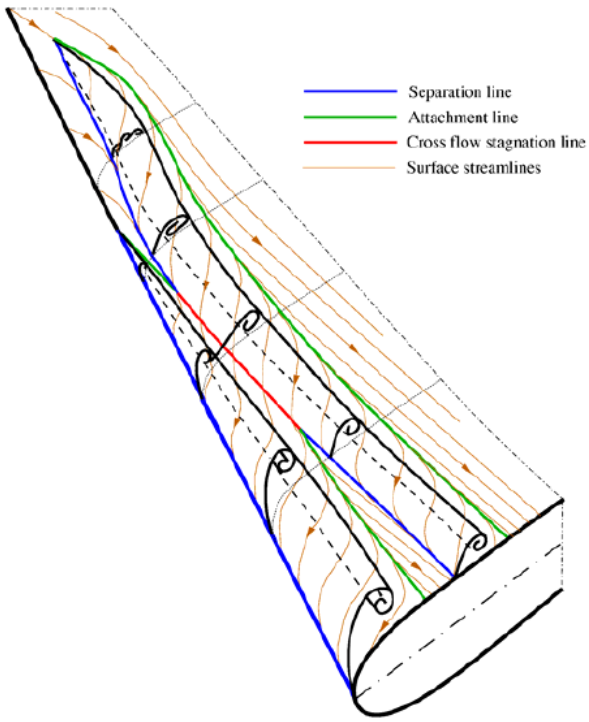

Figure 3.2 Schematic view on the vortex formation on the VFE-2 configuration with medium rounded leading-edge at M=0.4 and Re_{mac}= 3x10^6 and α= 13° based on numerical data (Hummel, 2008 b).

During AVT-113 it was established that Eddy Viscosity Models (EVMs) are often not able to predict the main vortex characteristics properly. The separation onset of the vortex is possibly not accurately predicted for medium rounded leading-edges (MRLEs) which affects the entire vortex development (Fritz and Cummings, 2008; Schuette et al., 2012; Crippa and Rizzi, 2008).

But also, configurations with sharp leading ledges (SLEs) lack in accuracy especially when it comes to VBD. It is assumed that this may be due to an underprediction of the axial velocity, which results in the prediction of VBD at lower α. Thus, the modelling of the eddy viscosity may be improper for vortical flow in current RANS methods (Fritz and Cummings, 2008; Schuette et al., 2012; Crippa and Rizzi, 2008; Schuette et al. (b), 2012). The eddy viscosity produced in the vortex is excessive resulting in an over-prediction of vortex size and velocities for wings with SLEs and MLEs. This causes differences in the size of the suction peak and pressure distribution from experimental data. The prediction of the secondary vortex has been found to be either stronger or weaker, shifted or not present at all, having an impact on the primary vortex's position and development (Fritz and Cummings, 2008). Also, the VBD is usually not predicted correctly with regards to position and strength, which again affects also the surrounding flow. This is a particular drawback of the EVMs as VBD has a significant impact on the aerodynamic coefficients of a delta wing (Moioli et al., 2018). However, it was found that for subsonic cases with SLE the agreement between numerical and experimental results is good until VBD. Generally, VBD is predicted to occur at lower angles for numerical simulations due to the under prediction of the axial velocity in the vortex core. Thus, higher-order models are recommended when investigating VBD (Fritz and Cummings, 2008).

The general disadvantage of RANS models in predicting vortex dominated flows is that they use second order numerical methods which introduce significant amounts of numerical dissipation into the solution, yielding an artificially diffused vorticity field. This in turn has an impact on the prediction of the small-scale features such as the secondary and tertiary vortices. Additionally, the turbulence models used for the closure of the Navier-Stokes equations assume the velocity fluctuation correlations to be isotropic. However, this is not the case on delta wings where the flow is influenced by rotational effects (Dzanic and Martinelli, 2019).

Moioli et al. (2018) enhanced the SA one-equation model based on experimental data collected on the VFE-2 configuration. They concluded that the mismatch between numerical and experimental data is due to the poor prediction of the eddy viscosity destruction in the vortex flow. Thus, they added additional eddy viscosity destruction terms which exclusively affect the vortex flow region. Also, several additional terms were formulated having different effects on different topologies and zones of the LEV in order to enable more flexibility of the turbulence model. The results obtained with the altered SA model proved to be significantly better especially with regards to surface Cp prediction. However, their model is only limited to simple geometries and small angles of attack (Moioli et al., 2018).

Therefore, when investigating configurations with round leading-edges or VBD on delta wings, higher order methods are recommended. However, these methods increase the computational time drastically and require the availability of massively parallel CPU. Despite the availability of such computing facilities for big research institutions this is still lacked at smaller ones. However, general trends can be established and conclusions be drawn despite not having the "perfect" solution.

Based on the literature review above it was decided that this study focuses on the SST model and the Linear Pressure-Strain Reynolds Stress model.

The SST model was selected as it shows to predict the vortex core best when comparing it to other turbulence models also with regards to VBD location (Wibowo et al., 2018; Anwar-ul-Haque et al., 2008; Al_Garni et al., 2012). Furthermore, the surface flow topological structure at lower angles of attack ($\alpha < 18°$) is known to be predicted with considerable accuracy for delta wing applications (Saha and Majumdar, 2012; Anwar-ul-Haque et al., 2008) but may not be appropriate at higher angles of attack where VBD is dominating the flow. The vortex onset and consequently its location may be subject to change when considering boundary layer transition and require more accurate turbulence models, such as DES and LES (Fritz and Cummings, 2008; Schütte and Luedeke, 2010; Schütte et al., 2012). However, the SST model is very robust and good for predicting separated flows where the separation point is dictated by the geometry, as is the case for SLEs. It further offers the best trade-off between accuracy and computational costs. Although SST can be used in the viscous sublayer, it is not designed to take into account wall effects. Its performance is also limited in flows with strong curvature and flows with secondary flows (Skillen, 2011), but computationally less expensive than DES and LES methods.

The Reynolds Stress Model was selected as studies by Cecora et al. (2015) and Crippa and Rizzi (2006) have shown that a RSM is superior to an EVM and suitable for flows with strong streamline curvature, secondary flows and complex strain fields as can be expected for a vortex dominated flow field (Cecora et al., 2015). They are known to represent the flow very well, but are very sensitive to initial conditions, require a high-quality grid and come at a high computational cost (Wassermann, 2016).

3.5 Steady vs. Unsteady Simulations for Delta Wing Simulations

In fluid dynamics a flow is considered to be steady when its properties are not a function of time. Unsteady flows on the other hand do change with time and therefore require the modelling

of the time component. Menke et al. (1999) identified the unsteady aspects of leading-edge vortices. These include aerodynamic manoeuvres, oscillations of breakdown location, vortex shedding, helical mode instabilities and Kelvin-Helmholtz instabilities. This study is not concerned with manoeuvring nor the impact of vortex breakdown and thus helical mode instabilities. Vortex shedding has been shown to result in significant asymmetry in the pressure distribution on the wing planform, which can have significant consequences on the stability of the aircraft. However, for most practical cases this is coupled with the motion of the aircraft, also known as wing rock (Rediniotis et al., 2012) but again manoeuvring is not part of this investigation. Kelvin-Helmholtz instabilities are encountered within the shear layer of delta wing configurations, which emanates from the leading-edge to the primary vortex (Gordnier, 1990). For the establishment of the differences between the configurations with regards to performance and longitudinal stability, the unsteady aspects of the flow are not deemed important enough to justify the increased computational costs of simulating unsteady flow. Furthermore, studies by Crippa and Rizzi (2006) on the VFE-2 have shown that at $\alpha = 18.5°$ the steady RANS EARSM resolved the apex region of delta wings better than the unsteady DES model, however, the trend was reversed close to the trailing edge. It was further shown that DES solutions overpredicted the strength of the secondary vortex as well as the primary suction peak. It was concluded that no substantial benefit of using DES is obtained with regards to the mean surface pressure coefficient. However, using the unsteady approach is recommended when investigating VBD, vortical substructures and primary vortex development (Crippa and Rizzi, 2006; Visbal and Gordnier, 2003). For blunt leading-edges it was found that advanced RANS methods gave superior boundary layer characteristics, resulting to an increased accuracy in primary separation prediction. DES, albeit having a higher accuracy with respect to vortex core development, suffered from the inability to predict vortex separation onset, location and thus strength correctly. It was concluded that DES models are recommended for angles of attack above $\alpha = 20°$ but due to the finer grid requirements no apparent improvement over steady runs could be found (Crippa and Rizzi, 2006). Studies by Schiavetta (2007) on the VFE-2 configuration have also shown that the main difference between steady and unsteady runs lies in the prediction of VBD onset. However, most studies investigating the differences between unsteady and steady runs focused on angles of attack above $\alpha = 18°$ (Morton et al., 2002; Mitchell at al., 2012; LeRoy et al., 2003).

This study is not concerned with high angle of attack flow, where ignoring flow unsteadiness would have dramatic effects on the structure nor with the impact of VBD and its location, further justifying the choice of steady RANS modelling. VBD will however be evaluated

qualitatively with the assumption that the reader has been informed sufficiently that VBD onset is predicted at lower α when using steady RANS modelling.

Based on the above, all simulations were using the steady state approach as they provide sufficient flow resolution for the purpose of this study. VBD was not investigated in detail and despite RANS predicting earlier onset of VBD (Crippa, 2006) the general trend will not differ when assuming steady state flow. Also, vortex flow visualisations were limited to angles of attack where VBD was not present for the majority of configurations tested. Finally, based on the fact that most runs were lying in the low to medium angle of attack range, the additional expense and computer resources required for unsteady flow simulations and/ or hybrid turbulence models could not be justified for this study.

3.6 Conclusion Chapter 3

Summarising it can be said that much care has to be taken when setting up a simulation in CFD. An appropriate mesh needs to be generated and the creation of an appropriate mesh takes up a significant amount of time based on the complexity of the geometry under investigation and can be an iterative process if errors or convergence problems are encountered during the solving process. Also, the case needs to be set up correctly in terms of including the appropriate flow physics. It needs to be established whether the problem is steady-state, where the flow characteristics do not change with time or whether it is unsteady, meaning the flow characteristics do change (like it is the case for vortex shedding). Traditionally, when dealing with turbulent flows using RANS approaches, a turbulence model has to be chosen which is appropriate for the problem under consideration.

From the work of others presented in this literature review, it was found that configurations with SLEs can be sufficiently simulated numerically using steady state methods and RANS turbulence models up until VBD. Investigations of different turbulence models on the VFE-2 showed that the SST model was the best when being limited to EVMS (Wibowo et al., 2018; Anwar-ul-Haque et al., 2008). Studies by Moioli (2018) have shown that the correct modelling of the eddy viscosity production is crucial to accurately predict vortex dominated flows. Using RSM models may have an effect on the eddy viscosity production as it calculates the Reynolds stresses independently as opposed to the EVMs which are relating the Reynolds stresses to the eddy viscosity. Additionally, the RSM models do not assume isotropic turbulence opposed to EVMs, which results in a more realistic prediction of vortical flow. The literature review has

further shown that multiple studies have been conducted on the VFE-2 configuration numerically as well as experimentally, thus, resulting in a multitude of available data for validation purposes. This makes it a valuable benchmark configuration for further studies investigating the flow physics on delta wings.

Chapter 4 Grid Refinement & Turbulence Model Study

This chapter deals with the verification of the numerical grid and chosen turbulence model by comparing it to the experimental results obtained during the international Vortex Flow Experiment 2 (VFE-2) of the Applied Vehicle Technology panel (AVT) of NATO during AVT-113. It further verifies the grid for the B05 3.4% configuration using the UWE wind tunnel conditions. To replicate the experiments numerically, first the methodology needs to be established based on the findings of the literature review. Then the similarity parameters (Mach and Reynolds numbers) need to be matched which is detailed in Appendix A.3.1.- A.3.4. The geometric characteristics and the numerical setup are discussed in section 4.1. to 4.5 followed by the grid independence study for both B05 and VFE-2 configuration. The final grid is then assessed regarding its overall quality before a turbulence model study is conducted for the VFE-2 configuration using the two RANS models SST and Linear Pressure Strain RSM for reasons discussed in Chapter 3.

4.1 Test Case Determination for the Grid Refinement & Turbulence Model Study

As mentioned in Chapter 1, NATO's AVT-113 research group conducted an extensive study on the VFE-2 configuration. Also, other institutions outside the AVT continue to use this configuration for research on LEVs. Due to the amount of computational and experimental data available it was decided to use this configuration as a benchmark case to validate the numerical and experimental results presented in this thesis.

In this investigation, the test data obtained by Furman and Breitsamter (2007) at the wind tunnel at TU Munich (TUM) were used to validate the mesh and turbulence model choice. They conducted tests at M=0.07, Re= 1×10^6 and α= 18° for MRLE and SLE. The angle was chosen as it has been established that separate vortical flow is fully developed at this incidence and VBD is not occurring yet (Fritz and Cummings, 2008). For better comparison between numerical and experimental data it was recommended to model the VFE-2 configuration with a sting mount. The results of the grid refinement study were compared to the findings at TUM for the mean axial velocity contours and surface pressure distribution at chord positions x/c= 0.2, 0.4, 0.6, 0.8 and 0.95. This was done following the recommendations by the AVT-113 group (Fritz and Cummings, 2008). It should be noted that only experimental data from TUM was available but no numerical data. The Mach and Re number were matched using the methodology described in Appendix A. 3.2.

Another grid refinement study was conducted on the clean B05 3.4% configuration at M=0.1, Re= 750,000 and α=13°, which is equivalent to the conditions investigated in the current study. An angle of attack of 13° was chosen as it marks the onset of vortical flow (Fritz and Cummings, 2008) and was used in the remainder of this study to evaluate the differences in flow structures when varying aerofoil shape.

Once the test cases were validated, the same meshing strategy and turbulence model choice were applied to the other configurations under investigation. A detailed explanation of the geometries used during the grid and turbulence model study is provided in the following section.

4.1.1 Geometries used for the Grid Refinement and Turbulence Model Study

The VFE-2 model shown in Figure 4.1 is an uncambered flat plate with special considerations given to the leading-edge and trailing edge. The leading-edge is designed to be interchangeable and is defined with a NACA-like aerofoil polynomial (Chu and Luckring, 1996, Luckring, 2009). The leading-edge contours matched the flat-plate wing over a distance of 15 percent root chord and the wing was closed out over the last 10 percent of the root chord to a sharp trailing edge. The model was sting mounted as can be seen in Luckring (2009). An analytical definition of the sting is also provided by Chu and Luckring (1996) and can be found together with the mathematical description of the leading-edge in the Appendix A.3.1. The other configuration used for the grid refinement study was a biconvex profile with maximum thickness location at x/c= 0.5 and 3.4% thickness (B05 3.4%) as shown in Figure 4.2. Opposed to the VFE-2 configuration shown in Figure 4.1 it was simulated without sting attachment.

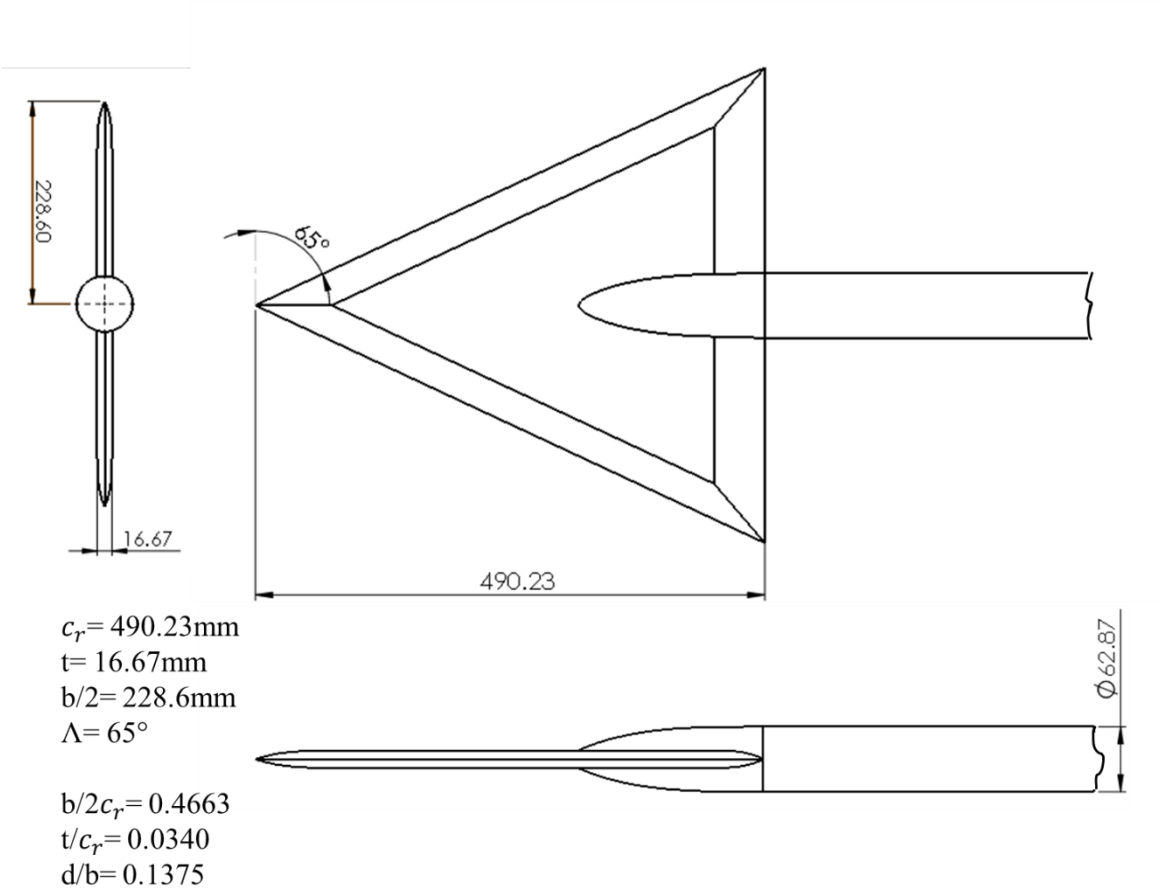

Figure 4.1 Schematic of the VFE-2 delta wing as used by Luckring (2009).

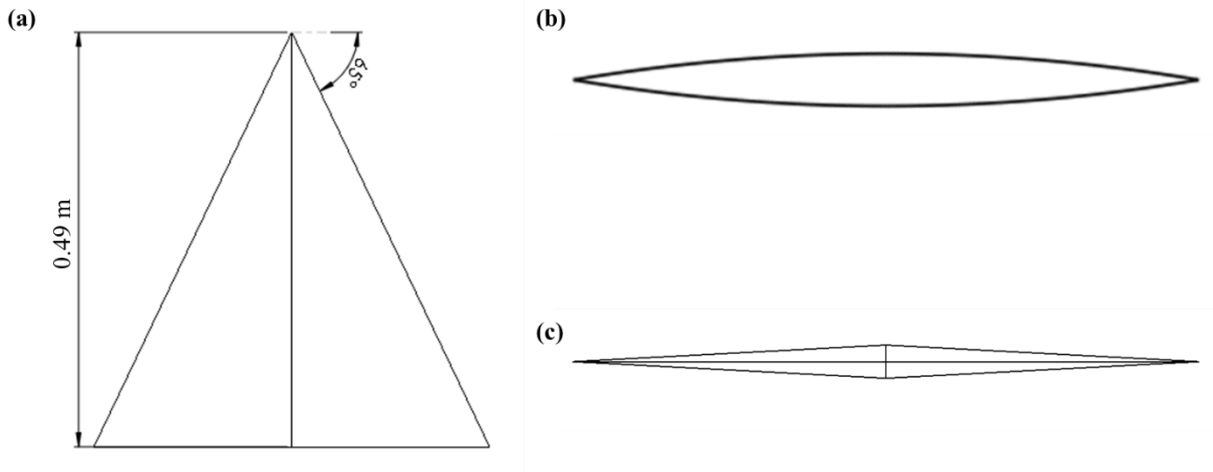

Figure 4.2 B05 3.4% configuration as used for the grid convergence study. (a) Top View, (b) Profile View, (c) Back view (spanwise thickness distribution).

4.2 Methodology

The behaviour of the fluid flow affecting the delta wing was simulated by using the CFD software ANSYS FLUENT. Here the compressible, three-dimensional, steady or unsteady Reynolds-Averaged Navier-Stokes equations are solved using a finite volume approach.

The grids used for the simulations in this study were created with ANSYS MESHING. A hybrid unstructured grid approach was chosen, making use of the advantages of prismatic elements for the resolution of the viscous shear layers near the wall and the flexibility in grid generation offered by unstructured discretisation methods (Schuette and Luedeke, 2009).

ANSYS FLUENT uses a finite- volume approach to discretize the Navier-Stokes equations. The finite volume method is used to satisfy the strict global conservation by enforcing local conservation over the control volumes. The finite element method was used in order to describe the solution variation within each element.

All simulations in this study were run in FLUENT 19.2 using the SIMPLE pressure-velocity coupling scheme of second order accuracy combined with the Green-Gauss Node Based spatial discretisation (a detailed description of the methods can be found in the FLUENT manual). The use of the density-based solver was deemed unnecessary due to the low Mach number resulting in weakly compressible flow. The simulations were carried out on an Intel® Core™ i7-3770 CPU @ 3.40GHz, 3401 MHz workstation with 4 cores and 8 logical processors with 32GB RAM for grids below 10,000,000 elements. For grids consisting of more than 10,000,000 elements an Intel® Xeon® X5690 with 3.46GHz CPU, 74 GB RAM, 8 cores and 16 logical processors was used.

The simulations were conducted using the steady state SST $k-\omega$ model and the linear pressure-strain RSM. The latter was chosen as vortex dominated external flows experience shear forces where the vortex re-attaches and by modelling the stress terms directly it was hoped that the vortex can be captured more accurately. The convergence criteria were set to be $1x\ 10^{-6}$ for all flow properties. The conditions for the VFE-2 CFD set up, derived in Appendix A. 3.4, are shown in Table 4.1 and that of the B05 3.4% configuration is shown in Table 4.2.

Table 4.1 Conditions for CFD set up to match experimental results by TUM.

Mach Number	0.07
Reynolds Number	1×10^6
Mean Aerodynamic Chord [m]	0.327
Temperature [K]	288
Pressure $[\frac{N}{m^2}]$	189980.405
Angle of Attack [°]	18

Table 4.2 Conditions for CFD set up for the B05 3.4% configuration using the UWE wind tunnel conditions.

Mach Number	0.1
Reynolds Number	750,000
Mean Aerodynamic Chord [m]	0.327
Temperature [K]	300
Pressure $[\frac{N}{m^2}]$	101,325
Angle of Attack [°]	13

4.3 Computational Grids

The following section describes the discretisation of the computational domain. As the cases under investigation were symmetric around their longitudinal axis and no asymmetric manoeuvres were studied it was sufficient to model only half of the wing and apply a symmetry boundary condition. The model setup is shown in Figure 4.3, Figure 4.4 and Figure 4.5 .The sting has been modelled partially (one chord length) and rounded off at the end. This was deemed sufficient for modelling the effect of the mount on the flow around the delta wing by AVT-113. The mounting sting was modelled as TUM's experimental data was used for the validation of CFD during AVT-113. An unstructured grid was used where the near wall region was modelled by prism layers to resolve the strong transverse gradients of the solution within the boundary layer. The mesh was refined within a rectangular region of size $3c_r$, $1c_r$ and $1.5c_r$,

in X, Y and Z direction respectively, around the wing. The element size within that region was 1 x 10^{-2} m. The rest of the domain had a maximum element size of 0.25m.

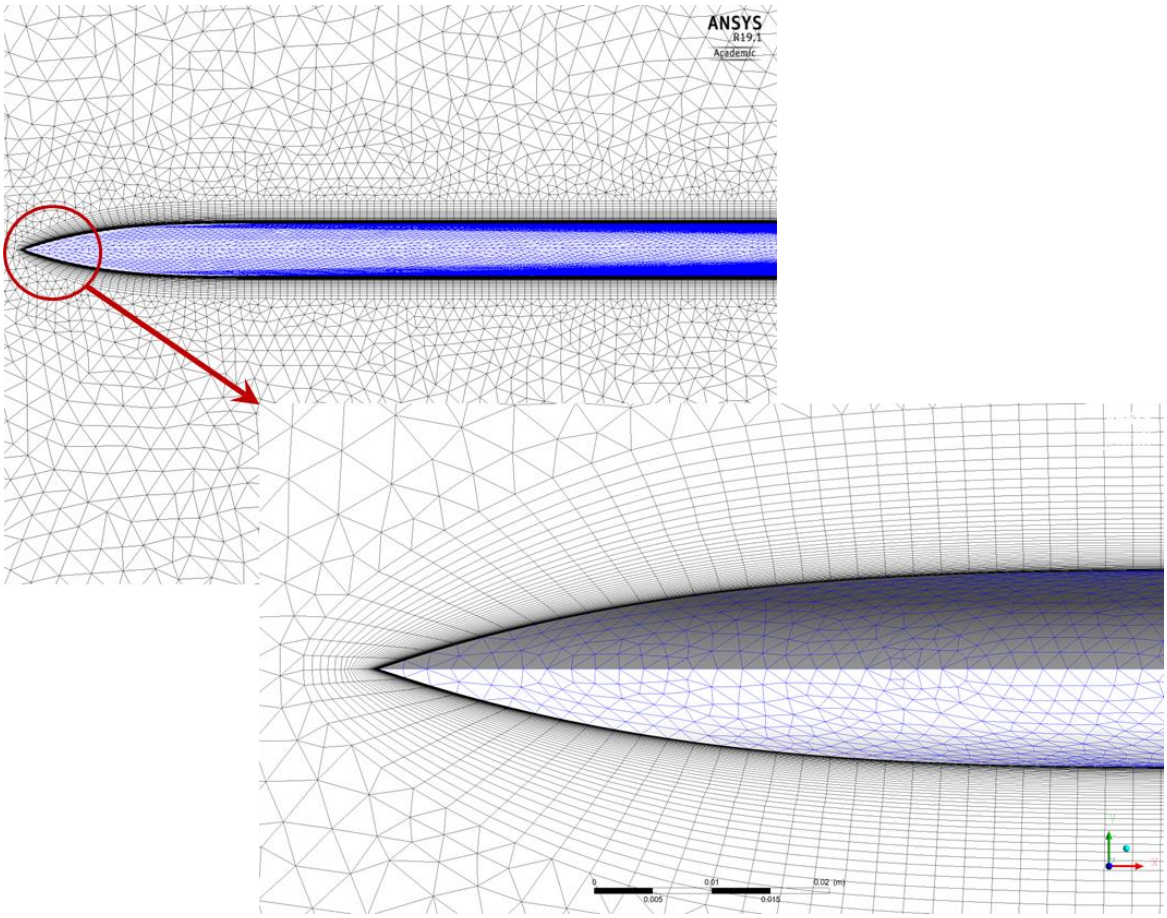

Figure 4.3 Prism layers and surrounding grid for the VFE-2 configuration.

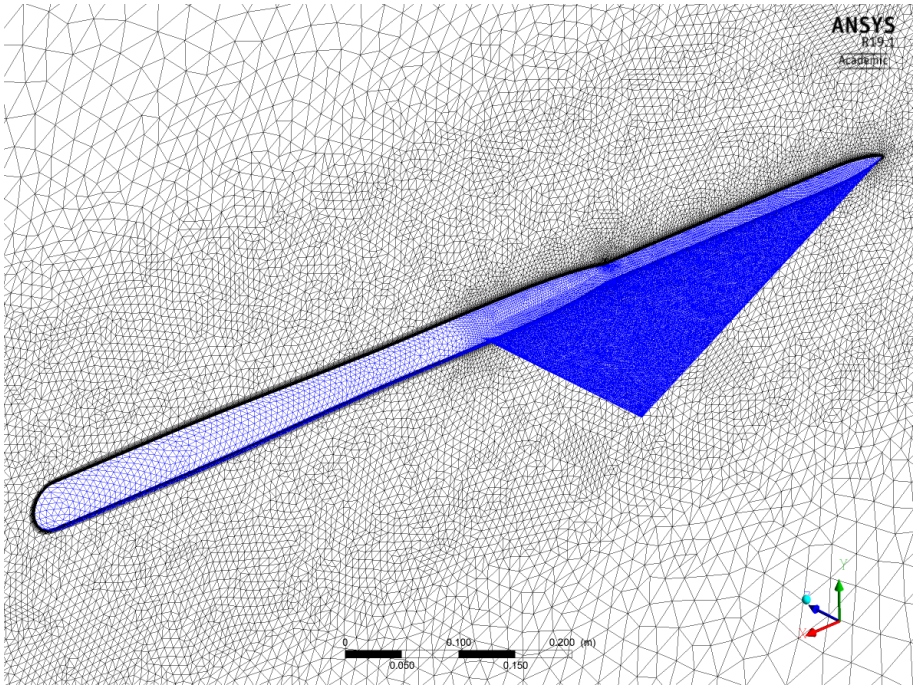

Figure 4.4 Generated grid of the VFE-2 as tested by TUM.

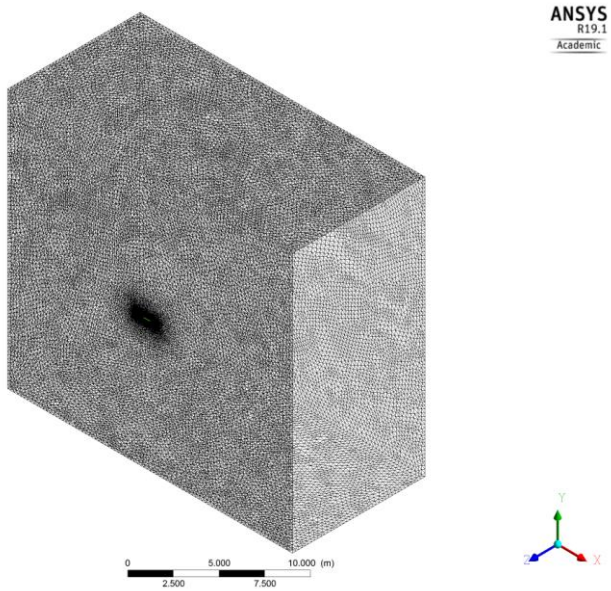

Figure 4.5 Grid resolution of the entire domain for the VFE-2 benchmark configuration.

The grids generated for the other configurations with varying spanwise thickness used a similar mesh, however, it proved to be more difficult to discretise them. This was due to the spanwise thickness change resulting in a singularity near the tip. To overcome this issue the geometry was split along the leading-edge, thus, reducing the sharpness of the corner.

4.4 Y^+ Value

The y^+ value (see Chapter 3 section 3.4 for details) was chosen based on flat-plate boundary layer theory (White, 2002). Generally, the choice of y^+ value depends on the turbulence model and the solver's near wall treatment. For most turbulence models and problems, a y^+ value less than one is desired as it ensures that the viscous sublayer of the boundary layer is resolved, thus, avoiding the use of wall functions.

The first layer height was chosen to be 2x 10^{-5} m. The boundary layer height was estimated using flat-plate theory to select a sufficient amount of prism layers. The simulation was run steady state and the turbulence model chosen was SST with curvature correction. All runs were run with an inlet turbulence intensity of 5%, which is the default setting in FLUENT. The runs were compared to the Linear Pressure-Strain RSM. It was found that for a convergence criterion of 1×10^{-6} the simulations were converging for the SST model and the RSM.

The y^+ value averaged to one with a standard deviation of around 0.15 one around the entire wing and was resolved by 45 prism layers with a growth rate of 1.1 resulting in a total height of 0.0113 m. Additional surface sizing had been applied as previous investigations on other delta wing configurations have shown that without a sufficient representation of the leading-edge contour the progression of the different vortices within the flow structure cannot be predicted correctly (Schuette et al., 2010).

4.5 Numerical Investigation

The quality of numerical simulations is dependent on the type and size of the chosen grid for a given turbulence model (Kulkarni et al., 2016). The quality of an element can be determined based on different characteristics, the ones chosen for this project being their aspect ratio, skewness, orthogonality and quality. These have a significant impact on the accuracy and stability of the numerical computation (FLUENT). This chapter deals with the process of determining the optimum grid for the numerical simulations by using the Grid Convergence Index (GCI) developed by Roache (1994). After the final grid had been established its quality was checked and sufficiency confirmed based on recommendations provided by ANSYS. A comparison of two RANS turbulence models were then conducted (SST and Linear- pressure strain RSM) to determine which one was more appropriate in capturing the important flow physics of delta wing configurations.

4.6 Grid Convergence Index (GCI)

In CFD, a grid is said to be successively refined when the discretisation error is asymptotically approaching zero whilst element size and time step are decreasing (Slater, 2008). The GCI was developed by Roache (2010) and applies the concept of Richardson extrapolation for improving the rate of convergence. It enables one to determine the order of convergence and the discretisation error.

The GCI is based on the assumption that the nature of the discretisation error can be defined as

$$Error = f_h - f_{exact} = Ch^p + H.O.Ts \tag{4.1}$$

where Error refers to the discretisation error, f_h is the solution with the current mesh density, f_{exact} is the exact solution, C is a constant, h is a measure of the mesh discretisation, p is the order of convergence and H.O.T.s are the higher order terms.

The exact solution here refers to the numerical solution which can differ from the mathematically exact solution due to approximations and limitations applied in the FVM formulation (Schwer, 2008).

The following derivation is focused on the situation where the error bound is determined based on the finest mesh solution. The order of convergence can be estimated by reading it as a slope on the logarithmic plot of the error versus the mesh density parameter (log(E) vs. log(h)).

Neglecting H.O.Ts in Equation (4.1) and taking the logarithm of both sides leads to (NASA NPARC):

$$log(E) = log(C) + p\ log\ (h) \tag{4.2}$$

By considering the results on three successive meshes f_1, f_2, f_3 and repeating Equation (4.1) for those three meshes, one can eliminate C and H.O.T.s to arrive at

$$p = \frac{ln\left(\frac{f_3 - f_2}{f_2 - f_1}\right)}{ln(r)} \tag{4.3}$$

with r being the mesh refinement ratio defined as

$$r = \frac{h_{i+1}}{h_i} \tag{4.4}$$

with h_i being the finer mesh. The measure of discretisation h is chosen by the user and depends on their judgement. For a delta wing, where it is known, that surface refinement has a great impact on the accuracy of the result, different levels of surface refinement were chosen as the discretisation parameter h. Note, that the refinement ratio can be uniform or non-uniform. If a non-uniform refinement ratio is chosen the GCI is obtained differently (see Appendix A.3.5 for details).

The error between the fine grid solution and the unknown exact solution can be estimated using (Schwer, 2008) using (4.1) and (4.4)

$$f_{exact} = f_1 - \frac{f_2 - f_1}{r^p - 1} \tag{4.5}$$

Note that Equation (4.5) is only valid for a constant r.

The estimated relative error E_1 can then be calculated using

$$E_1 = \frac{\varepsilon}{r^p - 1} \tag{4.6}$$

with ε being defined as the relative error between the two finest grids

$$\varepsilon = \frac{f_2 - f_1}{f_1} \tag{4.7}$$

The GCI is defined as (Roache, 1998):

$$GCI = \frac{F_s|\varepsilon|}{r^p - 1} \times 100\% \qquad (4.8)$$

where F_s is a factor of safety which is

$F_s = 3$ when two meshes are considered and

$F_s = 1.25$ when three meshes or more are considered.

The GCI shows how much the solution would change with a further refinement in mesh. Therefore, the smaller the value of the GCI the better. Note, that the safety factors given above are based on experiences on CFD calculations (Roache, 1998). It also represents with a confidence of 95% that the converged solution is within range of

$\left[f_1\left(1 - \frac{GCI_{12}}{100\%}\right), f_1\left(1 - \frac{GCI_{23}}{100\%}\right)\right]$ (Schwer, 2008).

Additionally, if all results f_i are in the asymptotic range of convergence then two GCIs computed over three meshes satisfy (Slater, 2008):

$$GCI_{23} = r^p GCI_{12} \qquad (4.9)$$

The extrapolation error in Equation (4.6) can further be used to calculate the uncertainties of the numerical findings. This is particularly useful when comparing numerical data with that obtained during wind tunnel testing (see Yao, 2013; Celik et al., 2008, Eca and Hoekstra, 2014 and Groves et al., 2014). Many options to calculate the uncertainty exist (see Yao, 2013; Celik et al., 2008, Eca and Hoekstra, 2014), however, here the approach of Groves et al. (2014) was used which is based on the student t-distribution:

$$U = t \times \left|\frac{1}{2}(S_u - S_L)\right| \qquad (4.10)$$

with t=2.92, which is the t value of the student t-distribution for three grids, and S_u and S_L being the upper and lower bounds of the solution variable respectively.

4.7 Grid Convergence Study

The grid refinement study was conducted on different grids by changing different meshing parameters such as surface refinement, element size in the vicinity of the wing, element growth

rate and domain size. The grids were labelled from Grid I to Grid VII and are summarised in Table 4.3.

In order to establish whether an appropriate domain size and grid refinement had been chosen the normal and axial force as well as the pitching moment were plotted against the grid refinement level (1 being the finest and 3 being the coarsest grid) to establish as to whether the grids were within the asymptotic range of convergence. Based on this the GCI was calculated. This gave a conclusion on the error percentage and provided a confidence bound on the estimated error band of the converged numerical solution.

Table 4.3 Summary of Grids tested.

	1st Order	2nd Order	Face Sizing	Body of Influence (BOI)	BOI Growth Rate	Domain Size (in terms of chord c)	No. of Elements
Grid I	x	x	3.375×10^{-3} m	1×10^{-2} m	1.2	20c	7,472,012
Grid II		x	2.25×10^{-3} m				9,540,829
Grid III		x	1.5×10^{-3} m				17,300,896
Grid IV		x	2.25×10^{-3}m	1.3×10^{-2} m	1.125		6,547,254
Grid V		x					3,174,841
Grid VI		x		8×10^{-3} m		10c	8,786,838
Grid VII		x		1×10^{-2} m		40c	9,540,829

4.8 Grid Convergence Study on the VFE-2 configuration at M= 0.07, Re=1×10^6 and α= 18°

The following mesh experiments were performed to investigate the effect of the mesh design on the aerodynamic forces and moments. Similar studies have been conducted during AVT-113 by Crippa and Rizzi (2008) as well as others. None of them used the GCI however, making the comparison somehow subjective. The experiments are:

1. Changing the maximum surface element size on the VFE-2 configuration with sting mount at M=0.07, Re= 1×10^6 and α= 18°
2. Changing the element size within the body of influence for the VFE-2 with sting mount M=0.07, Re= 1×10^6 and α= 18°
3. Changing the domain size around the VFE-2 configuration with sting mount M=0.07, Re= 1×10^6 and α= 18°

4. Changing the element size within the body of influence for the B05 configuration with no sting mount M=0.1, Re= 0.75×10^6 and α= 13°
5. Changing the maximum surface element size for the B05 configuration with no sting mount M=0.1, Re= 0.75×10^6 and α= 13°

For surface and body of influence refinement the mesh quality was assesses using the following mesh metrics (ANSYS Workshop, 2015):

1. Orthogonal Quality: acceptable values are >= 0.15
2. Skewness: acceptable values are =< 0.94
3. Aspect Ratio: acceptable values >1

4.8.1 Surface Refinement Study on the VFE-2 Configuration

The mesh refinement study focused on the refinment of the wing's surface elements. This aspect was chosen due to the shear forces acting on the wing's surface being major contributors to the separation of the flow and the vortex roll up. Therefore, the mesh study used a different element size for each mesh of the face of the thin benchmark configuration. The maximum element size for the three different meshes can be found in Table 4.4. Table 4.4 also shows the total number of elements and nodes as well the number of wing surfaces elements.

Equation (4.9) allows for checking that each grid level yields a solution that is in the asymptotic range of convergence for the axial and normal force as well as the pitching moment. These are in the column called "Convergence Check" and should have a value close to one when lying in the asymptotic range of convergence.

All simulations fully converged to 1×10^{-6} for the aerodynamic coefficients Cn and Cm. The axial force coefficient only converged to 1×10^{-5}. The details of each grid including the run time can be seen in Table 4.4 where the convergence is given as 1×10^{-5} for all cases. The different surface grids are shown in Figure 4.6. Note, that the surface mesh of the sting was kept constant for each grid.

Table 4.5 shows the average mesh metrics for the different grids. It can be seen that all three grids are of good quality, with quality increasing with surface mesh refinement.

Table 4.4 Surface Refinement Seeding Parameters for Grid I, Grid II and Grid III of the VFE-2 Configuration.

	Grid I	Grid II	Grid III
Maximum Face Sizing [m]	0.343125	0.225	0.1475
Number of wing surface elements	20,826	56,456	106,827
Total Number of Elements	7,472,012	9,540,829	17,300,896
Total Number of Nodes	1,626,412	2,489,763	4,787,289
Run Time (16 cores) [h:min:s]	26:32:54	30:12:27	40:56:38
Convergence	$1x10^{-5}$	$1x10^{-5}$	$1x10^{-5}$
	coarse	medium	fine

Table 4.5 Surface Refinement Mesh Metrics for Grid I, Grid II and Grid III of the VFE-2 Configuration.

	Grid I	Grid II	Grid III
Mean Orthogonal Quality	0.7915	0.794	0.798
Mean Skewness	0.276	0.277	0.2721
Mean Aspect Ratio	8.085	9.21	9.647

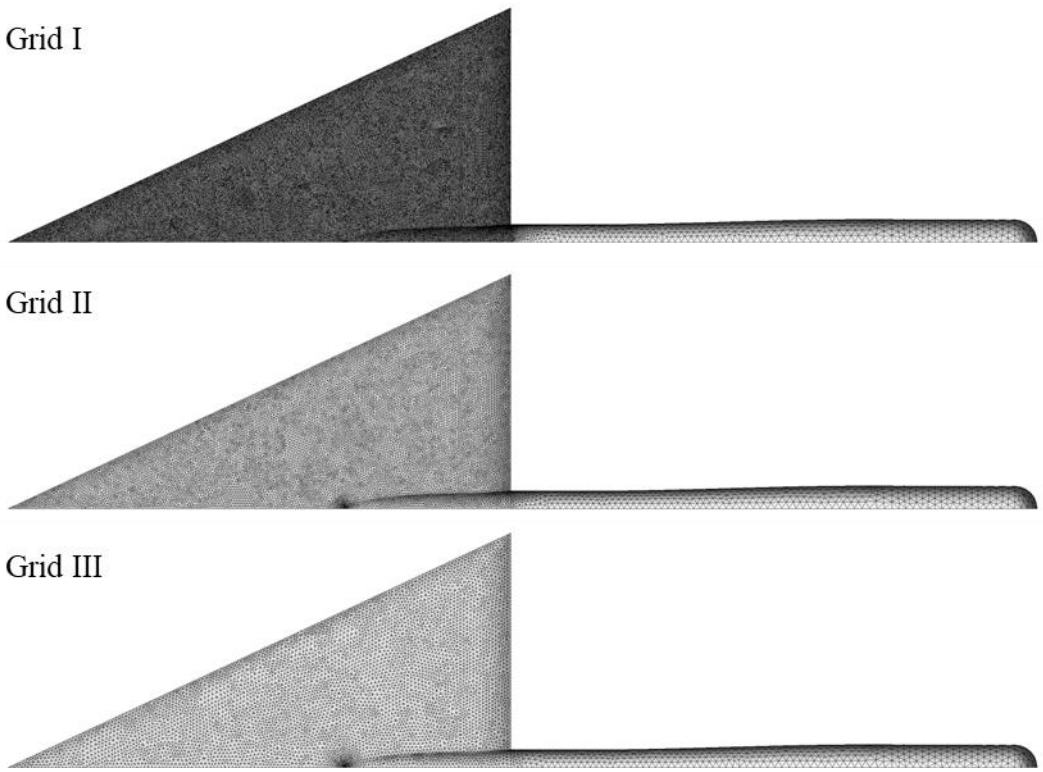

Figure 4.6 Grid I, Grid II and Grid III with maximum surface element sizes of 0.343125m, 0.225m and 0.1475m respectively.

Table 4.6 shows the aerodynamic forces obtained for each mesh and Table 4.7 shows the results for the grid convergence index and the Richardson extrapolation. It can be seen that the three meshes were not within the asymptotic range of the solution for the normal and axial force and pitching moment, indicating that further refinement would be required in order to use the GCI. The relative error of the axial force is high; around 23.5% and shows the importance of surface elements when predicting vortex dominated flows. Despite the results not lying in the asymptotic range the GCI was used in order to have some quantification of the numerical error when comparing the results later with those obtained in the wind tunnel.

Table 4.6 Aerodynamic loads of Grids I, II and III at α= 18°.

	Normal Force [N]	Axial Force [N]	Moment [Nm]
Grid I	25.9355	-0.113609	6.84479
Grid II	25.6688	-0.160798	6.71473
Grid III	25.8313	-0.210157	6.7702

Table 4.7 Grid Convergence Study of Grids I, II and III for different aerodynamic loads.

	GCI_{12}	GCI_{23}	Convergence Check	Order of Convergence p	95% Interval		Estimate of exact solution
					Lower bound	Upper bound	
Pitching Moment	1.802%	0.762 %	1.009	2.018	6.5937	6.8357	6.8115
Normal Force	2.027%	1.226%	1.007	1.173	25.5145	26.1481	26.0847
Axial Force	798.258%	638.430%	0.707	0.106	1.1315	-1.5519	-0.9126

For better judgement the numerical results and the Richardson extrapolate have been plotted for each force and moment against the normalised grid spacing. They can be found in Figure 4.7 and show that forces and moment are not in the asymptotic range of convergence.

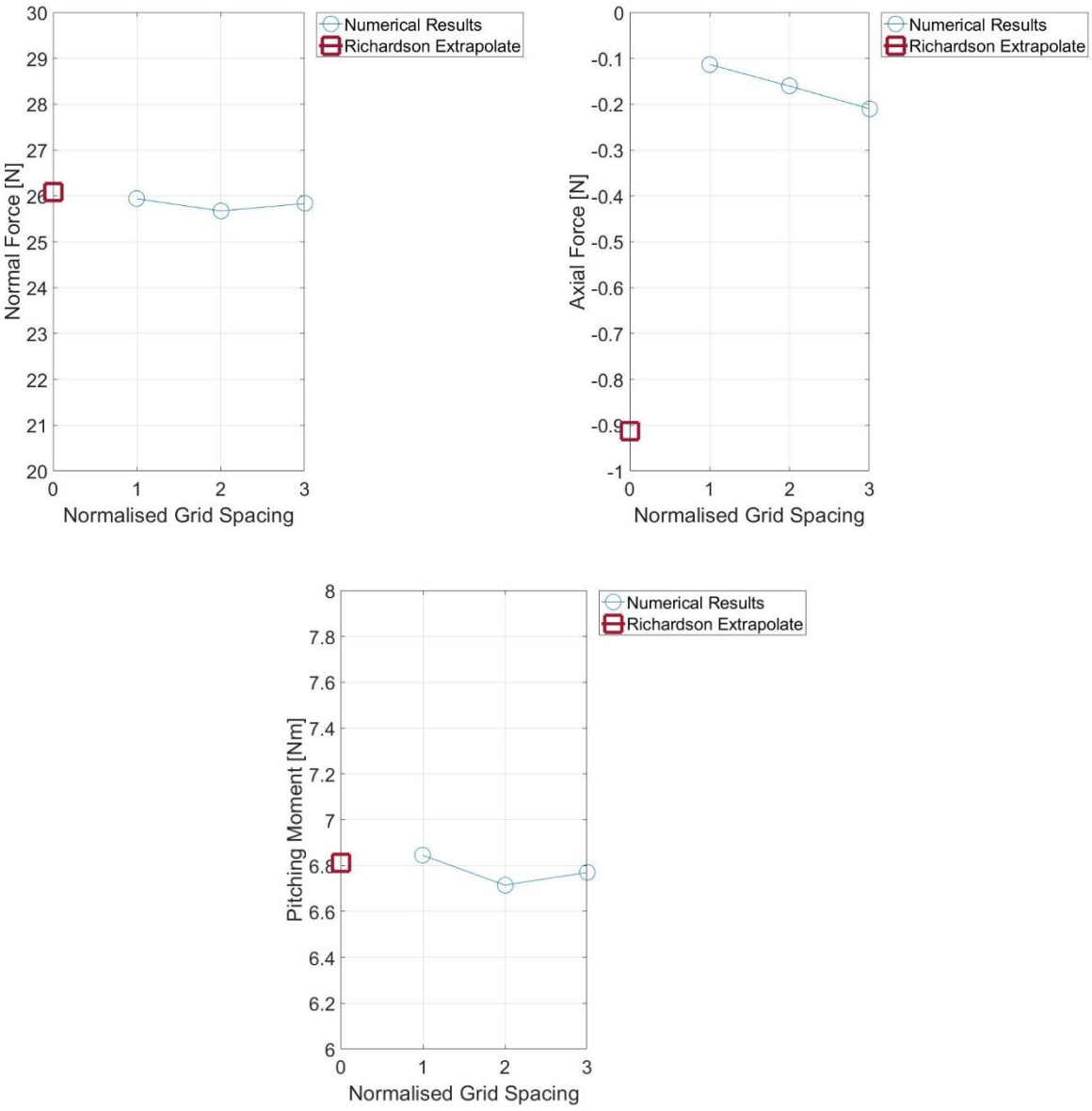

Figure 4.7 Richardson Extrapolate and numerical results for different grids and aerodynamic loads.

Since the flow features are very important; the pressure distribution at different chordwise locations was also compared between the meshes. The results are depicted in Figure 4.8. It can be seen that all three grids have a similar spanwise pressure distribution. The only noticeable difference can be found at x/c=0.2. Here, the coarsest grid predicted the pressure peak to be much lower than the other grids. Grid III predicted the highest pressure peak for most chord locations whereas the coarsest grid (Grid I) predicted the lowest pressure peaks throughout.

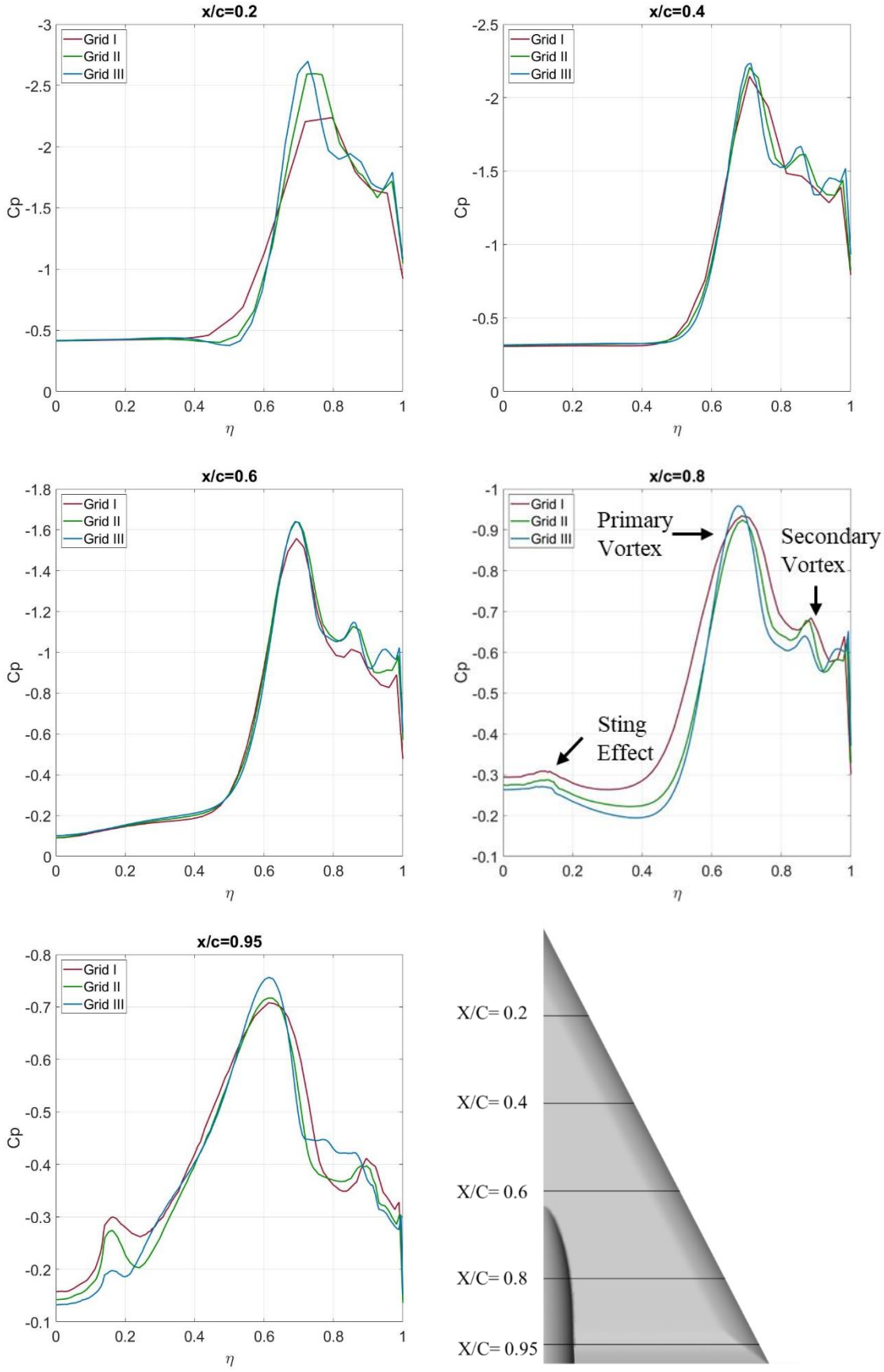

Figure 4.8 Comparison of the Spanwise Cp distribution at different chord locations for different levels of surface refinement at α= 18°.

Figure 4.9 shows the mean axial velocity contours for the three grids. It can be seen that there was barely any observable difference between the coarser grids. Grid II predicted a vortex core of slightly higher velocity from x/c=0.8 onwards compared to Grid I but not compared to Grid III. The axial velocity close to the trailing edge further increases with surface refinement, indicating that higher surface refinement is required when simulating higher angle of attack to avoid early VBD prediction.

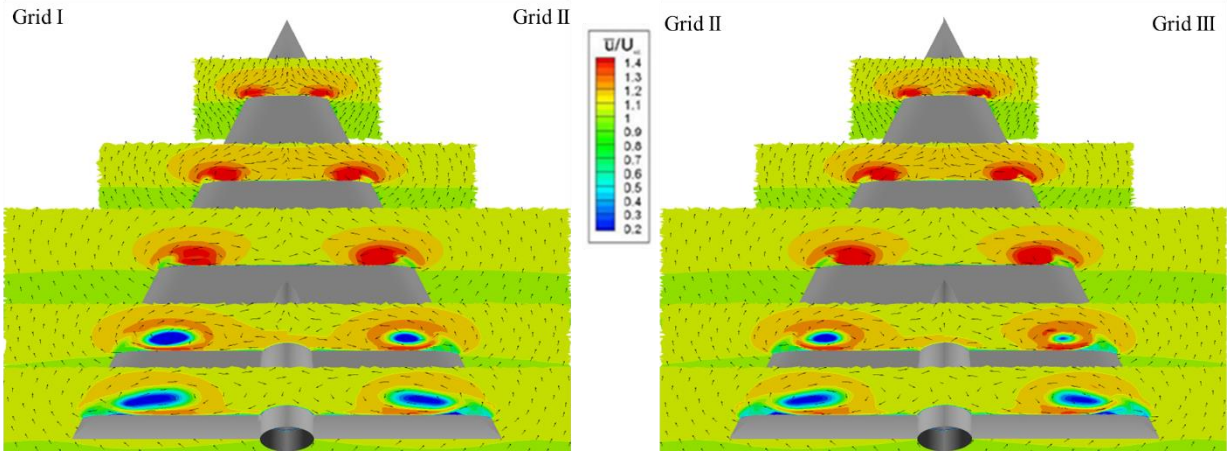

Figure 4.9 Comparison of the axial velocity contours and velocity vectors for different surface refinements at α= 18°.

Based on the findings above it was concluded that using the mesh with face sizing 0.225m (Grid II) would be sufficient as it gave the best accuracy whilst keeping computational time at an acceptable level. This was decided despite the non-convergence of the axial force component and the prediction of VBD at x/c=0.8.

Whilst using grids with higher surface refinement may not be an issue for big research institutions with high computational power available, it did prove to be a problem for the computational capabilities at the University of the West of England, Bristol (UWE). Therefore, the maximum angle of attack was limited to 18° as incidences above this would need a finer surface mesh in order to make meaningful physical predictions, due to the occurrence of VBD introducing time dependent effects.

4.8.2 Impact of Element Size within the Body of Influence for the VFE-2 Configuration

To investigate the effect of the element size in the vicinity of the wing on the flow physics another GCI study was conducted. Three different element sizes were used, each 1.3 times smaller than the previous, with Grid II being used as the benchmark grid. This resulted in Grid IV and V, where Grid IV was the coarsest and Grid V was the finest mesh. The details of the three grids is shown in Table 4.8 with the mesh metrics being depicted in Table 4.9. It can be seen from Table 4.9 that orthogonal quality and skewness improve with decrease in element

size whilst aspect ratio worsens. This implicates that there is an optimum element size for the body of influence given a certain surface refinement. Table 4.10 shows the force components and pitching moment, which were found to lie in the asymptotic range of convergence (Figure 4.10), thus, allowing for the use of the GCI.

Table 4.8 BOI Element Size Seeding Parameters for Grid IV, Grid II and Grid V of the VFE-2 Configuration.

	Grid IV	Grid II	Grid V
Maximum Face Sizing [m]	0.225		
BOI max. Element Size [m]	1.3×10^{-2}	1×10^{-2}	7.67×10^{-3}
Number of wing surface elements	56,456		
Total Number of Elements	6,547,254	9,540,829	14,194,916
Total Number of Nodes	1,886,395	2,489,763	3,174,841
Run Time (16 cores) [h:min:s]	24:59:23	30:12:27	37:13:58
Convergence	$1x10^{-5}$	$1x10^{-5}$	$1x10^{-5}$
	coarse	medium	fine

Table 4.9 BOI Element Size Mesh Metrics for Grid IV, Grid II and Grid V of the VFE-2 Configuration.

	Grid IV	Grid II	Grid V
Mean Orthogonal Quality	0.792	0.794	0.796
Mean Skewness	0.278	0.277	0.276
Mean Aspect Ratio	12.312	9.21	6.159

The results for the aerodynamic components are presented in Table 4.10 with the GCI study shown in Table 4.11. It can be seen that grid convergence is achieved for the axial and normal force as well as for the pitching moment (Figure 4.10). To further investigate the effect of BOI element size the surface pressure distribution as well as the normalised axial velocity contours were investigated (see Figure 4.11 and Figure 4.12).

Table 4.10 Aerodynamic loads of Grids IV, II and V at α= 18°.

	Normal Force [N]	Axial Force [N]	Moment [Nm]
Grid IV	25.6488	-0.158675	6.70774
Grid II	25.6688	-0.160798	6.71473
Grid V	25.7	-0.159074	6.72567

Table 4.11 Grid Convergence Study of Grids IV, II and V for different aerodynamic loads.

	GCI_{12}	GCI_{23}	Convergence Check	Order of Convergence p	95% Interval		Estimate of exact solution
					Lower bound	Upper bound	
Pitching Moment	0.216%	0.337%	0.409	1.707	6.7015	6.7499	6.7450
Normal Force	0.163%	0.255%	0.409	1.707	25.6304	25.7696	25.7557
Axial Force	7.131 %	5.853%	0.995	0.793	-0.1498	-0.1684	-0.1516

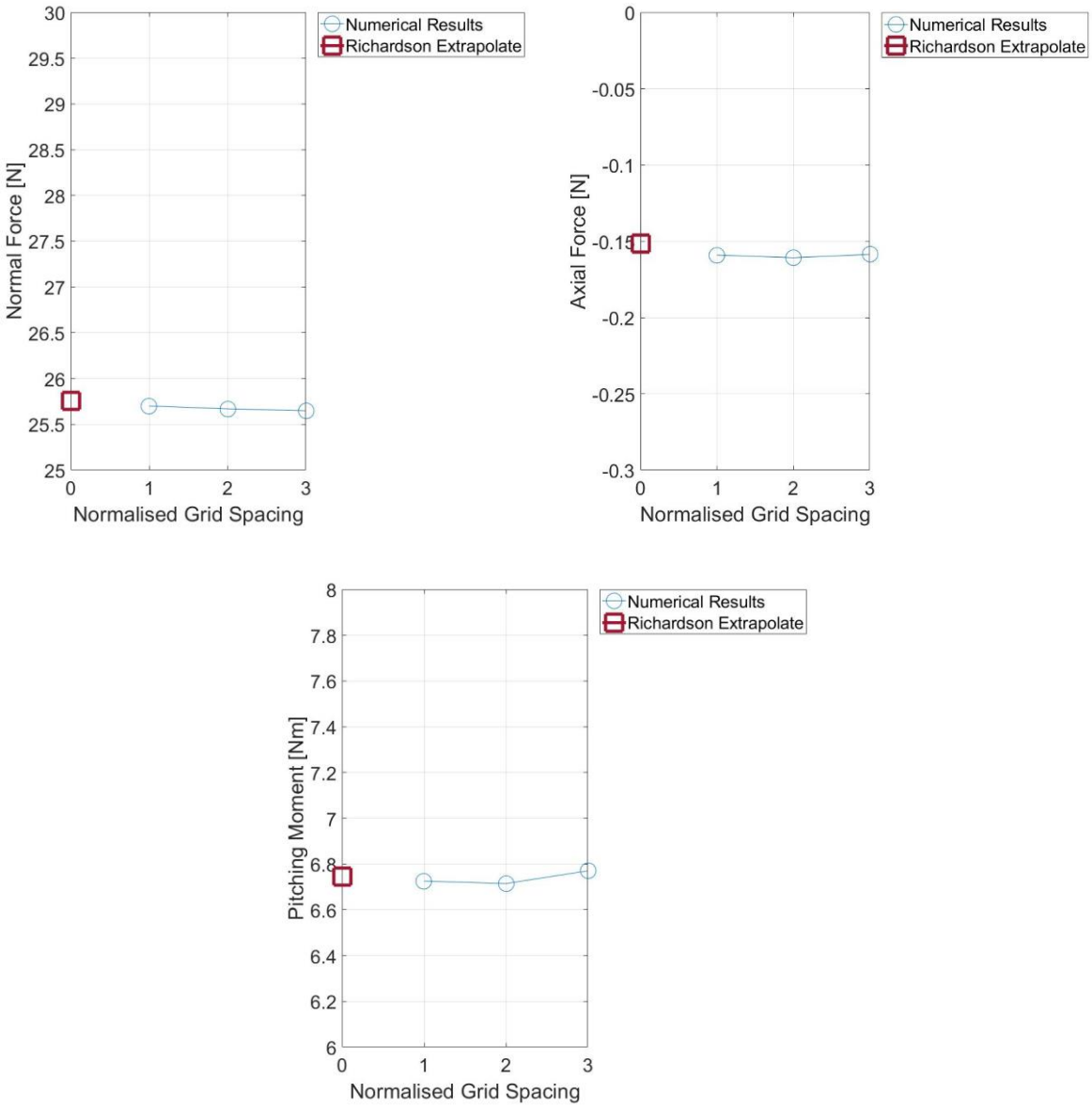

Figure 4.10 Richardson Extrapolation and numerical results for Grids IV, II and V.

The surface pressure distribution (Figure 4.11) as well as the axial velocity contours (Figure 4.12) were identical for all grids, despite the GCI indicating that the grids have not converged yet. This was due to the GCI evaluating the change in force or moment compared to the previous grid. However, the changes in normal force and pitching moment with smaller BOI element size were very small, but not in relative terms. This gave the impression that the grids had not converged, despite there being no differences in flow physics observed.

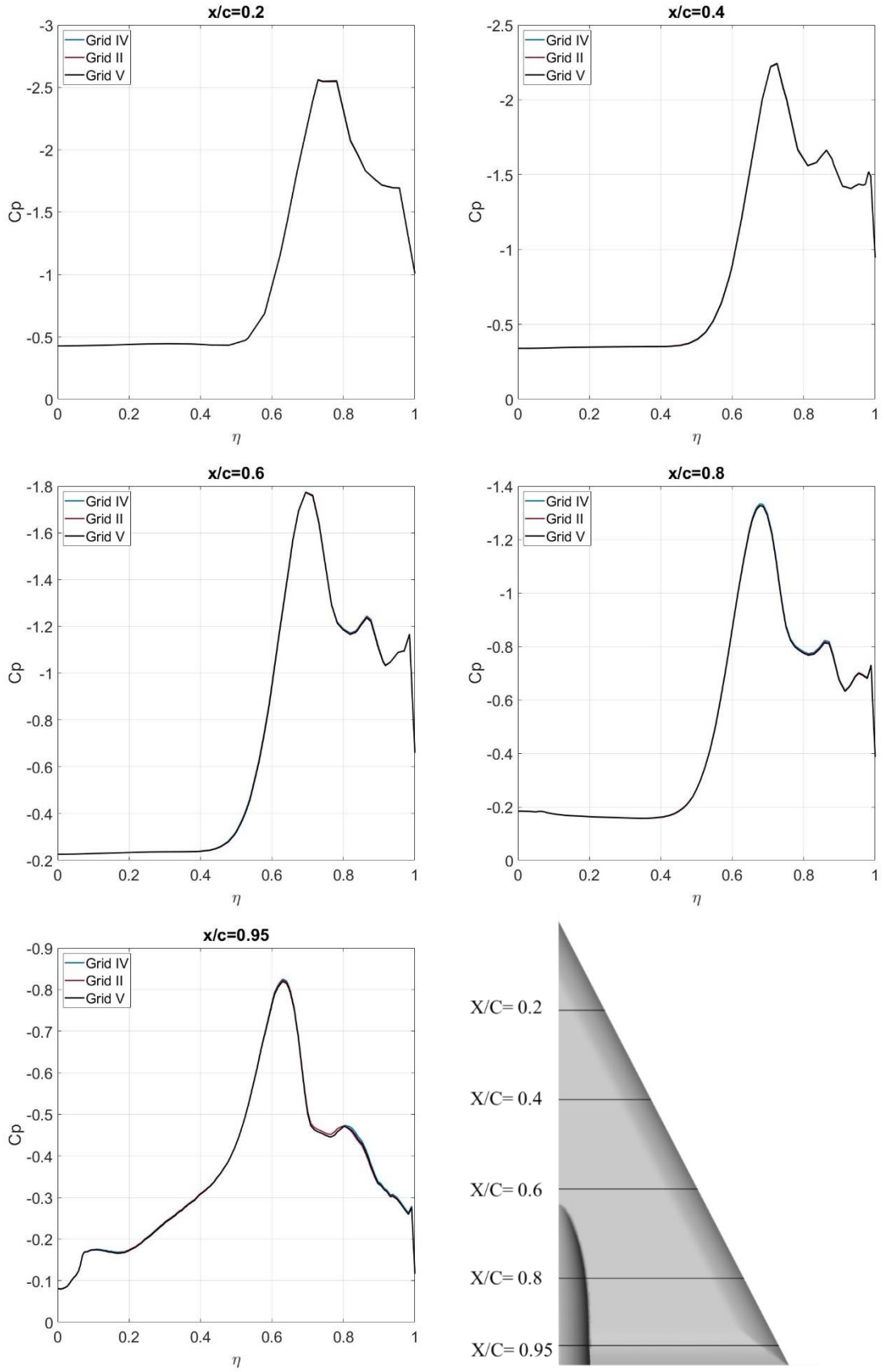

Figure 4.11 Comparison of the spanwise pressure distribution at different chord locations between Grid IV, Grid II and Grid V at α= 18°.

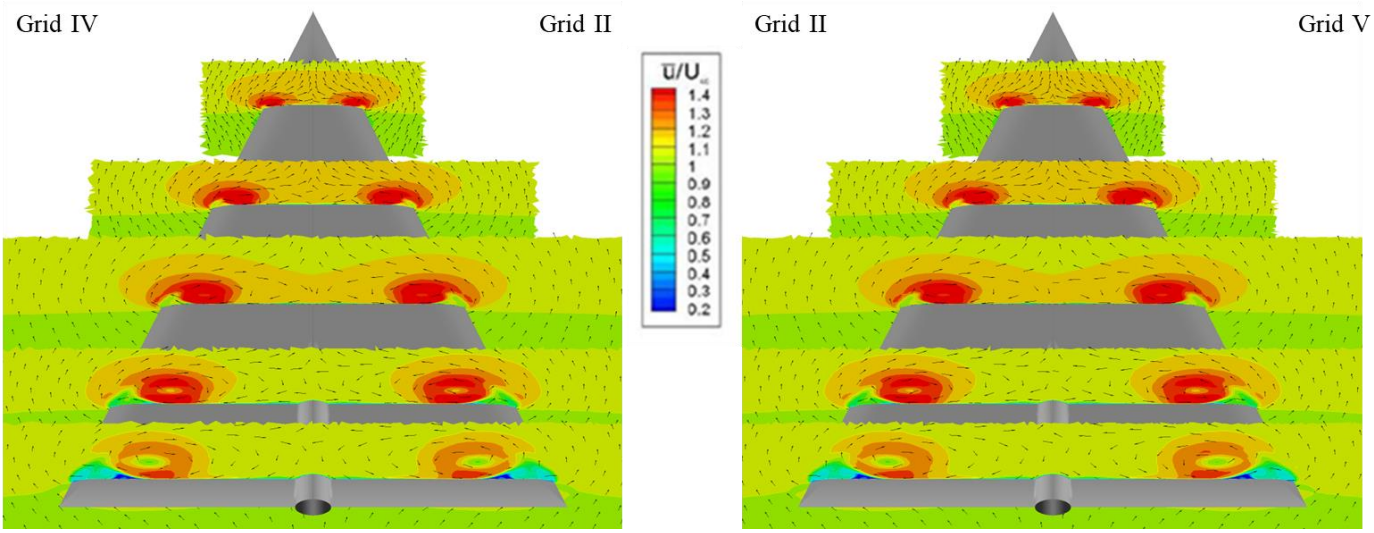

Figure 4.12 Mean axial velocity contours and velocity vectors for Grids IV, II and V at α= 18°.

4.8.3 Domain Size Study of the VFE-2 Configuration

A domain size study was conducted for Grid II for domains of size 10c, 20c and 40c at α= 13°. The details of each domain are presented in Table 4.12.

Table 4.12 Specifications of Grid II, VI and VII of the VFE-2 Configuration.

	Grid II	Grid VI	Grid VII
Face Sizing [m]	0.225		
Number of wing surface elements	56,456	56,456	56,456
Total Number of Elements	9,540,829	8,786,838	9,540,829
Total Number of Nodes	2,489,763	2,339,262	2,489,763
Run Time (16 cores) [h:min:s]	30:12:27	26:34:45	27:01:36
Convergence	$1x10^{-5}$	$1x10^{-5}$	$1x10^{-5}$
Domain Size [c]	20	10	40

The forces obtained from CFD can be found in Table 4.13 and lie within the asymptotic range of convergence (Figure 4.13) with GCI study results shown in Table 4.14. It can be seen that

the grids did converge for the normal force and pitching moment, but not the axial force (see also Table 4.14). Here, the relative error was calculated to be 6.5%, which was concluded to be acceptable. A comparison of the spanwise pressure distribution and mean velocity contour plots (Figure 4.14 and Figure 4.15) shows no significant difference between the different domain sizes. It was therefore concluded that a $20c_r$ domain will suffice for this investigation.

Table 4.13 Aerodynamic loads obtained for Grids II, VI and VII at α= 18°.

	Normal Force [N]	Axial Force [N]	Moment [Nm]
Grid VI	25.6544	-0.144186	6.70577
Grid II	25.7097	-0.142593	6.72154
Grid VII	25.7429	-0.152451	6.73543

Table 4.14 GCI obtained for Grids II, VI and VII.

	GCI_{12}	GCI_{23}	Convergence Check	Order of Convergence p	95% Interval		Estimate of exact solution
					Lower bound	Upper bound	
Pitching Moment	2.167%	1.905%	1.002	0.183	6.607	6.864	6.838
Normal Force	0.404%	0.242%	1.001	0.736	25.5586	25.681	25.793
Axial Force	0.269%	1.558%	0.028	2.63	-0.1501	-0.1548	-0.1544

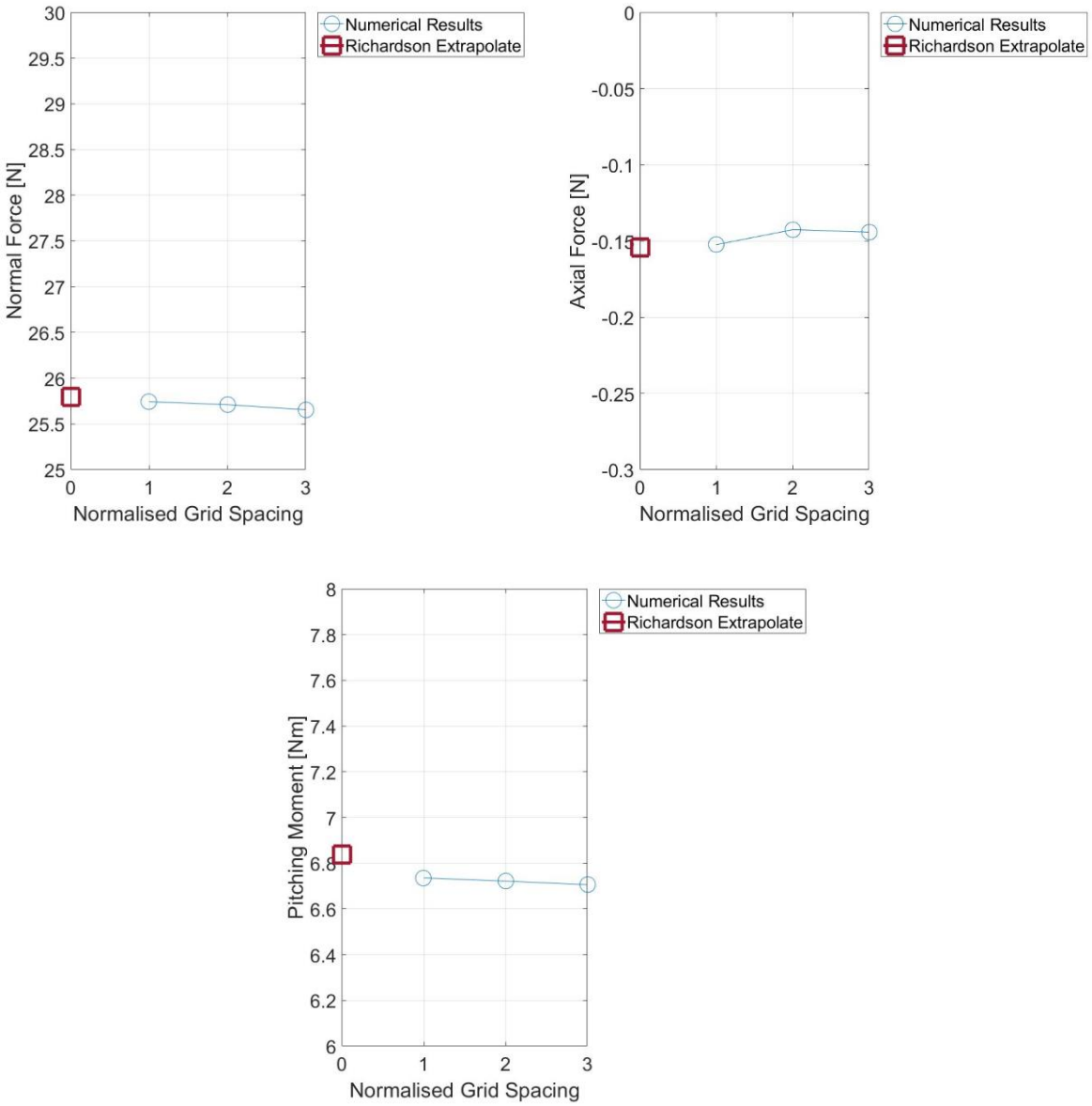

Figure 4.13 Richardson Extrapolation and numerical results for Grids II, VI and VII.

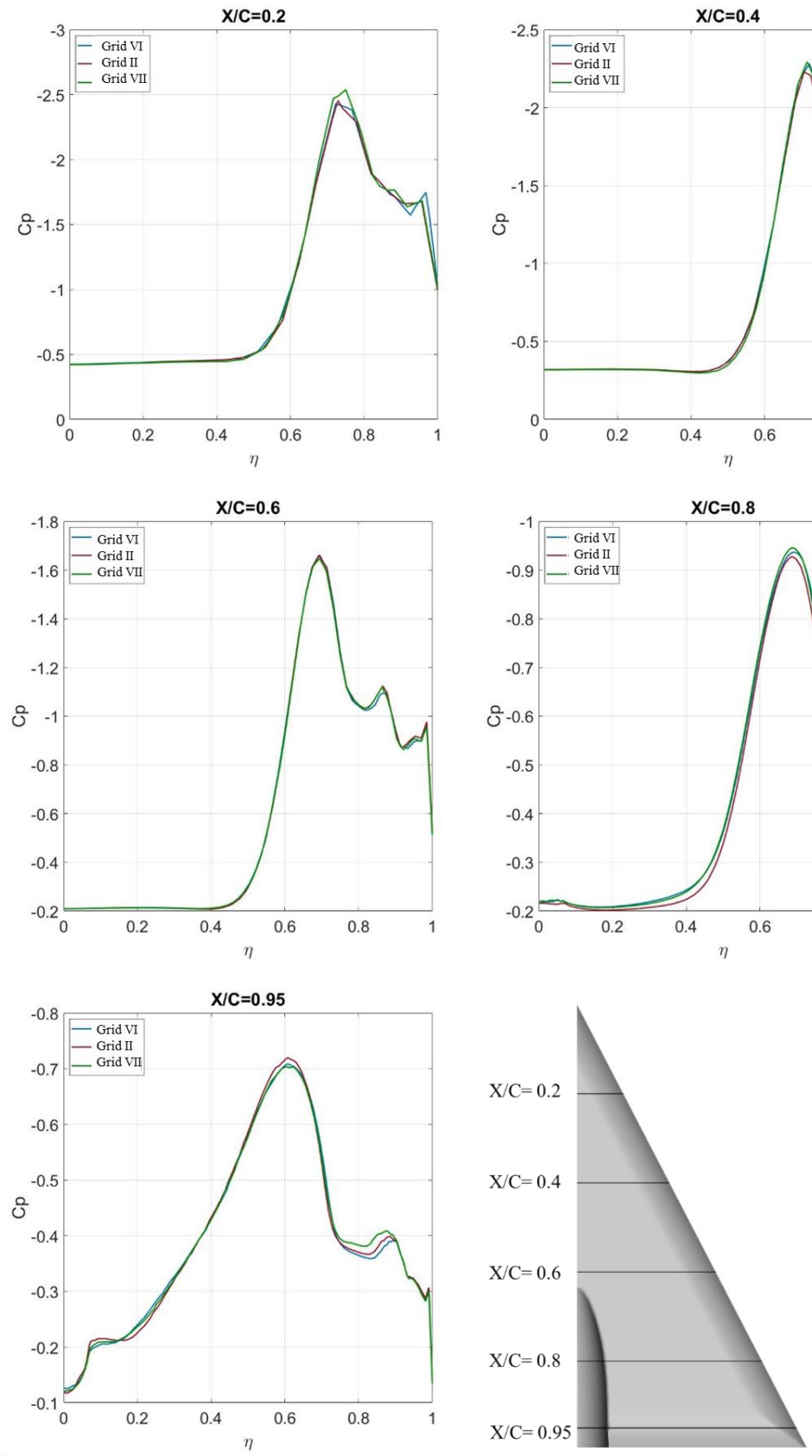

Figure 4.14 Comparison of the spanwise pressure distribution at different chord locations between grids Grid II, Grid VI and Grid VII at α= 18°.

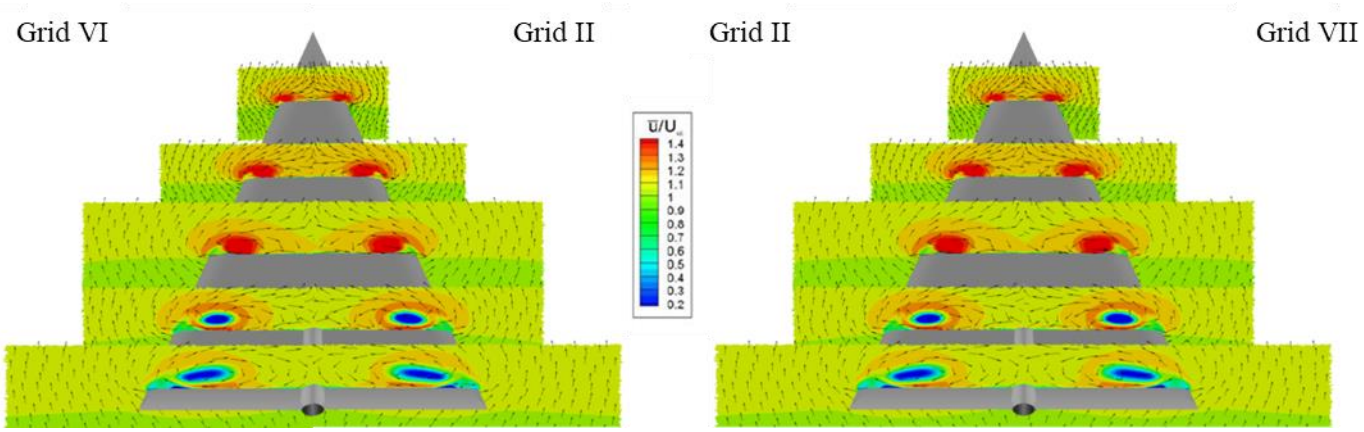

Figure 4.15 Mean axial velocity contours and velocity vectors for Grids II, VI and VII at α= 18°.

4.9 Grid Convergence Study on the B05 3.4% configuration at M= 0.1, Re=750,000 and α= 13°

Similar as to the GCI study for the VFE-2 configuration a mesh study was conducted for the B05 3.4% thick wing at test conditions (M=0.1, Re=750,000 and α=13°). These were the wind tunnel test conditions at UWE Bristol. A separate mesh study was necessary as the configurations were simulated not including a sting mount. This in combination with the different speed could have an effect on mesh convergence and therefore a separate mesh study was required. In contrast to the VFE-2 GCI study, a domain study was not conducted for the B05 configuration as the subtle changes in geometry between the configurations were not assumed to necessitate a large change in size of computational domain.

If it was found that a similar grid arrangement could be applied to cases where there is just a change in spanwise thickness than this could save computational time as the biconvex configurations also vary in spanwise thickness. If it was shown that a slight change in geometry has an impact on the mesh refinement region than this could yield information about the importance of different flow properties on the flow physics of delta wing configurations and would provide useful guidance on improved meshing techniques.

4.9.1 Surface Refinement Study on the B05 3.4% Configuration

The study on different surface refinement levels is discussed in the following paragraph. Three different maximum face sizings were applied (0.225m, 0.15m and 0.1m). The details of the grids as well as the GCI can be found in Table 4.15 and Table 4.17. The mesh metrics are shown in Table 4.16. Opposed to the VFE-2 configuration not all mesh metrics are improving. Skewness worsens with increase in surface refinement though only marginally.

All three grids reached the convergence criteria of 1×10^{-6}, with the normal force and pitching moment lying in the asymptotic range of convergence (Figure 4.16).

Table 4.15 Specifications of Grids I, II and III of the B05 Configuration.

	Grid I	Grid II	Grid III
Face Sizing [m]	0.343125	0.225	0.1475
Number of wing surface elements	20,163	43,217	93,168
Total Number of Elements	7,572,738	8,835,881	15,646,197
Total Number of Nodes	1,605,491	2,170,559	4,079,234
Run Time (16 cores) [h:min:s]	14:31:37	39:59:27	61:00:16
Convergence	1e-6	1e-6	1e-6
	coarse	medium	fine

Table 4.16 Surface Refinement Mesh Metrics for Grid I, Grid II and Grid III of the B05 Configuration.

	Grid I	Grid II	Grid III
Mean Orthogonal Quality	0.787	0.788	0.788
Mean Skewness	0.277	0.277	0.279
Mean Aspect Ratio	6.867	8.153	8.897

Table 4.17 Aerodynamic loads obtained for Grids I, II and III at α= 18°.

	Normal Force [N]	Axial Force [N]	Moment [Nm]
Grid I	22.813	0.120	6.414
Grid II	22.990	0.117	6.398
Grid III	23.087	0.098	6.330

The convergence check in Table 4.18 shows that for both forces and moment the values were close to unity indicating good grid convergence. The relative error for the axial force was around 10% despite the good convergence check value, again showcasing that the surface mesh primarily affects the prediction of the axial force component. This was due to it being two orders of magnitude smaller than the normal force and one order of magnitude smaller than the pitching moment, thus, being more sensitive to changes in discretisation.

Table 4.18 GCI obtained for Grids I, II and III.

	GCI_{12}	GCI_{23}	Convergence Check	Order of Convergence p	95% Interval		Estimate of exact solution
					Lower bound	Upper bound	
Pitching Moment	0.094%	0.408 %	1.008	3.607	6.304	6.355	6.309
Normal Force	0.81 %	0.354%	1.005	1.948	22.627	23.0	23.152
Axial Force	1.066%	6.159%	0.036	3.897	0.094	0.103	0.093

Table 4.18 and the Richardson extrapolate plots in Figure 4.16 show that Grid II is within the asymptotic region of the solution for normal force and pitching moment but not for the axial force. Examining the spanwise pressure distribution as well as the mean velocity contour plots (Figure 4.17 and Figure 4.18) showed further that the grids converged.

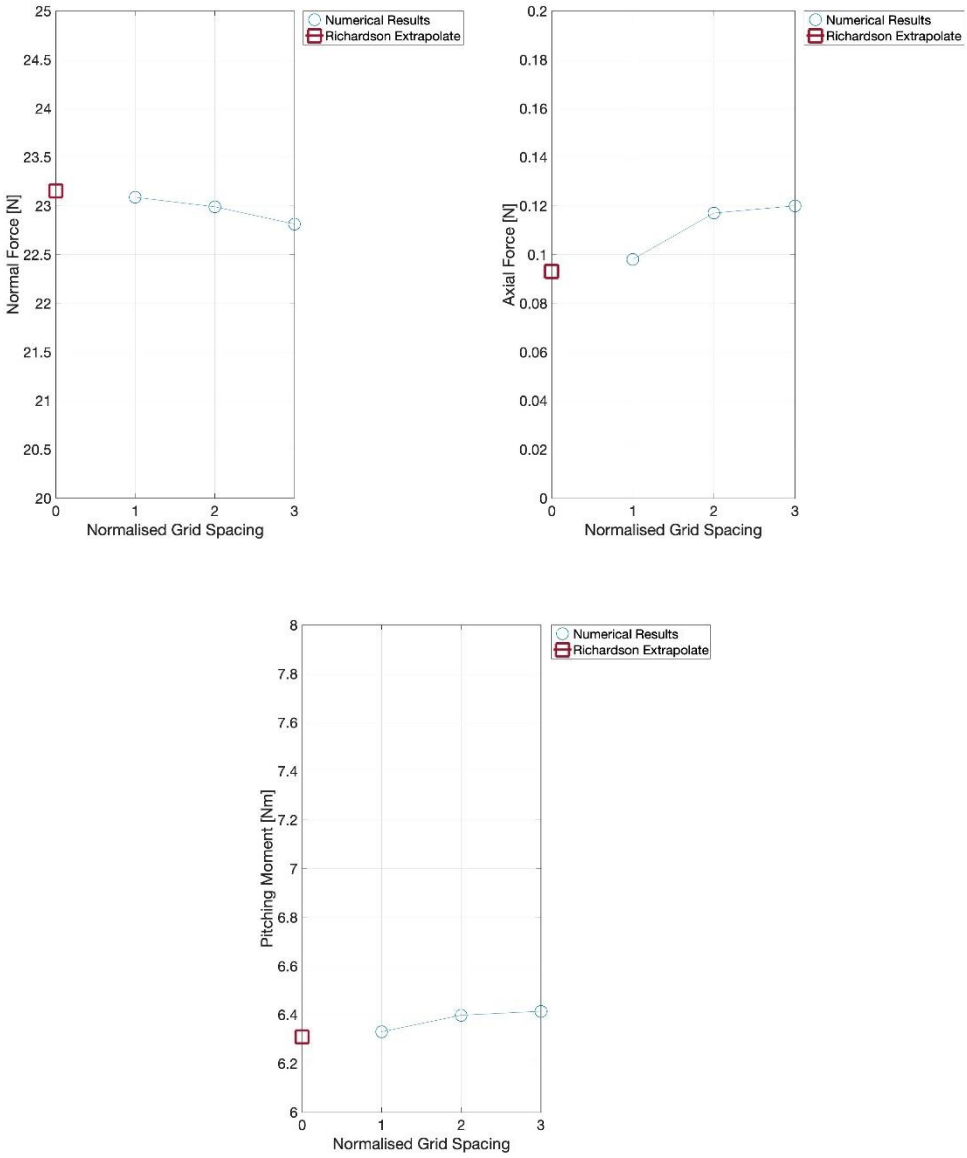

Figure 4.16 Richardson Extrapolation and numerical results for Grids I, II and III.

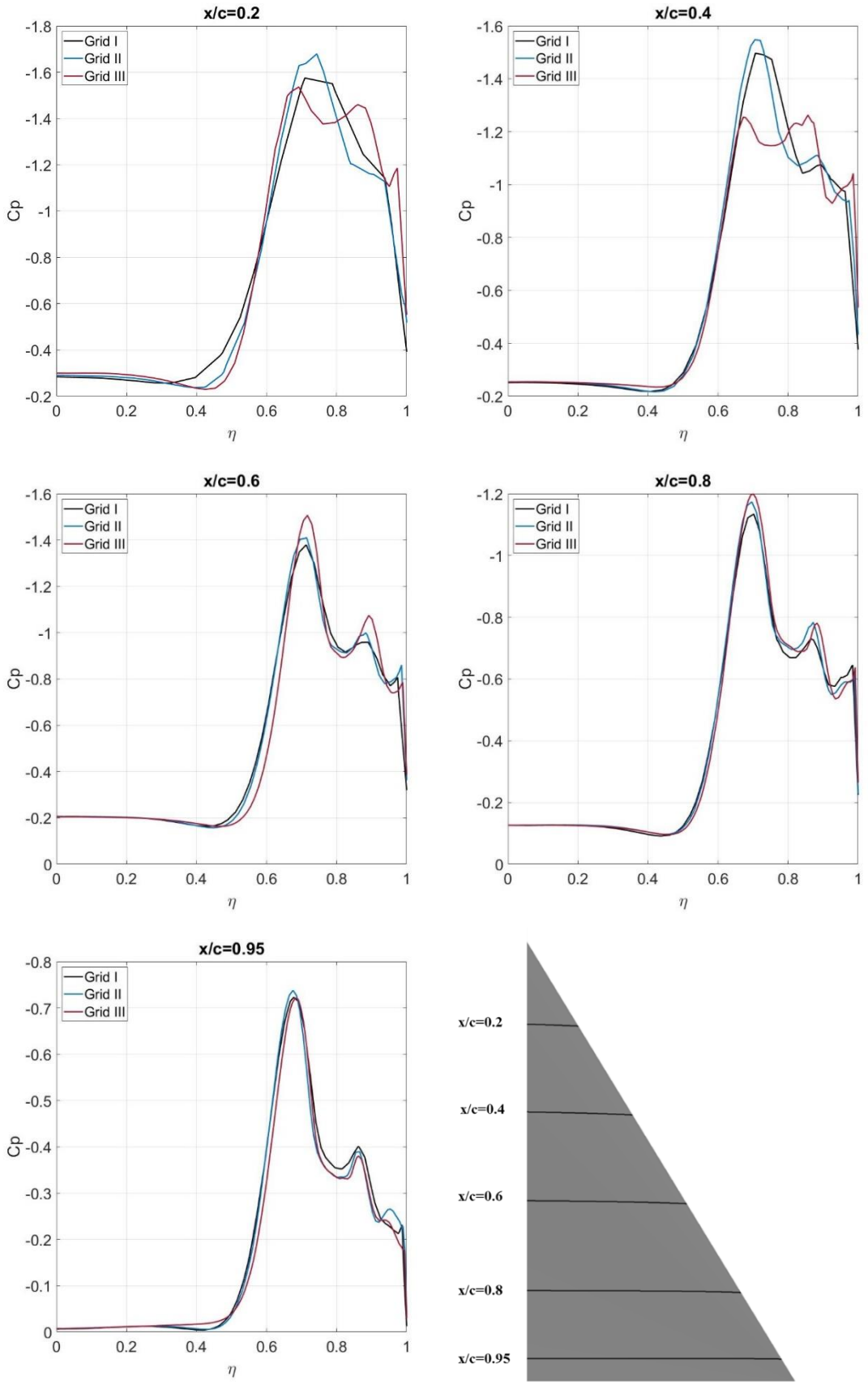

Figure 4.17 Comparison of the spanwise pressure distribution at different chord locations for different surface refinement levels at M=0.1, Re= 750,000 and α= 13°.

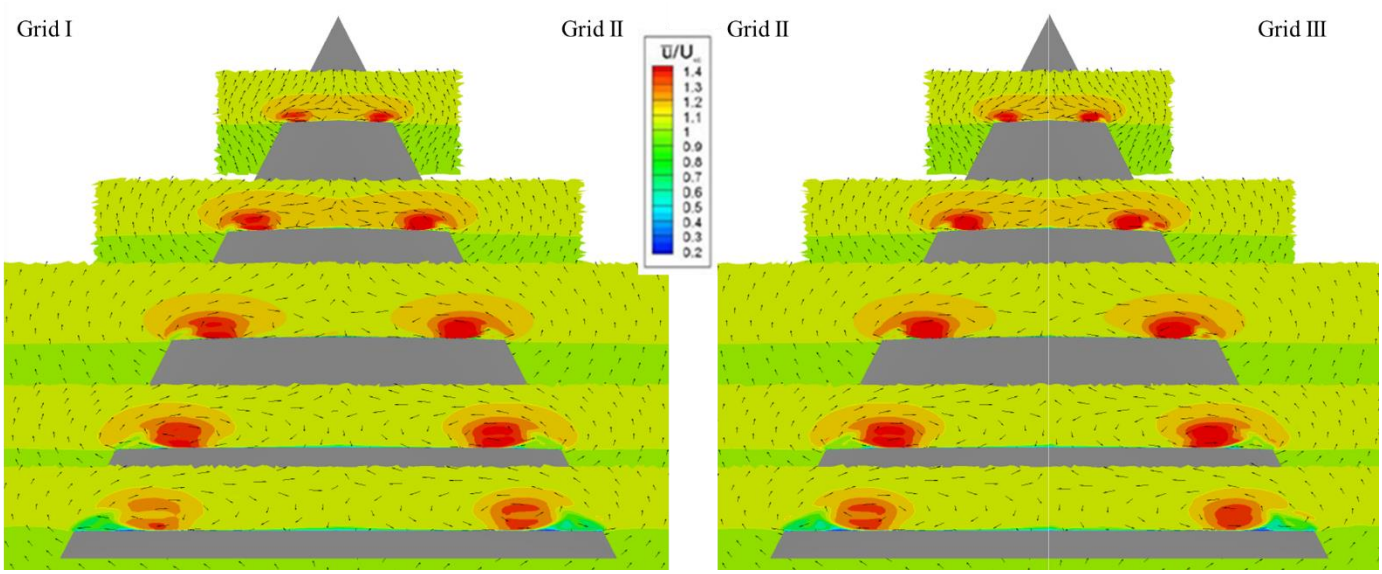

Figure 4.18 Mean axial velocity contours and velocity vectors for Grids I, II and III at α= 13°.

4.9.2 Impact of Element Size within the Body of Influence on the B05 3.4% Configuration

As for the VFE-2 an additional study was carried out for the element size within the Body of Influence (BOI). Here, Grid II served as the benchmark grid based on which a finer (Grid IV) and a coarser grid (Grid V) were generated. All aerodynamic loads lie in the asymptotic range of convergence (Figure 4.19) and the details of each grid as well as the convergence level and run time can be found in Table 4.19 with the mesh metrics shown in Table 4.20 and the results for the force component and pitching moment shown in Table 4.21.

Table 4.19 Specifications of Grid II, IV and V of the B05 configuration.

	Grid IV	Grid II	Grid V
Face Sizing [m]	0.225		
BOI Element Sizing [m]	8×10^{-3}	1×10^{-2}	1.135×10^{-2}
Number of wing surface elements	43,217		
Total Number of Elements	14,078,001	8,835,881	6,269,539
Total Number of Nodes	3,053,774	2,170,559	1,737,695
Run Time (16 cores) [h:min:s]	49:34:29	39:59:27	24:40:16
Convergence	1×10^{-6}	1×10^{-6}	1×10^{-6}
	coarse	medium	fine

Table 4.20 BOI Element Size Mesh Metrics for Grid IV, Grid II and Grid V of the B05 Configuration.

	Grid IV	Grid II	Grid V
Mean Orthogonal Quality	0.791	0.788	0.784
Mean Skewness	0.277	0.277	0.278
Mean Aspect Ratio	5.801	8.153	11.1

Table 4.21 Aerodynamic loads obtained for Grid IV, II and V at α= 18° of the B05 configuration.

	Normal Force [N]	Axial Force [N]	Moment [Nm]
Grid IV	23.003	0.102969	6.398
Grid II	22.990	0.116584	6.393
Grid V	22.892	0.116467	6.371

From Table 4.22 can be seen that grid convergence was not achieved for pitching moment and normal force, but only for the axial force component. A finer mesh would result in a grid with over 25 million elements, which was outside the limits of the computers at the University of the West of England Bristol. It was therefore decided to use Grid II as this was the best option considering computational limitations and time restrictions. The findings of the grid convergence study give an error estimate which was considered in the evaluation of the results as well as in the comparison with the experimental data.

Table 4.22 GCI obtained for Grid IV, II and V of the B05 configuration.

	GCI_{12}	GCI_{23}	Convergence Check	Order of Convergence p	95% Interval		Estimate of exact solution
					Lower bound	Upper bound	
Pitching Moment	0.036%	0.144%	0.064	5.222	6.362	6.380	6.364
Normal Force	0.011%	0.082%	0.018	7.695	22.874	22.911	22.877
Axial Force	0.127%	0.001%	0.999	18.13	0.1165	0.1165	0.1165

The results for the aerodynamic forces and moment for each grid and the Richardson extrapolate are shown in Figure 4.19 showcasing that the results for axial and normal force as well as pitching moment were in the asymptotic range. However, to get a more detailed understanding on how the resolution of the BOI influences the flow physics the surface pressure coefficient as well as the contours of the mean axial force component were compared for each grid.

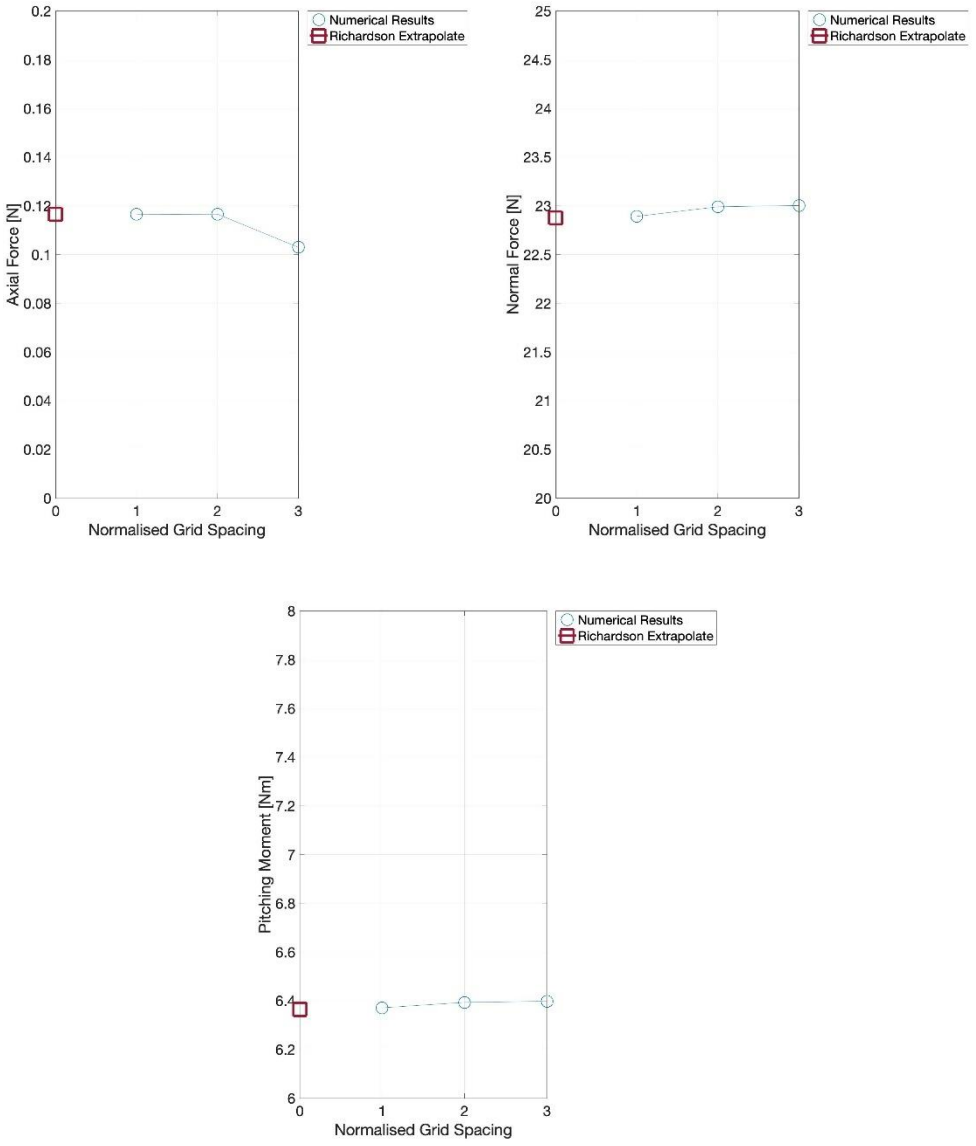

Figure 4.19 Richardson Extrapolation and numerical results for Grid IV, II and V.

The surface pressure distribution and the axial force contour plots are shown in Figure 4.20 and Figure 4.21. It can be seen that the difference in pressure distribution is greatest towards the apex. Here, a pattern cannot be determined. The coarsest and the finest grids were very similar at x/c=0.2 but after that the medium and finest meshes predicted a similar pressure distribution. Also, no significant difference could be found between grids regarding the normalised axial velocity component. This justified the use of Grid II for the remainder of the study. It could also be shown that surface refinement as well as the element size around the wing had a significant impact on the surface pressure distribution especially near the apex. However, it was found that the element quality was more sensitive to the surface meshing as the elements of poorer quality were found close to the wing's leading and trailing edge. It is

therefore recommended to prioritise surface meshing when generating grids for the investigation of vortical flow around delta wing configurations.

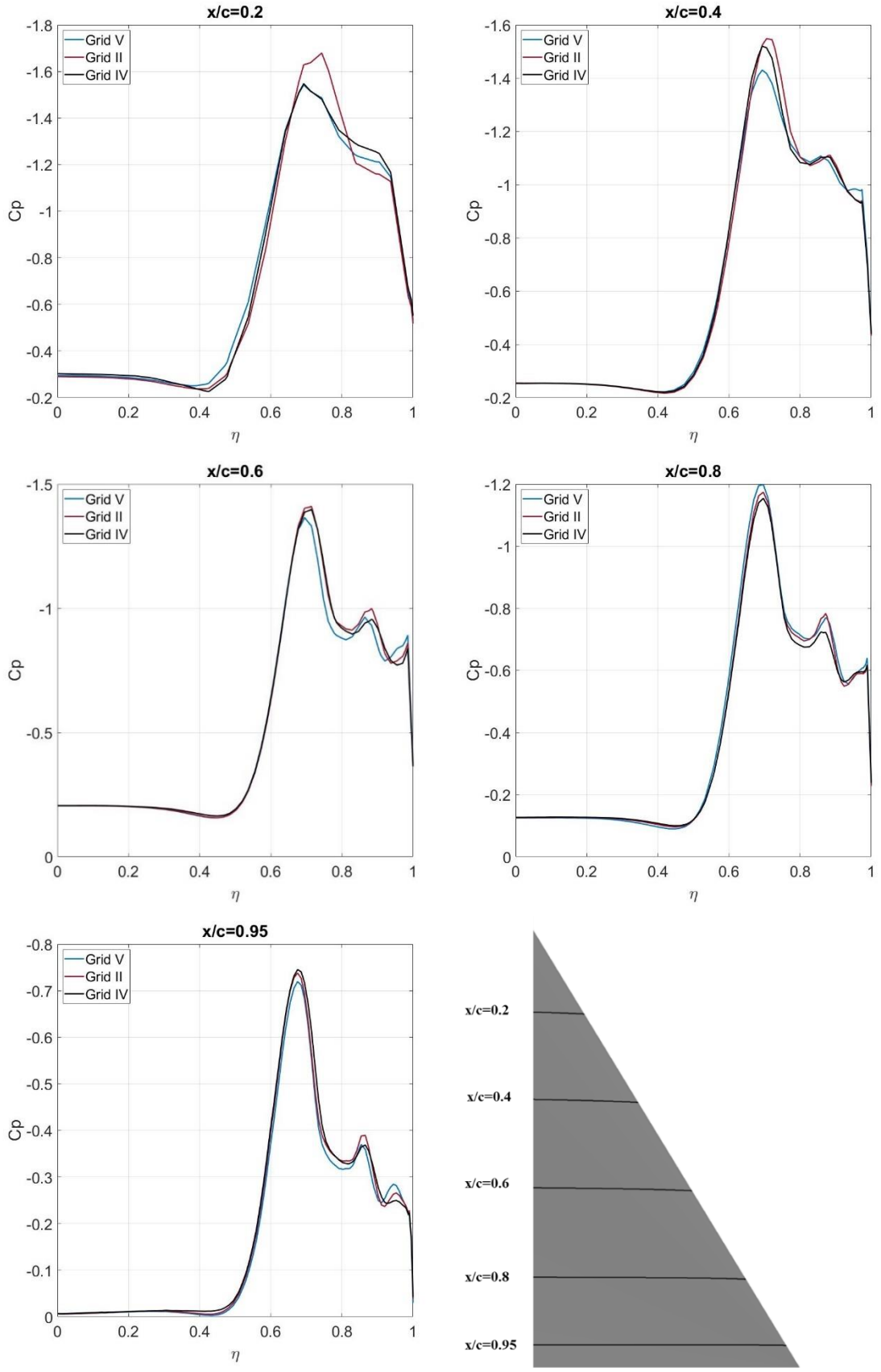

Figure 4.20 Comparison of the spanwise pressure distribution at different chord locations for different BOI element size at M=0.1, Re= 750,000 and α= 13°.

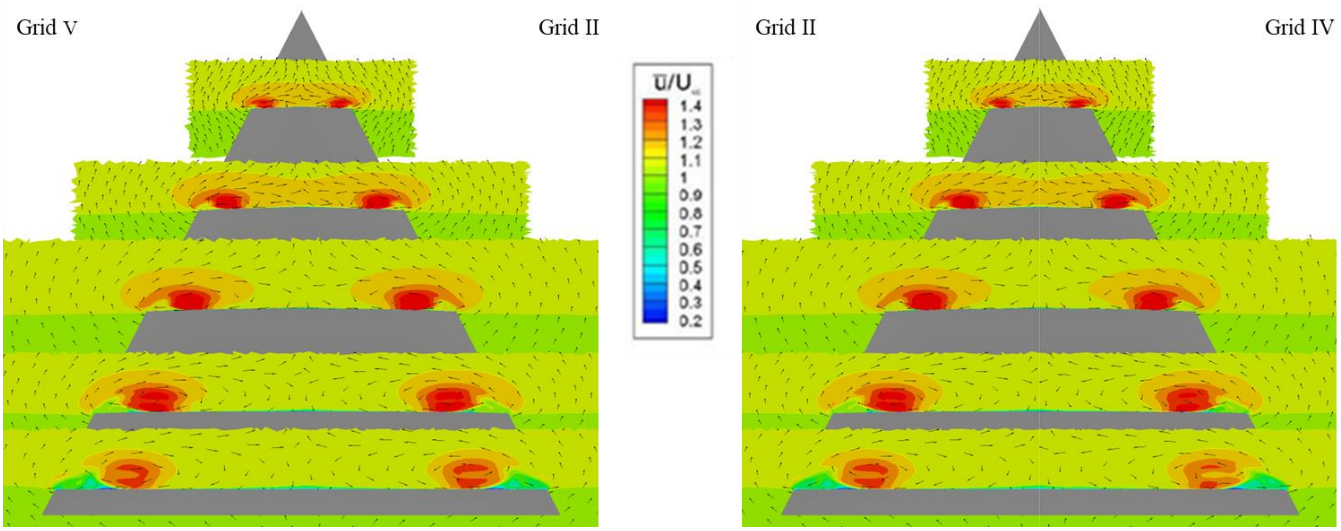

Figure 4.21 Mean axial velocity contours and velocity vectors for Grid V, II and IV at α= 13°.

4.10 Conclusion Chapter 4: Grid Refinement Study

From the grid refinement study, it was concluded that surface resolution is of major importance for the prediction of vortical flows. This was especially true with regards to the axial force component, which plays a major role in LEV prediction, as it determines the suction force generated by the vortices, which plays a major role in vortex lift prediction. It can further be seen that the surface pressure distribution was affected by surface grid refinement, resulting in different magnitudes in the pressure peaks, especially near the apex. This in particular is important as the initial vortex development affects the vortex behaviour further downstream, thus, its correct modelling is crucial. However, a very fine surface mesh results in a drastic increase in overall element count, increasing computational time significantly. Therefore, it is not always feasible to conduct numerical simulations on a high-resolution grid and compromises have to be made.

Further it has been found that the element size surrounding the area close to the wing had an impact on the aerodynamic characteristics predicted. However, the effect was less than for the surface refinement. This is shown in Figure 4.22 based on the example of the B05 3.4% configuration. Here the difference in spanwise pressure distribution are depicted for different areas of grid refinement.

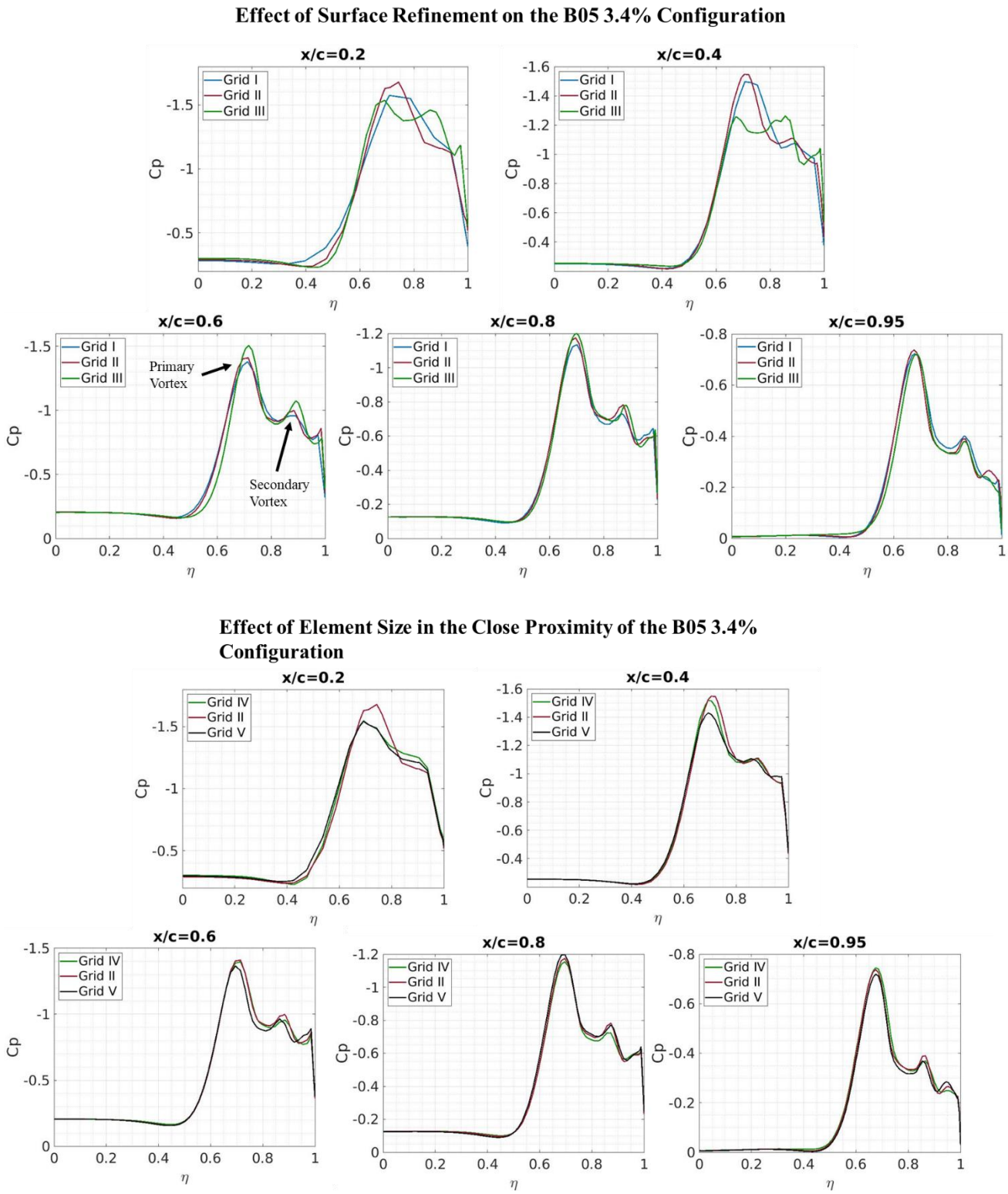

Figure 4.22 Comparison of the effect of surface grid refinement and grid size in the close proximity of the wing on the spanwise pressure distribution at different chord positions at α=13° for the B05 3.4% configuration at M=0.1 and Re= 750,000.

The major differences were found near the apex and diminished further downstream. This was in particular true for the clean configuration, whereas barely any differences were noted for the VFE-2 configuration with sting. There are multiple reasons as the VFE-2 included a sting and

was tested at different Reynolds number and angle of attack. Thus, no definite conclusions could be drawn and the investigation of different grids also lay outside the scope and computational power of this project.

From the above can be concluded, that a high-quality mesh requires an initial knowledge of the expected flow physics in order to adapt the grid in these regions accordingly. Grid adaption algorithms appear to be a solution but have not been implemented as standard features in most meshing codes.

Another finding of the grid refinement study was that domain size only has little impact on the results obtained, despite the axial force still being a more sensitive parameter. Surface refinement should be given priority when generating a computational grid as it has more impact than a fine grid in the vicinity of the configuration.

Generally, it was shown that evaluating the convergence of a run was difficult and depended on the variables considered. However, it should be ensured that every required variable was captured to a chosen accuracy.

Surface refinement and change in the element size within the BOI were found to increase the total number of elements drastically, which results in a trade-off between accuracy and computational costs. The GCI for the surface grid converged for both configurations whereas the element size of the BOI did not. However, it was found that this was more due to relative effects rather than due to a complete misprediction of the flow structure. Considering the limitations of computational resources at the University of the West of England it was decided to use Grid II as it showed the best compromise between accuracy and computational time. The mesh settings of Grid II as well as the general mesh settings of this project are summarised in Table 4.23 and Table 4.24.

Table 4.23 Final grid parameters based on the Grid Convergence Study.

Max Face Sizing [m]	2.25×10^{-3}
Max. Element Size BOI [m]	1×10^{-2}
Growth Rate BOI	1.125
Domain size	20c

Table 4.24 Specifications of the final grid.

Domain Size in root chord length c	20 c
1st Layer Height	2 x10^{-5} m
Growth Rate of Prismatic Layers	1.1
Number of Prismatic Layers	45
Total Height	0.0113 m
Maximum y^+	2.12
Mean y^+	1
Growth rate of Body of Influence	1.125
Number of Elements	9,704,007
Wing Surface Elements	48,898

Table 4.25 shows the summary of the mesh quality criteria mentioned earlier. It can be seen that apart from the orthogonal quality the grid was of good condition. The elements with an orthogonal quality below 0.15 (0.18% of all elements) are depicted in Figure 4.23. They are dependent on the face area of the element as well as on the distance between cell centroid and face and the distance between the centroid of the cell and the centroid of the neighbouring cell. As can be seen from Figure 4.23 the elements with poor quality were located along the leading and trailing edge of the configuration. In order to improve quality either the face sizing would have need reducing or the first layer height increasing. The former was not possible due to the restriction in computational memory and the latter would have resulted in an increase in y^+ which would also not be recommended.

Table 4.25 Summary of the mesh quality of the final grid.

Criterion	Min	Max	Average
Orthogonal Quality	1.1131x10^{-2}	0.99898	0.79505
Skewness	2.4368x10^{-4}	0.80301	0.20277
Aspect Ratio	1.1648	673.54	11.522

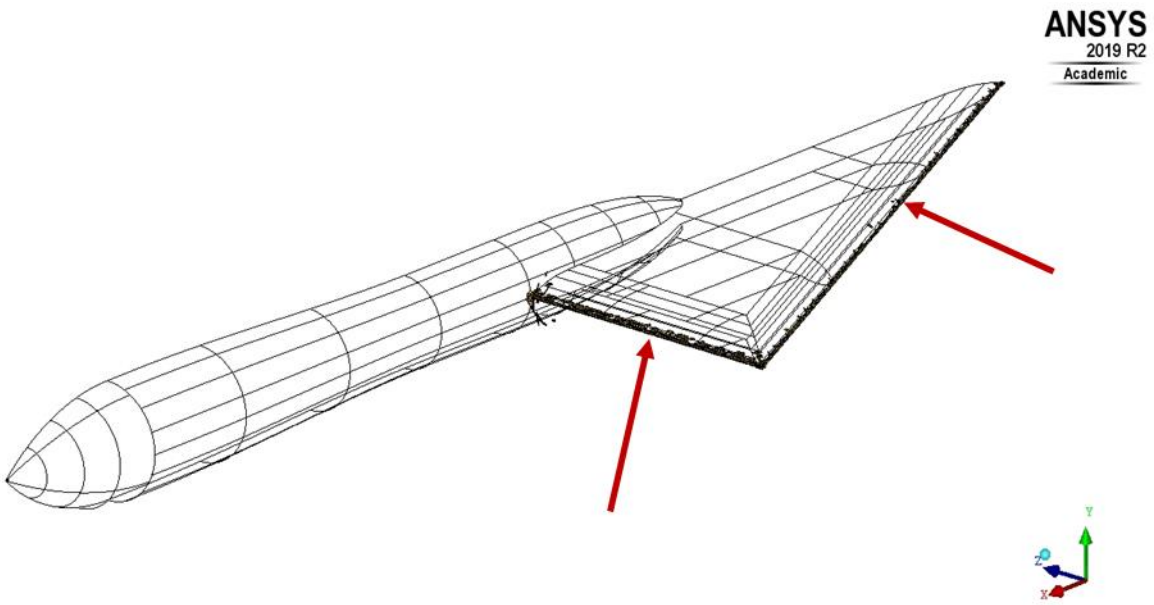

Figure 4.23 Elements with orthogonal quality < 0.15.

4.11 Turbulence Model Study on the VFE-2 Configuration comparing the k-ω SST model and the Linear Pressure Strain Reynolds Stress Model

Additional to the grid refinement study a turbulence model study was conducted using the SST model and the linear pressure strain RSM. An RSM was chosen as vortex dominated external flows experience shear forces where the vortex re-attaches. By modelling the stress terms directly, it was hoped that the vortex could be captured more accurately than with the turbulence models which are based on the Boussinesq assumption.

The RSM chosen was the linear pressure strain model which is based on the dissipation rate of the turbulence kinetic energy ε. Though turbulence models based on the specific dissipation rate (ω) have been proven to be more appropriate for flows with adverse pressure gradient, free shear flows and separated flows, it was decided to use the ε-based model as it has an additional pressure-strain term (Argyroppulos and Markatos, 2015). This additional term is the wall-reflection term, responsible for the redistribution of the normal stresses near the wall. Its characteristic is to dampen the normal stress perpendicular to the wall whilst enhancing the stresses parallel to the wall (FLUENT, 2009). It was thought that this term could provide a more accurate solution as the vortex re-attaches and separates a couple of times, which could be interpreted as a reflection at the wall.

To evaluate the vortical flow different flow visualisation techniques can be used, one of them being the normalised Q-criterion developed for incompressible flows (Martins et al., 2016) and is shown in Figure 4.24 at different chord locations (x/c= 0.2, 0.4, 0.6, 0.8 and 0.95). The normalised Q criterion was used and plotted for values >= 1 as this allows for the identification of the vortex boundary as suggested by Kamkar et al. (2011). It can be seen from Figure 4.25 that both turbulence models predicted a similar vortex in location and shape. The vortex predicted by the RSM, however, maintained its strength until the trailing edge whereas the vortex predicted with the SST turbulence model experienced a reduction in strength at x/c=0.95. The location of the LEV appeared to be the same for both turbulence models but needed to be confirmed by investigating the spanwise Cp distribution. However, conclusions regarding vortex strength and position cannot solely be based on surface pressure distribution and Q-criterion, therefore, also the mean velocity contours at different chord positions as well as the wall shear surface streamlines were examined.

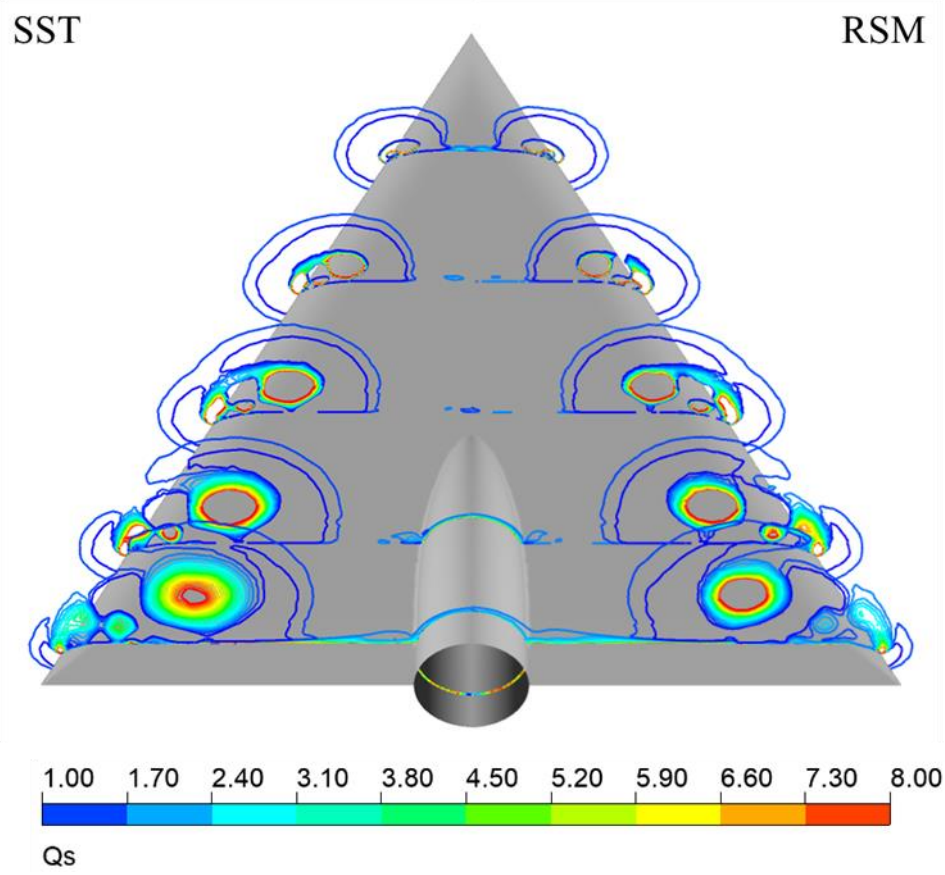

Figure 4.24 Normalised Q-Criterion for different turbulence models on the VFE-2 configuration at α= 18° and M=0.07.

The surface streamlines for both turbulence models are depicted in Figure 4.25. Again, a difference between the turbulence models was noticed downstream. The SST model seemed to

produce a multiple vortex structure indicated by the pooling of the streamlines at multiple locations within the primary vortex re-attachment line. Figure 4.26 shows the surface Cp contours. Again, both turbulence models seem to predict similar flow physics until close to the tip region (approximately x/c= 0.98). Here, the SST model predicted lower Cp values than the RSM.

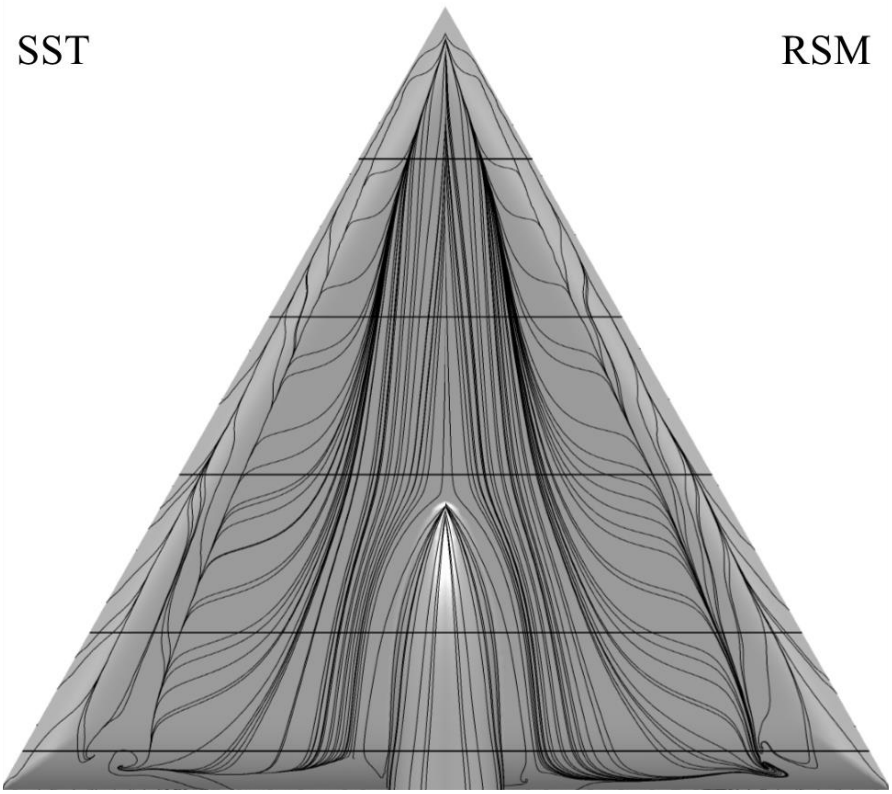

Figure 4.25 left: Surface Shear Streamlines of the RSM and SST model.

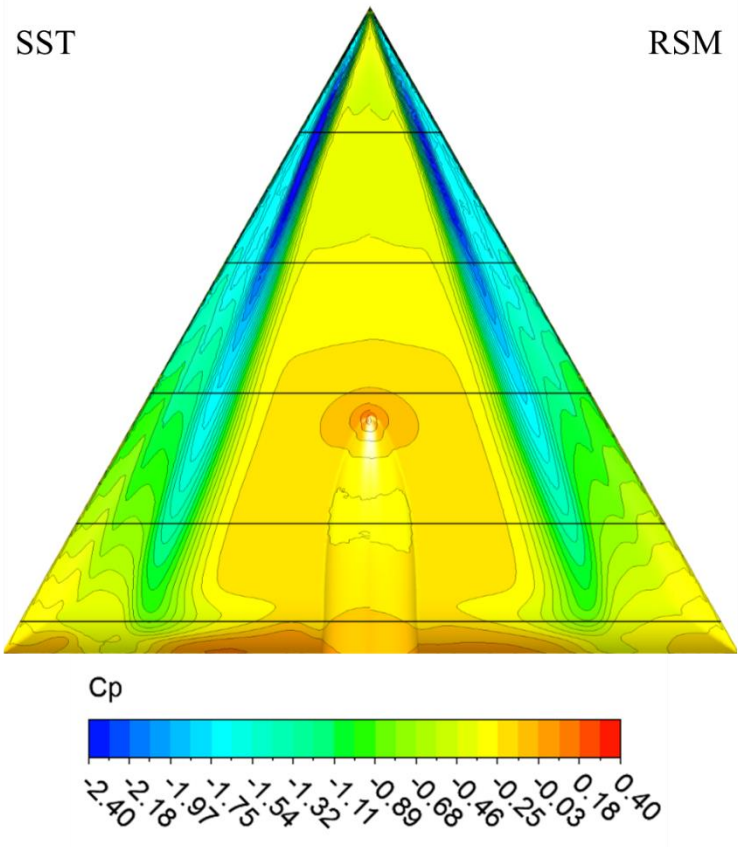

Figure 4.26 Surface Cp comparison M= 0.07 and Re= 1 million at α= 18°.

The experimental data provided by Furman and Breitsamter (2007) generated at TU Munich was used to compare the numerical results with those from experiments. It can be seen from Figure 4.27 that the surface streamlines of the experiment appear similar apart from near the tip. Here, some form of re-circulation seems to be occurring for the experimental results, which are not as pronounced in the numerical solution.

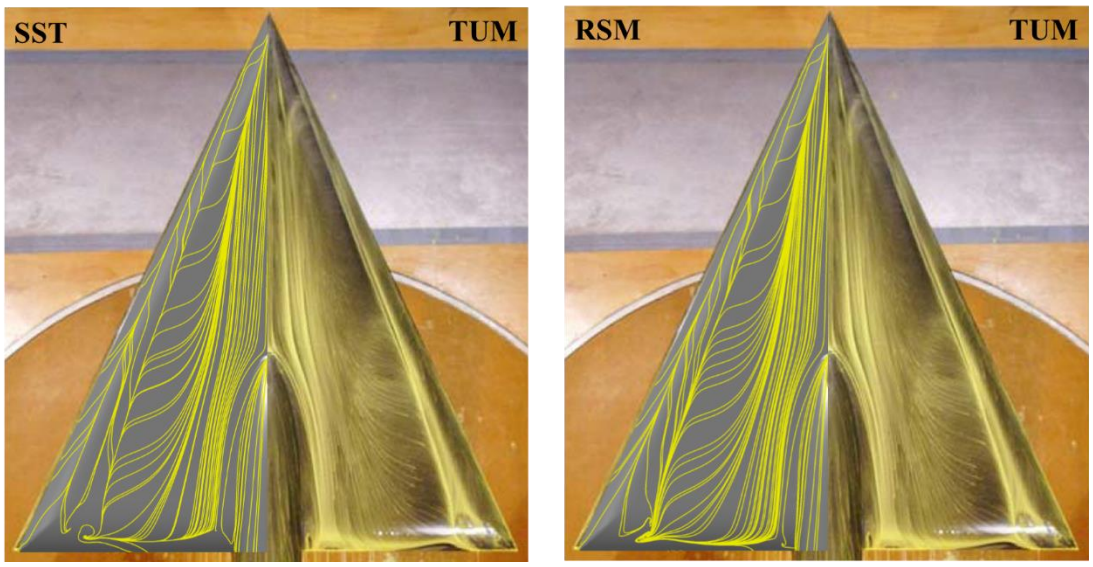

Figure 4.27 Surface Streamline comparison between experiments conducted by TU Munich and CFD SST and RSM (Furman and Breitsamter, 2007).

A comparison of the Cp between the numerical and experimental results (TUM) was done at the different chordwise locations mentioned above and are shown in Figure 4.28. It is clear that irrespective of turbulence model choice the numerical results did not match the experimental data apart from x/c= 0.2. The discrepancies between experiment and computational results increased with downstream location. The experimental results predicted the Cp suction peak to be further outboard and stronger. The SST model predicted a similar position of the suction peak as the RSM. The suction predicted by the RSM is similar to that of the SST model apart from x/c=0.2, where there was a significant difference between RSM and SST model. Generally, it appeared that the RSM did not predict the occurrence of a secondary vortex near the surface as there was no surface pressure decrease. However, the Q-criterion plots indicated a presence of a secondary vortex. It was concluded that the secondary vortex maybe offset from the surface, thus, no trace could be found in the Cp plots.

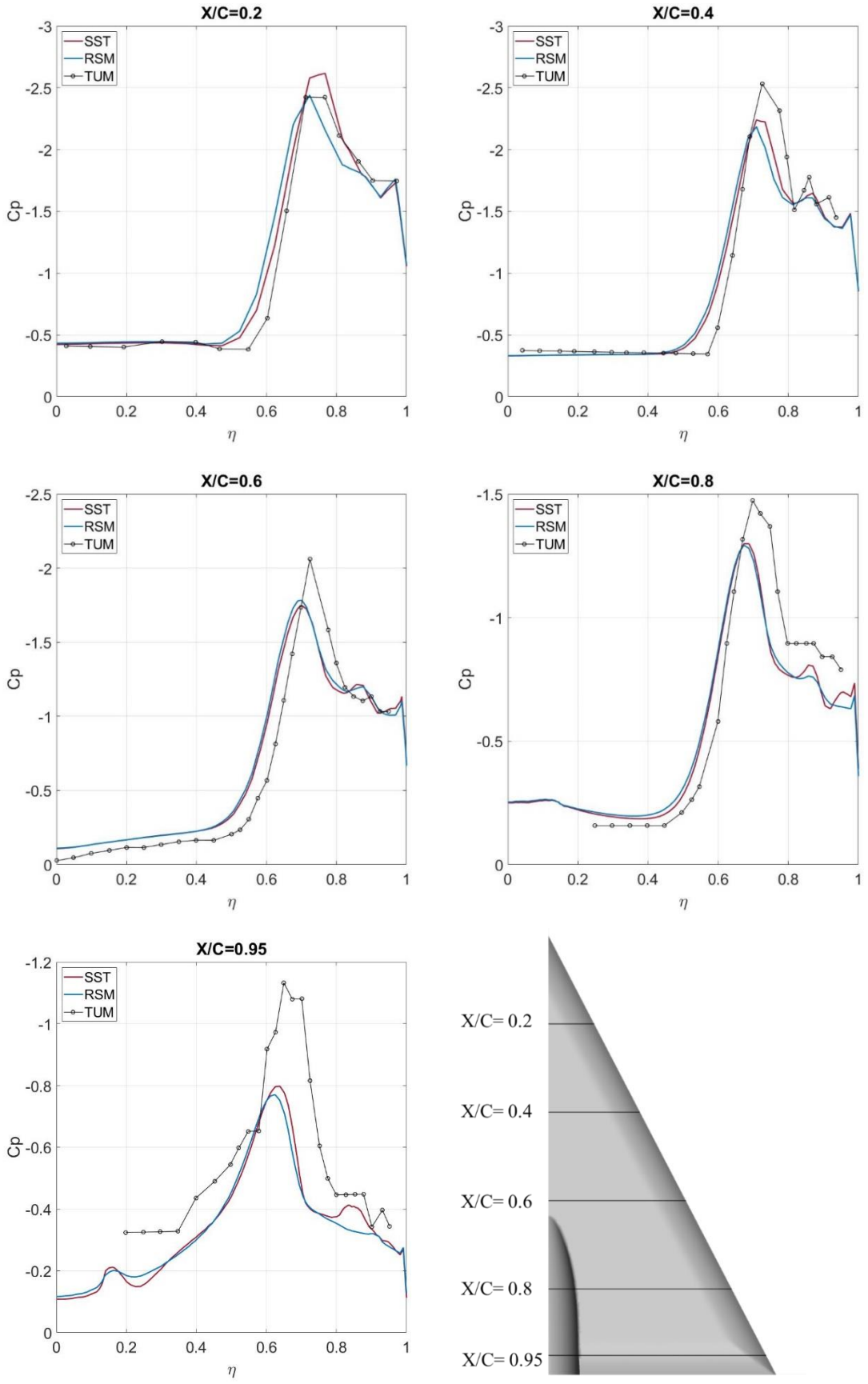

Figure 4.28 Comparison of the spanwise pressure distribution at different chord locations between the SST model, the RSM and experimental data from TUM at α= 18°.

Figure 4.29 shows the difference between the numerical results and the experiment regarding the mean axial velocity distribution at different chord locations. It can be seen that the RSM matched the experimental data better than the SST model close to the trailing-edge (x/c=0.8 and x/c=0.95). However, the numerical results still under predicted the axial velocity close to the trailing edge. Also, the location of the vortex core was further offset from the wing's surface for the experimental data. The vortex core was predicted bigger for the numerical solution and also showed an elliptical shape opposed to a circular shape as predicted by TUM. It can also be seen, due to the reduction in axial core velocity, that the numerical results predicted VBD. The SST predicted this already at x/c=0.8 whereas the RSM predicted the onset further downstream at x/c=0.95.

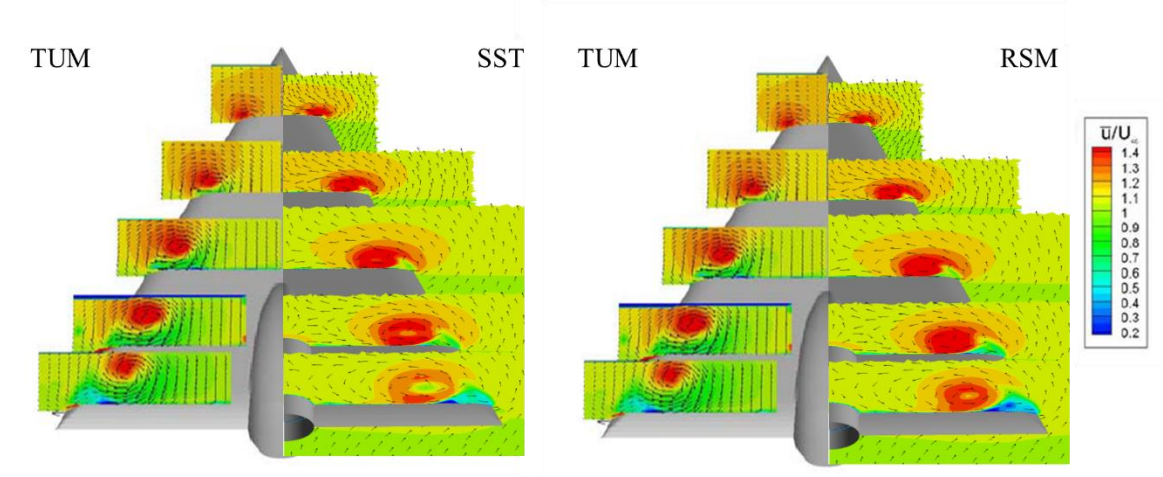

Figure 4.29 Comparison of axial velocity contours and velocity vectors of different turbulence models with experimental results from TUM.

Overall, it was found that the RSM model seemed to predict most of the LEV features better than the SST model. However, due its robustness and lower computational costs the SST model is used in the remainder of the study, despite its inferior performance. Nonetheless, the turbulence model study suggested that RSM may be more advantageous regarding the prediction of LEVs. If this turns out to be true, then this suggests that the correct prediction of the surface shear is essential in capturing the flow physics of vortices. Further studies on this are recommended for future research but are not covered in this study.

4.12 Conclusion Chapter 4: Turbulence Model Study

Based on the mesh study conducted it was found that a mesh of around 9 million elements was sufficient for the current investigation, though additional studies with higher number of surface

elements are recommended as it was found that the axial force was not converging within the three grids used. However, due to limitations in available computational power and a limited angle of attack range (0° to 18°) a grid of 9 million elements was deemed sufficient. A turbulence model study using the RSM (Linear Pressure Strain model) and eddy viscosity model (SST) was conducted and compared against experimental data obtained by TUM. It was found that the RSM was giving promising results, which compared better to those of the experiments. As the simulations were only conducted at $\alpha = 18°$, due to the detailed experimental data only being available at this particular angle, results cannot be extrapolated to lower angles. Further numerical and experimental studies over a wider range of incidences are required to draw conclusions on the overall impact of turbulence model choice on flight predictions of delta wing bodies.

For the purpose of this study the SST turbulence model with low Re and curvature corrections was chosen as it is known to provide good results for external aerodynamic cases, where flow is fully turbulent and is also one of the more popular turbulence models used in industry. A mesh study conducted on the B05 3.4% thick wing at test conditions of this study showed that the settings for the VFE-2 configuration with sting mount were still within the asymptotic range of convergence.

Comparison between the experimental findings and CFD would suggest that the modelling method was not suitable, however, the comparison between numerical and experimental data was conducted at an angle of attack where VBD occured. Experimental data for lower angles would be necessary to make a definite conclusion. Therefore, experiments at the UWE wind tunnel were conducted for the 3.4% thick VFE-2 and VST configuration as well as the 12% thick biconvex configurations.

Chapter 5 CFD Validation by Wind Tunnel Measurements

The CFD simulations were validated by performing experimental tests in the subsonic wind tunnel of the University of the West of England (UWE) Bristol. A limited number of configurations were used, namely, VFE-2, VST (t/c=3.4%) and two biconvex configurations, both of 12% thickness and with maximum thickness locations at 30% and 50%, referred to as B03 and B05. The VFE-2 was used to validate not only the CFD but also the wind tunnel as the data could be compared to the experimental findings at ONERA during AVT-113.

5.1 Wind Tunnel Specifications

The wind tunnel tests were conducted by the author in the high-speed section of the subsonic wind tunnel at the University of the West of England, Bristol. The wind tunnel (Figure 5.1) is a Gottingen-type closed loop single air return tunnel with a contraction ratio of 3.9:1. The tunnel has an octagonally shaped test section of width 2.14 m, and height 1.53 m. It can run speeds up to 50 m/s or Mach 0.148.

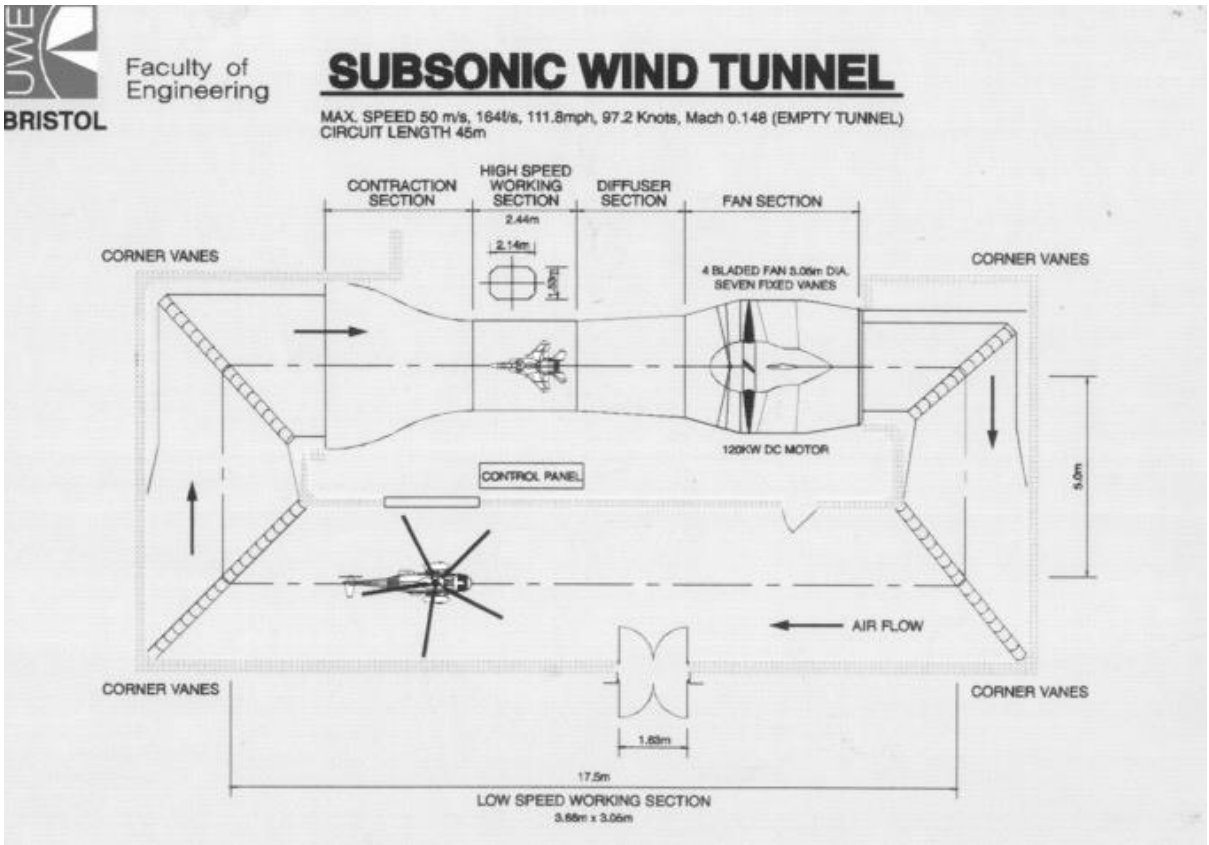

Figure 5.1 Sketch of the UWE subsonic wind tunnel with high and low speed sections with maximum speed of v=50m/s. M=0.148 (for empty tunnel) and circuit length of 45m.

The UWE wind tunnel uses an external roof balance system of strut type to record load values. The struts transmit the model loads down into a system of linkages that separates them into their six components. Strain gauges are used which return a voltage which can then be converted into a force.

The load ranges can be seen in Table 5.1 below and lie within an accuracy of +/- 0.2N.

Table 5.1 Load ranges of the UWE Wind Tunnel (Tuling and Kanaa, 2017).

Component	**Range [N, Nm]**	**Uncertainty [N, Nm]**
Lift	± 450	0.5
Pitching Moment	± 30	0.044
Drag	+80, -150	0.17 (+), 0.28 (-)

The uncertainties of the instruments used to measure pressure, temperature and angle of attack are listed in Table 5.2 (Tuling and Kanaa, 2017).

Table 5.2 Uncertainties of the UWE subsonic test section instruments excluding the overhead balance (Tuling and Kanaa, 2017).

Instrument	**Uncertainty**	**Units**
Dynamic Pressure	2.0	Pa
Static Pressure	100	Pa
Static Temperature	0.4	K
Angle of Attack	0.03	degrees

5.2 Wind Tunnel Test Conditions

The wind tunnel tests were conducted at 34 m/s yielding a Reynolds Number of 750,000, based on the mean aerodynamic chord. This was chosen so as to compare the results with AVT-113's VFE-2 configuration. The angle of attack ranged from -10° to 20° and was increased in steps of 1° with a measurement uncertainty of ± 0.03°. It was measured using a high-resolution inclinometer. The wind-off zero and the wind-on first point were repeated at the end of the run

as suggested by Rae and Pope (1984). The turbulence intensity in the test sections is 0.8% and was determined by Ackerman (2005) using a sphere and the methods described by Phoreman et al. (2000).

5.3 Wind Tunnel Test Rig Design

For the wind tunnel experiments a rig and model mount needed to be designed as the current mounting system was not suitable for the delta wing configurations. The candidate rig designs and the detailed calculations done to arrive at the final mounting system can be found in Appendix A.4.1. to A.4.3. The final wind tunnel rig and mounting system is depicted in Figures 5.2 and 5.3. Care was taken when designing the rig allowing for adjustments in width, sting location and position, whilst trying to minimise interference with the flow.

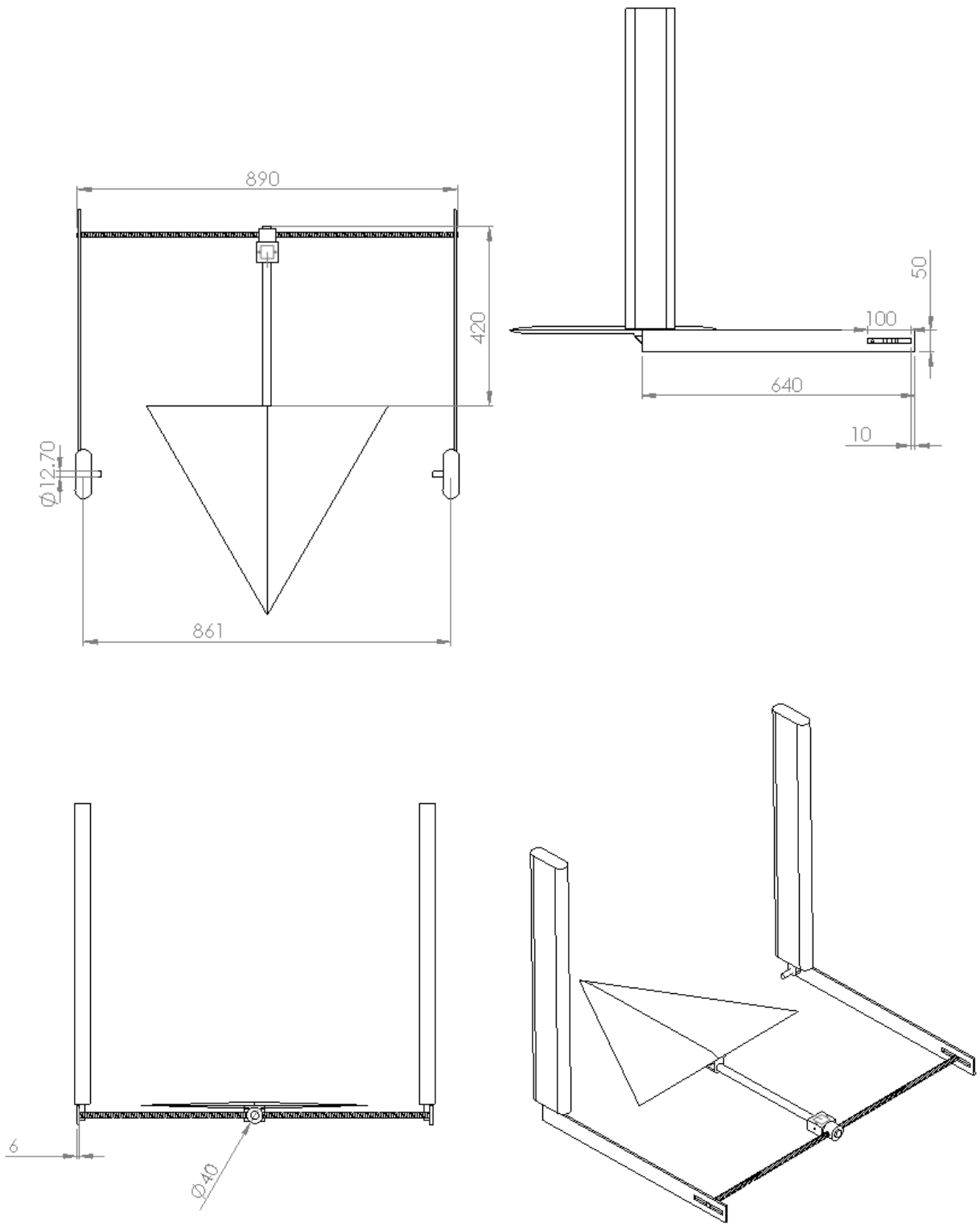

Figure 5.2 Geometry of the wind tunnel rig for the delta wing experiments with units provided in mm.

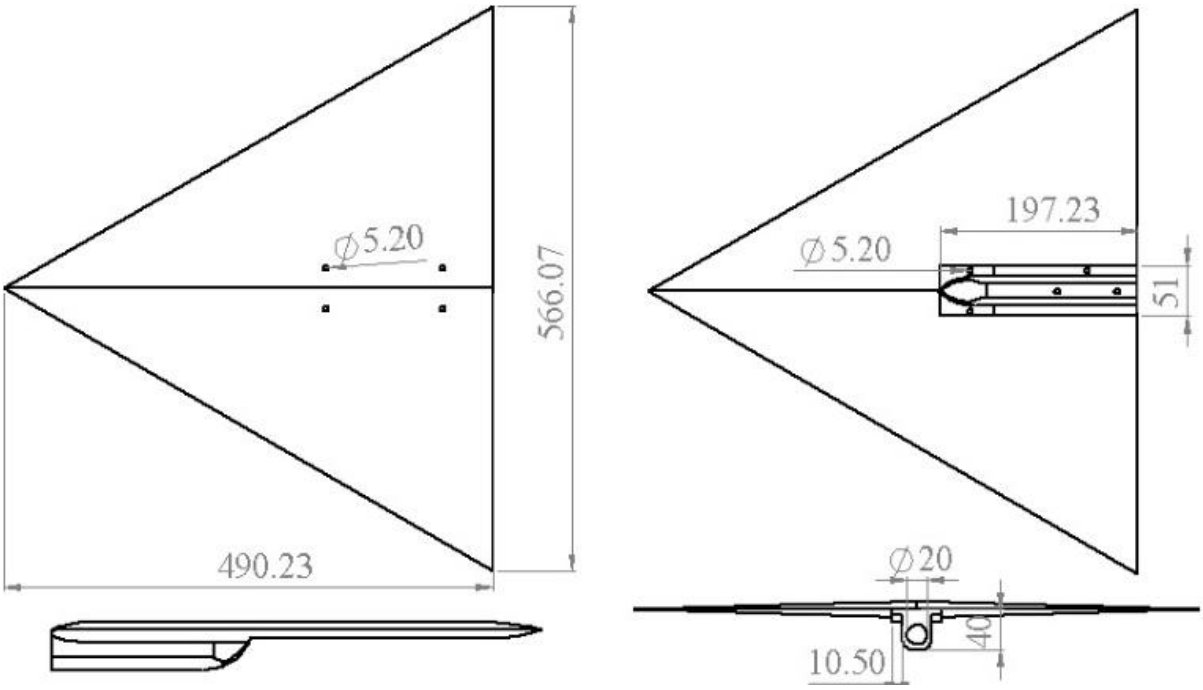

Figure 5.3 Geometry of the wind tunnel model mounts for the delta wing experiments in mm. Shown for the VST configuration as the mounts are the same in size for all configurations.

5.4 Use of statistics in Wind Tunnel testing

Wind tunnel data can be considered valid if it can be reproduced or consistently compared with other tunnels. This makes it necessary to determine the quality of the flow data which rquires a detailed calibration process in which flow features and uncertainties are determined (Yen and Braeuchle, 2000). Additionally, the experimental results need to be statistically analysed using an ISO standard uncertainty method (ISO 21748:2017) where the confidence level needs to be 95% or above. This method is an AMSE/ANSI Standard which recommends that uncertainties can be divided into two components; systematic bias (B_j) and random precision (P_j) (Yen and Braeuchle, 2000). Accuracy measures how close the measured value is to the actual (true) value and precision is defined as how close the measured values are to each other (ASTM International). Therefore, bias can also be related to repeatability of the experiment.

Next to calculating the bias and the precision, outliers in the measured dataset need to be detected and for the calculation of the aerodynamic forces acting on the wing linear regression had to be used. This is detailed in Appendix A.4.4 to A.4.9.

5.5 Wind Tunnel Calibrations

Before the experiments could be conducted different systems of the wind tunnel needed to be calibrated. This included the inclinometer, responsible for measuring the angle of attack, and the wind tunnel balance as well as the E-rig. The process of calibration is described in the following sections.

5.5.1 Calibration of the Inclinometer

The inclinometer, responsible for measuring the angle of attack, was positioned on a separate mount close to the threaded bar of the E-rig as shown in Figure 5.4. It was calibrated using a spirit level inclinometer which was positioned on top of the mounting block. This way the spirit level inclinometer could be set to the desired angle of attack and the voltage given by the transducer (DAS-30-A) could be read out. Using regression analysis, the relationship between voltage and angle of attack was established and fed into the numerical data system of the wind tunnel. The values of the curvefit coefficients of the calibration as well the standard deviation and uncertainty of the DAS-30-A inclinometer can be found in Table 5.3

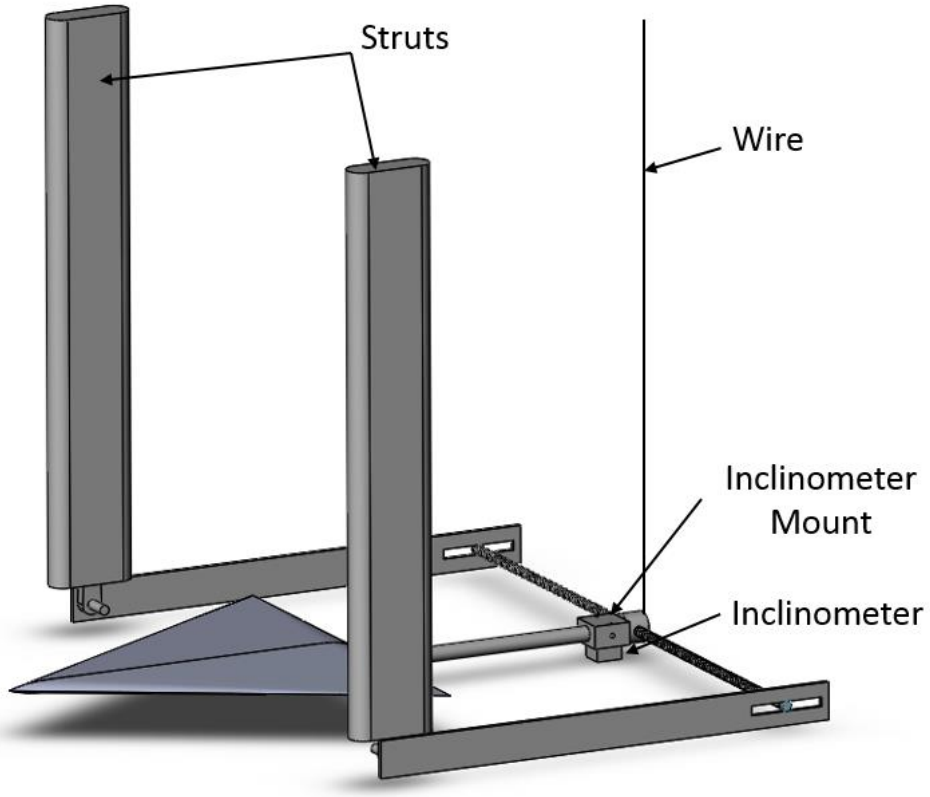

Figure 5.4 Drawing of the final E-rig design mounted in the wind tunnel including model and inclinometer.

Table 5.3 Inclinometer calibration curvefit coefficients, standard deviation and uncertainty.

C_0	-34.708
C_1	13.611
C_2	0.168
Standard Deviation of Residuals	0.0187°
Uncertainty	0.0375°

5.5.2 Calibration of the Balance and the E-Rig

Before testing, the wind tunnel balance system needed to be calibrated. First a testing rig was installed with zero angle of attack. At the end of it masses were mounted ranging from 0.5 kg to 5 kg in steps of 0.5 kg. For each mass the output voltage of the balance system was noted. The theoretical forces were then calculated multiplying the mass with the local acceleration due to gravity (9.811395 ms^{-2}). Based on this the theoretical normal force was calculated and mapped against the output voltage. Using linear regression, a function linking output voltage to force could be found. This was then be entered into the wind tunnel computer system.

After this, the E-rig was installed and a check calibration was done by repeating the test described above. This time the output values of the computer system were compared to the theoretical values, a match of values confirmed that the balance and the E-rig were working correctly.

Next, the pitching moment needed to be checked for accuracy. In opposition to the forces, the pitching moment was not measured via the struts but the wire attached to the end of the mounting sting. It was found that the readings were very sensitive to the attachment position of the wire to the balance system. This is because a change in angle of the balance results in a change in angle between sting and wire. Preferably, the wire should be perpendicular to the balance at all times. But due to its limited stiffness this is not the case. A solution for this would be to use a rod with greater diameter, however, this would also add additional drag to the overall system and was thus ruled out.

A final check calibration was done by a wind-off tare test. For each angle of attack it is necessary to take both wind-off (tare) and wind-on readings. Preferably, first a wind-off reading is taken at a certain angle of attack and then a wind-on reading is taken for the same angle of

attack. As this is often very time-consuming wind-off readings can be taken all at once before taking all wind-on readings (Simpson, 2011). This is done as most models do not have their centre of gravity located on their hinge-point. When the model changes its incidence angle, the centre of gravity of the model changes relative to its hinge point, resulting in a change in pitching moment. Also, forces are slightly affected by this change, but can be accounted for during tare-runs by subtracting it from the wind-on results (Broughton, 1999).

5.6 Experimental test conduction

As mentioned in the wind tunnel specifications and test conditions sections (5.2 and 5.3), the experimental tests were conducted at the UWE wind tunnel which has a 5’ high by 7’ ft wide octagonal test section. The loads were measured using the overhead balance and the models were sting mounted using an E-type rig attached to the overhead balance via two struts. The angle of attack was measured using a DAS-30 inclinometer at the base of the sting of the rig. The VFE2 model as mounted in the test section is shown in Figure 5.5.

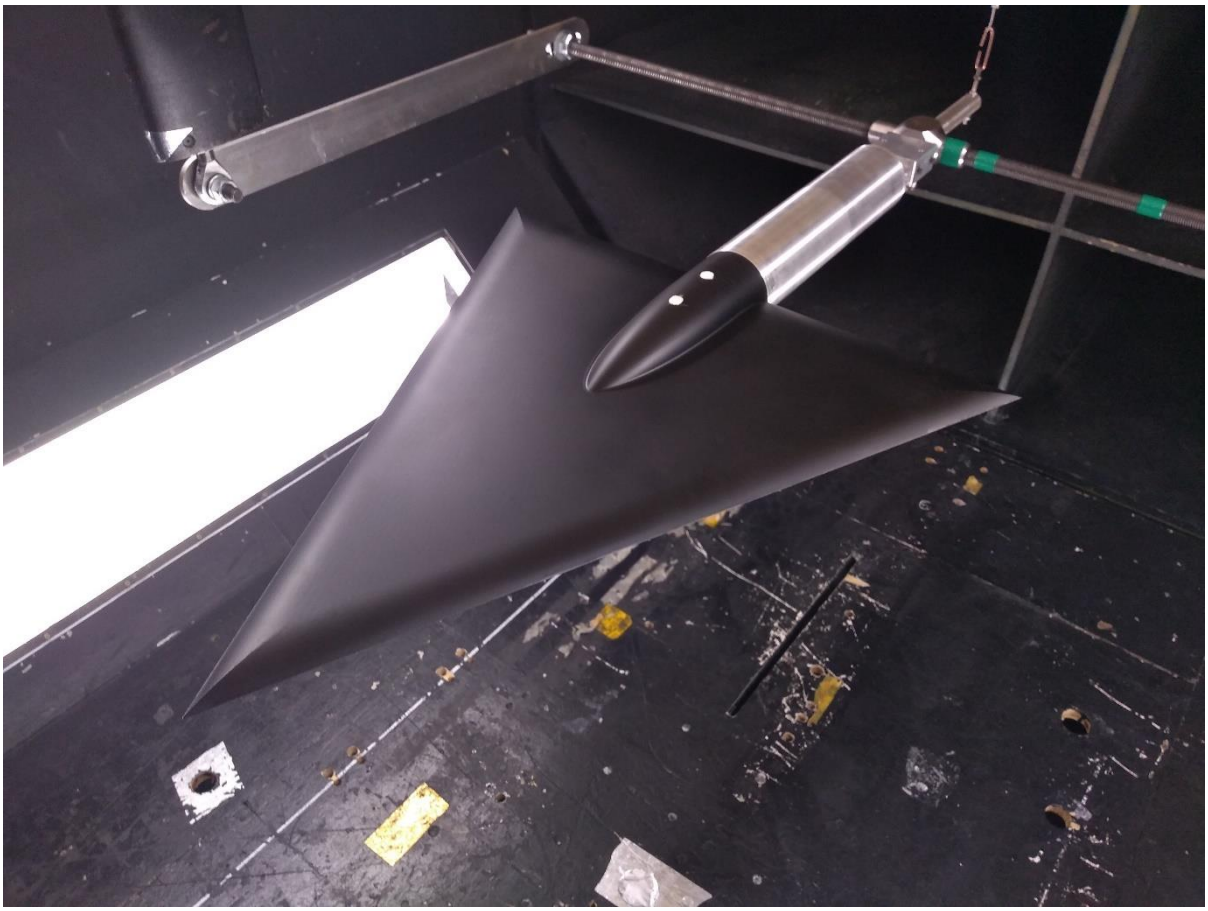

Figure 5.5 Looking down on the arrangement of the experimental rig in the wind tunnel at UWE Bristol showing the VFE-2 delta wing test model, and parts of the E-rig and strut support.

The net aerodynamic loads were obtained by removing the effects of struts, E-rig and model base pressure drag using a separate air-on run for a slender body dummy model with the same base area, performed at the same dynamic pressure as the model configuration. This yields the following equations for the aerodynamic load calculation (with a more detailed discussion in Appendix A.4.10.):

$$F_{Wing_{Clean}} = F_{VFE-2} - F_{Wing_{Tare}} - F_{Dummy} - F_{Dummy_{Tare}} \quad (5.1)$$

During the tare or air-off runs neither lift nor drag is produced but solely a moment due to the shift in centre of gravity with increased angle of attack. Hence, Equation (5.1) becomes

$$F_{Wing_{Clean}} = F_{VFE-2} - F_{Dummy} \quad (5.2)$$

$$M_{Wing_{Clean}} = M_{VFE-2} - M_{Wing_{Tare}} - M_{Dummy} - M_{Dummy_{Tare}} \quad (5.3)$$

The data were collected as a steady state behaviour by averaging the 1 kHz data of the DAS-30 inclinometer for two seconds. The VFE-2 dummy tare model used the same forebody as the centrebody of the VFE-2 model. The VFE-2 sting aftbody was extended for a distance of 0.65 root chords. Repeatability of the runs in upright and inverted positions was ensured and is covered in Appendices A.5.10. and A.5.11.

The root chord of all configurations was 0.49 m, identical to the VFE-2 model used by Leroy et al. (2007). This equates to 75% of the root chord used by Chu and Luckring (1996).

The loads were converted to coefficients using the planform as the reference area and the mean aerodynamic chord as the reference length as was done by previous studies on the configuration by LeRoy et al. (2007). The formulae are detailed in Appendix A.4.12.

The uncertainties of the experimental data were estimated using the method of Küchemann (1972) and are detailed in Appendix A.4.15 together with a detailed explanation on the wind tunnel data reductions.

The maximum uncertainties are listed in Table 5.4.

Table 5.4 Maximum uncertainties of the wind tunnel aerodynamic coefficients.

Parameter	Description	Uncertainty
C_L	Lift coefficient	0.0064
C_D	Drag coefficient	0.0022
C_m	Pitching moment coefficient	0.0036

The data were corrected for flow angularity by performing upright and inverted runs for each configuration (Appendix A. 4.7). Flow angularity is a non-uniformity of the flow within the wind tunnel and is defined as the angle between the wind tunnel centreline and the local velocity vector (Ljungskog et al., 2019). The two runs were plotted on the same graph and should overlay each other in absence of flow angularity. The corrections applied to α are equal to half of the angle offset between the curves at $C_L = 0$ (Barlow et al., 1999). The upwash angle α_{up} for the different configurations is shown in Table 5.5 and was obtained using step 8 in Appendix A.4.15.7.

Table 5.5 Upwash angle of the different delta wing configurations.

Configuration	Upwash angle α_{up}
VFE-2	-0.08971°
VST	0.15502°
B03	0.28143°
B05	0.45814°

The measured drag also needs correction, as the lift vector is non-orthogonal to the flow direction, meaning a small component of measured lift is actually drag. The additive correction to the drag coefficient to the upright model is defined by Barlow (1999) as:

$$\Delta C_D = C_L \times tan(\alpha_{up}) \tag{5.4}$$

No other corrections were applied to enable comparison with LeRoy et al. (2007). The only corrections missing are the blockage corrections. For the purpose of completeness, they are mentioned in Appendix A.4.13.

The tests were performed in three test entries allowing repeatability to be assessed across test entries. The VST configuration was used for this during the test campaign. The lift, drag and pitching moment coefficients repeated to within 1.5 times the uncertainties quoted in Table 5.4.

5.7 Comparison of the CFD results with the experimental data

The CFD predictions of this study using the SST turbulence model are compared with the experimental test data for each configuration in Figure 5.5 to Figure 5.9. The results for the VFE-2 configuration compared well with the wind tunnel tests conducted by ONERA, though the tests at UWE were run at a lower Re. ONERA conducted their tests at Re = 1 million, so differences in coefficients were expected. The pitching moment compared well as the difference between the ONERA and UWE data is within the uncertainty of the measurement. The drag coefficient also compared well as it was also found to be within the uncertainty of the measurement. The lift coefficient had a constant offset above and below zero degrees angle of attack. However, the lift curve slope values were very close in value. The good comparison and replication of the flow features to the ONERA test results gave confidence in the experimental setup.

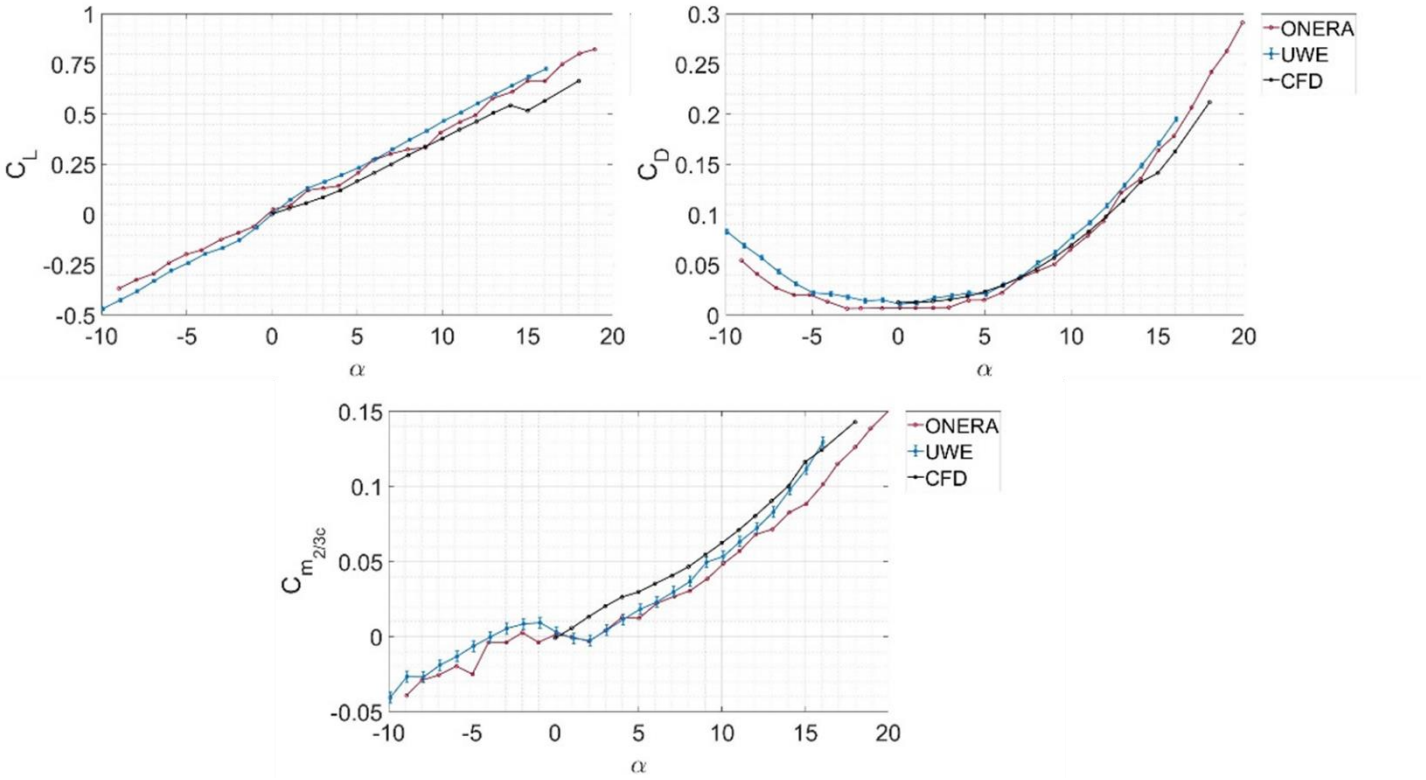

Figure 5.6 Comparison of CFD predictions and experimental tests for the lift, drag and pitching moment coefficients for the VFE-2 configuration.

The comparison between the numerical and experimental results for the VFE-2, VST, B03 and B05 (Figure 5.6 to Figure 5.9) configurations showed that the numerical simulations were predicting the curve slopes well for all configurations. However, they did not predict the change in lift curve slope at around zero-degree angle of attack for the VFE-2 and VST configurations, yielding a constant offset of 0.07 and 0.06 respectively.

The lift curve slope of the B03 and B05 configuration were within the uncertainty of the experiments. The drag prediction was good for angle of attack below 10 degrees whilst the simulations for the B05 configuration were matching very well, with the CFD slightly over-predicting the drag generation. The drag coefficient of the B03 configuration showed an over-prediction at an early angle of attack, thus affecting the lift-to-drag (L/D) ratio.

The pitching moment coefficient was captured well for the VST configuration and B03 at negative angle of attack. At positive incidences the pitching moment was over-predicted by the numerical simulations for the B03 by up to 0.0198, whilst being under-predicted for the B05 configuration. The differences here were larger at low angle of attack (up to 0.0116) and diminished with increase in incidence. Though the differences may appear large the

uncertainties in the CFD calculations have not been accounted for. These arise due to discretisation, truncation, iteration and rounding errors. The discretisation error can be accounted for using the methods described in Chapter 3.

The uncertainties due to discretisation error are shown in Table 5.6 and were calculated using Equation (4.10) from section 4.6. It can be seen that the uncertainties due to discretisation error were larger for the biconvex configurations, which explains the larger difference between the tunnel and CFD data. It further shows that the results between experiment and numerical simulation were within the uncertainty.

Table 5.6 Uncertainty in the prediction of the CFD pitching moment coefficient for different configurations.

Configuration	Uncertainty in C_m due to discretisation
VFE-2	0.0127
VST	0.0002
B03	0.0167
B05	0.0041

Generally, it is a common issue to predict the pitching moment accurately in CFD (see Boelens, 2009 and Vallespin et al., 2012). The wind tunnel pitching moment values are extremely sensitive to the pressure distribution, which is easily affected by wind tunnel walls and sting mounting. Schuette et al. (2012 (c)) concluded that the differences in pitching moment between numerical simulations not using a sting mount show differences in pitching moment coefficient compared to experimental data. This is however, not due to turbulence model choice (RANS vs DES) or steady and unsteady conditions. It was found that the flow oscillations behind the sting were influencing change in the pressure in a wide area at the base of the model. It was also shown that a high grid density around the leading-edge was required, making the runs computationally expensive (Schuette et al., 2012 (c)).

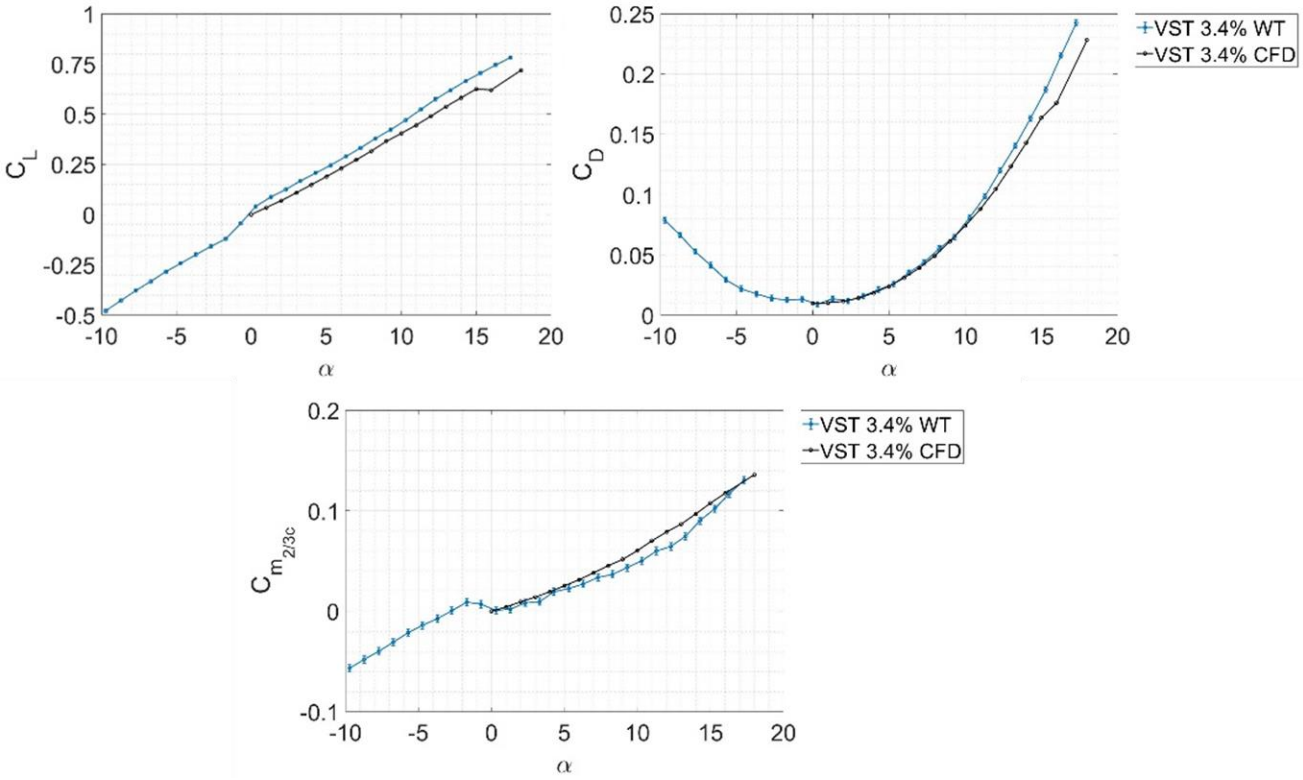

Figure 5.7 Comparison of CFD predictions and experimental tests for the lift, drag and pitching moment coefficients for the VST configuration.

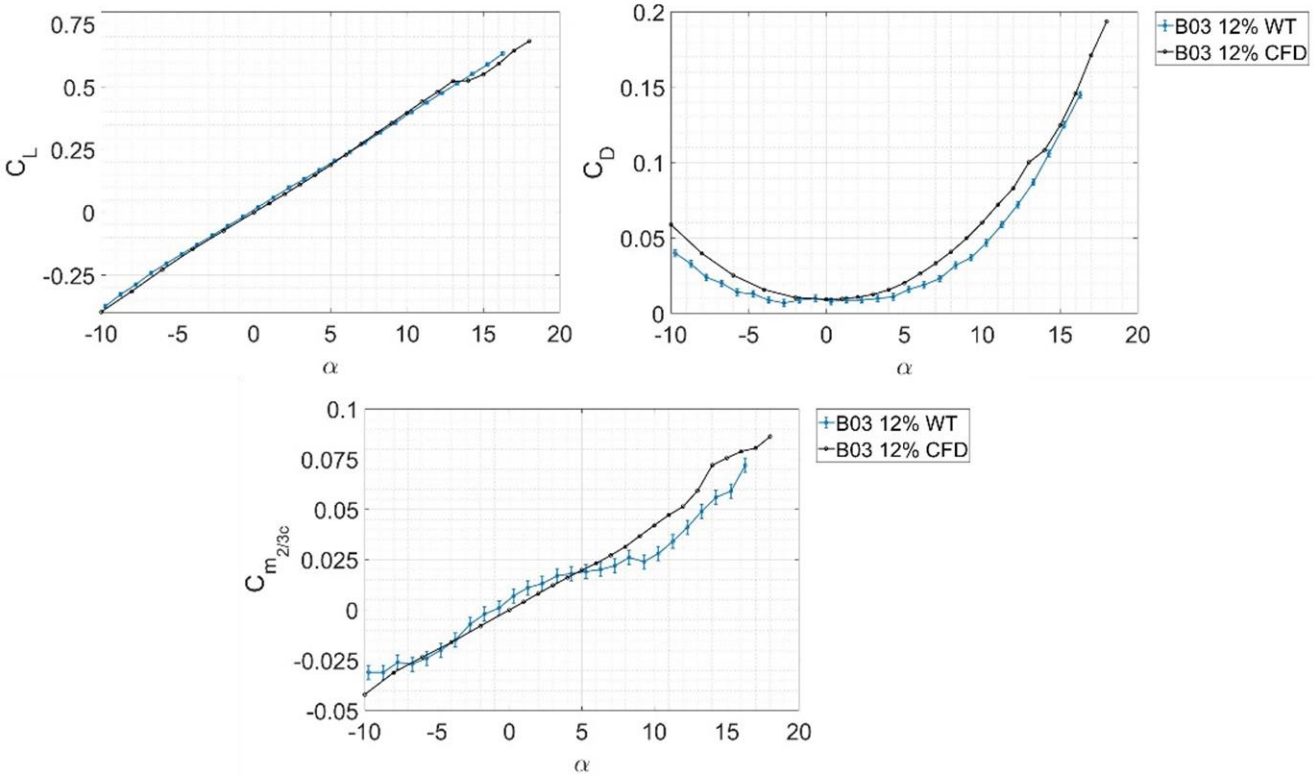

Figure 5.8 Comparison of CFD predictions and experimental tests for the lift, drag and pitching moment coefficients for the B03 configuration.

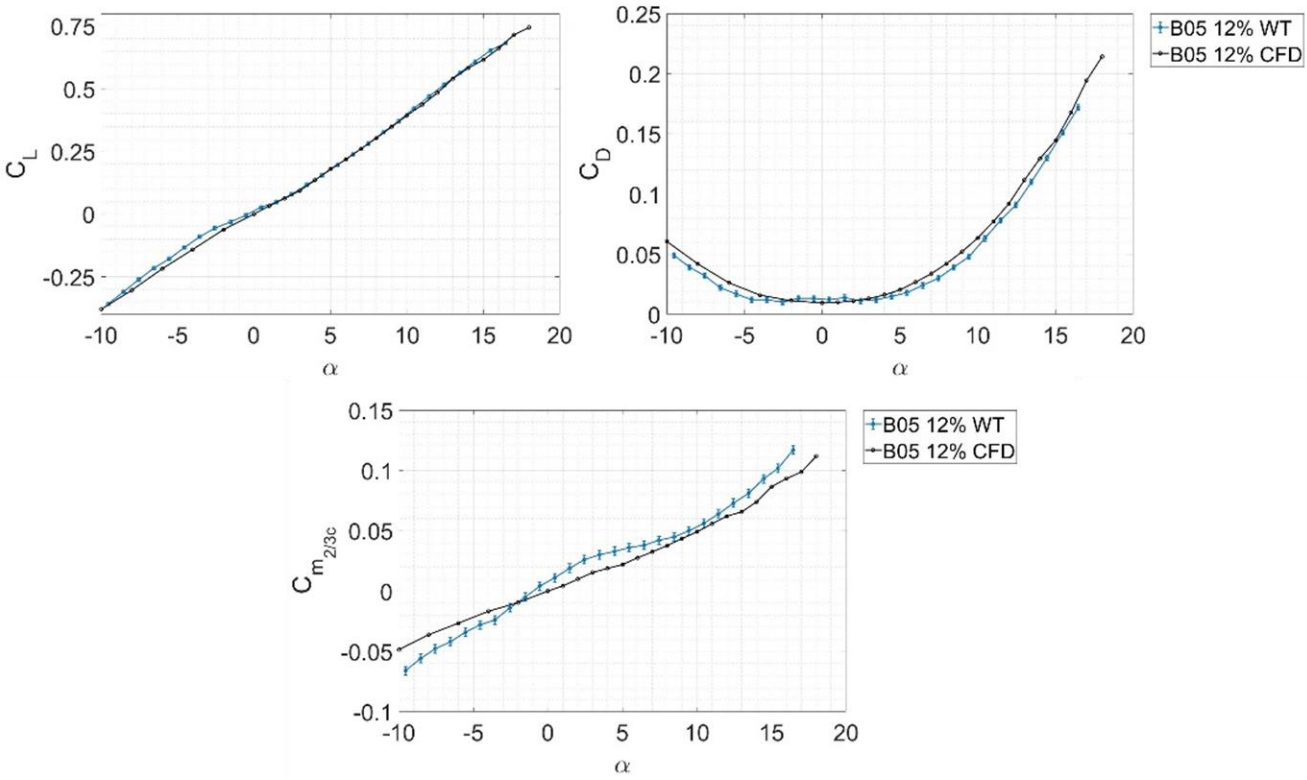

Figure 5.9 Comparison of CFD predictions and experimental tests for the lift, drag and pitching moment coefficients for the B05 configuration.

A comparison of the experimental and numerical data of the normal and axial force components for the different configurations is depicted in Figure 5.10 and Figure 5.11. Here, the normal and axial force coefficients were plotted against angle of attack.

For this the experimental data was transformed into its axial and normal force components using (Kirby and Kirkpatrick, 1969):

$$C_N = C_L \cos(\alpha) + C_D \sin(\alpha) \tag{5.5}$$

$$C_A = -C_L \sin(\alpha) + C_D \cos(\alpha) \tag{5.6}$$

It can be seen in Figure 5.10 that the numerical results under-predicted the forward suction generated for all cases. The prediction of the forward suction at zero lift varied with configuration, but was predicted to be larger for the numerical simulations. For the B05 configuration there was a discrepancy of 0.002 between experimental and numerical data, with the CFD results predicting a lower axial force component at zero lift. However, this was within

the uncertainty of the wind tunnel's aerodynamic coefficients. Differences in slope at low angle of attack can be observed for $\alpha < 5°$, after that the slope of the axial force coefficient appears to have the same gradient for both numerical and experimental results. The numerical simulations for the VFE-2 predicted VBD too early compared to the experimental data, whilst the behaviour of the VST, B03 and B05 configurations was predicted better with regards to VBD. The experimental results for the VST and VFE-2 configuration show rapid changes in slope at low angle of attack, which is not observed for the B03 and B05 configurations. The change in slope of the wind tunnel data at low angle of attack is also observed for the lift and pitching moment coefficient of the VFE-2 in Figure 5.6 and is consistent with the experimental findings at ONERA. Here, the effect measured was not as large as for the UWE wind tunnel, which could be due to the difference in Re. However, both point to the conclusion that the rapid changes in slope at low angle of attack are due to the aerofoil geometry.

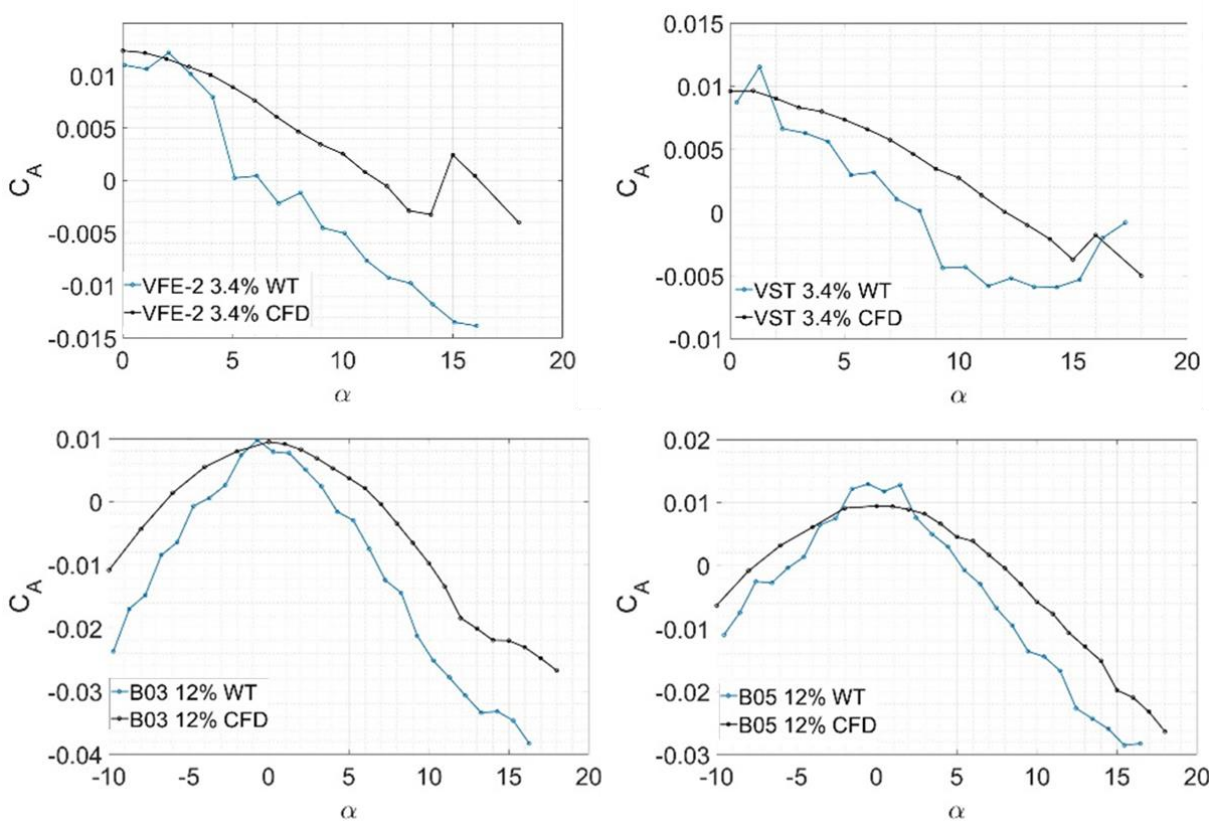

Figure 5.10 Comparison of CFD predictions and experimental tests for the axial force component for the four different configurations.

As for the lift coefficient the normal force data of the VFE-2 and VST is offset, whereas that of the B05 and B03 configuration is in good agreement. The numerical results captured the slope well at higher angle of attack for the VFE-2, VST and B05 configurations, whereas the

numerical results predicted a steeper slope for the B03 configuration. At lower incidences the slope was much steeper for the experimental results.

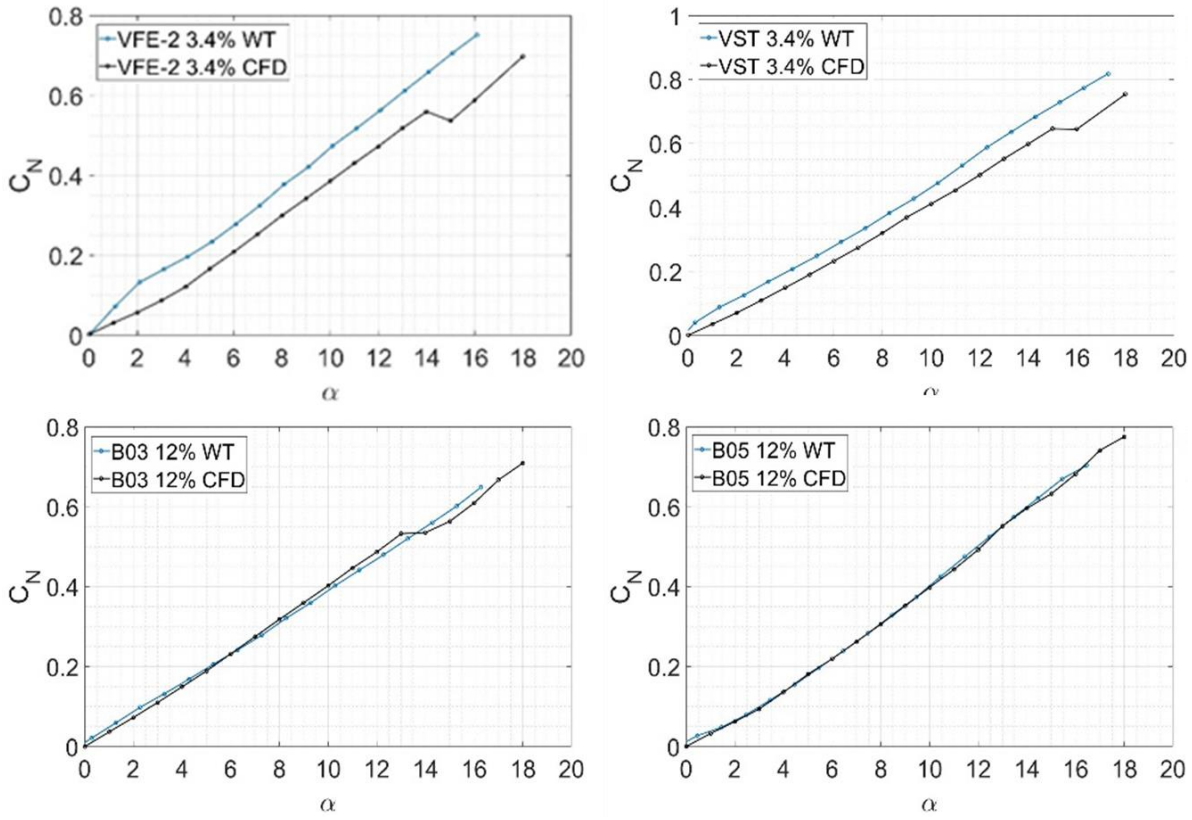

Figure 5.11 Comparison of CFD predictions and experimental tests for the normal force component for the four different configurations.

The L/D ratio is plotted against lift coefficient in Figure 5.12. It can be seen that the wind tunnel results show a larger L/D ratio especially in the range of moderate incidences. This is due to the lower drag values measured in the experimental tests. It can further be seen that the maximum L/D ratio for the B03 configuration is very high. This is due to the under-prediction of the drag at zero lift C_{D_0}. The same is observed for the VFE-2 configuration. The maximum L/D ratio is predicted approximately at the same lift coefficient for numerical and experimental results, when not taking into account the outliers.

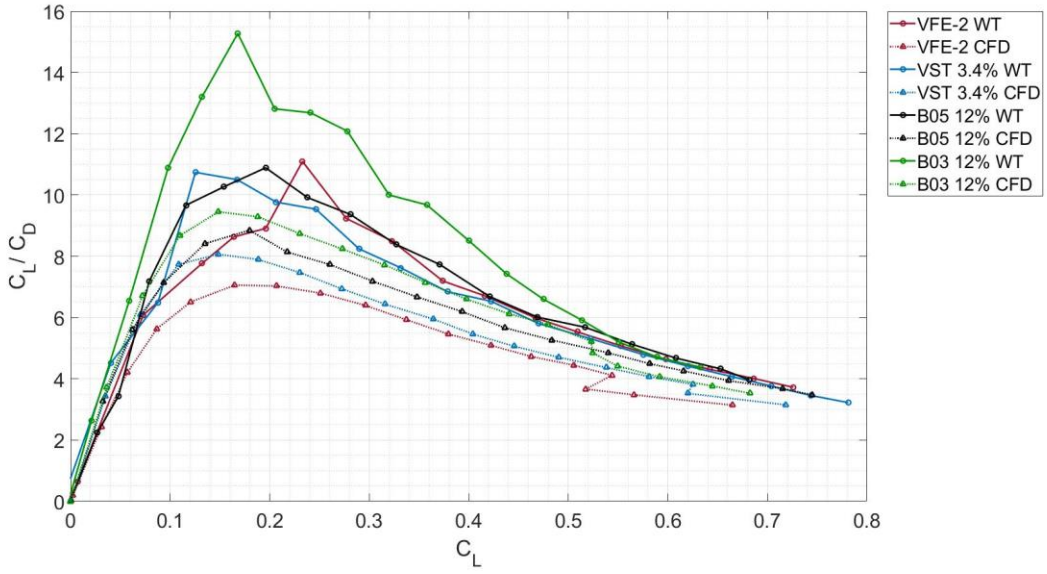

Figure 5.12 Comparison of CFD predictions and experimental tests for the L/D ratio for the four different configurations.

For the stability of an aircraft, the knowledge of the location of the aerodynamic centre (x_{ac}) is crucial. To understand the pressure distribution, one refers to the centre of pressure (x_{cp}).

The former can be determined using (Kirby and Kirkpatrick, 1969)

$$x_{ac} = \frac{\partial C_m}{\partial C_N} \tag{5.7}$$

And the latter using (Anderson, 2011)

$$x_{cp} = \frac{M}{N} \tag{5.8}$$

Therefore, to evaluate the accuracy between experimental and numerical findings both parameters were plotted against the normal force coefficient as depicted in Figure 5.13 for the B03 configuration. It can be seen that the wind tunnel data as well as the CFD data are fairly noisy. To enable an easier evaluation the pitching moment coefficient and normal force coefficient were curve fitted (first order) and centre of pressure and aerodynamic centre were recalculated. The raw data plots for both numerical and experimental findings can be found in Appendix A.4.14.

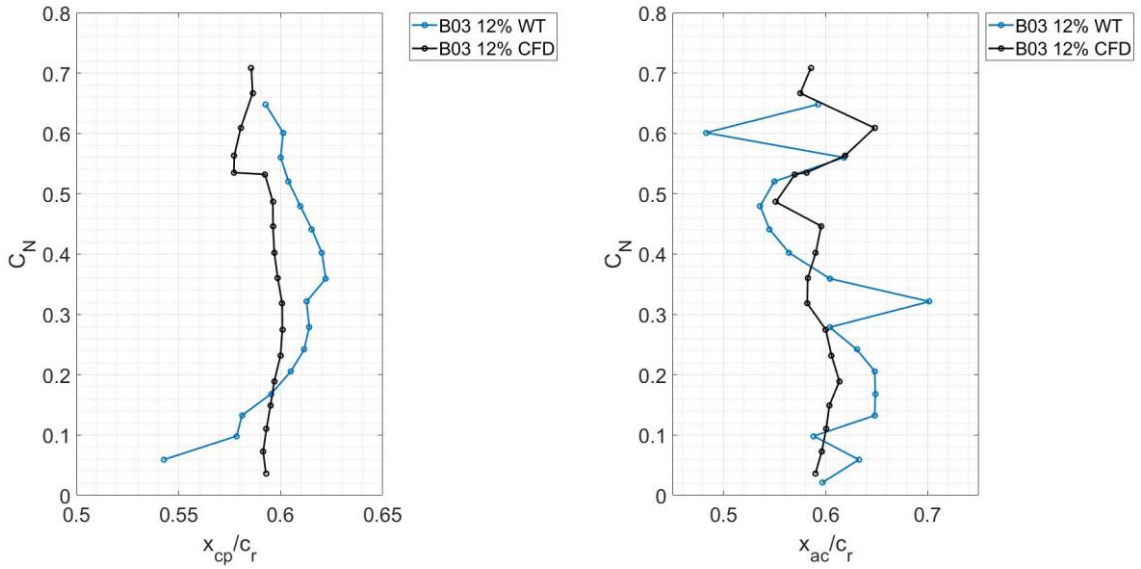

Figure 5.13 Comparison of CFD predictions and experimental tests for the centre of pressure and aerodynamic centre for the B03 configuration (non-dimensionalised with root chord). For each line the set-up shows variation in the angle of attack.

The results are presented in Figure 5.14 to Figure 5.17 for the different configurations. It can be seen there is a difference in the prediction of the centre of pressure between experimental and numerical findings, but this difference varies with configuration. The differences in the pressure distribution are up to 10% of the root chord length c_r. However, these differences are at low angle of attack and only observed on the VFE-2 configuration. For the VST the difference in x_{cp} position is 5% whereas for the thicker biconvex wings the difference is around 2%.

The aerodynamic centre prediction was very good and variation between experimental and numerical findings were 0.5% c_r. This implies that changes in angle of attack are captured well. The kinks in the aerodynamic centre curves were due to VBD, which is pre-maturely predicted by the numerical results. Overall, the numerical findings were predicted well compared to the experimental data regarding the pressure distribution. Large differences in centre of pressure location only occurred at very low incidences. It had been shown earlier that there is a slope change occurring at lower angle of attack for the experimental results, which was deemed to be due to interferences with the rig. The change in pitching moment with regards to change in normal force predicted by CFD was in good agreement with the experimental findings, thus, validating the numerical data.

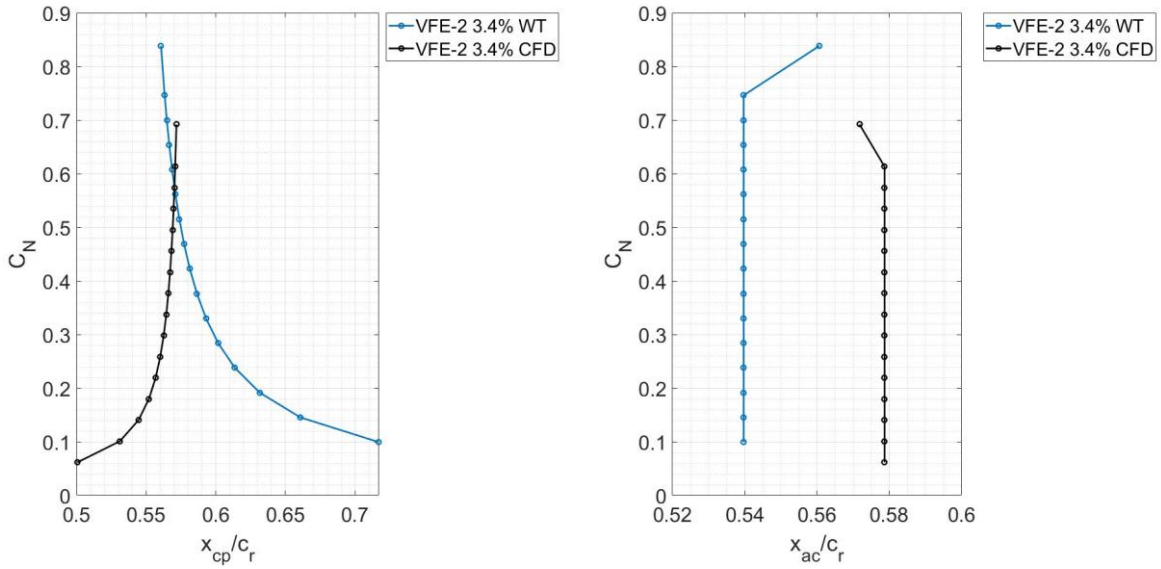

Figure 5.14 Comparison of the curve fitted CFD predictions and curve fitted experimental tests for the centre of pressure and aerodynamic centre for the VFE-2 configuration.

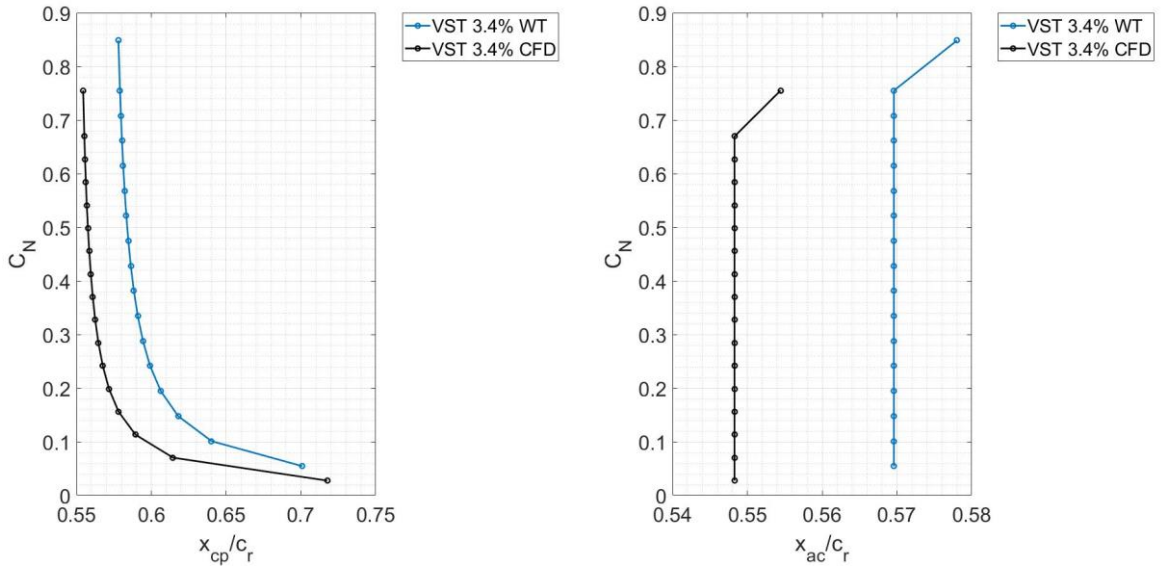

Figure 5.15 Comparison of the curve fitted CFD predictions and curve fitted experimental tests for the centre of pressure and aerodynamic centre for the VST configuration.

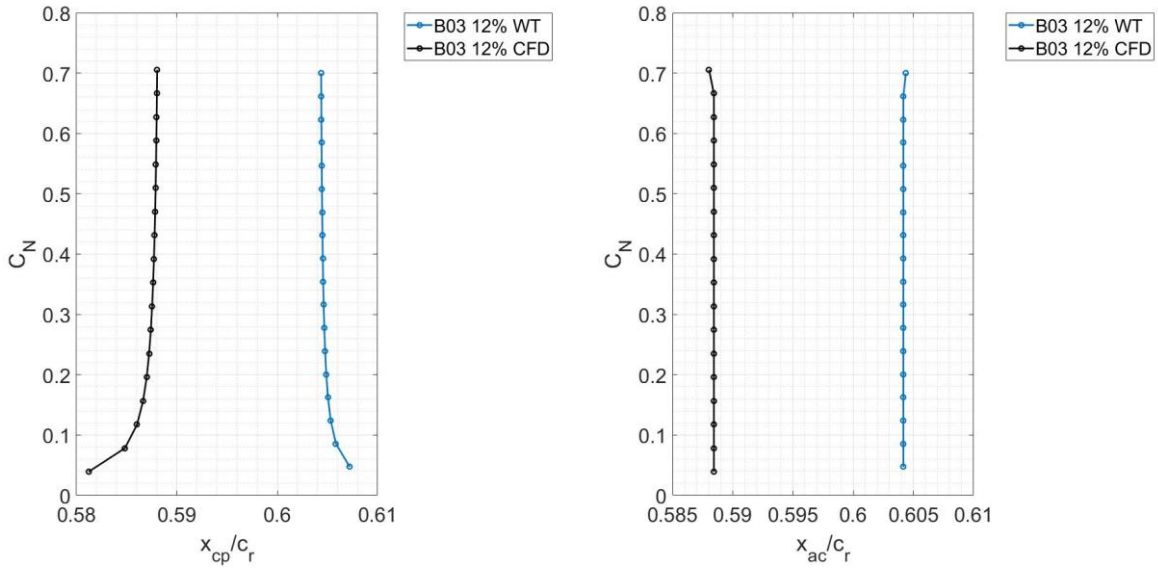

Figure 5.16 Comparison of the curve fitted CFD predictions and curve fitted experimental tests for the centre of pressure and aerodynamic centre for the B03 configuration.

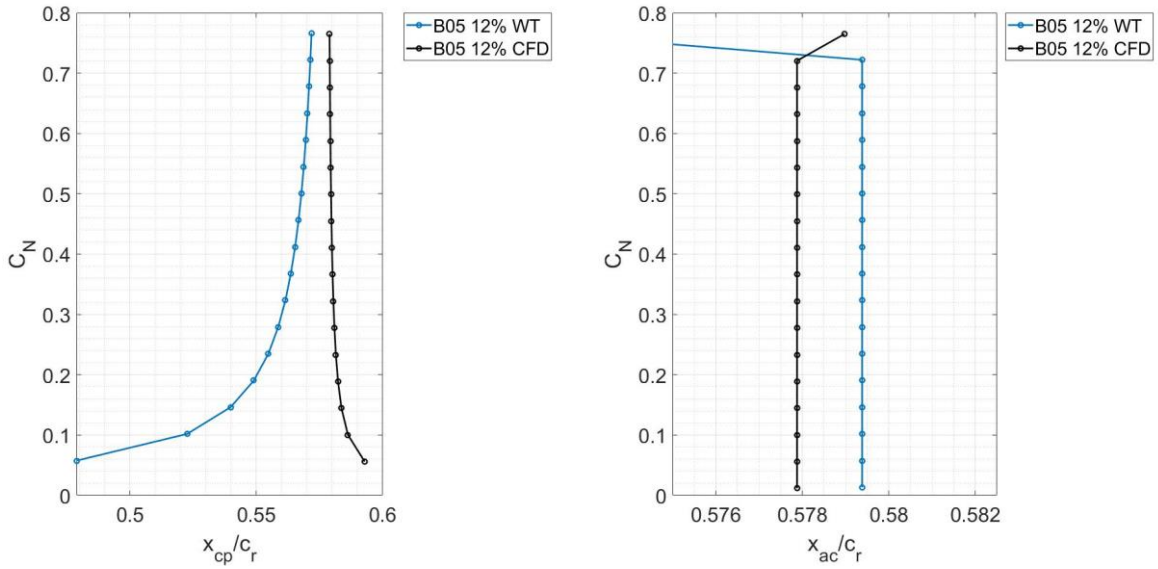

Figure 5.17 Comparison of the curve fitted CFD predictions and curve fitted experimental tests for the centre of pressure and aerodynamic centre for the B05 configuration.

Despite the discrepancies in numerical and experimental data it was shown that the general trend was captured; the differences between the VST, B03 and B05 configurations were predicted by the numerical simulations. Factors contributing to the differences in coefficients were model quality, rig design and interferences on the experimental side; and turbulence modelling and grid quality on the numerical side. In order to validate the findings even further advanced flow visualisation techniques would have been required. These were not available at the facilities of UWE at the time the project was undertaken. However, it was shown that rates of change in polar plots with change in maximum thickness location and maximum thickness

were sufficiently well predicted. The numerical simulations are, for the purposes of this study, which is investigating the trends with thickness and thickness location, considered validated.

5.8 Conclusion Chapter 5

This chapter detailed the design of the wind tunnel rig and mounting, as well as the design considerations for minimising the mounting interference. Furthermore, the statistical analysis necessary to ensure repeatability and uncertainty was discussed. It had been shown that the tests were repeatable and lay within the uncertainty of the measurement. Wind tunnel corrections were reviewed and applied where appropriate.

The experiments were carried out on four configurations of two different maximum thicknesses namely, VFE-2 (t/c=3.4%), VST (t/c=3.4%), B03 (t/c=12%) and B05 (t/c=12%). The number of configurations tested were limited by the manufacturing costs and it was assumed that validating the thinnest and thickest wings would suffice.

The experimental data of the VFE-2 was compared to the experimental findings at the ONERA L1 wind tunnel by Leroy et al. (2007) and it was shown that the data matched those conducted by ONERA well, despite the lower Re. Changes in Re did have an impact on the results and particularly the leading-edge suction as shown by Kurun (2008), who compared the VFE-2 wind tunnel results obtained at ONERA for M=0.13 and Re= 1×10^6 with those obtained at TUBITAK-Sage at M=0.2 and Re= 1.5×10^6.

The experimental findings were then compared to the numerical simulations. It was found that the lift data for the VFE-2 and VST was offset, due to the prediction of a different slope at very low angle of attack. The drag coefficient was over-predicted for the biconvex configuration at moderate angles of attack but was in good agreement at low and high incidences. The pitching moment was predicted satisfactorily given that its correct prediction depends on the inclusion of the sting modelling.

Axial and normal forces were predicted well, with the forward suction force being under-predicted by the numerical simulations. The slope of the normal force coefficient at very low incidences was over-predicted by the experiments for all configurations but was predicted well for higher angles of attack. Vortex onset and change in flow physics (such as separation bubble interaction or VBD) were predicted at similar normal coefficients for the biconvex

configurations. VBD was predicted too early by the numerical simulations especially for the VFE-2 and VST configuration.

The aerodynamic centre and centre of pressure values were predicted within 0.5% and 3% accuracy respectively. The differences between numerical and experimental findings at low angle of attack for the centre of pressure were found to be high (up to 10%) whereas these differences became smaller at higher incidences, showing that the numerical data did predict the pressure distribution very well.

The major differences were found in pitching moment prediction between the numerical simulations and the experimental results. It was shown that the discretisation error has a major effect on the prediction of the pitching moment. Taking its uncertainties into account resulted in a good match between experiment and simulation. Furthermore, it has to be considered that errors are arising during numerical prediction such as truncation, iteration and rounding errors. Also, turbulence model choice can lead to differences between experiments and simulations. These were not accounted for but are sources for errors.

Despite the discrepancies between the experimental and numerical findings the general trend and the differences between configurations were captured. It was shown that even with the constant developments in turbulence modelling and higher order methods as well as an increase in computational power the current methods are sufficient for making predictions on the behaviour of configurations subject to vortical flow. The numerical simulations were thus considered validated for the purposes of this study.

For a further validation and interpretation of the differences between experimental and numerical findings more flow features would need to be captured during the experiment. These include, surface pressure, PIV, hot wire anemometry and surface flow visualisations. This would enable a more thorough comparison between numerical and experimental data, in particular at higher incidences, where it has been found that the numerical models predict premature VBD.

As the validation of the numerical results was proven in this chapter, the next chapter evaluates the findings for the B03, B05, VFE-2 and VST configuration for the three different thicknesses (3.4%, 6% and 12%). Here, the focus will lie on the aerodynamic performance and longitudinal stability as well as the flow physics.

Chapter 6 CFD Findings and Evaluations

This chapter deals with the results evaluation of the numerical findings only. First the effect of thickness will be investigated, followed by the investigation of the effect of maximum thickness location. This is done using the biconvex configurations. Finally, differences between span tapered and untapered wings are shown using the VFE-2 and VST configurations. This is followed by a discussion of the findings. Conclusions are drawn and presented and suggestions regarding further work are made.

6.1 Configuration Geometries

The final CFD investigations are carried out on multiple configurations of either different profile shape (Figure 6.1) or different spanwise thickness

Table 6.1 lists the configurations assessed, their thicknesses and maximum thickness locations. The thickness was varied for only the biconvex configurations because the VFE-2 configuration used was the baseline configuration. A schematic of the different profiles and the planform are shown in Figure 6.1. The planform design as well as the shape of the profile for the VFE-2 configuration were obtained from Chu and Luckring (1996) as discussed in Chapter 3.

The baseline configuration VFE-2 was modified by changing its spanwise thickness distribution and was named VST. This is resulted in the VST having a thickness of 3.4% of the local chord, whereas the VFE-2 has a thickness of 3.4% root chord.

The same tip taper was applied for the biconvex configurations, which had a maximum thickness location at 50% and 30% and were named B05 and B03 respectively.

In this investigation, all four profiles are simulated at different thicknesses of 3.4%, 6% and 12%. A schematic of the profiles and planforms being depicted in Figure 6.1.

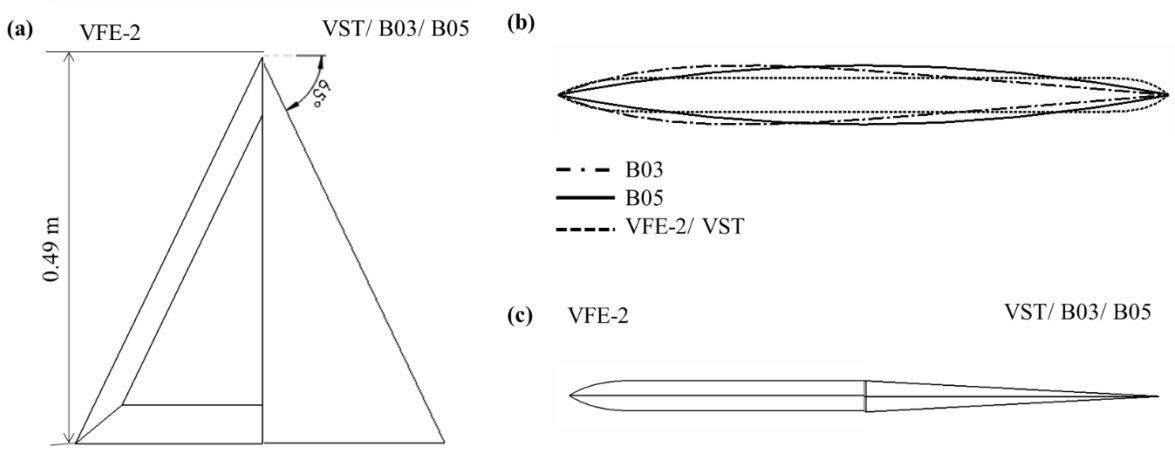

Figure 6.1 (a) The different planforms of the configurations. (b) Profile shape of the different configurations (c) Spanwise thickness distribution of the three different configurations.

Table 6.1 Test matrix of the different delta wing profiles.

Name of configuration	**Max t/c [%]**	$x_{max\ t/c}$ **[%]**
VFE-2	3.4*	constant
VST	3.4	constant
Biconvex 30%	3	30
Biconvex 50%	3	50
Biconvex 30%	6	30
Biconvex 50%	6	50
Biconvex 30%	12	30
Biconvex 50%	12	50

*Based on root chord, not local chord

6.2 CFD Simulations

Based on the investigations done in Chapter 4, the grid and solver settings were chosen and are repeated in a concise form as a reminder for the reader.

The numerical simulations were performed on an Intel® Core™ i7-3770 CPU @ 3.40GHz, 3401 MHz workstation with 4 cores and 8 logical processors using the RANS finite volume solver ANSYS FLUENT. Grids were created in ANSYS Design Modeler using a hybrid mesh approach. The advection fluxes and turbulence were second order accurate. The pressure-

velocity scheme used was SIMPLE with a Green-Gauss Node Based gradient scheme. The $\kappa - \omega$ SSTwith low Reynolds number and curvature corrections was used. The mesh had around 9 million elements with around 43,000 surface elements. The domain extended 20 root chords and the y^+ averaged to unity and was resolved by 45 prism layers with a growth rate of 1.1 resulting in a total height of 0.0113m.

The test conditions used for the simulations are summarised in Table 6.2.

Table 6.2 Test conditions for the numerical simulations.

Static Temperature	300K
Velocity	34m/s
Reynolds Number	750,000
Turbulence Model	k-ω SST with low Re and curvature corrections
Static Pressure	101,325Pa
Angle of attack	0° to 18° in 1° steps

A half-model was used and a symmetry boundary condition was applied to the central vertical symmetry plane enabling efficient use of the computational power available. The vertical plane upstream of the model's apex and the horizontal bottom plane are defined as velocity inlets, and all other surrounding surfaces are declared as pressure openings with the background turbulence being equal to that of the inlet. No-slip wall conditions are applied to the hydraulically smooth model surfaces. The angle of attack was altered by changing the inflow velocity vector to the flow domain. The solution was initialised with the free stream condition throughout the entire domain.

Numerical convergence was achieved by ensuring the standard FLUENT residuals, and the axial, normal and pitching moment coefficients (C_A, C_N , C_M respectively) converged to their constant values, with the residuals also reducing by at least three orders of magnitude. The typical residuals and force coefficient convergence behaviour is depicted in Figure 6.2. A convergence of the coefficients of $1x10^{-6}$ was obtained for most cases, however, not for the thicker wings of the VST and VFE-2 configurations at $\alpha > 13°$. For these cases, the residuals started oscillating as shown in Figure 6.3 and a convergence criterion of only $1x10^{-4}$ could be reached for the aerodynamic coefficients. When analysing the contour plots, it was found that

VBD reached the TE, which caused oscillations in the residuals and thus convergence issues, as the flow became unsteady and therefore a steady state simulation may no longer be physically accurate. To evaluate the impact of this on the validity of the study, the runs were stopped in specific time intervals (peak and trough between oscillations) and the normalised Q-Criterion, mean axial velocity component and surface pressure distributions where compared with each other. As no significant differences could be identified and as the focus of the study is not concerned with the flow physics in the shear layer the simulations were not changed to account for unsteadiness.

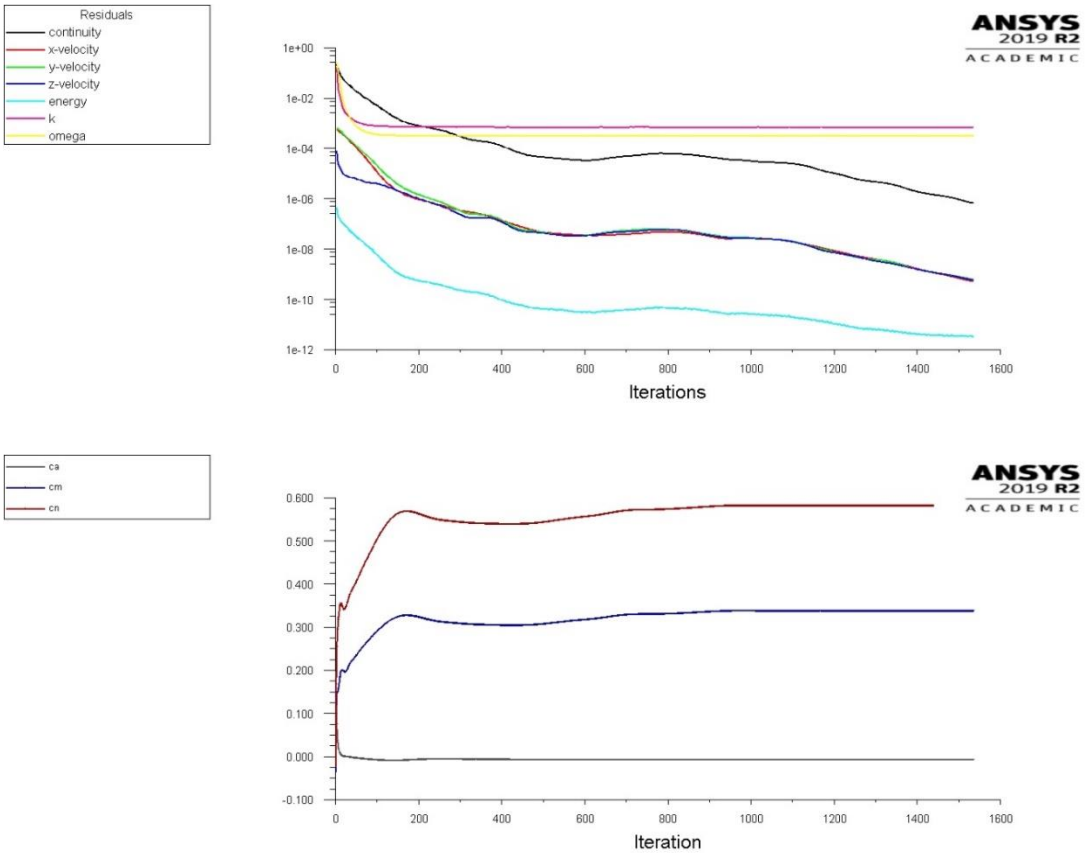

Figure 6.2 Convergence plot of the FLUENT solver residuals and force coefficient for the B05 configuration of 6% thickness at α=13°.

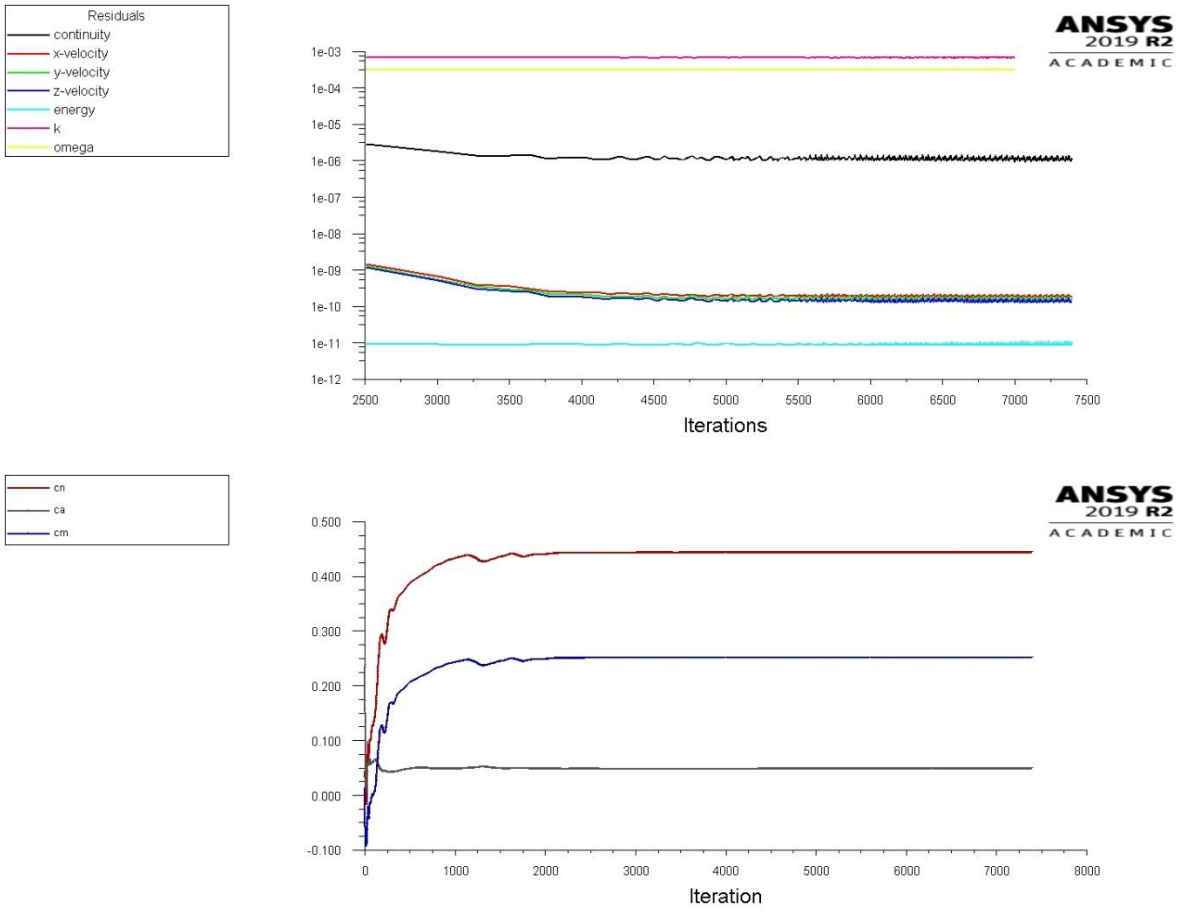

Figure 6.3 Convergence plot of the FLUENT solver residuals and force coefficient for the VFE-2 configuration of 12% thickness at α=13°.

The flow physics were visualised using surface streamlines, vorticity and normalised Q-criterion plots. The normalised Q criterion was used and plotted for values >= 1 as this allows for the identification of the vortex boundary as suggested by Kamkar et al. (2011). It is defined as

$$Q_S = \frac{1}{2}\left(\frac{\|\Omega\|^2}{\|S\|^2} - 1\right) \tag{6.1}$$

where Ω is the vorticity and S the strain rate.

Flow visualisation techniques varied depending on which aspects of the flow needed to be highlighted.

6.3 Change in Flow Structures when varying thickness

Before the general behaviour is evaluated by means of the aerodynamic loads, a closer look at different angle of attack will be taken to establish the effect of thickness and maximum thickness location on the wing loading and the flow behaviour.

For this the spanwise pressure distribution at different chord locations is evaluated (x/c = 0.2, 0.4, 06, 0.8 and 0.95) and the vorticity contours are displayed (at x/c = 0.1, 0.2, 0.3, 0.4, 0.5 0.6, 0.7, 0.8 and 0.95).

This will be done at α=4° and α=13° as the former is close to the location of maximum L/D ratio and the latter is in the angle of attack where fully developed vortical flow can be expected. It is noted that the formation of the secondary vortex may influence the location of the suction peak of the primary vortex so that it is no longer located below the location of the primary vortex core (Goertz, 2005). The investigation of Cp distribution and vorticity contours is conducted for the B03 configuration in the main body of text and the results for the other configurations can be found in Appendix A.5.1 to A.5.3.

6.3.1 Low Angle of Attack Flow

Figure 6.4 shows the vorticity and normalised axial velocity contours for the B03 configuration of three different thicknesses. A separation and reattachment cascade can be seen in the vorticity plots which are further explained in Figure 6.5. The contours also show that a LEV forms for the thinner wings, but not for the 12% thick wing

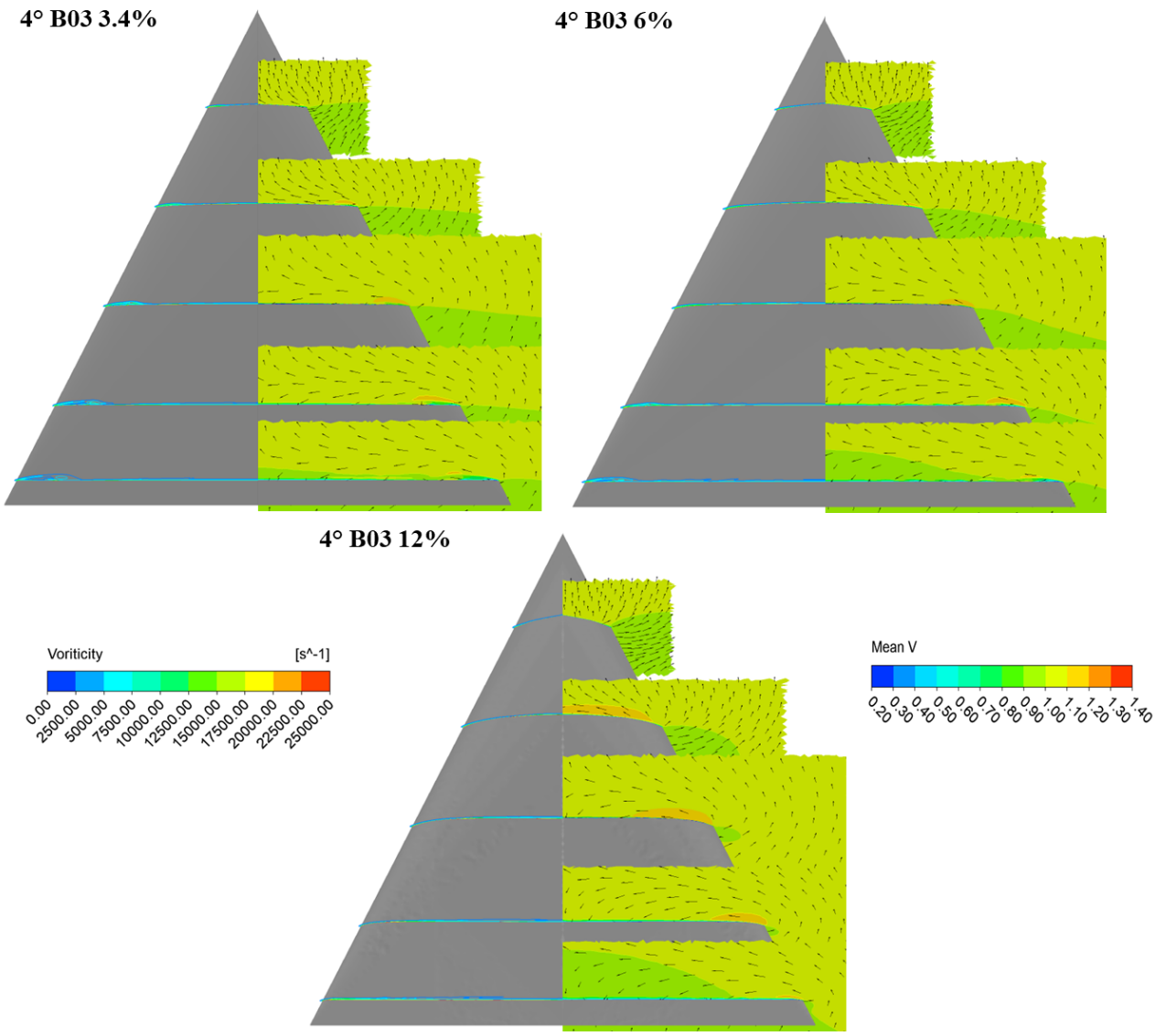

Figure 6.4 Vorticity and mean axial velocity contours at different chord locations for the B03 configuration of different thicknesses at α=4° Note the lack of a LEV on the 12% case.

Figure 6.5 shows the normalised spanwise pressure distribution at different chord locations for the B03 configuration of three different thicknesses. It can be seen that the pressure peaks are highest in the mid-section (x/c=0.6 and x/c=0.8) of the wing and that the front portion of the wing generates the least suction force. It can further be seen that the impact of the primary vortex reduces with increase in thickness. The 3.4% and 6% wings' pressure distribution still looks similar whilst that of the 12% thick wing does not. Here, the initial pressure peak is due to a separation bubble rather than the formation of a LEV. At x/c=0.4 and x/c=0.6 it can be seen that the flow separates again further inboard thus resulting in pressure peaks. For the thinner wings it can be observed that the section affected by the suction force reduces with increase in thickness (i.e. from y/s=0.82 to y/s=0.8 for all x/c)

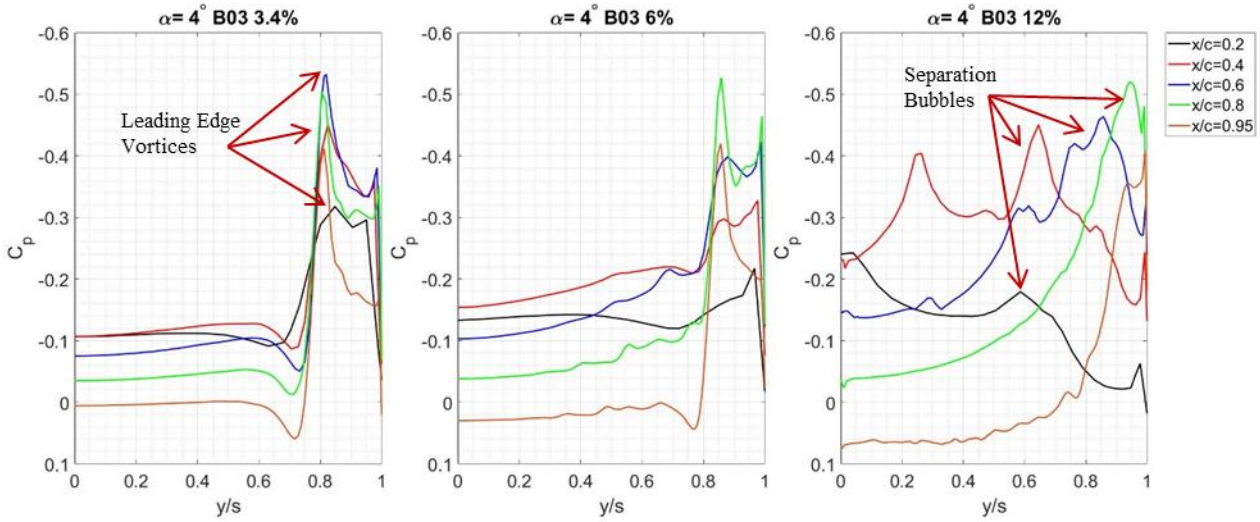

Figure 6.5 Spanwise pressure distribution of the B03 configuration for 3.4, 6 and 12% thickness at α=4°.

At 13° angle of attack the spanwise loadings between the 3.4% and 6% thickness wings are becoming more alike with regards to vortex pattern and location (see Figure 6.6). Secondary vortices have formed on the thinner configurations indicating the strength of the primary vortex and its position relative to the surface (Pershing, 1964). The front loading is diminishing with increase in thickness, whilst the rear loading is enhanced resulting in favourable longitudinal stability for thicker wings as illustrated in Figure 6.38. Further, it can be seen that the maximum suction peak is confined to a smaller area when increasing the thickness, which is due to the more oval shape of the vortex, compared to the 3.4% thick wing, as can be seen from the vorticity and mean axial velocity contours in Figure 6.7. This effect was already observed at α=4°. The cross-sectional area is not necessarily an indicator of the surface suction force generation or the area of the wing affected by it. Surface Cp is also affected by the distance between vortex and surface. It can further be seen from Figure 6.6 that the primary vortex of the 6% thick wing is displaced inboard due to the formation of the secondary vortex at x/c=0.2 and x/c=0.4. This is an effect already observed by Kirkpatrick and Kirby (1971). For the 12% thick wing the axial velocity is less than for the thinner wings, making the vortex less energetic with less effect on the surrounding flow. Thus, small separation bubbles are induced inboard of the vortex, as indicated by the oscillations in the pressure distribution curves.

Looking at the vorticity and mean axial velocity contours in Figure 6.7 no apparent differences between the thinner wings can be identified, apart from the vorticity increasing near the trailing edge when increasing the thickness of the wing. The leading-edge vortices can be seen to rotate counter-clockwise as indicated by the velocity vectors.

The 12% thick wing shows to have formed a vortex like structure whereby an actual LEV does not develop until x/c=0.8. The vortex structure is stretched and can be found closer to the wing's surface than for the thinner configurations.

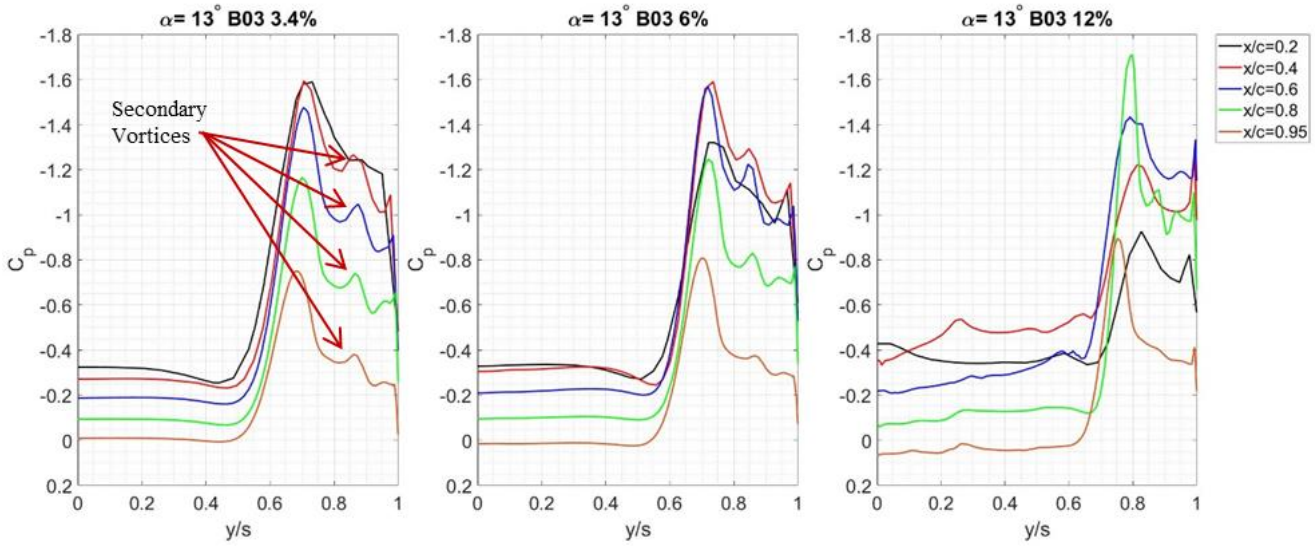

Figure 6.6 Spanwise pressure distribution of the B03 configuration for 3.4, 6 and 12% thickness at α=13°.

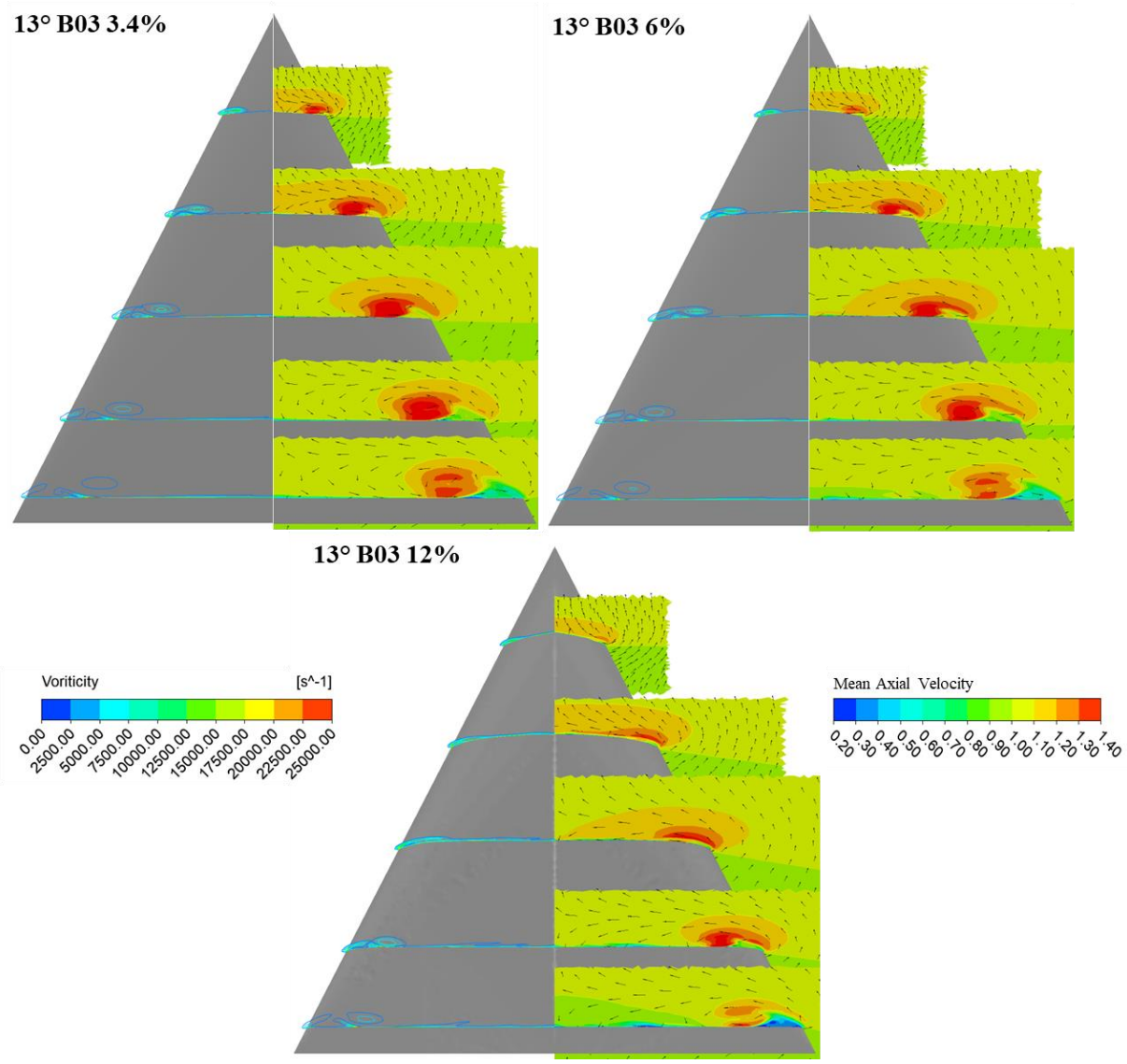

Figure 6.7 Vorticity and mean axial velocity contours at different chord locations for the B03 configuration of different thicknesses at α=13° Note the secondary vortices on the 3.4% and 6% thickness wings. Also, the vortex becomes more oval in shape as the wing thickness increases.

6.4 Change in Flow Structures when varying the maximum thickness location

For the investigation of the effect of maximum thickness location on the flow structure the B03 and B05 configurations for the different thicknesses. As a reminder it is restated that the B03 configuration has its maximum thickness location at 30% chord and thus further upstream than the B05 configuration, which has its maximum thickness location at 50% chord.

A comparison of spanwise pressure distribution at 4° angle of attack between the B03 and B05 configurations of 3.4% thickness is depicted in Figure 6.8 together with the vorticity contours.

From the pressure coefficient plots, it can be seen that the suction force is larger for the B03 configuration in the rear part of the wing (x/c> 0.4) whereas the B05 is more front loaded. The

vortex pattern of both wings is very similar; however, the location of the pressure peaks is located further outboard for the B05 configuration. This may be due to a higher adverse pressure gradient delaying reattachment. It can further be seen, that secondary vortices are forming on the B05 configuration, which displace the vortex inwards and upwards (Nelson and Visser, 1990). The Cp and contour plots of the VFE-2 and VST configuration can be found in Appendix 5.3. It was found that a constant spanwise thickness increases the suction in the last 5% of the wing of the 3.4% and 6% thick wings. The effect is reversed for the 12% thick wings. Overall, the effects of spanwise thickness distribution on the Cp distribution are small at low angle of attack

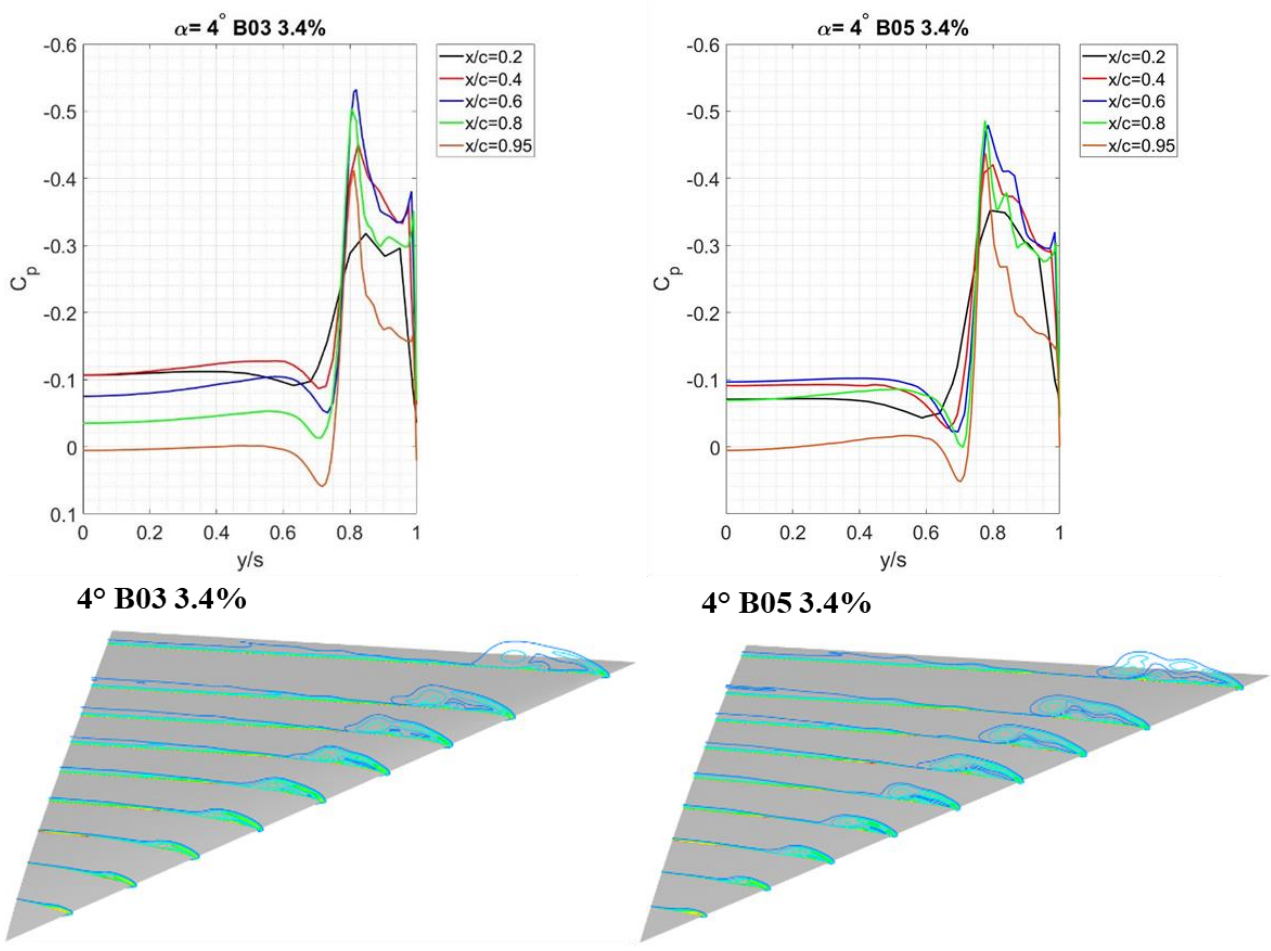

Figure 6.8 Comparison of the spanwise pressure distribution of the B03 and B05 configurations at 3.4% thickness and their associated vorticity contours at α=4°.

The trend that the upstream movement of maximum thickness location results in higher stability due to reduced front loading and increased rear loading can also be observed for thicker wings (see Figure 6.9 and Figure 6.10 for the 6% and 12% wings respectively). It can be seen from Figure 6.9 that for the B03 6% configuration vortex formation is delayed until the second half of the wing (x/c > 0.5) whilst being formed at x/c=0.2 for the B05 configuration.

Before that the B03 only shows the formation of a separation bubble. Due to the reduced thickness towards the rear, the B03's LEV persists until the TE, thus still producing a relatively high suction force in that region. The suction of the B05 configuration is dropping in magnitude after x/c=0.6 and is around 25 to 35% lower compared to the B03 configuration. From the vorticity contours it can be seen that less vorticity is fed into the LEV of the B05 configuration further downstream resulting in reduced suction force.

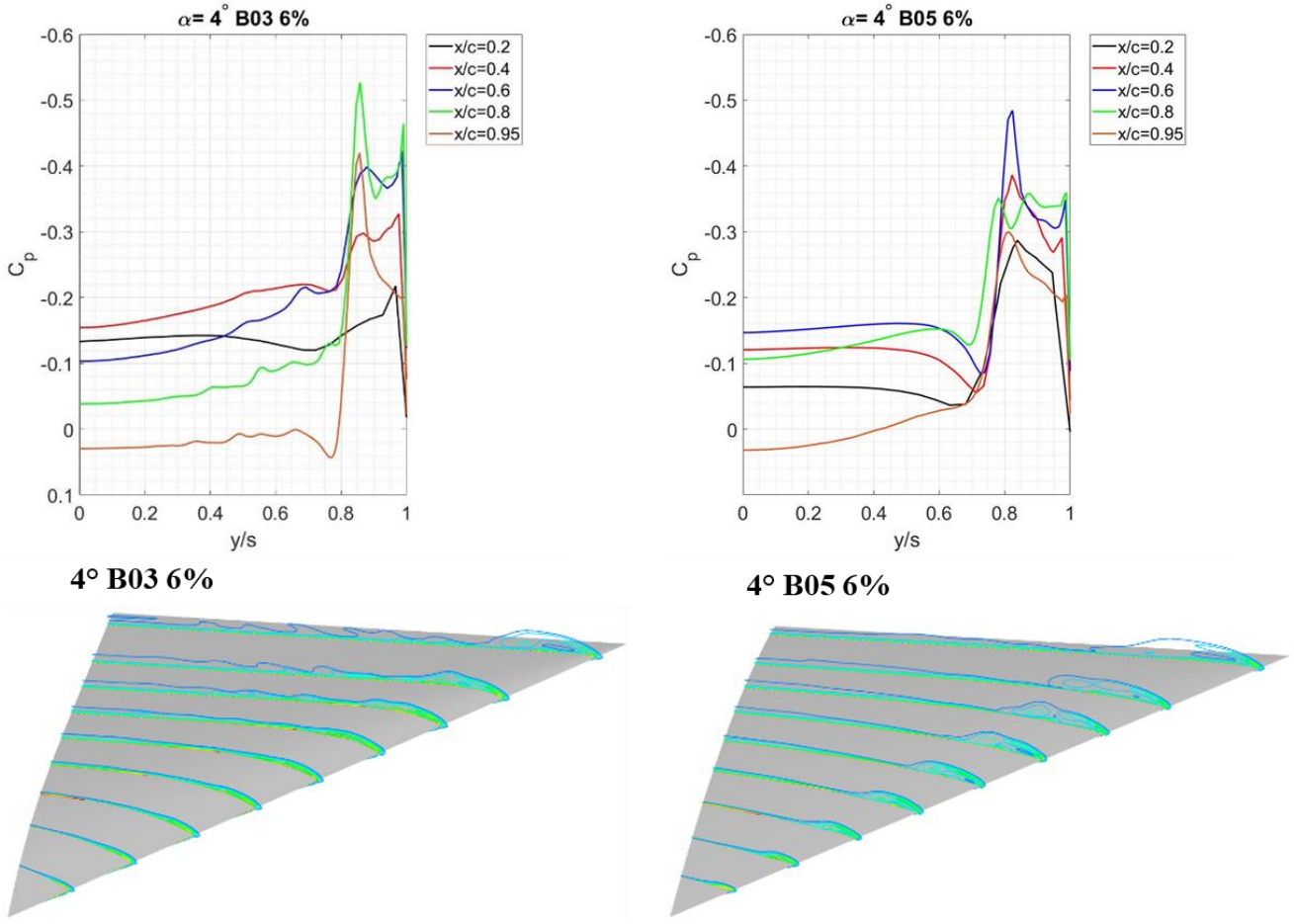

Figure 6.9 Comparison of the spanwise pressure distribution versus local normalised span of the B03 and B05 configurations at 6% thickness and their associated vorticity contours at α=4°.

At 12% thickness the flow around the B03 configuration is dominated by constant flow separation and reattachment as discussed earlier. Particularly, the region near the apex (x/c=0.2 and x/c= 0.4) shows the development of two vortices indicated by two suction peaks. However, these inner vortices decrease in strength after x/c= 0.4 and are no longer present beyond x/c= 0.8. A flow field dominated by multiple separation and reattachment can also be seen on the B05 configuration, however, here the flow disturbance is only affecting the outer half of the wing. The main difference between the configurations is the delayed vortex onset on the B03

configuration, with the flow being dominated by separation bubbles. The B05 shows a more structured separation pattern starting from the apex.

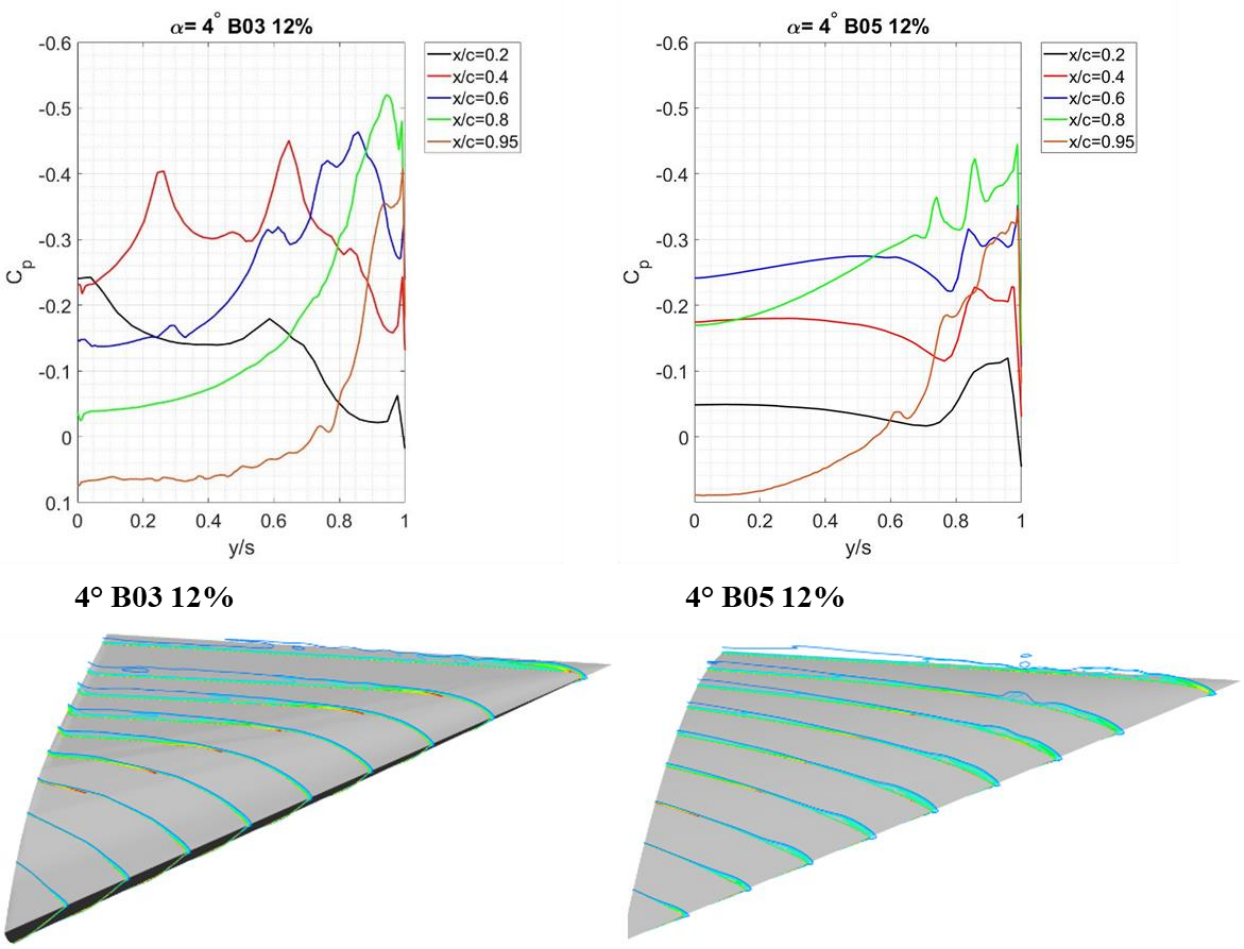

Figure 6.10 Comparison of the spanwise pressure distribution of the B03 and B05 configurations at 12% thickness and their associated vorticity contours at α=4°.

To establish the differences when moving the maximum thickness location when vortical flow is fully established, the different configurations are compared against each other at α=13°. Figure 6.11 shows the spanwise pressure distribution and vorticity contours for the B03 and B05 configuration of 3.4% thickness. It can be seen that the flow pattern does look more alike between configurations once vortex flow is fully established. However, the higher rear loading for the B03 configuration still holds true.

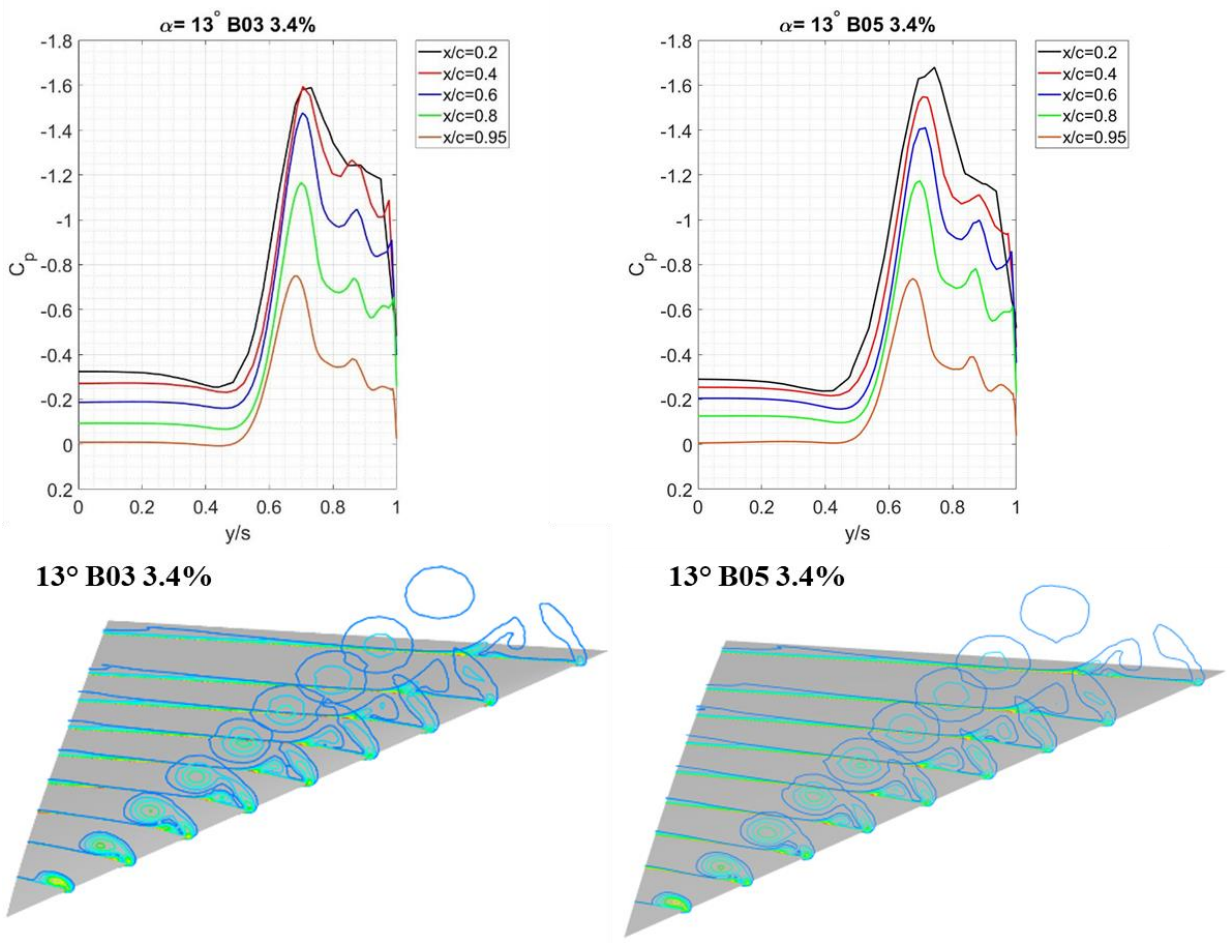

Figure 6.11 Comparison of the spanwise pressure distribution of the B03 and B05 configurations at 3.4% thickness and their associated vorticity contours at α=13°.

Differences in vortex shape start to occur once thickness is increased as depicted in Figure 6.12 for the 6% thick wings. The vortex of the B03 configuration is stretched compared to that of the B05. This effect becomes more severe when increasing the thickness even further as depicted in Figure 6.13. Here, the B03 configurations is dominated by separation bubbles over the majority of the wing, whereas for the B05 configuration vortex onset is only delayed until x/c=0.4. The position of the suction maxima is slightly more outboard for the B03 configuration of 6% thickness, but this effect is enhanced when thickness is increased.

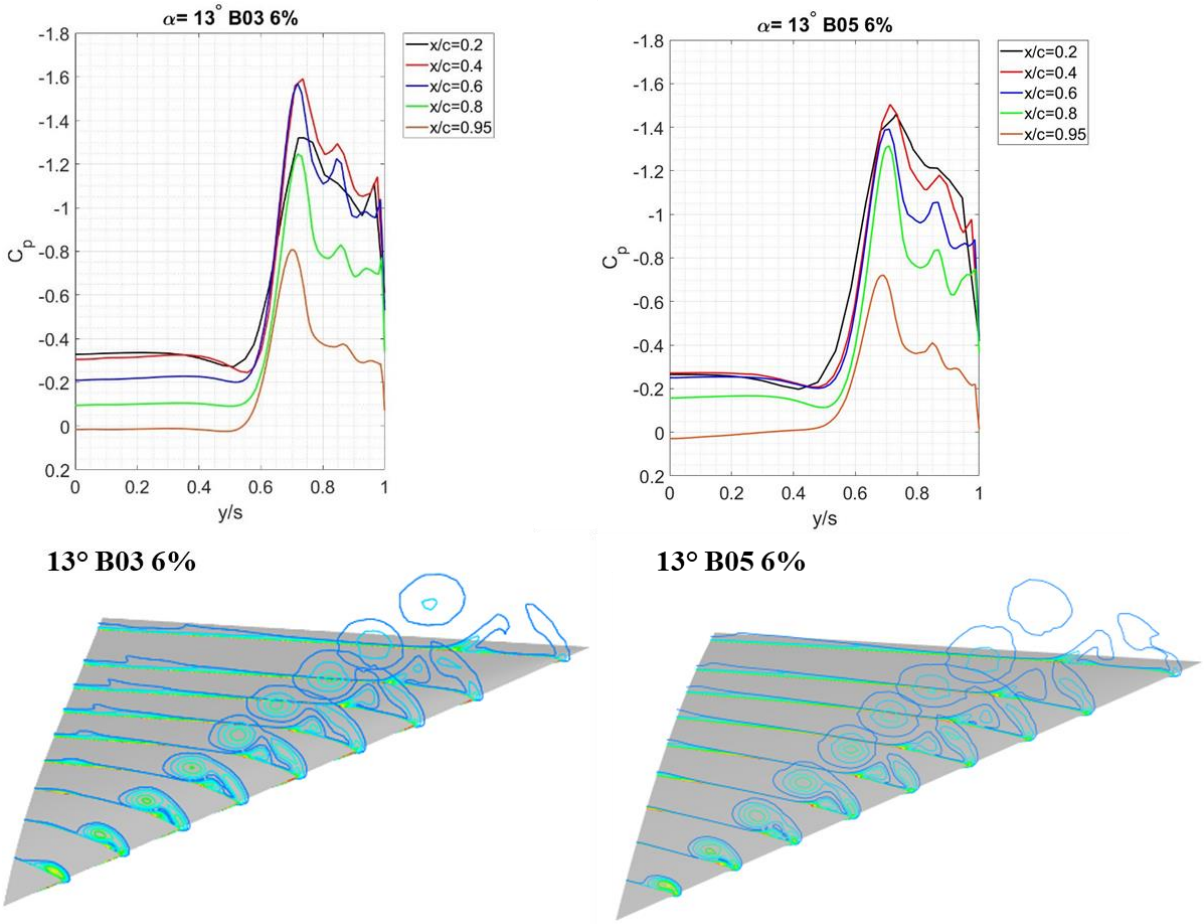

Figure 6.12 Comparison of the spanwise pressure distribution of the B03 and B05 configurations at 6% thickness and their associated vorticity contours at α=13°.

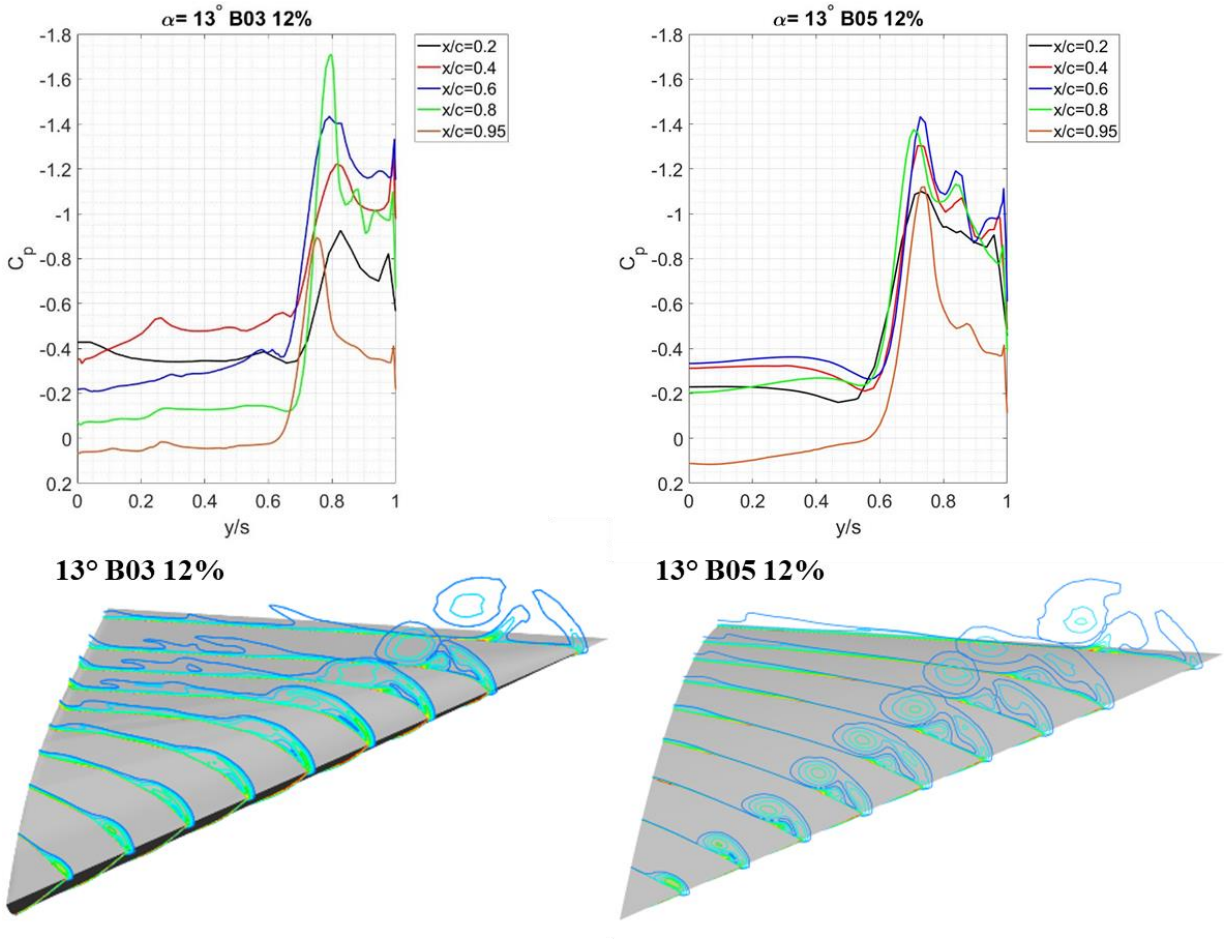

Figure 6.13 Comparison of the spanwise pressure distribution of the B03 and B05 configurations at 12% thickness and their associated vorticity contours at α=13°.

6.5 Change in Flow Structures with span taper

In the following section the effect of spanwise taper is discussed. As a reminder the geometric differences in spanwise thickness distribution are depicted in Figure 6.14.

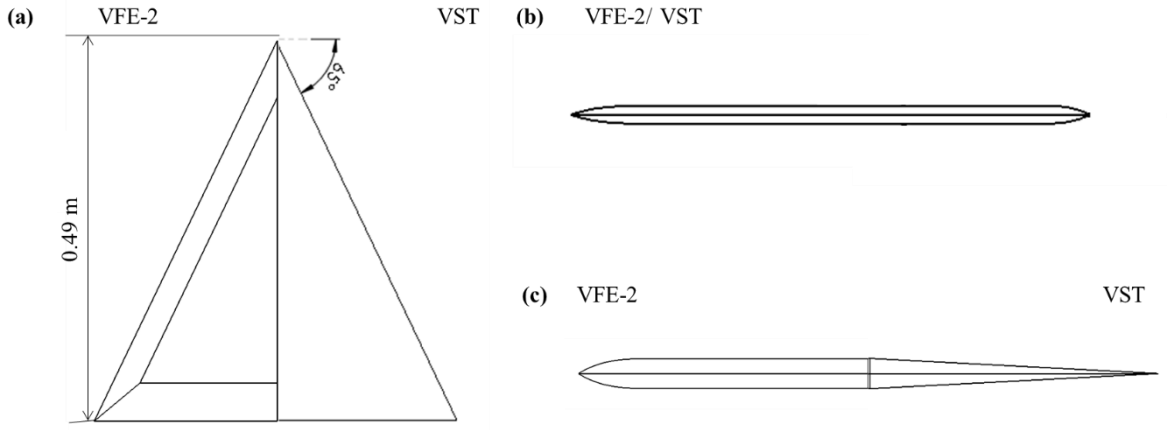

Figure 6.14 Geometric differences between the VFE-2 and VST configuration. (a) planform view, (b) wing profile, (c) back view (spanwise thickness distribution).

The effect of span taper on the Cp distribution and the overall flow at α=4° is depicted for the VST and VFE-2 at different thicknesses in Figure 6.15 to Figure 6.17. It can be seen that for the 3.4% thick configurations, the flow behaves very similarly and the biggest differences are seen close to the trailing edge. This is expected as here the difference in frontal area is most noticeable. The flow near the trailing edge is also influenced by the flow further upstream, and alterations in spanwise pressure distribution are already noticeable at x/c=0.4. Here, the suction generated near the leading-edge is significantly higher for the VST and a vortex structure is forming around x/c=0.6 which is not the case for the VFE-2. The flow of the VFE-2 is characterised by separation bubbles, due to the adverse pressure gradient introduced by the constant spanwise thickness.

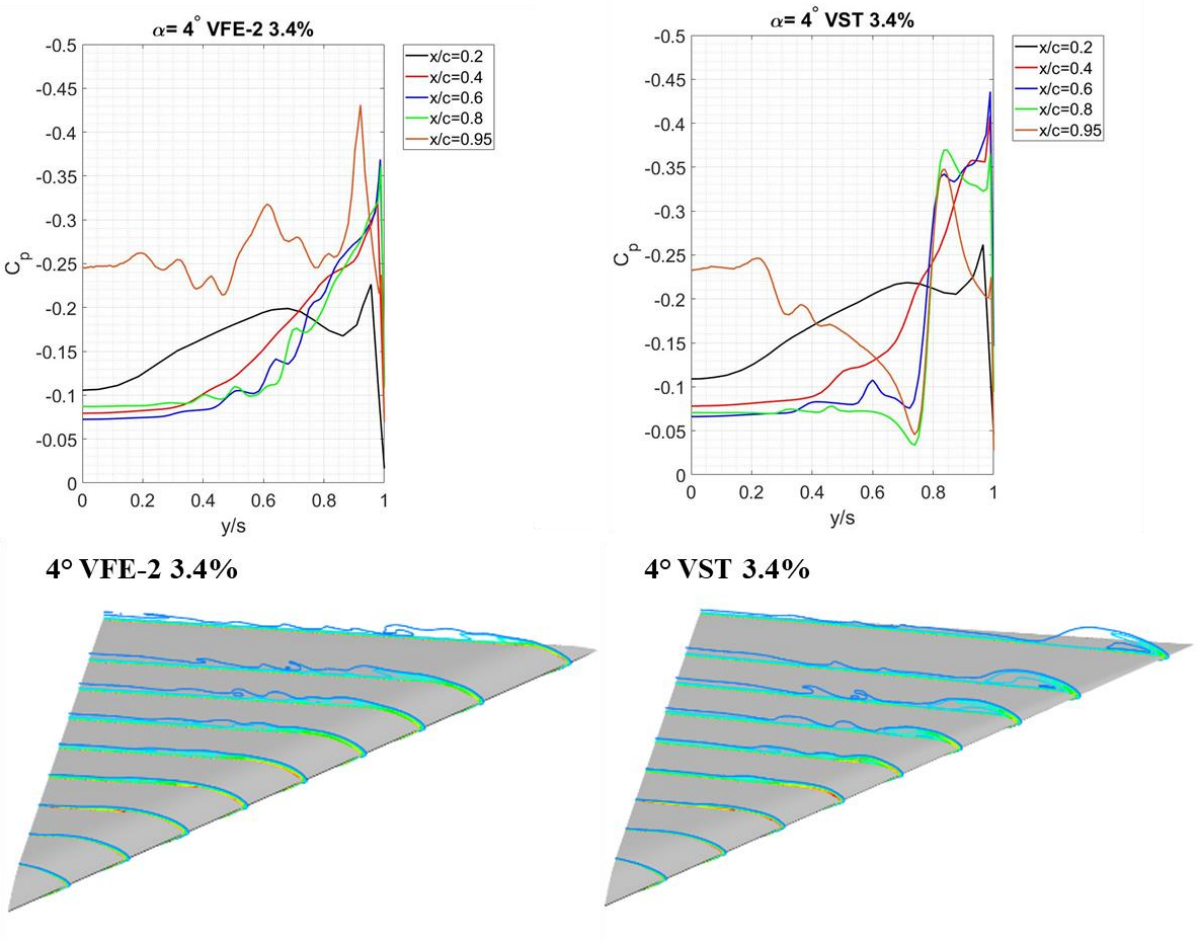

Figure 6.15 Comparison of the spanwise pressure distribution of the VFE-2 and VST configurations at 3.4% thickness and their associated vorticity contours at α=4°.

Increase in thickness makes the trailing edge effects even more pronounced as depicted in Figure 6.16 and Figure 6.17 for the 6% and 12% thick wings. The flow over the VFE-2 is mainly attached apart from the initial separation at the SLE. This is also true for the VST configuration, apart from the area close to the trailing edge. Here, the flow shows multiple

separation bubbles and the formation of a tip vortex. Constant spanwise thickness seems to magnify the effect resulting in a high suction peak near the tip. Inner vortices or separations occur for both VST and VFE-2 for the thicker wings and can thus be concluded being due to their flat profile. The inner vortices form on the 12% thick configurations at x/c=0.2 as the local flow has enough energy due to the relatively sharper leading-edge. With downstream direction, this changes and separation bubbles are forming close to the leading-edge resulting in the inner vortex to lose strength with downstream direction, as less vorticity is fed into it.

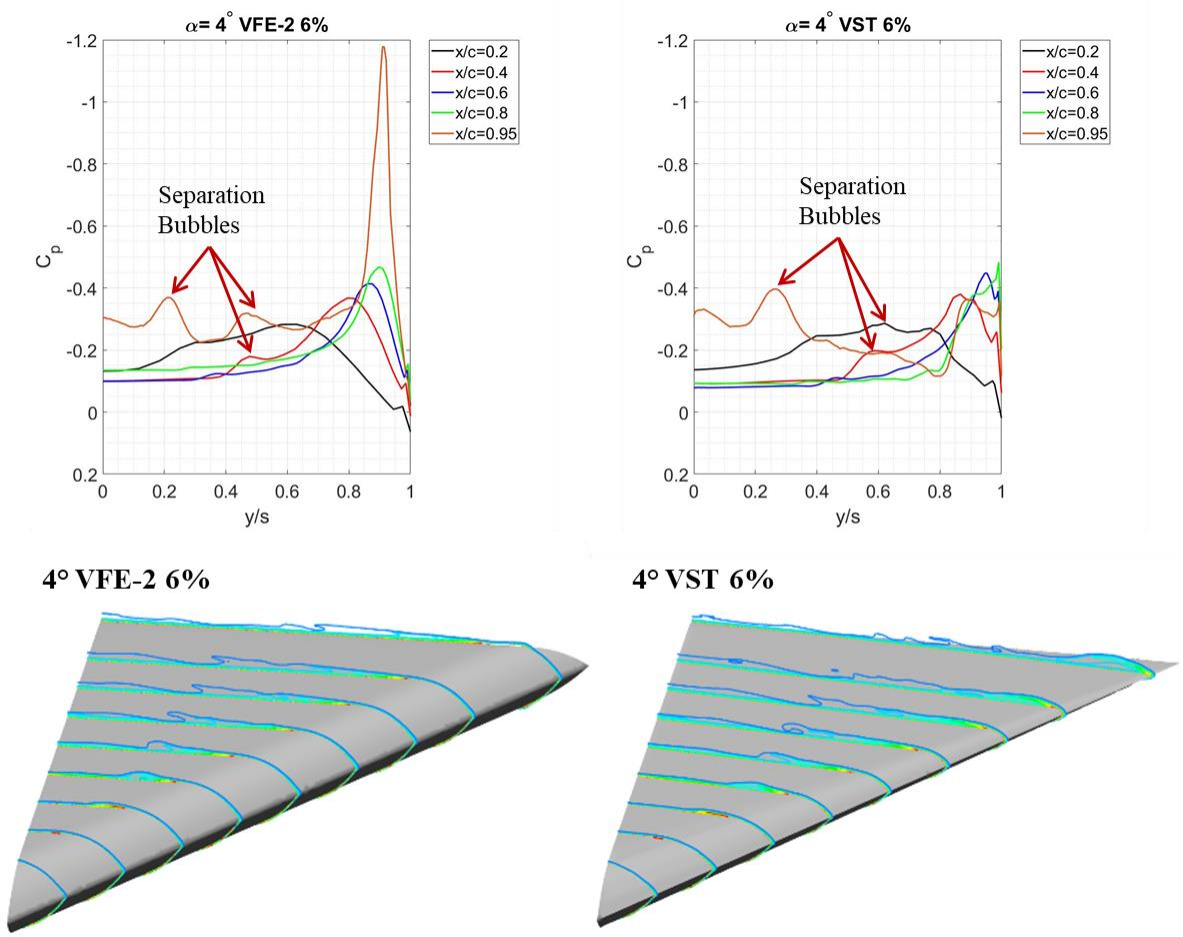

Figure 6.16 Comparison of the spanwise pressure distribution of the VFE-2 and VST configurations at 6% thickness and their associated vorticity contours at α=4°.

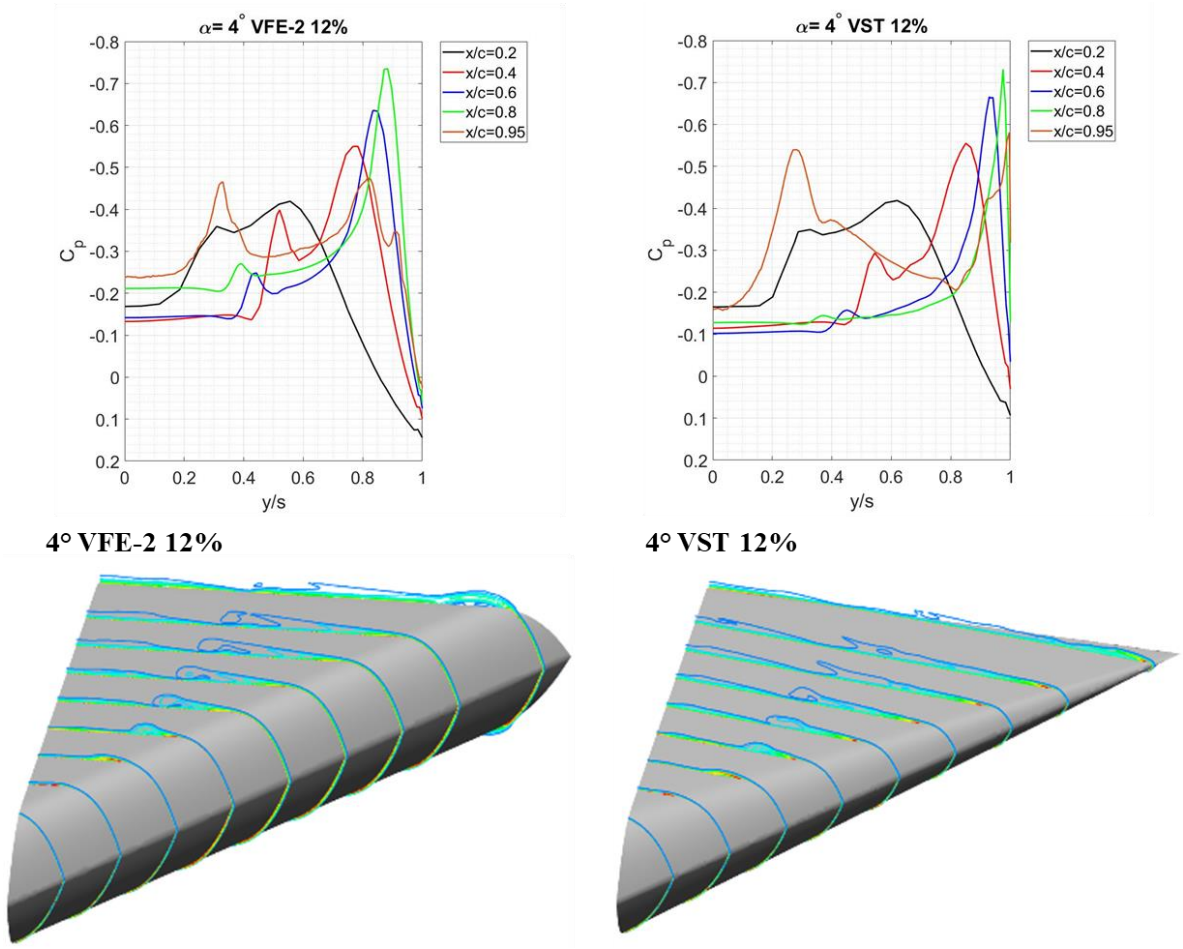

Figure 6.17 Comparison of the spanwise pressure distribution of the VFE-2 and VST configurations at 12% thickness and their associated vorticity contours at α=4°.

Once vortical flow is established at higher incidences the differences in flow physics diminishes for the 3.4% thick wing. This is seen in both the pressure and vorticity plots shown in Figure 6.18. Differences in wing loading are seen especially near the apex of the wing. Here, the loading of the VST configuration is much higher than for the VFE-2 configuration reducing its longitudinal stability. The small differences in flow physics seen on the 3.4% thick wing result in similar lift and drag generation. Differences in flow physics are therefore more significant at lower angles of attack and are less significant once vortical flow is fully developed, for thin wings.

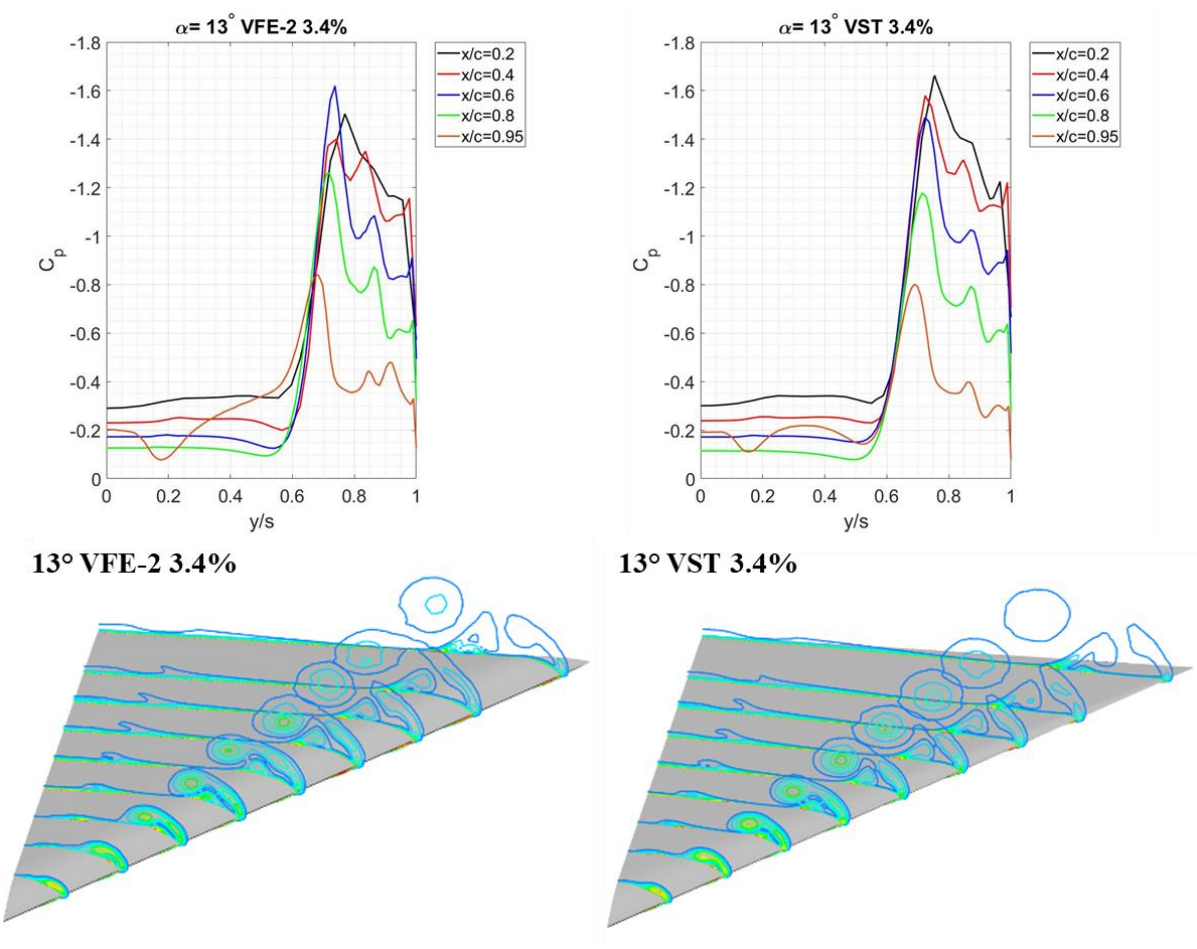

Figure 6.18 Comparison of the spanwise pressure distribution of the VFE-2 and VST configurations at 3.4% thickness and their associated vorticity contours at α=13°.

When increasing the thickness to 6% the differences in flow field and wing loading become more significant (see Figure 6.19). Whilst a typical pressure distribution for vortex dominated can be identified for the VST configuration this is not the case for the VFE-2. Here, the flow is heavily affected by inboard separations and vortex merging. The initial separation suction peaks of the VST are located further inboard, but the VFE-2's vortex system affects more of the span across the majority of the wing.

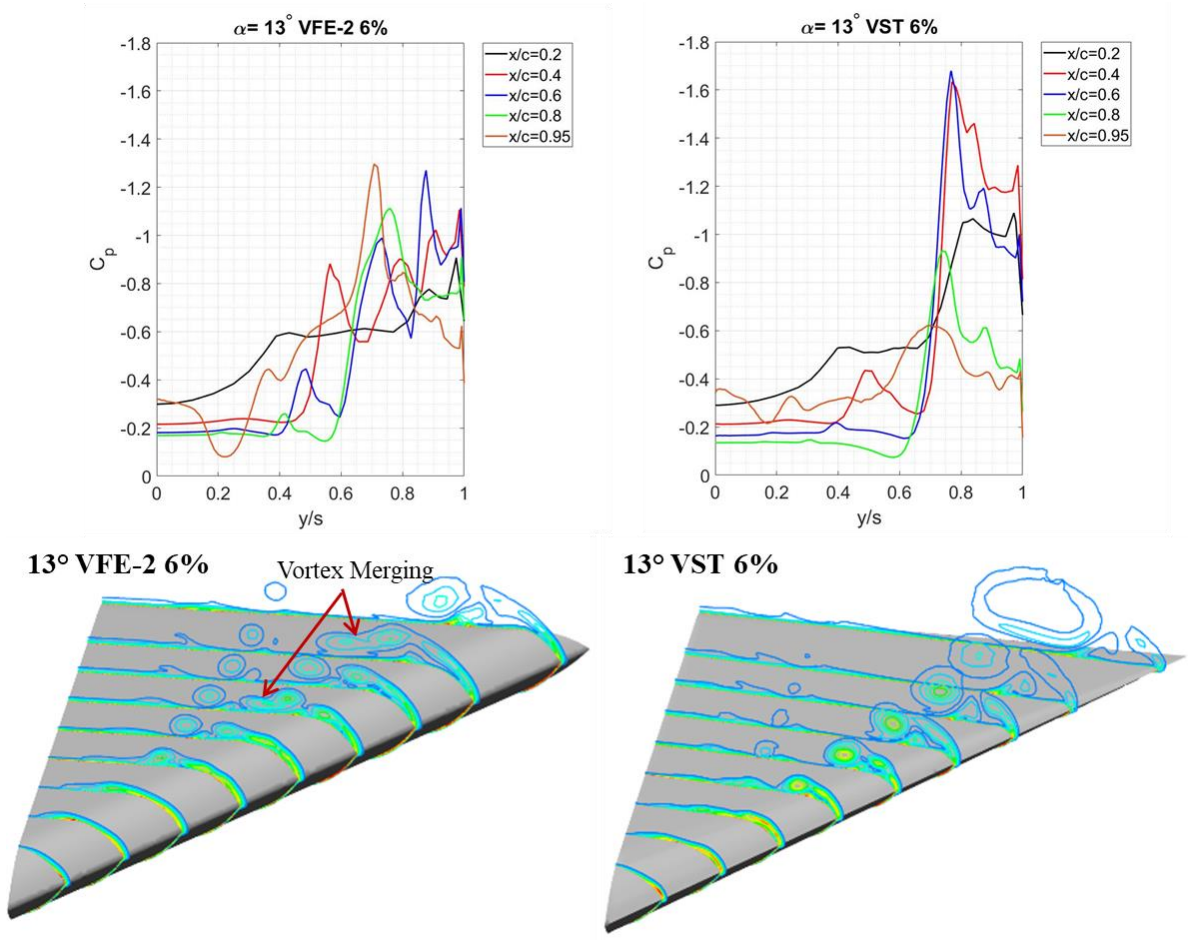

Figure 6.19 Comparison of the spanwise pressure distribution of the VFE-2 and VST configurations at 6% thickness and their associated vorticity contours at α=13°.

Increasing the thickness further to 12% shows again significant differences between configurations. This is because the effect of the relative leading-edge radius downstream becomes larger. Therefore, close to the apex the pressure distribution looks similar between both wings (x/c=0.2). After that the flow pattern changes, though inboard separation still occurs for both configurations, but affects the wing loading more for the VST than the VFE-2 configuration. The initial separation suction peaks of the VST are located further inboard due to span taper as could already be observed for the 6% thick wing.

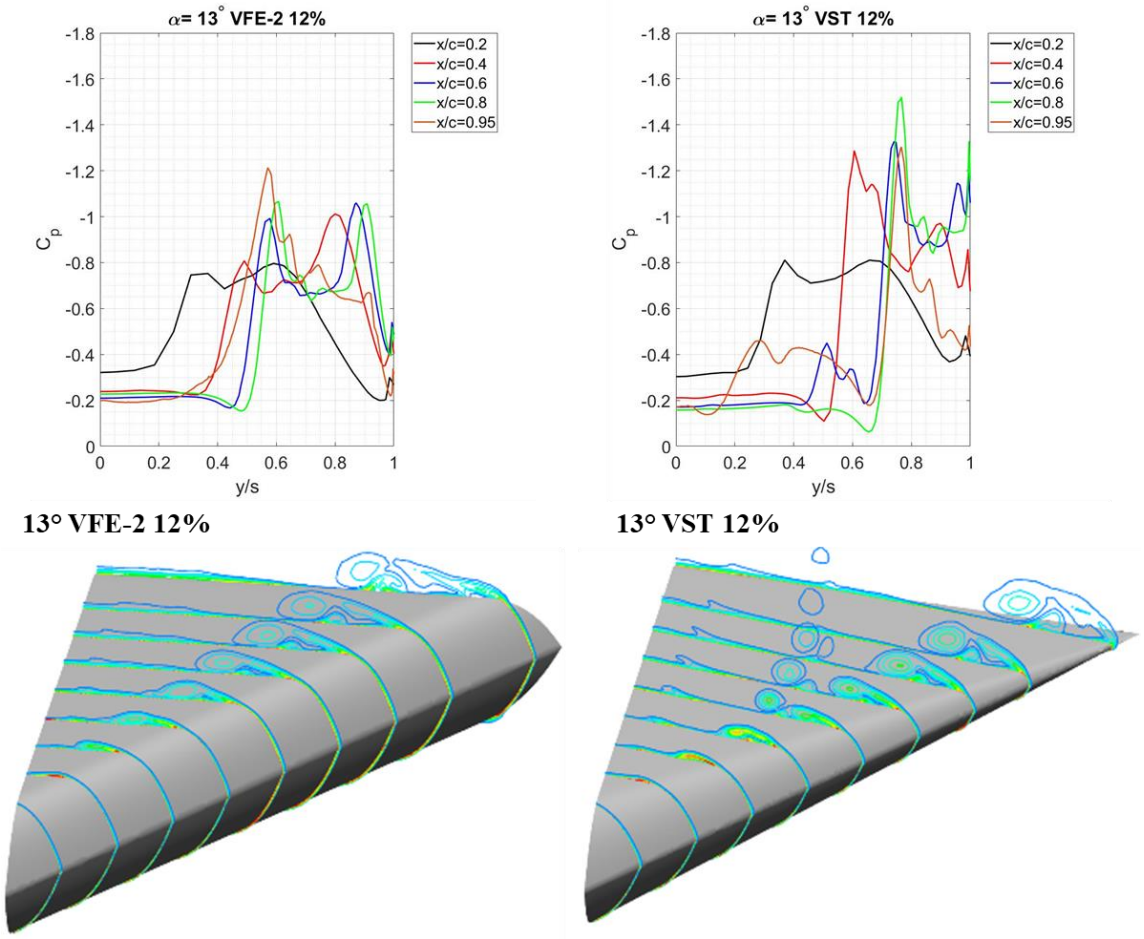

Figure 6.20 Comparison of the spanwise pressure distribution of the VFE-2 and VST configurations at 12% thickness and their associated vorticity contours at α=13°.

6.6 Effect of profile shape on the lift coefficient

After the effects of thickness, maximum thickness location and tip taper on the flow physics have been established, the aerodynamic loads are evaluated. First the effect on the lift coefficient is established.

Figure 6.21 depicts the lift coefficients for different configurations at different angle of attack. It can be seen that for all cases the lift decreased with increase in thickness. This phenomenon is attributed to the vortex lift as the total lift is proportional to thickness for aerofoils (Hoerner, 1985). Though differences are small at lower incidences they become more noticeable at higher angles. The differences between the 3.4% thick wing and the 6% thick wing are relatively small, however, the lift significantly decreases when doubling the thickness from 6% to 12%. It can be seen that a typical take-off lift coefficient of 0.5 (Kirby and Kirkpatrick, 1969) requires a higher incidence for thicker wings (1-2° more than for thinner wings). This angle lies between

10° and 13° angle of attack and can be considered disadvantageous as during take-off the aircraft would also consist of an undercarriage, limiting the rotation rate.

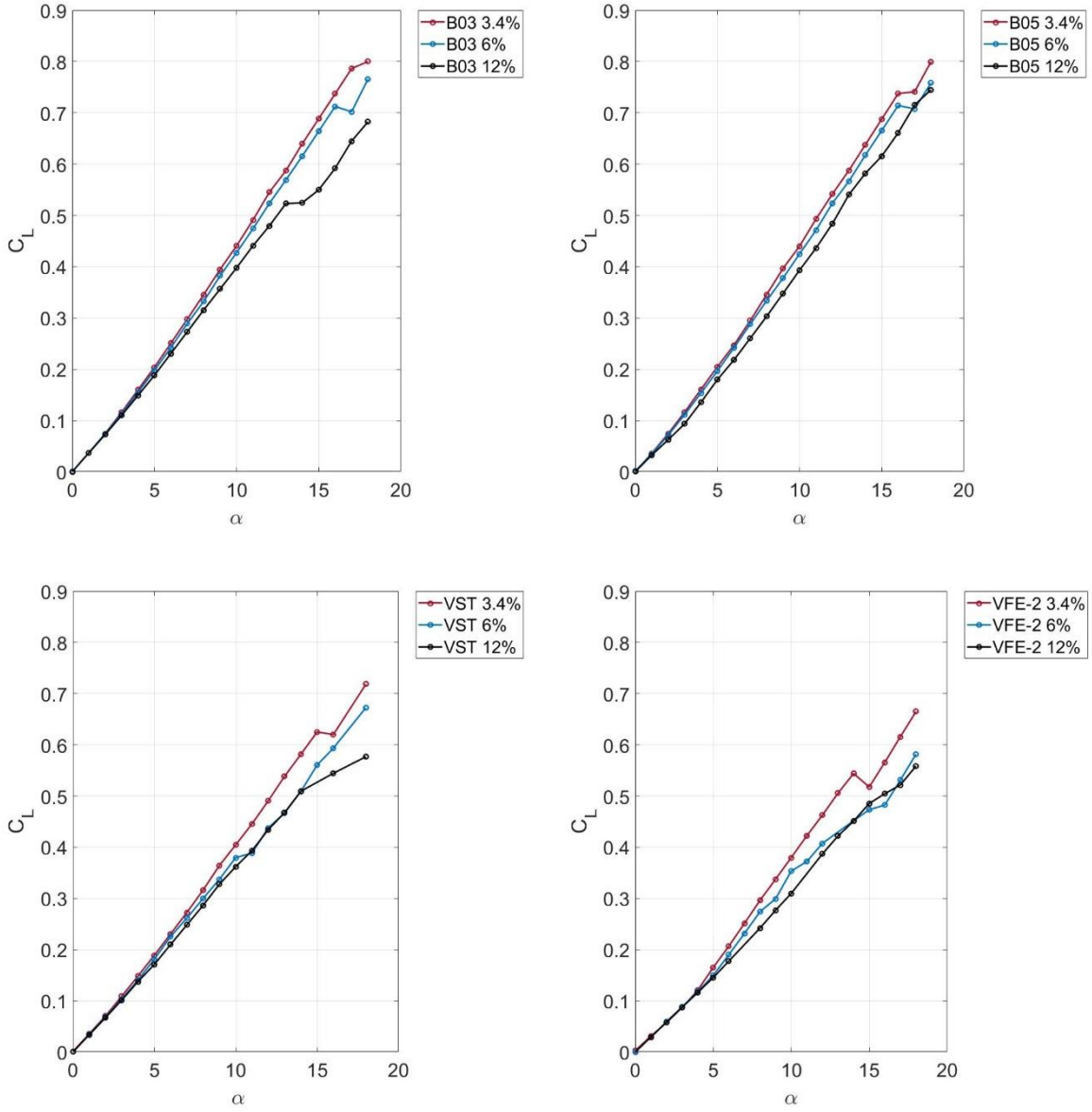

Figure 6.21 Lift coefficient versus angle of attack for the B03, B05, VST and VFE-2 configurations for varying thickness.

From Figure 6.21 can also be seen that the differences in lift are also affected by the maximum thickness location; i.e. the lift between the 3.4% and 6% thick wings of the B03 and B05 configurations does not vary much, whereby that of the VFE-2 and VST configurations does. However, no differences in lift are observed between the 6% and 12% thick wings of the VFE-2 between α=0°-5° and α=13°-18°. Between 5° and 13° angle of attack the 6% thick VFE-2 generates up to 17% more lift, though this varies between data points and could be due to numerical inaccuracies. No significant change in slope can be observed between the VST 6%

and VST 12% configuration between 0° and 14° angle of attack. After this VBD reduces the slope of the VST 12% resulting in up to 15% lift loss compared to the VST 6% and is different to the VFE-2 due to the taper towards the tip.

For easier evaluation Figure 6.22 illustrates the change in lift coefficient for different thickness locations. It can be seen that the differences between the VST and VFE-2 configurations are minimal for thinner wings. However, for thicker wings the effect of varying spanwise thickness distribution appears to become more significant. It can be seen that varying the spanwise thickness results in an increase in lift generation for all thicknesses, whereby the lift difference increases with increase in thickness. For the thinner wings it is interesting to see that the differences between VST and VFE-2 become more pronounced at higher angles of attack. The reason for the reduced lift generation are due to the trailing edge and tip effects, which are more significant for wings with constant spanwise thickness.

The B05 and B03 configurations show no differences for thinner wings between 0° and 15° angle of attack. Early VBD onset on the B03 3.4% results in a difference in C_L of approximately 5%. However, at a thickness of 12% it can be seen that the B05 outperforms the B03 configuration at higher angles of attack ($\alpha >= 13°$) by up to 12%.

Generally, the biconvex configurations generate the most lift across all thicknesses, followed by the VST and VFE-2 configurations. Those differences seem to be insensitive to thickness change. Overall, the lift generation is reduced with increase in thickness across all profiles and thus is a feature of thickness change.

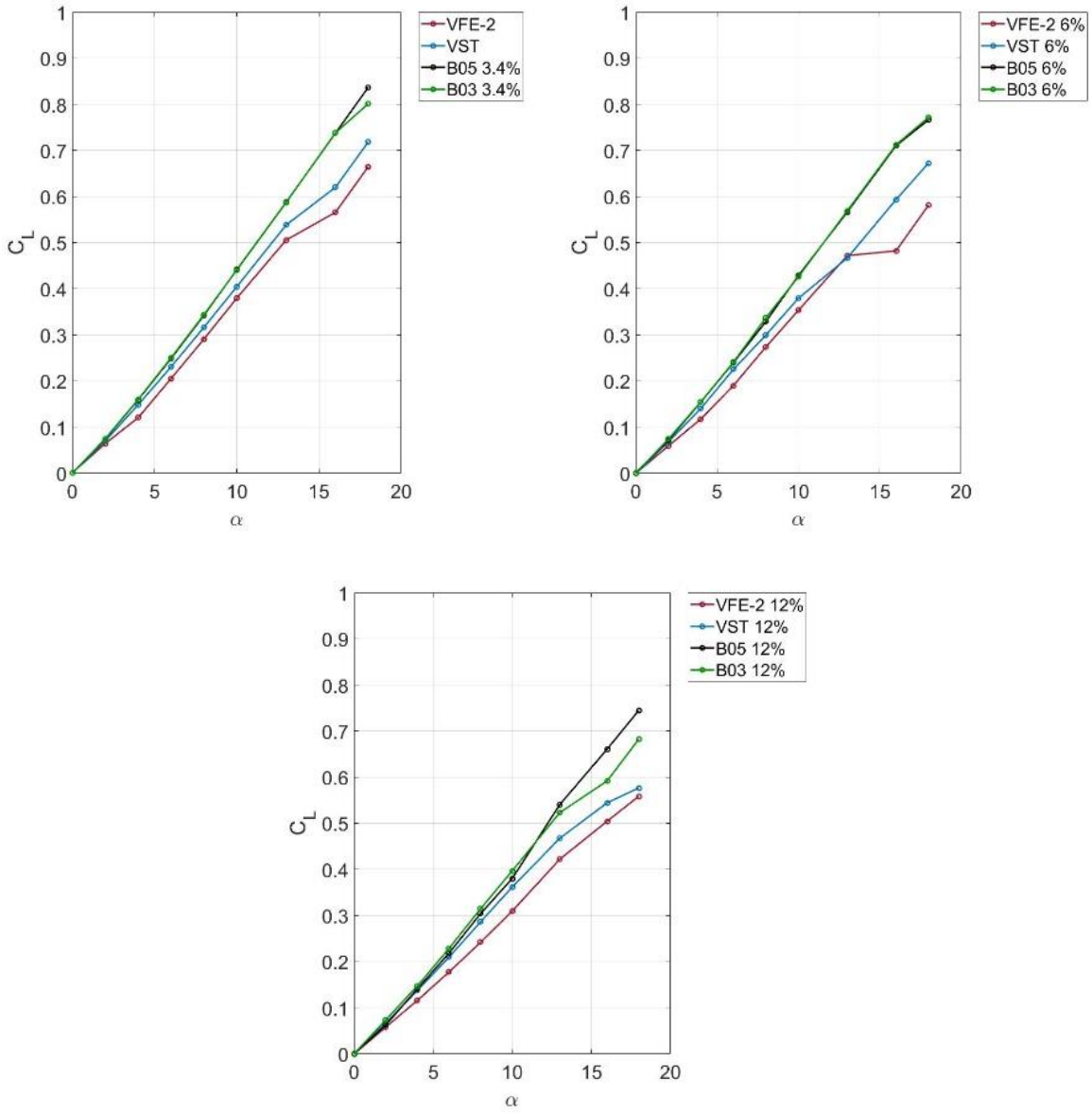

Figure 6.22 Comparison of the lift coefficient for different angles of attack between the B03, B05, VST and VFE-2 configurations.

6.7 Effect of profile shape on the normal force coefficient

From theory it is known that the flow past a slender wing with sharp edges can be considered as the sum of two velocity fields, namely, the linear and the non-linear velocity fields. The linear part of the flow is due to attached flow whereas the non-linear part is due to LEV. The former is said to be proportional to the angle of attack, whereas the latter is not. Thus, the normal force coefficient can be written as (Kirby and Kirkpatrick, 1969):

$$C_N = C_{N_{linear}} + C_{N_{non-linear}} = a\alpha + C_{N_{non-linear}} \quad (6.2)$$

where a is the slope of the normal force at zero incidence as the models investigated are symmetric. For symmetrical, sharp-edged wings the constant a should be determined from plots of C_N/α against angle of attack. The point where the plot intercepts the C_N/α axis is the constant a.

The value of a can then be taken to calculate the non-linear component of the normal force using (Kirby and Kirkpatrick, 1969)

$$C_{N_{non-linear}} = C_N/\alpha - a \quad (6.3)$$

and are due to the separated flow (Table 6.3 & Table 6.4). These values are plotted against angle of attack in Figure 6.23 and Figure 6.24.

Table 6.3 Linear and non-linear normal force components for the B03 and B05 configurations for different thicknesses.

		B03			B05		
	α [°]	3.4%	6%	12%	3.4%	6%	12%
Linear a		2.15	2.14	2.1	2.07	1.94	1.88
Non-linear $C_N/_\alpha - a$	2	0	0	0	0.08	0.002	0.008
	4	0.158	0.098	0.055	0.261	0.009	0.077
	6	0.271	0.196	0.130	0.325	0.125	0.223
	8	0.365	0.274	0.195	0.351	0.278	0.321
	10	0.428	0.355	0.221	0.514	0.344	0.411
	12	0.526	0.423	0.239	0.597	0.267	0.480
	14	0.561	0.461	0.106	0.642	0.176	0.568
	16	0.608	0.515	0.097	0.699	0.975	0.570
	18	0.539	0.424	0.173	0.629	0.218	0.596

Table 6.4 Linear and non-linear normal force components for the VFE-2 and VST configurations for different thicknesses.

		VFE-2			VST		
	α [°]	3.4%	6%	12%	3.4%	6%	12%
Linear a		1.93	1.73	1.76	2.01	2	1.95
Non-linear $C_N/_\alpha - a$	2	0.018	0	0	0.015	0.028	0
	4	0.03	0.009	0.004	0.136	0.037	0.056
	6	0.08	0.125	0.031	0.220	0.181	0.094
	8	0.232	0.278	0.073	0.293	0.183	0.147
	10	0.297	0.344	0.119	0.357	0.219	0.177
	12	0.736	0.267	0.197	0.396	0.145	0.183
	14	0.377	0.176	0.199	0.451	0.149	0.2
	16	0.194	0.075	0.163	0.309	0.21	0.078
	18	0.308	0.218	0.138	0.401	0.245	0.022

Figure 6.23 and Figure 6.24 show that the non-linear lift is majorly driven by maximum thickness location, which will be discussed later. An increase in thickness for the B03 configuration results in a decrease in non-linear lift component (Figure 6.5), which becomes more severe at higher incidences. A break in non-linear lift can be observed at 16 degrees angle of attack for the thinner wings, whereby the non-linear lift component drops after at 13 degrees for the 12% thick wing. The drop in non-linear lift for the thinner wings is due to VBD as can be seen from the normalised Q-Criterion (Q- Criterion normalised by the shear strain (Kamkar et al., 2011)) plots combined with the surface streamlines (Figure 6.24). The initial dip of the 12% thick configuration is also due to VBD. However, at 18 degrees angle of attack, unlike for the thinner wings, an additional inner vortex is forming and increasing in strength, thus, adding to the non-linear normal force component. The initial dip due to VBD is important when choosing a particular thickness and thickness location since it is not feasible to fly a

configuration above the VBD angle of attack, considering the lift loss and increased drag penalty.

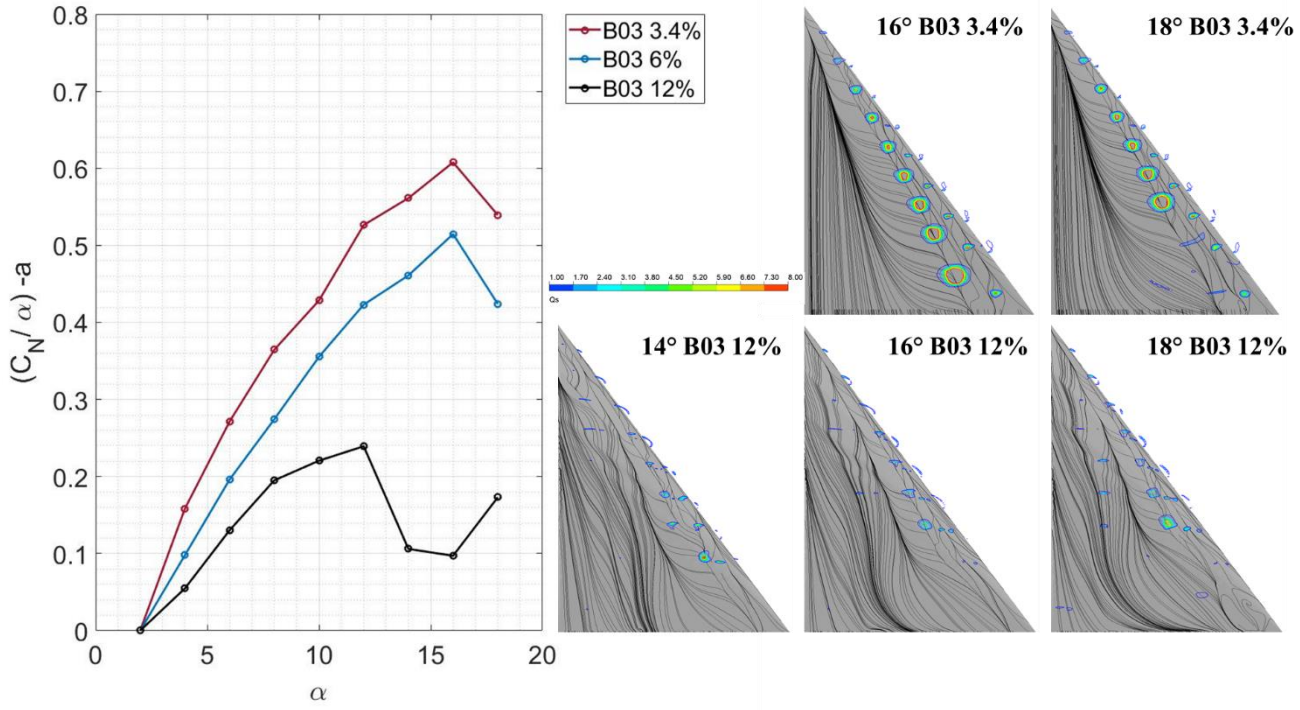

Figure 6.23 Non-linear normal force coefficient component versus angle of attack for the B03 configuration for varying thickness and normalised Q-criterion contour plots and surface streamlines at angles of attack where VBD occurs.

The non-linear normal force component for the other configurations is depicted in Figure 6.24. It can be seen that the non-linear force component decreases with increase in thickness, when excluding the numerical uncertainties. It also appears that moving the maximum thickness location backwards decreases the impact of thickness change on the non-linear lift generation.

For take-off and landing conditions (between 10 and 13deg) the non-linear component is not significantly affected by the wing thickness for the B05 configuration but the opposite is true for the B03 wing, again suggesting an effect of thickness distribution. The VFE-2 and VST vary significantly between thicknesses, however, they are sole research configurations and thus just serve as benchmarks. The drop in their curves is due to the same phenomenon as for the B03 configuration. However, VBD can be an unsteady phenomenon, based on the type of breakdown, thus, treating them numerically as steady could potentially introduce errors. Thus, they will not be considered in the evaluation.

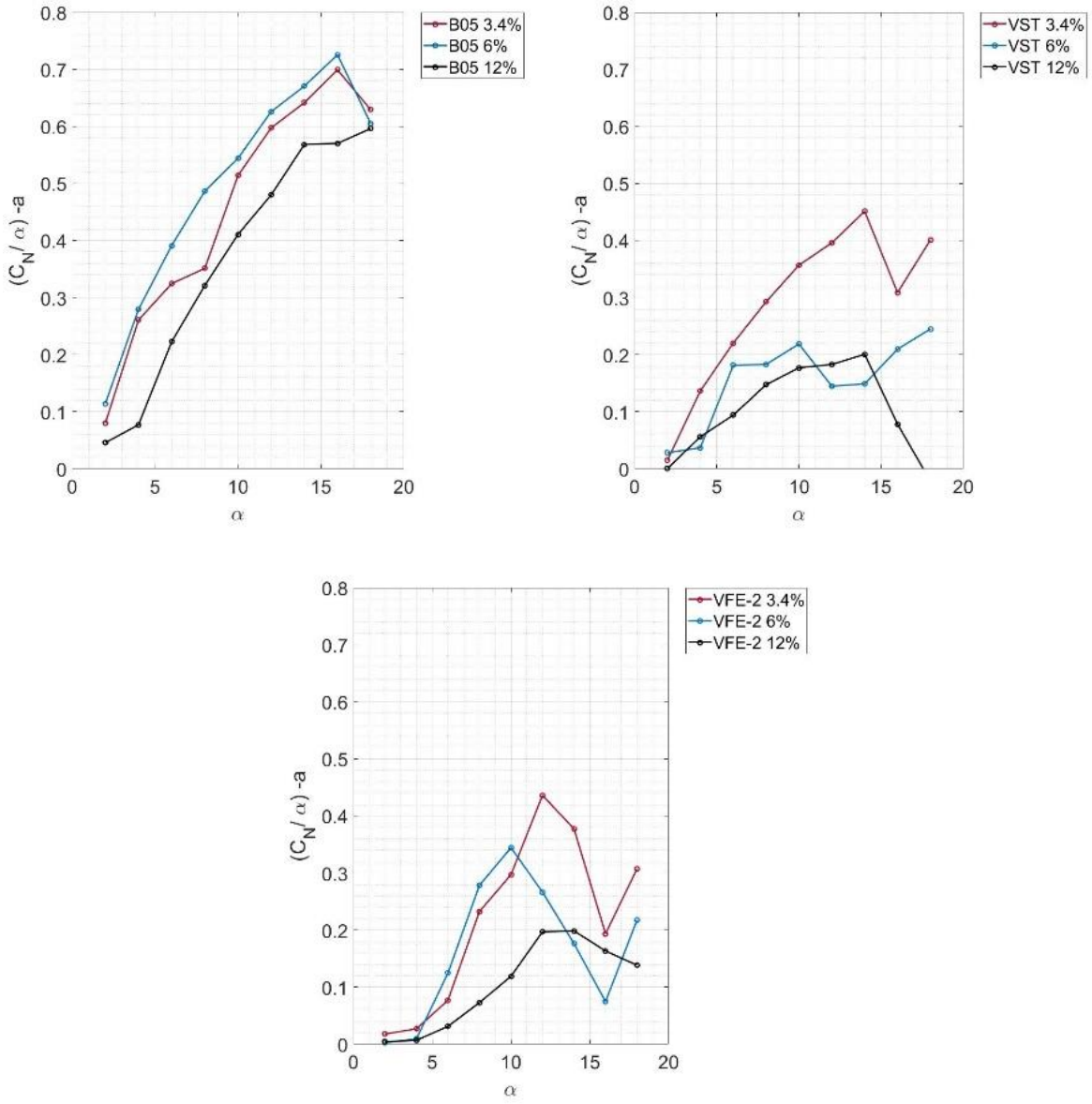

Figure 6.24 Non-linear normal coefficient versus angle of attack for the B05, VST and VFE-2 configurations for varying thicknesses.

Figure 6.25 shows the non-linear component of the normal force against angle of attack for the different profiles, to emphasise the effect of moving the maximum thickness location. It can be seen that moving the maximum thickness has a significant effect on the non-linear lift force particularly when increasing thickness. Moving the maximum thickness location forward results in a decrease in nonlinear lift, with the effect being enhanced when increasing thickness. Flow structure seems to completely change for very thick wings when shifting the maximum thickness as illustrated in Figure 6.28. This is due to the wing behaving more and more like that with a rounded leading-edge. The flow still separates at the sharp leading-edge but reattaches again forming a separation bubble rather than a LEV as also shown in Figure 6.28.

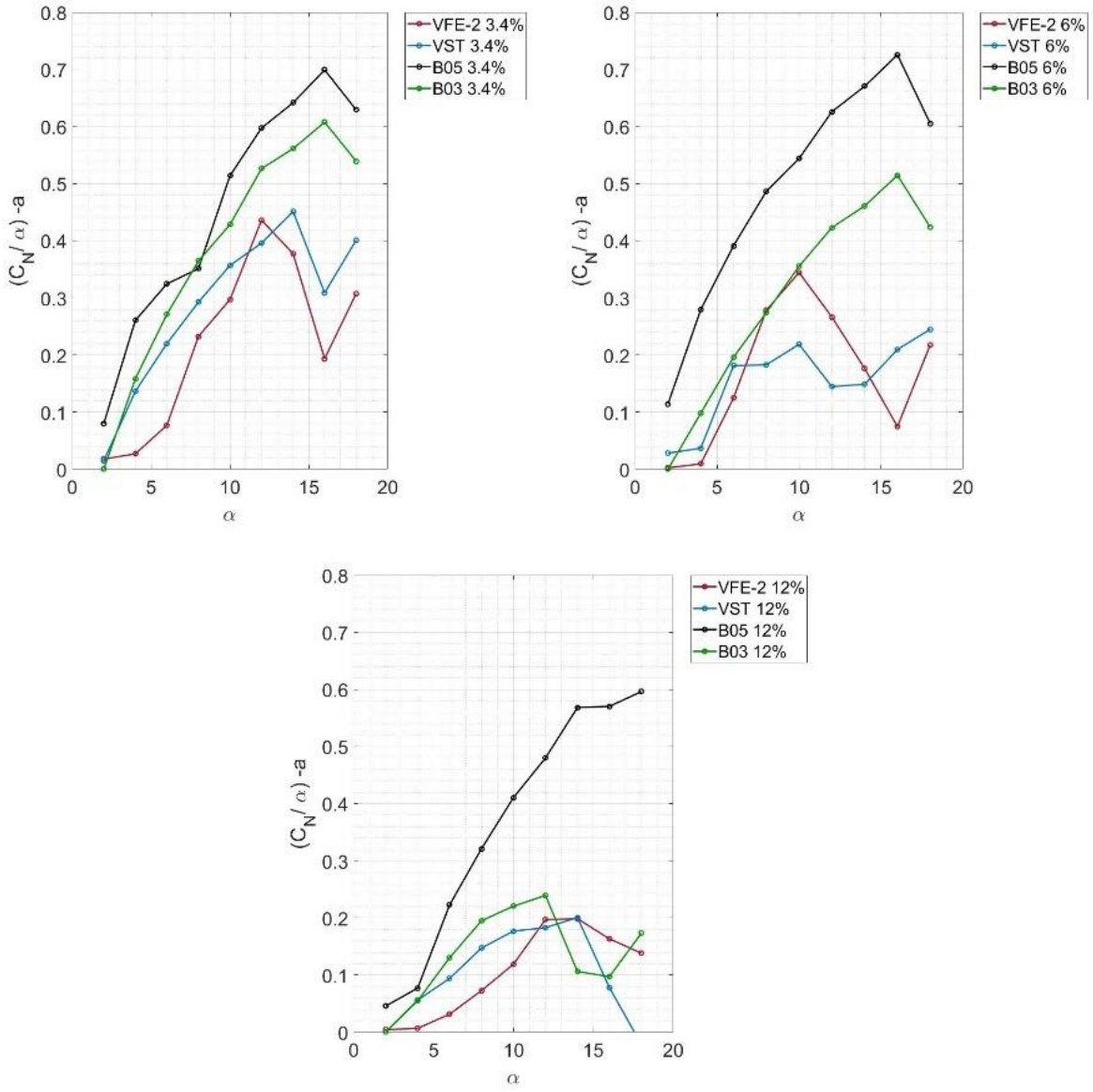

Figure 6.25 Comparison of the non-linear normal coefficient against angle of attack for the B03, B05, VST and VFE-2 configurations for varying thicknesses.

Changing the spanwise thickness distribution (see Chapter 4, Figure 4.1) also has a significant effect on the non-linear lift generation even for low thicknesses. For the 3.4% and 12% maximum thickness wings, having a constant spanwise maximum thickness decreases the non-linear lift for the most part of the angle of attack range. This can also be seen in Figure 6.26 and Figure 6.28, where the normalised Q-criterion is smaller in magnitude for the VFE-2 configurations of 3.4% and 12% thickness compared to the VST. For the 6% thick wings this effect is reversed, and a constant spanwise thickness seems to produce more non-linear lift between 7° and 14° angle of attack. However, the VFE-2 generates higher non-linear lift in the medium angle of attack range across all thicknesses, but not in the lower or higher angle of

attack range. This indicates that having a constant spanwise thickness delays vortex onset and favours VBD, which is not desirable for aircraft design and therefore, wings with spanwise taper should be preferred. The reason for delayed vortex onset is due the relative leading-edge roundness (ratio of leading-edge radius to local span) changing for the VST whereas it does not for the VFE-2. At 12% thickness the VST still forms vortices at the rear part of the wing, whereas this is not the case for the VFE-2. This is further illustrated in Figure 6.26 to Figure 6.28. Here, the normalised Q-criterion and the surface streamlines are plotted for all three thicknesses at 13° angle of attack. Figure 6.26 shows that there are barely any differences in surface streamline pattern between the biconvex configurations- The normalised Q-criterion plots indicate small differences in vortex core strength especially in the mid region of the wing (x/c=0.3 to x/c=0.5). Also, the differences between the VFE-2 and VST configuration are small with regards to the surface streamlines. The normalised Q-criterion shows slightly higher values for the VST configuration at x/c=0.5, 0.6 and 0.8.

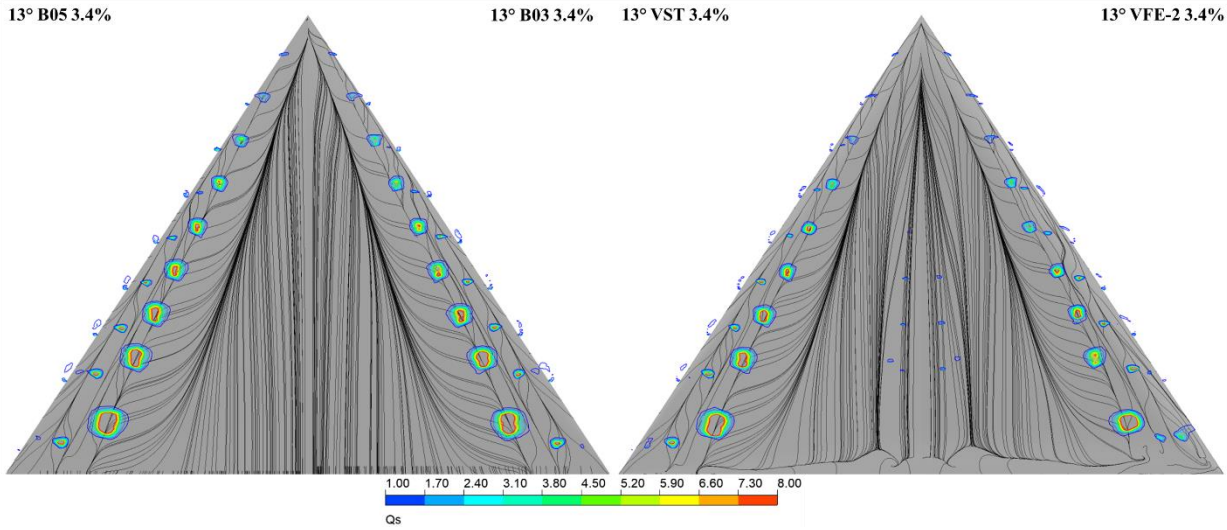

Figure 6.26 Normalised Q-criterion and surface streamlines for the for the B05, B03, VST and VFE-2 configurations of 3.4% thickness at α=13°, with Q_S=1 indicating the vortex boundary.

For the 6% thick wings a difference can be seen between the B03 and B05 configurations particularly close to the apex. The LEV is more stretched for the B03 wing especially in the part of the wing prior to the maximum thickness location, resulting in the reduced nonlinear-lift generation. This effect is enforced with increase in thickness, where only separation bubbles can be identified in the first half of the wing. It can further be seen that the VFE-2 generates a much weaker vortex for the 12% thick wing and vortex onset is delayed. As for the B03 leading-edge separation bubbles are dominating the flow. This is not the case for the VST

especially close to the trailing edge, as explained earlier, due to the effective leading-edge slope (leading-edge angle/ local span) decreasing.

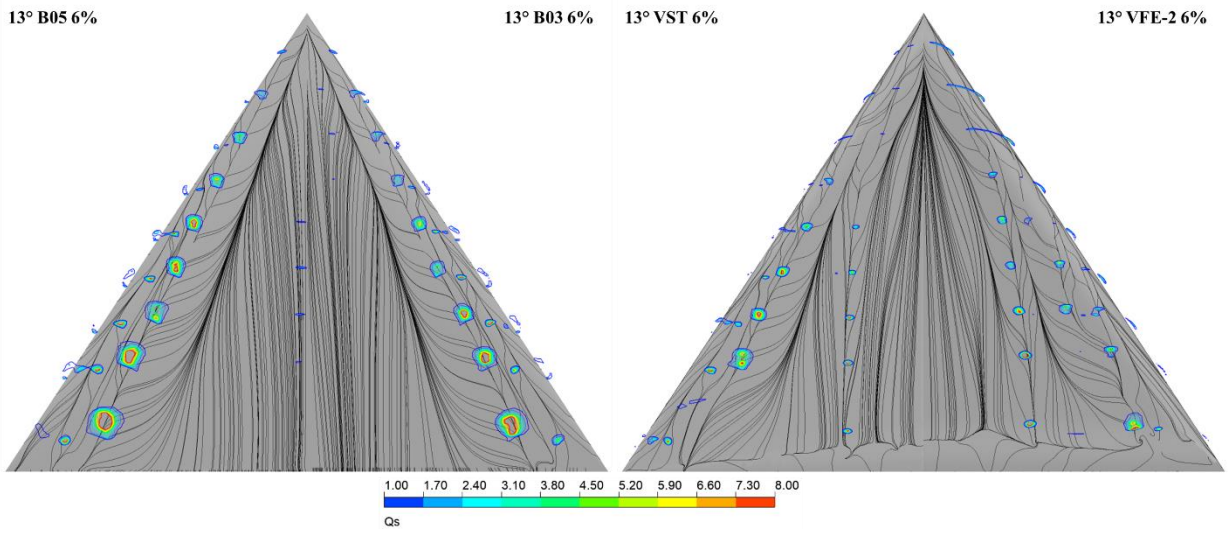

Figure 6.27 Normalised Q-criterion and surface streamlines for the for the B05, B03, VST and VFE-2 configurations of 6% thickness at α=13°, with Q_S=1 indicating the vortex boundary.

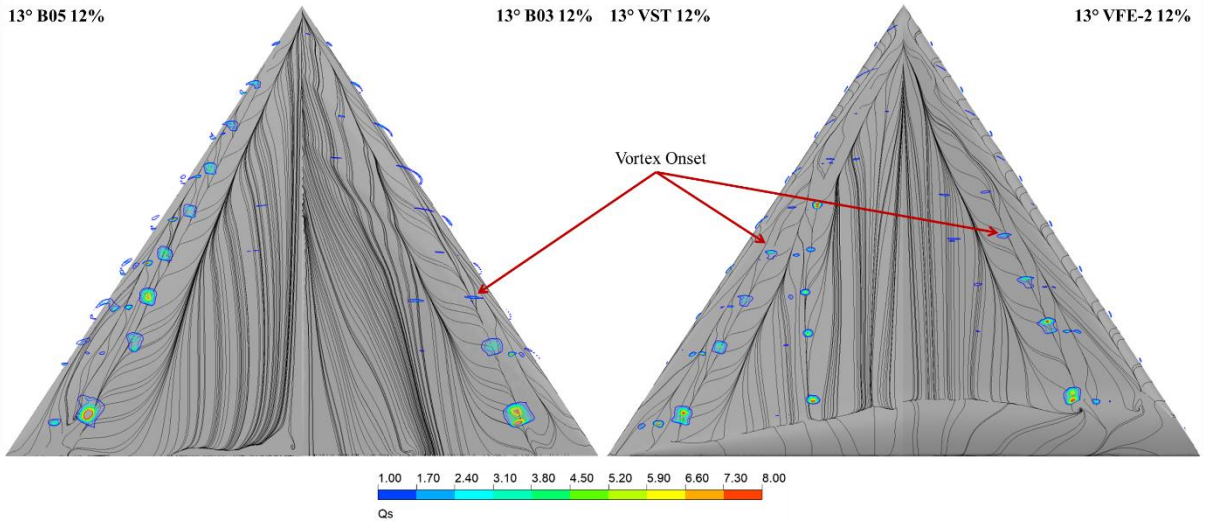

Figure 6.28 Normalised Q-criterion and surface streamlines for the for the B05, B03, VST and VFE-2 configurations of 12% thickness at α=13°, with Q_S=1 indicating the vortex boundary.

6.8 Effect of profile shape on the drag and axial force coefficient

To investigate the effect of profile shape on the drag coefficient, it has been plotted against the angle of attack for the different configurations and is depicted in Figure 6.29. It can be seen that for the biconvex wings the drag decreases with increase in thickness. This is particularly

true for angles of attack higher than 5 degrees and a result of vortex onset delay, due to a reduction in effective angle of attack. The effective angle is defined here as the actual angle minus the upper surface nose angle (Kulfan, 1979).

It can be further seen from Figure 6.29 that the VST's and VFE-2's profile drags are contributing more to the overall drag than at lower incidences. At higher angles however, they generate less drag and are exceeded by the thinner wings, which are having a more dominant vortex structure.

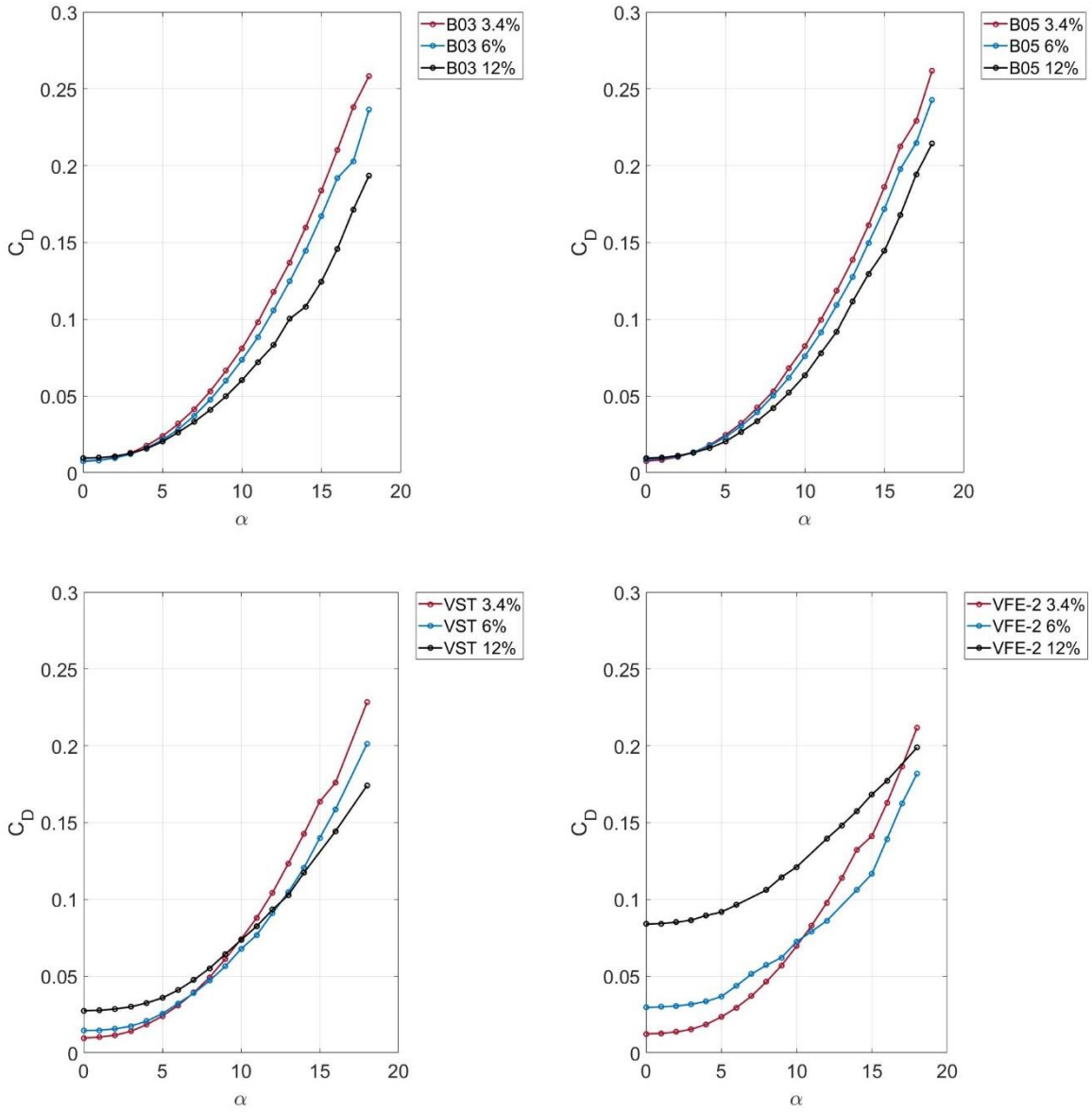

Figure 6.29 Drag coefficient versus angle of attack for the B03, B05, VST and VFE-2 configurations for varying thicknesses.

A comparison of the different configurations with each other is depicted in Figure 6.30. As in the case of the lift, barely any differences in the drag can be spotted between the B03 and B05

configurations at lower thicknesses. At 12% thickness however, the differences become more apparent at higher angles of attack. From 10° onwards the B05 configuration generates significantly more drag. This is because a LEV is forming at this angle whereas the flow on the B03 is still predominantly attached, apart from the separation bubbles forming due to the SLE (see Figure 6.28 surface streamlines and Q-criterion contours at x/c=0.1-0.4). The drag generation between the VFE-2 and VST is similar for 3.4% thickness. However, with increase in thickness the zero lift drag coefficient is increasing significantly for the VFE-2 configuration due to increased profile drag, thus resulting in a higher drag generation. For the 6% thick wings the difference is not as significant as for the 12% thick configurations. The VFE-2 6% generates higher drag at lower angle of attack until about α=10°. After that it generates less drag than the VST. At 12% thickness the VFE-2 generates a significant higher drag from 0° to 13° angle of attack. After that the difference in drag is reduced. This is because the profile drag is pre-dominant at lower angle of attack. For the VFE-2 having a constant spanwise thickness results in increased frontal area, explaining the differences in profile drag compared to the VST. At higher angle of attack the drag due to lift contributes more to the overall drag explaining as to why the VFE-2 approaches the values of the other configuration here. The VFE-2's flow experiences delayed vortex onset, due its constant leading-edge radius across the entire chord. With downstream location the leading-edge upwash increases, resulting in an increase in local angle of attack towards the trailing edge. Meanwhile, the relative leading-edge sharpness increases towards the trailing edge. Both mechanism favour flow separation which can result in a flow field, where the flow on the upstream portion of the wing remains attached whilst the downstream portion encounters leading-edge vortex formation.

Generally, it can be seen that an increase in thickness yields a reduction in drag generation, when the wing is tapered towards the tip. This is due to the reduced drag due to lift for thicker configurations due to delayed vortex onset. For configurations with constant spanwise thickness there is a certain thickness beyond which the profile drag is so high that the benefit of having attached flow and thus, less lift induced drag, is lost.

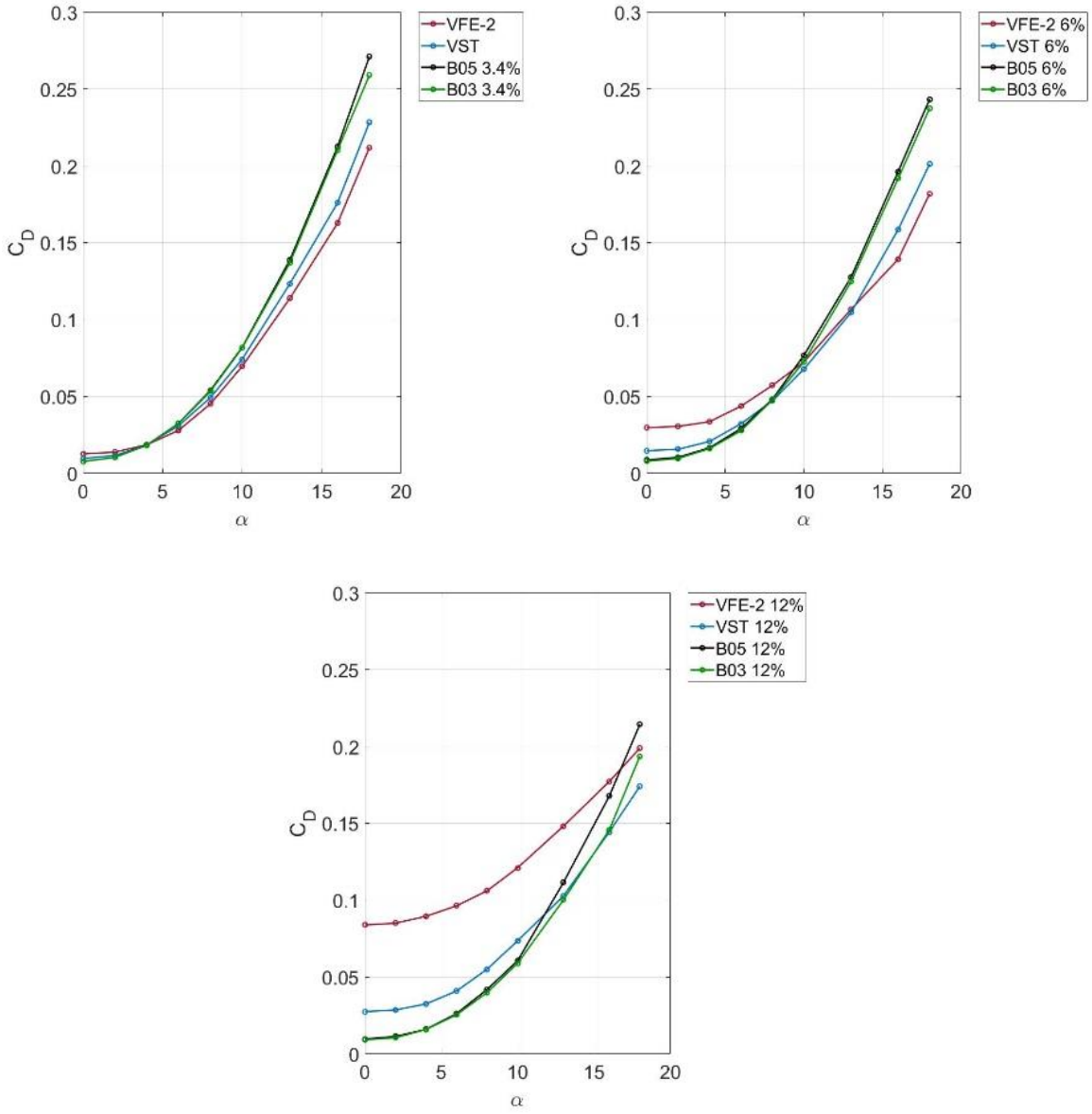

Figure 6.30 Comparison of the drag coefficient against angle of attack for the B03, B05, VST and VFE-2 configurations for varying thicknesses.

To analyse the effect of the flow field on the drag further, the lift-dependent drag factor, K, is calculated, and so for each case, the part of the drag due to the increased frontal area and that due to the LEVs can be distinguished.

Therefore, for each thickness case of 3.4%, 6% and 12%, the drag at zero lift C_{D_0} has been established. For symmetric wings this is at α=0°. The calculated value of C_{D_0} has been plotted against the total frontal area φ, which is non-dimensionalised relative to the wing planform area, S, for the three different thicknesses in Figure 6.31. It can be seen that the biconvex configurations' drag at zero lift is very similar. The VST's, however, is significantly higher

despite the same value of frontal area. This is due to the increased pressure drag of this configuration and the VFE-2 because of their flattened profiles.

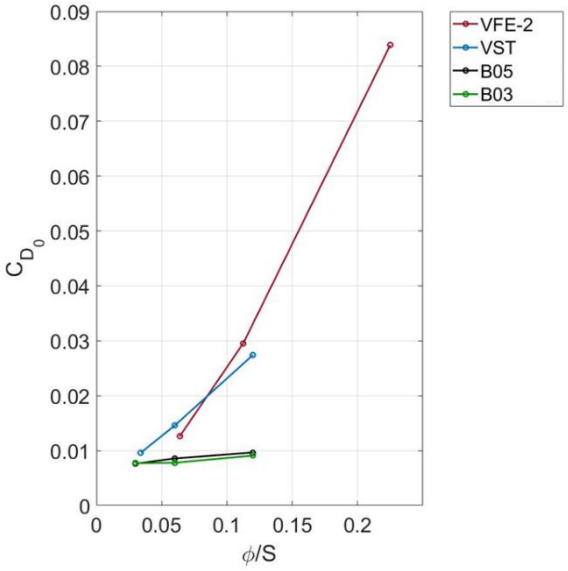

Figure 6.31 Drag at zero lift as a function of frontal area for the B03, B05, VST and VFE-2 configurations. For each curve the values for 3.4%, 6% and 12% are plotted from left to right (respectively).

The lift-dependent drag factor K (Equation (6.3)) was then calculated using (Kirby and Kirkpatrick, 1969)

$$K = \frac{\pi A}{C_L^2}\left(C_D - C_{D_0}\right) \tag{6.4}$$

The lift-dependent drag factor for the B03 configuration is plotted in Figure 6.32 and for the other configurations in Figure 6.33. It can be seen that the lift-dependent drag factor reduces with increase in thickness at lower and medium angle of attack for all configurations apart from the VFE-2. Here, K is the lowest for the 6% wing followed by the 12% and 3.4% wing. This is due to the attached flow over the VFE-2 12% wing in comparison to the other 12% thick wings, which form vortices in the region close to the tip. At higher α the flow forms more separation bubbles and thus reduces the lift-dependent drag factor for the VFE-2 12%, dropping below that of the 6% and 3.4% thick wings. This trend can already be seen in Figure 6.28. For the other configurations the differences at higher angle of attack become much smaller, whilst it is observed that for wings with maximum thickness location located further forward, the thickest wing overtakes the thinner wing in lift-dependent drag generation.

The behaviour of lift dependent drag factor, K, with C_L can show sudden discontinuous changes, for example, the change in K is significant for the B03 configuration. The discontinuity for the 12% thickness case occurs around C_L=0.526, and so additional flow visualisation plots have been added at locations prior, at and behind the discontinuity (Figure 6.14). It can be seen from the normalised Q-criterion that the discontinuity is due to VBD, which already occurs at very low lift coefficients for the 12% thick wing.

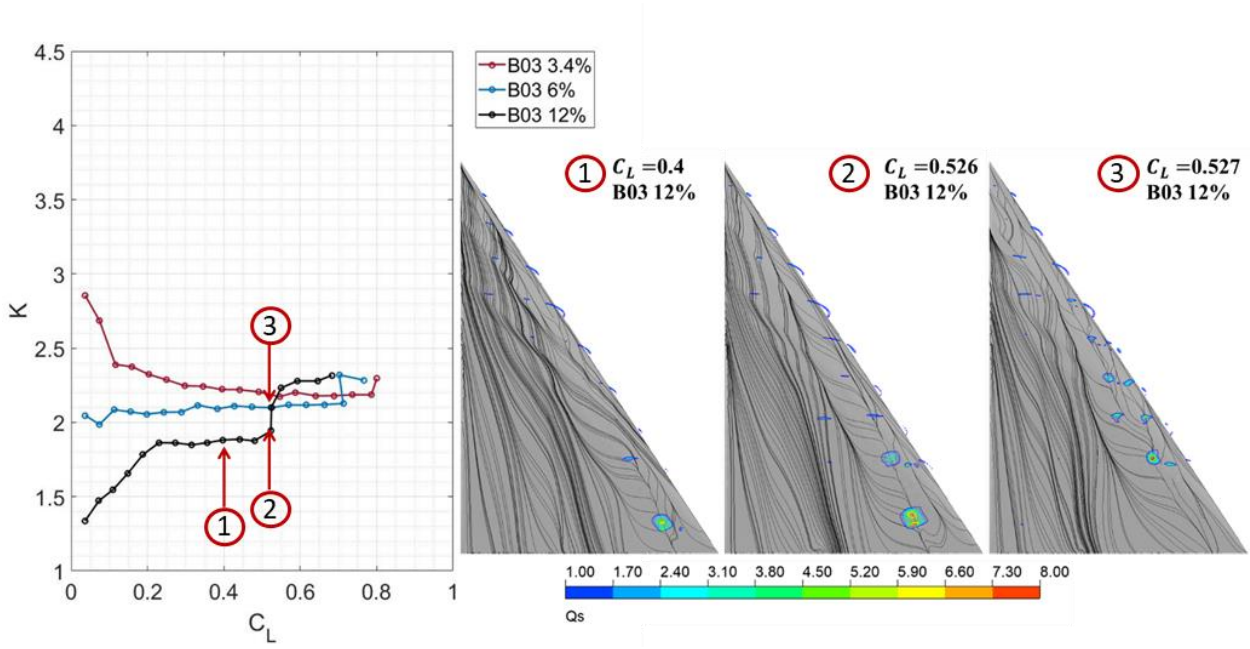

Figure 6.32 Lift dependent drag factor K versus lift coefficient for the B03 configuration for varying thicknesses.

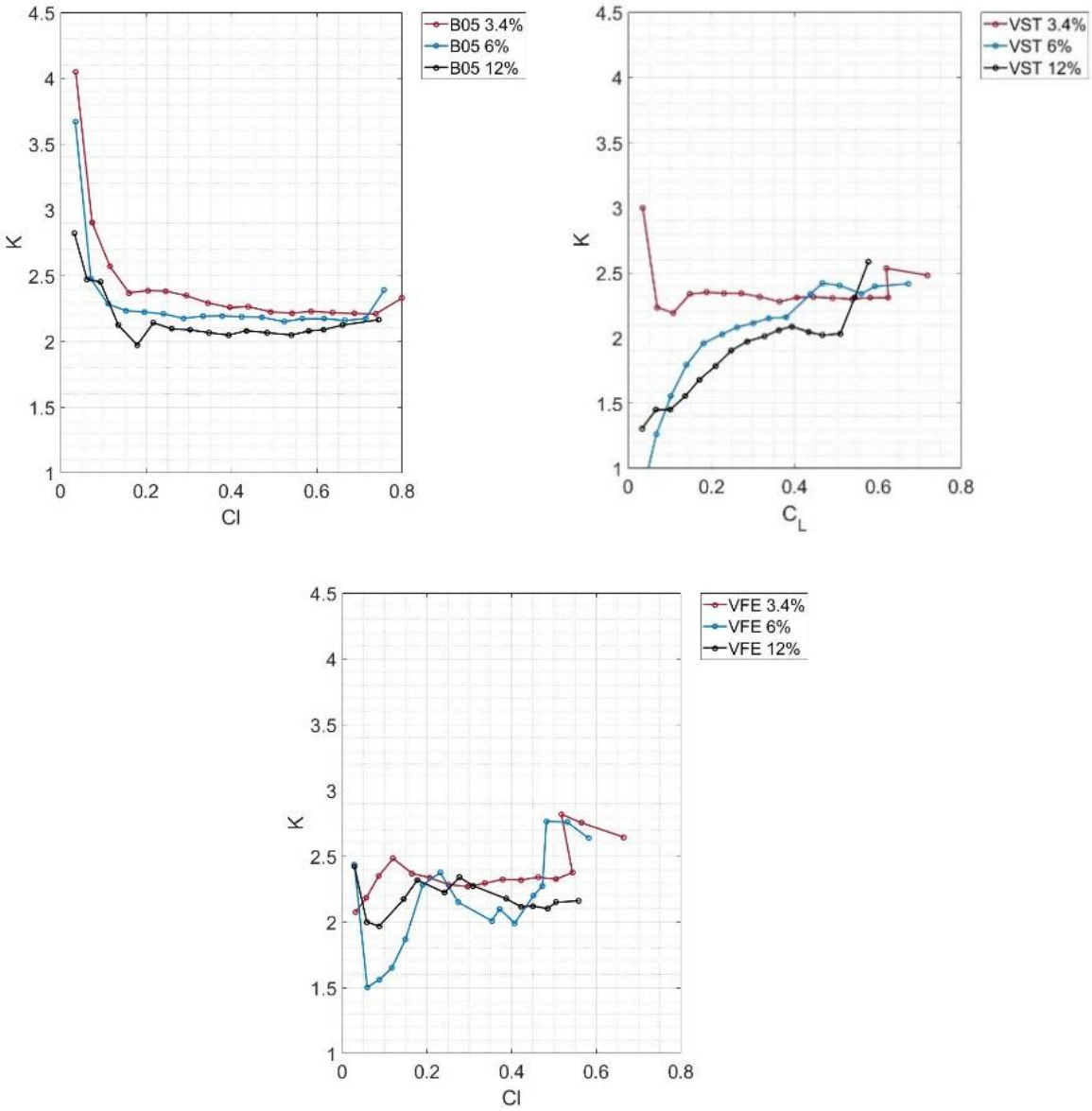

Figure 6.33 Lift dependent drag factor K versus lift coefficient for the B05, VST and VFE-2 configurations for varying thicknesses.

For each wing thickness value, a comparison plot of the different profiles is depicted in Figure 6.34 to emphasise the effect of the thickness location. It can be seen that differences between profiles are small when the maximum thickness is low (3.4%). The only noticeable difference is at high lift coefficients where the VFE-2 and VST experience VBD which yields a sudden increase in lift-induced drag.

With increase in thickness the effect of maximum thickness location and spanwise thickness distribution becomes more noticeable. A forward movement (towards the leading-edge) in maximum thickness location (so B05 to B03) results in a decreased lift-dependent drag factor at low C_L. These effects diminish at higher incidences. Having a constant spanwise thickness

(VFE-2) results in an early onset of VBD and thus increased K value for the two thinnest wings. Considering the lift-dependent drag factor alone, would make a constant spanwise thickness distribution undesirable. The 12% thick wings show that a forward movement in maximum thickness location results in a significant decrease in lift-dependent drag at lower incidences, but a drastic increase at higher angles. Moving the maximum thickness rearward or altering the spanwise thickness distribution results in a more constant behaviour of the K value across a wide range of lift coefficient.

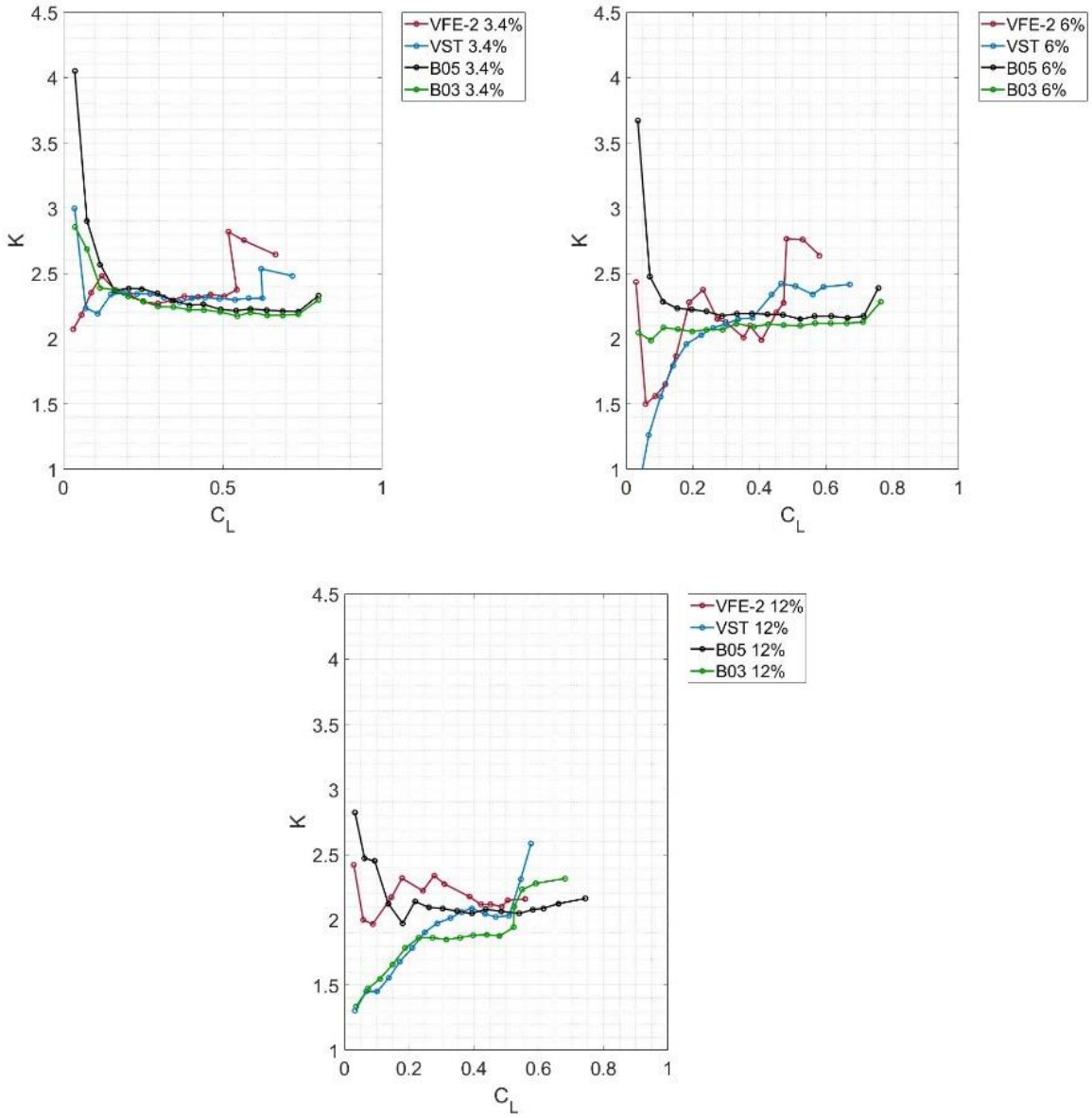

Figure 6.34 Comparison of the lift-dependent drag factor K against lift coefficient for the B03, B05, VST and VFE-2 configurations for varying thicknesses.

To better understand the reason for the reduction in lift-dependent drag with increasing thickness at low to moderate angle of attack and varying thickness, the lift and drag force

coefficients are replaced with axial and normal force coefficients using (Kirby and Kirkpatrick, 1969)

$$C_L = C_N \cos(\alpha) - C_A \sin(\alpha) \tag{6.5}$$

$$C_D = C_N \sin(\alpha) + C_A \cos(\alpha) \tag{6.6}$$

Equations (6.5) and (6.6) are substituted into the expression for K (Equation 6.3), and $C_{D_0} = C_{A_0}$, as the wings are symmetric. This yields to the approximation of (Kirby and Kirkpatrick, 1969)

$$K = \frac{\pi AR}{C_L}\left(\tan(\alpha) + \frac{C_{A_0} - C_A}{C_N}\right) \tag{6.7}$$

From the equation above it can be seen that a reduction in forward suction force C_A results in a reduction in K.

Figure 6.35 plots the forward suction force against the normal force. Tramlines for K=1 (flow fully attached) and K=0 (flow fully separated) are included to identify vortex onset and breakdown. It can be seen that with increase in thickness the wing behaves like one of fully attached flow at lower angle of attack irrespective of maximum thickness location. This means that the thrust component is increased with increase in thickness. VBD, represented by a sudden change in slope, is delayed with decrease in thickness.

For thicker wings the frontal surface area is increased which results in a decrease in axial force coefficient (see Figure 6.35) or increase in thrust component and thus decreases lift-dependent drag. The size of the thrust component is determined by planform shape and thickness distribution. The increase in frontal area is important as it increases the area for the LEV to act upon. However, this also depends on the presence of a LEV rather than a separation bubble.

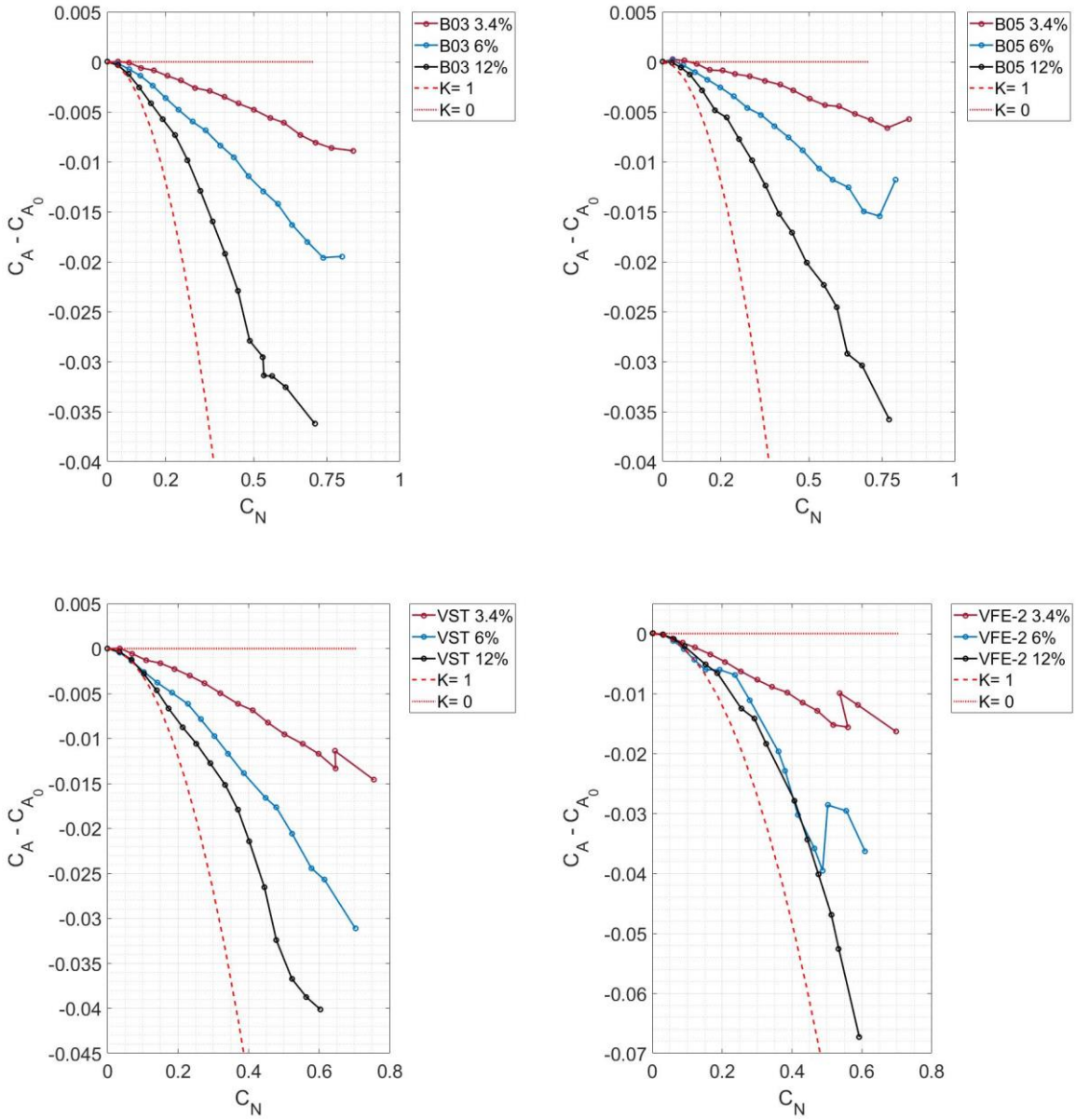

Figure 6.35 Axial force coefficient versus normal force coefficient for the B03, B05, VST and VFE-2 configurations for varying thicknesses.

The effect of the thickness distribution on the axial force component can be emphasised when plotting the axial force against the normal force for different configurations as shown in Figure 6.36. Though the changes in frontal area are small between configurations (up to $1mm^2$) the differences are still reflected in the axial force polar. Changing the overall thickness does not have a huge impact on the effect of thickness location. However, it can be seen that forward suction increases when moving the thickness towards the leading-edge, as due to the roundness effect the flow is attached for longer. An increase in thickness, however, does seem to reduce the difference in forward thrust generation at low incidences between configurations, due to the LEV not being present over the entire wing for most wings. Constant spanwise thickness

distribution (VFE-2) is of advantage when wanting to increase the forward suction coefficient as the region of attached flow is greater especially near the tip region.

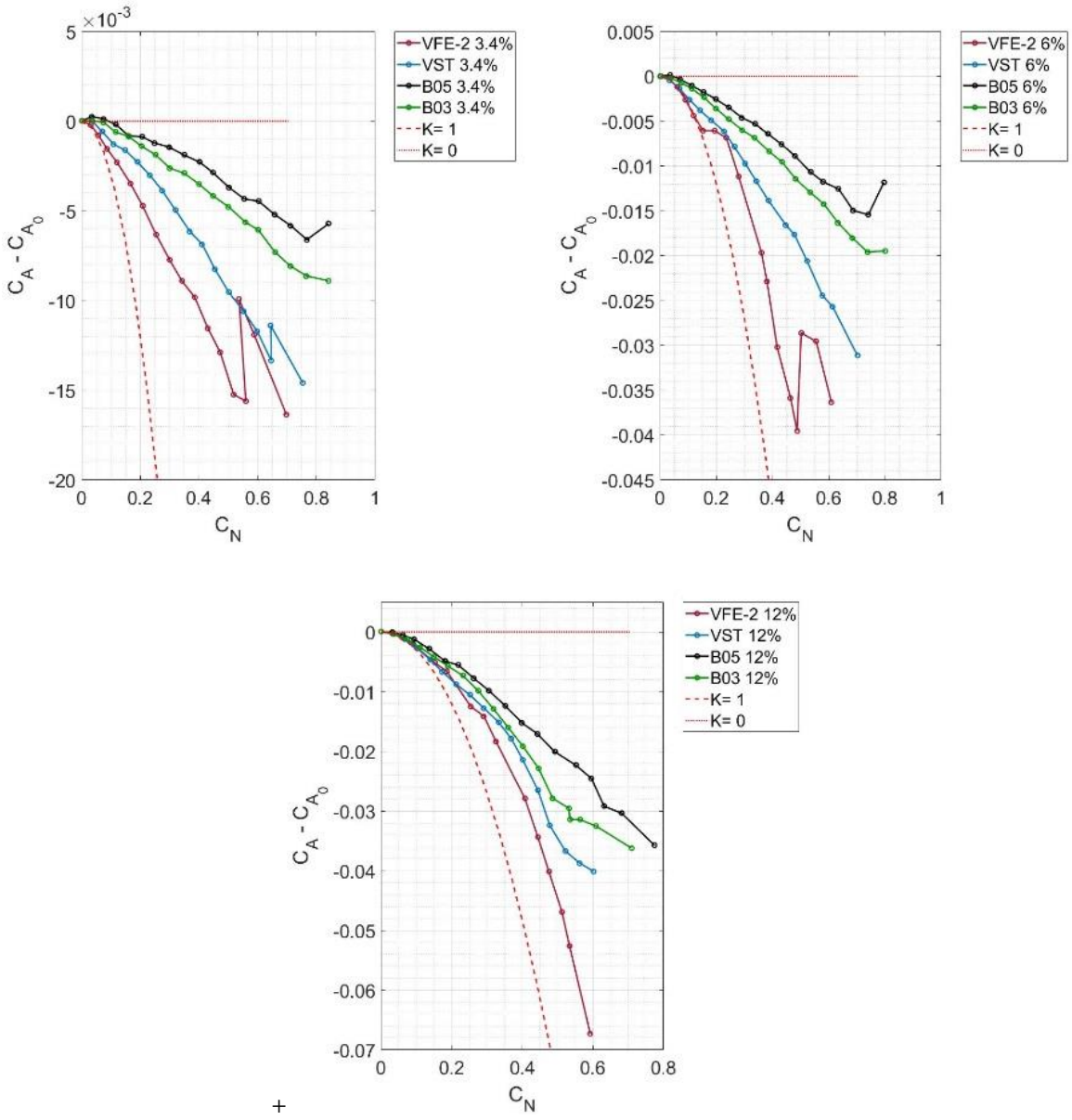

Figure 6.36 Comparison of the axial force coefficient against normal force coefficient for the B03, B05, VST and VFE-2 configurations for varying thicknesses.

The lift-dependent drag (in equation 6.5) is a function of the difference between two terms: $\tan(\alpha)$ and $\frac{C_{A_0}-C_A}{C_N}$. The former represents the lift curve slope at small angles of attack, which decreases with increase in thickness (see Figure 6.3). It can further be seen that $C_A - C_{A_0}$ is much lower for thicker wings at low to moderate C_N and thus, angle of attack, in comparison to the steepness of the lift curve slope. Hence, at low angles the K value is lower for thicker wings. This is in accordance with the findings by Kirby and Kirkpatrick (1969). Once the LEV

is fully established the change in lift with angle of attack increases for the thinner wings whereas the difference in thrust component does not change as rapidly, thus, resulting in the K values being lower.

6.9 Effect of profile shape on the pitching moment and longitudinal stability

When designing an aircraft one major aspect is developing a certain degree of stability around all three axes. Longitudinal stability is defined as the quality that makes an aircraft stable around its lateral axis. Aircraft which are longitudinally unstable have the tendency to climb progressively, even into stall, making the aircraft difficult and sometimes dangerous to fly. Whether an aircraft is longitudinally stable depends on the location of the wing with respect to the centre of gravity, the position of the horizontal stabilisers with respect to the centre of gravity as well as their overall area (Cook, 2013).

Therefore, the pitching moment should be taken with respect to the centre of gravity location in order to evaluate the stability of a configuration. For the delta wings in this configuration this location varies as shown in Table 6.8. and is on average at around 0.6 c_r. However, for this study the pitching moment coefficient was taken slightly further upstream at 0.58 root chord and plotted against the normal force coefficient in Figure 6.37. The reference point was chosen, for ease of interpretation as most points are lying on the abscissa, and deviation from it indicates change in stability. In the following an unfavourable behaviour regarding longitudinal stability is indicated by a positive gradient in the curve, a favourable behaviour by a negative gradient and a maintenance in stability by no change in slope.

It can be seen that increasing the thickness results in an increase in longitudinal stability irrespective of thickness distribution. For the B03 configuration the stability is enhanced from C_N= 0.2 to C_N=0.5 (or between 8 to 13 degrees) when doubling the thickness from 6% to 12%. For the B05 the stability is enhanced starting from C_N=0.05, equivalent to about 3 degrees, so thickness distribution affects longitudinal stability. At coefficients common for take-off and landing the two thicker wings of the biconvex configurations show stable behaviour whilst the thinner wings do not. The sudden changes in gradient are indicators for changes in flow physics. This can be, for example, the formation of a LEV or the occurrence of additional separation bubbles as well as VBD onset. The rapid change in gradient at higher C_N seen in Figure 6.37 is due to VBD whereas the changes at lower normal force coefficients are due to

separation bubbles for the 12% thick configurations and due to vortex onset for the thinner wings.

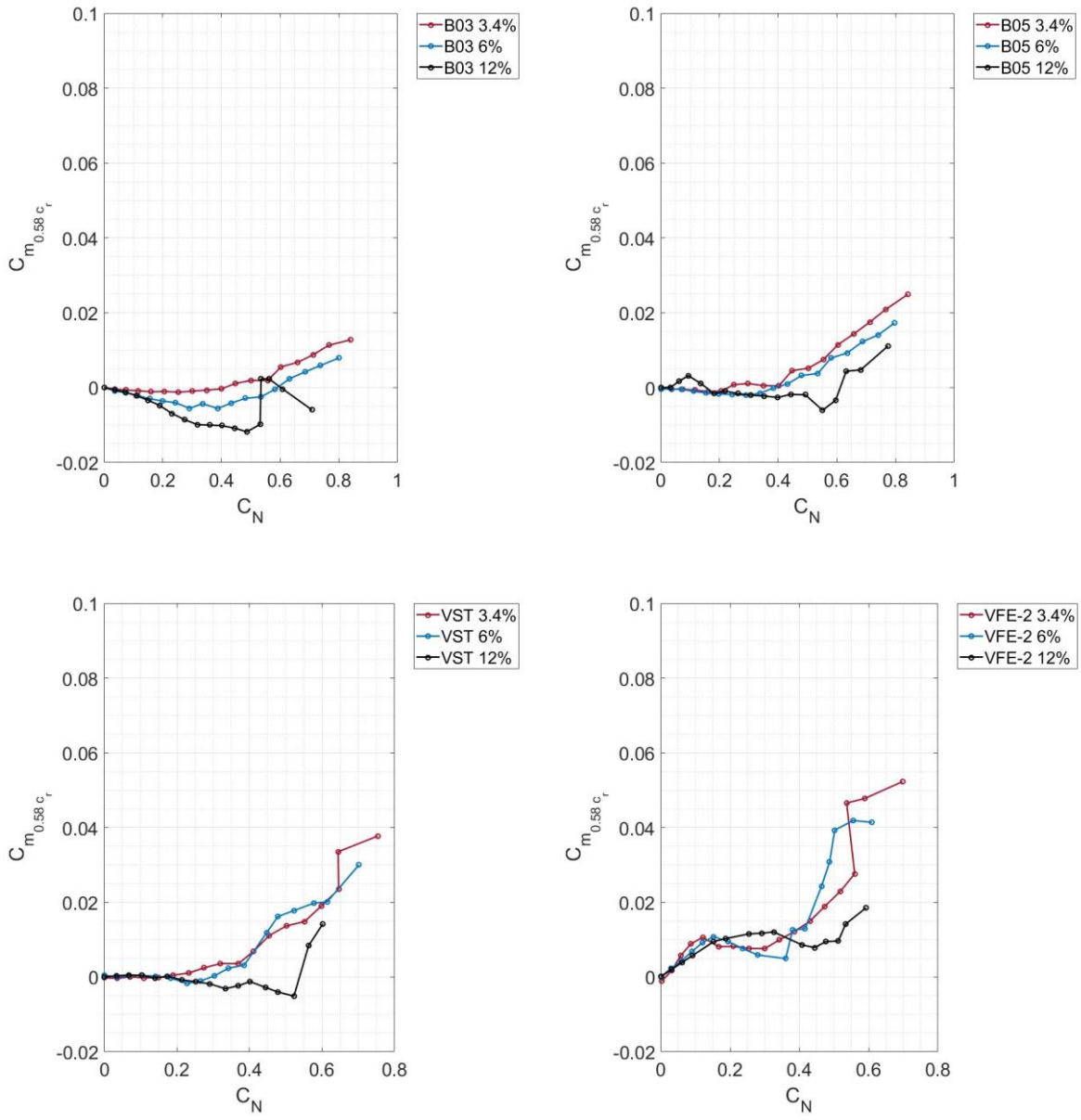

Figure 6.37 Pitching moment coefficient taken at $0.58c_r$ versus normal force coefficient for the B05, VST and VFE-2 configurations for varying thicknesses.

To better understand the pitching moment behaviour the wing loading is displayed in Figure 6.38 to Figure 6.41 for all configurations at 13° and for different thicknesses at x/c 0.2, 0.4, 0.6, 0.8 and 0.95. For the biconvex configurations shown in Figure 6.38 and Figure 6.39 can be seen that the stability increases with thickness, due to the reduced suction force generated by the LEV in the first 20% of the wing. The negative relative pressure generated between x/c=0.4 and x/c=0.8, is little affected by increase in thickness, but the last 20% of the wing

experience an increase in suction force with increase in thickness. Therefore, the reduction in the first and last 20% of the wing affects the stability of the biconvex configurations. It can further be seen that the pressure peaks move outboard with increase in thickness, which may have structural implications, such as thicker root chord due to a higher bending moment.

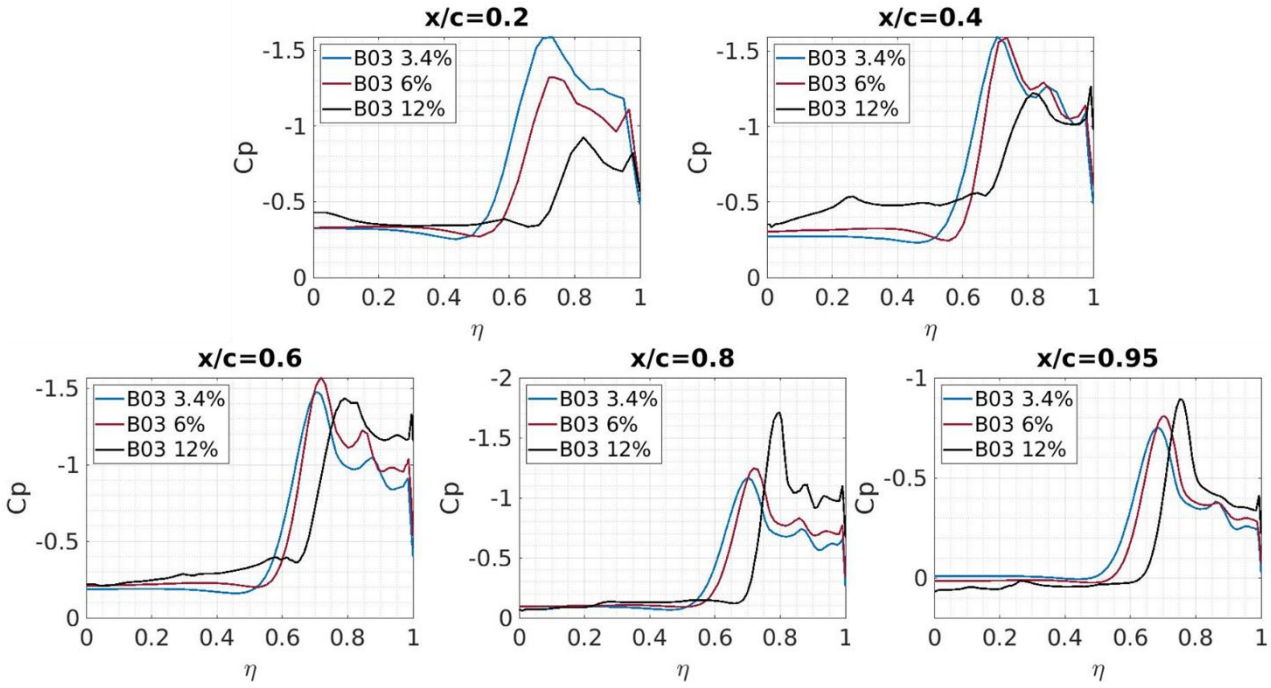

Figure 6.38 Spanwise pressure distribution of the B03 configuration at different chord positions for 3.4, 6 and 12% thickness at α= 13°.

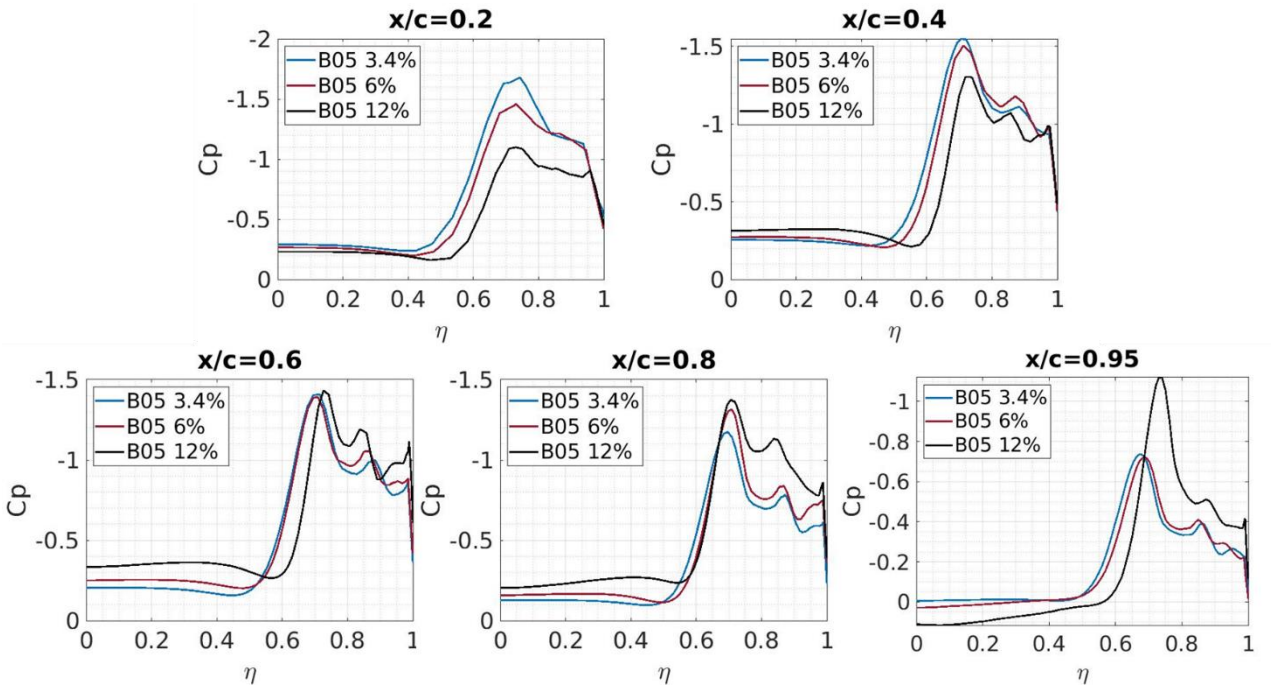

Figure 6.39 Spanwise pressure distribution of the B05 configuration at different chord positions for 3.4, 6 and 12% thickness at α= 13°.

The behaviour of the VST and VFE-2 is different to that of the biconvex wings as can be seen from Figure 6.40 and Figure 6.41. Here, an increase in thickness causes a very complex flow structure for the 6% and 12% thick wings, with multiple separations and reattachments occurring especially for the VFE-2. The VST's spanwise taper appears to ensure a better LEV development even when thickness is increased. The stabilising effect for VFE-2 is again due to decrease in upwards force in the first 20% and an increase in the last 5% of the wing, whereas the stability increase with thickness for the VST is due to an increased suction between 60% and 80% of the wing. The VST and VFE-2 pressure peak is not as clear as for the biconvex wings, though also a move of the vortices outward with increase in thickness can be observed.

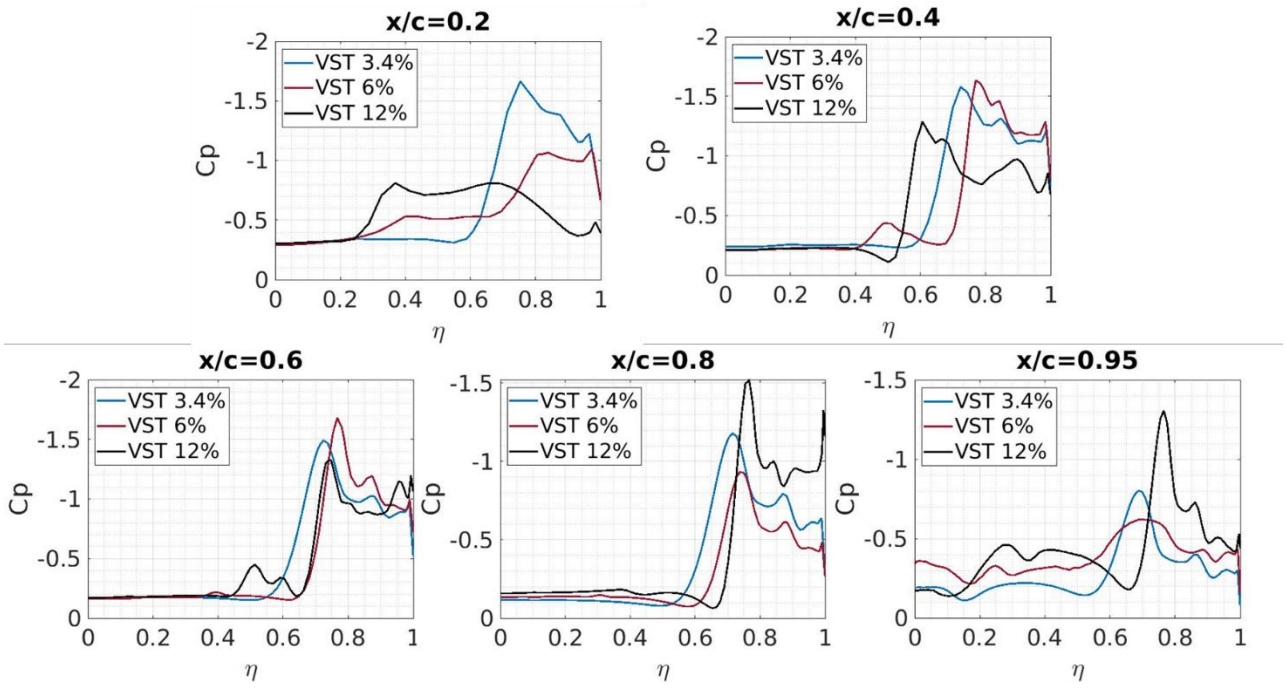

Figure 6.40 Spanwise pressure distribution of the VST configuration at different chord positions for 3.4, 6 and 12% thickness at α= 13°.

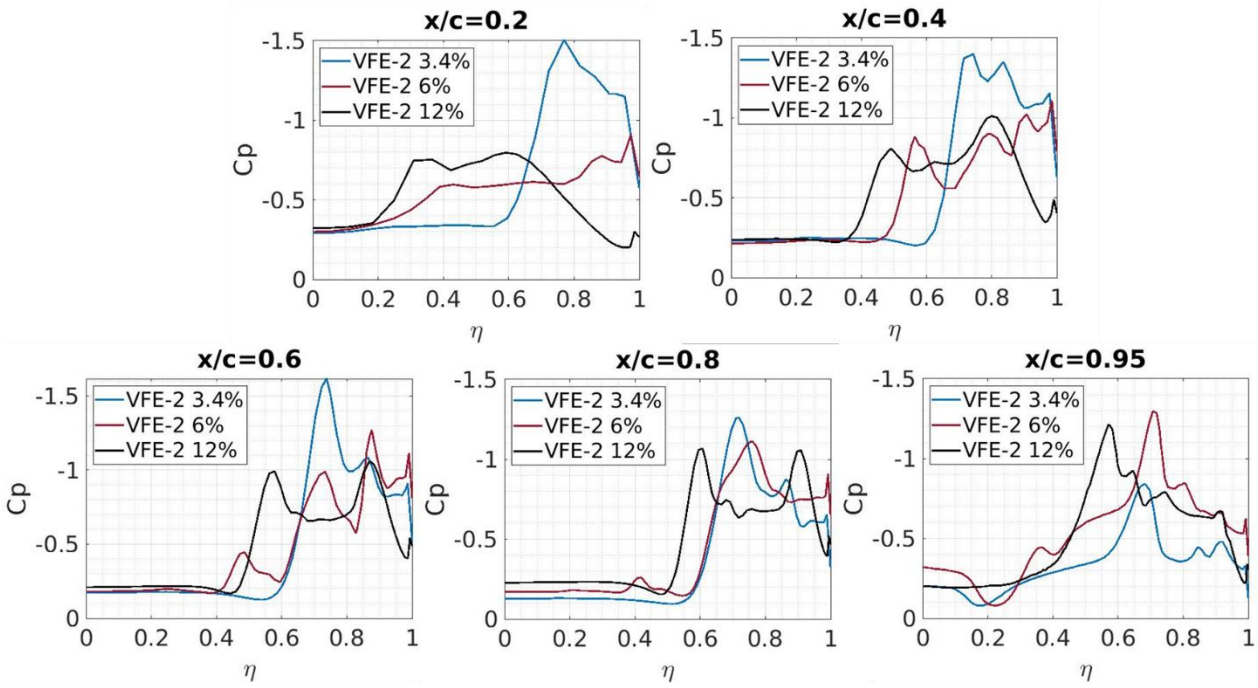

Figure 6.41 Spanwise pressure distribution of the VFE-2 configuration at different chord positions for 3.4, 6 and 12% thickness at α= 13°.

The pitching moment is plotted against the normal force coefficient for different profiles in Figure 6.42. It can be seen that a shift in maximum thickness location towards the front (cases comparing B05 at 50% chord to B03 at 30% chord) has a stabilising effect. As can be seen from Figure 6.38 and Figure 6.39 this is due a decreased suction force close to the apex, due to delayed vortex onset and a stronger suction force near the trailing edge. This effect is enhanced when increasing the thickness. However, once a certain thickness is reached VBD is shifting to lower incidences and reduces the natural stability of these configurations. Changing the spanwise thickness distribution as it has been done for the VST (constant slope from root to tip) has a stabilising effect irrespective of thickness, whilst a constant thickness along the span (VFE-2) leads to highly unstable wing. Based on the application purposes of the design and the onboard systems, this effect may or may not be desired.

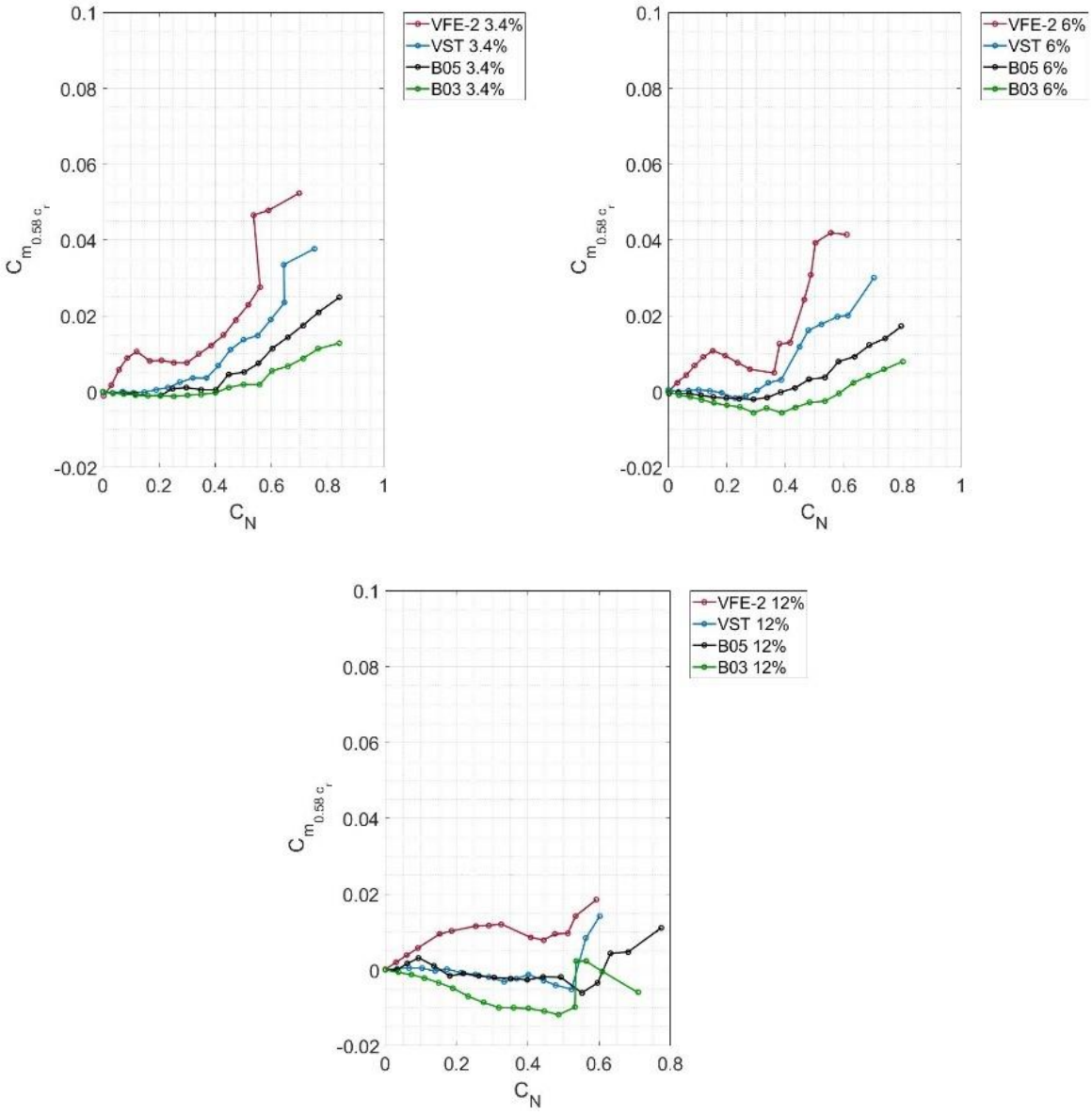

Figure 6.42 Comparison of the pitching moment coefficient taken $0.58c_r$ normal force coefficient for the B03, B05, VST and VFE-2 configurations for varying thicknesses.

To assess how thickness affects longitudinal stability the position of the aerodynamic centre needs to be determined. Its location is of high importance as it determines the position of the aircraft's centre of gravity and its maximum deviation with various fuel and payloads. The aerodynamic centre was determined using (Houghton et al., 2013)

$$\frac{x_{ac}}{c_{mac}} = \frac{x_{ref}}{c_{mac}} - \frac{\partial C_{m_{ref}}}{\partial C_N} \tag{6.8}$$

Where x_{ac} is the position of the aerodynamic centre, x_{ref} is the reference distance of the pitching moment coefficient $C_{m_{ref}}$ and c_{mac} is the mean aerodynamic chord.

Here, $\frac{\partial C_{m_{ref}}}{\partial C_N}$ was calculated by determining the slope at each point in relation to neighbouring data points rather than using curve fitting.

Furthermore, the centre of pressure was calculated using (Houghton et al., 2013)

$$\frac{x_{cp}}{c_{mac}} = \frac{x_{ref}}{c_{mac}} - \frac{C_{m_{ref}}}{C_N} \tag{6.9}$$

The position of aerodynamic centre x_{ac} and the centre of pressure x_{cp} are expressed relative to the root chord length and plotted against the normal force coefficient in Figure 6.43 and Figure 6.44.

As for the data in Chapter five the normal force coefficient and pitching moment have been linearly curve fitted to account for the scatter in the data. The uncorrected data plots can be found in Appendix A.5.4.

Due to the linear approximation of the normal force and pitching moment the aerodynamic centre is fixed, which is different to the raw numerical data plots, but sufficient for evaluation purposes.

It can be seen that the aerodynamic centre not only varies with thickness but also with maximum thickness location. It can be seen to move rearwards with increase in thickness. However, the position does not vary much more than 0.5% between the thinnest and thickest wing. Generally, a rearward movement of the aerodynamic centre is desired as it is increasing the aircraft's static margin, thus, making the effect of increased thickness very useful and therefore worth considering when utilising wing morphing. The static margin is then defined as the distance between the vehicle's centre of gravity and the neutral point, the location where the vehicle is neutrally stable in pitch (Cook, 2013). For a simple delta wing configuration without control surfaces the neutral point is equal to the aerodynamic centre. The position of the aerodynamic centre is also an indicator of trailing edge effects (as was shown in sections 6.3 to 6.5). When decreasing the thickness, the aerodynamic centre moves upstream/ the static margin reduces (see Figure 6.43), which corresponds to an increase in trailing edge effects as could already be seen in Figure 6.39 to Figure 6.41. The discontinuities observed in the curves

in Figure 6.43 are due to VBD which creates a rapid change of pitching moment and normal force. However, the position of the aerodynamic centre is difficult to predict once VBD is occurring and is only shown here to indicate that stability changes with VBD onset. It does not imply that the configurations become more stable when VBD is occurring.

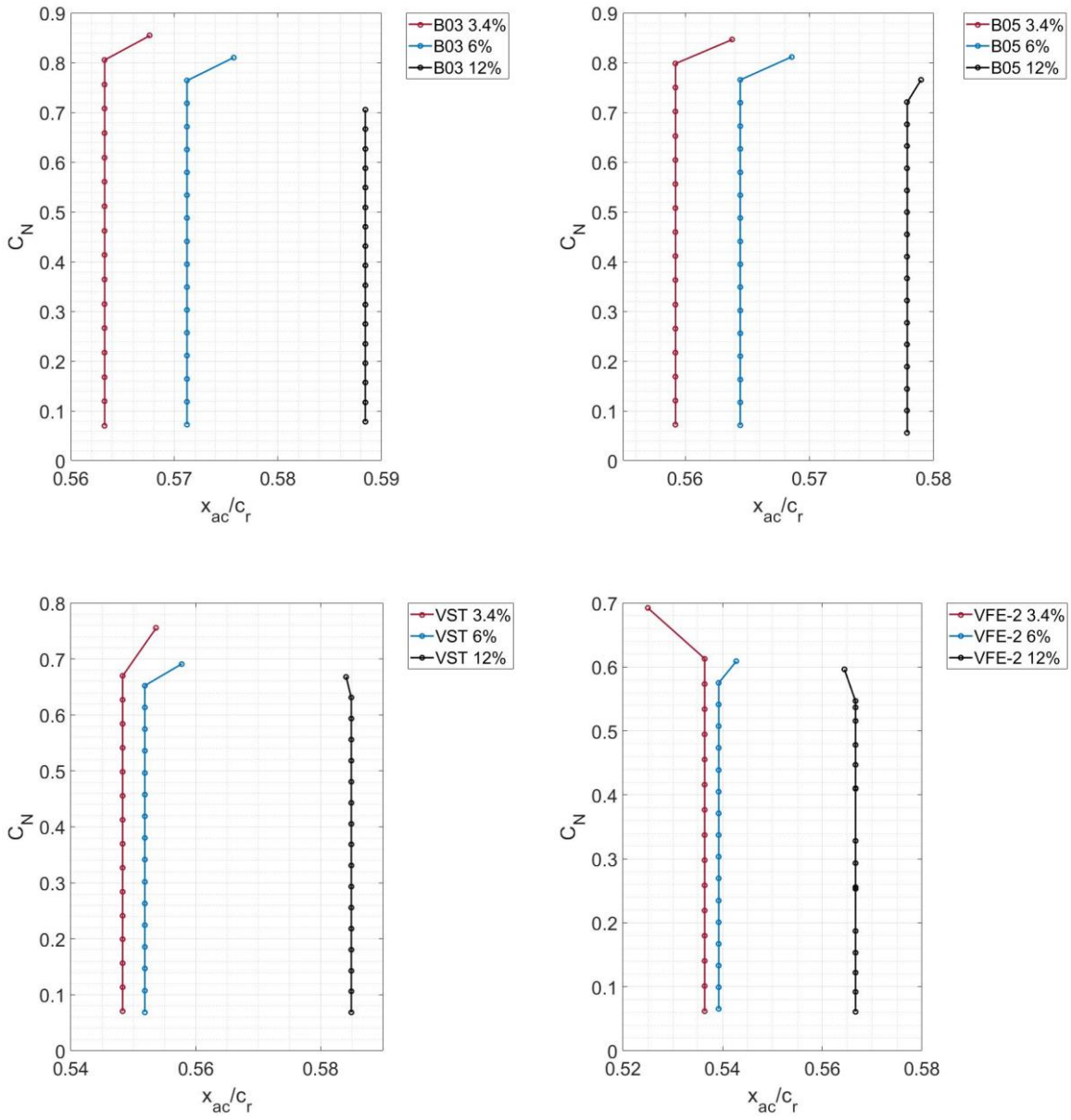

Figure 6.43 Normal force coefficient versus curve fitted, normalised aerodynamic centre position for the B03, B05, VST and VFE-2 configurations for varying thicknesses.

As discussed earlier this study is particularly interested in the stability at the approximate lift coefficient during take-off and landing. To evaluate how the stability is affected with thickness the aerodynamic centre at C_L=0.5 of the thinnest wing of each configuration is taken as the

baseline. Then the change is calculated as a percentage for the 6% and 12% thick configurations, with a positive value indicating a rearward movement in aerodynamic centre and thus increased stability. The effect of thickness on stability is shown in Table 6.5. It can be seen that the stability improves with increase in thickness, whereby the biconvex configuration's stability increases approximately linearly whilst that of the flat plate profiles does not.

Table 6.5 Change in aerodynamic centre at C_L=0.5 with increase in thickness based on the thinnest configuration.

Configuration	Thickness [%]	3.4	6	12
B03	Change in x_{ac}/c_r [%]	0	1.41	4.46
B05		0	0.93	3.34
VST		0	0.64	6.68
VFE-2		0	0.52	5.65

The centre of pressure is plotted relative to the aerodynamic centre in Figure 6.44. It can be seen that the centre of pressure is found behind the aerodynamic centre for the two thinnest wings of the B03 and B05 configurations. The centre of pressure is moving forward with increase in normal force coefficient, which results in the destabilising effect seen in Figure 6.37 around C_N= 0.6 for the 3.4% thick wing and C_N=0.7 for the 6% thick wing. The same is true for the 12% thick configuration. The centre of pressure moves also towards the aerodynamic centre with increase in normal force. However, the distance between centre of pressure and aerodynamic centre is relatively small initially (between 0.2%). The results for the 12% thick wings of both configurations are found to be quite noisy, as it was found that for thicker wings the flow tends to become more unsteady.

For the VST configuration the centre of pressure is located behind the aerodynamic centre for the two thinner wings, again with the differences reducing with increase in thickness. The same is true for the VFE-2 3.4% and 6% configuration. The 12% thick wings of both configurations have the centre of pressure lying very close to that of the aerodynamic centre as already observed for the biconvex wings. However, here the centre of pressure is moving rearwards with increase in normal force coefficient, which is counter intuitive. The reason lies within the very complex flow field arising for these wings.

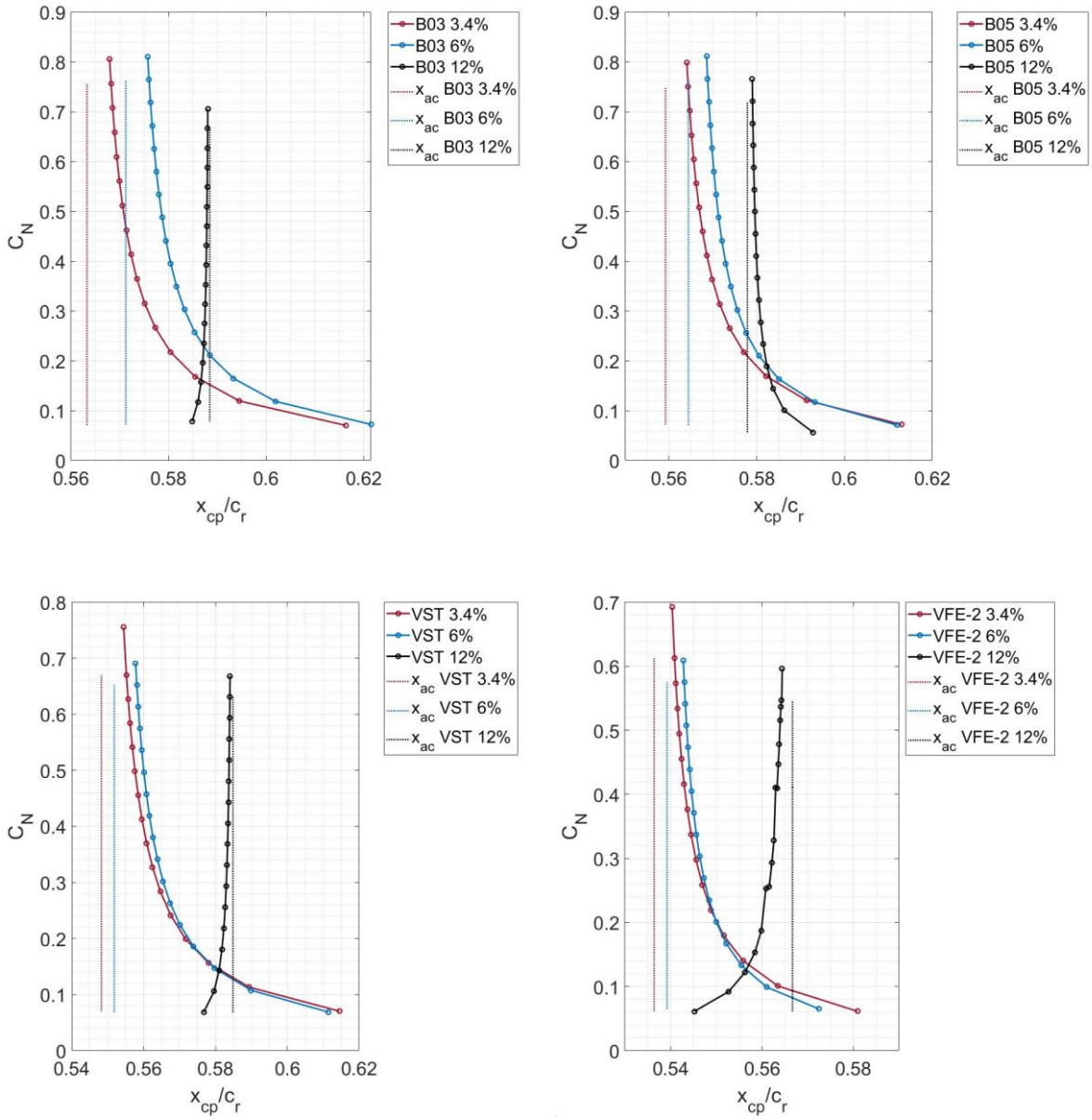

Figure 6.44 Normal force coefficient versus curve fitted normalised centre of pressure location for the B03, B05, VST and VFE-2 configurations for varying thicknesses.

To compare the effect of maximum thickness location both, aerodynamic centre and centre of pressure are plotted against the normal force coefficient and depicted in Figure 6.45. It can be seen that shifting the maximum thickness location barely has an effect on the centre of pressure's and aerodynamic centre's locations. Though both move rearwards when moving the maximum thickness location forward, this shift is only about 0.1% due to the wings being symmetric. The aerodynamic centre and centre of pressure appear to be more sensitive to tip taper, with tapering resulting in a shift of both centres rearward. However, the movement is

only about 0.2% of the root chord. As this increases stability, tapering towards the tip appears to be of advantage, which is a valuable insight for aircraft design.

As for thickness, Table 6.6 shows the change in aerodynamic centre when shifting the maximum thickness location forward, whilst Table 6.7 shows the effect of tip taper on longitudinal stability at C_L=0.5. It can be seen that the positive effect of stability is enhanced with thickness when changing the maximum thickness location forward and that tip taper has more significant impact on longitudinal stability, which is relatively insensitive to thickness.

Table 6.6 Change in aerodynamic centre at C_L=0.5 with shift in maximum thickness upstream.

Thickness [%]	Configuration	B05	B03
3.4	Change in x_{ac}/c_r [%]	0	0.72
6		0	1.2
12		0	1.82

Table 6.7 Change in aerodynamic centre at C_L=0.5 with tip taper.

Thickness [%]	Configuration	VFE-2	VST
3.4	Change in x_{ac}/c_r [%]	0	2.22
6		0	2.34
12		0	3.21

The prediction of the aerodynamic centre is not in accordance with conical flow theory, which predicts the aerodynamic centre of a delta wing to be at 2/3 of the chord (Gates, 1949). However, conical flow theory assumes inviscid flow, therefore, neglecting the impact of the boundary layer. The vortex formation and thus the pressure distribution have been shown to be highly sensitive to boundary layer status and the modelling of the viscous region (Hummel, 2004), which in turn affects the location of the aerodynamic centre.

The differences between the results of this study and conical flow theory are up to 13%, which is quite significant. For design purposes the position of the aerodynamic centre determines the location of the centre of gravity (cg). For a stable aircraft this has to be in front of the aerodynamic centre.

The cg position x_{cg} can be calculated and is presented in Table 6.8 for the current configuration. Note, this is not representative of an actual aircraft as cg position would also depend on the placement of various other system components. Comparing the position of the cg for the different configurations with the aerodynamic centre it can be seen that all but the B03

configurations are naturally unstable and would require additional measures such as control surfaces or artificial shift in weight towards the front.

Table 6.8 Location of the centre of gravity of the different configurations as obtained from Solid Works.

Configurations	B03	B05	VFE-2	VST
x_{cg}/c_r	0.56	0.63	0.66	0.63

However, the graphs presented here are curve fitted and the raw data shows a forward movement in aerodynamic centre of up to 0.5% (see Appendix A.5.4). In real flight conditions this would yield a decrease in static margin and needs to be accounted for by either moving the cg further forward or by implementing control surfaces.

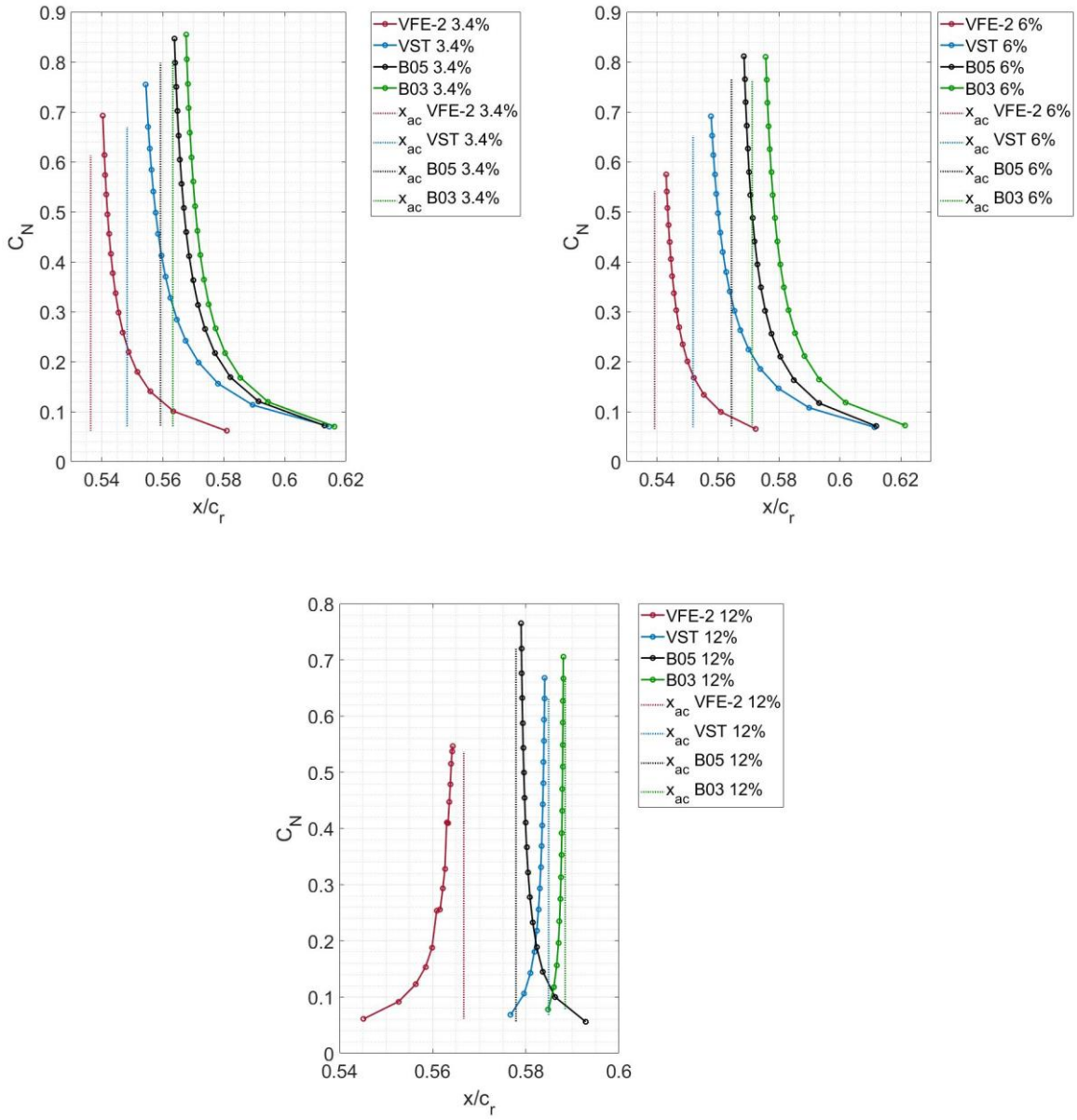

Figure 6.45 Comparison of the normal coefficient against curve fitted normalised position of the aerodynamic centre and centre of pressure for the B03, B05, VST and VFE-2 configurations for varying thicknesses.

Similar to the normal force, also the pitching moment can be considered to consist of a linear and non-linear component. This has been done by Kirby and Kirkpatrick (1969) for the experimental results of biconvex delta wings of different thickness and offers a means of comparison for the current numerical investigation. The pitching moment coefficient around a moment centre of $0.58c_r$ can be expressed as (Kirby, 1974)

$$C_{m_{0.58c_r}} = C_{N_{linear}}\left(0.58 - \frac{x_a}{c_r} + \frac{\Delta h_L}{c_r}\right) + C_{N_{non-linear}}\left(0.58 - \frac{x_a}{c_r} + \frac{\Delta h_{NL}}{c_r}\right) \qquad (6.10)$$

Where x_a is the distance between the apex and the centre of area and $\Delta h_L = x_a - x_{cp_l}$ and $\Delta h_{NL} = x_a - x_{cp_{Nl}}$ being the distances between the centre of pressure and the centre of area for the linear and non-linear force components respectively. $\frac{\Delta h_L}{c_r}$ is given by the value of $\frac{dC_m}{dC_n}$ at α=0°, which is the aerodynamic centre position at zero incidence for symmetric aerofoils. The non-linear component can be found by rearranging Equation (6.10) for $\frac{\Delta h_{NL}}{c_r}$.

The values obtained earlier in section 6.7 for $C_{N_{linear}}$ and $C_{N_{non-linear}}$ were then substituted into Equation (6.10), together with $\frac{dC_m}{dC_n}$ at small angles of attack in order to obtain $x_{cp_{Nl}}$. The linear and non-linear centre of pressure locations are shown in Table 6.9 and Table 6.10 for C_L=0.5 to visualise the effect of thickness change on linear and non-linear lift generation. Note, that the aerodynamic centre is the sum of linear and non-linear aerodynamic centres. Further note that the linear and non-linear normal force coefficients are obtained using $\frac{dC_N}{d\alpha}$ at low angles of attack. However, these values are the most challenging to obtain experimentally and numerically, and inaccuracies here, will affect the results obtained for the aerodynamic centres by up to 20%. Figure 6.46 shows the change in non-linear and linear centre with change in thickness. It can be seen that the linear component of the normal force is moving slightly forward with increase in thickness. Maximum thickness location has an impact of the severity of this movement, with a more forward located maximum thickness location resulting in a reduced movement of the linear force component but an increased movement of the non-linear component. The non-linear force component moves rearward with increase in thickness for the B03 configuration, but not for the B05 configuration. This has a stabilising effect for thicker wings of the B03 configuration, which is favourable for take-off and landing.

The movement of the linear and non-linear component of the VST and VFE-2 configurations is again different to that of the biconvex wings. Here, the linear component of the centre of pressure is moving rearward for the VFE-2 but that of the VST moves initially rearward before moving upward again. This can only be explained by the complex flow physics of the configuration especially at higher thicknesses. The non-linear force component acts significantly further rearward for the VST compared to the biconvex wings and for the VFE-2 the non-linear force acts no longer on the wing's surface. The reason for this is that the thicker wings of the VFE-2 are not producing much non-linear lift, due to an absence of LEV. The same can be said for the VST, however, here a more defined vortex structure is present close to the trailing edge (see Cp distribution in Figure 6.40 and Figure 6.41).

Table 6.9 Linear and non-linear aerodynamic centre location for the B03 and B05 configurations.

	B03			B05		
	3.4%	6%	12%	3.4%	6%	12%
$\frac{x_{cp}}{c_r}_{linear}$	0.5918	0.59272	0.59283	0.5875	0.577	0.561
$\frac{x_{cp}}{c_r}_{non-linear}$ at C_L=0.5	0.382	0.479	0.749	0.355	0.367	0.392

Table 6.10 Linear and non-linear aerodynamic centre location for the VST and VFE-2 configurations.

	VST			VFE-2		
	3.4%	6%	12%	3.4%	6%	12%
$\frac{x_{cp}}{c_r}_{linear}$	0.578	0.5814	0.575	0.515	0.528	0.539
$\frac{x_{cp}}{c_r}_{non-linear}$ at C_L=0.5	0.459	0.884	0.910	0.368	1.466	1.081

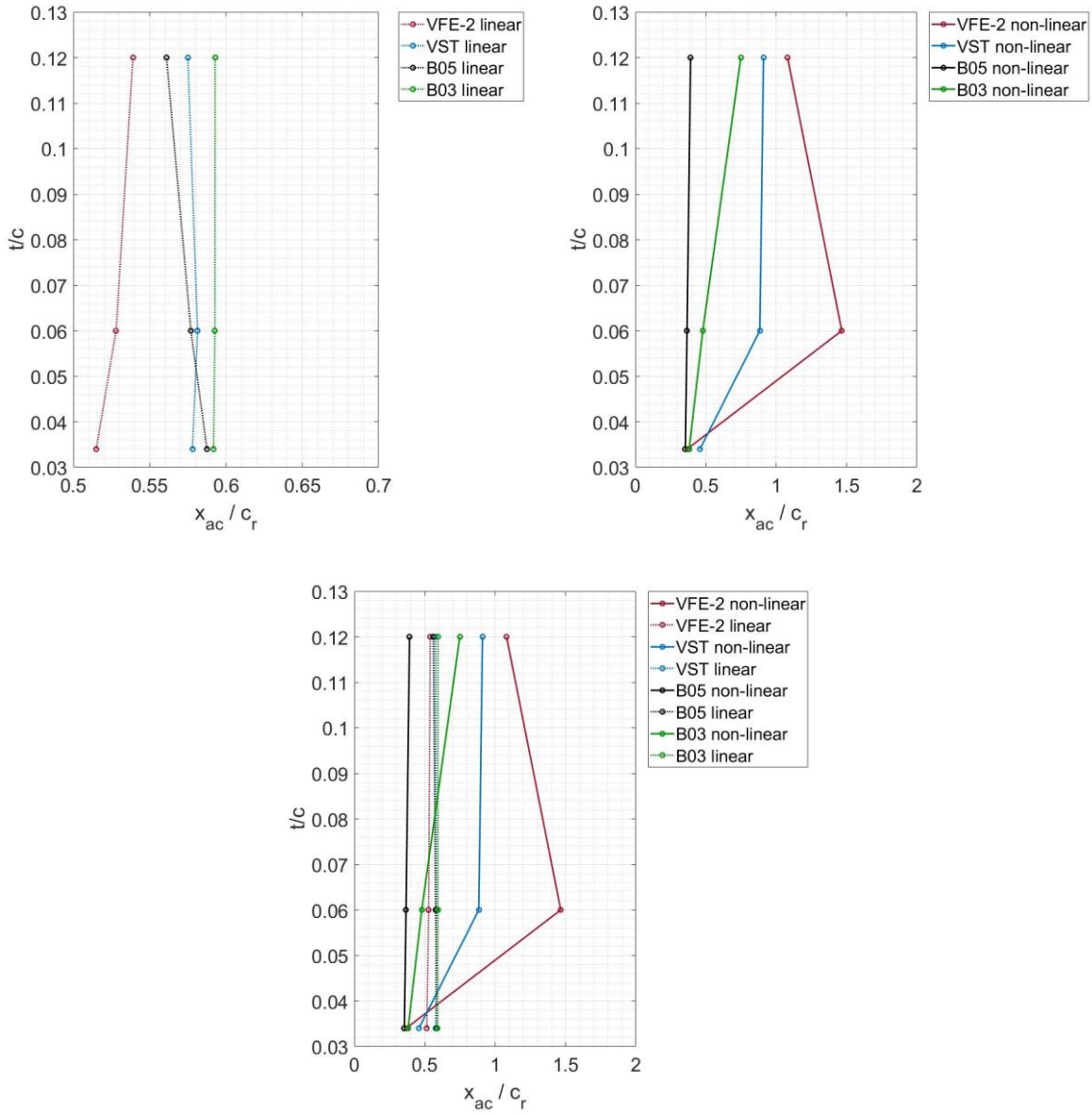

Figure 6.46 Comparison of the relative thickness against the position of the linear and non-linear aerodynamic centre of the B03, B05, VST and VFE-2 configurations for varying thicknesses.

6.10 Effect of profile shape on the L/D drag ratio

The measure of aerodynamic efficiency is the lift-to-drag ratio and determines the design point for most aircraft and is thus important in the evaluation of the overall performance of a configuration.

To investigate how the L/D ratio varies with increase in thickness, it has been plotted against angle of attack and lift coefficient in Figure 6.47 to Figure 6.50. This has been done to better evaluate differences between configurations. It can be seen that increasing the thickness results

in an increase in maximum L/D ratio, with the best value at 4 degrees. However, these differences decrease with further increase in thickness, due to an increase in profile drag. Furthermore, the L/D ratio is increased over a large range of incidences when increasing thickness, whereas the differences in L/D for a given lift coefficient are existent, but to a lesser extent. At around C_L=0.5 performance drastically reduces for the 12% thick wing as the lift coefficient only increases minimal from there onwards, whilst drag increases at a similar rate. This is due to the LEV moving upstream from the trailing edge, which increase the lift induced drag more than the non-linear lift. Additionally, for the B03 configuration VBD reduces the L/D at higher lift coefficients.

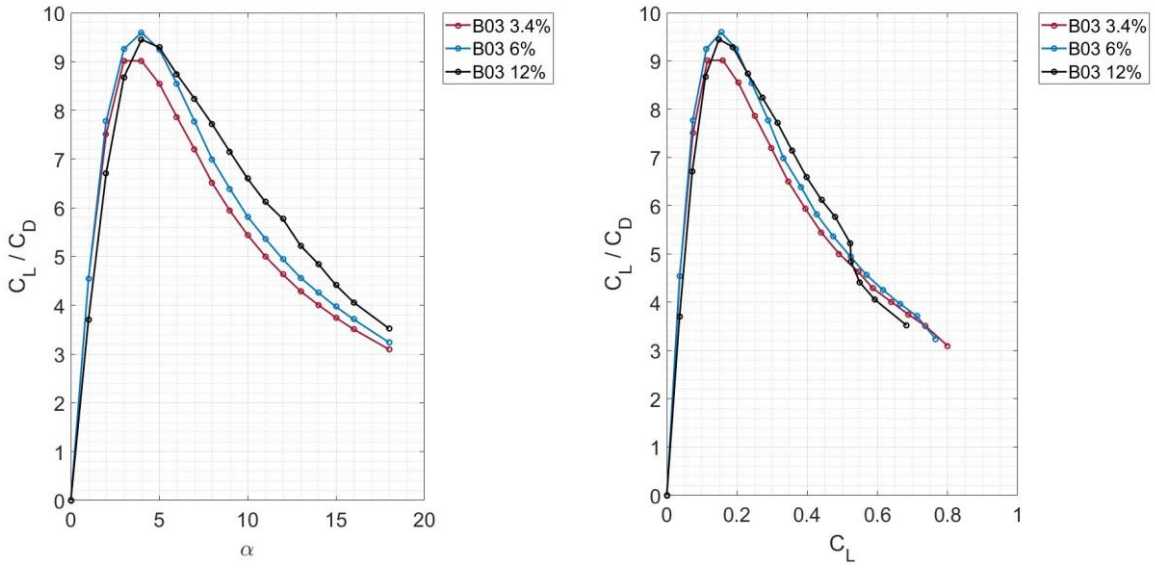

Figure 6.47 Lift to drag ratio versus angle of attack and lift to drag ratio versus lift coefficient for the B03 configuration for varying thicknesses.

For the B05 configuration depicted in Figure 6.48 it can be seen that the increase in thickness also yields differences in L/D ratio but to a lesser extent. It appears that the maximum L/D ratio is reached at higher angles when increasing thickness, which was not observed for the B03 configuration (the maximum L/D is now at 5 degrees). Therefore, this may be attributed to the maximum thickness location.

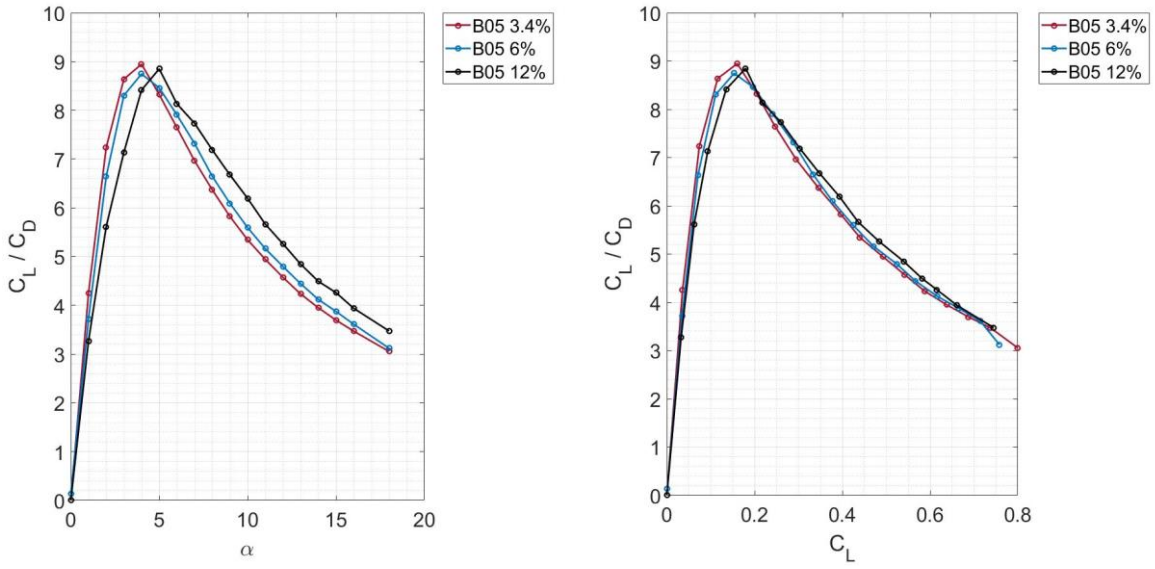

Figure 6.48 Lift to drag ratio versus angle of attack and lift to drag ratio versus lift coefficient for the B05 configuration for varying thicknesses.

However, for the non-biconvex cases, as can be seen from Figure 6.49 and Figure 6.50, L/D ratio decreases with increase in thickness due to a combination of increased profile drag and friction drag due to the dominance of separation bubbles on the thicker wings. These separation bubbles also do not contribute much to the overall lift force, resulting in a decreased L/D ratio. At higher angles of attack the discrepancy between the L/D ratio of the different thicknesses becomes smaller for VST and VFE-2. The reason could be that for the thicker wings, the flow is mostly attached, therefore, the lift-induced drag is smaller for thicker wings, which has a greater impact at higher α, where vortical flow is fully established for the thinner wings. The differences between the VFE-2 and VST are likely due to reduced profile drag close to the tip for the VST configuration.

In conclusion it can be said that the lift-dependent drag increases at higher angle of attack (as mentioned in section 6.8) whilst the lift curve slope remains constant. Therefore, the changes in the L/D versus C_L curve are reduced at higher angle of attack. The angle of maximum L/D changes for some configurations but not for others, leading to the conclusion that this is a feature of thickness distribution rather than overall thickness change.

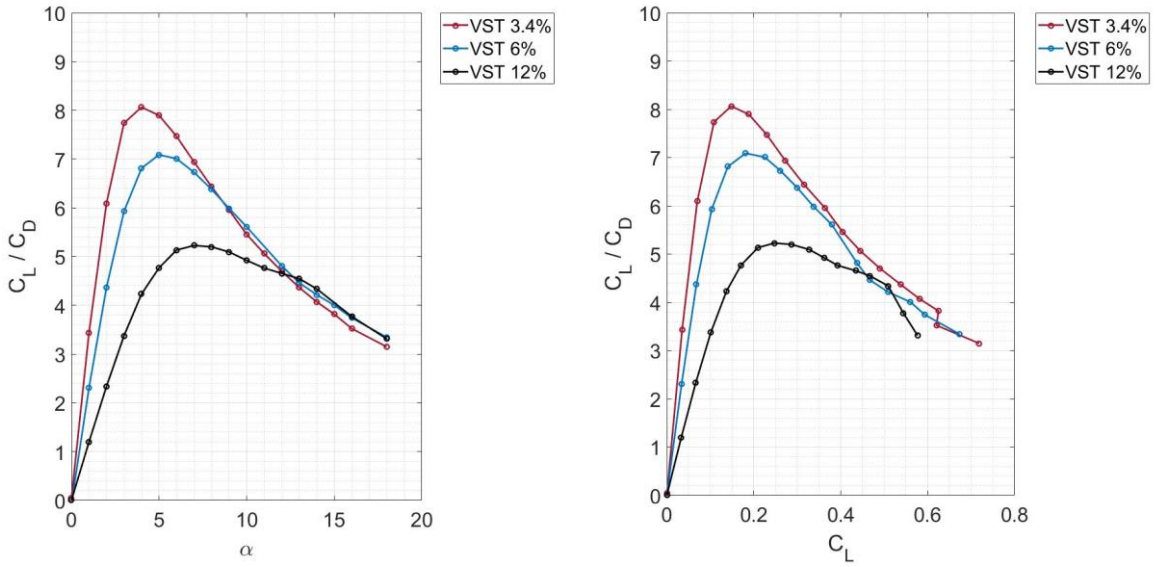

Figure 6.49 Lift to drag ratio versus angle of attack and lift to drag ratio versus lift coefficient for the VST configuration for varying thicknesses.

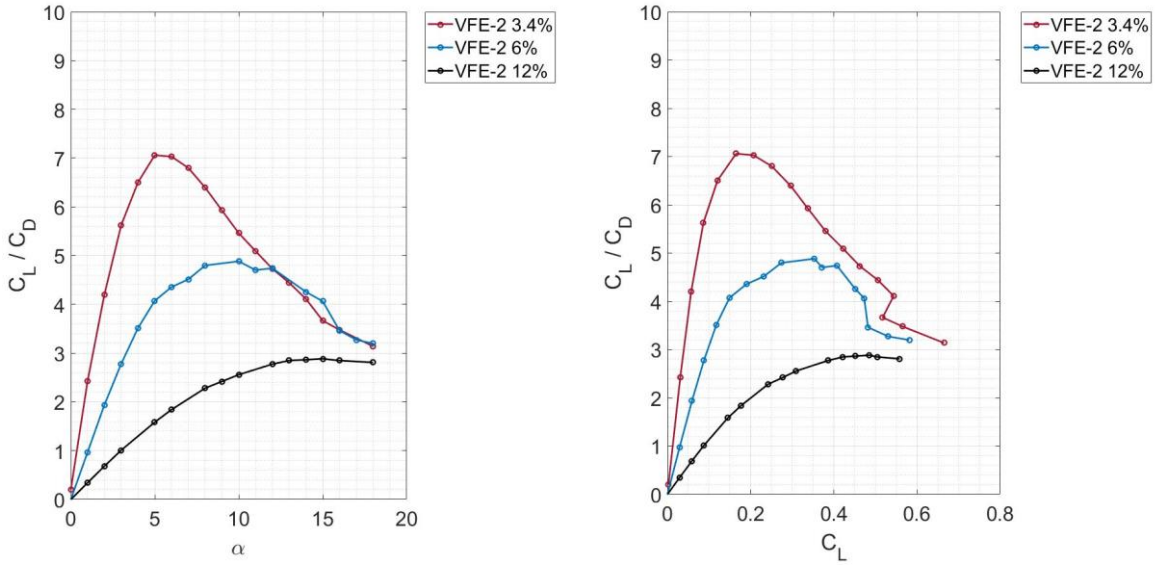

Figure 6.50 Lift to drag ratio versus angle of attack and lift to drag ratio versus lift coefficient for the VFE-2 configuration for varying thicknesses.

To investigate the effects of maximum thickness location, the previous graphs have been replotted for different thicknesses and profiles. These are shown in Figure 6.51 to Figure 6.53.

It can be seen that the effects of maximum thickness location become more apparent with increase in thickness. At 3.4% thickness the B03 and B05 configurations perform identical across the angle of attack range and across all C_L values. However, the differences in changing

spanwise thickness are already apparent at low thicknesses. Here, tapering the tip results in a drastic increase in L/D ratio until the maximum L/D is reached. After this the wings perform identically. Also, the maximum L/D is reached at lower incidences when changing the spanwise thickness. The maximum L/D is obtained at around α=4° for the B05 and VST configuration, whereas the B03 reaches its maximum L/D ratio at α=3° whilst the VFE-2 obtains its maximum at α=5°. Also, the VFE-2 generates a significantly lower L/D between 2° and 6° angle of attack. As the difference between the VFE-2 and VST configuration are spanwise thickness distribution, which results in a slightly higher profile drag for the VFE-2. This dominates at lower angles of attack. Additionally, the VFE-2 generates less lift over the entire angle of attack range, which is possibly due to trailing edge effects, which decrease the lift generation in that area.

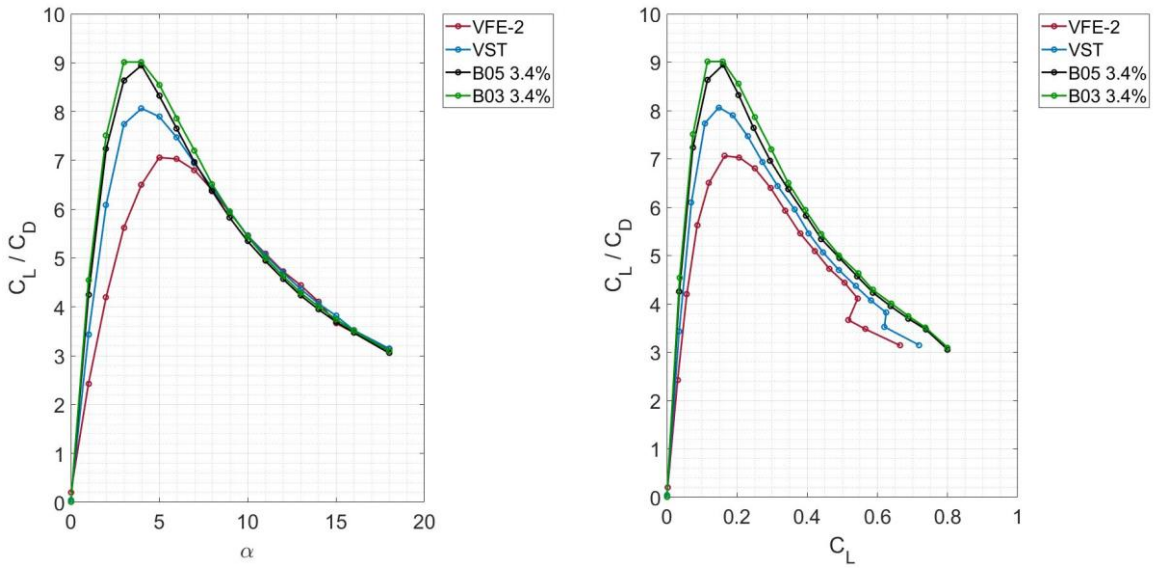

Figure 6.51 Comparison of the lift to drag ratio against angle of attack and lift to drag ratio against lift coefficient for the B03, B05, VST and VFE-2 configurations of 3.4% thickness.

Increasing the thickness does not impact nor change the maximum thickness location's impact on the angle at which maximum L/D is obtained. However, the maximum attainable L/D increases with forward movement of maximum thickness location, due to reasons discussed earlier. Spanwise thickness distribution and overall thickness in the area near the trailing edge has a significant effect on the performance at higher angle of attack. As shown in Figure 6.53 for the 12% thick wings, the L/D ratio suddenly drops for the B03 and VST configurations, which both have a very low thickness near the tip region compared to the B05 and VFE2 configuration. Here, the drop is due to the drop in lift curve slope as shown in Figure 6.22, which is due to VBD.

Tapering the tip (see Figure 6.14), as has been done for the VST, has been found to lead to a drastic improvement of L/D ratio, whilst moving the angle of maximum L/D to lower angles. When the tip is not tapered, as has been done for the VFE-2, an increase in thickness results in a shift in incidence of the maximum L/D to higher angles, showing the potential use of morphing to alter the performance of delta wing configurations.

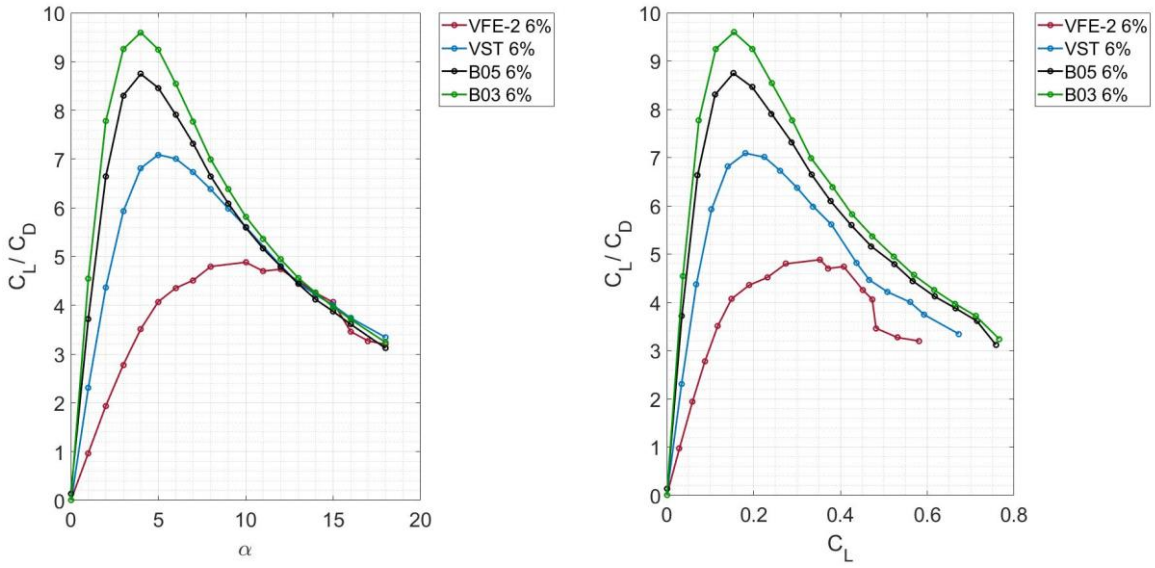

Figure 6.52 Comparison of the lift to drag ratio against angle of attack and lift to drag ratio against lift coefficient for the B03, B05, VST and VFE-2 configurations of 6% thickness.

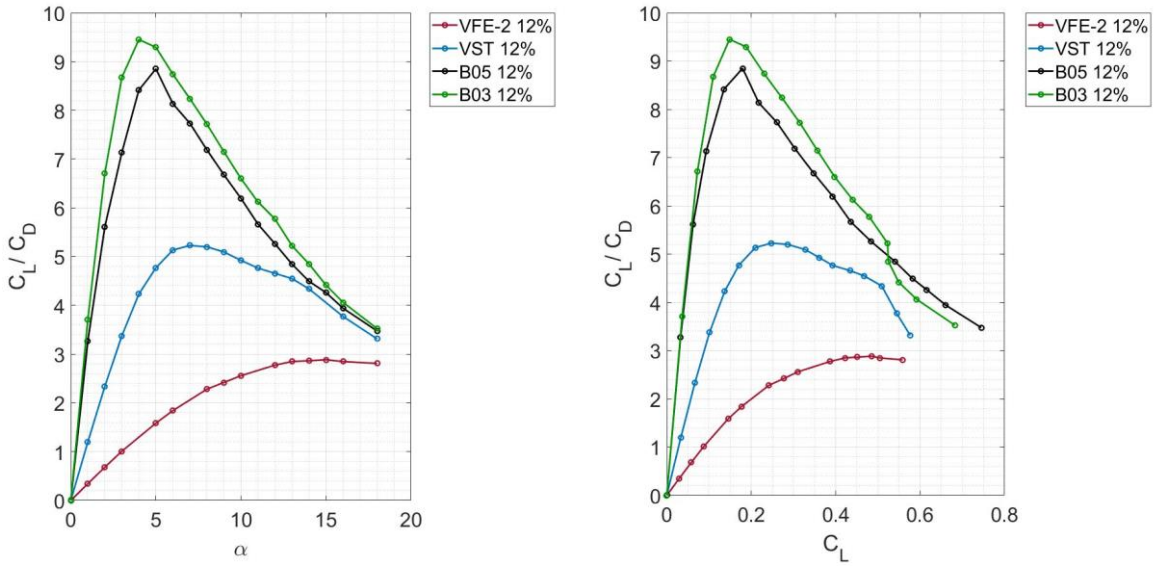

Figure 6.53 Comparison of the lift to drag ratio against angle of attack and lift to drag ratio against lift coefficient for the B03, B05, VST and VFE-2 configurations of 12% thickness.

6.11 Comparison of Findings with Literature

The VFE-2 and the VST delta wings were used as benchmark configurations and the focus of the effect of parameter changes focused on the two biconvex wings. The VFE-2 was used to validate numerical and experimental findings, whilst the VST was used to show the impact of tip tapering. It was shown that introducing tip taper results in lift due to increase in non-linear lift. Further, it was found that drag was dependent on thickness and tip taper and was found to increase for thin wings but decrease for thick wings. The thin wings' drag increased as the vortex is stronger in the mid-section of the wing, which is due to the relative leading-edge sharpness. For thicker wings the increased pressure drag due to constant spanwise thickness is the dominating factor yielding to the increased drag for the VFE-2. The pitching moment is increasing with tip taper whilst L/D is increasing. This leads to the conclusion that morphing of the outer part of the wing can be used to alter performance and stability significantly and may have a more significant effect than overall thickness alteration or shift in maximum thickness location. This is valuable knowledge for future UCAV design.

The findings regarding tip taper are partially correlating with those of Kirby and Kirkpatrick (1969). They did a preliminary investigation on tip taper on a 4% thick, 70° swept back biconvex wing. It was found that the non-linear lift component decreases when tip taper is introduced which is opposed to the findings of this study. Furthermore, they showed an increase in lift induced drag at low α and a decrease at high α. Both were confirmed in this study. Stability was shown to decrease with tip taper another aspect which could not be confirmed here. However, the findings regarding suction force, lift and drag coefficient and aerodynamic centre location correlated. The differences in some of the findings could be attributed to the fact, that both of Kirby and Kirkpatrick's (1969) configurations did have tip taper, however, one of them to a lesser extent. Also, the investigation was done on biconvex wings, whereas in the present study this was not the case. Both could have an effect on the vortical flow pattern, resulting in the differences mentioned above.

It was shown that the area for the vortex to act upon increases when increasing thickness or moving the maximum thickness location forward. It was hypothesised that this may result in similar flow patterns observed for wings with rounded leading-edges. Kuflan's (1971) observations confirm this partially as vortex onset is delayed for thickness as well as for increased leading-edge radius. The suction force plotted in Figure 6.17 and 6.18 was shown to increase, solely by altering the shape of the upper surface.

Increase in thickness also results in a reduction in drag up to a given thickness where form drag dominates. The same could be observed when shifting the maximum thickness location forward. In section 6.4 the lift induced drag was shown to decrease with thickness as well as with forward movement in maximum thickness location. Co-rotating inner vortices were found on the VFE-2 and VST configuration at 6% thickness, similar to those observed by AVT-113 on the VFE-2 configuration with MRLE. As most on their tests were conducted at M=0.4 and Re >= 3×10^6 no direct comparisons could be made. However, it is believed that they occur due to the same flow physics: an increased adverse pressure gradient between the primary suction peak and the local suction minimum at the symmetry plane (Furman and Breitsamter, 2013). A comparison between the topology of vortex systems for the VFE-2 configuration with round leading-edge at α=13° $\mathrm{Re_{mac}} = 2 \times 10^6$ and M=0.14 (Furman and Breitsamter,2013) and the CFD surface streamlines for the VFE-2 configuration of 6% thickness of this thesis at α=13° $\mathrm{Re_{mac}} = 7.5 \times 10^5$ and M=0.1 are shown in Figure 6.54. It shows the similarity in flow pattern, though more vortex structures are found on the VFE-2 configuration of increased thickness.

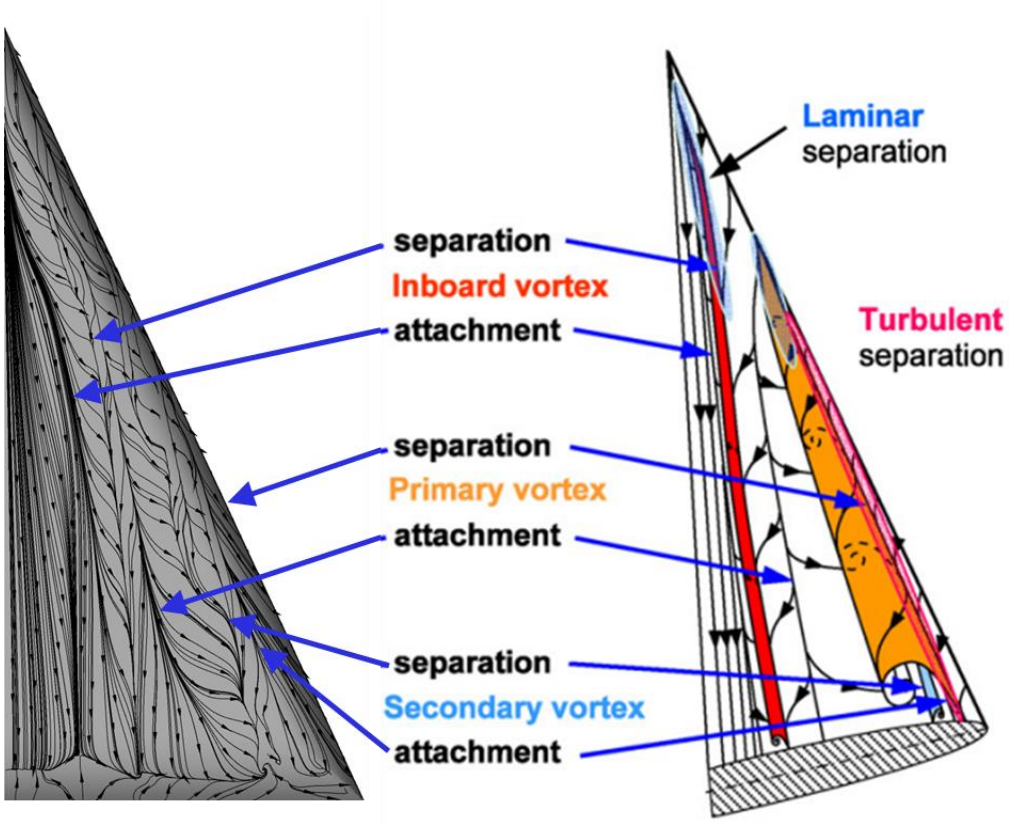

Figure 6.54 Flow Topology based on the surface streamlines of the VFE-2 6% (left side) at α=13°, M=0.1 and $Re_{mac} = 7.5 \times 10^5$ on the left and the flow topology based on laser light sheet and oil flow visualisation for α=13°, M=0.14 and $Re_{mac} = 2 \times 10^6$ on the right (Furman and Breitsamter, 2013). Note, the rear flow separation occurring on the VFE-2 6% wing indicated by the streamlines moving upstream.

Overall, it was found that the wing performing the best is the B03 6% maximum thickness to chord (t/c) configuration followed by the B05 6% t/c. It delays VBD the furthest, provides the best L/D ratio whilst also being stable over a wide range of angle of attack. The shift of the maximum thickness forward may be advantageous regarding stability as the centre of gravity for the B03 configuration is located further forward. Due to the aerodynamic centre being further back than for the B05 configuration this increases the B03 wing's static margin. The thickness also affects the structural weight, as thinner wings are more prone to bending. Equations, derived from statistical data from existing aircraft, for wing weight show that the structural weight of a shell type wing varies approximately inversely with the square root of the thickness ratio; meaning a decrease in thickness results in an increase in structural weight (Raymer, 1992). This is a drawback of the 6% thick wing compared to the 12% thick wing, as the wing weight increases by about 41% causing the empty weight to increase by about 6% (assuming the wing is typically about 15% of the total empty weight) (Raymer, 1992). The configurations of this study were investigated at low speeds, typical for take-off and landing. These configurations could have transonic or supersonic design speeds, depending on their application. If designed for high speeds these configurations would generally use thicknesses ratios of t/c= 0.016 and t/c= 0.04, assuming cruise speeds of M<=1.0 and M=2.0 respectively (Raymer, 1992). The increase in weight is a clear disadvantage, but may be compensated by the higher L/D ratio, as form drag is lower for thinner wings, of this configuration.

The findings of this study can be used for the evaluation of take-off and landing characteristics of high-speed vehicles. Here, the main considerations are increased stability at high α as this is not only beneficial for rapid manoeuvring but also for take-off and landing. It has been shown, that moving the maximum thickness location forward whilst keeping the thickness as low as possible is desired. Furthermore, designers are concerned to delay the onset of VBD as much as possible, as it allows the aircraft to be flown at higher lift coefficients. The angle of attack at which VBD occurs has been found to be a function of thickness and thickness location. Generally, a movement of maximum thickness forward triggers VBD, resulting in a trade-off between stability and VBD angle of attack. At low α a shift in maximum thickness location upstream was shown to be most beneficial from a performance perspective. When agility is required increase in wing taper would have the most destabilising effect followed by a downstream movement of maximum thickness location. This adds valuable knowledge regarding the effect of maximum thickness location and spanwise thickness change for future UCAV design. It suggests that for a morphing UCAV one would like to have a thick wing with

a maximum thickness location located further upstream (B03) during take-off and landing, as it not only results in greater L/D ratio, but also higher longitudinal stability. During cruise flight, where, depending on the mission, the UCAV may require higher agility, the configuration would have the option of either reducing thickness, shifting the maximum thickness location downstream, change in spanwise thickness distribution or a combination of the three. Here, a decrease in tip taper would have the most significant effect, but comes with a great drag penalty. A shift of maximum thickness location rearward would have the second most destabilising effect whilst maintaining a good L/D ratio and therefore should be the preferred option. However, the study was conducted at a very low speed and not cruise conditions of common UCAVs and therefore the recommendations given here would need to be verified by conducting numerical simulations at higher speeds. Using the above measures for controllability of the UCAV needs also further investigation, however, it can be seen that a smart design, with a thick front part and a very thin rearward shape with little tip taper could achieve this, as this would lead to delayed vortex onset whilst utilising the increased lift near the trailing edge due to reduced tip taper to move the wing loading rearwards. However, when implementing control surfaces on the UCAV a strong vortex near the trailing edge would not be desired, thus, a thicker rear part with a maximum thickness location further upstream may be required.

6.12 Conclusion Chapter 6

Chapter 6 described the findings of the numerical simulations at M=0.1 and Re=750,000 for the B03, B05, VST and VFE-2 configuration at thickness 3.4%, 6% and 12%. Emphasis was put on the performance and stability, namely, L/D ratio and position of aerodynamic centre. The differences in the parameters seen in Table 6.11 were explained using the flow physics by means of vorticity and axial velocity contours as well as spanwise pressure distribution.

Table 6.11 Summary of the numerical findings.

	Increase in t (Biconvex profiles)	Increase in t (VFE-2/ VST profiles)			Moving max. thickness location upstream (B05 → B03)	Introducing Tip Taper (VFE-2 → VST)			
C_l					Apart from very thick wings at high α				
C_d		Low α (0°- 12°)			Apart from very thick wings at high α where B03 is lower	Low α (0°-12°)	3.4%	6%	12%
		High α (12°- 18°)	VST	VFE-2 highest to lowest: 12%, 3.4%, 6%		High α (12°-18°)	3.4%	6%	12%
$C_{m_{0.58}}$									
$C_A - C_{A_0}$									
L/D					For 6% and 12% thickness				
Non-linear Lift	B03 highest to lowest: 3.4%, 6%, 12% B05 highest to lowest: 6%, 3.4%, 12%	Low α (0°- 12°)	VST	VFE-2 highest to lowest: 6%, 3.4%, 12%		Low α (0°- 8°)			
		High α (12°- 18°)	VST highest to lowest: 3.4%, 12%, 6%	VFE-2 highest to lowest: 3.4%, 12%, 6%		High α (8°- 18°) Highly dependent on thickness			
Lift-induced drag K									
Stability									
x_{ac}	downstream	downstream			downstream	downstream			
Non-linear x_{cp}	downstream	downstream			upstream	upstream			
Linear x_{cp}	B03: downstream B05: upstream	downstream			upstream	downstream			

Legend	
	Increase in value
	Decrease in Value
	No change in Value

Regarding the change in thickness it was found that maximum L/D ratio could be improved by up to 6.25% on the biconvex configurations when increasing the thickness. However, this was also affected by the maximum thickness location. The improved maximum L/D ratio was a result of decreased lift induced drag due to vortex onset being delayed with increase in thickness. Stability was increased as delayed vortex onset decreased the upward suction force in the front part of the wing whilst still being high in the rear part where vortical flow was present.

An increase in thickness for the VST and VFE-2 configurations significantly influenced the wing performance depending on angle of attack and spanwise thickness distribution. L/D ratio was found to decrease with thickness as lift decreased. The maximum L/D ratio showed a reduction of up to 57% depending on thickness. The drag increased at lower α mainly due to profile drag with increase in thickness, thus, resulting in significant differences in L/D at that range. At higher angles of attack the differences became smaller, as drag decreased due to reduced lift induced drag factor.

Leading-edge suction, was found to increase with thickness for the biconvex and flat profiles and is associated with an increase in L/D ratio. A forward movement in maximum thickness had the same effect, whereas the opposite was observed when introducing tip taper.

The stability, defined as the rearward movement in aerodynamic centre, at C_L= 0.5 increased by up to 4.5% compared to the thinnest wing when altering the thickness of the biconvex configurations, whereas the VFE-2 and VST showed improvements of up to 6.7%. The stability was enhanced due to increased rear loading whilst front loading was decreased. The former was due to the trailing edge having less of an effect on the flow for thicker wings, whilst the latter was due to the delay in vortex formation.

Moving the maximum thickness location upstream did not show significant differences especially for the 3.4% thick wing. However, it could be shown that L/D ratio increased by up to 8% when moving the maximum thickness location upstream for thicker wings as the leading-edge suction became stronger. This was true for the entire angle of attack range, though the most noticeable differences were between α= 3° and α= 6° and due to the reduction in drag, which compensated for the decrease in lift with upstream movement. Drag was decreased because the vortical flow onset is delayed for the wings with maximum thickness location further upstream. The reason being is that the leading-edge slope is increased, thus, reducing the effective angle of attack.

Moving the maximum thickness location forward increased the stability of the wings, as linear and non-linear normal force components are moving towards the trailing edge, thus, increasing the static margin. Furthermore, moving the maximum thickness location forward resulted in a forward movement of the centre of volume, which is a fair representative of the centre of gravity. This also added to the longitudinal stability of these configurations. Another aspect is the enhanced rear loading and decreased front loading for wings with maximum thickness location further forward. The latter is due to delayed vortex onset as the frontal area is greater. Therefore, at C_L= 0.5 stability was shown to improve by up to 1.8% when moving the maximum thickness location forward. The change was observed to be constant with thickness change.

It was further found that for thicker wings a shift in maximum thickness upstream results in additional separation occurring inboard. Furthermore, it was found that that the LEV moves outboard and is more oval shaped for the same reasons mentioned earlier. Those effects, however, are pronounced with increase in thickness and not noticeable for thin wings.

Moving the maximum thickness location downstream was shown to result in an increase in leading-edge suction force and a more developed vortical flow pattern, whereby the differences become more significant at higher incidences. This is due to the relative leading-edge sharpness (leading-edge radius/ local span), which is greater for wings with maximum thickness location located rearwards.

Introducing tip taper resulted in an increase in lift-to-drag ratio as well as in an increase in stability, due to the backward shift of the aerodynamic centre. Stability improved by up to 3.21%, with the static margin changing more drastically when thickness was increased. Generally, it was found that the thicker the wing the larger were the improvements in stability when altering maximum thickness location and tip taper. L/D ratio also increased with tip taper. That was due to large differences in drag generation, which was dominated by the frontal area of the non-tapered wing. The leading-edge vortices were stronger for the VST configuration due the effective leading-edge slope being lower. This was reflected in the non-linear lift, which increased, thus, further contributing to the differences in L/D ratio. The angle of attack of maximum L/D was shifting to higher incidences when the spanwise thickness was held constant, and maximum L/D ratio was reduced by up to 45%. Tapering the tip also resulted in an inboard movement of the LEV, whilst the area close to the trailing edge was more effective for non-tapered wings especially at low incidences.

Generally, the findings suggest that an increase in thickness yields a decrease in aerodynamic loads and an increase in longitudinal stability. The reduced loads are due to a decrease in effective angle of attack as a result of leading-edge slope (Kulfan, 1979) with increase in thickness. Regardless of the upper surface shape, the flow separates at the sharp leading-edge. For thicker wings, a separation bubble forms over the majority of the chord, whereas leading-edge vortices form for thinner wings. The presence of separation bubbles impacts the non-linear component of the lift, which is reduced for thicker wings, but is not influenced by maximum thickness location.

The drag has been found to decrease with increase in thickness, whilst also being insensitive to maximum thickness location. The decrease is due to the reduction in axial force component. As frontal area increases so does the thrust component of the axial force, yielding in a reduction in lift-dependent drag. Since the lift-dependent drag is also a function of lift curve slope, the effect on the lift-dependent drag is larger at lower angles of attack, but vanishes at higher α. This is also reflected in the L/D.

The maximum obtainable L/D ratio was shown to depend on the maximum thickness location and to be higher for the thicker wings, even though not significantly. At lower angles of attack the L/D ratio is higher for thinner wings, but this effect is reversed after the maximum L/D value is reached. For the VST and VFE-2 it was shown that the maximum achievable L/D ratio reduced significantly with increase in thickness, which was concluded to be due the dominance of the pressure drag and reduction of the non-linear lift component for the thicker wings.

The angle of attack at which the maximum L/D ratio occurs is insensitive to thickness and profile shape and can be found at α=4° for M=0.1. The stability increases with thickness and a shift in aerodynamic centre to higher angle of attack. This is due to the delay for thicker wings of vortex onset, which is also responsible for the reduced drag generation. It was shown that an increase in thickness yields an increase in profile drag (or drag at zero lift). This has particularly an effect at lower α. At higher angles of attack the lift induced drag becomes more dominant for the thinner configurations with vortical flow whilst the pressure drag remains constant, thus, the drag of these configurations becomes higher.

The LEV was found to move outboard with increased thickness whilst the surface area of the wing affected by the vortex decreases, thus causing a reduced lift force. This is because of the secondary vortices reducing in size as adverse pressure gradient below the primary vortex decreases. It was further found that the vortex becomes more oval shaped with rise in thickness, due to increased re-attachment length, and that separation bubbles are dominating the flow due to the frontal area increasing.

The investigations on the effects of altering the thickness correlate with the findings of Kirby and Kirkpatrick (1969). Their study on a 70° swept back delta wing with biconvex profile showed an increase in leading-edge suction, decreased lift-dependent drag and increased longitudinal stability at high angles of attack with increase in thickness. It was conducted at a higher Re than the present study (Re= $2.24 \times 10^6 c_r$), which gives confidence that the geometrical effects are transferable to higher Re.

However, the observed effects disagree with the study by Wang (2005) on a delta wing of 50° sweep. Wang (2005) concluded that drag increases with increase in thickness so does the L/D ratio. This cannot be said for the biconvex wings in this study. However, it has been found true for the VFE-2 and VST configuration. Wang (2005) investigated delta wings with bevelled LEs, therefore the wing acted like a flat plate, where increase in thickness yields higher drag.

The findings above are limited by errors in the numerical simulation due to grid quality, turbulence model choice and initial boundary conditions, such as turbulence intensity value. However, these will always result in uncertainty, but general trends such as the aerodynamic coefficients have shown not to vary much (Wibowo et al., 2018), whereby elements, such as surface Cp distribution, Q-criterion and axial velocity may proportionally change more.

Chapter 7 Conclusions & Recommendations

7.1 Contributions to the Field

The presented study contributes to the existing knowledge in the area of slender delta wing flow physics and their effects on performance and longitudinal stability. Both, stability and performance are of major importance especially for aircraft design. Though restricted to SLEs, longitudinal stability is worsening when round leading-edges are used (Luckring and Hummel, 2008), so this study is also a good estimator for the design of subsonic configurations.

This investigation further contributes by showcasing the improvement of stability and performance of a high-speed delta wing during take-off, landing and rapid manoeuvring when altering two geometrical parameters; thickness and maximum thickness location. It uses a profile which is more realistic to general application than some previous studies on the VFE-2 configuration, whilst offering another benchmark configuration for future investigations. It further builds on the work done on the effects of thickness by Kirby and Kirkpatrick (1969) by adding flow visualisations and pressure distribution at a slightly lower Re.

This thesis also adds to the work done by the AVT-113 group by adding the impact of the use of a RSM turbulence model using the TUM test case at $\alpha = 18°$ as suggested in the further work section of their report (Fritz and Cummings, 2008). It further confirms the findings by Crippa regarding the importance of the surface discretisation on the prediction of the flow physics of delta wings (Crippa, 2008).

Further, it contributes by using a combination of most recent CFD flow visualisations with classic wind tunnel evaluation methods for validation, to evaluate the flow physics and characteristics of delta wings, thus adding new judgement parameters.

New insights on delta wing vortical flows in terms of the effects of the specific parameters are summarised below and have been sub-divided into the different categories

7.1.1 Increase in thickness

It has been found that an increase in thickness yields:

- Longitudinal static stability is enhanced with an increase in thickness and the angle at which the configuration becomes unstable is delayed. This is due to the wing being more rear-loaded, as front-loading decreases and rear-loading increases with thickness. The latter is a result of decrease in trailing edge effect.

- The aerodynamic centre moves backwards (downstream) with increase in thickness thus increasing the static margin and enhancing longitudinal stability.
- That there is an optimum thickness at which L/D is maximised. This has been found to be t/c=0.06 for all three configurations
- The angle of attack of maximum L/D is insensitive to thickness change, but does change when constant spanwise thickness is introduced
- There is a certain thickness which depends on the maximum thickness location, at which VBD is moving to lower incidences.
- With increase in thickness the flow around the delta wing becomes more dominated by separation bubbles which do not fully roll up into a LEV. When leading-edge vortices do form, they become more stretched compared to thinner wings.
- The LEV moves outboard with increase in thickness and the wing area affected by the vortex decreases.

7.1.2 Maximum thickness location

For a change in maximum thickness location it has been found that:

- Moving the maximum thickness location downstream results in a reduction in suction force and a more developed vortical flow patter, whereby the differences become more significant at higher incidences.
- Moving the maximum thickness location downstream results in an earlier onset of vortical flow.
- Shifting the maximum thickness location upstream results in enhanced stability over a wider angle of attack range irrespective of thickness. This is due to delayed vortex onset which results in enhanced rearward loading. Also, the aerodynamic centre and the centre of pressure are moving rearwards, thus, increasing the wing's static margin.
- A shift in maximum thickness location rearward results in a rise of non-linear lift with increase in thickness. This is due to the frontal area being less impacted by thickness change.
- The thickness distribution is affecting the area the LEV is acting on, which in turn impacts the non-linear lift generated. A movement rearward enlarges the effective area used by the leading-edge vortices.
- Moving the maximum thickness location backwards results in a more drastic forward movement of the linear component of the normal force, whilst moving the maximum thickness forward results in a rapid backward movement of the non-linear component.

- Moving the maximum thickness location forward enhances the maximum attainable lift-to-drag ratio.
- Lift has been found to be unaffected by maximum thickness change, though moving the thickness location forward can trigger VBD at lower angles of attack, thus, reducing lift generation.
- Moving the maximum thickness location forward results in additional separation occurring inboard for wings of high thickness. This may be due to similar effects as discovered by Furman and Breitsamter (2013) for wings of round leading-edges.
- Vortex formation is delayed with forward movement in maximum thickness location, though this is only true for higher thicknesses.
- The LEV moves outboard when shifting the maximum thickness location upstream. This effect is enhanced when increasing the thickness.

7.1.3 Tip Taper

Introducing tapering towards the tip has been found to:

- result in the angle of maximum L/D moving to lower angles. This angle is subject to change for wings with constant frontal area depending on thickness.
- have a significant effect on stability and especially on the location of the aerodynamic centre and centre of pressure. Both quantities move upstream when the wing has a constant spanwise thickness and are insensitive to thickness change.
- move the LEV inboard whilst the trailing edge generates a higher suction force when not tapered, especially at lower incidences.
- decrease the suction force due to the frontal area no longer being constant.

7.1.4 General observations

Finally, general observations can be summarised as:

- The aerodynamic centre for all configurations lies between 55% and 60% of the root chord.
- The best performing aerofoil is the biconvex wing of 6% thickness and t/c= 0.3, followed by the biconvex profile of 6% thickness and t/c=0.5.
- Thickness and maximum thickness do not affect the angle of attack at which the maximum L/D ratio is occurring.
- Profiles using no curvature but being flat cause the formation of an inner vortex especially on thicker wings.

- The shape of the upper surface of a delta wing with SLE has a significant impact on the leading-edge suction generation and thus on the L/D ratio.

7.2 Satisfying the objectives and research questions

This study investigated the effect of thickness and different thickness locations on a 65° delta wing, with the aim to demonstrate the effectiveness of change in thickness and maximum thickness location on the performance of slender delta wings at low speed. The aim was satisfied as evidenced by the findings detailed above.

Next to the main aim, research questions were defined and answered.

Objective (i): Reviewing the current literature on the topic of slender delta wings revealed that despite there being a significant amount of studies done on slender delta wings there is a large scatter in data. Rarely any consistency in certain parameters such as profile shape or Reynolds number was found. This makes it difficult to evaluate the effect of certain parameter changes as vortical flow is extremely sensitive to many geometric and environmental parameters. The studies conducted on the VFE-2 configuration showed and gave the scientific community a benchmark configuration for future studies.

Objective (ii) & (iii): The objective regarding grid sensitivity and turbulence model choice were answered, showing that the simulation of delta wing configuration requires a very fine grid, particularly close to the leading-edge, making its simulation quite computationally expensive. It was further shown that the axial force component experiences the highest sensitivity to grid size and was shown to cause the highest variation between consecutive grid refinements. Turbulence model choice was shown to have an effect on the prediction of axial velocity component and VBD location. Two models were evaluated; SST and the FLUENT pressure strain Reynolds Stress Model (RSM). It was shown that the predictions by RSM were in better agreement with the wind tunnel data by TUM regarding axial velocity component and VBD location, thus showing that the directional effects of the Reynolds stresses and complex turbulent flow interactions are important in vortex dominated flows.

Objective (iv): In order to achieve the overall aim of this study, wind tunnel validation runs were conducted on a selection of configurations. To verify the wind tunnel the VFE-2 configuration was tested and compared to available data of other research institutions. It was shown that the UWE wind tunnel was capable to reproduce their findings, thus, giving confidence in the accuracy of the data obtained for the other models.

Objective (v): Objective (v) on verifying the numerical findings was met. Lift and drag coefficients were in very good agreement with the wind tunnel data. The pitching moment was not predicted as well but was still within the uncertainty of the grid resolution.

Research Questions 1: The research question - “to what extent changing the overall thickness as well as the maximum thickness location affects performance an longitudinal stability” - showed that the maximum L/D ratio can be increased by up to 6.25% on biconvex configurations, whilst moving the maximum thickness location forward results in an increase of up to 8%. Lift coefficients, typical for take-off, landing and loitering, can be enhanced by up to 4.5% when thickness is increased. Shifting the maximum thickness location forward increases the stability by up to 1.82%. Therefore, it can be said that changing the thickness has a significant effect on the performance and stability of delta wings whilst the effect of changing the maximum thickness location is more significant for performance than for longitudinal stability.

Research Question 2: The second research question regarding the confidence level of the prediction was answered by the achievement of objectives (ii), (iii) and (iv). Numerical simulations of the flow up to VBD can be predicted with a high confidence level using RANS methods. Furthermore, knowing the effect of thickness and maximum thickness location can help designing configurations, with wing morphing in mind, to utilise the benefits of different aerofoil geometries.

7.3 Limitations

Most of the studies referred to in the literature review are from a time when CFD was in development and computational power was limited. Therefore, most findings are experimental. This doctoral study adds to the body of knowledge on delta wings by using mainly numerical methods. Although numerical methods come with uncertainty due to their dependence on an appropriate grid, domain size, boundary conditions and turbulence model choice, there accuracy can be determined by using different polar plots. This was done throughout Chapter 6, with focus lying on those polar plots, which were also used by different authors in the literature review to enable comparison of findings.

In Chapter 4 section 4.7 to 4.10 the VFE-2 benchmark case was used to verify grid, turbulence model choice and boundary conditions by running a test case with sting mount and compare the findings against those experimentally done at TUM in the framework of AVT-113. The experimental tests conducted at ONERA were used to verify the results obtained at the UWE wind tunnel as presented in Chapter 5. It was shown, that the experimental findings at the UWE wind tunnel were within the uncertainties of the ONERA wind tunnel. The numerical comparison at $\alpha=18°$ showed that current RANS turbulence models struggle with the detailed prediction of flow details in vortex dominated flows due to their highly unsteady nature

especially for very thick wings. This is also in agreement with the findings of AVT-113. It was shown in Chapter 4 section 4.9.1 that the RSM turbulence model may be a viable option as findings in this study suggest, that their prediction of flow parameters, such as axial velocity, is more accurate than for other RANS models.

The findings on the VFE-2 configuration by the NATO-AVT-113 task group are largely replicated in the UWE wind tunnel. Furthermore, the numerical findings are also replicated. It is shown, that current RANS turbulence models struggle with the detailed prediction of flow details in vortex dominated flows at high angle of attack. Here, the flow becomes unsteady, which is especially true for very thick wings.

The limitations of this study in the area of the numerical findings are; grid quality, domain size, turbulence model, steady flow assumption and boundary condition choice. Especially, the wings of 12% thickness showed unsteady behaviour at higher angles of attack, which was expected due to the combination of increased nose radius and sharp-leading-edge. A quantitative evaluation of vortex location and position was omitted as multiple studies have shown that vortex location is highly dependent on the accurate prediction of vortex onset, which in turn depends highly on turbulence model choice as well as grid resolution (Fritz and Cummings, 2008; Schütte and Luedeke, 2010; Schütte et al., 2012). It was shown in Appendix 3 sections 3.3 and 3.4 that the prediction of axial velocity and pressure distribution is highly sensitive to surface grid refinement. The drawback is however a drastic increase in element count, resulting in a drastic increase in computational time. Therefore, when investigating vortical flow a high surface grid resolution should be prioritised over a refinement of the surrounding domain.

Considering the computational limitations and the proven under prediction of the axial velocity in Chapter 4 section 4.9 it was decided not to focus on the quantitative evaluation of vortex location and position, as no valid conclusion could be drawn from this. However, a qualitative investigation was conducted. The experimental results are limited by the interference of the tunnel with the model and the chosen rig design. The wind tunnel model was not completely steady during the runs at higher α.

As can be seen from the literature review and the findings of this study, multiple geometrical factors affect the behaviour of vortices on the aerodynamic coefficients. The contributions made and the recommendations for further work are discussed in the next chapter.

7.4 Recommendations and Further Work

Based on the findings and limitations of this study it is recommended to conduct further numerical studies at higher Re and Mach numbers to investigate the effect of both on the flow characteristics, especially on vortex onset and vortex development. Furthermore, it is recommended to extend this study to higher α. Especially for higher angles of attack it is suggested to use DES or LES models to more accurately predict VBD onset. Further studies can be conducted to investigate the effects of thickness and maximum thickness change on different flow parameters. Distance of the vortex core from the surface and away from the leading-edge can be determined. However, this requires a higher order turbulence model and sufficient resolution of the numerical grid.

Further it is encouraged to conduct studies using a RSM model as it proved to be promising in this study. Additionally, by using multiple turbulence models conclusions could be drawn as to which modelling parameters cause enhanced results. This could yield to improved turbulence models for external vortical flows.

Also, other flight conditions require investigating, such as sideslip effects as well as a combination of thickness and maximum thickness location with other geometric features, such as camber and twist.

It was shown that the absence of tip taper had a big impact on the performance and longitudinal stability of the delta wing. However, this study was limited to the VFE-2 profile and it would be suggested that further studies are conducted on the biconvex configurations. Also, other variations in geometric parameters such as camber, sweep and leading-edge radius could be added to give the study more breadth.

On the experimental side further studies using PIV and surface pressure tappings are recommended. This way, the numerical findings could be validated further. To investigate whether the effects observed here are universal similar investigations on non-slender delta wings would need to be conducted.

References

Abernethy, R. B., Benedict, R. P., Dowdell, R. B. ASME Measurement Uncertainty. Journal of Fluids Engineering, 107 (161).

Ackerman, M. (2005). Tunnel Turbulence [Microsoft Excel spreadsheet]. University of the West of England, Bristol.

Adams M. C. (1953). Leading-Edge Separation from Delta Wings at Supersonic Speeds. Journal of Aeronautical Sciences, 10 (6).

Ahmadi, G. (2016). ME 639: Advanced Turbulence, Clarkson University. Available from: http://webspace.clarkson.edu/projects/fluidflow/courses/me639/downloads/32_Prandtl.pdf [Accessed 30 May 2017]

Al-Garni, A. Z., Saeed, F., Al-Garni, A. M. (2008). Experimental and Numerical Investigation of 65 Degree Delta and 65/40 Degree Double- Delta Wings. Journal of Aircraft, 45 (1), pp. 71-76.

Anderson, J. D., Jnr (1995). Computational Fluid Dynamics. McGraw-Hill

Anderson, J. D. Jnr. (1999). Aircraft Performance and Design. Cambridge: WCB/McGraw-Hill.

Anderson, J. D. (2011). Fundamentals of Aerodynamics. (5th ed.): McGraw-Hill Education.

Ansys Workshop. (2015). Lecture 7: Mesh Quality & Advanced Topics, Introduction to Ansys Meshing, 12.02. 2015. Available Online: https://www.academia.edu/16970000/MESH_QUALITY_AND_ADVENCED_TOPICS_ANSYS_WORKBENCH_16.0, Accessed: 26.05.2019.

Ansys (2011). Ansys CFX-Solver Theory Guide. Release 14.0.

Anwar-ul-Haque, Khawar, J., Ch, S. R. (2008). Influence of Turbulence Modeling In Capturing Separated Flow Over Delta Wing At Subsonic Speed. Engineering Applications of Computational Fluid Mechanics, 2 (3), pp. 252-263.

Ariff, M., Samlim, M. S., Cheah, S.C. (2009). Wall Y+ Approach for Dealing with Turbulent Flow over a Surface Mounted Cube: Part 1- Low Reynolds Number. 7th International Conference on CFD in the Minerals and Process Industries CSIRO, Melbourne, Australia.

Bahrami, M. (2014). Dimensional Analysis and Similarity. Fluid Mechanics (S09), Simon Fraser University, Available at: http://www.sfu.ca/~mbahrami/ENSC%20283/Notes/Dimensional%20Analysis%20and%20Similarity.pdf, Accessed: 27.06.2017.

Baker, C., Johnson, T., Flynn, D., Hemida, H., Quinn, A., Soper, D., Sterling, M. (2019). Chapter 4- Computational Techniques. Train Aerodynamics, Fundamentals and Applications, pp. 53-71.

Bakker, A. (2002). Lecture 5- Solution Methods, Lecture Notes, Computational Fluid Dynamics (ENGS 150), Dartmouth College. Delivered between 2002-2006.

Barlow, J.B., Rae, W. H., Pope, A. (1999). Low Speed Wind Tunnel Testing. 3rd edition, New York: A Wiley–Interscience Publication.

Bazargan, M., Mohseni, M. (2009). The significance of the buffer zone of boundary layer on convective heat transfer to a vertical turbulent flow of a supercritical fluid. The Journal of Supercritical Fluids, 51 (2), pp. 221-229.

Betyaev, S. K., Brysov, O. P. (1994), Delta Wing in a Subsonic Flow. Mekhanika Zhidkosti I Gaza, 29, pp. 282-284.

Blazek, J. (2005). Computational Fluid Dynamics: Principles and Applications. Second Edition.

Boelens, O. J. (2009). Numerical Solutions for the VFE-2 Configuration on Structured Grids at NLR, The Netherlands. Chapter 27, RTO-TR-AVT-113 Final Report.

Boelens, O.J., Spekreijse, S., Sytsma, H. and de Cock, K. (2009). Numerical Solutions for the CAWAPI Configuration on Structured Grids at NLR, The Netherlands. Chapter 5, RTO-TR-AVT-113 Final Report.

Bolsunovsky, L., Buzoverya, N. P., Gurcvich B. I., Denisov, V. E., Dunacsky, A. I., Shkadov, L.M., Sonin, O. V., Udzhuhu, A. J., Zhurihin, J.P. (2001). Flying Wing Problems and Decisions. Aircraft Design, 4, pp. 193-219.

Bozhkov V.M, Mozol'kov A.S. & Shalaev, V.I. (1975). Visual Study of the Three-Dimensional Flow Diagram around a Delta Wing in Subsonic Stream. Mekhanika Zhidkosti I Gaza. Page 334-338.

Brett, J., Ooi, A. (2014). Effect of Sweep Angle on the Vortical Flow over Delta Wings at an Angle of Attack of 10°. Journal of Engineeing Science and Technology, 9 (6), pp. 768-781.

Broughton, B. A. (1999). Low Speed Wind Tunnel Testing and Data Correction Methods for Aircraft Models in Ground Effect. Master of Mechanical Engineering, University of Pretoria.

Brown, CE, Michael Jr. (1954). WH, Effect of leading-edge separation on the lift of a delta wing. Journal of Aeronautical Science, 21, pp 690- 706.

Budynas, R.G., Nisbett, J.K. (2015) Shingley's Mechanical Engineering Design. Third Edition, McGraw-Hill Education.

Buie, M. (2017). Problem Solving for New Engineers: What Every Engineering Manager Wants You to Know. 1st Edition, Productivity Press.

Burr, K.P., Akylas, T.R., Mei, C.C. 2003. Chapter Two- Two-Dimensional Laminar Boundary Layers, High Re Flows. MIT School Wide Modular Program on Fluid Mechanics. Available Online: http://web.mit.edu/fluids-modules/www/highspeed_flows/ver2/bl_Chap2.pdf, Accessed: 17.02.2019.

Campbell, J.F. (1976). Augmentation of Vortex Lift by Spanwise Blowing. Journal of Aircraft, 13 (9), pp. 727-732.

Cecora, R-D., Radespiel, R., Eisfeld, B., Probst, A. (2015). Differential Reynolds-Stress Modeling for Aeronautics. AIAAJ, 53 (3).

Celik, I. B., Ghia, U., Roache, P. J., Freitas, C. J., Coleman, H., Raad, P. E. (2008). Procedure for Estimation and Reporting of Uncertainty Due to Discretisation in CFD Applications. Journal of Fluids Engineering, 130 (7).

Chegg. (n.d.). Inertia-elasticity Force Ratio. [Online] Available at: https://www.chegg.com/homework-help/definitions/inertia-elasticity-force-ratio-5 [Accessed 13 Nov. 2019].

Chen, H., Wang, J- J. (2014). Vortex structures for flow over a delta wing with sinusoidal leading-edge. Experiments in Fluids, 55 (6).

Chu J., Luckring J. M. (1996). Experimental surface pressure data obtained on 65° delta wing across Reynolds number and Mach number ranges. NASA TM-4645.

Coe Jr, PL, Chambers, JR, Letko, W. (1972). Asymmetric lateral-directional characteristics of pointed bodies of revolution at high angles of attack, NASA TN D-7095.

Colak-Antic. (1971). Visuelle Untersuchungen von Laengswirbeln im Staupunktsgebiet eines Kreiszylinders bei turbulenter Anstroemung. DL M 71 (13).

Coleman, H.W., Steele, W.G. (1989). Experimentation and Uncertainty Analysis for Engineers. John Wiley & Sons, New York.

Coleman, G. N., Sandberg, R. D. (2010). A Primer on Direct Numerical Simulation of Turbulence- Methods, Procedures and Guidelines. Aerodynamics & Flight Mechanics Research Group, Technical Report AFM-09/01a.

Cook, M. V. (2013). Flight Dynamics Principles: A Linear Systems Approach To Aircraft Stability And Control. 3rd Edition. Butterworth-Heinemann

Corda, S. (2017). Introduction to Aerospace Engineering with a Flight Test Perspective. Aerospace Series. 1st ed.. Wiley.

Cousteix, J. (2003). Encyclopedia of Physical Science and Technology. Third Edition, pp. 301-317.

Crippa, S., Rizzi, A. (2006). Initial Steady/Unsteady CFD Analysis of Vortex Flow over the VFE-2 Delta Wing. 25th International Congress of the Aeronautical Sciences.

Crippa, S., Rizzi, A. (2008). Steady, Subsonic CFD Analysis of the VFE-2 Configuration and Comparison to Wind Tunnel Data. AIAA Paper 2008- 397.

Cummings, R. M., Forsythe, J.R, Morton, S. A., Squires, K. D. (2003). Computational challenges in high angle of attack flow prediction. Progress in Aerospace Sciences, 39, pp 369-384.

Cummings, R. M., Schütte, A. (2009). Numerical solutions for the VFE-2 Configuration on Unstructured Grids at USAFA, United States. Chapter 32. AVT-113.

Delery, J.M. (1992). Physics of Vortical Flow. Journal of Aircraft, 29 (5), pp. 856-876.

Delery, J. M. (1994). Aspects of Vortex Breakdown. Progress in Aerospace Sciences, 30, pp. 1-59.

Delery J, Pagan D, Solignac JL. (1987). On the breakdown of the vortex induced by a delta wing. Colloquium on Vortex Control and Breakdown Behavior, Baden, Switzerland, ONERA TP 1987-105.

Dzanic, T., Martinelli, L. (2019). Higher-Order Implicit Large Eddy Simulations of a VFE-2 Delta Wing. AIAA Scitech 2019 Forum, AIAA 2019-0276.

Earnshaw, P. B., Lawford, J. A. (1964). Low Speed Wind Tunnel Experiments on a Series of Sharp-Edges Delta Wings, R & M 3424, Aeronautical Research Council.

Eca, L., Hoekstra, M. (2014). A procedure for the estimation of the numerical uncertainty of CFD calculations based on grid refinement studies. Journal of Computational Physics, 262 (C).

Edwards, R. H. (1954). Leading-edge Separation from Delta Wings. Journal of the Aeronautical Sciences, 21: 134-135.

Eisfeld, B. (2006). Numerical simulation of aerodynamic problems with a Reynolds stress turbulence model. Notes on Numerical Fluid Mechanics and Multidisciplinary Design (NNFM). pp.413-421.

Elle, B. J. (1958). An investigation at low speed of the flow near the apex of thin delta wings with sharp leading-edges, Reports and Memoranda 3176, Aeronautical Research Council.

Erickson, G. E. (1982). Water-Tunnel Studies of Leading-edge Vortices. Journal of Aircraft, 19 (6), pp. 442-448.

Ericsson, L.E., King, H.H.C. (1992). Effect of Leading-Edge Geometry on Delta Wing Unsteady Aerodynamics. Journal of Aircraft. 30 (5), pp. 793 – 795.

Ericsson, L. E. (1984). The fluid mechanics of slender wing rock. Journal of Aircraft, 21(5), 322–328. doi:10.2514/3.44967

Fink, P.T. (1966). Some Early Experiments on Vortex Separation, Part 1: Some Low Speed Aerodynamic Properties of Cones. Aeronautical Research Council Reports and Memoranda, No. 3489.

Flierl, G., Ferrari, R. (2007). 'Chapter 5: Isotropic homogeneous 3D turbulence', lecture notes distributed in the topic 12.820 Turbulence in the ocean and atmosphere. MIT, Massachusetts in Spring 2007.

FLUENT Theory Guide. (2009). Wall Boundary Conditions. ANSYS Inc. Release 12.0.

Frink, N. T. (2014) Stability and Control CFD Investigation of a Generic 53° Swept UCAV Configuration. 32nd AIAA Applied Aerodynamics Conference, AIAA 2014-2133.

Fritz, W. (2008). Numerical Solutions for the VFE-2 Configurations on Structured Grids at EADS-MAS, Germany. RTO-TRAVT-113, Chapter 25, pp. 25-1 – 25-21.

Fritz, W. (2009). Numerical Solutions for the CAWAPI Configuration on Unstructured Grids at EADS-M. Germany, Chapter 8, RTO-TR-AVT-113 Final Report.

Fritz, W. (2013). Numerical simulation of the peculiar subsonic flow-field about the VFE-2 delta wing with rounded leading-edge. Aerospace Science and Technology. 24 (1), pp. 45-55.

Fritz, W., Cummings, R. M. (2008). What was learned from the numerical simulations for the VFE-2?. AIAA Paper 2008-0399.

Furman, A., Breitsamter, C. (2008). Experimental Investigations on the VFE-2 Configurations at TU Munich, Germany. RTO-TR-AVT-113.

Gates, S. B. (1949). Notes on the transonic movement of wing aerodynamic centre. R&M 2785.

Gatsis, J. (2000). Investigating the Spalart- Allmaras Turbulence Model. University of Toronto, Available from: http://oddjob.utias.utoronto.ca/john/courses/vis/vis_report.pdf [Accessed 31 May 2017]

Gatski, T. B., Hussaini, M. Y., Lumley, J. L. (1996) Simulation and Modeling of Turbulent Flows. Volume 1, Oxford Press.

Gerasimov, A. (2006). Modeling Turbulent Flows with FLUENT. Europe, ANSYS, lnc.

Goertz, S. (2005). Realistic Simulations of Delta Wing Aerodynamics Using Novel CFD Methods. PhD Dissertation KTH Sweden.

Goertz, S. (2009). Unsteady Euler and Detached-Eddy Simulation of a Full-Span ONERA 70° Delta Wing. Chapter 12, RTO-TR-AVT-080 Final Report, U.S.A.

Gordnier, R. E. (1990). Computation of a Kelvin-Helmholtz Instability for Delta Wing Vortex Flows. Wright Laboratory Final Report WL-TR-91-3098.

Gordnier, R. E., Visbal, M.R. (2003). Higher-Order Compact Difference Scheme Applied to the Simulation of a Low Sweep Delta Wing Flow. 41st Aerospace Sciences Meeting and Exhibit, Aerospace Sciences Meetings.

Greenwell, D. I. (2001). Pitfalls in the Interpretation of Delta Wing Flow Visualisation. NATO RTO Symposium on Advanced Flow Management, RTO MP-069(I)-(SYA)-05, Loen, Norway.

Grecu, I. S., Bucur, D. M., Dunca, G., Panaitescu, V. N., Cervantes, M. J. (2017). Implementation of the standard wall function in numerical computation software. International Conference on Energy and Environment.

Gresham, N. T., Wang, Z., Gursul, I. (1993). Vortex Dynamics of Free-to-Roll Slender and Nonslender Delta Wings. Journal of Aircraft, 47 (1), pp. 292-302.

Groves, C. E., Ilie, M., Shallhorn, P. A. (2014). Numerical Uncertainty Analysis for CFD using Student T-Distribution. AIAA SCITECh Conference, USA.

Gudmundsson, S. (2014). General Aviation Aircraft Design: Applied Methods and Procedures. 1st Edition. Oxford: Butterworth- Heinemann. Chapter 9, pp. 340-345.

Gursul, I. (1994). Unsteady Flow Phenomena over Delta Wings at High Angle of Attack. AIAA Journal, 32 (2), pp.225-231.

Gursul, I. (2004). Recent Developments in Delta Wing Aerodynamics. Aeronautical Journal, pp. 437–452.

Gursul, I. (2005). Review of Unsteady Vortex Flows over Slender Delta Wings, Journal of Aircraft, 42 (2), pp. 299-319.

Gursul, I., Gordnier, R., Visbal, M. (2005). Unsteady Aerodynamics of Nonslender Delta Wings. Progress in Aerospace Sciences, 41, pp. 515-557.

Gursul, I., Vardaki, E., Wang, Z. (2006). Active and Passive Control of Reattachment on Various Low-Sweep Wings. AIAA-2006-506, 44th AIAA Aerospace Sciences Meeting and Exhibit, Reno, NV.

Gursul, I.; Wang, Z., Vardaki, E. (2007). Review of flow control mechanisms of leading-edge vortices. Progress in Aerospace Sciences, 43 (7-8), pp. 246-270.

Hall, M. G. (1961). A theory for the core of a leading-edge vortex. Journal of Fluid Mechanics, 11(02), 209.doi:10.1017/s0022112061000470

Hall, N. (2015). Boundary Layer, Available Online: https://www.grc.nasa.gov/www/k-12/airplane/boundlay.html, Accessed: 17.02.2019.

Hall, N. (2018). Speed of Sound. Available Online: https://www.grc.nasa.gov/www/k-12/airplane/sound.html, Accessed: 30.05.2019.

Hantrais- Gervois, J-L. (2012). A Methodology to Derive Wind Tunnel Wall Corrections from RANS Simulations. 5th Symposium on Integrating CFD and Experiments in Aerodynamics.

Harrell FE. Jr., Lee, KL, Matchar, DB, Reichert, TA. (1985). Regression models for prognostic prediction: advantages, problems, and suggested solutions. Cancer Treatment Reports, 69 (10), pp.1071-1077.

Hemsch, M. J., Luckring, J. M. (1990). Connection between Leading-Edge Sweep, Vortex Lift, and Vortex Strength for Delta Wings. Journal of Aircraft, 27, pp. 473-475.

Henderson WP. (1976). Effects of Wing Leading-Edge Radius and Reynolds Number on Longitudinal Aerodynamic Characteristics of Highly Swept Wing-Body Configurations at Subsonic Speeds. NASA TN D-8361, Washington D. C., USA.

Hengartner, N. (1997). Linear regression, Introductory to Data Analysis. Yale Univeisity, Available Online: http://www.stat.yale.edu/Courses/1997-98/101/linreg.htm, Accessed: 31.01.2019.

Hibbeler, R. C. (2012). Engineering Mechanics: Statics. 13th Edition. Prentice Hall.

Hitzel, S. M., Boelens, O. J., van Rooj, M., Hoevelmann, A. (2015). Vortex Development on the AVT-183 Diamond Wing Configuration- Numerical and Experimental Findings. Aerospace Science and Technology, 57, pp.90-102.

Hoerner, S. F. (1985). Lift Characteristics of Foil Sections. In: Fluid-Dynamic Lift: Practical Information on Aerodynamic and Hydrodynamic Lift. 2nd Edition New York City: Liselotte A. Hoerner, pp. 2-12.

Honkan, A., Andreopoulos, J. (1997). Instantaneous Three-Dimensional Vorticity Measurements in Vortical Flow over a Delta Wing. AIAA Journal, 35, pp. 1612- 1620.

Houghton, E. L., Carpenter, P. W., Collicott, S. H., Valentine, D. T. (2013). Aerodynamics for Engineering Students. 6th Edition. Butterwort-Heinemann.

Huang, X. Z., Hanff, E. S. (1998). Flow Physics of Leading-Edge Vortex-Breakdown. AIAA Paper 98-31536.

Huang, A, Folk, C., Silva, C., Christensen, B., Chen, Y., Ho, C.M., Jiang, F., Grosjean, Tai, Y.C., Lee, G.B., Chen, M., Newbern, S. (2001). Application of MEMS Devices to Delta Wing Aircraft: From Concept Development to Transonic Flight Test. 39th AIAA Aerospace Sciences Meeting & Exhibit. AIAA 2001-0124.

Huang, X.Z., Verhaagen, N.G. (2009). Chapter 1- Introduction and Highlights. RTO Technical Report TR-AVT-080, Vortex Breakdown over Slender Delta Wings, NATO.

Hunt, J. C. R., Wray, A. A., Moin, P. (1988). Eddies, stream, and convergence zones in turbulent flows. Centre for Turbulence Research Report CTR-S88, pp. 193-208.

Hummel, D. (1965). Untersuchungen ueber das Aufplatzen der Wirbel an schlanken Deltafluegeln. Zeitung fuer Flugwissenschaften, 13 (5).

Hummel, D. (1978). On the Vortex Formation over a Slender Wing at Large Incidence. AGARD CP-247, High Angle of Attack Aerodynamics.

Hummel, D., Oelker, H.C. (1989). Vortex Interference Effects on Close-Coupled Canard Configuration at Low Speed. Aerodynamics of Combat Aircraft Controls and of Ground Effects, CP-465, AGARD, pp. 7-1 to 7-18.

Hummel, D. (2004). Effects of Boundary layer Formation on the vortical Flow above Slender Delta Wings. RTO specialist Meeting on Enhancement of NATO military Flight Vehicle Performance by Management of Interacting Boundary Layer transition and Separation. Meeting Proceedings RTO-MPAVT- 111, pp. 30-1 to 30-2.

Hummel, D. (2006). The Second International Vortex Flow Experiment (VFE-2): Objectives and first results. Proceedings of the Institution of Mechanical Engineers Part G, Journal of Aerospace Engineering, 220 (6).

Hummel, D. (2007)). The International Vortex Flow Experiment 2 (VFE-2): Objectives and Present Status. 25th AIAA Applied Aerodynamics Conference, Miami, Florida.

Hummel, D. (2008). The Second International Vortex Flow Experiment (VFE-2): Results of the first phase 2003- 2008. 26th International Congress of the Aeronautical Sciences.

Hummel, D. (2009). The second International Vortex Flow Experiment (VFE-2) Objectives and First Results. 26th International Congress of the Aeronautical Sciences, Anchorage, Alaska, USA.

Hummel, D., Luckrin, J.M. (2008). What was learned from the new VFE-2 experiments?. 46th AIAA Aerospace Sciences Meeting and Exhibit, Reno, Nevada.

Hummel, D., Redeker, G. (2003). A New Vortex Flow Experiment for Computer Code Validation. RTO AVT Symposium on “Advanced Flow Management: Part A- Vortex Flows and High Angle of Attack for for Military Vehicles, Loen, Norway.

Hummel, D., Srinivasan, P.S. (1967). Vortex breakdown effects on the low speed aerodynamic characteristics of slender delta wings in symmetrical flow. Journal of the Aeronautical Society, 71, pp. 319-22.

James, G., Witten, D., Hastie, T., Tibshirani, R. (2013). An Introduction to Statistical Learning. Springer Science & Business Media.

Jiang, F., Lee, G.B., Tai, Y.C., Ho, C.M. (2000). A flexible Micromachine based Shear Stress sensor array and its application to separation point detection. Sensors and Actuators, 79, pp. 194-203.

Johnson, D. A., and King, L. S. (1985). A Mathematically Simple Turbulence Closure Model for Attached and Separated Turbulent Boundary Layers. AIAA Journal, 23 (11), pp. 1684–1692.

Jones, R.T., Cohen, D. (1960). High Speed Wing Theory. Princeton University Press, Princeton, New Jersey, USA.

Jumper, E.J., Nelson, R. C., Cheung, K. (1993). A Simple Criterion for Vortex Breakdown. AIAA-93-0866.

Jung, D. W., Lowenberg, M. H. (2005). Stability and control assessment of a blended-wing-body airliner configuration. AIAA Atmospheric Flight Mechanics Conference and Exhibition. San Francisco, California.

Kamar, S. J., Wissink, A. M.., Sanaran, V., Jameson, A. (2011). Feature-driven Cartesian adaptive mesh refinement for vortex-dominated flows. Journal of Computational Physics. 230 (16), pp. 6271- 6298.

Kegelman, J., Danehy. (2010). Advanced Capabilities for Wind Tunnel Testing in the 21st Century. American Institute of Aeronautics and Astronautics.

Kegelman, J., Roos, F. (1989). Effects of Leading-Edge Shape and Vortex Burst on the Flowfield of a 70 Degree Sweep Delta-Wing. AIAA Paper 89-0086, 27th Aerospace Sciences Meeting, Reno, NV, USA.

Kirby, D. A. (1974). Low-Speed Wind Tunnel Measurements of the Lift, Drag and Pitching Moment of a Series of Cropped Delta Wings, Aerodynamics Department, R.A.E. Farnborough, Reports and Memoranda No. 3744.

Kirby, D. A., Kirkpatrick, D. L. I. (1969). An experimental investigation of the effect of thickness on the subsonic longitudinal stability characteristics of delta wings of 70 degree sweep-back, Aerodynamics Department, R.A.E. Farnborough, Reports and Memoranda No. 3673.

Kirby, D. A., Kirkpatrick, D. L. I. (1971). An experimental investigation of the subsonic longitudinal stability characteristics of five slender-wing models with gothic planforms, Aerodynamics Department, R.A.E. Farnborough, Reports and Memoranda No. 3720.

Koelzsch, A., Breitsamter, C. (2014). Vortex-Flow Manipulation on a Generic Delta-Wing Configuration. Aerospace research Central, 51 (5).

Kohlman, D. L., Wentz, JR, W. H. (1971). Vortex breakdown on slender sharp-edged wings. Journal of Aircraft, 8 (3), pp. 156-161.

Kolar, V. (2007). Vortex identification: New requirements and limitations. International Journal of Heat and Fluid Flow, pp. 638-652.

Konrath, R., Klein, C., Engler, R.H., Otter, D. (2006a). Analysis of PSP Results Obtained for the VFE-2 65° Delta Wing Configuration at Sub- and Transonic Speeds. 44th AIAA Aerospace Sciences Meeting and Exhibit.AIAA 2006-60.

Konrath, R., Schröder, A., Kompenhans, J. (2006b). Analysis of PIV Results Obtained for the VFE-2 65° Delta Wing Configuration at Sub- and Transonic Speed. 24th Applied Aerodynamics Conference. AIAA 2006-3003.

Konrath, R., Klein, C., Henne, U., Sachs, W., Wiedemann, A., Otter, D. Schroder, A., Agocs, J., Mattner, M., Egami, Y., Fey, U. & Groot, K.D. (2008a). The International Vortex Flow Experiment 2, DNW-KKK. DNW Report, Goettingen, Germany.

Konrath, R., Klein, C., Schröder, A., Groot, K.D. (2008b). PSP and PIV Investigations on the VFE-2 Configuration in Sub- and Transonic Flow. 46th AIAA Aerospace Sciences Meeting and Exhibit, Reno, Nevada.

Kralik, J. (2016). CFD Simulation of Air Flow over an Object with Gable Roof, Revised with y+ Approach. Transactions of the VŠB – Technical University of Ostrava, De Gruyter Open, pp. 85- 94.

Krasnov, N. F. (1970). Aerodynamics of bodies of revolution. American Elsevier Publishing Company, Inc. New York.

Küchemann, D. (1972). Standard: Assessment of Experimental Uncertainty With Application to Wind Tunnel Testing. AIAA S-071A-1999.

Küchemann, D. (1978). The Aerodynamic Design Of Aircraft: A Detailed Introduction To The Current Aerodynamic Knowledge And Practical Guide To The Solution Of Aircraft, Technology, Engineering, And Social Studies. Pergamon Press.

Kulfan, R. M. (1979). Wing Airfoil Shape Effects on the Development of Leading-edge Vortices. AIAA Atmospheric Flight Mechanics Conference, Colorado, USA.

Kulkarni, S. S., Chapman, C., Shah, H. (2016). Computational Fluid Dynamics (CFD) Mesh Independency Study of a Straight Blade Horizontal Axis Tidal Turbine. Conventry University's Repository.

Kundu, P. K., Cohen, I. M., Dowling, D. R. (2016). Turbulence. Fluid Mechanics, pp.603-607.

Kurun, S. (2007). Experimental Investigations on the VFE-2 Configuration at TUBITAK-SAGE, Turkey. RTO Technical Report, TR-AVT-113. Chapter 23.

Kuzmin, D. (2010). A Guide to Numerical Methods for Transport Equation. Friedrich-Alexander-Universität Erlangen-Nürnberg. Available Online http://www.mathematik.uni-dortmund.de/~kuzmin/Transport.pdf, Accessed: 16.02.2019.

Kwak, D., & Nelson, R. (2010). Vortical Flow Control over Delta Wings with Different Sweep Back Angles Using DBD Plasma Actuator. 5th Flow Control Conference.doi:10.2514/6.2010-4837

Kwaśniewski, L. (2009). On practical problems with verification and validation of computational models. Archives of Civil Eng. LV (3), pp. 323–346.
Kwasniewski, L. (2013) Application of grid convergence index in FE computation. Bulletin of the polish academy of sciences, Technical Sciences, 6 (1), pp. 123-128.

Lamar, J. E. (2002). Understanding and Modeling Vortical Flows to Improve the Technology Readiness Level of Military Aircraft. NATO RTO Advanced Vehicle Technology Panel AVT-E-10/RTG.

Lamar, J. E., Abdol-Hamid, K. S. (2009). Numerical Solutions for the CAWAPI Configuration on Unstructured Grids at NASA LARC, United States. RTO-TR-AVT-113, Chapter 15.

Lamar, J. E., Clifford, J.O. (2009). The cranked arrow wing aerodynamics project (CAWAP) and its extension to the international community as CAWAPI: Objectives and Overview. RTO-TR-AVT-113, Chapter 3.

Lambourne, N. C., Bryer, D. W. (1962). The Bursting of Leading-Edge Vortices- Some Observations and Discussions of the Phenomenon. Reports and Memoranda 3282, Aeronautical research Council.

Lamar, J. E. (1968). A Modified Multhopp Approach for Predicting Lifting Pressures and Camber Shape for Composite Planforms in Subsonic Flow. NASA TN D-4427.

Lamar, J. E. (1976). Prediction of Vortex Flow Characteristics of Wings at Subsonic and Supersonic Speeds. Journal of Aircraft, 13(7), pp. 490-494.

Lamar, J.E., Campbell, J.F. (1984). Vortex Flaps – Advanced Control Devices for Supercruise Fighters. Aerospace America, pp. 95-99.

Le Moigne, Y.; Rizzi, A. (2009). Grid Study for Euler Simulations of a 70° Delta Wing with the unstructured Flow Solver EDGE, Sweden. RTO-TR-AVT-080 Final Report, Chapter 15.

LeRoy, J. F., Mary, I., Rodriguez, O. (2003). CFD Solutions of a 70° Delta Wing Flows. 21st AIAA Applied Aerodynamics Conference.

LeRoy, J.-F., Rodriguez, O. (2009). RANS Solutions of 70° Delta Wing in Steady Flow, ONERA, France. RTO-TR-AVT-080 Final Report, Chapter 16.

LeRoy, J. F., Rodriguez, O., Kurun, S. (2007). Experimental and CFD Contribution to Delta Wing Vortical Flow Understanding. AIAA Paper 2008-0380.

Legendre, R. (1952). Ecoulement Au Voisinage De La Ponte Avant D'Une Aile A Forte Fleche Aux Incidences Moyennes. La Recherche Aeronautique Bulletin Bimestriel, No. 30.

Limb, B.J., Dalon, Work, D. G., Hodson, J., Smith, B. L. (2017). The Inefficacy of Chauvenet's Criterion for Elimination of Data Points. Journal of Fluids Engineering, 139 (5).

Ljungskog, E., Sebben, S., Broniewcz, A. (2019). Flow Angularity Investigation in an Automotive Slotted Wall Wind Tunnel. Recent Advances in Vehicle Aerodynamics, 12 (23).

Luckring, J. M. (2002). Reynolds Number and Leading-Edge Bluntness Effects on a 65 degree Delta Wing at Transonic Speeds. AIAA-2002-0419, 40th AIAA Aerospace Sciences Meeting & Exhibit, Reno, NV, USA.
https://archive.org/stream/nasa_techdoc_20040139861/20040139861#page/n1/mode/2up

Luckring, J. M. (2009). Experimental Investigation of the Flow about a 65° Delta Wing in the NASA Langley National Transonic Facility. AVT-080 Final Report, Chapter 4, pp.4-1 – 4-8.

Luckring, J. M. (2010). A Survey of Factors Affecting Blunt Leading-Edge Separation for Swept and Semi-Slender Wings. 28th AIAA Applied Aerodynamics Conference, Chicago, Illinois.

Luckring, J. M., Boelens, O. J. (2010). A Reduced-Complexity Investigation on Blunt-Leading-Edge Separation Motivated by UCAV Aerodynamics. AiAA 53rd Aerospace Sciences Conference. Kissimmee. USA.

Luckring, J. M., Hummel, D. (2008), What was learned from the new VFE-2 Experiments. 46th AIAA Aerospace Sciences Meeting and Exhibit. Reno, Nevada.

Majumdar, B. (2015). Fluid Mechanics with Laboratory Manual. PHI Learning. 2nd Edition.

Mangler, K.W., Smith, J.H.B. (1959). A Theory of the Flow Past a Slender Delta Wing with Leading-edge Separation. Proceedings of Royal Society, 251, pp. 200- 217.

Martins, R. S., Pereira, A. S., Mompean, G., Thais, L., Thompson, R. L. (2016). An objective perspective for classic flow classification criteria. Comptes Rendus Mecanique. 344 (1), pp. 52-59.

Menke, M., Yang, H., Gursul, I. (1999). Experiments om the Unsteady Nature of Vortex Breakdown over Delta Wings. Experiments in Fluids, 27 (3), pp. 262-272.

Menter, F. R. (1993). Zonal Two Equation k–ω Turbulence Models for Aerodynamic Flows. AIAA Paper 93-2906.

Miau, J. J., Kuo, K. T., Liu, W. H., Hsieh, S. J., Chou, J. H. (1995). Flow Development Above 50-Deg Sweep Delta Wing with Different Leading-Edge Profiles. Journal of Aircraft, 32 (4), pp. 787-794.

Mitchell, A., Morton, S. Forsythe, J. (2006). Analysis of Delta Wing Vortical Substructures using Detached-Eddy Simulation. AIAA Journal, 44 (5).

Moioli, M., Breitsamter, C., Sorensen, K.A. (2018). Turbulence Model Conditioning for Vortex Dominated Flows Based on Experimental Results. 31st Congress of the International Council of the Aeronautical Sciences. Belo Horizonte, Brasil.

Morton, S., Forsythe, J., Mitchell, A., Hajek, D. (2002). DES and RANS Simulations of Delta Wing Vortical Flow. 40th AIAA Aerospace Sciences Meeting & Exhibit.

Muir, R. E., Arredondo-Galeana, A., Viola, I. M. (2017). The Leading-Edge Vortex of swift Wing-Shaped Delta Wings. Royal Society Open Science, 4 (8).

Nangia, R., Palmer, M., Doe, R. (2002). A study of supersonic aircraft with thin wings of low sweep. 40th AIAA Aerospace Sciences Meeting & Exhibit. doi:10.2514/6.2002-709

Nangia, R. (2003). Applying Vortex Breakdown Empiricisms to Predict Aerodynamic Characteristics in Symmetric & Asymmetric Situations. AIAA Applied Aerodynamics Conference & Exhibit. Florida, USA.

Nasir, R.E., Kuntjoro, W., Wisnoe, W. (2014). Aerodynamic, Stability and Flying Quality Evaluation on a Small Blended Wing-body Aircraft with Canard Foreplanes. Procedia Technology, 15, pp. 783-791.

Nelson, R. C., Pelletier, A. (2003). The unsteady aerodynamics of slender wings and aircraft undergoing large amplitude maneuvers. Progress in Aerospace Sciences, 39, pp185- 248.

Nelson, R. C., Visser, K. D. (1990). Breaking Down the Delta Wing Vortex. AGARD Symposium on Vortex Flow Aerodynamics. Scheveningen, The Neterhlands.

Nguyen, H. T., Rogers, G. S. (1989). Fundamentals of Mathematical Statistics: Probability for Statistics V.1. Springer Verlag.

Ning, A. (2017). Matching Mach and Reynolds Number. Flight, Optimization and Wind Laboratory, Brigham Young University, Utah. Available at: http://flowlab.groups.et.byu.net/me412/hw/ReMmatching.pdf. [Accessed: 30.06.2017]

Nosakhare, U. H., Bright, A. F. (2017). Evaluation of Techniques for Univariate Normality Test Using Monte Carlo Simulation, American Journal of Theoretical and Applied Statistics, 6 (5-1), pp. 51-61.

O'Neil, P., Roos, F., Kegelmann, J., Barnett, R., Hawk, J. (1989). Investigation of Flow Characteristics of a Developed Vortex. Final Report NADC-89114-60, McDonell Aircraft Company

Ol, M. V. (2011). An Experimental Investigation of Leading-edge Vortices and Passage to Stall of Nonslender Delta Wings. RTO-MP-069(I).

Ozgoren, M. (2002). Vortex structure on a delta wing at high angle of attack. AIAA Journal. 40 (2), pp. 285-292.

Pallant J. (2007). SPSS survival manual, a step by step guide to data analysis using SPSS for windows. 3 ed. Sydney: McGraw Hill. pp. 179–200.

Pashilkar, A.A. (2001). Surface Pressure Model for Simple Delta Wings at High Angle of Attack. Sâdhana, 26 (6), pp. 495-515.

Payne, F. M., Ng, T. T., Nelson, R. C. (1986). Vizualisation and Flow Surveys of the leading-edge Vortex Structure on Delta Wing Planforms. AIAA Paper 86-0303, 24th Aerospace Sciences Meeting, Reno, NV, USA.

Payne, F. M., Ng, T. T., Nelson, R. C. (1987). Experimental Study of the Velocity Field on a Delta Wing. AIAA paper 87-1231, AIAA, 19th Fluid Dynamics, Plasma Dynamics and Lasers Conference, Honolulu, HI, USA.

Peake, D.J., Tobak, M. (1980). Three-Dimensional Interactions and Vortical Flows with Emphasis on High Speeds. AGARD-AG-252.

Peckham, D.H., Atkinson, S.A. (1958). Low-Speed Wind-Tunnel Tests on a Series of Uncambered Slender Pointed Wings with Sharp Edges. Aeronautical Research Council Technical Report No. 3186.

Peckham, D.H., Atkinson, S.A. (1960). Preliminary Results of Low Speed Wind Tunnel Tests on a Gothic Wing of Aspect Ratio 1.0. Aeronautical Research Council Technical Report. R21836.

Pershing, B. (1964). Separated Flow Past Slender Delta Wings with Secondary Vortex Simulation. TDR-269(4560-10)-4.

Phoreman, J., Saephan, S., Vander Kam, J. C. (2000). Determination of Turbulence Level in the UC Davis Aeronautical Wind Tunnel.

Pitsch, H. (2014). Turbulence. CEFRC Combustion Summer School, Princeton. Available Online at: https://www.princeton.edu/cefrc/Files/2014%20Lecture%20Notes/Pitsch/Lecture7_Turbulence_2014.pdf, Accessed 24.05.2017.

Polhamus, E. C. (1966). A Concept of the Vortex Lift of Sharp-Edge Delta Wings based on a Leading-Edge-Suction Analogy, NASA Technical Note, NASA TN D-3767.

Polhamus, E. C. (1971). Predictions of Vortex-Lift Characteristics by a Leading-Edge Suction Analogy. Journal of Aircraft. 8 (4). pp. 193-199.

Rae, W. H., Pope, A. (1984). Low-Speed Wind Tunnel Testing. 2nd Edition, John Wiley & Sons, United States.

Raymer, D., P. (1992). Aircraft Design: A Conceptual Approach. AIAA Educational Series, Washington DC.

Rediniotis, O. K., Stapountzis, H., Telionis, D. P. (2012). Vortex Shedding over Delta Wings. AIAA Journal, 28 (5).

Renac F., Barberis D., Molton P. (2005). Control of Vortical Flow over a Rounded Leading-Edge Delta Wing. AIAA Journal. 43 (7), pp. 1409-1417.

Richardson, L. F. (1910). The approximate arithmetical solution by finite differences of physical problems involving differential equations, with an application to the stresses in a masonry dam. Trans. Roy. Soc. London, Ser. A, 210, pp. 307-357.

Ridder, S-O. (1971). On the Induced Drag of Thin Plane Delta Wings, An Experimental Study of the Spanwise Distribution of the Leading-edge Forces at tow Speeds. KTH AERO TN-57, Stockholm.

Rinoie, K. (1996a). Low Speed Aerodynamics Characteristics of 60° Rounded Leading-Edge Delta Wing with Vortex Flaps: Part 1: 457 mm Span Delta Wing. Cranfield University. COA Report No. 9611.

Rizzi, A., Engquist, B. (1987). Selected Topics in the Theory and Practice of Computational Fluid Dynamics. Journal of Computational Physics, 72 (1).

Roache, P. J. (1998). Verification and validation in computational science and engineering. Computing in Science Eng.1, pp. 8–9.

Rodriguez, O. (2008). Experimental Investigation on the VFE-2 Configuration at ONERA, France. RTO-TR-AVT-113, Chapter 20.

Roj, C. J. (2003). Grid Convergence Error Analysis for Mixed-Order Numerical Schemes. AIAA Journal, 41 (4).

Sack, A. H., Lundberg, R. E., Hanson, C.W. (1967). A Theoretical Investigation of the Aerodynamics of Slender Wing-Body Combinations Exhibiting Leading-edge Separation. NASA CR-719.

Saephan, S., Van Dam, C. P. (2008). Simulation of the tumbling behaviour of tailless aircraft. 24th Applied Aerodynamics Conference. San Francisco, California.

Sahini, D. (2004). Wind Tunnel Blockage Corrections: A computational study. Master Thesis in Mechanical Engineering, Texas Tech University, available online: http://edge.rit.edu/edge/P14414/public/Reference%20Documents/Wind%20Tunnel%20Blockage%20Corrections.pdf, Accessed: 22.01.2019.

Saha, S., Majumdar, B. (2012). Flow visualization and CFD simulation on 65° delta wing at subsonic condition. Procedia Engineering 38, pp. 3086-3096.

Salim, M. Cheah, S.C. (2009). Wall y+ Strategy for Dealing with Wall-Bounded Turbulent Flows. Proceedings of the International MultiConference of Engineers and Computer Scientists Volume 2, March, Honkong.

Schiavetta, L. (2007). Evaluation of URANS and DES Predictions of Vortical Flows over Slender Delta Wings. Thesis submitted to the Faculty of Engineering in fulfilment of the requirements for the degree of Doctor of Philosophy. University of Glasgow.

Schneider, A., Hommel, G., Blettner, M. (2010). Linear Regression Analysis- Part 14 of a Series on Evaluation of Scientific Publications. Deutsche Aerzteblatt International, 107 (44), pp. 776-782.

Schütte, A., Hummel, D., Hitzel, S. M. (2010). Numerical and experimental analyses of the vorical flow around the SACCON configuration. 28th AIAA Applied Aerodynamics Conference, Chicago, Illinois.

Schütte, A., Boelens, O. J., Oehlke, M., Jirásek, A., Loeser, T. (2012). Prediction of the flow around the X-31 aircraft using three different CFD methods. Aerospace Science and Technology, Vo.20, No.1, pp 21-37.

Schütte, A., Hummel, D., Hitzel, S. M. (b) (2012). Flow Physics Analyses of a Generic Unmanned Combat Aerial Vehicle Configuration. Journal of Aircraft, Vol. 49, No. 6, pp 1638-1651.

Schütte, A., Cummings, R. M., Stern, F., Toxopeus, S. (c) (2012). Summary of AVT-161, Lessons learned and the way ahead. Chapter 26, RTO-AVT-161.

Schütte, A., Luedeke, H. (2010). Numerical Solutions for the VFE-2 Configuration on Unstructured Grids at DLR, Germany. Final Report AVT-113, Chapter 31.

Schwer, L. E. (2008). Is your mesh refined enough? Estimating discretization error using GCI. 7th LS DYNA Anwenderforum I-I-45-54, CD-ROM.

Schwer, L.E. (2007). Guide for Verification and Validation in Computational Solid Mechanics. The American Society of Mechanical Engineers.

Sforza, P. M. (2014). Commercial Airplane Design Principles. Butterworth-Heinemann.

Sharov, D., Nakahashi, K. (1998). Hybrid Prismatic/Tetrahedral Grid Generation for Viscous Flow Applications. AIAA Journal, 36 (2), p. 157.

Simpson, R. (2011). F-14 Wind Tunnel Experiment. Aerospace and Ocean Engineering, Available Online: http://www.dept.aoe.vt.edu/~simpson/aoe4154/f14lab.pdf, Accessed: 28.01.2019.

Skillen, A. (2011). Shear Stress Transport Model. Manchester University. Available Online: http://cfd.mace.manchester.ac.uk/twiki/bin/view/Saturne/SSTMode. [Accessed: 18.02.2019]

Slater, J. W. (2008). Examining Spatial (Grid) Convergence. NPARC Alliance CFD Verifiction and Validation Web Site. Available Online:

http://www.grc.nasa.gov/WWW/wind/valid/tutorial/spatconv.html, Accessed: 23.01.2019.

Sodja, J. (2007). Turbulence models in CFD. University of Ljubljana. Available from: http://www-f1.ijs.si/~rudi/sola/Turbulence-models-in-CFD.pdf [Accessed 31 May 2017]

Soltani, M. R., Bragg, M. B. (1990). Measurements on an Oscillating 70-Deg Delta Wing in Subsonic Flow. Journal of Aircraft, 27 (3), pp. 211-217.

Spalart, P. R., Allmaras, S. R. (1992). A One-Equation Turbulence Model for Aerodynamic Flows. AIAA Paper 92-0439.

Spalart, P. R., Jou, W.-H., Stretlets, M., Allmaras, S.R. (1997). Comments on the Feasibility of LES for Wings and on the Hybrid RANS/LES Approach. Advances in DNS/LES. Proceedings of the First AFOSR International Conference on DNS/LES

Spanier, J. and Oldham, K. B. (1987)."The Error Function erf(x) and Its Complement erfc(x)" and "The exp(x) and erfc(sqrt(x)) and Related Functions.". An Atlas of Functions. Washington, DC: Hemisphere, pp. 385-393 and 395-403.

Stallings RL. (1986). Low aspect ratio wings at high angles of attack. In: Progress in astronautics and aeronautics. Tactical missile Aerodynamics, 104. New York: AIAA, Chapter 3.

Stanbrook A, Squire L. C. (1964). Possible types of flow at swept leading-edges. The Aeronautical Quarterly, 15: 72–82.

Taylor, G. S., Gursul, I. (2004). Buffeting flows over a low-sweep delta wing. AIAA Journal, 42(9), 1737-1745.

Taylor, G., Schnorbus, T., Gursul, I. (2003). An Investigation of Vortex Flows over Low Sweep Delta Wings. 33rd AIAA Fluid Dynamics Conference and Exhibit. doi:10.2514/6.2003-4021.

Thompson, J. F., Warsi, Z. U. A., Mastin, C. W. (1985). Numerical Grid Generation. Elsevier Science Publishers.

Tu, J., Yeoh, G.-H., Liu, C. (2018). CFD Mesh Generation: A Practical Guideline. Computational Fluid Dynamics: A Practical Approach (Third Edition), 125-154, Butterworth Heinemann.

Tuling, S., Kanaa, Z. (2017). UWE Subsonic Tunnel Instrument Uncertainties (2017). Technical Report. FET-EDM-SUB-REP-0003.

Vallespin, D.; Boelens, O., Badrock, K. J. (2012). SACCON CFD Simulations using Structured Grid approaches. 28th AIAA Applied Aerodynamics Conference. Chicago, Illinois.

Vengadesan, D. (2015). Week 6 Module 3: Foundation of CFD, lecture notes, NPTEL Online Certification Course, Available Online at: https://www.youtube.com/watch?v=nQNE9nmK1XQ, Accessed 24.04.2017.

Verhaagen, N.G., Jenkins, L.N., Kern, S.B., Washburn, A.E. (1995). A Study of the Vortex Flow over a 76/40-deg Double-Delta Wing. AIAA 95-0650, 33rd Aerospace Sciences Meeting and Exhibit, Reno, NV, USA.

Verhaagen, N. G. (2002). Effects of Reynolds Number on Flow over 76/40- Degree-Double-Delta Wings. Journal of Aircraft, 39 (6).

Visbal, M. R.; Gordnier, R. E. (2003). On the Structure of the Shear Layer Emanating from a Swept Leading-edge at Angle-of-Attack. 33rd AIAA Fluid Dynamics Conference and Exhibit, Orlando, Florida, USA.

Visbal, M. R.; Gordnier, R. E. (2009). Origin of stationary Shear-Layer Sub-Structures above Delta Wings, U.S.A. RTO-TR-AVT-080 Final Report, Chapter 12.

Visser K.D. (1991). An experimental analysis of critical factors involved in the breakdown process of leading-edge vortex flows. PhD dissertation, University of Notre Dame, Notre Damne, France.

Visser KD, Nelson R.C. (1993). Measurements of circulation and vorticity in the leading-edge vortex of a delta wing. AIAA Journal, 31(1), pp. 104–11.

Wang, J.J., Lu, S.F. (2005). Effects of Leading-Edge bevel Angle on the Aerodynamic Forces of a Non-Slender 50° Delta Wing. The Aeronautical Journal. Paper No. 2918, pp. 403 – 407.

Warrington, D.C. (2016). Statistical Rejection of "Bad" Data – Chauvenet's Criterion. Available Online: https://chetaero.files.wordpress.com/2016/11/chauvenet.pdf, Accessed: 31.01.2019.

Wassermann, S. (2016). Turbulence Models Offered by CFD Simulation Vendors. Available at: https://www.engineering.com/ResourceMain.aspx?resid=484 (Downloaded: 28 July 2020).

Wentz, W. H., Kohlman, D.L. (1968). Wind Tunnel investigations of vortex breakdown on slender sharp-edged wings. PhD thesis, University of Kansas, Kansas, USA.

Wentz, W. H., Kohlmann, D. L. (1971). Vortex Breakdown on Slender Sharp-Edged Wings. Journal of Aircraft, 8, pp. 156-161.

White, F. M. (2002). Fluid Mechanics, 5th Edition. McGraw-Hill.

Wibowo, S. B., Sutrisno, Rohmat, T. A. (2018). An Evaluation of Turbulence Model for Vortex Breakdown Detection Over a Delta Wing. PAN Journal LXV (3), pp. 399- 414.

Wilcox D. C. (1988). Reassessment of the Scale Determining Equation for Advanced Turbulence Models. AIAA Journal, 26 (11).

Wilcox, D. C. (1998). Turbulence Modeling for CFD. 2nd ed., DCW Industries, La Cañada, CA.

Williams, N., Wang, Z., Gursul, I. (2008). Active Flow Control on a Nonslender Delta Wing. AIAA, 46th Aerospace Sciences Meeting, Reno, NV, USA.

Wolffelt, K. W. (1986). Investigation of the Movements of Vortex Burst Position with Dynamically Changing Angle of Attack for a Schematic Delta Wing in a Water Tunnel With Correlation to Similar Studies in a Wind Tunnel. AGARD CP-4123.

Xin-Cheng, H., Ling, X. A. (2014). Iteration and Parallel Computation on Computational Fluid Dynamics. 7th International Conference on Intelligent Comutation Technology and Automation, pp. 318-321.

Yamamoto, K., Tanaka, K., Murayama, M. (2010), Comparison Study of Drag Prediction for the 4th CFD Drag Prediction Workshop using Structured and Unstructured Mesh Methods. 28th AIAA Applied Aerodynamics Conference, pp. 1-18.

Yaniktepe B., Rockwell D. (2004). Flow Structure on a Delta Wing of Low Sweep Angle. AIAA Journal, 42 (3), pp. 513-523.

Yao, Z. (2013). A new Methodology for the CFD Uncertainty Analysis. Journal of Hydrodynamics, 25 (1), pp. 131-147.

Yen, D., Braeuchle, F. (2000). Calibration and Uncertainty Analysis for the UC Davis Wind Tunnel Facility. UCD Wind Tunnel Calibration Document. Available Online: http://research.engineering.ucdavis.edu/flight/wp-content/uploads/sites/33/2015/01/Calibration.pdf, Accessed: 29.01.2019

Zhiyin, Y. (2015). Large-eddy simulation: Past, present and the future. Chinese Journal of Aeronautics, 28 (1), pp. 11-24.

Zohar, Y. (1984). The Effects of Vortex Breakdown on the Aerodynamic Properties of Delta Wings. M.Sc. Thesis, Technion—Israel Institute of Technology, Haifa.

Zohar, Y., Er-El, J. (1988). Influence of the Aspect ratio on the Aerodynamics of the Delta Wing at High Angle of Attack. Journal of Aircraft, Volume 25 (3).

Appendix 1 Chapter 2: Literature Review on the Flow Physics of Delta Wings

A.1.1 Vortex Breakdown

Appendix A.1.1 ((from section 2.1.1) provides more information about VBD in general. The burst of the vortices results in unsteady aerodynamic loading which in turn may cause structural and aerodynamic problems. Delaying VBD is one of the goals when designing delta wings as it is increasing the stability, controllability and manoeuvrability of the aircraft.

VBD can occur on delta wings in two different forms; bubble or spiral form (Lambourne and Bryer, 1961).

The spiral-type of breakdown is characterised by a rapid deceleration of the core flow, causing the vortex core filament to kink and to spiral around the axis of the structure. This results in a corkscrew-like distortion of the vortex core, which can spiral for one or two turns before breaking up into large-scale turbulence (Payne et al., 1987).

An example of a spiral type VBD is depicted in Figure A. 1.1.

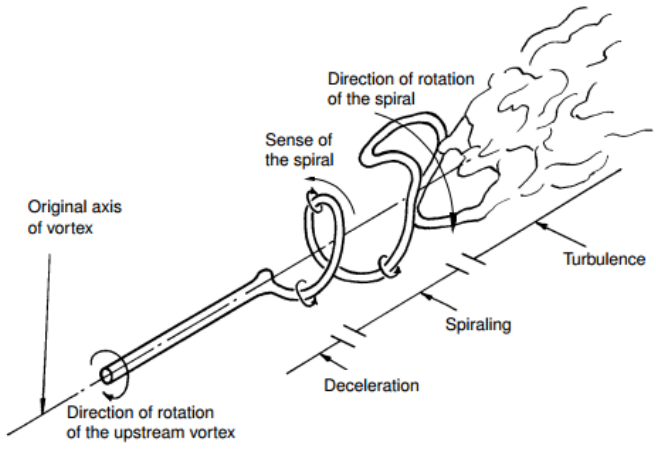

Figure A. 1.1 Spiral Breakdown (Lambourne and Bryer., 1961).

The bubble type of VBD is characterised by the stagnation of the flow on the vortex axis thereby forming an oval-shaped recirculation zone as shown in Figure A. 1.2.

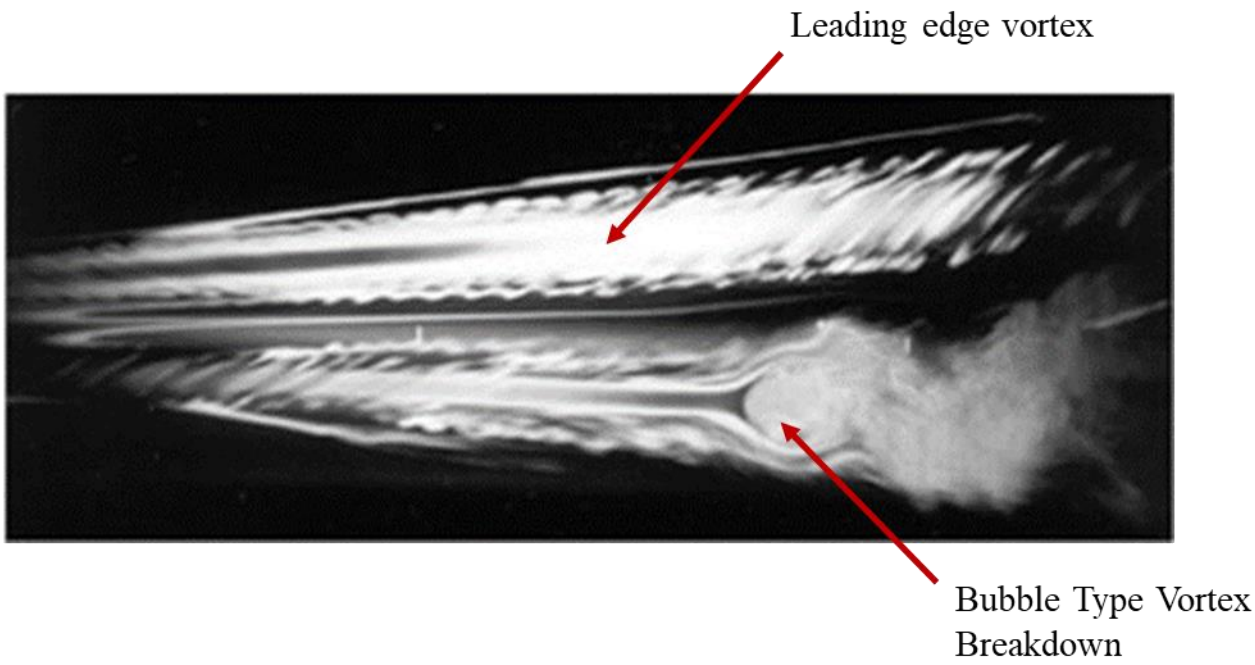

Figure A. 1.2 Bubble-type of Vortex breakdown (Payne,1987).

There is no agreement on how the two types of breakdown are related and some researchers (Jumper et al., 1993 and Payne et al., 1991) think that the bubble form is basic and that the spiral type is a result of the instability of the bubble form. Other opinions are that the bubble type is an artefact of the visualization technique used (Greenwell, 2001).

VBD onset is dependent on sweep angle, thickness, leading-edge shape and other geometric parameters but is generally found at high angles of attack. Here, the primary vortex experiences instabilities near the trailing edge causing the vortex to break down. Increasing the angle of attack provokes a rapid displacement of breakdown location forward, whereas increasing leading-edge sweep reduces the strength of the LEV and delays VBD (Hemsch and Luckring, 1990). Studies by Kegelmann and Roos (1989) and Miau et al. (1995) have shown that leading-edge shape has a significant effect on the burst location due to the variation of separation location and vortex strength. Nonetheless, the effect of leading-edge shape on the flow pattern decreases with increase in Mach number (Goertz, 2005). Positive camber has been shown to delay breakdown whereas thicker wings seem to encourage breakdown (Wentz and Kohlman, 1971).

VBD is a result of a destabilizing agent, such as the longitudinal adverse pressure gradient near the trailing edge. The adverse pressure gradient is dependent on angle of attack and sweep, thus, they are also contributing parameters to the burst (Erickson, 1982, Lambourne and Bryer,

1962). Research has also shown that vorticity shedding from the leading-edge might encourage VBD. The vortex filaments can tighten up when the vorticity-feeding rate from the leading-edge exceeds a certain value, thus causing VBD (Elle, 1958).

Studies have also revealed that the Reynolds number has little effect on vortex burst and thus may be an inviscid phenomenon (Lambourne and Bryer, 1962). However, breakdown points located further forward were also measured with increasing Reynolds number. Soltani and Bragg (1990) concluded that for delta wings with SLEs the Reynolds number effects only appear once the burst point moves onto the wing. According to Wolffelt (1986), thicker wings may be more Reynolds number sensitive.

Although VBD causes a drastic change in the flow pattern over a delta wing, the global strong circulatory flow pattern does not disappear suddenly at breakdown location but persists (Hummel, 1965). Therefore, the vortex upstream of the burst is barely affected. A study by Delery (1994) suggested that the secondary vortex is not affected by the breakdown of the primary one, but a kink in the secondary separation line can be observed (Huang and Hanff, 1998). When breakdown occurs near or at the apex a variety of reversed flow patterns have been reported and also a “whorl” near the outboard tip has been observed (Huang and Hanff, 1998, Earnshaw and Lawford, 1964) as depicted in Figure A. 1.3.

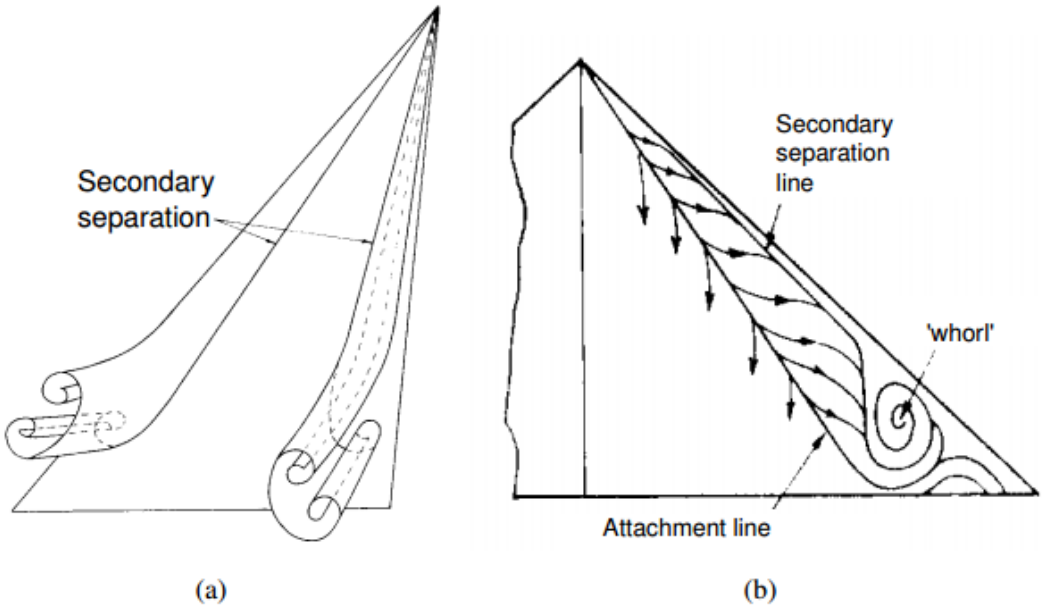

Figure A. 1.3 (a) Suggested secondary vortex system during vortex breakdown (b) secondary separation associated with 'whorl' upper surface skin friction pattern at high angle of attack (Earnshaw and Lawford, 1964).

A.1.2 Internal Structure of Leading-edge Vortices

Appendix A.2.2 (from section 2.1.1) provides further information regarding the internal vortex structure and the impact of the boundary layer status on sharp-edged wings. Understanding the flow physics of sharp-edged configurations and how they are affected by boundary layer status is important for this project, as the numerical simulations are conducted assuming fully turbulent flow, which may cause inaccuracies as flow starts off laminar and the location of the transition point depends on geometric and flow variables.

A.1.2.1 Internal Vortex Structure

The internal structure of the primary vortex can be divided into three regions (Nelson and Pelletier, 2003), see Figure A. 1.4:

1. **Shear Layer:** generated at the leading-edge and feeding vorticity into the vortex core. Increases in thickness with distance from the leading-edge.
2. **Rotational Core:** approximately 30% of the local semi-span in diameter. Circumferential and longitudinal velocity distribution within the core is barely affected by the shear layer. Also, the vorticity distribution is continuous. The velocity distribution in this region is jet-like with a tangential velocity up to approximately 1.5 times freestream velocity.
3. **Viscous Sub-core:** approximately 5% of the local semi-span in diameter. The gradients of local heat, static pressure and velocity are very high within that region. The axial velocity of the viscous sub-core can exceed three times the freestream velocity value. It is smaller than the rotational core and remains nearly constant in size with increase in angle of attack. Also, most of the axial vorticity can be found here.

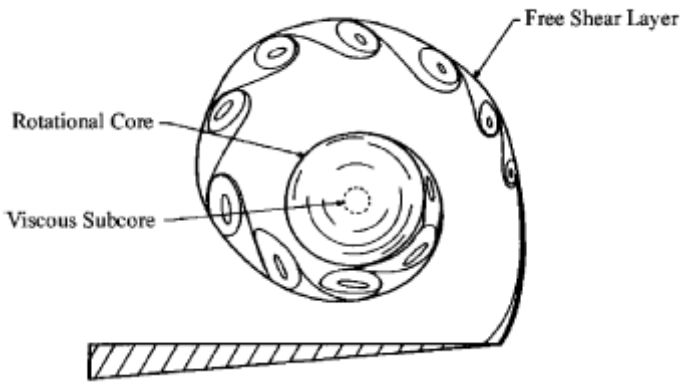

Figure A. 1.4 Three regions within a leading-edge vortex (Nelson and Pelletier, 2003).

A.1.2.2 Laminar Flow

Laminar flow on delta configurations can result in laminar separation on the wing's surface. Hummel (2004) investigated the effect of laminar separation on a delta wing using flow visualisation. He reported that the primary vortex increased in size and was located further inboard than would be expected for turbulent flow. Underneath the primary vortex the flow separates earlier due to an adverse pressure gradient between the attachment line and leading-edge. The secondary vortex formed in this process is relatively large. Additionally, a tertiary vortex is formed (Hummel, 2004).

The strength of the primary vortex in the subsonic region formed by laminar separation is weaker in intensity than in the turbulent case (Betyaev, 1994). Figure A. 1.5 shows the difference between the vortices generated with laminar and turbulent flow (Visbal and Gordnier, 2003).

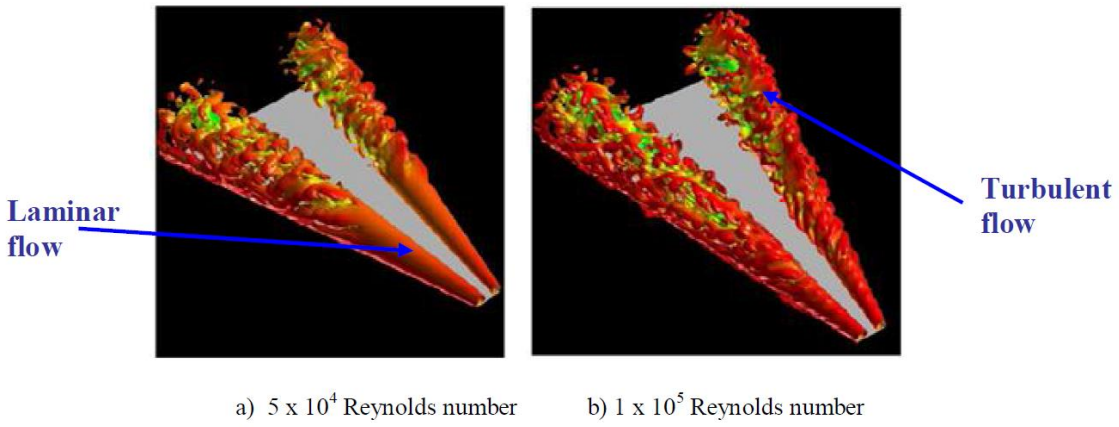

Figure A. 1.5 Flow structure of a (a) laminar and (b) turbulent boundary layer (Visbal and Gordnier, 2003).

A.1.2.3 Turbulent Flow

At a sufficiently high Reynolds number the flow on the upper surface of the wing becomes turbulent resulting in an irregular, highly mixed and unpredictable flow with additional cross flow (TF-12DFRC, 2004). A turbulent boundary layer causes turbulent separation which creates different characteristics in the flow topology. The primary vortex has a higher intensity and is also located further outboard than the laminar case. Due to the increased energy within the boundary layer, the turbulent flow can sustain the adverse pressure gradient longer, thus, delaying secondary separation. This results in a smaller secondary vortex (Hummel, 2004). Next to this, VBD is delayed, but drag is increased as an effect of higher viscous forces.

A.1.3 Effects of Leading-edge Radius on Leading-edge Vortex Development

Appendix A.1.3 (from section 2.1.2) provides further information regarding the internal vortex structure and the impact of the boundary layer status on round-edged wings. Understanding the flow physics of round-edged configurations is important for this project as increasing the thickness changes the effective leading-edge radius, where a SLE wing may behave similar to one with a round leading-edge. Hence, a detailed understanding of the effects of different leading-edge shapes is required.

A.1.3.1 Primary Vortex

For round or blunt-edged delta wings the separation line of the primary vortex is not fixed to the leading-edge (Hummel, 2004). The major differences between the flow topology of round-edged and sharp-edged delta wings is summarised in Figure A. 1.6 (Luckring, 2004a).

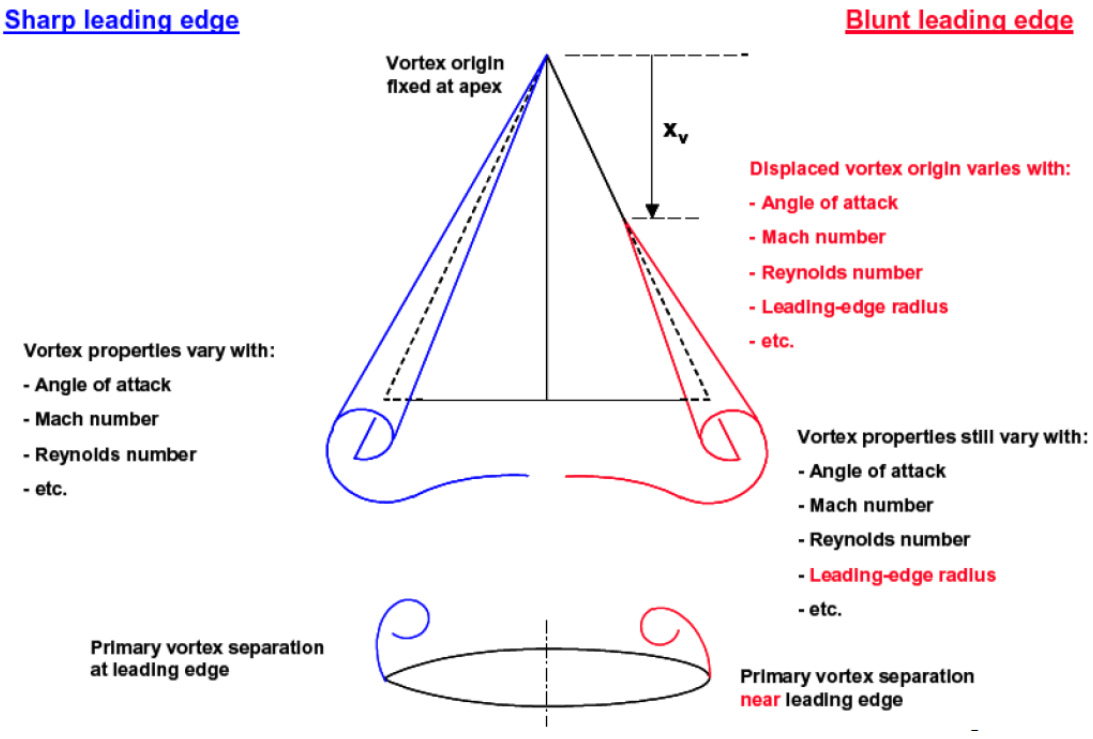

Figure A. 1.6 Difference between the flow topology of sharp and blunt-edged delta wings (Luckring, 2004a).

The extent of the primary vortex, as well as its properties, were found to depend on angle of attack, Mach number, Reynolds number and leading-edge radius. The reason why separation on blunt leading-edges is delayed is that the leading-edge radius stays constant over the entire span whereas the local half span thickness ratio increases further downstream. This means that the radius to local span ratio decreases towards the trailing edge (as the span increases with chord for the delta), thus making it effectively sharper, which in turn increases the suction and

adverse pressure gradient. The rise of those gradients causes separation (Luckring and Hummel, 2008; Konrath et al., 2006).

Next to this, the upwash created by the wing increases towards the trailing edge making the local angle of attack higher near to the trailing edge compared to the apex region. This also yields an increase in adverse pressure gradient and the promotion of separation along the leading-edge (Luckring, 2008). If the flow in the vicinity of the trailing edge is turbulent, the primary vortex is formed in the same manner as is the case for sharp-edged wings (Furman and Breitsamter, 2008). The vortex created will then also have a stronger magnitude than in the laminar case (Pashilkar, 2001).

In summary, the effect of bluntness on the flow field around a delta wing has two obvious effects:

1. Increase in leading-edge radius results in a shift in the position of the primary vortex outboard towards the leading-edge.
2. Increase in leading-edge radius yields to a decrease in physical size and strength of the primary vortex.

A.1.3.2 Secondary Vortex

As for the sharp-edged configuration, a secondary vortex forms underneath the primary vortex due to the separation induced by the adverse pressure gradient. However, the secondary vortex can form later and aft the onset of the primary vortex. Its location mainly depends on the boundary layer status underneath the primary vortex (Rodriguez, 2008). The type of boundary layer also affects the primary separation process.

A.1.3.3 The Effect of Boundary Layer Status on Delta Wings with Round Leading-edges

Hummel (2004) observed different flow phenomena for the same angle of attack but different Reynolds numbers, which are stated below:

1. Laminar flow around the leading-edge without flow separation.
2. Laminar flow around the leading-edge followed by the onset of laminar flow separation on the upper surface.
3. Laminar separation line on the upper surface moves towards the leading-edge until laminar flow separation occurs at the leading-edge.
4. Laminar flow separation ends at a certain point along the leading-edge and is then replaced by laminar to turbulent transition if the Reynolds number is further increased.

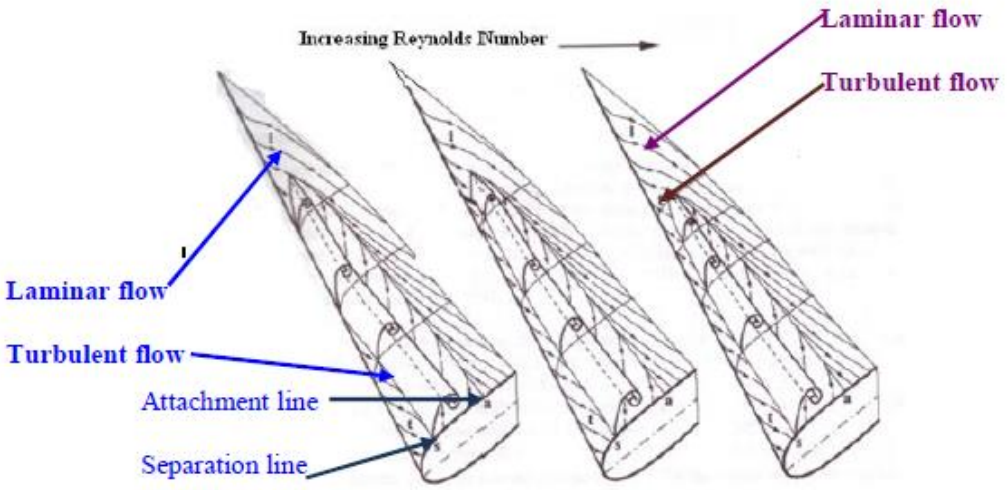

Figure A. 1.7 Boundary Layer underneath primary vortex (Hummel, 2004).

Figure A. 1.7 shows the effect of increasing Reynolds number on the boundary layer status and separation onset. It can be seen that increasing the Reynolds number yields to upstream progression of the transition point, thus reducing the region of laminar primary separation. At a certain Reynolds number the laminar primary separation disappears completely and only turbulent separation is present. As the turbulent boundary layer is able to withstand the adverse pressure gradient longer, the region of attached flow in the apex region is larger (Bozhkov and Mozol'kov, 1975; Hummel, 2004).

A.1.3.4 The Effect of Leading-edge Radius on Separation Onset

The most distinctive feature between configurations having a SLE as opposed to a round leading-edge is the point of separation onset. At low to moderate incidences the majority of the flow around the round leading-edge is attached. At higher incidences the flow starts to separate close to the wing tips (Fink, 1966; Peckham and Atkinson, 1960).

Studies conducted by Hummel (2004) and Peake & Tobak (1980) concluded that the primary separation point depends on the flow characteristics on the lower surface. Hence, the boundary layer status on the lower surface of the wing plays a significant role in determining the location of the primary separation line. This is also depicted in Figure A. 1.8, where S_1 marks the primary separation line. Figure A. 1.8 also shows the shear layer zone between S_3 and S_4, which is associated with high turbulence levels (Honkan and Andreopoulus, 1997).

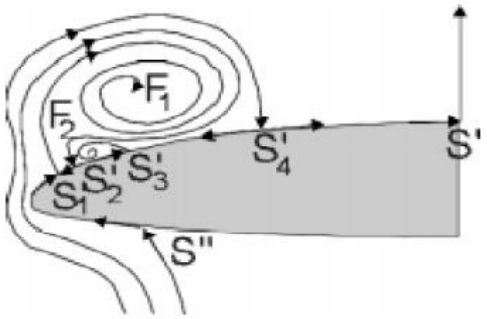

Figure A. 1.8 Primary vortex topology of the round-edged wing (Lang, 1998).

It is also worth noting that the primary separation line S_1 can also be on the lower surface and that it is not necessarily a straight line along the leading-edge of the wing (Renac et al., 2005, Jiang et al., 2000, Huang et al., 2001).

Figure A. 1.9 shows the separation line of the primary vortex along a 65° swept back wing. Furthermore, it displays an additional vortex inboard of the primary vortex; this inner vortex is characteristic of the effect of blunt leading-edges. It can be noted that the inner vortex is generated further upstream than the primary vortex, but both lines curve inboard downstream of the wing (Luckring, 2004).

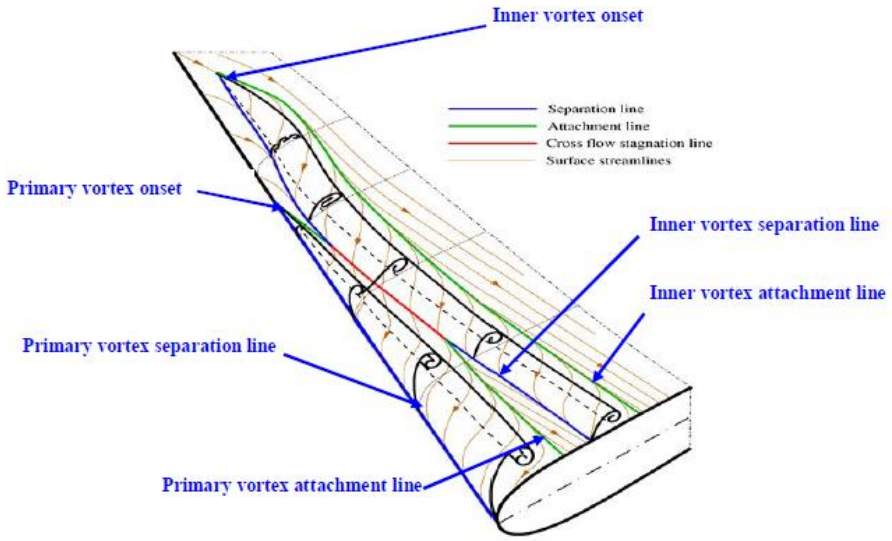

Figure A. 1.9 Attachment and separation lines on the round-edged delta wing:VFE-2 configuration; Mach number= 0.4, Remac=3x106 and α=13.3° (Luckring, 2004).

A.1.3.5 The Effect of Leading-edge Radius on the development of Leading-edge Vortex Structures

As shown earlier, (Figure A. 1.9) one distinctive feature of medium-radius wings is the occurrence of an inner vortex, rotating in the same sense as the primary vortex (Hummel, 2004). At moderate incidences a weak suction peak is observed, at around 1/3rd of the wing chord. This peak is located inboard of the primary vortex. Research conducted by Fritz (2008) and Hummel (2006) found that the inner vortex appears earlier than the primary vortex due to boundary layer separation near the apex. It increases in strength while moving downstream but only up to a certain chordwise position. It starts to decay in strength as the primary vortex is formed. Note that the primary vortex has a higher overall vortex strength (Figure A. 1.10) than the inner vortex (Hummel, 2009).

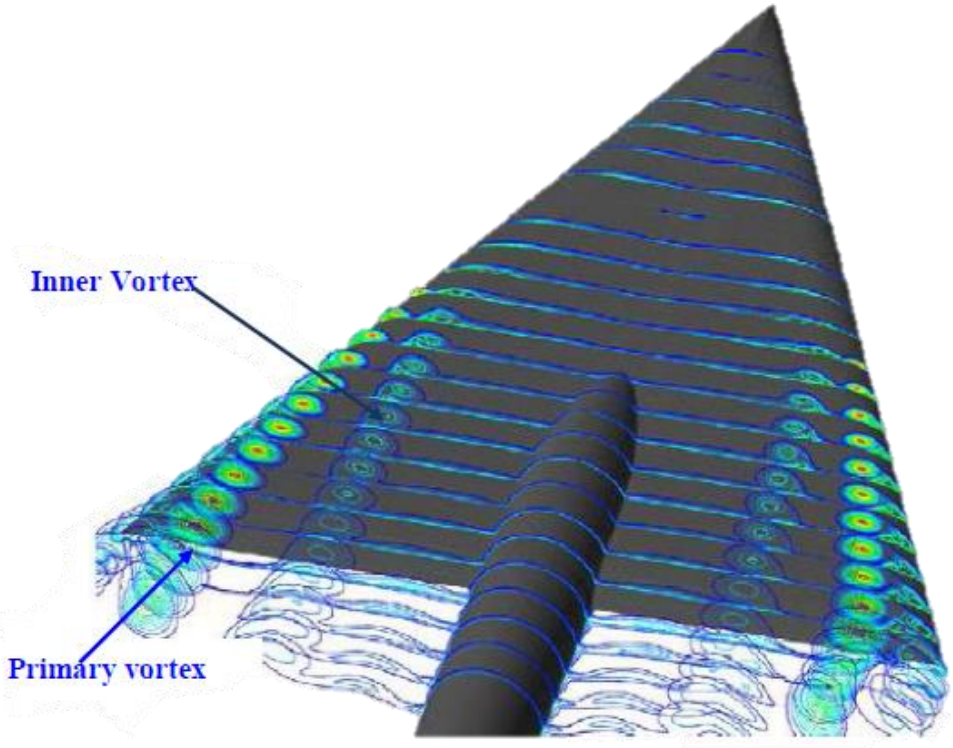

Figure A. 1.10 Calculated pressure contour on the 65° medium radius delta wing at Remac=3x105 and α=13.3° (Hummel, 2009).

Both vortices are located close to each other but do not merge during the initial stage of their development. With increasing distance from the apex the stronger primary vortex shifts the inner vortex inboard (Konrath et al., 2008a & 2008b).

One theory is that the inner vortex is caused by a boundary-layer separation bubble (Delery, 1992). Hummel (2007) reported that the separation bubble can occur first in a region close to

the apex, where the body is relatively thick. At the beginning of its formation the inner vortical structure appears as a flat vortex close to the wing's surface but grows with increasing distance from the apex. At a certain chord position it starts to lift off the surface and its strength decreases as the primary vortex starts developing (Konrath et al., 2008b). This can be explained by the vorticity shed from the leading-edge feeding into the primary vortex rather than in the inner vortex (Luckring and Hummel, 2008).

A.1.4 Summary of Investigations conducted by Kulfan (1979)

The geometric effects discussed in section 2.5 of the main report refer majorly to the studies conducted by Kulfan. A summary of her work including speed and geometric features is shown in Table A. 1.1.

Table A. 1.1 Summary of investigations done by Kulfan (1979).

	Sweep [°]	Profile	t/c	x/c	Mach	Notch angle ζ $\zeta = \frac{\Delta c}{c_r}$	Taper Ratio $\lambda = \frac{c_T}{c_r}$	Nose Radius
Nose Radius Study	70	NACA 66-00XX	0.0336	0.1	0.2	0	0	Small
		NACA 00XX	0.0336	0.1	0.2			Intermediate
		NASA Arrow Wing Profile	0.0336	0.1	0.2			Round
Sweep Effect	67.4	14° lower surface bevel	0.01	Flat Top	0.1	0	0	Intermediate
	71.6							
	76							
Sweep Effect	63	NACA -0003.36	0.0336	0.1	Assume 0.1	0	0	Intermediate
	70							
	74							
Notch angle	70	NACA -0003.36	0.0336	0.1	0.2	0	0	Intermediate
						0.2		
						0.4		
Taper ratio	70	NACA -0003.36	0.0336	0.1	0.2	N/A	0	Intermediate
							0.1	

							0.3	
Spanwise Nose Radius Variation	60				0.16		0.1	Constant percent chord
								Cylindrical, constant across span
								Conical, linear increase from root to tip
Twist	71.2	NACA 0003.36	0.0336	0.1	0.85		0.1	Intermediate
		Sharp nose thin aerofoil	0	0				

Appendix 2 Chapter 3: Literature Review Computational Methods

This appendix supports Chapter 3 in terms of background theoretical information on CFD meshing, turbulence models and factors affecting delta wings.

A.2.1 Grid Types

A.2.1.1 Structured Mesh

The simplest grid generation methods are classic methods which generate a structured mesh, e.g. algebraic and elliptic methods (Thompson et al., 1985). For a two-dimensional domain the mesh elements take the shape of rectangles as illustrated in Figure A. 2.1. The grid points here are addressed by indices (i, j), where the index i represents the numbering of points in the x-direction and j represents numbering points in the y-direction. If (i, j) are indices for a point P (see Figure A. 2.1) then the neighbouring points in each direction are defined by increasing or decreasing indices (Tu et al., 2018).

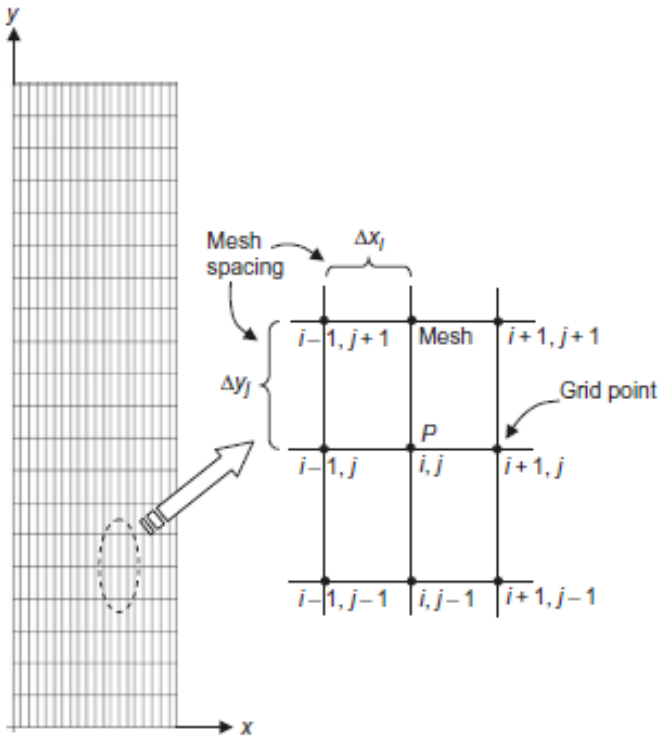

Figure A. 2.1 Uniform rectangular mesh (Tu et al., 2018).

A form of a structured mesh for bodies with complex (i.e. curved) shapes is called body-fitted mesh (Tu et al., 2018) as shown in Figure A. 2.2. Here, compromises are required on curved sections to fit an orthogonal mesh to the geometry. This is done by introducing a curvilinear coordinate domain with coordinates η and ζ, which can be transformed into the coordinates of the physical domain and vice versa.

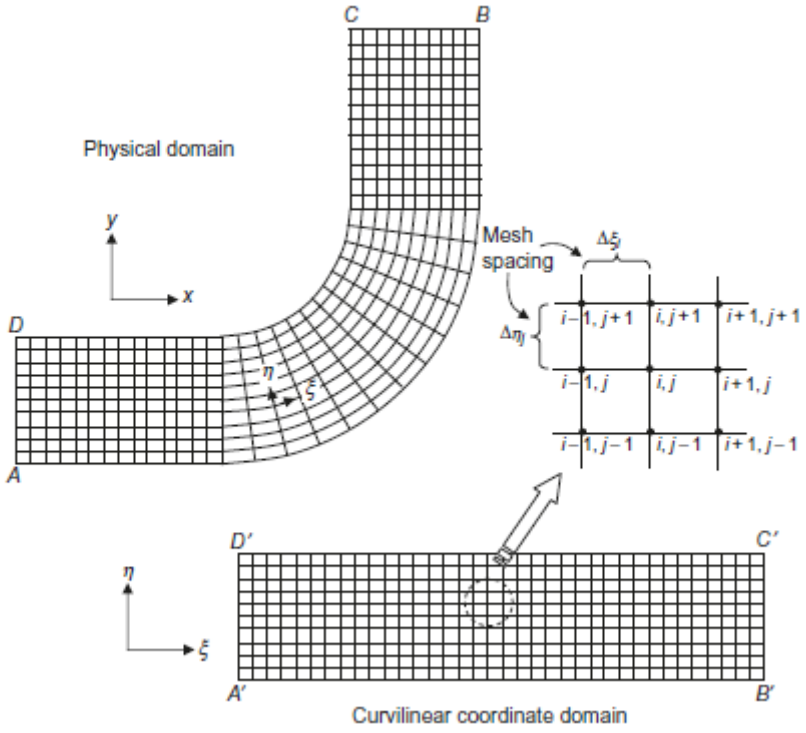

Figure A. 2.2 An example of a body-fitted or curvilinear mesh for a 90° bend geometry and corresponding computational geometry (Tu et al., 2018).

A.2.1.2 Unstructured Mesh

Unstructured meshes are also suitable for complex geometries and characterised by a non-regular arrangement of the elements as can be seen in Figure A. 2.3. The benefit of this type of mesh is its flexibility as it does not need to stick to certain coordinate lines as the structured mesh. This is particularly handy for highly complex geometries. The most common element form of unstructured meshes are triangles and tetrahedrons (Tu et al., 2018).

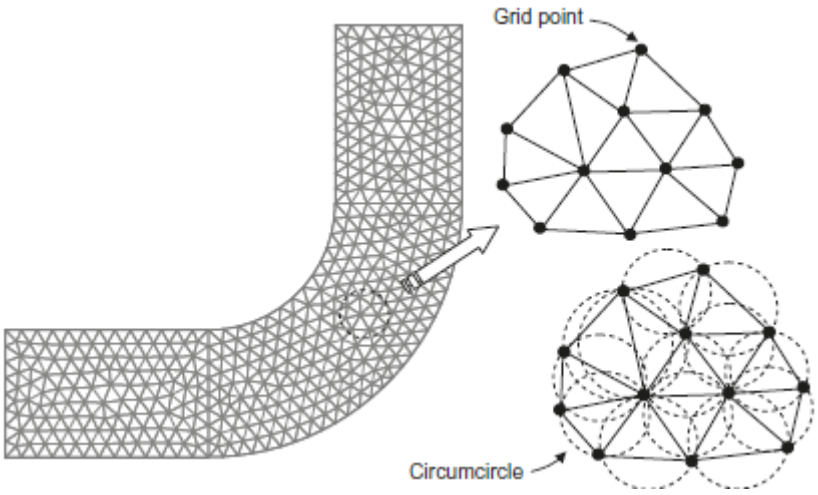

Figure A. 2.3 An example of a triangular mesh for the 90° bend geometry (Tu et al., 2018).

A.2.1.3 Advantages and Disadvantages of certain Mesh Types

The different mesh types stated above come with certain advantages and disadvantages. Using a structured mesh approach allows easy access to each elemental cell due to its indexing and connectivity. This makes programming and data management simple. The downside of structured meshes is that grid non-orthogonality and skewness increases for complex geometries which can yield to unphysical solutions due to the transformation of the algebraic equations. A special case is the block-structured or multi-block grid, where the issue of high non-orthogonal and skewed elements in a domain can be reduced by subdividing it into a number of structured blocks which are attached to one another. The cell faces within each block do not need to match necessarily thus reducing the number of problematic elements due to complex geometries (Tu et al., 2018). An example of matching and nonmatching faces in a mesh is shown in Figure A. 2.4.

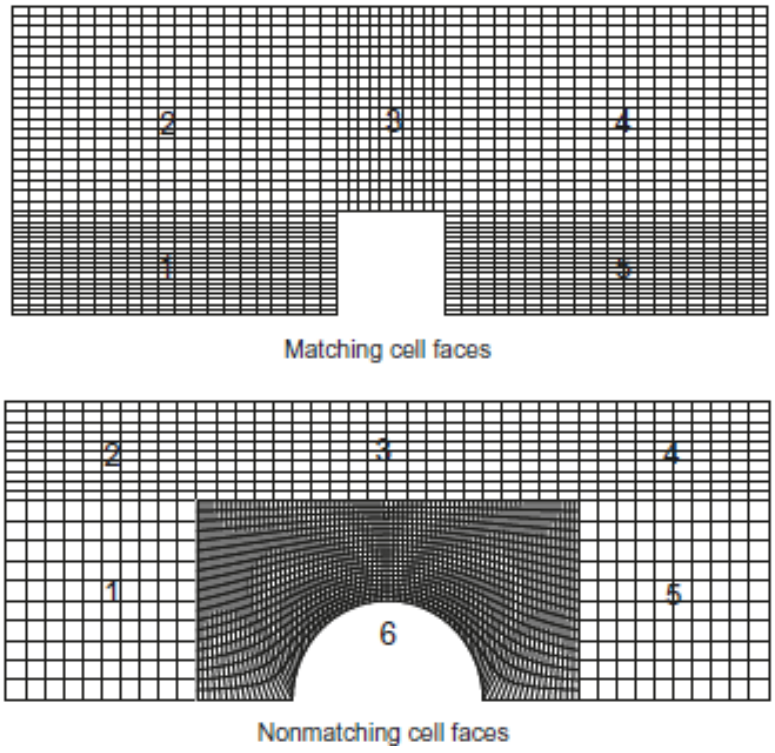

Figure A. 2.4 Multiblock-structured mesh with matching and nonmatching cell faces (Tu et al, 2018).

Most CFD codes are based on the use of unstructured grids with the most typical element shape being a triangle in two dimensions or a tetrahedron in three dimensions. However, also other element types are used such as quadrilateral or hexahedral cells. The benefit of this method is its suitability for domains with high-curvature boundaries, which can lead to improved numerical stability. The disadvantages of unstructured meshes are that they cannot be simply treated or addressed by their indices making data treatment and connection complicated. This

results in increased computational time. Also, triangular or tetrahedral cells in comparison with quadrilateral or hexahedral cells are ineffective in resolving wall boundary layers especially when it comes to approximating the diffusive fluxes. A way to overcome this is by using a combination of different element types, so that quadrilateral or hexahedral elements can be placed near walls and triangular or tetrahedral elements are generated for the rest of the domain (Tu et al., 2018).

A.2.2 Y^+ Value

When a viscous fluid moves past a rigid surface the velocity at any point relative to the wall is zero (Burr et al., 2003). This yields to a modification of the flow not only at the surface but also at a certain distance away from it. In order to evaluate if the near-wall region is sufficiently modelled Gerasimov (2006) suggested the use of y^+ in order to select the most suitable near-wall treatment (wall functions or near-wall modelling) and the corresponding turbulence model (Salim and Cheah, 2009). The y^+ value is defined as a non-dimensional distance from the wall to the first mesh node and determines whether the influences in the wall adjacent cells are laminar or turbulent (Kralik, 2016).

It is similar to the local Reynolds number and can be calculated using the formula (Ariff et al., 2009)

$$y^+ = \frac{\rho u_\tau y_P}{\mu} \qquad \text{(A. 2.1)}$$

where $u_\tau = \sqrt{\frac{\tau_w}{\rho_w}}$ is the friction velocity at the nearest wall, y_P is the distance from a given point P to the wall, ρ is the fluid density and μ is the fluid viscosity at point P.

A.2.2.1 Boundary Layer

Experiments have shown that the near-wall region or boundary layer can be subdivided into three layers. The layer closest to the surface is called viscous sublayer (y^+ =5) in which the flow is almost laminar. Here, the molecular viscosity plays a dominant role in momentum and heat or mass transfer. The outer layer is called fully-turbulent layer or log-law region (y^+ >60), where turbulence plays a significant role. In between those two layers is an interim region, called buffer layer or blending region, where viscosity and turbulence are equally important

(Bazargan and Mohseni, 2009). A schematic of the relation between y^+ and different boundary layers is shown in Figure A. 2.5.

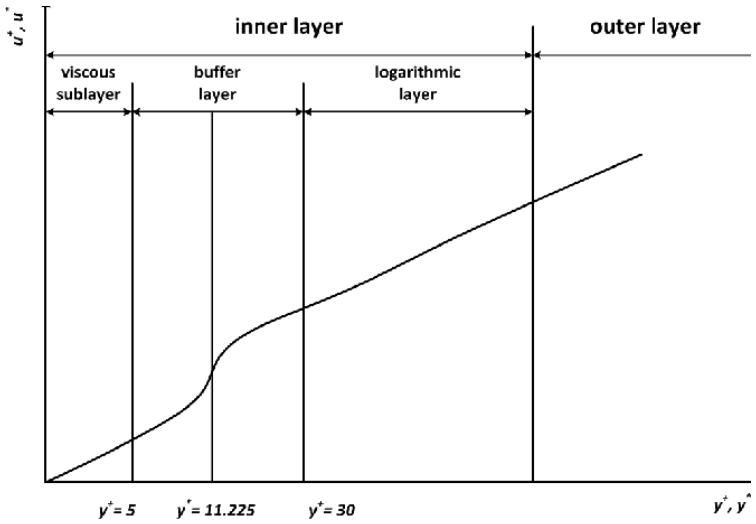

Figure A. 2.5 Boundary Layer Structure (Grecu et al., 2017).

A.2.3 Wall Functions versus. Near-Wall Model

Under the assumption that the boundary layer can be reasonably approximated via a logarithmic profile the fluid shear stress can be computed as a function of the velocity at a given distance from the wall. This is commonly referred to as a "wall function" and the logarithmic nature of the boundary layer profile gives rise to the well-known "log law of the wall" (Ansys, 2011).

Generally, there are two approaches when modelling near-wall regions.

- **The wall function method** which does not resolve the inner region (viscous sublayer and buffer layer) affected by viscosity, but uses semi-empirical formulae, so called "wall functions" to bridge between the near-wall region and the fully-turbulent region. Consequently, when using the wall function method, a very low y^+ value (y^+~ 30) is not required resulting in saving computational time.

  The advantages of using this approach are twofold; the shear-layers near the wall can be modelled with relatively coarse meshes saving CPU and storage and there is no necessity of modifying the turbulence models to account for the presence of the wall (ANSYS FLUENT Theory Guide, 2009). Next to this, the wall function approach is robust, economical and reasonably accurate (FLUENT Theory Guide, 2009).

  However, the wall function approach is inadequate in situations where low- Re-number effects are predominant in the flow domain. For those cases the near-wall model

approach has to be picked, which is available in ANSYS Fluent (FLUENT Theory Guide, 2009).

- The Low-Reynolds Number method or **Near-Wall method** resolves the boundary layer thus requiring a very fine mesh in the direction normal to the wall (y^+=1). In the near-wall method, turbulence models are modified to enable a viscosity-affected region to be resolved with a mesh all the way to the wall, including the viscous sublayer. Therefore, turbulence models based on the ω- equation (where ω is the specific dissipation or turbulent mixing length frequency), such as Shear Stress Transport (SST) or Second Moment Closure (SMC)-ω models, are suitable for using this approach. Note that the low- Renumber approach is not referring to the device Re (as in using the length or width of the device as the reference length) but to the turbulent Re, which is low in the viscous sublayer.

  The downside of this method is its requirement for a fine mesh in the near-wall zone thus resulting in higher computational storage and runtime requirements. Also, care must be taken to ensure good numerical resolution in order to capture the rapid variation in variables (Ansys, 2011).

The modelling of the near wall regions is solver dependent and is explored here for ANSYS FLUENT as it was the flow solver used in this study.

In ANSYS FLUENT, scalable wall functions are used by default for all turbulence models which are based on the ε-equation for turbulence dissipation and enhanced near-wall treatment when k-ω based models (based on turbulent kinetic energy k and the specific turbulence dissipation rate ω) are used (including SST) (FLUENT Theory Guide, 2009). The use of the standard wall function implies that the boundary layer mesh lies entirely within the log-law region of the boundary layer. However, this is difficult to achieve for most flow problems due to the varying local velocity around the model. The scalable wall function displaces the mesh to a y^+~11.225 irrespective of the first layer height of the mesh. This avoids erroneous modelling of the laminar sublayer and buffer region. For grids with y^+>11.225 the scalable wall function will give identical results to the standard wall function.

Enhanced wall treatment in ANSYS automatically switches from wall-function to a low-Re near wall treatment as the mesh is refined (FLUENT Theory Guide, 2009). The choice of wall treatment depends on the flow physics and turbulence model. K-ε, Reynolds Stress (RSM) and

Large Eddy Simulation (LES) turbulence models are primarily designed for flows with turbulent cores, somewhat far from walls, and hence coupled with wall function. SA, k-ω and SST are applicable throughout the boundary layer when near-wall mesh resolution is sufficient and therefore needs near-wall modelling (Salim and Cheah, 2009). In order to use the scalable wall functions or enhanced wall treatment accurately it is required to fully resolve the boundary layer, by placing at least 10 nodes into it (FLUENT Theory Guide, 2009).

A.2.4 Turbulence Modelling

This section gives a detailed explanation and derivation of the eddy viscosity models (EVMs). First the Reynolds Averaged Navier-Stokes (RANS) equations are derived and then three different EVM closure models are discussed: zero-, one- and two-equation EVMs.

A.2.4.1 Statistical Turbulence Models and the Closure Problem

Starting from the Navier- Stokes equation for incompressible flow as the flow under investigation in this thesis is incompressible, the continuity and momentum equations are defined respectively as (Pitsch, 2014):

$$\frac{\partial u_j}{\partial x_j} = 0 \qquad \text{(A. 2.2)}$$

$$\frac{\partial u_j}{\partial t} + u_i \frac{\partial u_j}{\partial x_i} = -\frac{1}{\rho}\frac{\partial p}{\partial x_j} + \upsilon \frac{\partial^2 u_j}{\partial x_i^2} \qquad \text{(A.2.3)}$$

with i=[1,3] and j=[1,3]. A characteristic of turbulence is its fluctuation in time and space. When looking at large time scales, however, then turbulent flow can be said to have average characteristics with an additional time-varying fluctuating component (Ansys, 2011). The turbulent velocity components and the pressure, p, can therefore be decomposed as follows (Anderson, 1995):

$$u_j = \bar{u_j} + u_j' \tag{A.2.4}$$

$$p = \bar{p} + p' \tag{A.2.5}$$

where u_j is the momentary velocity component, $\overline{u_j}$ is the time-averaged velocity component and u_j' is the fluctuating velocity component.

The time averaging is done by taking the mean values at a fixed place in space and averaging them over time. Note, that the time span has to be large enough so that the mean values are independent of it (Anderson, 1995).

$$\bar{u_j} = \frac{1}{\Delta t} \int_{t_0}^{t_0+t_1} u_j \, dt \tag{A.2.6}$$

The time-averaged values of the fluctuating values are defined to be zero, so (Anderson, 1995):

$$\overline{u_j'} = 0 \tag{A.2.7}$$

The simplification above is significant for turbulence modelling. The averaged and fluctuating quantities are substituted into the Navier-Stokes equations thus forming the Reynolds Averaged Navier-Stokes (RANS) equations (Ansys, 2011).

The following rules for time-averaging apply (Anderson, 1995):

$$\overline{\frac{\partial \bar{u}}{\partial x}} = \frac{1}{\Delta t} \int_{t_0}^{t_0+t_1} \frac{\partial u}{\partial x} \, dt = \frac{\partial}{\partial x} \frac{1}{\Delta t} \int_{t_0}^{t_0+t_1} u \, dt = \frac{\partial \bar{u}}{\partial x}$$

$$\overline{\frac{\partial u'}{\partial x}} = \frac{1}{\Delta t} \int_{t_0}^{t_0+t_1} \frac{\partial u'}{\partial x} \, dt = \frac{\partial}{\partial x} \frac{1}{\Delta t} \int_{t_0}^{t_0+t_1} u' \, dt = 0$$

$$\bar{\bar{f}} = \bar{f}$$

$$\overline{f + g} = \bar{f} + \bar{g} \qquad \text{(A.2.8)}$$

$$\overline{\bar{f} \times g} = \bar{f} \times \bar{g}$$

$$\frac{\overline{\partial f}}{\partial s} = \frac{\partial \bar{f}}{\partial s}$$

$$\overline{\int f \, ds} = \int \bar{f} \, ds$$

But $\overline{f \times g} \neq \bar{f} \times \bar{g}$

where f and g are both functions.

The time averaged continuity equation therefore becomes (Anderson, 1995):

$$\frac{\partial \bar{u}_j}{\partial x_j} + \frac{\partial u_j'}{\partial x_j} = 0 \qquad \text{(A.2.9)}$$

Equation (A.2.9) shows that there is no correlation between the fluctuating quantities, thus, the continuum equation can be considered linear.

The Momentum equation, however, transforms to (Pitsch, 2014):

$$\frac{\partial \bar{u}_j}{\partial t} + \bar{u}_i \frac{\partial \bar{u}_j}{\partial x_i} = -\frac{1}{\rho}\frac{\partial p}{\partial x_j} + \frac{\partial}{\partial x_i}\left(\upsilon \frac{\partial u_j}{\partial x_i} - \overline{u_i' u_j'}\right) \qquad \text{(A.2.10)}$$

The term $\frac{\partial}{\partial x_i}\overline{u_i' u_j'}$, which results from time-averaging the convective transport term $u_i \frac{\partial u_j}{\partial x_i}$, is called the Reynolds Stress Tensor and is defined as

$$\tau_{ij} = -\rho\overline{u_i' u_j'} \tag{A.2.11}$$

as it only appears due to the Reynolds averaging. Due to the addition of the turbulent term in Equation (A.2.10) a Reynolds stress matrix forms (Vengadesan, 2015):

$$\begin{pmatrix} \sigma_x & \tau_{xy} & \tau_{xz} \\ \tau_{xy} & \sigma_y & \tau_{yz} \\ \tau_{xz} & \tau_{yz} & \sigma_z \end{pmatrix} = -\begin{pmatrix} \rho\overline{u'^2} & \rho\overline{u'v'} & \rho\overline{u'w'} \\ \rho\overline{u'v'} & \rho\overline{v'^2} & \rho\overline{v'w'} \\ \rho\overline{u'w'} & \rho\overline{v'w'} & \rho\overline{w'^2} \end{pmatrix} \tag{A.2.12}$$

It can be seen that the matrix is symmetric and thus contributes six additional unknowns to the already existing four unknowns in the continuity and the Navier-Stokes equations (the velocity fluctuation components u, v and w and pressure). This yields to a closure problem as there are only four equations to solve for ten unknowns (Vengadesan, 2015).

Therefore, in order to solve the system of the RANS the Reynolds stress needs to be modelled as a function of mean flow quantities.

This would normally be done by deriving a transport equation for τ_{ij}. Therefore, the momentum equation (Equation

(A.2.3)) is subtracted from the averaged momentum equation (Equation (A.2.10)) and Equation (A.2.4) is rearranged for u_j' leading to (Pitsch, 2014):

$$\frac{\partial \overline{u_j}}{\partial t} + \overline{u_i}\frac{\partial u_j'}{\partial x_i} + u_i'\frac{\partial u_j'}{\partial x_i} + u_i'\frac{\partial \overline{u_j}}{\partial x_i} = -\frac{1}{\rho}\frac{\partial p'}{\partial x_j} + \frac{\partial}{\partial x_i}\left(\upsilon\frac{\partial u'_j}{\partial x_i} - \overline{u_i' u_j'}\right) \tag{A.2.13}$$

Multiplying Equation (A.2.13) with the fluctuating velocity u_k' for k=1,2,3 and a corresponding equation for u_k' k=1,2,3 with u_j' j=1,2,3 results after summation in (Pitsch, 2014):

$$\frac{\partial u_j' u_k'}{\partial t} + \overline{u_i} \frac{\partial u_j' u_k'}{\partial x_i} + u_i' u_k' \frac{\partial \overline{u_j}}{\partial x_i} + u_i' u_j' \frac{\partial \overline{u_k}}{\partial x_i} + \frac{\partial}{\partial x_i}\left(u_i' u_j' u_k'\right) =$$
$$-\frac{1}{\rho}\left(u_k' \frac{\partial p'}{\partial x_j} + u_j' \frac{\partial p'}{\partial x_k}\right) + \upsilon\left(u_k' \frac{\partial^2 u'_j}{\partial {x_i}^2} + u_j' \frac{\partial^2 u'_k}{\partial {x_i}^2}\right) + u_k' \frac{\partial \overline{u_i' u_j'}}{\partial x_i} + \qquad (A.2.14)$$
$$u_j' \frac{\partial \overline{u_i' u_k'}}{\partial x_i}$$

where $\left(u_k' \frac{\partial p'}{\partial x_j} + u_j' \frac{\partial p'}{\partial x_k}\right)$ are the pressure based terms and $\upsilon\left(u_k' \frac{\partial^2 u'_j}{\partial {x_i}^2} + u_j' \frac{\partial^2 u'_k}{\partial {x_i}^2}\right)$ are the viscous terms.

The viscous terms can be transformed into

$$u_k' \frac{\partial^2 u'_j}{\partial {x_i}^2} + u_j' \frac{\partial^2 u'_k}{\partial {x_i}^2} = \frac{\partial^2}{\partial {x_i}^2}\left(u_j' u_k'\right) - 2 \frac{\partial u_k'}{\partial x_i} \frac{\partial u_j'}{\partial x_i} \qquad (A.2.15)$$

The pressure terms can be written with the use of the Kronecker Delta δ_{ij}as

$$u_k' \frac{\partial p}{\partial x_j} + u_j' \frac{\partial p'}{\partial x_k} = \frac{\partial}{\partial x_j}\left(p' u_k'\right) - p' \frac{\partial u_k'}{\partial x_j} + \frac{\partial}{\partial x_k}\left(p' u_j'\right) - p' \frac{\partial u_j'}{\partial x_k} =$$
$$-p'\left(\frac{\partial u_k'}{\partial x_j} + \frac{\partial u_j'}{\partial x_k}\right) + \frac{\partial}{\partial x_i}\left[p'\left(\delta_{ij} u_k' + \delta_{ik} u_j'\right)\right] \qquad (A.2.16)$$

Substituting Equation (A.2.15) and (A.2.16) into (A.2.13) leads to

$$\frac{\partial}{\partial t}\left(\overline{u_j' u_k'}\right) + \overline{u_i} \frac{\partial u_j' u_k'}{\partial x_i} = -\overline{u_i' u_k'} \frac{\partial \overline{u_j}}{\partial x_i} - \overline{u_i' u_j'} \frac{\partial \overline{u_k}}{\partial x_i} - 2\upsilon \overline{\frac{\partial u_k'}{\partial x_1} \frac{\partial u_j'}{\partial x_1}} +$$
$$\frac{p'}{\rho}\left(\frac{\partial u_k'}{\partial x_j} + \frac{\partial u_j'}{\partial x_k}\right) + \frac{\partial}{\partial x_i}\left[-\overline{u_i' u_j' u_k'} + \upsilon \frac{\partial}{\partial x_i}\left(\overline{u_j' u_k'}\right) - \right. \qquad (A.2.17)$$
$$\left. \overline{\frac{p'}{\rho}\left(\delta_{ij} u_k' + \delta_{ik} u_j'\right)}\right]$$

with

$$\frac{\partial}{\partial t}\left(\overline{u_j' u_k'}\right) \qquad (A.2.18)$$

being the Local derivative,

$$\overline{u_l}\,\frac{\partial \overline{u_j' u_k'}}{\partial x_i} \tag{A.2.19}$$

being the Convective or Advective Transport,

$$-\overline{u_i' u_k'}\,\frac{\partial \overline{u_j}}{\partial x_i} - \overline{u_i' u_j'}\,\frac{\partial \overline{u_k}}{\partial x_i} \tag{A.2.20}$$

being the Production of Reynolds Stresses,

$$-2\upsilon\,\overline{\frac{\partial u_k'}{\partial x_l}\frac{\partial u_j'}{\partial x_l}} \tag{A.2.21}$$

being the (Pseudo-) Dissipation of Reynolds Stresses,

$$\frac{p'}{\rho}\left(\frac{\partial u_k'}{\partial x_j} + \frac{\partial u_j'}{\partial x_k}\right) \tag{A.2.22}$$

being the Pressure- Rate- Of- Strain Correlation (it contributes to the redistribution of the Reynolds stresses similar to the diffusion term and

$$\frac{\partial}{\partial x_i}\left[-\overline{u_i' u_j' u_k'} + \upsilon\frac{\partial}{\partial x_i}\left(\overline{u_j' u_k'}\right) - \overline{\frac{p'}{\rho}\left(\delta_{lj} u_k' + \delta_{lk} u_j'\right)}\right] \tag{A.2.23}$$

being the Diffusion of the Reynolds Stresses (includes all terms under the divergence operator).

It can be seen from Equation (A.3.22) that the mean velocity gradients are responsible for the production of turbulence. Also note, that by trying to derive a transport equation for the Reynolds shear stress resulted in the creation of six additional equations (Equations (A.2.18) until (A.2.23)) and thus 27 more unknowns (Vengadesan, 2015). In order to reduce the number

of unknowns additional equations are required. However, Equation (A.3.22) can be simplified by replacing terms by using the principle of turbulence kinetic energy (TKE).

A.2.4.2 Derivation of an Equation for turbulent KE

In general, turbulence models work by providing additional equations in order to solve for the unknowns in the time-averaged momentum equation. This is done by the implementation of the so called, turbulence kinetic energy (TKE). The idea of TKE is very similar to the one of kinetic energy (KE) in mechanics. As for the velocity field in Equation (A.2.4) also the KE can be decomposed, thus, resulting in two types of KE (Savli, 2012):

$$\frac{\mathrm{MKE}}{\mathrm{m}} = \frac{1}{2}(\bar{u}_1^2 + \bar{u}_2^2 + \bar{u}_3^2) \tag{A.2.24}$$

$$\frac{\mathrm{TKE}}{\mathrm{m}} = \bar{k} = \frac{1}{2}\left(\overline{u'^2_1} + \overline{u'^2_2} + \overline{u'^2_3}\right) = \frac{1}{2}\overline{u_j^2} \tag{A.2.25}$$

With MKE being the mean turbulence kinetic energy and m being mass.

Replacing the index j in Equation (A.2.17) by the index k and apply Equation (A.2.25) leads to (Pitsch, 2014):

$$\frac{\partial \bar{k}}{\partial t} + \bar{u}_i \frac{\partial \bar{k}}{\partial x_i} = -\overline{u_i' u_k'} \frac{\partial \bar{u}_j}{\partial x_i} - \bar{\varepsilon} + \frac{\partial}{\partial x_i}\left[-\overline{u_i'\left(k + \frac{p'}{\rho}\right)} + \upsilon \frac{\partial \bar{k}}{\partial x_i} + \upsilon \frac{\partial}{\partial x_j}\left(\overline{u_i' u_j'}\right)\right] \tag{A.2.26}$$

with $\bar{\varepsilon}$ being the mean dissipation of TKE being defined as

$$\bar{\varepsilon} = \upsilon \overline{\left(\frac{\partial u_j'}{\partial x_i} + \frac{\partial u_i'}{\partial x_j}\right)\frac{\partial u_j'}{\partial x_i}} \tag{A.2.27}$$

Note, that due to the Continuity Equation being equal to zero (compare Equation (A.2.9)) also the pressure-rate-of-strain-correlation $\frac{p'}{\rho}\left(\frac{\partial u_k'}{\partial x_j}+\frac{\partial u_j'}{\partial x_k}\right)$ is equal to zero. Additionally, the dissipation $\frac{\partial u_k'}{\partial x_i}\frac{\partial u_j'}{\partial x_i}$ in Equation (A.2.27) can be rewritten such as (Pitsch, 2014):

$$\overline{\frac{\partial u_k'}{\partial x_1}\frac{\partial u_j'}{\partial x_1}}=\overline{\frac{\partial u_j'}{\partial x_1}\left(\frac{\partial u_j'}{\partial x_1}+\frac{\partial u_1'}{\partial x_j}\right)}-\frac{\partial^2}{\partial x_j x_i}\left(\overline{u_j' u_1'}\right) \tag{A.2.28}$$

Equation (A.2.26) is representing the transport equation for the TKE and can be interpreted in the same way as the equation for the Reynolds Stress Tensor with the local change and the convection of TKE on the left hand side (LHS) of Equation (A.2.26) and the production, dissipation and diffusion on the right hand side (RHS) (Pitsch, 2014).

The derivation of the TKE simplifies the Reynolds Stress Equation but does not solve the closure problem; there are still more unknowns than equations. One way to overcome this problem are so called turbulence models. Depending on the kind of model they are either providing additional equations or are replacing the unknowns with known variables (Vengadesan, 2015).

A.2.4.3 Turbulent Viscosity

As mentioned in the previous section the derived averaged equations are not closed. In order to solve this issue the Turbulent Stress Tensor has to be modelled:

$$\tau_{ij}=-\rho\overline{u_i' u_j'} \tag{A.2.29}$$

A.2.4.4 Boussinesq Approach

The starting point for all turbulence models is the Boussinesq eddy viscosity assumption which can predict the properties of the flow without knowing its turbulent structure. Boussinesq developed this concept in 1877 and it is based on similarity reasoning between turbulence and viscosity (University of Manchester, Bredberg, 2001).

In the Navier-Stokes equation the viscous term is given as (Bredberg, 2001):

$$D_v = \frac{\partial}{\partial x_j}\left[\upsilon\left(\frac{\partial u_i}{\partial x_j} + \frac{\partial u_j}{\partial x_i}\right)\right] \quad \text{(A.2.30)}$$

Boussinesq assumed that turbulence behaves similarly to viscosity as it also affects dissipation, diffusion and mixing processes. Therefore, the Reynolds stresses may be modelled in a closely related way to the viscous term. The Reynolds stress term produced by time-averaging is (Bredberg, 2001):

$$D_R = \frac{\partial R_{ij}}{\partial x_j} = \frac{\partial}{\partial x_j}\left(-\overline{u_i' u_j'}\right) \quad \text{(A.2.31)}$$

Note that the viscous term, shown in Equation (A.2.30), is representing laminar flow, therefore, an additional assumption has to be made, which is, that turbulent flow will enhance the effects of the above properties. This is accounted for by the use of a tensor as shown in the equation below (Bredberg, 2001):

$$-\overline{u_i' u_j'} = \alpha_{ijkl}(x, y, z, t)\left(\frac{\partial u_i}{\partial x_j} + \frac{\partial u_j}{\partial x_i}\right) \quad \text{(A.2.32)}$$

α_{ijkl} is a fourth rank tensor which could have spatial and temporal variations as well as directional properties (anisotropic). The eddy viscosity models assume isotropy of turbulence (same value of turbulence when measured in different directions) meaning rotation and buoyancy can be neglected and there is no mean flow. This is because rotation and buoyancy forces tend to suppress vertical motions, thus creating an anisotropy between the vertical and horizontal directions. The presence of a mean flow can also introduce anisotropy in the turbulent velocity and pressure fields due to having a particular direction (Flierl and Ferrari, 2007). The spatial variations of the fluctuations are modelled using algebraic relations whilst the temporal variation is generally dropped resulting in the following equation (Bredberg, 2001):

$$-\overline{u_i' u_j'} = \upsilon_t(x, y, z)\left(\frac{\partial u_i}{\partial x_j} + \frac{\partial u_j}{\partial x_i}\right) \quad \text{(A.2.33)}$$

In order to account for the normal stresses Equation (A.2.33) is modified to:

$$-\overline{u_i' u_j'} = \upsilon_t(x, y, z)\left(\frac{\partial u_i}{\partial x_j} + \frac{\partial u_j}{\partial x_i}\right) - \frac{2}{3} k \delta_{ij} \qquad \text{(A.2.34)}$$

With υ_T being the turbulent kinetic eddy viscosity and δ_{ij} being the Kronecker delta. Note that the eddy viscosity is a factor of proportionality and depends on the degree of turbulence in the flow. Thus, it varies within the fluid flow and depends on the flow conditions. The Kronecker delta ensures that the equation is also valid for normal tension where i=j and i=1, 2, 3 (Anderson, 1995, Vengadesan, 2015).

A.2.4.5 Eddy Viscosity Models (EVMs)

The problem of the prediction of turbulent flows is the appearance of the Reynolds stress. Even though it can be related to stress, its physics are very different from the viscous stress. Viscous stress is directly related to other flow properties. The Reynolds stress, however, arises from the flow itself leading to a closure problem (more unknowns than equations) (Bakker, 2002). Different turbulence models have been developed which address this problem.

All turbulence models are using the following steps in order to overcome the closure problem:

1. Solving the transport equations (PDEs) for k, ε and ω and the respective variables. Their relations can be seen below (Vengadesan, 2015):

$$\upsilon_t = \frac{k\rho}{\omega} \qquad \text{(A.2.35)}$$

$$\upsilon_t = \frac{k^2\rho}{\varepsilon} \qquad \text{(A.2.36)}$$

$$\varepsilon = \omega k \qquad \text{(A.2.37)}$$

2. Calculating the turbulence eddy viscosity.

3. Using the turbulence eddy viscosity to calculate the Reynolds stress term based on the Boussinesq assumption.

The most commonly known turbulence models in CFD can be subdivided into different categories (Majumdar, 2015);

- Zero-equation models or algebraic models
- One- equation models
- Two- equation models.

There are also other categories, however, not as popular and therefore omitted here. Those names relate to the way in which the turbulent stresses are expressed or how many additional conservation equations are required in order to overcome the closure problem.

The zero-equation turbulence models do not require the solution of any additional equations and are solely based on dimensional analysis (Pitsch, 2014). These models assume that the turbulent field is in equilibrium with the mean flow. This is achieved by comparing the turbulent length scale to some mean flow length scale such as the boundary layer thickness and by comparing the turbulent time scale to the mean flow time scale (Gatsis, 2000).

One example of an algebraic model is the Prandtl mixing length hypothesis. Prandtl postulates that the eddy viscosity can be expressed as the product of a velocity scale and a length scale (Pitsch, 2014):

$$\upsilon_t = l^2\left|\overline{S_{ij}}\right| \tag{A.2.38}$$

$$S_{ij} = \frac{1}{2}\left(\frac{\partial u_i}{\partial x_j} + \frac{\partial u_j}{\partial x_i}\right) \tag{A.2.39}$$

The value of the mixing length l depends on the nature of the flow and takes different values for different types of flows (e.g. free shear layer flows and boundary, boundary layer flows) (Ahmadi, 2016) and is determined empirically (Pitsch, 2014).

The downside of these turbulence models are the flow length scales chosen as they need to be clearly defined (Gatsis, 2000). When using the boundary layer thickness i.e. inaccurate results

will be generated where there is separation and or shock-boundary layer interaction (Gatsis, 2000). Additionally, zero-equation turbulence models show high inaccuracies when predicting heat transfer, recirculation or separation (Ahmadi, 2016). Other very well-known zero-equation models are the Baldwin- Lomax model and the Cebeci-Smith model (Bakker, 2002). Due to its disadvantages with regards to predicting complex flows the zero-equation model is barely implemented in commercial CFD programs today (Bakker, 2002). Therefore, it will not be further discussed but is only mentioned for completeness.

The zero-equation model assumes that the turbulent stresses are proportional to the flow velocity whereas the one-equation model uses additional partial differential equations for the velocity scale. The two-equation model uses additional PDEs for the length scale. Turbulence models based on stress models require PDEs for all components of the stress tensor (Anderson, 1995).

The one-equation models solve one turbulent transport equation, usually for turbulent kinetic energy, k (Bakker, 2002). Many of those models are based on the Prandtl-Kolmogorov equation (Ahmadi, 2016):

$$\upsilon_t = C_\mu l\sqrt{k} \qquad \text{(A.2.40)}$$

With C_μ being a constant whose value is often $C_\mu = 0.09$ (Pitsch, 2014).

The two-equation models are the most commonly used in CFD with the k-epsilon and k-omega models being the most popular ones.

By definition, those turbulence models solve two extra transport equations in order to represent the turbulent properties of the flow, thus, allowing to account for history effects such as diffusion and convection of turbulent energy.

The most commonly used transport variables are the turbulence kinetic energy k in combination with either the turbulent dissipation ε or the specific turbulence dissipation rate ω, depending on the type of turbulence model. The first variable of the two- equation models describes the energy in the turbulence while the second variable determines the scale of turbulence (length-scale or time-scale) (Bakker, 2002).

It is often argued, despite being mathematically more sophisticated, that two-equation models do not provide significant advantage over one-equation models whilst being computationally

more expensive. This is because they require a much finer grid near the wall, have stronger source terms which negatively impact convergence and require non-trivial upstream and freestream conditions for the turbulence variables (Spalart and Allmaras, 1992).

Nevertheless, it has been found that a compromise between the one-and two-equation models is most preferred by current researchers who are using EVMs (Gatsis, 2000).

A.2.5 Popular Turbulence Models

A.2.5.1 $k-\varepsilon$ Model

The k-ε model is a two-equation model with two separate transport equations (kinetic energy (k) and the dissipation rate (ε)) solving for the turbulent velocity and length scales independently. It is a standard model used by industry due to its robustness, economy and reasonable accuracy for a wide range of turbulent flows. The standard k-ε model is a semi-empirical model and is based on the assumption that the flow is fully turbulent and the effects of molecular viscosity are negligible. Therefore, it is limited to high Reynolds-number flows (FLUENT Theory Guide, 2009). Over the years improvements have been made to the standard k-ε model; two of these variants are the RNG (Re-normalisation Group method) k-ε model and the realizable k-ε model.

A.2.5.2 RNG $k-\varepsilon$ Model

The RNG $k-\varepsilon$ model has an additional term in the ε equation which improves the accuracy for rapidly strained flows. Additionally, this turbulence model improves the accuracy of predicting swirling flows and allows for low-Reynolds number effects under appropriate near-wall treatment, thus, making it more accurate and reliable for a wider range of flows (FLUENT Theory Guide, 2009).

A.2.5.3 Realizable $k-\varepsilon$ Model

In opposition to the standard $k-\varepsilon$ model, the realizable $k-\varepsilon$ model contains a new formulation for the eddy viscosity as well as a new equation for the transport dissipation rate. This model is called "realizable" as it satisfies certain mathematical constraints on the Reynolds stresses, consistent with the physics of turbulent flows and therefore has superior performance for rotating flows, flows with boundary layers subject to strong adverse pressure gradients, separation and recirculation (FLUENT Theory Guide, 2009). Furthermore, this model can be

integrated through the whole boundary layer provided that $y^+ \sim 1$ (Bigarella and Azevedo, 2007).

A.2.5.4 k − ω Model

The standard k-ω model in ANSYS FLUENT is based on the Wilcox model, designed for low Re-number effects, compressibility and shear flow spreading. This model has been developing over the years and corrections and improvements have been made in order to make it applicable for a wider range of flow cases. The model is a semi-empirical model based on transport equations for the turbulence kinetic energy (k) and the specific dissipation rate (ω). Its constants are obtained from calibration against key test cases for turbulent flows (Wilcox, 1998). The k-ω and SA model are both designed to be applicable throughout the boundary layer when the near-wall mesh resolution is sufficient ($y^+ = 1$) and hence require near-wall modelling (Salim and Chea, 2009).

The k- ω model is the model of choice in the sublayer of the boundary layer as unlike other two-equation models it does not involve damping functions and allows simple Dirichlet boundary conditions to be specified. It is a very simple model in comparison to other two-equation models thus yielding to higher numerical stability (Menter, 1993).

The k- ω model is also used in the logarithmic part of the boundary layer and proves to be superior over the k-epsilon model in particular when dealing with adverse pressure gradients in compressible flows (Menter, 1993).

The downside of the k- ω model, however, is that it fails to predict the asymptotic behaviour of the turbulence as it approaches the wall correctly. Next to this, in the wake region of the boundary layer the k-epsilon model proves to be better as it is not sensitive to freestream values ω_f specified for ω outside the boundary layer (Menter, 1993).

As stated earlier, the correct modelling of the logarithmic part of the boundary layer is of importance. However, for flows with moderate pressure gradients, the level of eddy viscosity in the wake region determines whether an eddy viscosity model can predict strong adverse pressure gradient flows correctly. That is also why the k- ω model fails to predict pressure-induced separation. This led to the development of the Shear Stress Transport (SST) model, which switches between the k-ω and k-ε approaches (Menter, 1993).

A.2.5.5 k − ω SST Model

As described in Chapter 3 section 3.4.2 the SST k-ω turbulence model is a two-equation EVM which combines the k-ω and k-ε formulation (Menter, 1993).

The original k- ω model is defined as (Menter, 1993):

$$\frac{\partial(\rho k)}{\partial t}+\frac{\partial(\rho k u_i)}{\partial x_i}=\tau_{ij}\frac{\partial u_i}{\partial x_j}-\beta^*\rho\omega k+\frac{\partial}{\partial x_j}\left[(\mu+\sigma_{k1}\mu_t)\frac{\partial k}{\partial x_j}\right] \quad \text{(A. 2.41)}$$

$$\frac{\partial(\rho\omega)}{\partial t}+\frac{\partial(\rho\omega u_i)}{\partial x_i}=\frac{\gamma_1}{\upsilon_t}\tau_{ij}\frac{\partial u_i}{\partial x_j}-\beta_1\rho\omega^2+\frac{\partial}{\partial x_j}\left[(\mu+\sigma_{\omega 1}\mu_t)\frac{\partial \omega}{\partial x_j}\right] \quad \text{(A. 2.42)}$$

where k is the turbulence kinetic energy, ω is the specific turbulence dissipation rate, ρ is the density, γ_1,β^*, $\sigma_{\omega 1}$, σ_{k1}, and β_1 are turbulence modelling constants, τ_{ij} is the Reynolds stress, μ_t is the turbulence eddy viscosity, t is the time, $\upsilon_t = {}^{\mu_t}/_{\rho}$ is the turbulence kinetic viscosity, μ is the molecular dynamic viscosity and u_i the flow velocity.

The transformed k-ε model, using the relation $\varepsilon = \omega \times k$, is defined as:

$$\frac{\partial(\rho k)}{\partial t}+\frac{\partial(\rho k u_i)}{\partial x_i}=\tau_{ij}\frac{\partial u_i}{\partial x_j}-\beta^*\rho\omega k+\frac{\partial}{\partial x_j}\left[(\mu+\sigma_{k2}\mu_t)\frac{\partial k}{\partial x_j}\right] \quad \text{(A. 2.43)}$$

$$\frac{\partial(\rho\omega)}{\partial t}+\frac{\partial(\rho\omega u_i)}{\partial x_i}=\frac{\gamma_2}{\upsilon_t}\tau_{ij}\frac{\partial u_i}{\partial x_j}-\beta_2\rho\omega^2+\frac{\partial}{\partial x_j}\left[(\mu+\sigma_{\omega 2}\mu_t)\frac{\partial \omega}{\partial x_j}\right]+2\rho\sigma_{\omega 2}\frac{1}{\omega}\frac{\partial k}{\partial x_j}\frac{\partial \omega}{\partial x_j} \quad \text{(A. 2.44)}$$

The transition between the two models is achieved by multiplying Equation (3.5) and Equation (3.6) by a function F_1 and Equation (3.7) and Equation (3.8) by a function (1-F_1) and adding them up together. F_1 is designed so that it equals one in the near wall region, thus activating

the k-ω model and zero away from the wall (activating only the k-ε model). By doing the above step one arrives at (Menter, 1993):

$$\frac{\partial(\rho k)}{\partial t}+\frac{\partial(\rho k u_i)}{\partial x_i}=\tau_{ij}\frac{\partial u_i}{\partial x_j}-\beta^*\rho\omega k+\frac{\partial}{\partial x_j}\left[(\mu+\sigma_k\mu_t)\frac{\partial k}{\partial x_j}\right] \quad \text{(A. 2.45)}$$

$$\frac{\partial(\rho\omega)}{\partial t}+\frac{\partial(\rho\omega u_i)}{\partial x_i}=\frac{\gamma}{\upsilon_t}\tau_{ij}\frac{\partial u_i}{\partial x_j}-\beta\rho\omega^2+\frac{\partial}{\partial x_j}\left[(\mu+\sigma_\omega\mu_t)\frac{\partial\omega}{\partial x_j}\right]+2\rho(1-F_1)\sigma_{\omega 2}\frac{1}{\omega}\frac{\partial k}{\partial x_j}\frac{\partial\omega}{\partial x_j} \quad \text{(A. 2.46)}$$

Here the turbulence eddy viscosity is calculated from

$$\mu_t=\frac{\rho k}{\omega} \quad \text{(A. 2.47)}$$

The constants of the model ($\varphi_1$and φ_2) are calculated as follows:

$$\varphi=F_1\varphi_1+(1-F_1)\varphi_2 \quad \text{(A. 2.48)}$$

The additional functions required are

$$F_1 = \tanh(arg_1^4) \tag{A. 2.49}$$

$$arg_1 = \min\left[\max\left(\frac{\sqrt{k}}{\beta^* \omega d}, \frac{500\nu}{y^2 \omega}\right), \frac{4\rho\sigma_{\omega 2} k}{CD_{k\omega} y^2}\right] \tag{A. 2.50}$$

$$CD_{k\omega} = \max\left(2\rho\sigma_{\omega 2} \frac{1}{\omega} \frac{\partial k}{\partial x_j} \frac{\partial \omega}{\partial x_j}, 10^{-20}\right) \tag{A. 2.51}$$

with d being the distance from the field point to the nearest wall (Menter, 1993). The constants for the baseline SST model were obtained empirically and are as follows:

$$\gamma_1 = \frac{\beta_1}{\beta^*} - \frac{\sigma_{\omega 1} \kappa^2}{\sqrt{\beta^*}}$$

$$\gamma_2 = \frac{\beta_2}{\beta^*} - \frac{\sigma_{\omega 2} \kappa^2}{\sqrt{\beta^*}}$$

$\sigma_{k1} = 0.5$ $\sigma_{\omega 1} = 0.5$ $\beta_1 = 0.075$

$\sigma_{k2} = 1.0$ $\sigma_{\omega 2} = 0.856$ $\beta_2 = 0.0828$

$\beta^* = 0.09$ $\kappa = 0.41$

Appendix 3 Literature Review Computational Fluid Dynamics (CFD)

A.3.1 Analytical Description of the Leading- and Trailing-Edge Geometry

The aerofoil geometry was created using the analytical definition of Chu and Luckring (Volume 1 Appendix A, 1996). According to them the shape is defined by

$$\varphi(\zeta) = \pm x_1\left(a\sqrt{\zeta} + b\zeta + c\zeta^2 + d\zeta^3\right) \qquad (0 \leq \zeta \leq 1) \qquad \text{(A. 3.1)}$$

and the boundary (the flat plate part of the wing) is defined by (Chu and Luckring, 1996)

$$\psi(\zeta) = \pm x_1\left[\frac{1}{x_1} + m(\zeta - 1) + \frac{n x_1}{2}(\zeta - 1)^2\right] \qquad (1 \leq \zeta) \qquad \text{(A.3.2)}$$

such that

$$\psi|_{\zeta=1} = l \qquad \left.\frac{d\psi}{dx}\right|_{\zeta=1} = m \qquad \left.\frac{d^2\psi}{dx^2}\right|_{\zeta=1} = n \qquad \text{(A.3.3)}$$

with ζ being defined as (Chu and Luckring, 1996)

$$\zeta = \frac{x - x_0}{x_1} \qquad \text{(A.3.4)}$$

and a, b, c and de being defined as (Chu and Luckring, 1996)

$$a = \sqrt{\frac{2r}{x_1}} \qquad \text{(A.3.5)}$$

$$b = -\frac{15}{8}a + 3\frac{l}{x_1} - 2m + \frac{mx_1}{2} \quad \text{(A.3.6)}$$

$$c = \frac{5}{4}a - 3\frac{l}{x_1} + 3m - nx_1 \quad \text{(A.3.7)}$$

$$d = -\frac{3}{8}a + \frac{l}{x_1} - m + \frac{nx_1}{2} \quad \text{(A.3.8)}$$

Note that for the flat plate part of the model represented by ψ; m and n are equal to zero and for a SLE the radius is r=0 thus reducing Equations (A.3.5)-(A.3.8).

An illustration of the above equations can be seen in Figure A. 3.1.

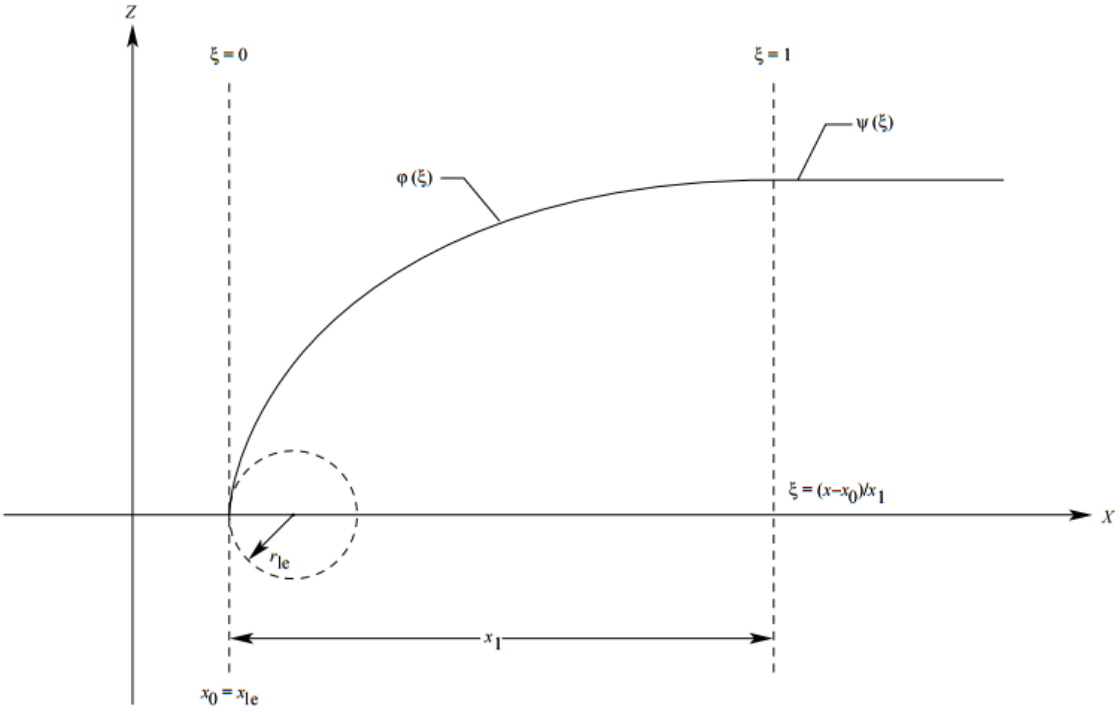

Figure A. 3.1 Semi-thickness functions of the VFE-2 configuration (Chu and Luckring, 1996).

The leading-edge is designed so it matches the flat plate wing at a streamwise distance of 15% of the root chord. Therefore x_0 and x_1 in the equations above for the leading-edge are (Chu and Luckring, 1996):

$$x_0 = x_{le} \tag{A.3.9}$$

$$x_1 = 0.15 \tag{A.3.10}$$

For the flat centre part of the wing the equation for x_0 and x_1 are (Chu and Luckring, 1996):

$$x_0 = x_{le} + 0.15 \tag{A.3.11}$$

$$x_1 = 0.9 - x_0 \tag{A.3.12}$$

The trailing edge closure is designed to produce a sharp trailing edge and to match the flat plate at 90% of the root chord and has the following coefficients for x_0 and x_1 (Chu and Luckring, 1996):

$$x_0 = 1 \tag{A.3.13}$$

$$x_1 = 0.1 \tag{A.3.14}$$

A.3.2 Similarity Parameters

In fluid mechanics, non-dimensional parameters are useful for planning, presentation, comparison and interpretation of experimental and numerical data as geometric scales do not need to be taken into account. This is especially true for fluid dynamics where problems are too complex to be solved analytically and must be tested by experiment or approximated by CFD. The use of non-dimensional similarity parameters with regards to geometric, kinematic and dynamic similarity provides insight on controlling parameters and the nature of the problem as well as enabling the use of scaling laws. This means aircraft testing can be conducted on a model level and conclusions on the behaviour of the prototype can be drawn as all the relevant dimensionless parameters have the same corresponding values (Bahrami, 2014).

Establishing complete similarity is highly unlikely, however, particular similarity can be obtained. One can distinguish between three types of similarity (Bahrami, 2014):

1. Geometric similarity: exists when the model and prototype are geometrically similar meaning all body dimensions in all three coordinates have the same linear scale ratio.
2. Kinematic similarity: exists when model and prototype are geometrically similar and have the same length and time scale ratio (matching Re number).
3. Dynamic similarity: exists when the model and the prototype are kinematically similar and when Re, M are equal between model and prototype, meaning they both have the same force scale ratio.

In order to investigate turbulence model choice and verify mesh density the simulation is set up using dynamic similarity.

A.3.3 Dynamic Similarity

A.3.3.1 Mach Number

The Mach number is defined as the ratio between the airspeed, v, to the speed of sound, a, and is often used in aerodynamics to categorise different regimes of flight (Corda, 2017).

When a body moves through the atmosphere it generates forces based on the body's geometry, attitude, altitude and velocity. However, these forces are also influenced by the properties of the air, including its viscosity and elasticity or compressibility. As the body moves through the fluid, it affects the gas surrounding it. The inertia force F_i is then the resistance of the fluid when varying the velocity of the body and is a consequence of the fluid's momentum and is defined as (Chegg, n.d.):

$$F_i \propto \rho l^2 v^2 \qquad \text{(A. 3.15)}$$

The elastic force F_e is due to the compressibility of the fluid, where a reduction in volume at constant pressure leads to an increase in elastic modulus E resulting in (Chegg, n.d.)

$$F_e \propto E l^2 \qquad \text{(A.3.16)}$$

To evaluate dynamic similarity both inertia and elastic forces are taken into consideration by forming the inertia-elasticity force ratio (Chegg, n.d.).

$$\frac{F_i}{F_e} \propto \frac{\rho v^2 l^2}{E l^2} \qquad \text{(A.3.17)}$$

$$\frac{F_i}{F_e} \propto \frac{\rho v^2}{E} \qquad \text{(A.3.18)}$$

The term $\frac{\rho v^2}{E}$ is also known as the Cauchy number. The speed of sound, a, depends on the elastic modulus of the medium and the density (Ling, Sanny and Moebs, 2019),

$$a^2 = \frac{E}{\rho} \tag{A.3.19}$$

Substituting Equation (A.3.19) into (A.3.18) results in (Chegg, n.d.)

$$\frac{F_i}{F_e} \propto \frac{v^2}{a^2} = M \tag{A.3.20}$$

Equation (A.3.20) is another physical interpretation of the Mach number. The ratio of inertia force to elastic force is related to the compressibility, or springiness, of the gas, thus, making the Mach number a governing parameter for compressible flows (Corda, 2017).

A.3.3.2 Reynolds Number

The Reynolds number is an important similarity parameter for the viscosity of a gas. It is defined as the ratio of inertial forces to viscous forces or stickiness of the gas (Anderson, 2011) and is given by (Corda, 2017)

$$Re = \frac{\text{inertia force}}{\text{viscous force}} = \frac{\rho V^2 L^2}{\mu V L} = \frac{\rho V L}{\mu} \tag{A. 3.21}$$

with μ being the dynamic viscosity of the gas.

If the Re of two independent experiments are the same, then the effects of the viscous forces relative to the inertial forces are modelled properly (Anderson, 2011).

A.3.4 Matching Mach and Reynolds Number

In CFD the freestream boundary condition can be specified by Mach number, pressure and temperature. In order to obtain kinematic similarity, Mach number and Reynolds number need to be matched. Once the Mach number is set, temperature and pressure need to be calculated in order to match the Reynolds number (Ning, 2017).

As stated earlier the Mach number and Reynolds number are defined as

$$M = \frac{V}{a}, \quad Re = \frac{\rho V c}{\mu} \tag{A. 3.22}$$

where V is the free stream velocity, c the chord length and a the speed of sound. In Equation (A. 3.22) density is a function of pressure and temperature defined by the ideal gas law and both the speed of sound and the dynamic viscosity are functions of temperature. Thus, Equation (A. 3.22) can be rewritten as (Ning, 2017):

$$M = \frac{V}{a(T)}, \quad Re = \frac{\rho(p,T) V c}{\mu(T)} \tag{A. 3.23}$$

where p is the ambient pressure and T is the ambient temperature. Rearranging the Mach number and Reynolds Number equations for the velocity V and substitute one into the other yields to (Ning, 2017)

$$Re = \frac{\rho(p,T) Ma(T) c}{\mu(T)} \tag{A. 3.24}$$

Equation (A. 3.24) has one degree of freedom as either temperature can be chosen to calculate the pressure satisfying the equation or vice versa.

The relationship between density, temperature and pressure is given by the ideal gas law. Substituting it into Equation (A. 3.24) results in (Ning, 2017)

$$Re = \frac{pM\sqrt{\gamma RT}c}{RT\mu(T)} = \frac{pMc\sqrt{\gamma}}{\mu(T)\sqrt{RT}} \tag{A. 3.25}$$

where R is the ideal gas constant, which is $R=287\frac{J}{kg\,K}$ for dry air and γ is the ratio of specific heat which is $\gamma=1.4$ for air.

The dependence of dynamic viscosity on temperature can be found from Sutherland's law (Ning, 2017):

$$\mu = \mu_{ref}\left(\frac{T}{T_{ref}}\right)^{3/2}\frac{T_{ref}+S}{T+S} \qquad \text{(A. 3.26)}$$

where $T_{ref} = 273.15K$, S is the Sutherland temperature $S = 110.4, \mu_{ref} = 1.716 \times 10^{-5}\frac{kg}{ms}$. Substituting Equation (A. 3.26) into Equation (A. 3.25) and rearrange for p then gives (Ning, 2017)

$$p = \frac{Re\mu(T)\sqrt{RT}}{Mc\sqrt{\gamma}} \qquad \text{(A. 3.27)}$$

By choosing a temperature T, Equation (A. 3.27) can now be solved directly for the pressure p.

Applying Equation (A. 3.27) to the benchmark case (M=0.07 and Re=1×10^6) and assuming a temperature of 288K leads to the following set up (Table A. 3.1).

Table A. 3.1 Conditions for CFD set up to match experimental results by TUM.

Mach Number	0.07
Reynolds Number	1×10^6
Mean Aerodynamic Chord [m]	0.327
Temperature [K]	288
Pressure [$\frac{N}{m^2}$]	189980.405

A.3.5 Non-Uniform Refinement Ratio

A constant mesh refinement ratio over three meshes can become computationally very expensive. Studies by Roache (1998) have shown that in order to obtain good results for GCI calculations the only requirement is a refinement ratio of $r => 1.3$ but not necessarily a constant refinement ratio (Schwer, 2008).

The order of convergence for non-uniform refinement ratios is (Schwer, 2008):

$$p = \frac{\left|\ln\left|{}^{f_{32}}/_{f_{21}}\right| + q(p)\right|}{\ln r_{21}} \tag{A. 3.28}$$

with q(p) being defined as (Schwer, 2008)

$$q(p) = \ln\left(\frac{r_{21}^{p} - s}{r_{32}^{p} - s}\right) \tag{A. 3.29}$$

and s being defined as (Schwer, 2008)

$$s = \text{sign}\left({}^{f_{32}}/_{f_{21}}\right) \tag{A. 3.30}$$

with $f_{ij} = f_i - f_j$ and $r_{ij} = \frac{h_i}{h_j}$. Note, that Equation (A. 3.28) until (A. 3.29) have to be solved iteratively using an initial guess for $q(p) = 0$. Assuming Equation (A. 3.29) to be equal to zero results in Equation (A. 3.28) being identical to the Equation for constant grid refinement ratio (Schwer, 2008).

The GCI can then be calculated using

$$GCI_{21} = F_s \frac{e_{21}}{r_{21}^{p} - 1} \tag{A. 3.31}$$

GCI_{21} is defined as the amount of discretisation error in the finest grid relative to the converged numerical solution (Schwer, 2008).

Based on the results obtained for the convergence rate p and the solutions of the two finest mesh an extrapolation of the numerical solution can be made providing a useful estimate of the numerically converged solution (Schwer, 2008).

$$f_{21}^{*} = \frac{r_{21}^{p} f_1 - f_2}{r_{21}^{p} - 1} \tag{A. 3.32}$$

Appendix 4 Wind Tunnel Rig Design and CFD Validation by Wind Tunnel Measurements

A.4.1 Wind Tunnel Test Rig Design (from Section 5.4)

For the wind tunnel experiments a rig needed to be designed as the current mounting system is not suitable for the delta wing configuration. Two ideas are considered and shown in Figure A. 4.1.

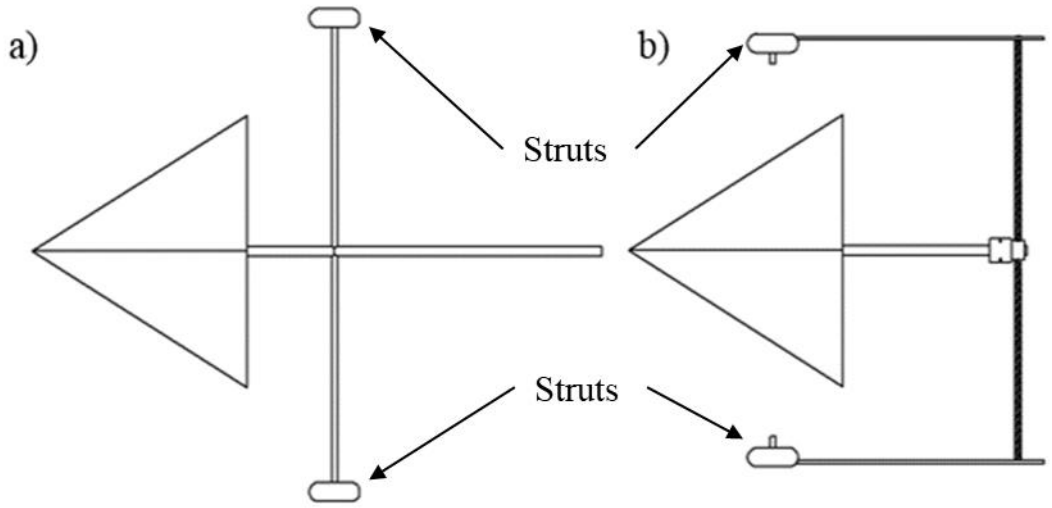

Figure A. 4.1 Possible wind tunnel rig designs for the delta wing experiment; a) initial idea b) final design.

The design limitations for the rig are the mounting joints at the struts and the power of the motor responsible for changing the angle of attack. The strut joints have a diameter of 12.7 mm and cannot be exchanged. After calculating the required sting diameter as well as the forces and moments involved, design a) is discarded as it is deemed too heavy for the motor.

Design b), from now on referred to as E-rig, is then designed as depicted in Figure A. 4.2. The rig allows for different strut positions (maximum distance=1m, minimum distance= 0.15m) but also for the wing being moved further upstream or downstream if required. Additionally, a block was manufactured to mount the high-resolution inclinometer to guarantee accurate readings for different angles of attack.

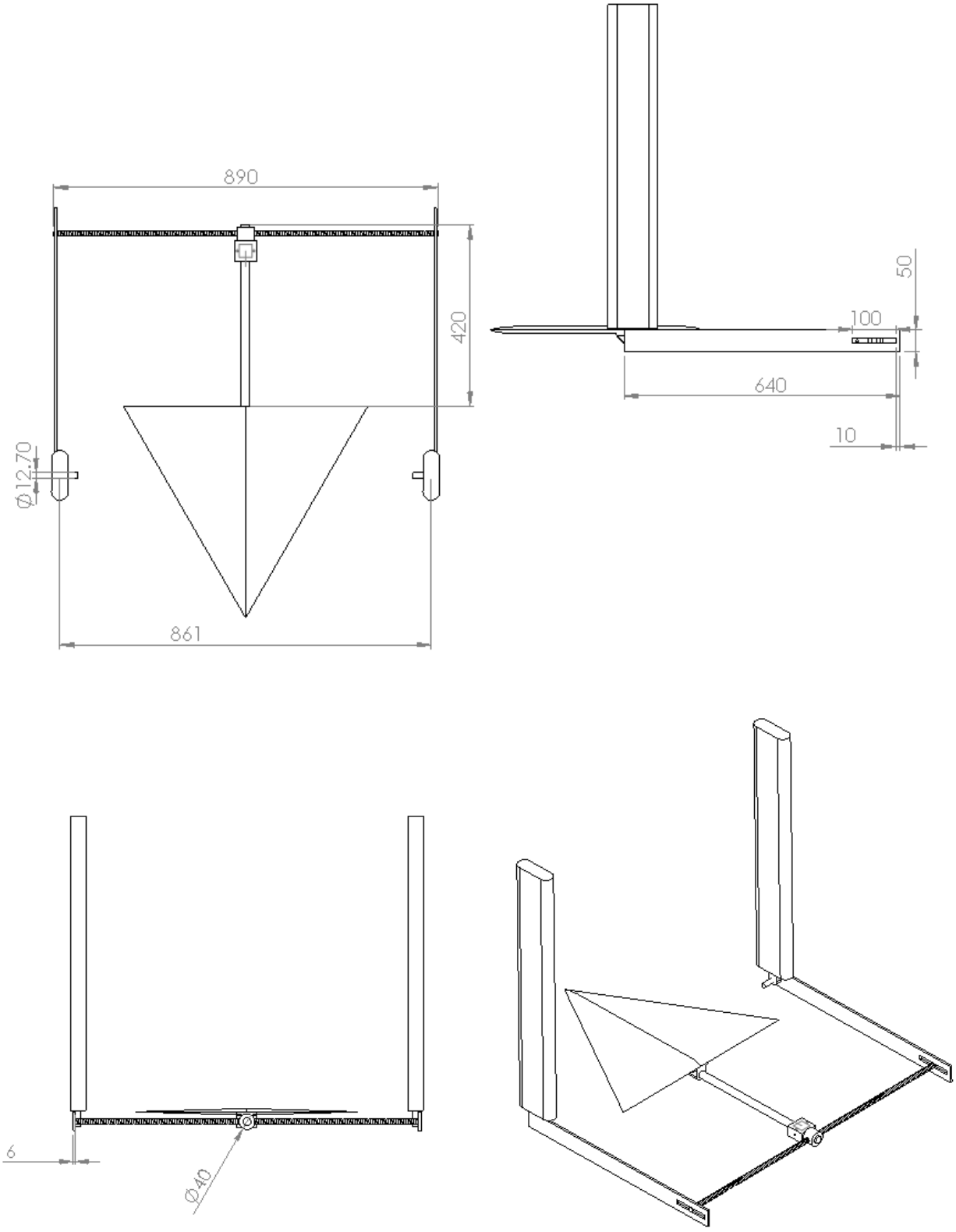

Figure A. 4.2 Final geometry of the wind tunnel rig for the delta wing experiments in mm.

In order to guarantee that the rig is able to withstand the forces during the experiment, it was designed based on the force data obtained by initial CFD runs.

A.4.2 Wing mount design (also see Section 5.4)

The model required a wing mount for attaching the sting. The final design can be seen in Figure A. 4.3.

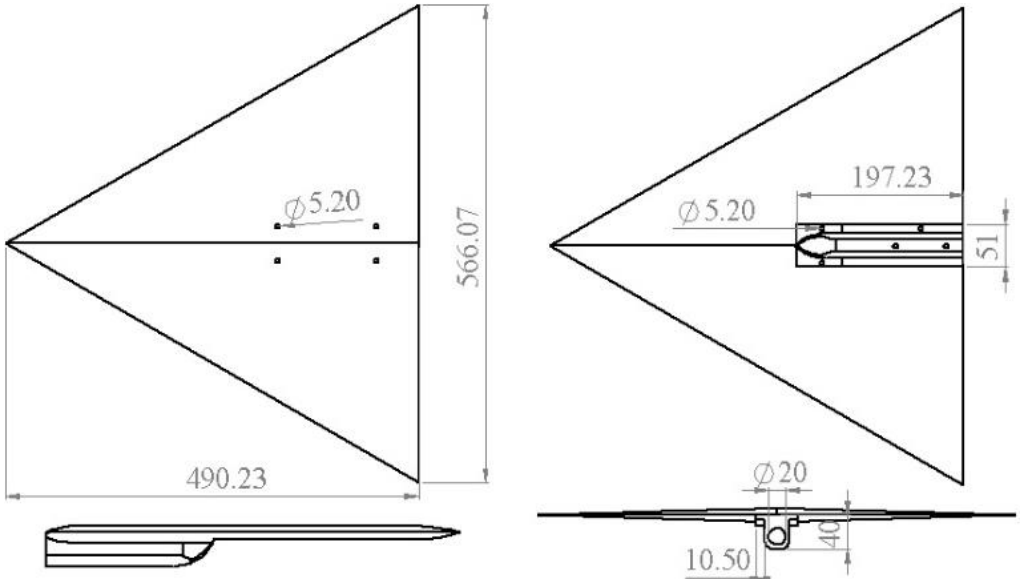

Figure A. 4.3 Geometry of the wind tunnel model sting mounts for the delta wing experiments with the dimensions in mm.

The wing mount is attached to the wing by four M6 bolts and attached to the mounting sting via two M6 fastener screws. The bolt loads were calculated to ensure the right diameter was chosen and the bolts would hold during wind tunnel testing. Figure A. 4.4 shows the free body diagram of the wing including the bolts. Here, F_{Lift} is the lift force acting through the centre of pressure, F_{B_1} and F_{B_2} being the bolt forces and F_C being the contact force between wing and wing mount.

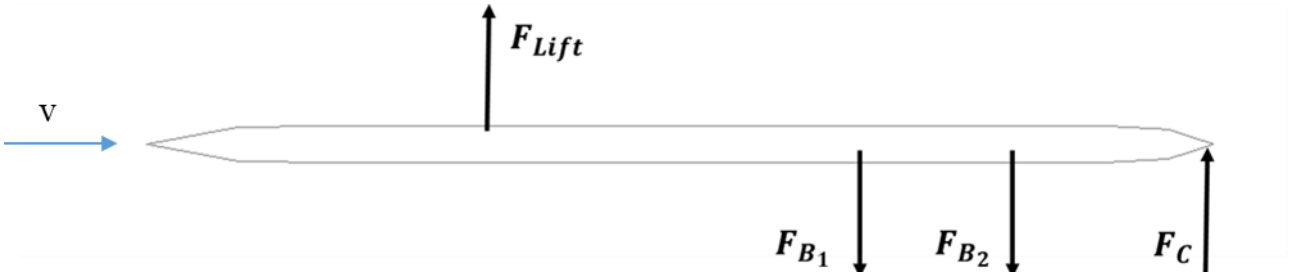

Figure A. 4.4 Free body diagram of one of the tested delta wings for bolt load calculation.

Assuming that F_C is located at the end of the wing and $F_{B_2} = 0$, as this would result in a higher bolt force for F_{B_1}, then a new free body diagram can be drawn. This is depicted in Figure A. 4.5.

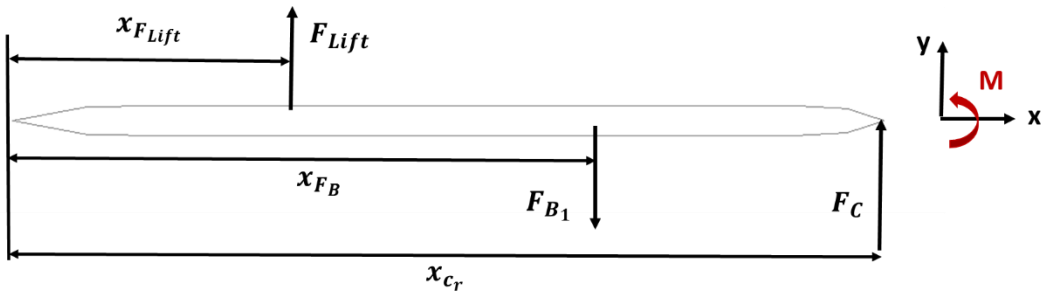

Figure A. 4.5 Free body diagram of one of the tested delta wings for bolt load calculation with assuming $F_{B_2} = 0$.

Assuming the worst-case scenario, where there is solely the lift force acting at the leading-edge and the rig is static balanced, then the moment around the leading-edge is defined as

$$\sum M = 0 = -F_{B_1} x_{F_B} + F_c x_{c_r} \qquad \text{(A. 4.1)}$$

$$\sum F = 0 = F_{Lift} - F_{B_1} + F_c \qquad \text{(A.4.2)}$$

From Equation (A. 4.1)and (A.4.2) it follows:

$$F_c = F_{B_1} - F_{Lift} \qquad \text{(A.4.3)}$$

$$F_c x_{c_r} = F_{B_1} x_{F_B} \qquad \text{(A.4.4)}$$

Substituting (A.4.3) into (A.4.4) gives

$$(F_{B_1} - F_{Lift}) x_{c_r} = F_{B_1} x_{F_B} \qquad \text{(A.4.5)}$$

$$F_{B_1} = F_{Lift} \left(\frac{x_{c_r}}{x_{c_r} - x_{F_B}} \right) \qquad \text{(A.4.6)}$$

From (A.4.6) can be seen that F_{B_1} is magnified by a ratio of $\left(\frac{x_{c_r}}{x_{c_r}-x_{F_B}}\right)$. When $x_{F_B} = \frac{x_{c_r}}{2}$ then $F_{B_1} = 2 \times F_{Lift}$. From CFD calculations it was found that the maximum lift force is around 30 N, which would give a maximum bolt loading of 60 N. From bolt loading tables it can be seen that the maximum loading of an M6 bolt is around 4.5 kN, thus justifying the use of M6 bolts.

A.4.3 Stress calculation for the wind tunnel rig: Force and moment estimation (also see Section 5.4)

The design of the E-rig requires the estimation of the forces expected in order to calculate the stresses in the structure. The forces of the wing are obtained from initial CFD simulations and the forces and stresses in the rig are obtained using the method of trusses (Hibbeler, 2012). The simplified E-rig is shown in Figure A. 4.6, where the forces are indicated by a capital F and the lengths indicated by the letter r.

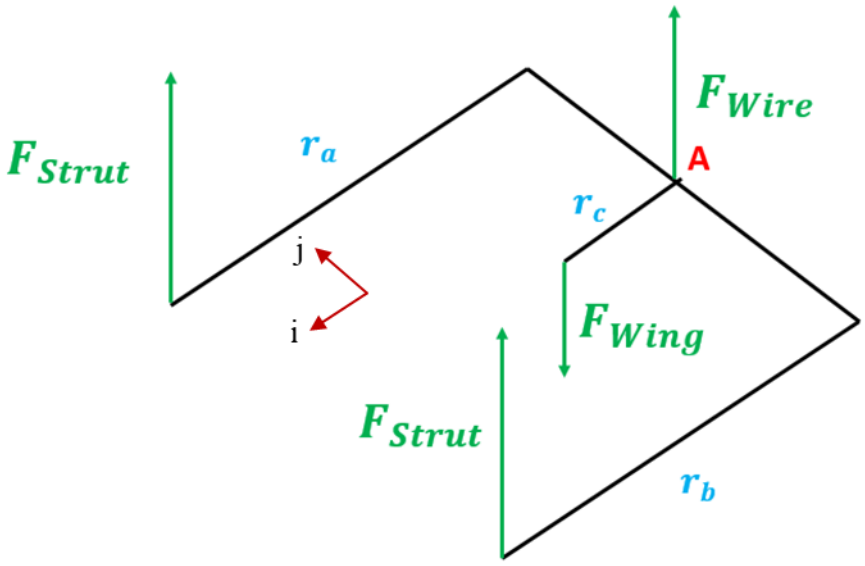

Figure A. 4.6 Free body diagram of the proposed wind tunnel rig.

The lift force generated at 20 degrees angle of attack is used for the stress analysis as it is the highest achievable angle in the wind tunnel and is estimated to be $F_{Wing} = 150N$. It is also assumed that this force acts through the apex as this results in the longest lever arm and thus the worst-case scenario.

Based on this the moment around A can be calculated by defining the vector for each truss as follows;

$$r_a = \left\{ l_{I\ beam} i - \frac{1}{2} l_{threaded\ rod} j \right\} \quad \text{(A.4.7)}$$

$$r_c = \{(c + l_{sting})i\} \quad \text{(A.4.8)}$$

The moment equation then becomes

$$M_{rA} = F_{Strut} r_a + F_{Strut} r_b + F_{wing} r_c = -35\text{Nm} \quad \text{(A.4.9)}$$

with

$$F_{Strut} = \{0\ 0\ F_{Strut}\}$$

$$F_{Wing} = \{0\ 0\ -F_{Wing}\}$$

The stress in the rig can then be estimated using the normal stress equation:

$$\sigma = \frac{M y_{max}}{I} \quad \text{(A.4.10)}$$

Where σ is the normal stress, $M = M_{rA}$ the bending moment, I the second moment of area and y_{max} the maximum distance from the neutral axis. For the sting the distance to the neutral axis is the radius $y_{max} = r$ and the second moment of area for a circular cross-section is given by:

$$I = \frac{\pi}{4} r^4 \quad \text{(A.4.11)}$$

The factor of safety (FoS) can be obtained by:

$$FoS = \frac{\sigma_{yield_{Steel}} \times I}{|M| \times r} = \frac{\sigma_{yield_{Steel}} \times \pi \times r^3}{4 \times |M|} \quad (A.4.12)$$

with $\sigma_{yield_{Steel}} = 250MPa$ and M is taken from equation A.5.9

Thus rearranging (A.5.12), the minimum radius of the sting and taking a FoS of three results in:

$$r = \sqrt[3]{\frac{4 \times FoS \times M}{\pi \sigma_{yield_{Steel}}}} = 7.1mm \quad (A.4.13)$$

The radius of the threaded rod can be determined in a similar fashion. The threading needs to be taken into account as it causes stress concentrations. This is done by applying a stress-concentration factor K_t, used to relate the actual maximum stress at a discontinuity to the nominal stress (Gudynas and Nisbett, 2015).

$$K_t = \frac{\sigma_{max}}{\sigma_0} \quad (A.4.14)$$

where σ_0 is the nominal stress.

For a given radius K_t can be found from relevant tables (Budynas and Nisbett, 2015) resulting in:

$K_t = 1.6$ for bending and

$K_t = 1.3$ for torsion

The equation for the determination of the radius using $K_t = 1.6$, as it the more critical value, and a FoS = 2 then becomes

$$r = \sqrt[3]{\frac{4 \times FoS \times M \times K_t}{\pi \sigma_{yield_{Steel}}}} = 8.3mm \quad (A.4.15)$$

Having determined the radii of the sting and the threaded rod, the shear flow in the rig can be determined using Equation (A.4.10). For this the geometry is simplified as depicted in Figure A. 4.7.

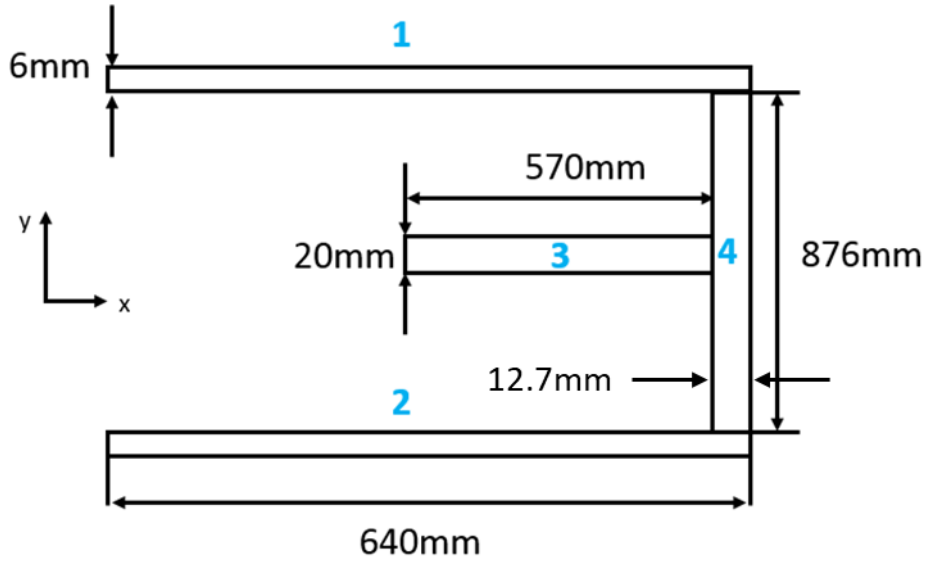

Figure A. 4.7 Top view of E-rig including dimensions.

The neutral axis can be calculated using

$$y_{max} = \frac{\sum Ay}{\sum A} \tag{A.4.16}$$

where A is the area of each beam section and y is the distance from the base of each section to the mid-point of each rectangle. The second moment of area for the beam structure can be calculated using the formula:

$$I = \sum Ah^2 + \sum \frac{xy^3}{12} \tag{A.4.17}$$

where h is the distance from the neutral axis to the mid-point of each rectangle.

$$h = |y_{max} - y| \tag{A.4.18}$$

The results for these calculations are shown in Table A. 4.1 below.

Table A. 4.1 Calculation of the distance to the neutral axis.

Rectangle No.	Area [mm^2]	x [mm]	y[mm]	y[mm] Distance from base of section to the mid-point of each rectangle
1	3840	6	640	320
2	3840	6	640	320
3	8985.512	20	570	402.6622
4	11125.2	876	12.7	633.65

The maximum moment experienced by the rig has been found to be 35Nm (see calculations above). The estimated stress in the structure is 0.005 MPa, which is far below the yield stress of steel of 250MPa. Therefore, it can be concluded that the rig is save to use for the experiments.

A.4.4 Use of Statistics in Wind Tunnel Testing (see Section 5.5)

Wind tunnel data is only valid if it can be reproduced or consistently compared with other tunnels. This makes it necessary to determine the quality of the flow data, requiring a detailed calibration process in which flow features and uncertainties are determined (Yen and Braeuchle, 2000). Additionally, the experimental results need to be statistically analysed using the ISO 17713-1:2007 standard uncertainty method where the confidence level needs to be 95%. This method is an AMSE/ANSI Standard which recommends that uncertainties can be divided into two components; systematic bias (B_j) and random precision (P_j) (Yen and Braeuchle, 2000). Accuracy measures how close the measured value is to the actual (true) value and precision is defined as how close the measured values are to each other (ASTM International). Therefore, bias can also be related to repeatability of the experiment.

The basic measure of precision, also called standard deviation, S, and thus repeatability is defined as (Yen and Braeuchle, 2000):

$$S = \sqrt{\left[\frac{1}{N-1}\sum_{i=1}^{N}(X_i - \overline{X})^2\right]} \qquad (A.4.19)$$

where the mean of the sample population $\overline{X}$ is defined as (Yen and Braeuchle, 2000):

$$\overline{X} = \frac{1}{N}\sum_{i=1}^{N} X_i \qquad \text{(A.4.20)}$$

with N being the number of samples. A high value of S indicates a low precision whereas a low value indicates high precision) (ASTM). The precision limit can then be reported by averaging data from multiple tests, which reduces the randomness of the error (Yen and Braeuchle, 2000):

$$\overline{P} = \frac{tS}{\sqrt{N}} \qquad \text{(A.4.21)}$$

where $\overline{P}$ is the precision limit of the sample mean and t is the coverage factor from the T-distribution table. Once the standard deviations are calculated S, 2S or 2.8S can be reported. 2S would mean that 95% of all data is expected to fall within 2S of the mean or that that 95% of all results will differ by less than 2S.

If the true value or an accepted reference value is available the bias is defined as the difference between the average of all data and the reference value (ASTM).

The recommended procedure using the ISO method for estimating the precision and the accuracy is as follows (Yen and Braeuchle, 2000):

1. Determine the data reduction equation and identify the important variables. Establish how well the final result needs to be known as it gives a guideline regarding the tolerated uncertainty of each variable.
2. Estimate the range of anticipated test conditions. Investigate the sensitivity of the uncertainty in the result to the uncertainties of the variables, with focus on those variables whose uncertainties affect the results the most.
3. Focus on obtaining detailed estimates of the uncertainties in the most important variables.

4. Perform detailed uncertainty analysis including systematic bias and precision uncertainties.
    - Usually variables have uncertainty sources which contribute to their uncertainty. Their relative significance needs to be determined. An order of magnitude analysis can be used to eliminate insignificant sources. A rule of thumb is that if uncertainties are smaller than $1/4^{th}$ or $1/5^{th}$ of the largest sources they can be neglected.

The data reduction equation is defined as

$$r = (X_1, X_2, \ldots X_j,)$$

where X_i are the contributing variables or measured variables and r is the final result of the measurement. Figure A. 4.8 shows how individually measured variables X_j are influenced by multiple errors and how these propagate into the final result (r).

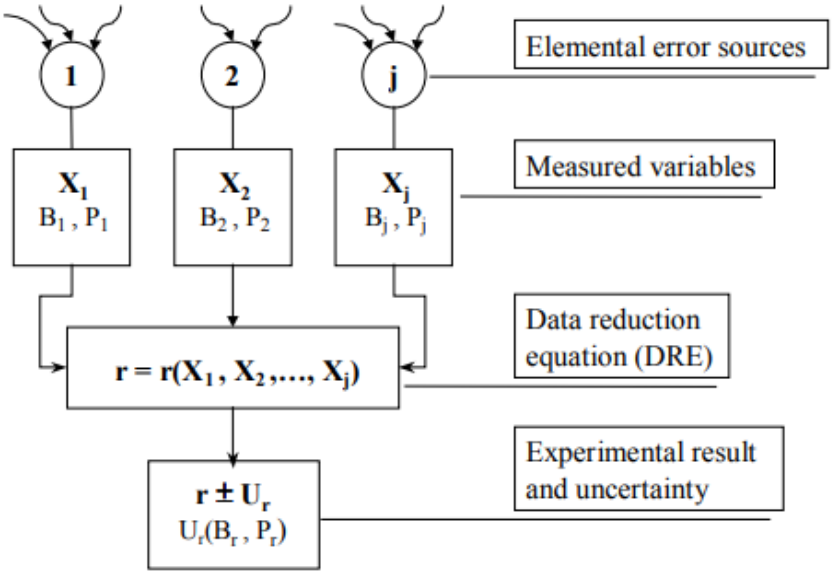

Figure A. 4.8 Influence of multiple errors on measured variables (Coleman and Steele, 1989).

The uncertainty of the result U_r can then be calculated using the ISO method (Yen and Braeuchle, 2000):

$$U_r^2 = \sum_{i=1}^{j} \theta_i^2 (tb_i)^2 + 2 \sum_{i=1}^{j-1} \sum_{k=i+1}^{j} \theta_i \theta_k (t^2 b_{ik}) + \sum_{i=1}^{j} \theta_i^2 (tS_i)^2 + 2 \sum_{i=1}^{j-1} \sum_{k=i+1}^{j} \theta_i \theta_k (t^2 S_{ik}) \quad \text{(A.4.22)}$$

where t is the coverage factor which can be assumed to be t=2, resulting in a 95% confidence interval, and S_i and S_{ik} are the precision indices for the individual and correlated effects. The

correlated bias indices are expressed as b_i and b_{ik}. As there are no correlated values in this study S_{ik} and b_{ik} are neglected.

The sensitivity coefficient θ_i can be determined by (Abernethy, Benedict and Dowdell, 1985)

$$\theta_i = \frac{\partial r}{\partial X_i} \tag{A.4.23}$$

The overall results can then be presented in the form of (Yen and Braeuchle, 2000):

$$r \pm U_r \tag{A.4.24}$$

A.4.4.1 Linear Regression

Linear regression is a statistical tool used to model the relationship between two variables by fitting a linear equation to the obtained data. Before applying this method, it needs to be established whether there is a significant association between the two variables. This can be done by using a scatterplot or by evaluating the correlation coefficient, which takes a value between -1 and 1 indicating the strength of the association of the observed data for the two variables. Here, 1 means a strong positive relationship, -1 a strong negative relationship and 0 indicates no relationship between the variables (Schneider, Hommel and Blettner, 2010).

A linear regression line has the equation of the form (Hengartner ,1997)

$$y = a + bX \tag{A.4.25}$$

where, X is the explanatory variable, y is the dependent variable, b is the slope of the line and a is referred to as the intercept.

The most common method is fitting the regression line, which minimises the sum of the squares of the vertical deviations from each data point to the line (Hengartner ,1997).

Linear regression will be used here mainly for the wind tunnel calibration. The output voltage for the inclinometer with varying angle of attack can be estimated this way for a wide range of angles and the regression line equation can be programmed into the wind tunnel's numerical data system.

A.4.4.2 Outlier Detection

Once the regression line has been plotted for a group of data it can be checked for extreme values which deviate from other observations in the sample. They can indicate either a variability in measurement, experimental errors or novelty (Ben-Gal, 2005). Therefore, outliers cannot be just discarded but need a statistical criterion which identifies points that can be considered for rejection. There are many methods to do so, however, Chauvenet's criterion is the most widely used criterion in engineering and physics (Limb et al. 2017). It states that all data points that fall within a band around the mean that correspond to a probability of 1-1/ (2N) should be retained. An illustration of this can be seen in Figure A. 4.9 (Warrington, 2016).

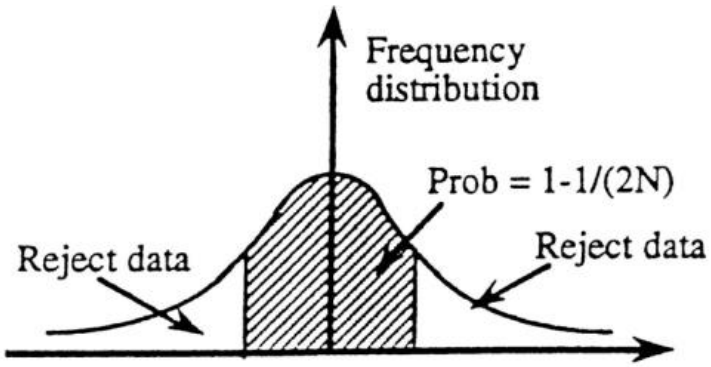

Figure A. 4.9 Visualisation of Chauvenet's Criterion (Warrington, 2016).

Chauvenet's criterion assumes that the data is normally distributed around the mean, which is true for sufficiently large sample sizes but can be flawed for small ones. The Z-score, which is a measurement of the number of standard deviations a data point is from the mean, can be calculated using Buie, (2017)

$$Z = \left| \frac{X_i - \overline{X}}{S_X} \right| \tag{A.4.26}$$

where $\overline{X}$ is the mean of a sample, X_i is the selected data point and S_X the standard deviation.

The probability can be calculated using Buie, (2017)

$$P = n\left(1 - \operatorname{erfc}\left(\frac{Z}{\sqrt{2}}\right)\right) \tag{A.4.27}$$

If

$$P < \frac{1}{2}$$

then data point X_i is rejected. Note erfc is the error function defined as (Spanier and Oldham, 1987)

$$\mathrm{erf}(z) = \frac{2}{\sqrt{\pi}} \int_z^{\infty} e^{-r^2}\, d \qquad \text{(A.4.28)}$$

The methods described above to calculate uncertainty and detect outliers are applied to the measured wind tunnel data with the results being found in Chapter 5 section 5.7.

A.4.5 Raw Data Analysis

A.4.5.1 Tare Runs

Before evaluating the wind tunnel results and applying wind tunnel corrections, a statistical analysis of the air-off tare runs is conducted. Three runs were conducted for each tare run; one being with the wing mounted and the other one with the dummy mounted.

The dummy has a cylindrical shape with rounded front as depicted in Figure A. 4.10 and serves as a simplification of the wing mount. The frontal area of the dummy matches the one of the wing mount. The simplifications were necessary due to the geometrical complexity of the mount. The mount itself could not be run as its lips would generate more drag when run without the wing mounted.

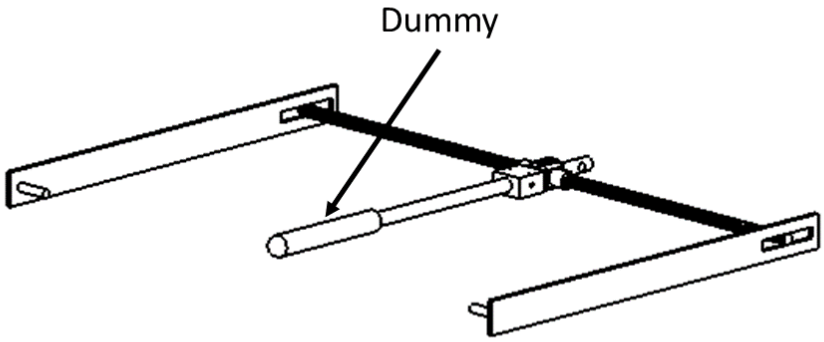

Figure A. 4.10 Wind tunnel rig plus dummy model.

The dummy represents the wing mounting system, which will be later deducted from the model runs to arrive at the aerodynamic forces and moments generated by the wing alone. Both tare (air-off) runs are expected to be within a certain range of each other. The raw data scatter plot for lift, drag and pitching moment of both tare runs is shown in Figure A. 4.11 to Figure A. 4.13.

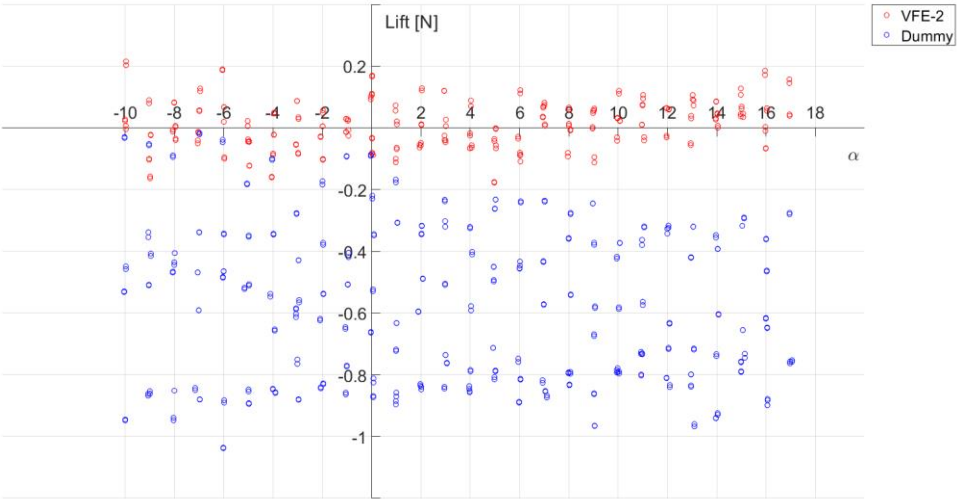

Figure A. 4.11 Raw data scatter plot of the tare run for the lift force against angle of attack (degrees).

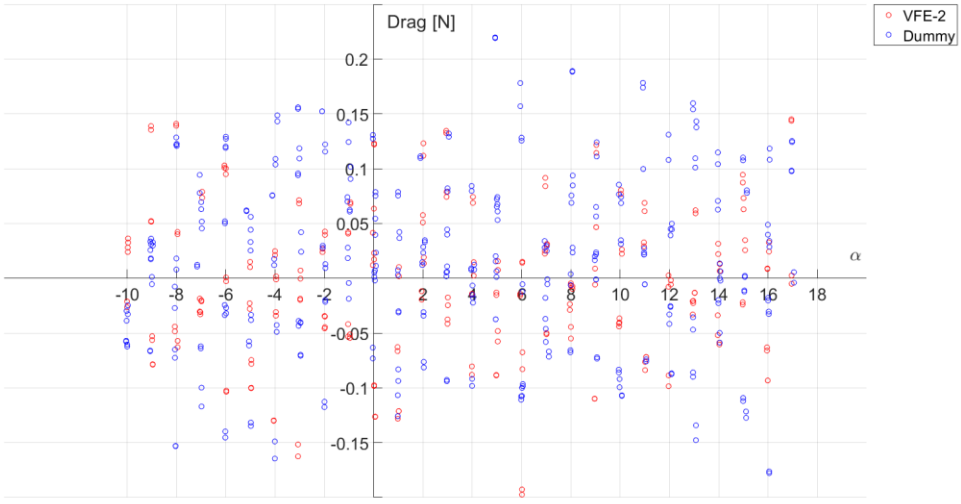

Figure A. 4.12 Raw data scatter plot of the tare run for the drag force against angle of attack (degrees).

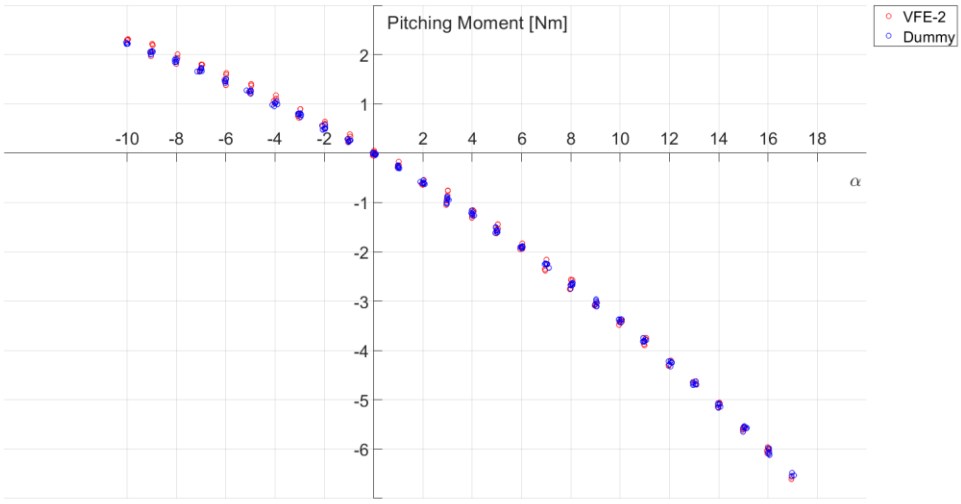

Figure A. 4.13 Raw data scatter plot of the tare run for the pitching moment against angle of attack (degrees).

The hypothesis for the lift and drag tare runs is that the expected force value is zero for every angle of attack. As the values for the different hysteresis runs seem to be randomly scattered a histogram is plotted showing how the lift and drag force data is distributed. The histograms are depicted in Figure A. 4.14 including the theoretical normal distribution curve.

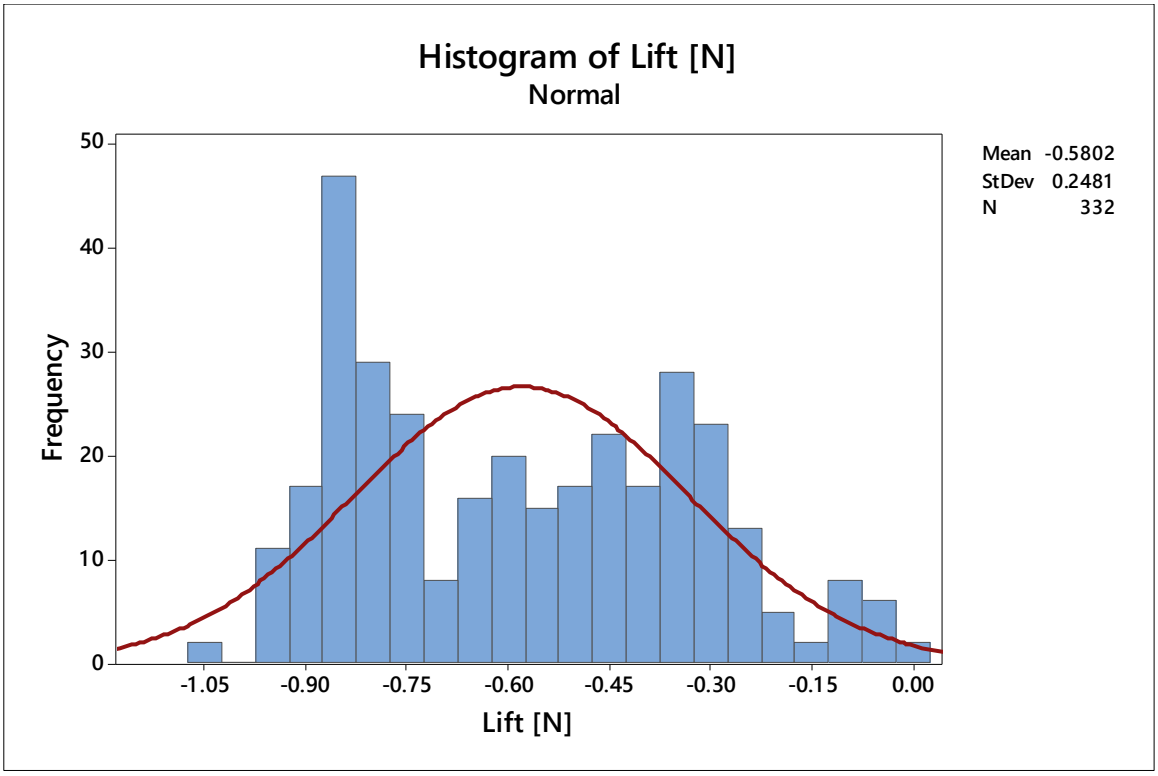

Figure A. 4.14 Lift force histogram of the VFE-2 dummy tare run.

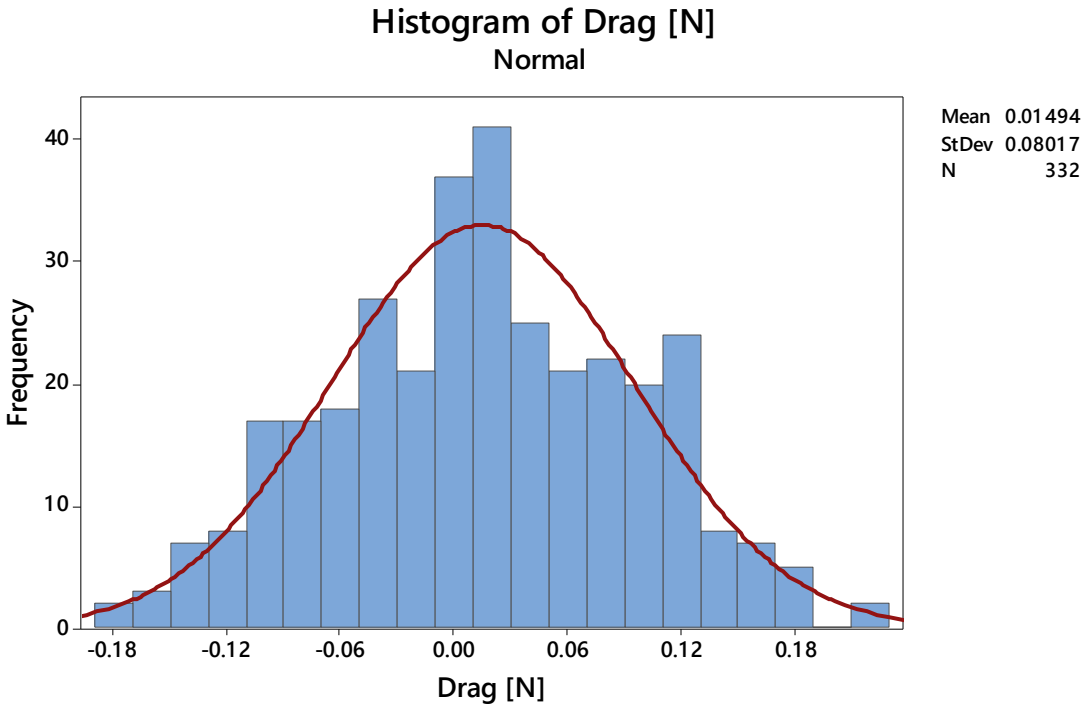

Figure A. 4.15 Drag force histogram of the VFE-2 dummy tare run.

It can be seen that the lift force of the VFE-2 does not appear to fit a normal but bimodal distribution. The drag force, however, appears to be normally distributed. To gain more

certainty on whether the data is distributed normally the Ryan-Joiner normality test is applied since it is most appropriate for large sample data (n > 30) (Nosakhare and Bright, 2017) as is encountered in this study. The null hypothesis is, that when the probability is greater than 0.05 the data is normal distributed. The results for the VFE-2 Dummy and the VFE-2 model can be seen in Figure A. 4.16 to Figure A. 4.19. The normality test confirms the result of the visual inspection.

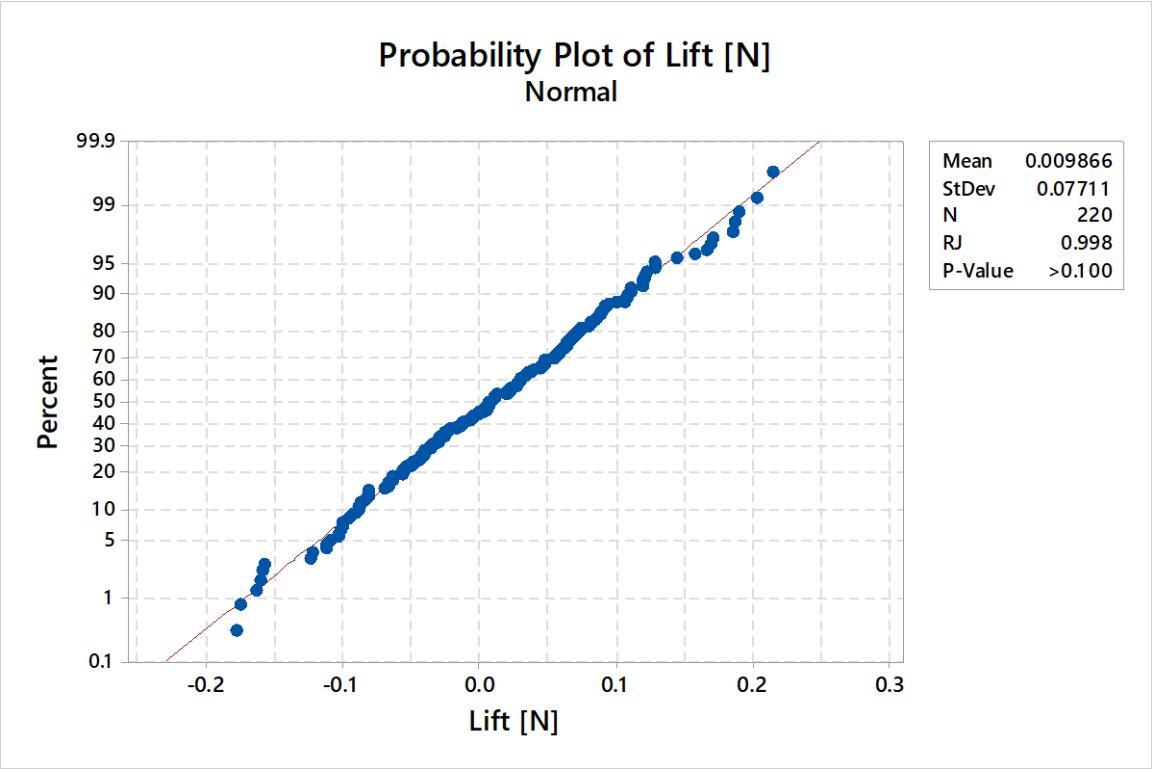

Figure A. 4.16 Ryan-Joiner normality test for the lift force measured for the VFE-2 tare.

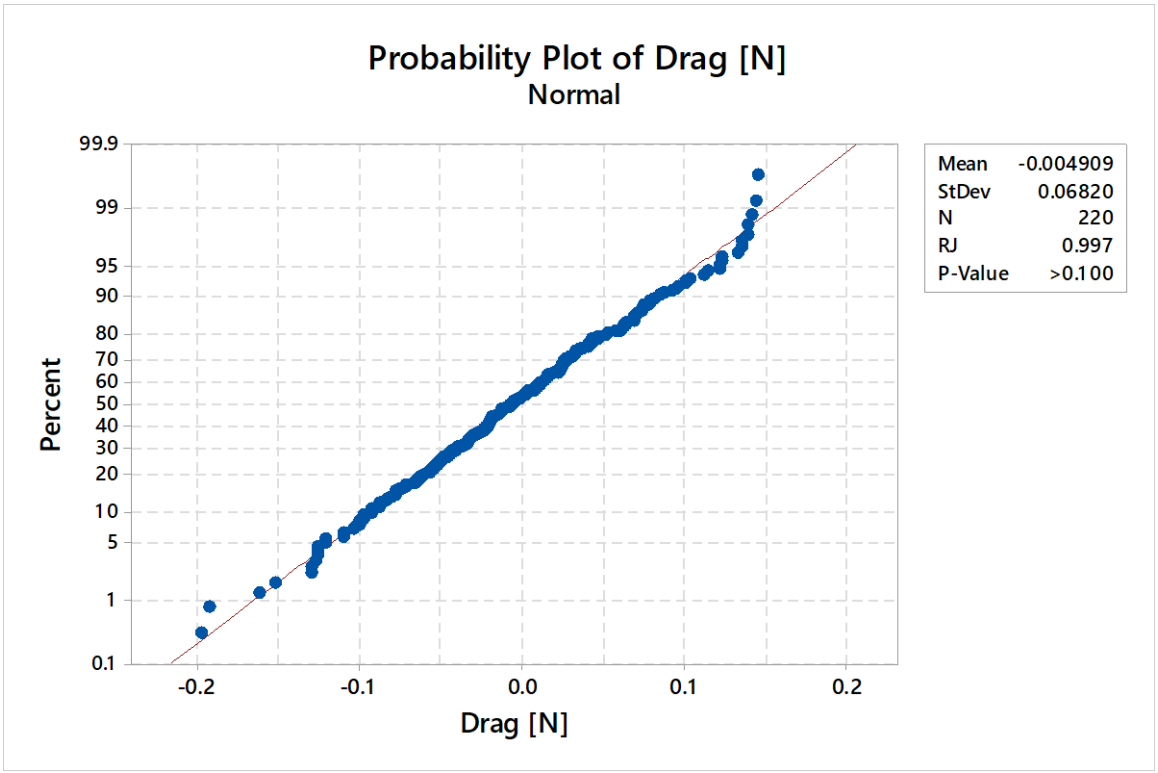

Figure A. 4.17 Ryan-Joiner normality test for the drag force measured for the VFE-2 tare.

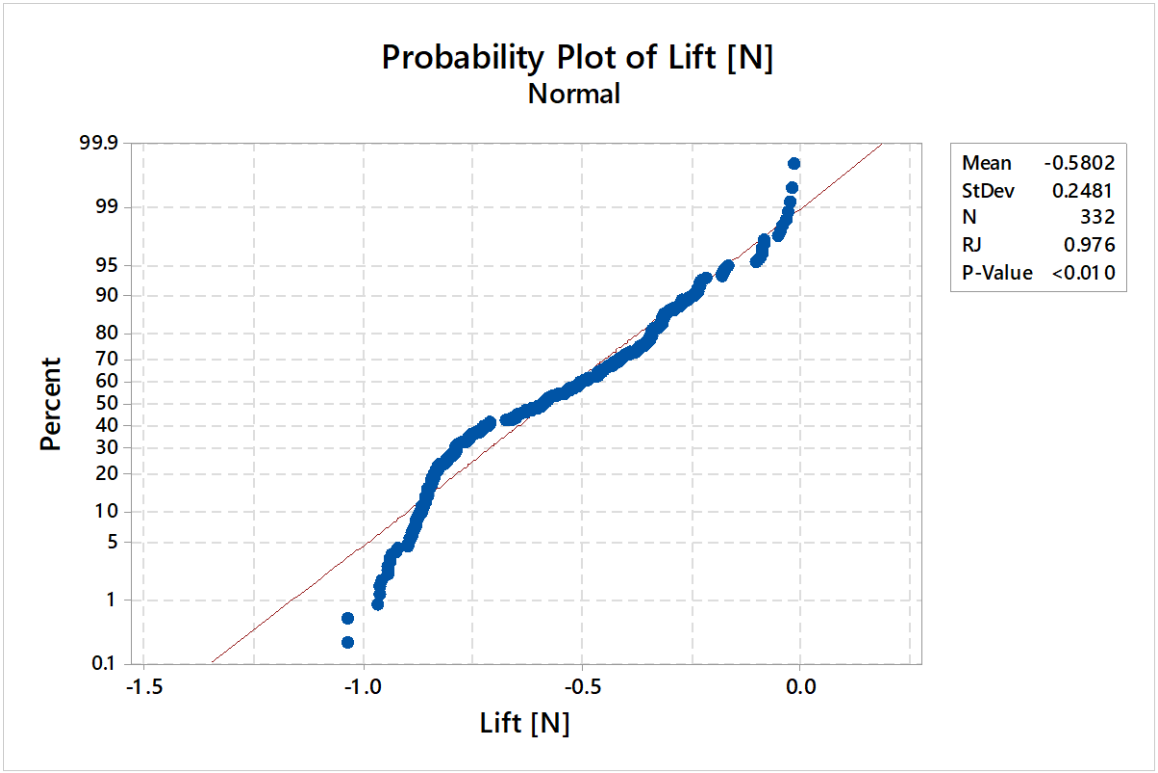

Figure A. 4.18 Ryan-Joiner normality test for the lift force measured for the VFE-2 dummy tare.

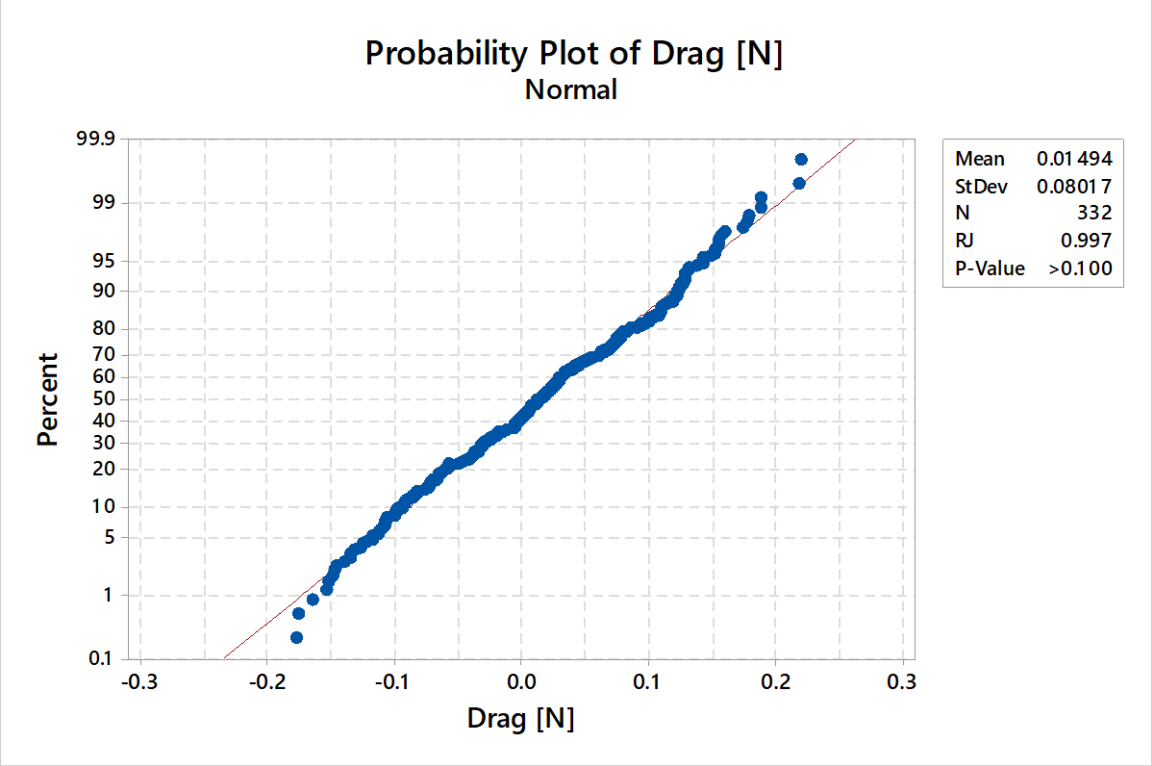

Figure A. 4.19 Ryan-Joiner normality test for the drag force measured for the VFE-2 dummy tare.

It can be seen from the above that apart for the lift forces of the VFE-2 dummy run the distributions are normal. Despite the lift force for the dummy run being random, a normal distribution will be assumed, as for sample sizes (n > 30 or 40) the violation of the normality assumption should not cause major problems (Pallant, 2007). Thus, the mean values can be calculated and used for the corrections done in later sections. The descriptive statistics can be seen in Table A. 4.2.

Table A. 4.2 Basic statistics for the model and dummy tare runs.

Variable	N	Mean	Standard Error of the Mean	Standard Deviation	Median	Minimum	Maximum
Lift VFE-2	220	0.00987	0.0052	0.07711	0.00807	-0.17746	0.21469
Drag VFE-2	220	-0.00491	0.0046	0.06820	-0.00635	-0.19742	0.14498
Lift Dummy	332	0.5802	0.2481	0.2481	-0.5909	-1.0375	-0.017
Drag Dummy	332	0.01494	0.08017	0.08017	0.01411	-0.17775	0.21970

The reason as to why there is a scatter in lift and drag data is that the wind tunnel's balance system comes with an uncertainty. This uncertainty is 0.5 N for the lift force and 0.17 N (+) and 0.28 N (-) for the drag force. As can be seen from Table A. 4.2 the maximum/ minimum value for lift is far are within the uncertainty of the measuring equipment. This explains the scattered readings for the air-off runs.

The data points for the pitching moment do not to appear to be random but rather appear to have a quadratic dependency.

Before curve fitting the data via linear regression the assumption that the curve fit will be of second order needs to be verified to avoid overfitting the data. Over fitted or under fitted models are unlikely to stand a validation test (Harrell et al., 1985).

For the wind tunnel pitching moment the model can be validated by estimating the theoretical moment based on a free body diagram whilst taking into account the wind tunnel system set up.

The free body diagram of the rig and the moment balance system is depicted in Figure A. 4.20. Note that the centre of gravity of the rig, according to Solid Works, is located approximately at

x= 0.00 m

y= 0.00012 m

z= - 0.35371 m

where the origin is located at the centre of the rig between the eye ball joints, and where z is the downstream direction and y is the direction parallel to the struts. Note, this is a different coordinate system to that in Figure A. 4.7.

For the calculation of the pitching moment note that the all forces and moments measured by the wind tunnel system are the change in forces and moments rather than the total forces and moments. Also note that the balance is generating a moment itself due to a geometric asymmetry of the lever arm. This moment was obtained by taking a tare run of the balance only and is referred to in Figure A. 4.20 as $M_{Balance}$.

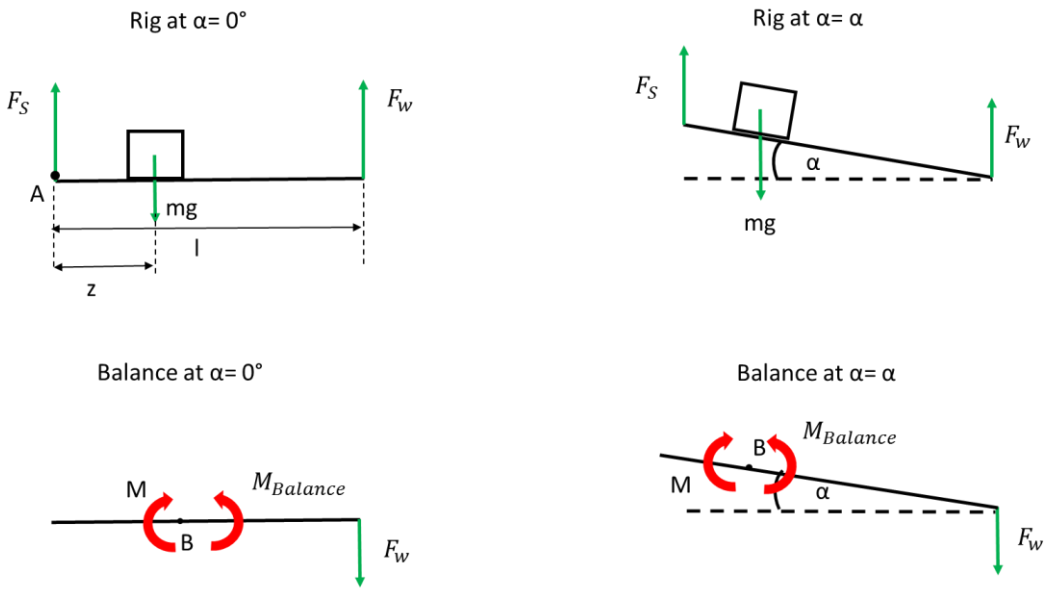

Figure A. 4.20 2-D free body diagram of the wind tunnel rig and moment balance system at α= 0° and α=α with F_W being the force of the wire F_{Wire} and F_S=F_{Strut}.

After rearranging the forces and moment equations for each system and forming the difference the pitching moment for the rig can be calculated using:

$$\Delta M = mgz(1 - \cos(\alpha + \beta)) - M_{Balance} \qquad (A.4.29)$$

where β is the angle between centre of gravity of the rig and pivot point of the balance B.

Plotting the data obtained by Equation (A.4.29) against angle of attack and comparing it with measured moment resulted in the graph shown in Figure A. 4.21. It can be seen that the theoretical data fits the measured data well. The maximum difference between the measured and theoretical data is 0.252 Nm, which is the difference in pitching moment at the origin. The 0.252 Nm were measured during the tare run of the balance only (neither dummy or model attached).

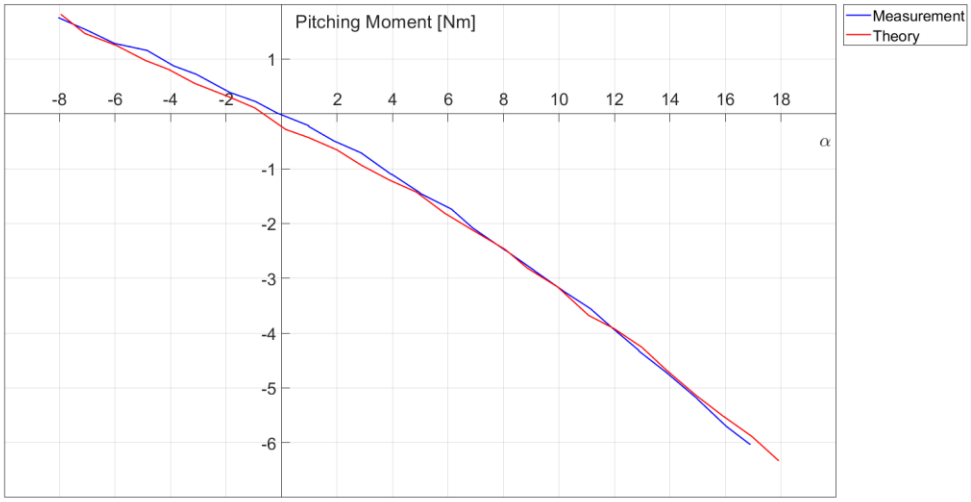

Figure A. 4.21 Comparison theoretical pitching moment vs measured pitching moment.

As Equation (A.4.29) is a function of cosine the data can be curve fitted using a second order polynomial. This is done using the linear regression in the statistics software MINITAB. The regression model alongside the observed data points is depicted in Figure A. 4.22.

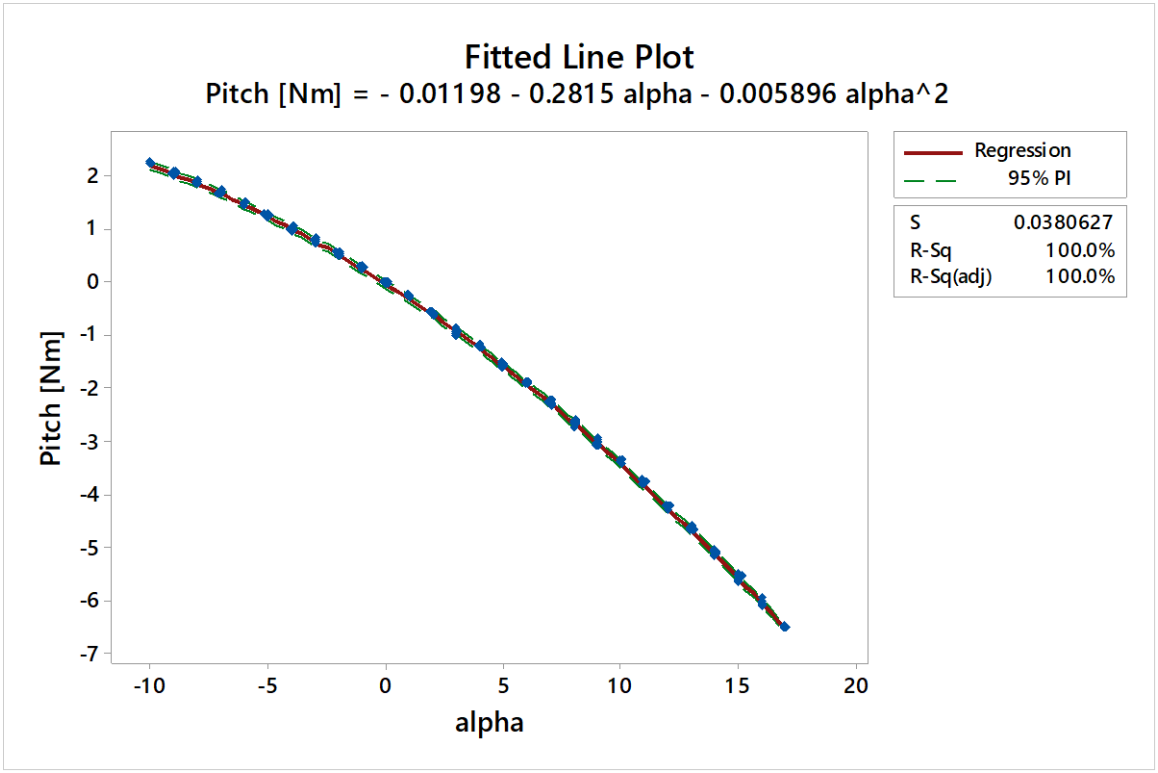

Figure A. 4.22 Fitted curve of the dummy tare run.

The polynomial fitting the data is determined to be:

$$PM(\alpha) = -0.01198 - 0.2815\alpha - 0.005896\alpha^2 \quad \text{(A.4.30)}$$

The first step is to determine whether the association between the response and the variable α is statistically significant, meaning the relationship between the variables is not due to chance. This can be done by evaluating the p-value and the standard error of the coefficients in Equation (A.4.30) which are shown in Table A. 4.3.

The p-value of Table A. 4.3 states whether a change in predictor yields a change in the response. A high value indicates that there is no change in response when changing the predictor. It can be seen from Table A. 4.3 that because the p-value is zero, that all coefficients are statistically significant with a confidence level of 95%. Therefore, the curvature is not due to change but due to the physics of the problem.

Table A. 4.3 Second order curve fitting coefficients for the dummy tare run.

Term	Coef	SE Coef	P-Value
Constant	-0.01198	0.00294	0.000
alpha	-0.281471	0.000372	0.000
alpha*alpha	-0.005896	0.000038	0.000

The standard error, defined as the approximate standard deviation of a statistical sample population (Nguyen and Rogers, 1989), of the coefficients is labelled SE Coef and indicates the variability between coefficient estimates. It can be used to determine the precision of the estimate of the coefficient. The smaller its value the more precise the estimate. As can be seen the standard error values for the angle of attack coefficients are extremely small and therefore the curve fit is very precise.

Evaluation of the dummy tare run curve fit coefficients

Next, it is determined how well the model fits the data. This is done by examining the goodness-of-fit-statistics in the model summary shown in Table A. 4.4.

Table A. 4.4 Goodness-of-fit-statistics for the dummy tare run pitching moment.

S	R-sq	R-sq(pred)
0.0380627	99.98%	99.98%

The standard error S represents the average distance that the observed data fall from the regression line. Smaller values are better as it means that the values are closer to the fitted line. The measured pitching moment for the dummy tare run is on average 0.05% away from the fitted line. S can also be used to assess the precision of the predictions. About 95% of the observations should fall within +/- 2S from the regression line, which would be 1% of the data for this case (James et al., 2013).

R^2 (R-sq) is the percentage of the variation in the response variable of the model. The higher the value the better the model fits the data. A value of 99.95% suggests that there is a very good fit of the data to the model (James et al., 2013). However, R^2 on its own cannot determine whether a regression model is adequate and therefore also the residuals versus fit plot has to be checked for its randomness (James et al., 2013)). The predicted R^2 (R-sq(pred)) indicates how well a regression model predicts responses of new data points. This helps in determining whether the regression model overfits the data, which is the case when R^2 (pred) << R^2 (James et al., 2013)

The last step is assessing as to whether the model meets the assumptions of the analysis by means of the residual plots. Here, it has to be checked if the residuals are randomly distributed on both sides of zero and have a constant variance whilst showing no recognisable patterns.

Table A. 4.5 shows patterns and their interpretation

Table A. 4.5 Interpretation of the residual plot pattern (James et al., 2013).

Pattern	**Potential indication**
Fanning or uneven spreading of residuals across fitted values	Non-constant variance
Curvilinear	A missing higher-order term
A point that is far away from zero	An outlier
A point that is far away from the other points in the x-direction	An influential point

The residual versus fit plot for the dummy tare run is shown in Figure A. 4.23. There appear to be some points which are away from zero thus indicating to be outliers. Apart from this the points are randomly distributed yielding to the conclusion that the curve fit is appropriate. Figure A. 4.23 also shows the residuals versus order plot, which is used to verify the assumption that the residuals are independent from one another. There should be no trends or patterns visible in the graph when the residuals are independent. As for the residual versus fit plot this plot should fall randomly around the centre line, which it does (James et al., 2013).

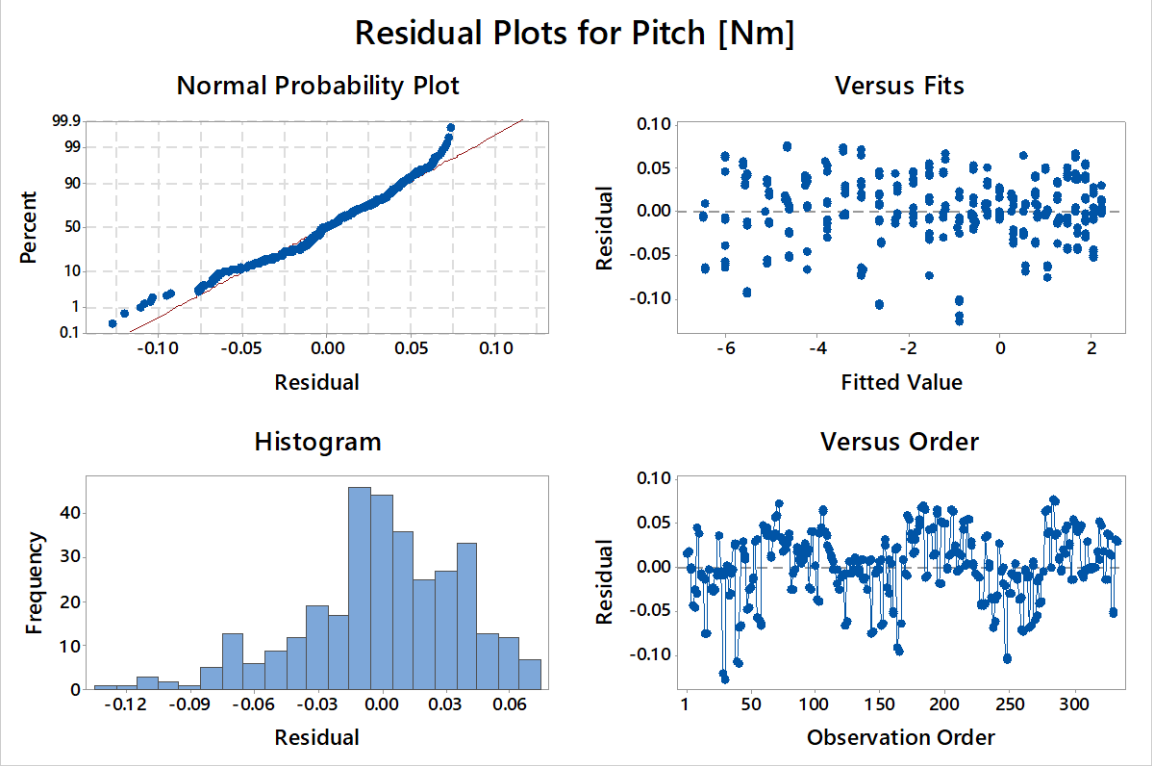

Figure A. 4.23 Residual plots of the dummy model pitching moment tare run.

One assumption in regression analysis is that the residuals are normally distributed. To verify this assumption the normal probability plot can be examined. A normal distribution is given when the residuals approximately follow a straight line. Table A. 4.6 shows the interpretation of patterns deviating from a straight line.

Table A. 4.6 Pattern interpretation of the dummy model pitching moment probability plot (James et al., 2013).

Pattern	**Potential indication**
Not a straight line	Non-normality
A point that is far away from the line	An outlier
Changing slope	An unidentified variable

The normality plot for the dummy tare is displayed in Figure A. 4.23. It can be said that the residuals do follow a straight line but also indicates a few outliers as do the residual plots before.

A regression model is also fitted to the pitching moment data of the VFE-2 tare run (Figure A. 4.24). The results can be seen below.

The polynomial of the curve fit is:

$$PM(\alpha) = 0.01569 - 0.285733\alpha - 0.005822\alpha^2 \qquad (A.4.31)$$

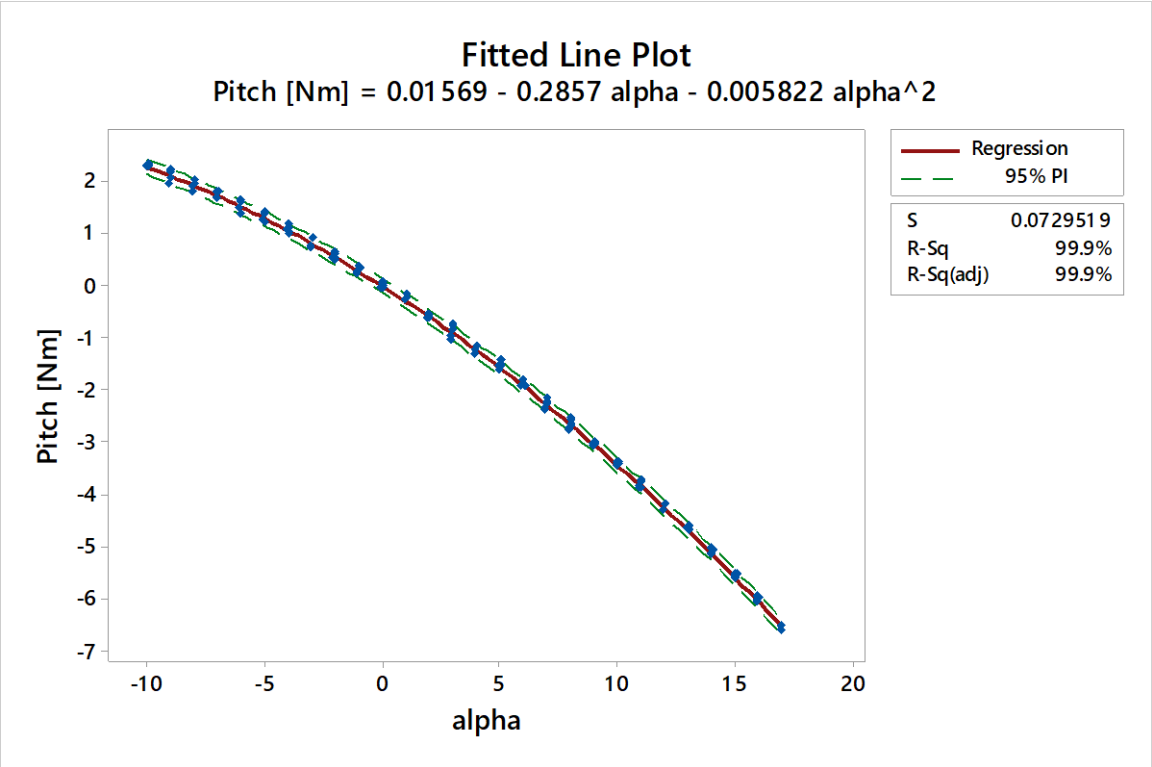

Figure A. 4.24 Second order curve fit of the VFE-2 pitching moment tare run.

As for the case of the dummy tare run, the error in the coefficients and the p-value for the VFE2 case indicate a good fit, which is confirmed by the model summary values in Table A. 4.7 and Table A. 4.8.

Table A. 4.7 Second order curve fitting coefficients for the VFE-2 tare run.

Term	Coef	SE Coef	P-Value
Constant	0.01569	0.00689	0.024
alpha	-0.285733	0.000870	0.000
alpha*alpha	-0.005822	0.000088	0.000

Table A. 4.8 Goodness-of-fit-statistics for the VFE-2 tare run pitching moment.

S	R-sq	R-sq(pred)
0.0729519	99.92%	99.92%

The results of the calculated values are confirmed by the residual plots as shown in Figure A. 4.25.

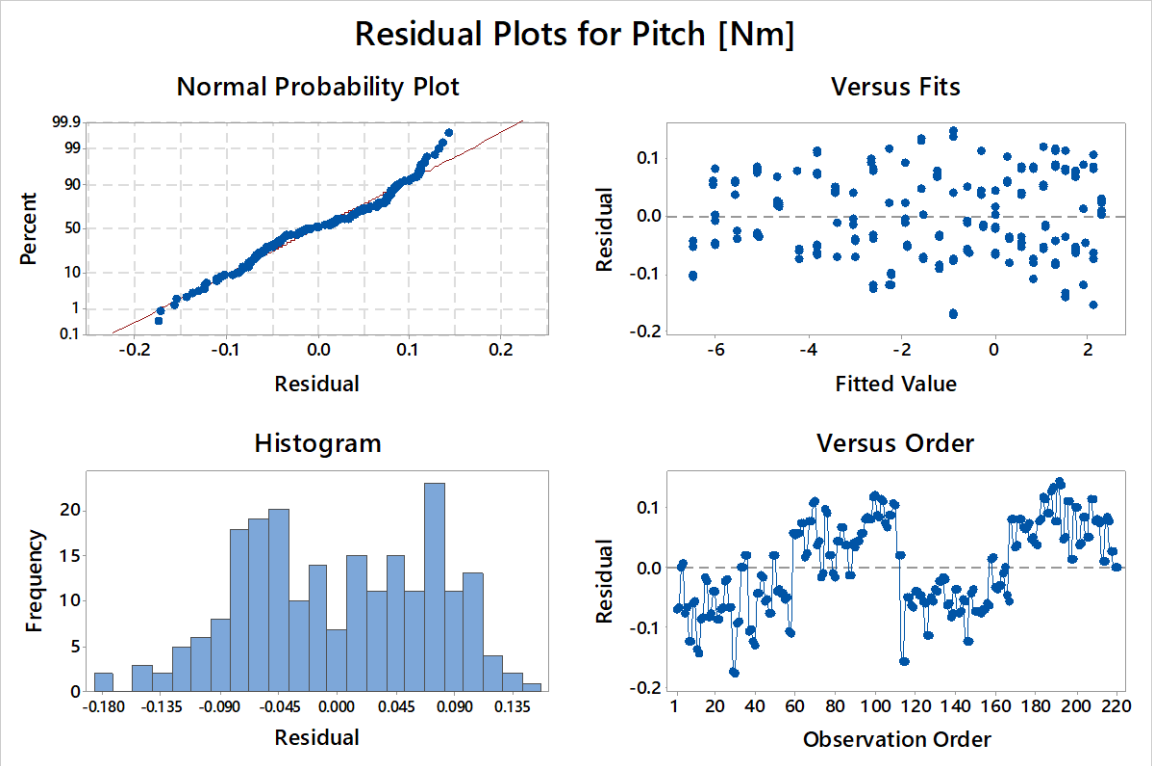

Figure A. 4.25 Residual plots for the VFE-2 pitching moment tare run.

As mentioned earlier the results of the dummy tare run and the VFE-2 tare run should lie within a certainty of each other. In order to test this the coefficient values are compared. Each coefficient comes with a standard error. The upper and lower limit of each coefficient can be calculated using

$$a_{UL} = a + 2 \times \text{SE Coeff} \tag{A.4.32}$$

$$a_{LL} = a - 2 \times \text{SE Coeff} \tag{A.4.33}$$

The standard error is taken twice as this captures the region in which about 95% of the data points lie. The upper and lower limit can be calculated for each coefficient of each run and then be compared with each other.

Figure A. 4.26 shows the coefficients of the polynomial for each tare run. It can be seen that the coefficients of each tare run lie within a 95% confidence interval to each other. This proves that both tare runs can be approximated by the same curve fit as they as they statistically prove to give the same result.

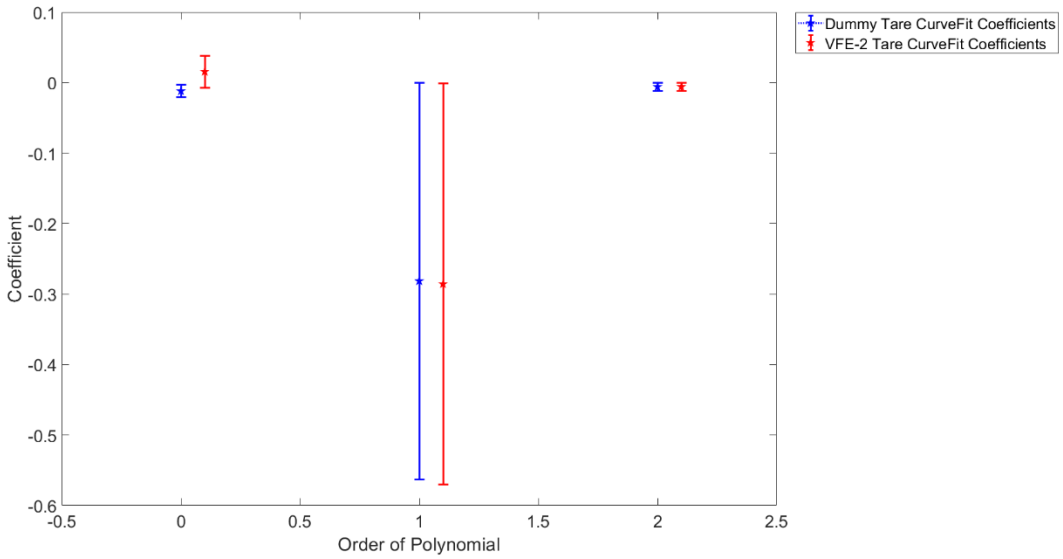

Figure A. 4.26 Plot of the coefficients of the polynomial for each tare run including their error bands.

A.4.5.2 Lift Force

The results for the lift force for the 34 m/s dummy run are depicted in Figure A. 4.27. It can be seen that the results are approximately of third order. The major components contributing to the lift are the square bars and the sting. That is because their chord length is large compared to the dummy. The dummy itself does not contribute majorly to the overall lift force seen in Figure A. 4.27. This conclusion is based on the lift formula for slender bodies (Krasnov, 1970)

$$L = \rho U^2 \pi \alpha R_B^2 \tag{A.4.34}$$

where R_B is the base radius of the body of revolution.

The solution for the lift coefficient C_l from potential flow theory is defined as (Anderson, 2011)

$$C_l = 2\pi \sin(\alpha) \tag{A.4.35}$$

Hence, the lift force also is a function of sine. Figure A. 4.27 can be interpreted as a shifted sine function. The shift may be explained by the aerodynamics of the given configuration.

To validate the lift curve one can resolve the free body diagram (FBD) for the lift force. This results in

$$L = \frac{M - mgx_{cg}(\cos(\alpha) - 1)}{x_{cp}\cos(\alpha)} - D\tan(\alpha) + L_0 \tag{A.4.36}$$

where x_{cp} is the centre of pressure and L_0 the distance between wire and eyeball joint centre obtained using

$$Sx_{cp} = \sum_{i=1}^{n} a_i \times d_i \tag{A.4.37}$$

where S is the total projected area of the system and a_i and d_i are the projected area and distance from the reference centre to the centre of gravity of each component respectively.

The first term in Equation (A.4.36) has the highest impact on the shape of the lift curve as it has the highest magnitude but is closely followed by the drag force and the lift generated at zero degrees angle of attack.

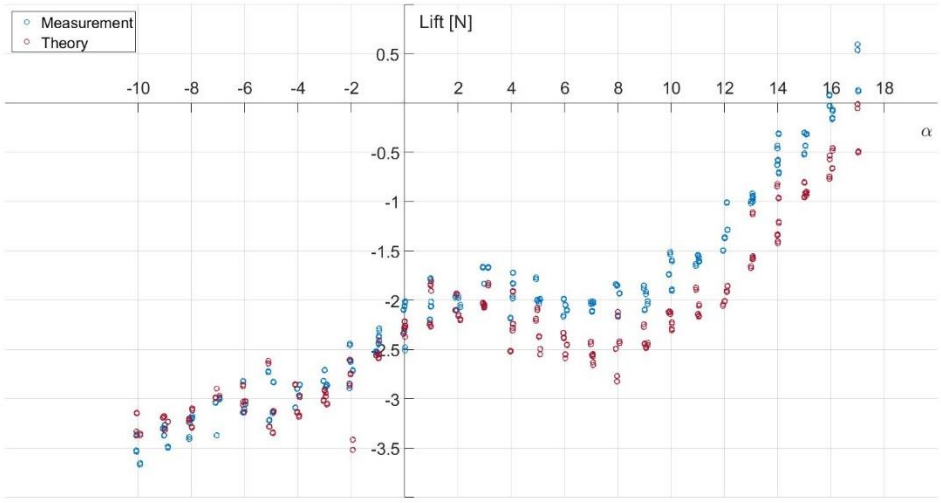

Figure A. 4.27 Raw data plot of the lift force vs. angle of attack for the dummy air on run.

For later corrections it is necessary to curve fit all the aerodynamic forces acting on the dummy. Using a third order polynomial regression results in the plot shown in Figure A. 4.28.

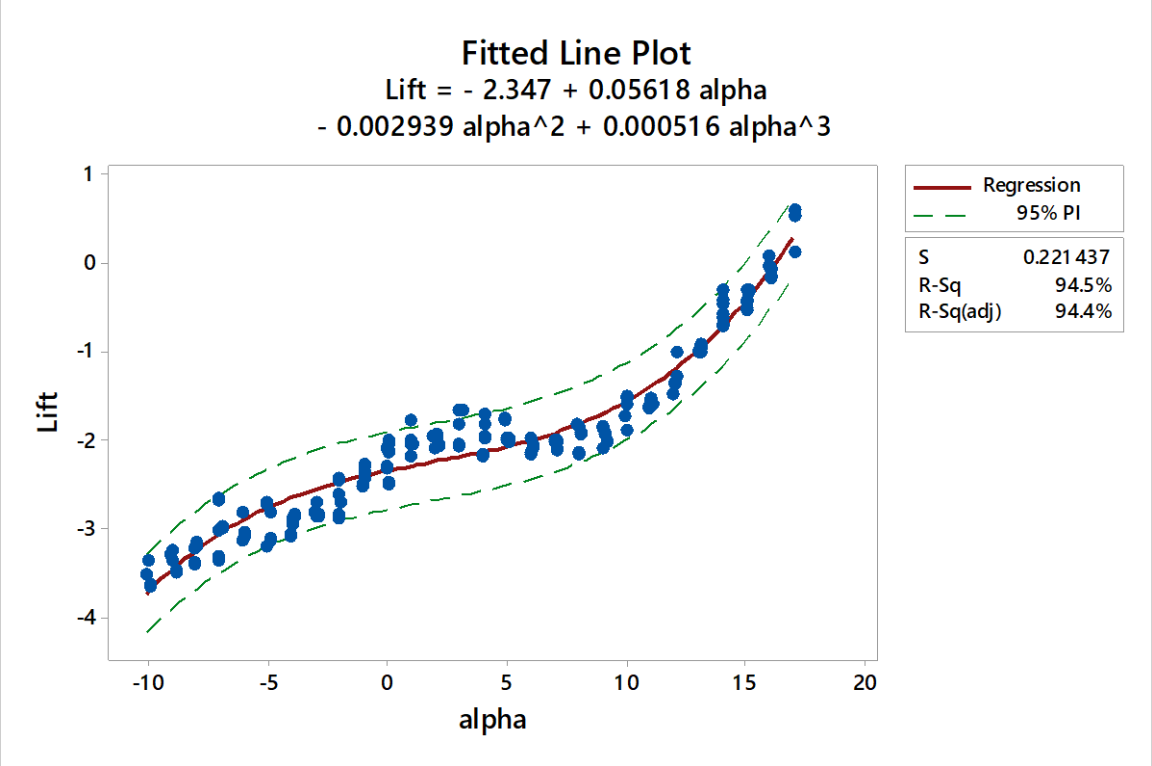

Figure A. 4.28 Curve fit of the lift force dummy air on run.

The function fitting the lift force of the dummy is

$$L(\alpha) = 0.000516\alpha^3 - 0.002939\alpha^2 + 0.05618\alpha - 2.347 \qquad (A.4.38)$$

The residuals are shown in Figure A. 4.29 and the model coefficients and errors are shown in Table A. 4.9 and Table A. 4.10. The residual versus order graph appears random and the normal probability plot seems to follow a straight line. It can thus be concluded that the curve fit is of the correct polynomial and an appropriate fit for the problem.

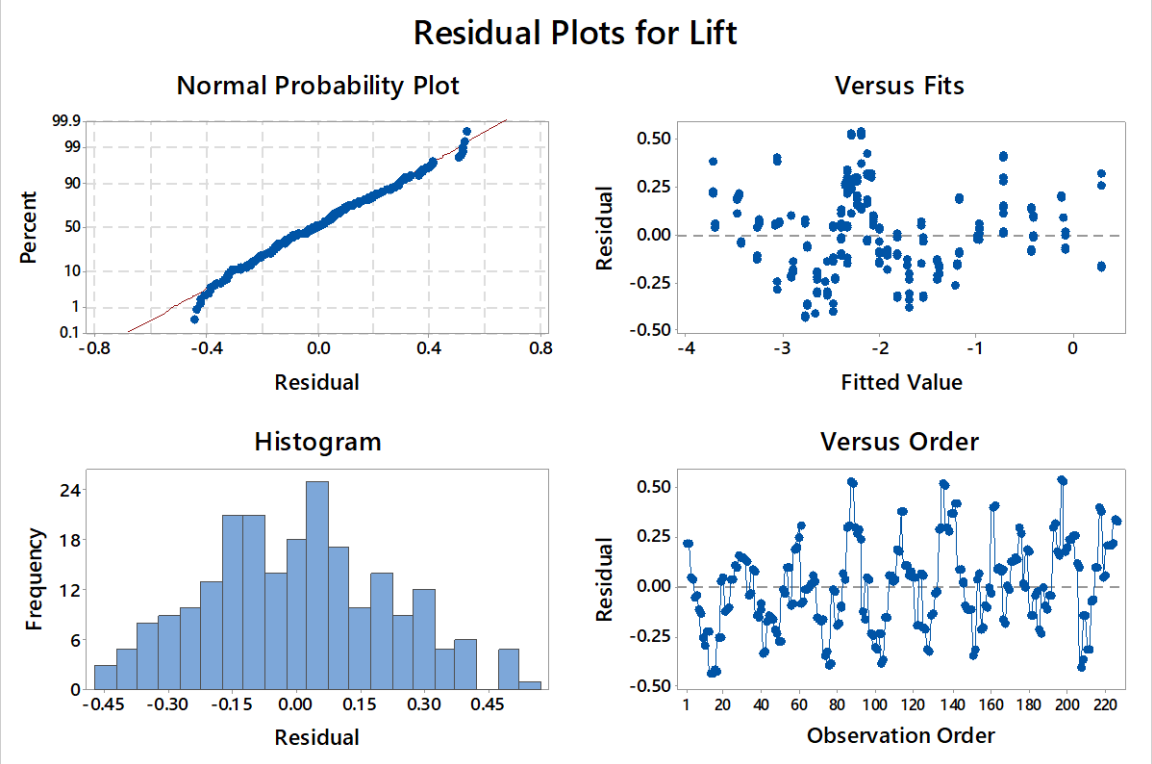

Figure A. 4.29 Residual plots for the dummy pitching moment air on run.

Table A. 4.9 Third order curve fitting coefficients for the lift force of the dummy air on run.

Term	Coef	SE Coef	T-Value	P-Value	VIF
Constant	-2.3475	0.0242	-97.20	0.000	
alpha	0.05618	0.00398	14.11	0.000	4.48
alpha*alpha	-0.002939	0.000466	-6.30	0.000	6.02

alpha*alpha*alpha	0.000516	0.000038	13.48	0.000	12.08

Table A. 4.10 Goodness-of-fit-statistics for the lift force of the dummy air on run.

S	R-sq	R-sq(adj)	R-sq(pred)
0.221437	94.47%	94.39%	94.28%

A.4.5.3 Drag Force

The drag force for the air-on dummy run is shown in Figure A. 4.30. It can be seen that the drag force is high. This can be explained by the drag generation of the threaded bar. The Re number for the threaded bar is 3.6×10^4 which yields a drag coefficient of approximately 1.2 and accounts for over 50% of the drag generated by the E-rig.

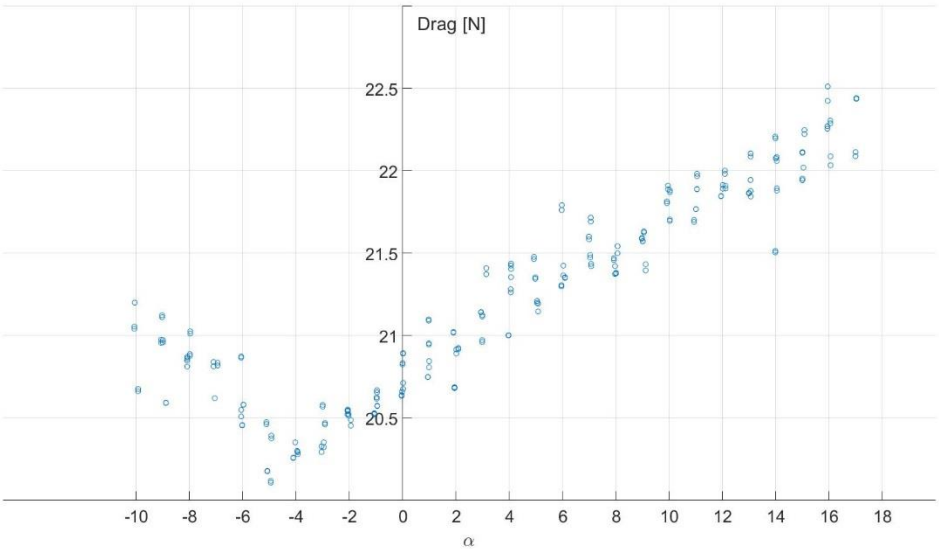

Figure A. 4.30 Raw data of the drag force vs. angle of attack for the dummy air on run.

The drag force is curve fitted using a cubic regression model with the results displayed in Figure A. 4.31 and Figure A. 4.32. It is shown by the R^2 value that the curve matches the data 76.91%. The details of the polynomial coefficients and their associated error as well as outliers are shown in Table A. 4.11 to Table A. 4.13.

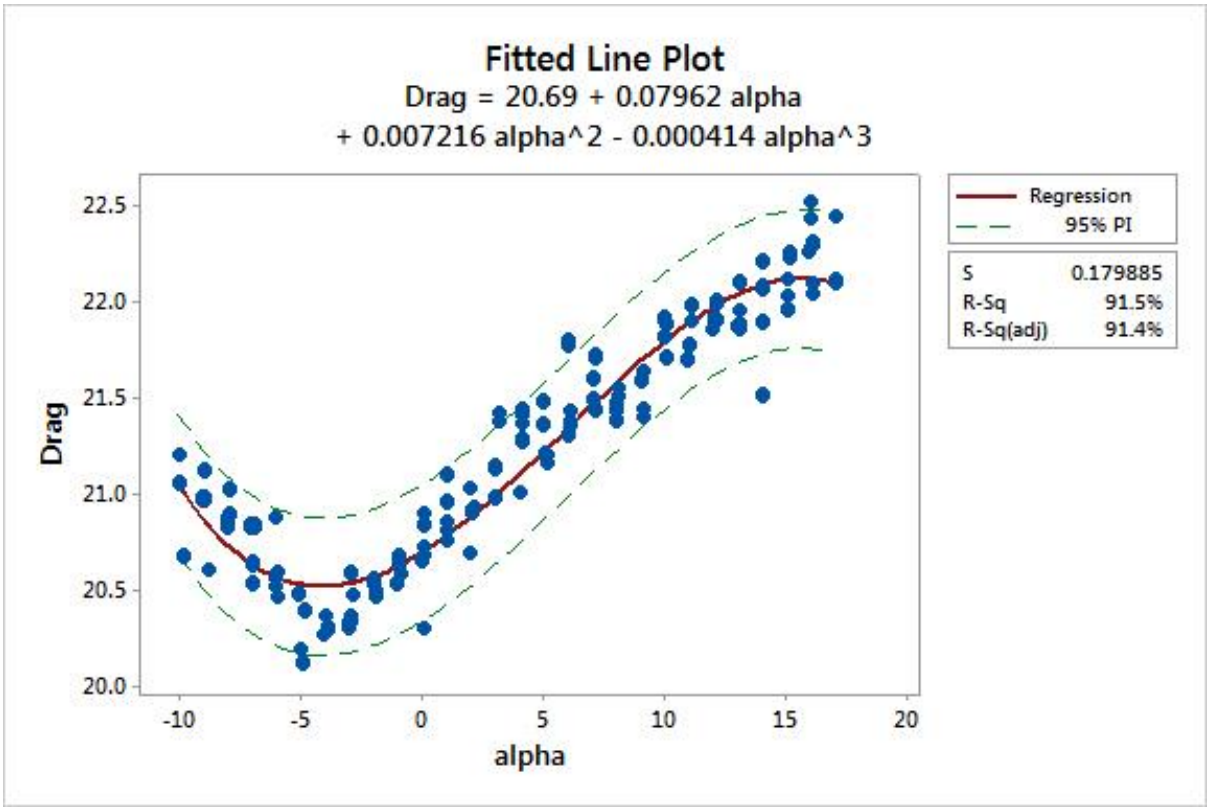

Figure A. 4.31 Curve fit of the drag force for the dummy air on run.

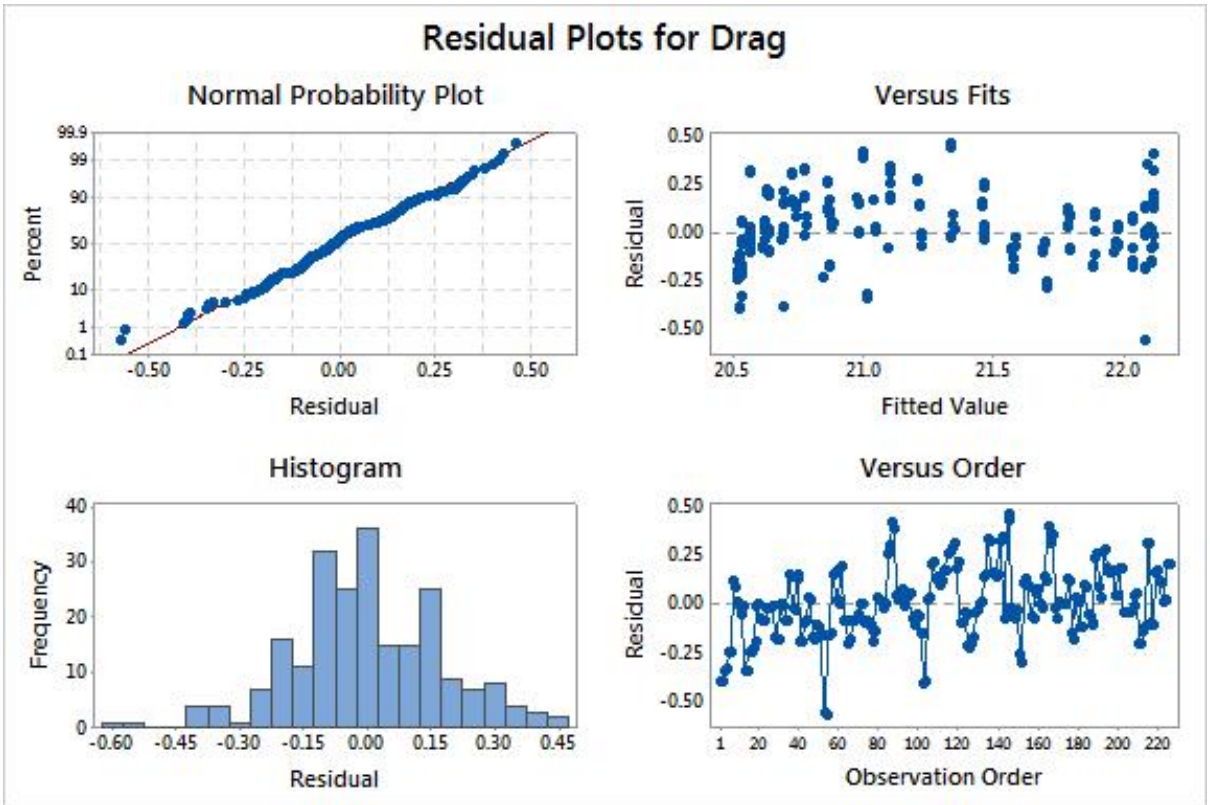

Figure A. 4.32 Residual plots for the dummy drag force air on run.

Table A. 4.11 First order curve fitting coefficients for the drag prediction of the dummy air on run.

Term	Coef	SE Coef	T-Value	P-Value	VIF
Constant	20.9744	0.0214	981.19	0.000	
alpha	0.06847	0.00251	27.32	0.000	1.00

Table A. 4.12 Goodness-of-fit-statistics for the drag force of the dummy air on run.

S	R-sq	R-sq(adj)	R-sq(pred)
0.294949	76.91%	76.81%	76.39%

Table A. 4.13 Fits and diagnostics for unusual observations for the drag force of the dummy air on run.

Obs	Drag	Fit	Resid	Std Resid	
1	20.2923	20.9752	-0.6829	-2.32	R
2	20.2889	20.9750	-0.6861	-2.33	R
111	20.9567	20.3538	0.6029	2.06	R
112	20.9765	20.3537	0.6228	2.13	R
113	21.1997	20.2863	0.9134	3.12	R
114	21.2003	20.2865	0.9138	3.13	R
115	21.1126	20.3568	0.7558	2.58	R
116	21.1241	20.3567	0.7674	2.62	R
118	21.0257	20.4288	0.5969	2.04	R
221	20.9729	20.3585	0.6144	2.10	R
222	20.9584	20.3584	0.5999	2.05	R
223	21.0419	20.2852	0.7567	2.59	R
224	21.0553	20.2853	0.7700	2.63	R

R Large residual

A.4.5.4 Pitching Moment

As mentioned above the accuracy of the lift and drag data can be proven by calculating the pitching moment based on the free body diagram shown in Figure A. 4.33.

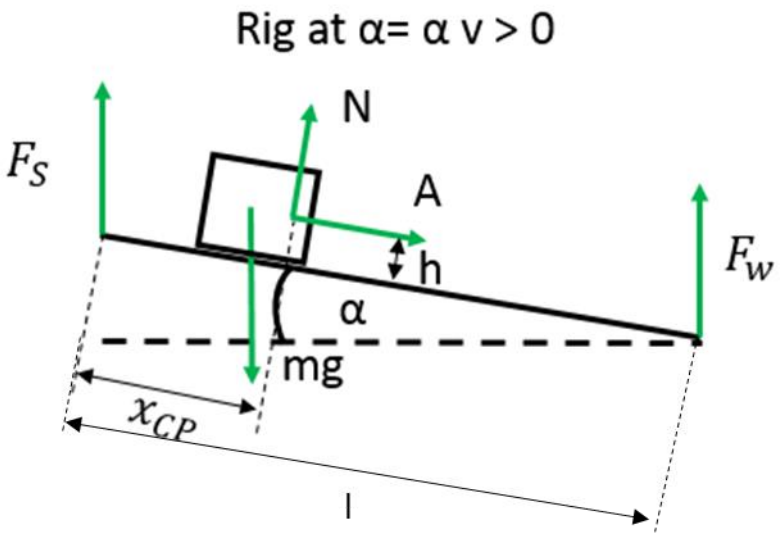

Figure A. 4.33 Free body diagram of the E-rig at velocity v.

This yields to the theoretical moment around F_S being defined as:

$$M_{th} = mgx_{cg_{rig}} \times (1 - \cos(\alpha)) + Nx_{cp} + Ah + M_0 + M_B + F_w \times l \sin(\alpha) \times (1 - \cos(\alpha)) \quad \text{(A.4.39)}$$

where N and A are the normal and axial forces respectively, M_0 is the moment generated at 0° angle of attack, l is the length of the square bar, $x_{cg_{rig}}$ is the distance between F_S and the centre of gravity of the rig and M_B the moment generated by the balance itself.

Figure A. 4.34 shows the comparison between estimated and measured pitching moment. It can be seen that the trend is accurately captured, the maximum difference between the curves being 0.768 Nm.

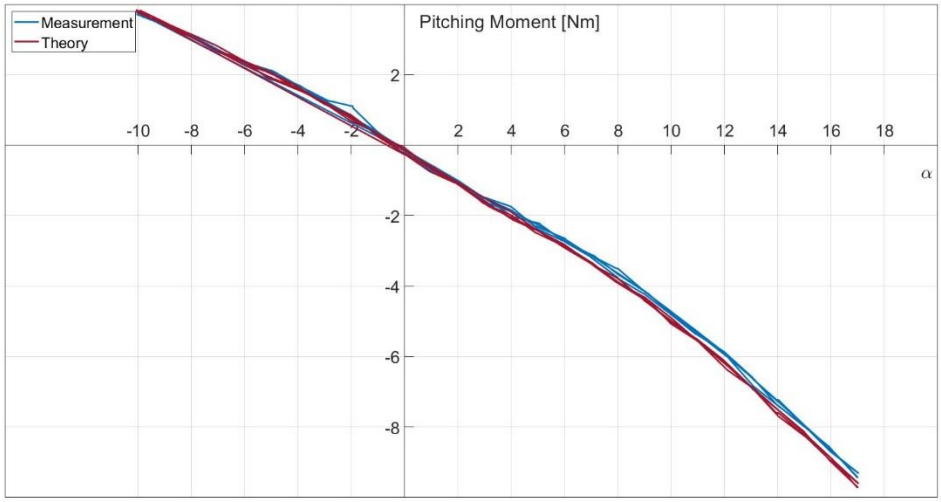

Figure A. 4.34 Theoretical and measured pitching moment plotted against α.

Curve fitting the pitching moment with a second order polynomial results in Figure A. 4.35. The residuals are displayed in Figure A. 4.36. The curve fits the data very well with a R^2 value of 99.86%. The details of the polynomial coefficients and their associated error as well as outliers are shown in Table A. 4.14 to Table A. 4.16.

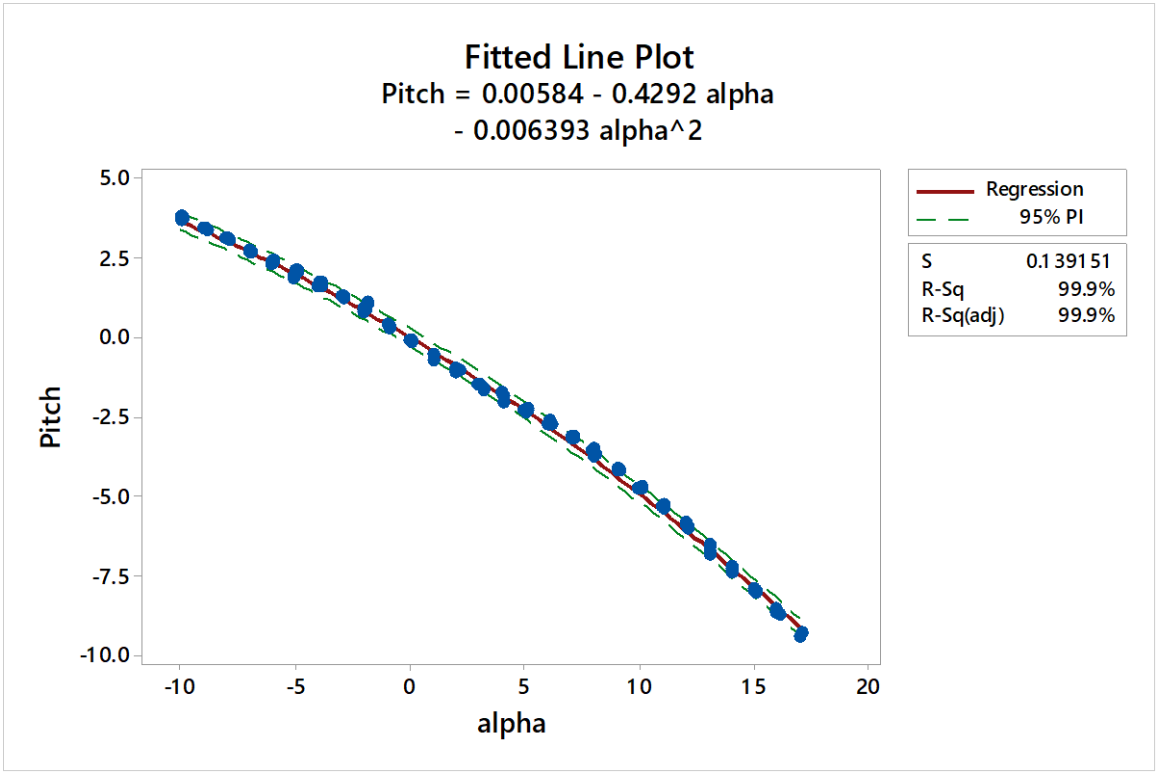

Figure A. 4.35 Curve fit of the pitching moment for the dummy air on run.

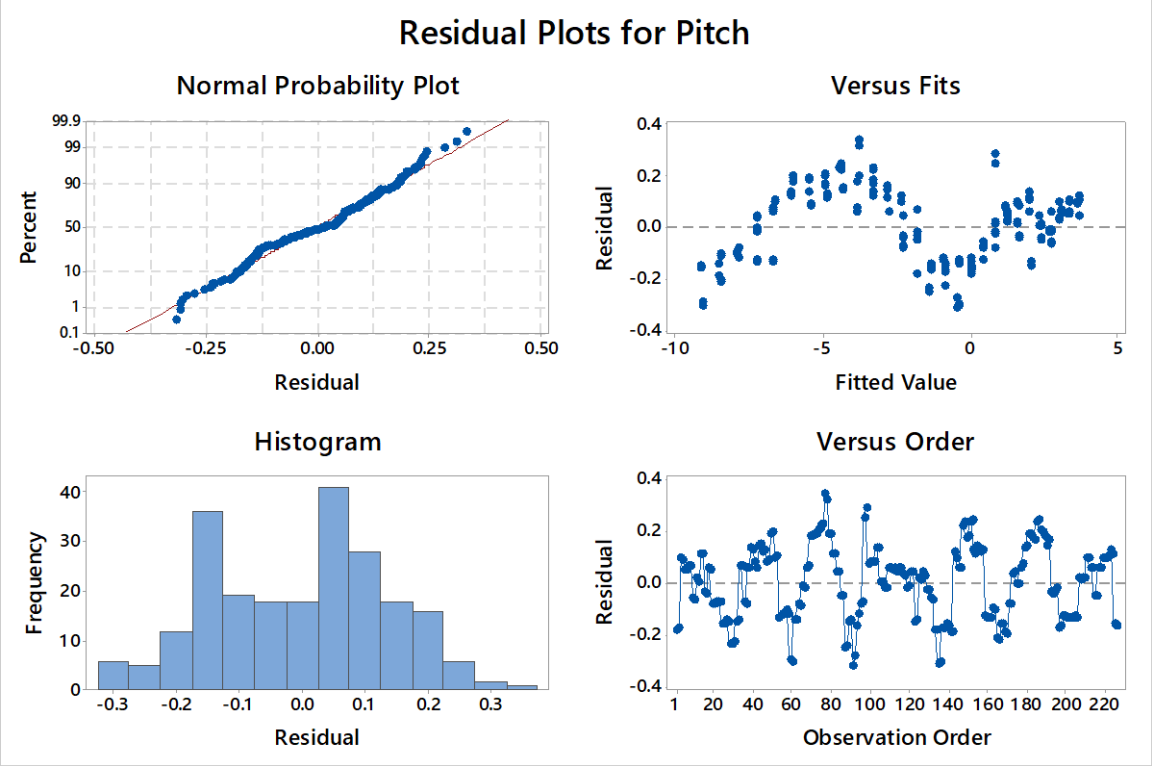

Figure A. 4.36 Residual plots for the dummy pitching moment air on run.

Table A. 4.14 Second order curve fitting coefficients for the pitching moment prediction of the dummy air on run.

Term	Coef	SE Coef	T-Value	P-Value	VIF
Constant	0.0058	0.0130	0.45	0.654	
alpha	-0.42925	0.00165	-260.23	0.000	1.95
alpha*alpha	-0.006393	0.000167	-38.37	0.000	1.95

Table A. 4.15 Goodness-of-fit-statistics for the pitching moment of the dummy air on run.

S	R-sq	R-sq(adj)	R-sq(pred)
0.139151	99.86%	99.86%	99.86%

Table A. 4.16 Fits and diagnostics for unusual observations for the pitching moment of the dummy air on run.

Obs	Pitch	Fit	Resid	Std Resid	
59	-9.4275	-9.1327	-0.2949	-2.16	R
60	-9.4395	-9.1314	-0.3081	-2.26	R
77	-3.4851	-3.8197	0.3346	2.41	R

78	-3.5096	-3.8195	0.3099	2.24	R
91	-0.7453	-0.4259	-0.3194	-2.31	R
92	-0.7081	-0.4273	-0.2808	-2.03	R
98	1.1011	0.8171	0.2840	2.05	R
135	-0.7286	-0.4171	-0.3115	-2.25	R
136	-0.7248	-0.4182	-0.3066	-2.21	R

R Large residual

A.4.6 Outlier Detection

The raw data has been plotted in the sections above to get a first impression of the accuracy of the results. After this has been established, the data has to be checked for statistical outliers. One method that has achieved a wide acceptance is Chauvent's criterion (Coleman and Steele, 1999). It defines that all points falling within a certain band, of probability 1-1/(2N), around the mean value should be retained.

The maximum allowable deviation from the mean x_{max} can be defined as

$$x_{max} = \tau \times S_x \qquad \text{(A.4.40)}$$

Where τ is the Chauvent's criterion which can be found from tables such as presented by Coleman and Steele (1999, page 36) and S_x being the standard deviation.

Chauvent's criterion is applied to all the test data prior to any further evaluation.

A.4.7 Comparison of upright and inverted runs

Upright and inverted runs were conducted to investigate the impact of the strut interference on the results. Normally, inverted runs are also conducted to establish the balance alignment to the tunnel flow. Wind tunnels do not have absolutely perfect flow, but up- and cross-flow. Both can critically impact on the accuracy of the drag measurement. Normally, this is accounted for by installing dummy struts to guarantee support strut interference (Rae and Pope, 1994). This could not be done at the facilities at the University of the West of England Bristol as dummy

struts are not available. Therefore, the inverted runs will not account solely for flow alignment but also for strut interference.

In order to investigate the effect of strut interference the moment and forces obtained were curve fitted by a second order polynomial using linear regression. The coefficients for the curvefits for the upright and inverted runs were then plotted with their respected standard error.

Figure A. 4.37 shows the results for the VFE-2 configuration for 34 m/s. It can be seen that for lift, drag and pitching moment the constants are within the limits between upright and inverted run, although the lift force constant of order zero is just about within the limits. This is due to an offset between the upright and inverted runs which is not due to strut interference. The results for the other configurations are depicted in Figure A. 4.38 to Figure A. 4.40. As for the VFE-2 run it can be seen that the upright runs are within the uncertainty of the inverted runs.

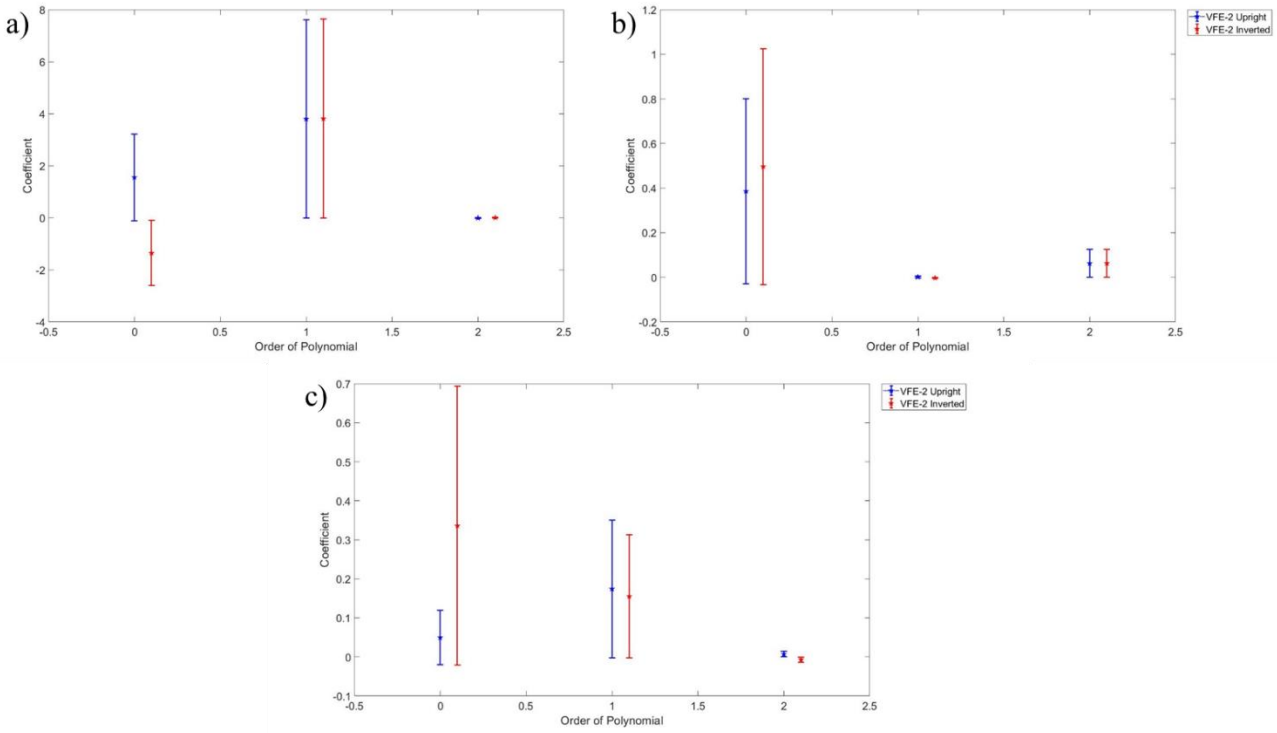

Figure A. 4.37 Comparison of curve fit coefficients for upright and inverted VFE-2 runs at 34 m/s for a) Lift b) Drag and c) Pitching Moment.

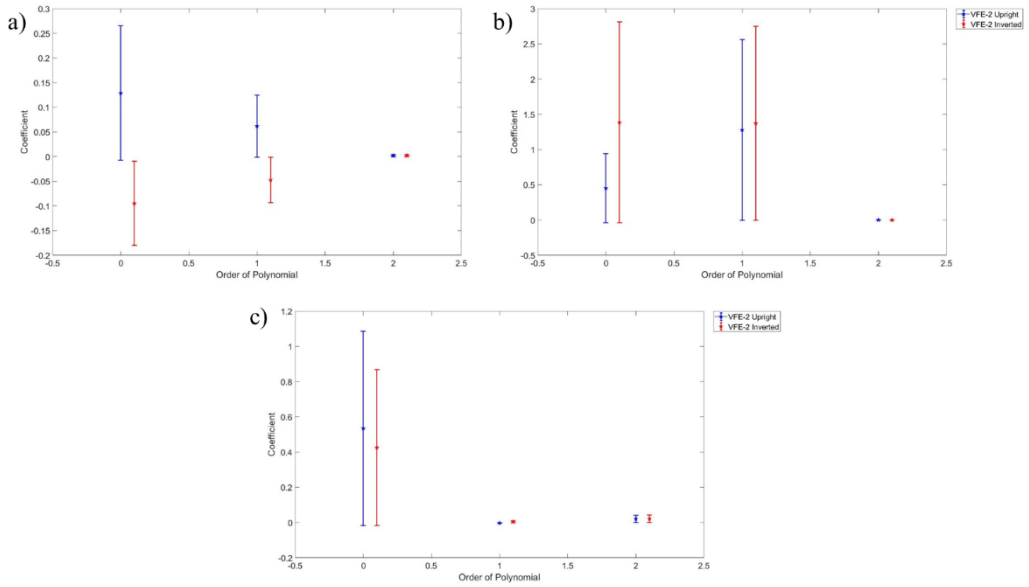

Figure A. 4.38 Comparison of curve fit coefficients for upright and inverted VST runs at 34 m/s for a) Lift b) Drag and c) Pitching Moment.

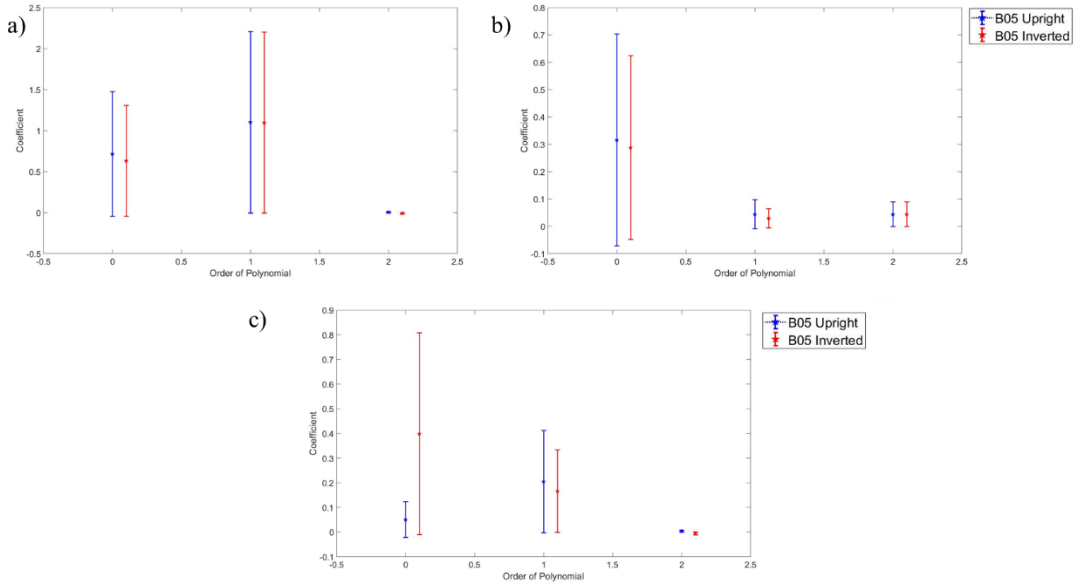

Figure A. 4.39 Comparison of curve fit coefficients for upright and inverted B05 runs at 34 m/s for a) Lift b) Drag and c) Pitching Moment.

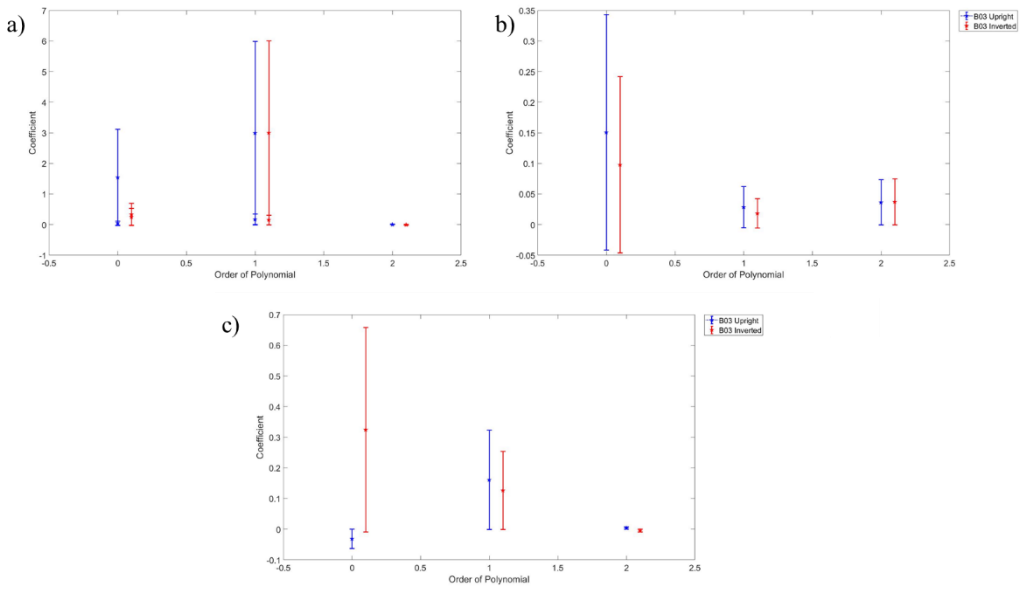

Figure A. 4.40 Comparison of curve fit coefficients for upright and inverted B03 runs at 34 m/s for a) Lift b) Drag and c) Pitching Moment.

A.4.8 Repeatability Tests

To show that the test set up and the results obtained are repeatable the VST configuration was run three times on three different dates. On each date the wind tunnel rig was re-installed in the tunnel and the instruments calibrated. The results of all three runs are depicted in Figure A. 4.41. Here, 4-16, 4-17 and 4-25 are indicating the month and day respectively.

It can be seen from Figure A. 4.41 that the data from all runs lie within the uncertainty of each other.

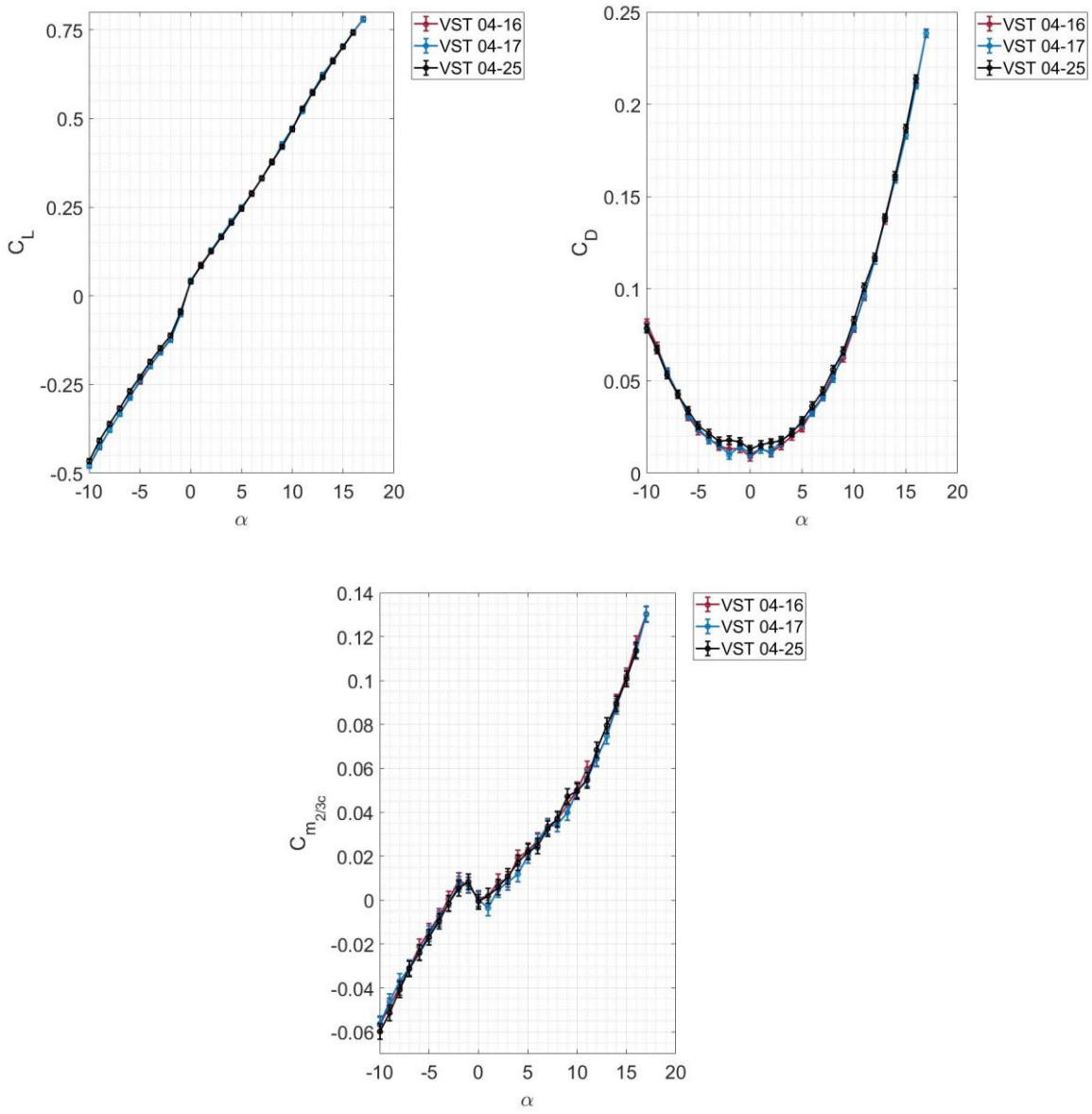

Figure A. 4.41 Aerodynamic coefficients of the repeatability runs of the VST configuration on three different dates.

A.4.9 Correction of weight tare and aerodynamic effects

To account for the aerodynamic forces and the weight of the rig and wing mount, the data obtained for the VFE-2 configuration needs to be corrected. The weight of the rig is accounted for by subtracting an air-off tare run of the wind-on set up. To account for the aerodynamic effects of the mount a separate wind-on and wind-off run is conducted for the rig and a dummy mount.

The forces of the clean wing can then be obtained using

$$F_{Wing_{Clean}} = F_{VFE-2} - F_{Wing_{Tare}} - F_{Dummy} - F_{Dummy_{Tare}} \quad (A.4.41)$$

$$M_{Wing_{Clean}} = M_{VFE-2} - M_{Wing_{Tare}} - M_{Dummy} - M_{Dummy_{Tare}} \quad (A.4.42)$$

During the tare runs neither lift nor drag is produced but solely a moment due to the shift in centre of gravity with increased angle of attack. Hence, equation A.5.41 becomes

$$F_{Wing_{Clean}} = F_{VFE-2} - F_{Dummy} \quad (A.4.43)$$

The forces and the pitching moment have been calculated by curve fitting the dummy air-on data as well as the moments obtained for each tare run to the angle of attack range of the wing air-on run. This is done as the tare runs were run for a different number of hysteresis cases than the air-on runs and because of slight differences in the angle of attack setting. The latter is due to the fact that the angle of attack is set manually and is measured to a fourth order accuracy by the wind tunnel system.

A.4.10 Coefficient Calculations

After the corrections have been made, the forces and moments can be transformed into coefficients using the following formulae (Anderson, 2011):

$$C_l = \frac{L}{q \times S} \quad (A.4.44)$$

$$C_d = \frac{D}{q \times S} \tag{A.4.45}$$

$$C_m = \frac{M}{q \times S \times mac} \tag{A.4.46}$$

where q is the dynamic pressure, S the planform area and "mac" the mean aerodynamic chord. The moment arm used in the test is 0.008 m in front of the 2/3c location. Therefore, the moment needs to be shifted by using:

$$M_{New} = M_{ref} + L \times (x_{new} - x_{ref}) \tag{A.4.47}$$

Where M_{ref} is the moment measured around a given reference point and x_{ref} is the location of the current moment reference point.

The mean aerodynamic chord and projected area, S, are calculated based on the measurements of the wind tunnel model. Due to inaccuracies in manufacturing, the following chord lengths and spans were measured for the different models (Table A. 4.17).

Table A. 4.17 Measured chord and span for the four different models.

	VFE-2	VST	B03	B05
Chord [m]	0.486	0.487	0.489	0.489
Span [m]	0.4543	0.4545	0.4555	0.456

A.4.11 Wind Tunnel corrections: Blockage Corrections

Wind tunnel testing differs from free flight for multiple reasons such as the test section boundaries and mounting system which influences the flow field. Corrections have to be applied in order to draw realistic conclusions for the model's performance in free flight. The different methods are discussed in the following sections.

Wind tunnel testing differs from free flight due to the test section boundaries and the support system required hindering the flow from expanding in the same way as it would in free flight (Hantrais-Gervois, 2012). This has an effect on the pressure field around the model, which needs to be accounted for before drawing conclusions about the model's free air behaviour.

During wind tunnel testing the model is affected by the dynamic pressure, Mach number and the change in angle of attack. These quantities change due to the wall interferences and need to be corrected for.

The dynamic pressure and Mach number corrections are also referred to as blockage corrections.

Maskell derived a blockage equation for thin plates, which is used for the VFE-2 configuration (Rae and Pope, 1984).

$$\varepsilon_{sb_W} = \frac{\text{Wing Volume}}{C^{\frac{3}{2}}} \qquad \text{(A.4.48)}$$

Where C is the tunnel test section area (see Table A. 4.18 for the measurements of the UWE wind tunnel high-speed section).

The increment in velocity due to blockage is defined as (Rae and Pope, 1984):

$$\Delta V = V_u \times \varepsilon_{sb_W} \qquad \text{(A.4.49)}$$

where V_u is the uncorrected velocity.

Table A. 4.18 Measurements of the UWE Wind Tunnel High-Speed Test Section.

Wind Tunnel Height [m]	1.53
Wind Tunnel Width [m]	2.14
C $[m^2]$	3.2742
Wing Volume $[m^3]$	0.001445
V_u $\left[\frac{m}{s}\right]$	33.7564

Every body generates a wake when subject to a flow. This wake has a lower velocity than the freestream. In a closed duct this means that the airspeed outside the wake must be larger than the velocity inside the wake so that the law of continuity can be maintained. This heightened velocity results in a lower pressure in this region which yields to a favourable pressure gradient causing a velocity increment at the model. This wake effect is referred to as wake blockage and need to be corrected for. The wake blockage is defined as (Rae and Pope, 1984):

$$\varepsilon_{wb} = \frac{S}{4C} C_{Du} \tag{A.4.50}$$

Where S is the projected area of the model and C_{Du} the uncorrected drag coefficient.

The total corrections can then be written as (Rae and Pope, 1984):

$$\varepsilon = \varepsilon_{wb} + \varepsilon_{sb} \tag{A.4.51}$$

The dynamic pressure can then be corrected by taking into account both; the correction of the solid and wake blockages as (Sahini, 2004):

$$q_c = q_u(1 + 2\varepsilon) \tag{A.4.52}$$

where q_u is the uncorrected dynamic pressure and q_c is the corrected dynamic pressure.

And the total corrected airspeed can be obtained by (Rae and Pope, 1984):

$$V = V_u(1 + \varepsilon) \tag{A.4.53}$$

where V_u is the uncorrected velocity and is the average velocity measured by the pitot tube for the four different runs.

The total corrected Reynolds number, Re, then becomes (Rae and Pope, 1984):

$$Re = Re_u(1 + \varepsilon) \tag{A.4.54}$$

The blockage corrections are required to obtain the correct dynamic pressure for calculating the coefficients.

A.4.12 Comparison of Aerodynamic Centre and Centre of Pressure locations between Numerical and Experimental data

As discussed previously, the aerodynamic centre and centre of pressure are important parameters; the former for stability analysis and the latter for the evaluation of pressure distribution. The raw wind tunnel data and experimental data have been plotted against normal force coefficient in Figure A. 4.42 to Figure A. 4.45. It can be seen, that CFD as well as wind tunnel results are quite noisy, especially when looking at the location of the aerodynamic centre. This is because the aerodynamic centre is predicted using the slopes of pitching moment and normal force, which are more sensitive to changes in normal force and pitching moment data. Ignoring the extrema, it can be seen that the aerodynamic centre is predicted very well by the CFD (right hand diagrams in Figure A. 4.42 to Figure A. 4.45). The centre of pressure is predicted further forward for the numerical simulations, apart from the B05 configuration,

where it is predicted slightly behind the location predicted by the wind tunnel data (left hand diagrams).

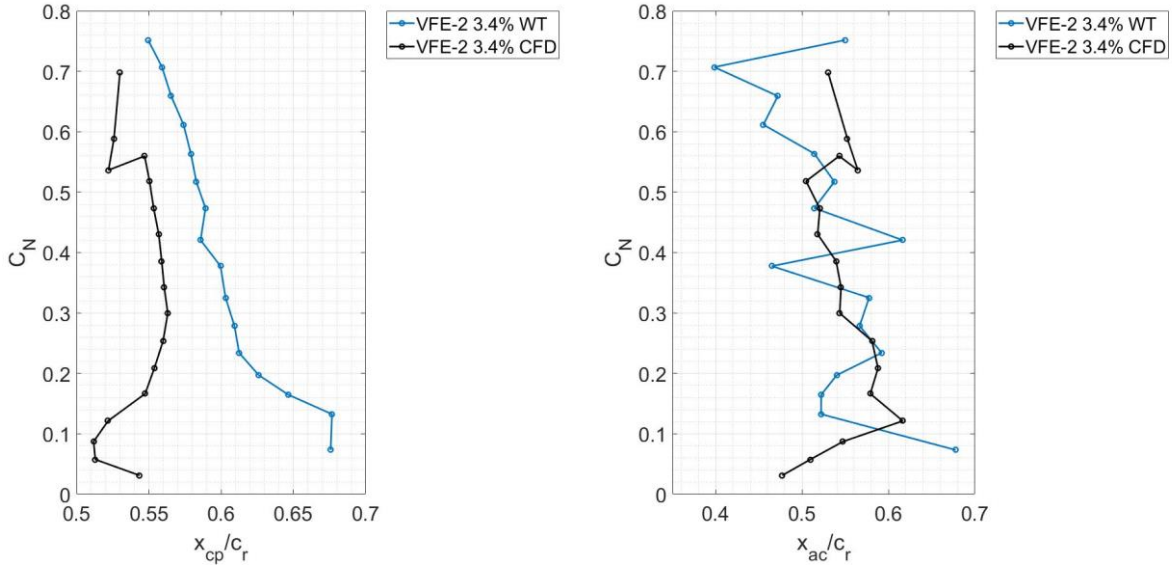

Figure A. 4.42 Comparison of CFD predictions and experimental tests for the centre of pressure and aerodynamic centre (referenced to root chord) for the VFE-2 configuration.

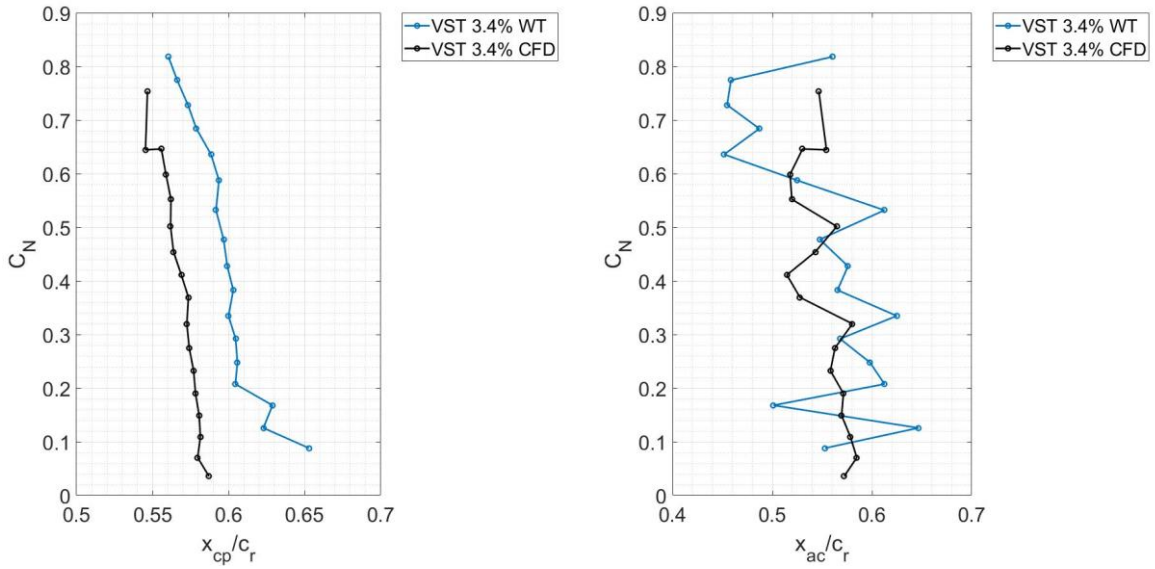

Figure A. 4.43 Comparison of CFD predictions and experimental tests for the centre of pressure and aerodynamic centre (referenced to root chord) for the VST configuration.

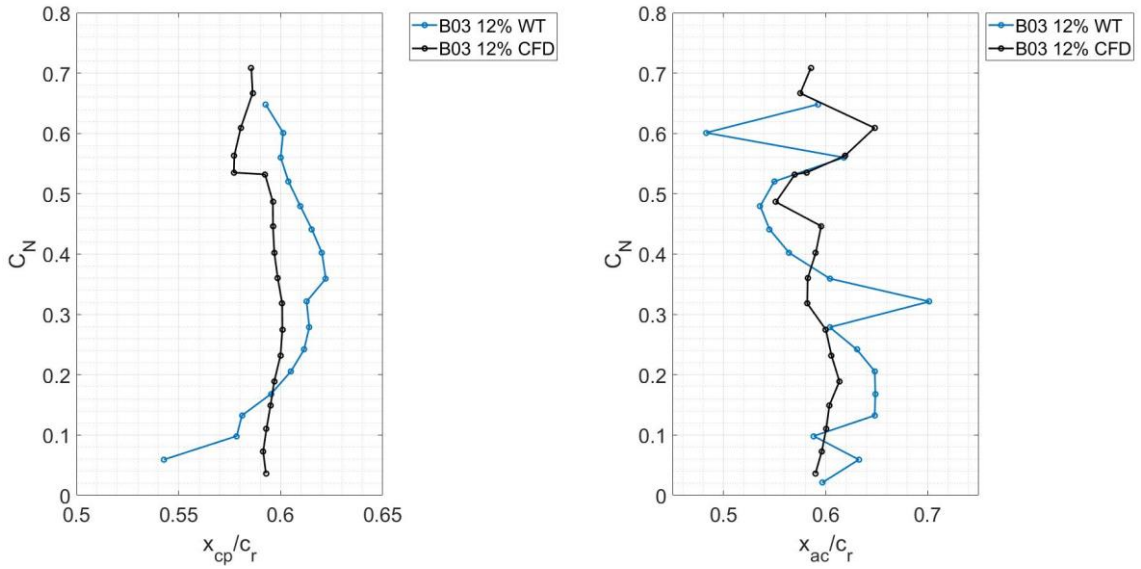

Figure A. 4.44 Comparison of CFD predictions and experimental tests for the centre of pressure and aerodynamic centre (referenced to root chord) for the B03 configuration.

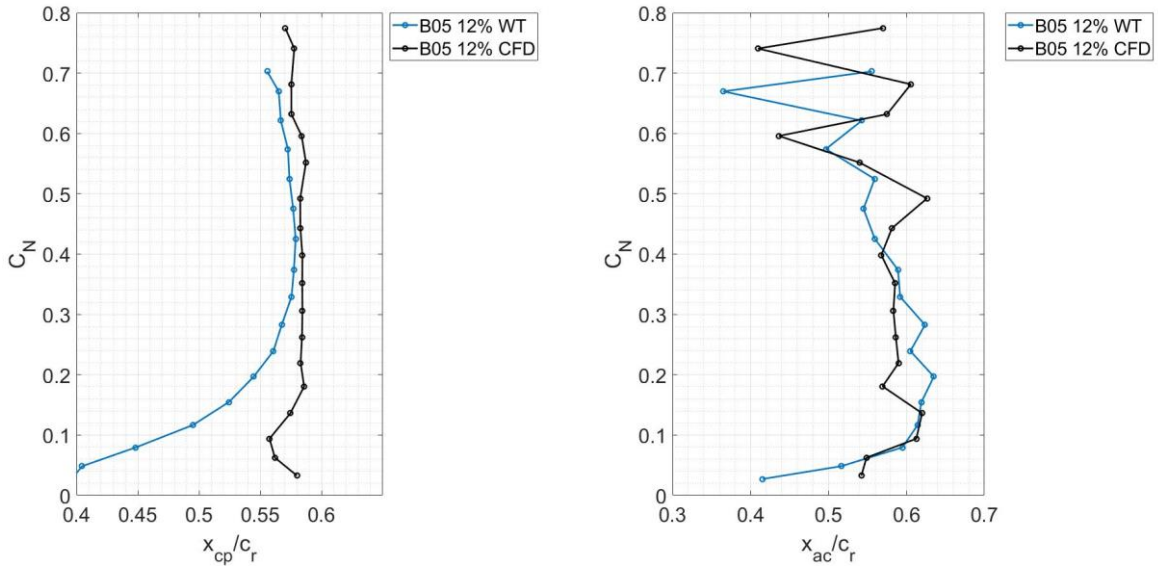

Figure A. 4.45 Comparison of CFD predictions and experimental tests for the centre of pressure and aerodynamic centre (referenced to root chord) for the B05 configuration.

A.4.13 Wind tunnel data reduction procedure

A.4.13.1 Tare Corrections Upright run

1. Curve fit the tare runs for pitching moment, PM, data and take the statistical average for Lift and Drag.
2. Calculate aerodynamic loads using

$$L_{aero} = L_{34ms} - L_{Tare} \quad \text{(A.4.55)}$$

and

$$D_{aero} = D_{34ms} - D_{Tare} \quad \text{(A.4.56)}$$

where L_{aero} and D_{aero} is the aerodynamic lift and drag respectively, L_{34ms} and D_{34ms} are the lift and drag measured at 34 m/s and L_{Tare} and D_{Tare} are the lift and drag measured during the tare run.

3. Calculate normal force using

$$N = L \times \cos(\alpha_{VST\_34}) + D \times \sin(\alpha_{VST\_34}) \quad \text{(A.4.57)}$$

4. Start iterations using $PM_{aero} = 0$
5. Calculate θ using (iteration, i= iteration number)

$$\theta_i = (N \times 0.5 + PM_{aero_{i-1}}) \times KTHETAM + N \times KTHETAN - C_{deflection} \times \cos(\alpha_{corr_{i-1}}) \quad \text{(A.4.58)}$$

with $C_{deflection} = 0.38$ for VST (deflection in sting caused when mounting the model on the rig), $PM_{aero_i} = 0$ and $\alpha_{corr_{i-1}} = \alpha_{uncorr}$ for the first iteration.

6. Calculating the first corrected angle of attack α_{corr} for the tare run

$$\alpha_{corr_i} = \alpha_{uncorr_i} - \theta_i \quad \text{(A.4.59)}$$

7. Calculate PM_{Tare_i} by substituting α_{corr_i} in the curvefit polynomial

8. Calculate

$$\mathrm{PM}_{\mathrm{aero_i}} = \mathrm{PM}_{34\mathrm{ms}} - \mathrm{PM}_{\mathrm{Tare_i}} \quad \text{(A.4.60)}$$

9. Repeat steps 5 to 8 until $\alpha_{\mathrm{corr_i}}$ reaches a convergence of 1×10^{-4} ($\alpha_{\mathrm{rig}} = \alpha_{\mathrm{corr}}$)
10. Curve fit L, D and PM for Dummy_{34} and $\mathrm{Dummy}_{\mathrm{Tare}}$ using α_{rig}
11. Calculate aerodynamic loads of the dummy

$$\mathrm{Dummy}_{\mathrm{aero}} = \mathrm{Dummy}_{34} - \mathrm{Dummy}_{\mathrm{Tare}} \quad \text{(A.4.61)}$$

12. Calculate the aerodynamic loads of the clean configuration

$$\mathrm{Clean} = \mathrm{VST}_{\mathrm{aero}} - \mathrm{Dummy}_{\mathrm{aero}} \quad \text{(A.4.62)}$$

13. Plot graphs using $\alpha_{\mathrm{VST\_34}}$

A.4.13.2 Tare Corrections Inverted Run

Same steps as for the upright run until step 13.

14. Invert $\alpha_{\mathrm{VST\_34}}$=-$\alpha_{\mathrm{VST\_34}}$
15. Invert lift and pitching moment

A.4.13.3 Shift moment to 2/3 chord

$$\mathrm{PM}_{2/3} = \mathrm{PM} + \mathrm{N} \times \mathrm{x} \times \cos(\alpha) + \mathrm{A} \times (\mathrm{y} + \mathrm{x} \times \sin(\alpha)) \quad \text{(A.4.63)}$$

With x being the distance to the 2/3c position (-0.0010609 m for VST upright) and y being the distance from wing midpoint at 2/3c to eye ball joint (0.02 m)

A.4.13.4 Data reduction Wind Tunnel

1. Interpolation of each hysteresis run for angle of attack in steps of 1 degree using Matlab function interp1()
2. Taking the mean for each hysteresis run for each angle of attack
3. Calculation of the standard deviation for each angle of attack
4. From students t-distribution t value for (n-1) = 3 degrees of freedom t= 3.182
5. Calculating precision, P, using

$$P = t \times \frac{std(\alpha)}{\sqrt{n}} \tag{A.4.64}$$

6. Bias (B) for each variable

Lift	+- 0.5
Drag	+0.17 and -0.28
PM	0.044
q	2

7. Calculating uncertainty, U, for the measured forces and moments using

$$U_x = \sqrt{P^2 + B^2} \tag{A.4.65}$$

8. Calculating the uncertainty for the different coefficients using (example for Cl)

$$U_{Cl} = \sqrt{\left(\frac{1}{\bar{q} \times S} \times U_L\right)^2 + \left(\frac{L}{\bar{q} \times S} \times U_q\right)^2} \tag{A.4.66}$$

A.4.13.5 Calculating Aerodynamic Forces on Clean Configuration

1. Calculate the aerodynamic forces for dummy and model separately using

$$F_{aero} = F_{Air\ On} - F_{Air\ off} \quad \text{(A.4.67)}$$

2. Calculate the aerodynamic forces on the clean configuration using

$$F_{Clean} = F_{Model\_aero} - F_{Dummy\_aero} \quad \text{(A.4.68)}$$

A.4.13.6 Shift Moment to 2/3c

1. Determine wing thickness t at 2/3c.
2. Determine distance between sting centreline and top of mounting box h
3. Vertical distance between eye ball joint and centre 2/3c of wing

$$y = h + {}^{t}/_{2} \quad \text{(A.4.69)}$$

4. Shift PM to 2/3c using

$$PM_{23} = PM + N \times x\cos(\alpha) + A \times (y + x\sin(\alpha)) \quad \text{(A.4.70)}$$

with x being

$$x = (x_{bar} - x_{ref}) - \left(\frac{1}{3}c + x_{half\ block} + x_{model}\right) \quad \text{(A.4.71)}$$

where $x_{bar} = 0.5$ m, $x_{ref} = 0.00015$m, $x_{half\ block} = 0.02$ m and x_{model} being the distance between the trailing edge of the model and the beginning of the half block.

A.4.13.7 Wind Tunnel Corrections (Rae and Pope, 1984)

1. Calculate ε_{SB}

$$\varepsilon_{SB} = \frac{K \times V_{Model}}{{}^{3}/_{2}\,C} \quad \text{(A.4.72)}$$

where K=0.9, V_{Model} is the volume of the model and C is the tunnel test section area.

2. Calculate ε_{WB}

$$\varepsilon_{WB} = \frac{S}{4C} \times C_{d_u} \tag{A.4.73}$$

3. Calculate ε_{total}

$$\varepsilon_{total} = \varepsilon_{SB} + \varepsilon_{WB} \tag{A.4.74}$$

4. Calculate q_c

$$q_c = q \times (1 + \varepsilon_{total})^2 \tag{A.4.75}$$

5. Calculate C_{l_c}

$$C_{l_c} = \frac{L}{S \times q_c} \tag{A.4.76}$$

6. Determine flow angularity α_{up}
7. Calculate ΔC_d

$$\Delta C_d = C_{d_{upright}} - C_{d_{inverted}} \tag{A.4.77}$$

8. Use linear regression with ΔC_d for x-values and $C_{l_{upright}}$ as y-values and then the x variable is $\tan(\alpha_{up})$
9. Calculate α_w using

$$\alpha_w = \frac{S \times \delta}{C} \times C_{l_c} \tag{A.4.78}$$

where δ=0.135, obtained from Rae and Pope (1984) for closed wind tunnels.

10. Correct alpha using

$$\alpha_c = \alpha_g + \alpha_{up} + \alpha_w \tag{A.4.79}$$

11. Drag coefficient correction using

$$C_{d_c} = C_{d_u} + \Delta C_{d_{up}} + \Delta C_{d_w} \tag{A.4.80}$$

with

$$\Delta C_{d_{up}} = C_l \alpha_{up} \tag{A.4.81}$$

with α_{up} in radians and

$$\Delta C_{d_w} = \frac{\delta S}{C C_{l_c}^2} \tag{A.4.82}$$

12. The pitching moment is then corrected using

$$C_{m_c} = \frac{PM}{q_c \times S \times mac} \tag{A.4.83}$$

Appendix 5 CFD Results evaluation

A.5.1. Effect of thickness on the flow features and pressure distribution of the B05 configuration (from section 6.2)

The spanwise pressure distribution at α=4° is presented in Figure A. 5.1 for the B05 configuration of different thicknesses (see Figure 6.33). It can be seen that the suction force increases with increase in chord location until it is dropping off rapidly close to the trailing edge to meet the ambient pressure. The location where a maximum pressure peak is formed depends on the thickness and varies between x/c=0.6 and x/c=0.8. It can be seen from Figure A. 5.1 that an increase in thickness increases the suction generated inboard of the LEVs. This is due to thicker wing generating separation bubbles rather than LEVs (see Figure A. 5.2). This results in an earlier reattachment and less disturbed flow. For the thinner wings the area of low pressure decreases with thickness as already observed for the B03 configuration and is due to earlier reattachment. It can be seen from the Cp plots that this is due to a more favourable pressure gradient for the thicker wings.

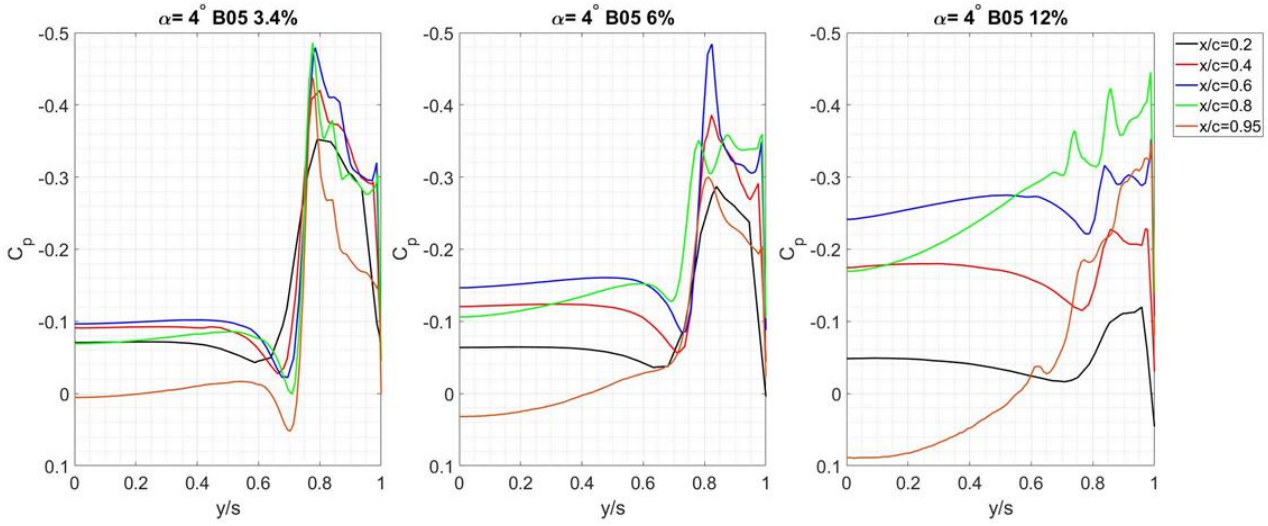

Figure A. 5.1 Spanwise pressure distributions of the B05 configuration for 3.4, 6 and 12% thicknesses at α=4° where y/s is the normalised spanwise coordinate from the centreline. Note that s is the local half-span and thus increases from apex to trailing edge.

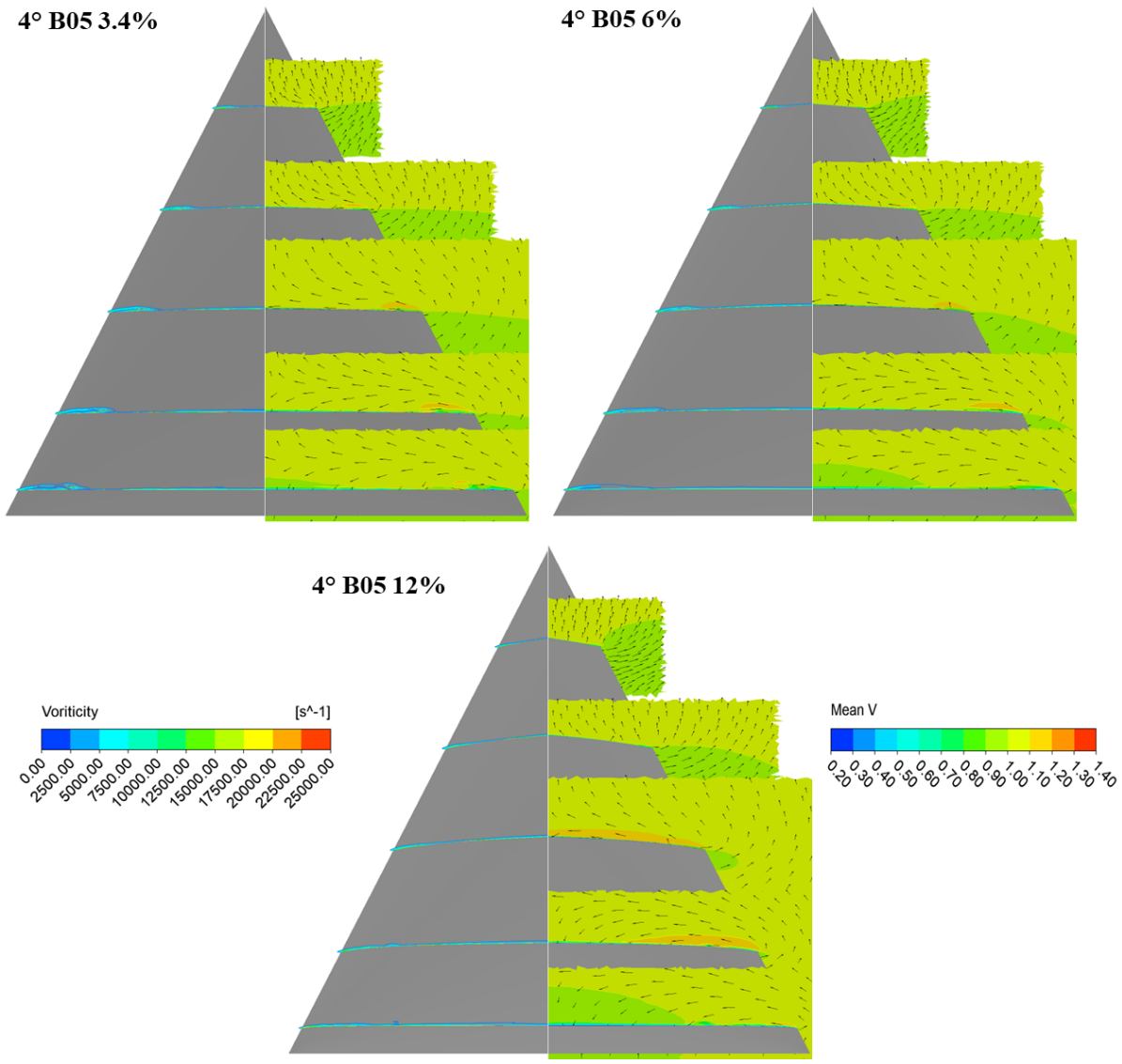

Figure A. 5.2 Vorticity contours and mean velocity at different chordwise locations for the B05 configuration with different thicknesses at α=4°.

The spanwise pressure distribution at 13° angle of attack is shown in Figure A. 5.3. On all three wings LEVs have formed as indicated by the pressure peaks. Even secondary vortices can be seen, which form due to either the increased strength of the primary vortex or its closeness to the surface. The flow pattern of the two thinner wings is very similar, but the vortex shape changes for the thickest wing; again, the vortex is more oval shaped. As before, this is due to the adverse pressure gradient being lower, thus, delaying reattachment, which in turn effects the vortex shape. The biggest difference however is close to the trailing edge, where an increase in thickness prevents a rapid suction force drop. A reason for this may be that due to the more favourable adverse pressure gradient of the thicker wings along most of the chord, the pressure has to increase more rapidly towards the trailing edge, favouring separation. This effect moves further downstream with increase in thickness and is also observed for the B03 configuration.

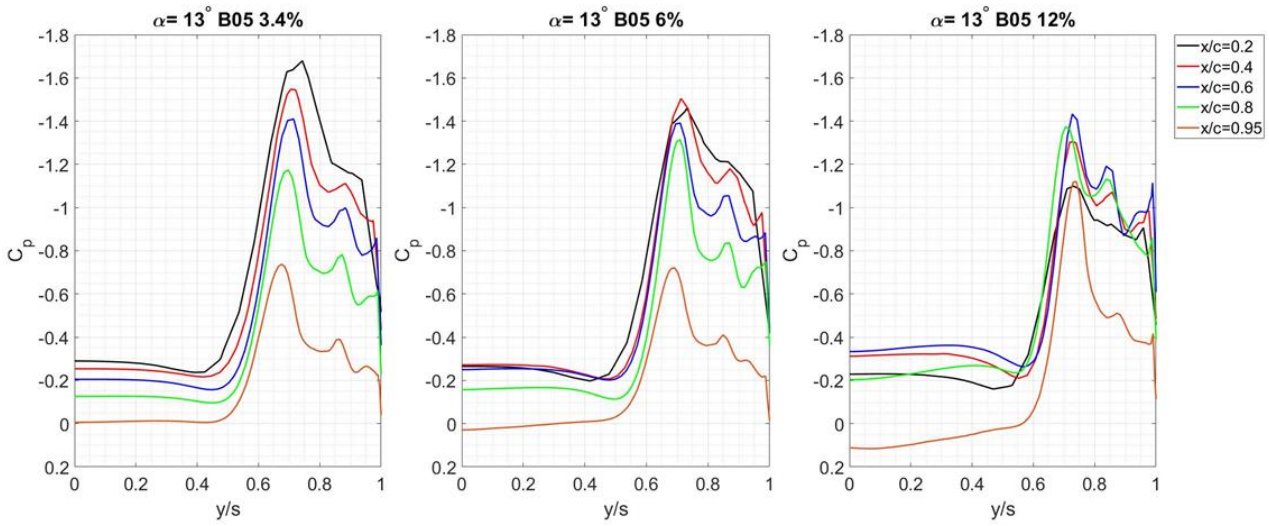

Figure A. 5.3 Spanwise pressure distributions of the B05 configuration for 3.4, 6 and 12% thicknesses at α=13°.

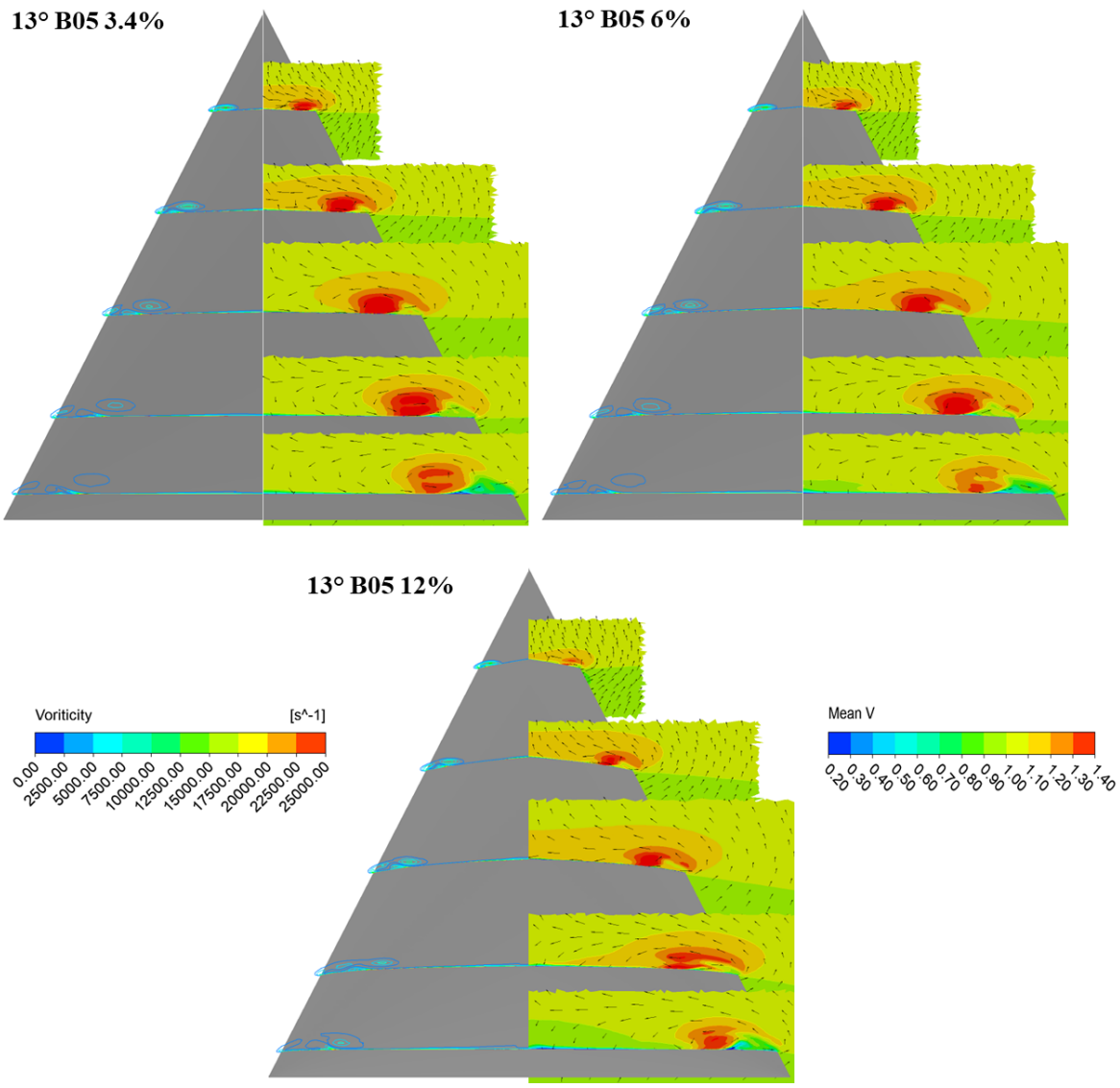

Figure A. 5.4 Vorticity contours and mean velocity at different chordwise locations for the B05 configuration of different thicknesses at α=13°.

A.5.2. Effect of the thickness on the flow features and pressure distribution of the VST configuration (from Section 6.2)

The spanwise pressure distribution of the VST configuration at 4° angle of attack is plotted against the normalised span in Figure A. 5.5. It can be seen that the pressure distribution looks very different for this profile which is flat for the majority of the surface (see Chapter 4 Figure 4.1). The flow on the 3.4% thick configuration is attached for the majority of the wing with separation bubbles forming in the second half. The flow is more complex for the thicker wings and is characterised by the formation of an inner vortex in the rear part of the wing. The initial separation is delayed towards the apex due to the effective leading-edge radius being higher there than closer to trailing edge. This results in the vortex lying more inboard. This can also

be seen when comparing the spanwise pressure distribution with the vorticity plots shown in Figure A. 5.6.

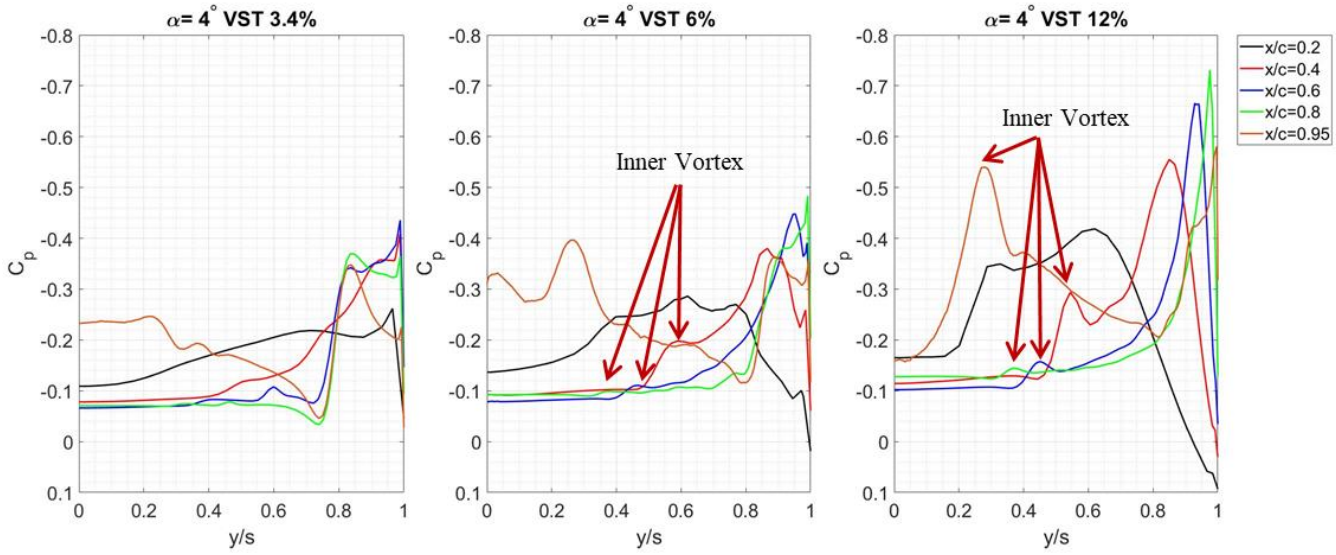

Figure A. 5.5 Spanwise pressure distribution of the VST configuration for 3.4, 6 and 12% thicknesses at α=4°.

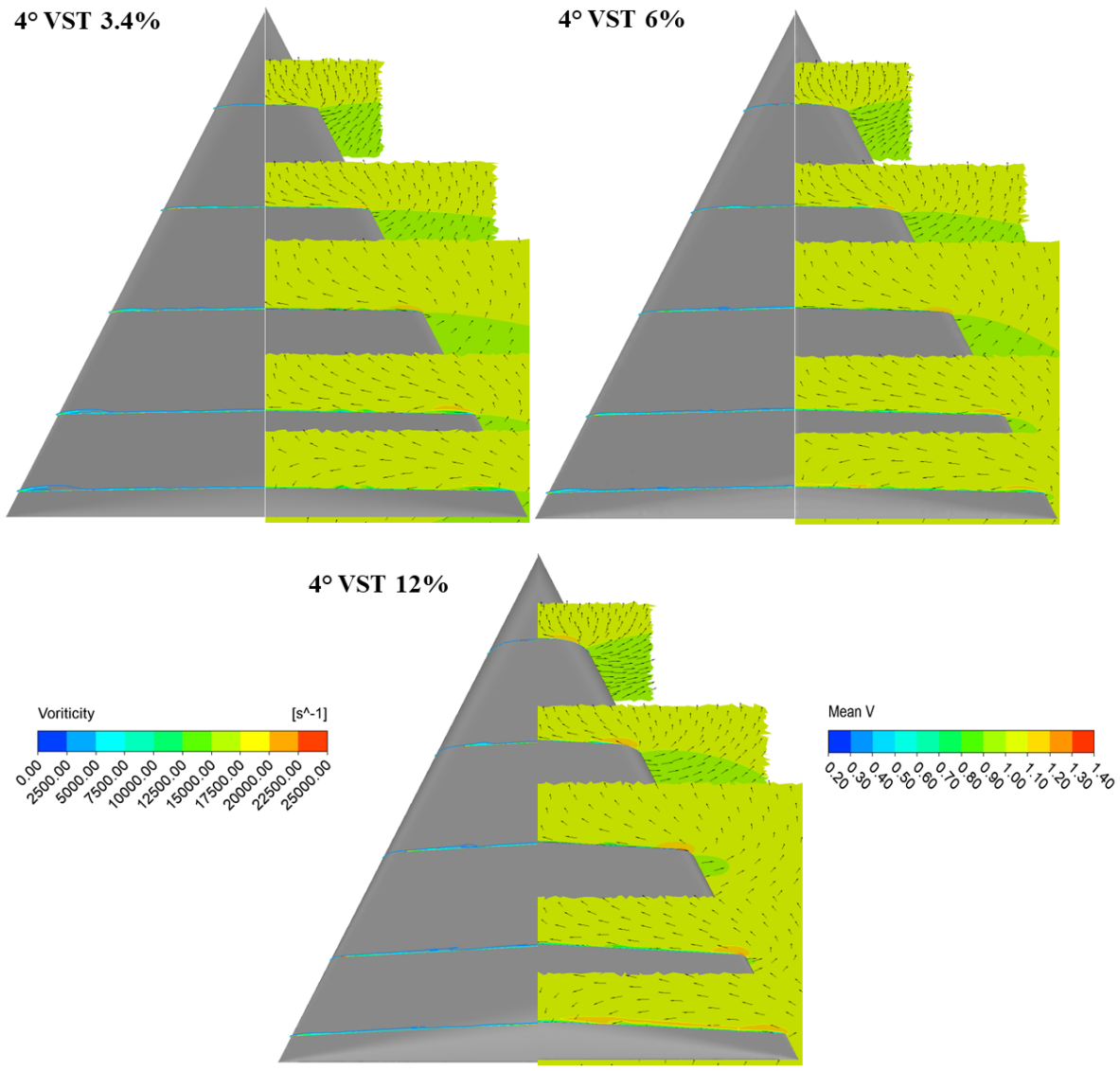

Figure A. 5.6 Vorticity contours and mean velocity at different chordwise locations for the VST configuration of different thicknesses at α=4°.

Figure A. 5.7 shows the spanwise pressure distribution of the VST configuration for different thicknesses. A fully developed vortical flow structure including secondary vortices can be seen on the thinnest wing. This is confirmed by the vorticity contours depicted in Figure A. 5.8. The wing is loaded in the front causing the wing to be unstable as discussed earlier. With increase in thickness the wing becomes more stable with the loading shifting downstream (see Chapter 6 Figure 6.40). For the thicker wings the effect of relative leading-edge roundness results in the flow forming separation bubbles in the first 30% of the wing. Only further downstream the flow rolls up into a vortex. As for the biconvex configurations, the suction force near the trailing edge remains powerful with increase in thickness, due to a more favourable pressure gradient and a relatively stronger primary vortex further upstream. However, from the mean axial velocity contours can be seen that the 6% thick wing experiences VBD at x/c=0.95. It can

further be seen, that the 3.4% and 6% wings are closer regarding their axial velocity, whereas the 12% thick wing shows a very different patter. This is due to the flow over the VST 12% being delayed so far downstream, that VBD is avoided. An inner vortex is forming around x/c=0.5 on the 6% and 12% thick configurations, which is an effect of the flat profile as it is not observed on the biconvex profiles and is also present on the VFE-2 configurations.

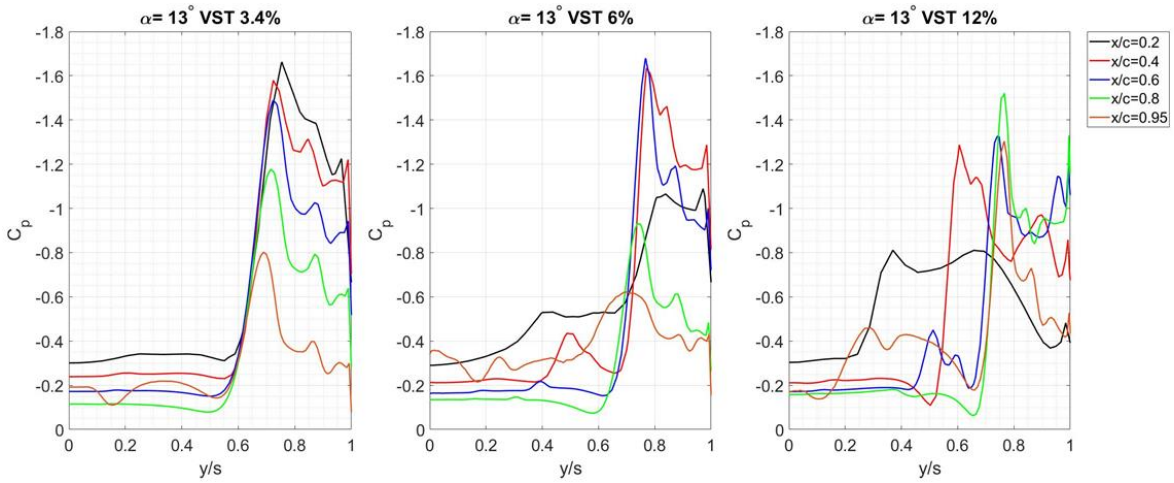

Figure A. 5.7 Spanwise pressure distribution of the VST configuration for 3.4, 6 and 12% thicknesses at α=13°.

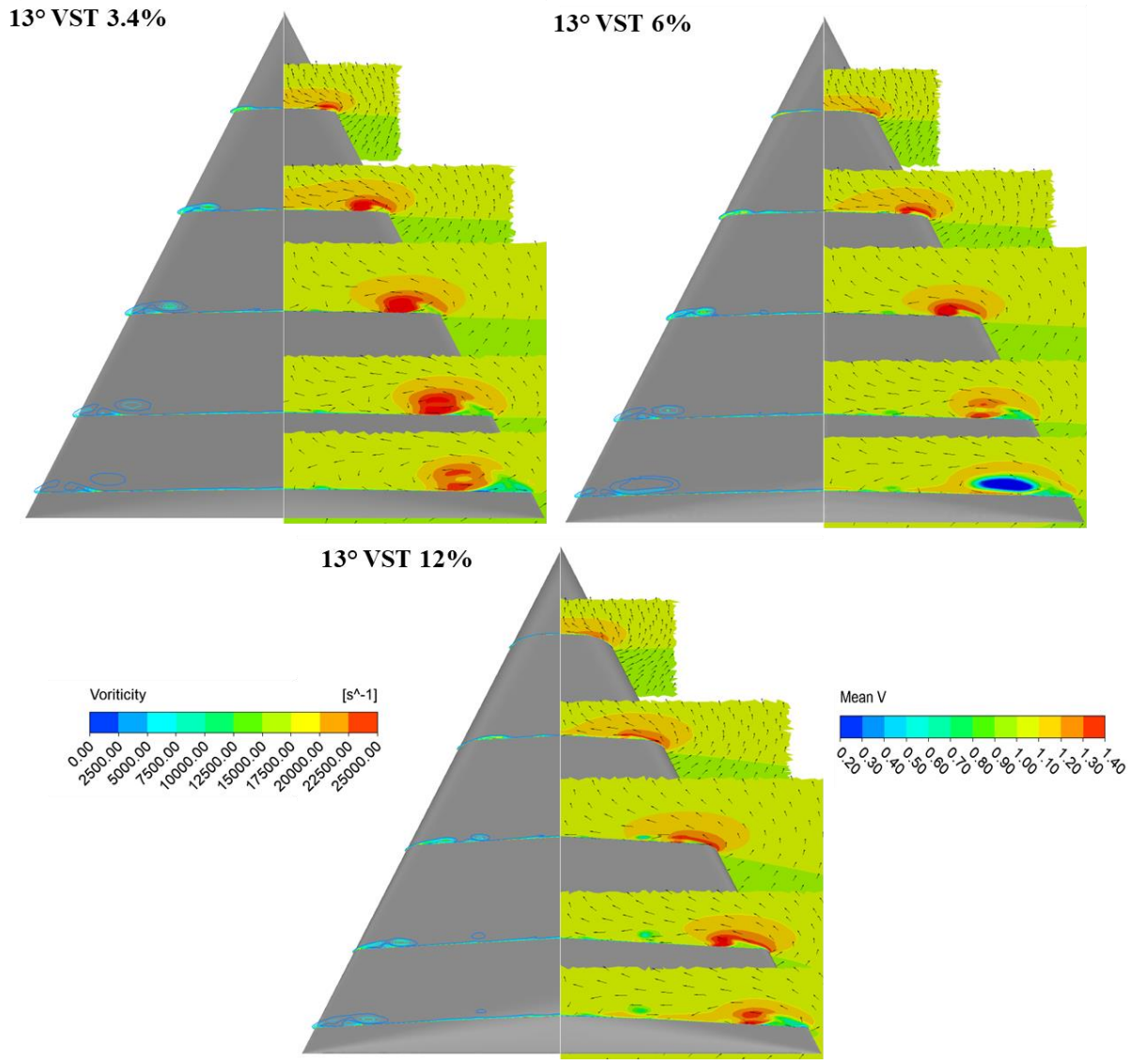

Figure A. 5.8 Vorticity and mean velocity and mean velocity contours at different chordwise locations (x/c=0.2, 0.4, 06, 0.8 and 0.95) for the VST configuration of different thicknesses at α=13°.

A.5.3. Effect of thickness on the flow features and pressure distribution of the VFE-2 configuration (from Section 6.2)

The spanwise pressure distributions for the VFE-2 configurations at α=4° are depicted in Figure A. 5.9 and their associated vorticity and mean axial velocity contours in Figure A. 5.10. It can be seen that the flow on the VFE-2 of 3.4% thickness is mainly attached and only small separation bubbles form due to the forced separation at the SLE. Pressure peaks arise near the trailing edge for the thicker wings where the flow rolls up into a vortex. The flow on the two thicker wings separates initially at the leading-edge resulting in the formation of vortices. The flow reattaches then only to separate again further inboard as captured in the surface pressure distribution. The inner vortices increase in strength with thickness. Here, the strength of the

inner vortex depends on the strength of the initial separation; with a higher initial suction resulting in a more powerful inner vortex. This can be explained by the drastic change in pressure causing a stronger adverse pressure gradient after reattachment of the primary vortex, thus enabling further separation inboard. The wing loading is rearward for low thicknesses but moves forward with an increase in thickness.

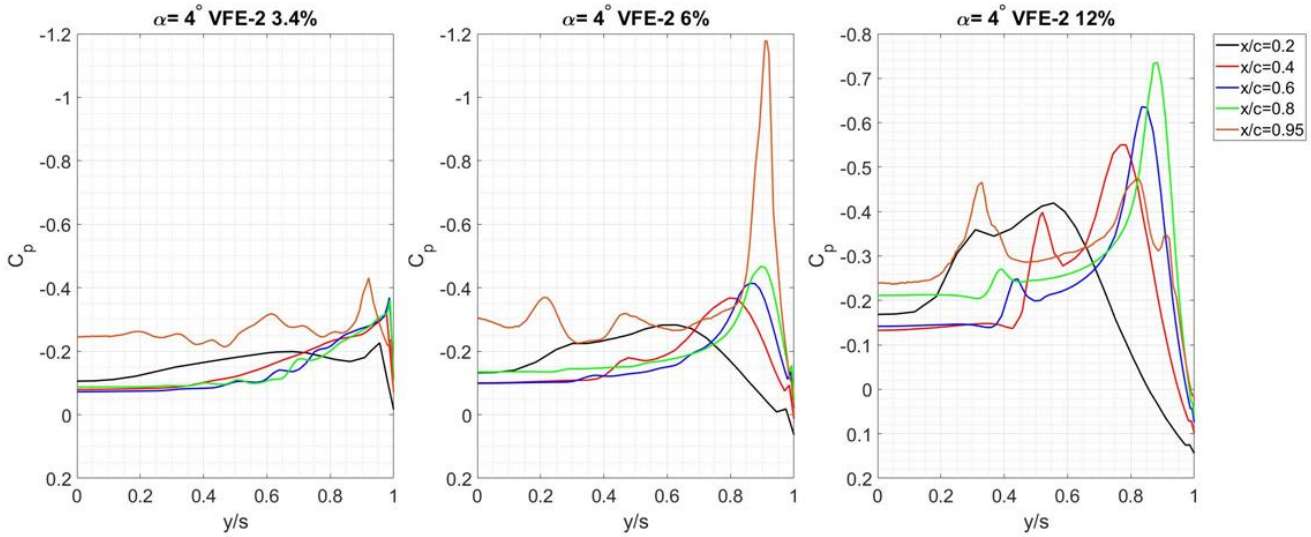

Figure A. 5.9 Spanwise pressure distribution of the VFE-2 configuration for 3.4, 6 and 12% thicknesses at α=4°.

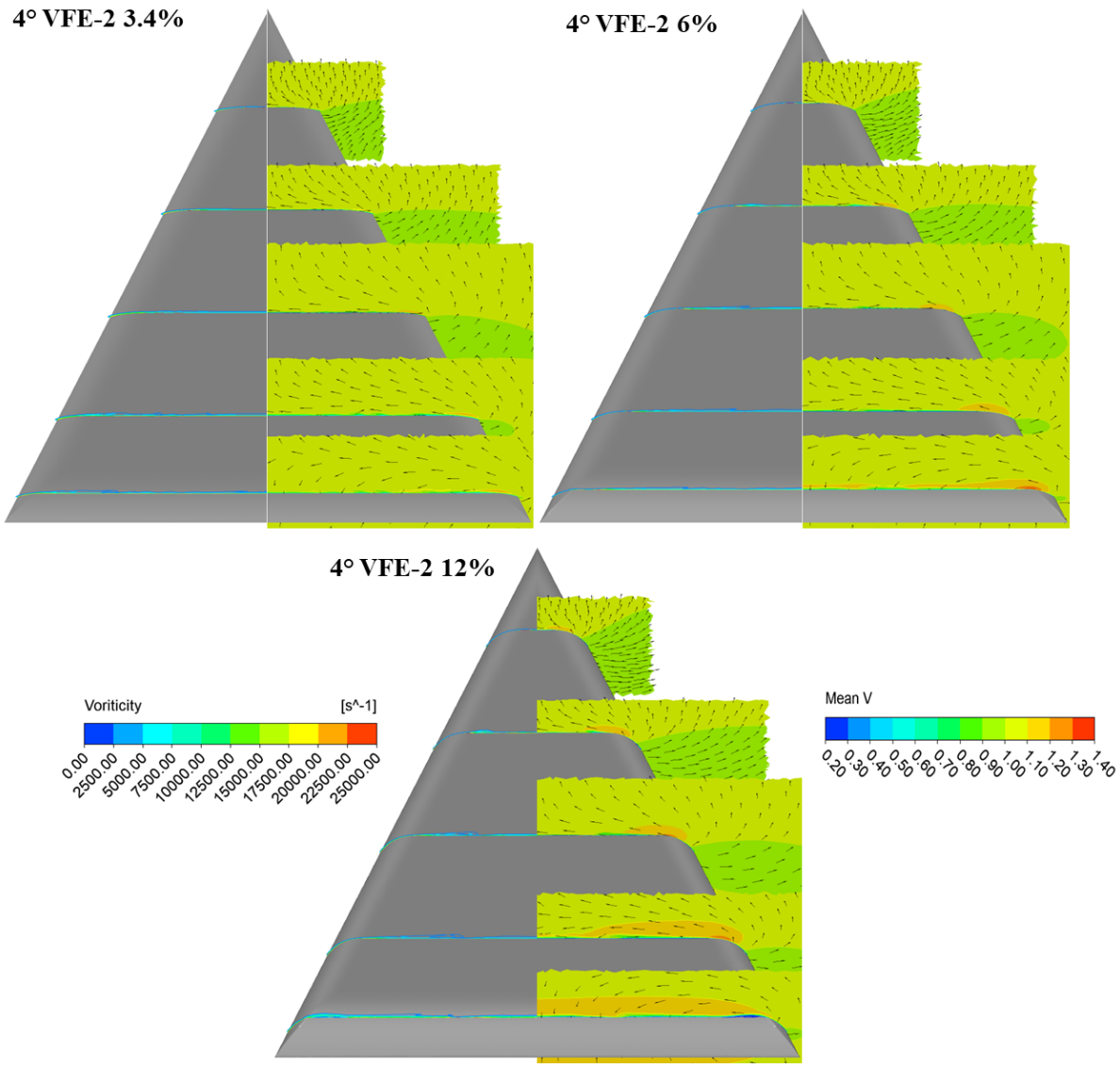

Figure A. 5.10 Vorticity contours and mean velocity at different chordwise locations for the VFE-2 configuration of different thicknesses at α=4°.

At 13° angle of attack vortical flow is fully developed on all three configurations (Figure A. 5.11 and Figure A. 5.12). The thin wing shows a vortex pattern typical for thin wings with the wing loading shifted towards the apex. The thicker wings generate a significantly lesser suction force but show the development of multiple vortex structures consisting of an inner and outer vortex. The thin wing on the other hand captures a primary and secondary vortex. The inner vortex is very dominant on the 6% thick wing, whilst much smaller in size for the 12% thick wing. They also vary in location with the inner vortex of the 6% thick wing being located further outboard (around y/s=0.7) than that of the 12% thick wing (y/s=0.5). Furthermore, the inner vortex of the 12% thick wing is connected by an area of high axial velocity with the primary vortex, which is not the case for the 6% thick wing. As described for the VST configuration in A.6.2 the inner vortex is believed to occur due to a combination of a less

favourable adverse pressure gradient for profiles which have a majorly flat section and a less energised boundary layer upon reattachment.

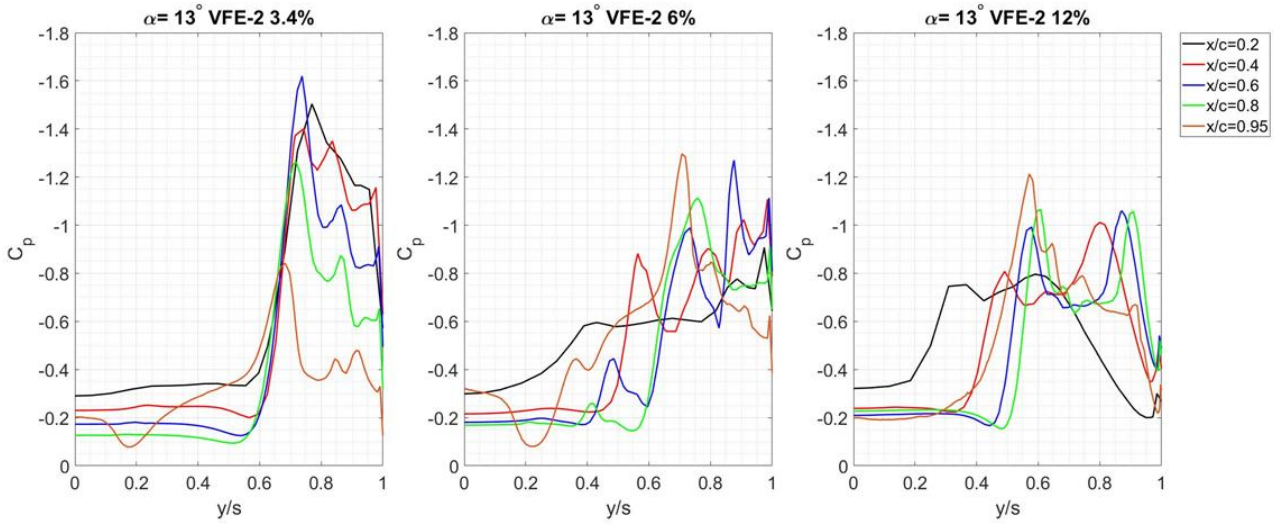

Figure A. 5.11 Spanwise pressure distribution of the VFE-2 configuration for 3.4, 6 and 12% thicknesses at α=13°.

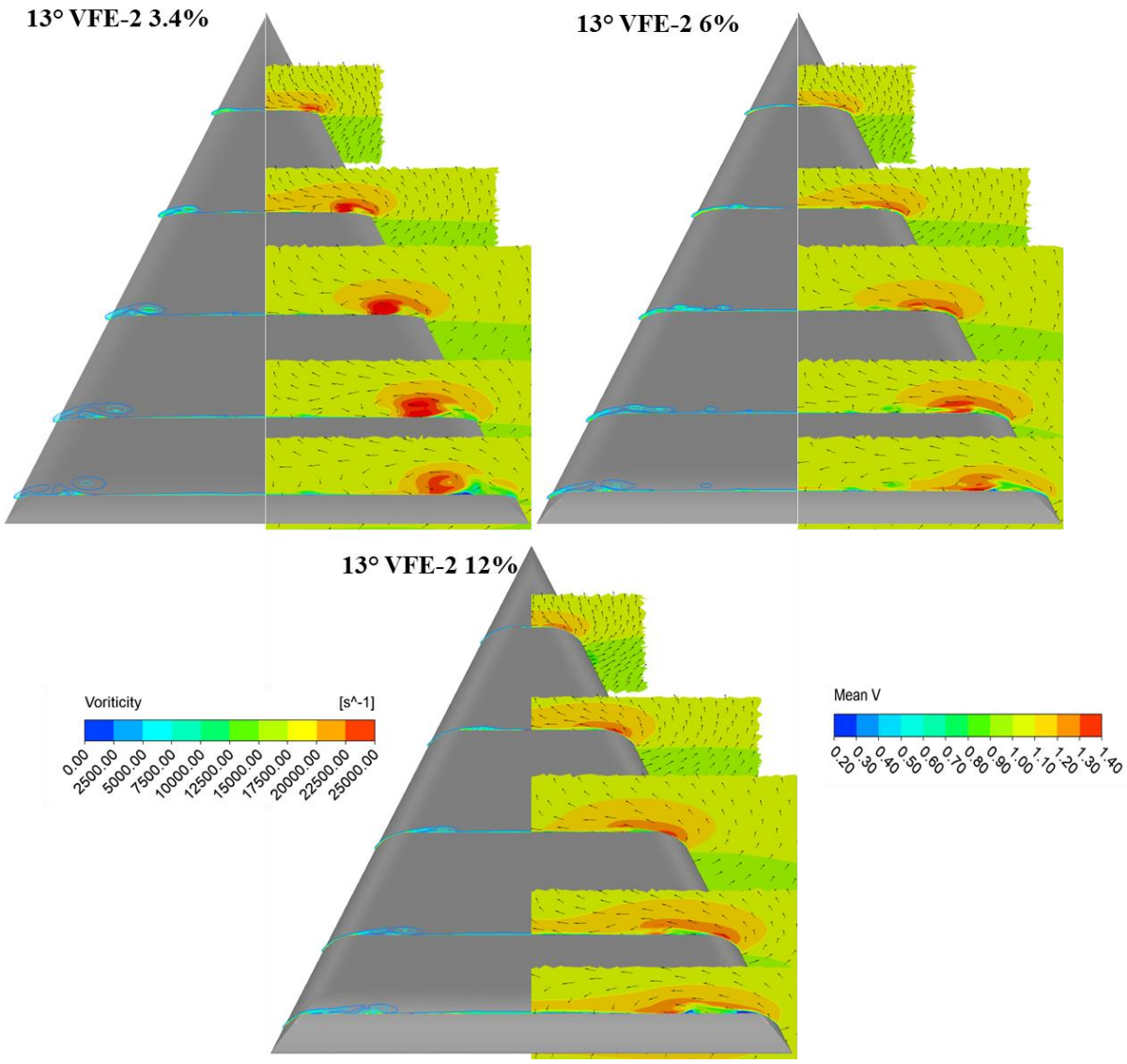

Figure A. 5.12 Vorticity and mean velocity contours at different chordwise locations for the VFE-2 configuration of different thicknesses at α=13°.

The investigations on the flow physics at 4° and 13° angle of attack for the B05, VST and VFE-2 configuration here, aided to reach the practical conclusions presented in Chapter 6 section 6.5. The reader is therefore referred to continue the report with the evaluation of the aerodynamic coefficients in chapter six in section 6.5.

A.5.4. Evaluation of the centre of pressure and the aerodynamic centre location

As explained in section 6.8, the position of aerodynamic centre x_{ac} and the centre of pressure x_{cp} is expressed relative to the root chord length and plotted against the normal force coefficient in Figure A. 5.13. The plots in this section present the raw data.

It can be seen that the aerodynamic centre not only varies with thickness but also with maximum thickness location. It can be seen that the aerodynamic centre moves rearwards with increase in thickness. However, the position does not vary much more than 0.5% between the thinnest and thickest wing. Generally, a rearward movement of the aerodynamic centre is desired, thus, making the effect of increased thickness very useful. The discontinuities observed in curves are due to VBD and they result in a rapid change of pitching moment and normal force.

The centre of pressure can be found behind the aerodynamic centre for the two thinnest wings of the B03 configuration (i.e. $x_{cp} > x_{ac}$). The B05's centre of pressure coincides with that of the aerodynamic centre of the majority of angles of attack. At higher incidences it is located behind the aerodynamic centre, thus, enhancing stability. However, the distance between centre of pressure and aerodynamic centre is relatively small (between 0.2%). The results for the 12% thick wings of both configurations are found to be quite noisy, as it was found that for thicker wings the flow tends to become more unsteady.

For the VST configuration the centre of pressure is located behind the aerodynamic centre for the thinner wings, whilst this is only the case for the 12% thick wing at higher incidences. Before that the centre of pressure and aerodynamic centre coincide. For the VFE-2 the centre of pressure is found prior the aerodynamic centre for the two thicker wings, whilst at higher angle of attack it moves behind the aerodynamic centre for the 3.4% thick wing.

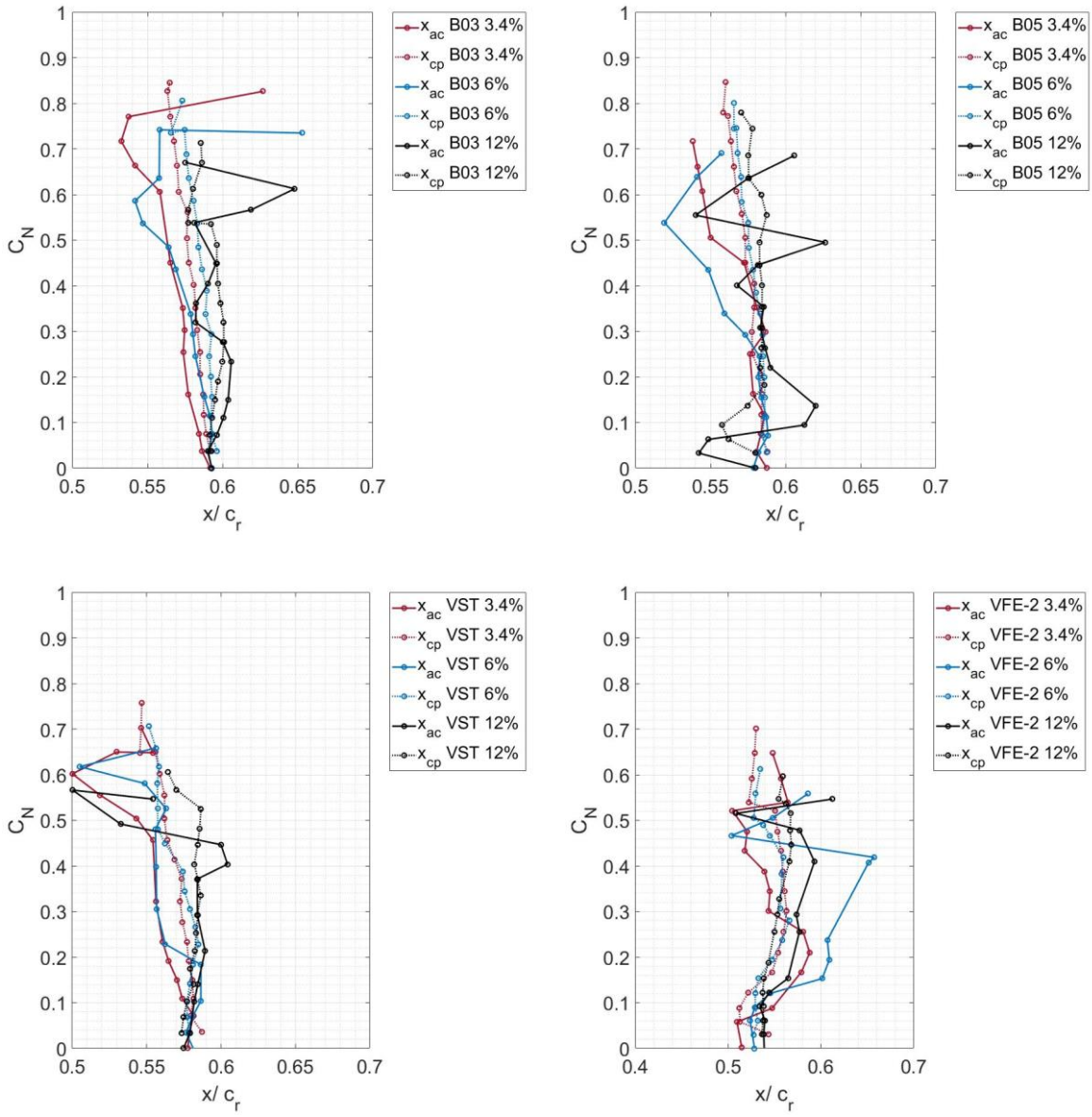

Figure A. 5.13 Normal force coefficient vs. normalised centre of pressure and aerodynamic centre locations for the B03, B05, VST and VFE-2 configurations for varying thicknesses.

To compare the effect of maximum thickness location only the aerodynamic centre is plotted against the normal force coefficient and depicted in Figure A. 5.14. It can be seen that shifting the maximum thickness location barely has an effect on the aerodynamic centre's location. Only for the 6% thick wing does a movement of maximum thickness location rearward move the aerodynamic centre location forward with increased incidence. The aerodynamic centre appears to move more rapidly for the VFE-2 configuration and it appears that tapering the tip results in a backward movement of the aerodynamic centre. As this increases stability, tapering towards the tip appears to be of advantage.

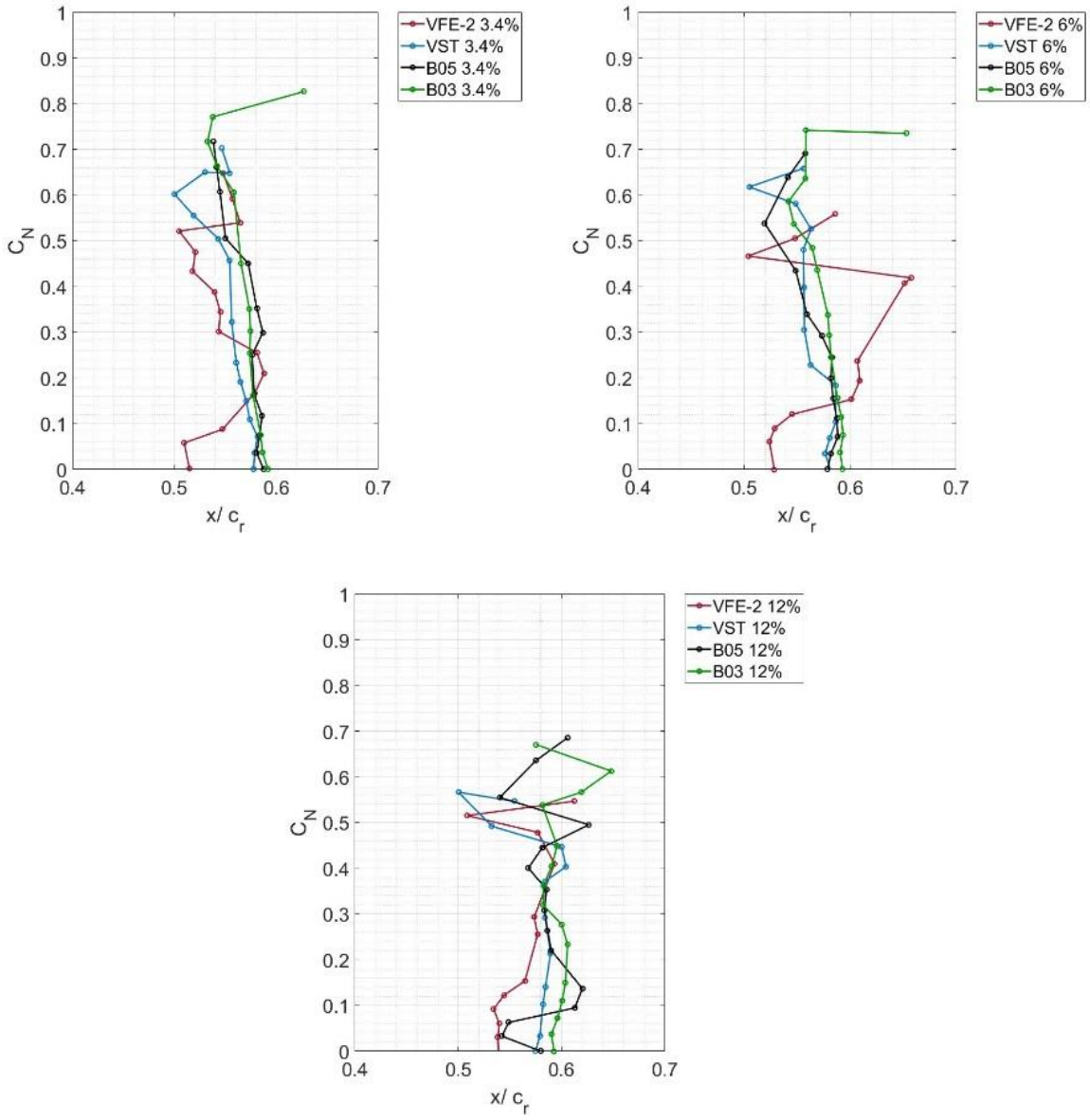

Figure A. 5.14 Comparison of the normal coefficient against normalised positions of the aerodynamic centre and centre of pressure for the B03, B05, VST and VFE-2 configurations for varying thicknesses.